

# **Customized ceramic granules for laser powder bed fusion of aluminum oxide**

Von der Fakultät für Maschinenbau, Verfahrens- und Energietechnik  
der Technischen Universität Bergakademie Freiberg

genehmigte

## **DISSERTATION**

zur Erlangung des akademischen Grades

Doktor-Ingenieur

(Dr.-Ing.)

vorgelegt

von Master of Science (M.Sc.) Stefan Pfeiffer

geboren am 30.04.1989 in Weißenhorn

Gutachter: Prof. Dr. Christos G. Aneziris, Freiberg, Deutschland

Prof. Dr. Thomas Graule, Dübendorf, Schweiz

Tag der Verleihung: 23.05.2022



...to my parents and siblings as well as my girlfriend Baiba and my daughter Luise for  
their loving support.





---

## **Eidesstattliche Erklärung**

Hiermit versichere ich, dass ich die vorliegende Arbeit ohne unzulässige Hilfe Dritter und ohne Benutzung anderer als der angegebenen Hilfsmittel angefertigt habe; die aus fremden Quellen direkt oder indirekt übernommenen Gedanken sind als solche kenntlich gemacht.

Freiberg, den

Stefan Pfeiffer

---

## Acknowledgements

My biggest thanks go to Prof. Thomas Graule and Prof. Christos Aneziris for the opportunity provided. I would like to thank Prof. Thomas Graule for the great discussions of new ideas, his patient way of supervising and his big involvement in the whole project. Furthermore, I thank Prof. Christos Aneziris for the constructive discussions, his valuable suggestions and critical questions during this work.

An exceptional thank goes to the ETH Board for funding the “FUORCLAM” project within the frame of the SFA (Strategic Focus Areas) Advanced Manufacturing. Hereby, I would like to thank my project partners Dr. Kevin Florio and Dr. Malgorzata Makowska for the interesting scientific discussions, the enjoyable sleepless nights during our beamtime and most importantly their friendship. Furthermore, I would like to appreciate the important advices of Prof. Konrad Wegener and Prof. Helena Van Swygenhoven regarding the project.

I also really enjoyed the collaboration with Dr. Xiaoyan Zhang on laser cladding within the scope of her research internship. Furthermore, I acknowledge the constructive discussions and nice working atmosphere with Dr. Yaroslav Romanyuk and Dr. Evgeniia Gilshtein in terms of photonic sintering of aluminum oxide.

I would like to acknowledge the Paul Scherrer Institut, Villigen, Switzerland for provision of synchrotron radiation beamtime at beamlines Tomcat, micro-XAS and MS of the Swiss Light Source. Furthermore, a special thank goes to Dr. Dario Ferreira Sanchez, Dr. Federica Marone and Dr. Nicola Casati for their assistance with the experiments conducted at the Paul Scherrer institute.

Additionally, I am grateful to all my co-workers for their support during my time at Empa, especially Dr. Clark Ligon and Dr. Jon Bell for proofreading of many different works.

---

## Abstract

Additive manufacturing experienced a huge upsurge in industry and research in the last decades, especially for metal and polymer applications. However, the implementation of AM for ceramics is more challenging, since most of the shaping methods require an additional thermal treatment. Laser powder bed fusion could hereby play an outstanding role, since it is in theory capable to shape ceramics in a direct manner without post-processing. However, low thermal shock resistance, weak densification and low light absorptance at room temperature and strongly temperature-dependent absorptance in the visible or near-infrared range limits laser processing of oxide ceramics. Powder properties can have a strong impact on the quality and performance of the laser manufactured aluminum oxide ceramic parts.

In this work, the challenges of part densification, powder flowability, laser light absorption and crack formation in laser powder bed fusion of aluminum oxide have been addressed by spray drying of customized granules. To improve the laser absorption by over eighty percent, the alumina granules were doped with colored oxide nanoparticles. Bimodal or trimodal distributions of aluminum oxide were chosen to test different particle packing theories. Dibasic ammonium citrate was found to be a suitable dispersant for all oxides. The appropriate amount of dispersant for consecutive water-based spray granulation was determined by Zeta Potential measurements. Thermal treatment of the spray dried granules and consecutive mixing with coarse alumina allowed to further improve the powder bed densities up to a maximum tapped density of 56.4% of the theoretical density. This led to laser processed parts with densities up to 98.6% evaluated by tomographic microscopy. The powder quality was characterized by apparent density, tapped density, Hausner ratio, moisture content, particle size distribution, avalanche angle and surface fractal. The improved absorptance of the laser light was verified by means of an integrating sphere and an UV-VIS-NIR spectrophotometer employing Kubelka-Munk theory. 3D mapping by X-ray  $\mu$ -beam fluorescence contrast tomography and high resolution synchrotron powder diffraction provided information about the uniform dopant distribution. Furthermore, several approaches were done to reduce crack formation caused by thermal stresses by addition of suitable additives.

---

---

# Table of Contents

<b>1</b>	<b>Introduction.....</b>	<b>1</b>
1.1	Motivation .....	1
1.2	State of the art.....	2
1.3	Aim of the project.....	2
<b>2</b>	<b>Literature review .....</b>	<b>5</b>
2.1	Additive manufacturing by laser powder bed fusion.....	5
2.1.1	Classification and process description .....	5
2.1.2	Advantages against other AM processes.....	9
2.1.3	Challenges of laser powder bed fusion .....	12
2.1.4	State of the art of laser powder bed fusion of aluminum oxide based ceramics	13
2.1.4.1	Powder bed preparation and impact on the process.....	13
2.1.4.2	Critical rating of the powder bed preparation techniques .....	17
2.1.4.3	Processing methods and properties .....	19
2.1.4.4	Part properties .....	26
2.2	Theoretical and experimental considerations for powder bed preparation.....	35
2.2.1	Spray granulation .....	35
2.2.2	Particle packing theories .....	39
2.3	Mechanisms for particle dispersing.....	41
2.3.1	DLVO-theory .....	41
2.3.2	Surface charge and electrical double layer.....	43
2.4	Conceptualization of new ideas for laser powder bed fusion of aluminum oxide.....	45
2.4.1	Densification, powder flowability and absorption issue .....	46
2.4.2	Reduction of crack formation.....	47
<b>3</b>	<b>Doped spray-dried granules to solve densification and absorption issue in laser powder bed fusion of alumina .....</b>	<b>55</b>
3.1	Dispersing of aluminum oxide, iron oxide and manganese oxide.....	55
3.1.1	Experimental .....	55
3.1.2	Particle characterization .....	57
3.1.3	Saturation amount evaluation of dispersant .....	59
3.1.4	Particle size distributions after dispersing.....	62
3.1.4.1	Particle size distributions of alumina powders .....	62
3.1.4.2	Particle size distribution of dopants .....	67

---

3.2	Packing density increase of spray-dried granules.....	76
3.2.1	Experimental .....	77
3.2.2	Influence of solid load and particle ratio on granules .....	83
3.2.3	Influence of dopant shape and multimodal distributions on granules.....	84
3.2.4	Evolution of pH-value during slurry preparation and slurry stability after mixing of all components.....	85
3.2.5	Influence of slurry viscosity on yield of granules .....	88
3.2.6	Addition of coarse alumina to spray-dried granules .....	89
3.2.7	Application of Andreasen model on mixtures of ceramic particles with spray-dried granules.....	94
3.2.8	Thermal pre-treatment of granules .....	98
3.2.9	Influence of surface tension of slurry on granule size and density .....	110
3.3	Investigation of laser manufactured parts.....	114
3.3.1	Experimental .....	115
3.3.2	Influence of different iron oxide dopants and multimodal particle distributions within granules.....	118
3.3.3	Influence of coarse alumina variation .....	121
3.3.4	Influence of thermal pre-treatment of powders.....	127
3.3.5	Grain structure of laser additive manufactured parts .....	135
3.3.6	Thermal expansion of laser processed parts.....	137
3.3.7	Influence of thermal pre-treatment and laser processing on manganese amount within granules and laser additive manufactured parts.....	138
<b>4</b>	<b>Additives to reduce crack formation in selective laser melting and sintering of alumina.....</b>	<b>143</b>
4.1	Experimental.....	144
4.2	Additives to reduce thermal stresses .....	150
4.2.1	Selective laser melting with mullite additives.....	150
4.2.2	Amorphous alumina formation by rare earth oxide doping .....	160
4.2.3	Formation of aluminum titanate by use of reduced titanium oxide .....	169
4.2.3.1	Dispersing of titanium oxide nanoparticles in water .....	170
4.2.3.2	Thermal treatment of $\text{Al}_2\text{O}_3/\text{TiO}_2$ granules under argon/hydrogen atmosphere .....	172
4.2.3.3	Laser manufacturing of parts .....	178
4.2.4	In-situ formation of negative thermal expansion materials.....	187

---

4.2.4.1	Dispersing of zirconia and tungsten oxide nanoparticles.....	187
4.2.4.2	Influence of spray drying process parameters .....	191
4.2.4.3	Preparation of final powders for laser powder bed fusion .....	197
4.2.4.4	Laser manufacturing of layers and parts .....	200
4.3	Mechanical properties of laser processed parts .....	205
<b>5</b>	<b>Flowability and inner structure of customized granules.....</b>	<b>209</b>
5.1	Experimental.....	209
5.2	Comparison of flowability in terms of Hausner ratio, Avalanche angle and surface fractal measurements .....	211
5.2.1	Influence of coarse alumina AA18 variation .....	211
5.2.2	Influence of thermal pre-treatment of powders.....	213
5.2.3	Influence of dopant content within granules .....	216
5.2.4	Flowability of zirconia-tungsten oxide granules and alumina granules with mullite or rare earth oxide addition.....	219
5.2.5	Flowability of titanium oxide doped alumina powders.....	221
5.3	Cross sections of customized granules to image inner structure .....	224
<b>6</b>	<b>Summary, conclusions and outlook.....</b>	<b>233</b>
6.1	Summary and conclusions .....	233
6.2	Outlook .....	241
	<b>References .....</b>	<b>245</b>
	<b>List of Figures.....</b>	<b>260</b>
	<b>List of Tables.....</b>	<b>269</b>

---



# 1 Introduction

## 1.1 Motivation

Shaping of complex geometries with high precision, meanwhile ensuring both high strength and fracture toughness is a key challenge in the processing of ceramics. In combination with the long processing times and cost-intensive post processing, this forms a major obstacle for the broader application of high tech ceramic parts. Additive manufacturing (AM), especially powder bed fusion - laser beam (PBF-LB), could be a solution to these problems [1]. PBF-LB is already an emerging technology in industry for shaping of parts with complex geometries. However, its industrial usage is limited to applications employing metals or polymers, since these materials undergo plastic deformation and are therefore less critical to cracking due to thermal stresses. For the production of high performance alumina ceramics with this technology, severe problems such as weak densification, low laser light absorption and crack formation, must still be solved. Nevertheless, PBF-LB has a great potential to produce highly complex ceramic prototypes and small series with high accuracy and short lead times and to avoid cost, energy and time consuming machining. Enlightenment of the limited understanding of the interaction of the laser with the ceramic materials and the slow sintering kinetics could master the challenges for consolidation of ceramic powders to dense structures with convenient material properties in high-tech ceramics by PBF-LB.

### 1.2 State of the art

In the past, several approaches to overcome the problems of low thermal shock resistance and weak densification during processing of oxide ceramics were demonstrated. For example, the use of different lasers (CO<sub>2</sub> [2-5], pulsed Nd-YAG [6, 7], high power diode [8] or femtosecond lasers [9]), various laser scanning strategies (special circular [10], single-track, zigzag or island scanning strategies using different laser powers [11] or powder feeding directly to the melt pool [12, 13]), preheating (by microwaves [14], with a second laser [15, 16] or applying a building platform with a vertical tube furnace [5]) and finally the addition of silica to form an amorphous phase [2, 3, 6, 7] were tested to improve the properties of the laser processed parts. Until now, none of these approaches proved to combine a high accuracy, a high bending strength and a total freedom of design. To achieve this, not only the laser process parameters and processing conditions have to be considered, but also powder properties, such as melting temperature, absorptance [17], flowability and powder bed density [18, 19].

### 1.3 Aim of the project

Up to now, PBF-LB of oxide ceramics revealed many obstacles, which hinder a broader application of laser processed high-performance oxide ceramic parts. The main identified obstacles were:

- Weak densification and limited powder flowability (especially for nano and submicron powders).
- Low laser light absorption of aluminum oxide in the visible and near infrared range of the light (only 3% absorption at a wavelength of 1064nm according to [20]).
- Low thermal shock resistance and therefore, crack formation.

The several approaches pursued in this work to overcome these obstacles were:

- Use of spray granulation to achieve a high powder bed density and to improve the final powder flowability, which is especially a solution to increase the low flowability and the final powder bed density in the case of using nanoparticles.
- Control of particle interactions in the dispersion by electrostatic stabilization prior to spray drying and additionally, use of an ultrasonic nozzle as an atomizer to achieve notably spherical granules for good flowability, which was evaluated by Hausner ratio and avalanche angle measurements.
- Doping of the spray dried granules with different coloured metal oxide nanoparticles for a better laser light absorption of the applied laser. The focus in this work was on the

optimization of particle size, powder composition and dopant distribution to improve the interaction between the laser and the granules.

- Test of different additives, suitable to reduce the thermal shock during laser processing. Direct addition of additives during spray drying possible due to the variable design of the granules. Additives included mullite as well as other materials, suitable to form an in-situ phase with a low or negative thermal expansion coefficient during processing.



## **2 Literature review**

Parts of this chapter were already published in the Journal of European Ceramic Society, Volume 41 (13), (2021) 6087-6114.

### **2.1 Additive manufacturing by laser powder bed fusion**

#### **2.1.1 Classification and process description**

Additive manufacturing (AM) is predicted to have a major influence on several industries in the future. It evolved from a rapid prototyping technology to produce physical models to a manufacturing technology today, which is capable to produce functional parts in a wide range of materials [21]. AM will facilitate entire new production and business strategies and open new uses and markets, since it broadens the range of products with those that can only be produced additively. In 2019 the volume of sales of products and services in AM was \$11.9 billion, and the average growth was 23.3% in the past 4 years [21, 22]. Polymers have by far the biggest market share, whereas ceramics only appear as a niche, accounting for less than 2% of the total AM material sales [22, 23].

AM offers the possibility to combine the geometrical design of a part with the materials design, which in consequence can reduce the fabrication time and the unit cost for a part with specific

required properties, compositions, microstructure and shape. The different AM techniques currently available for ceramics are summarized and classified in the ISO/ASTM 52900:2018 standard [24] and by different authors [1, 21, 23]. Several different nomenclatures have been used in the literature. In this study, we refer to the standard terminology defined in the ISO/ASTM 52900:2018 standard. A first classification can be done between single-step and multi-step AM processes. Single-step methods (also known as “direct” methods) allow the production of the part with desired geometry and material properties in one operation. Multi-step methods (also known as “indirect”) involve sequential operations. Commonly, the first operation is needed to obtain a given geometry by a point, line or planar addition of material [1], whereas the second step is aimed at consolidating the part to achieve target material properties such as a high part density, good mechanical properties and a low amount of cracks.

**Figure 1** shows a schematic classification of AM methods for ceramics into Laser additive manufacturing (LAM), binder jetting, Vat photopolymerization, material extrusion and sheet lamination. LAM processes for ceramics can be further classified into Powder Bed Fusion – Laser Beam (PBF-LB) and Directed Energy Deposition (DED) with laser source. PBF-LB of ceramics may involve two different underlying AM principles, i.e., direct and indirect PBF-LB. This PhD study focuses only on direct PBF-LB.

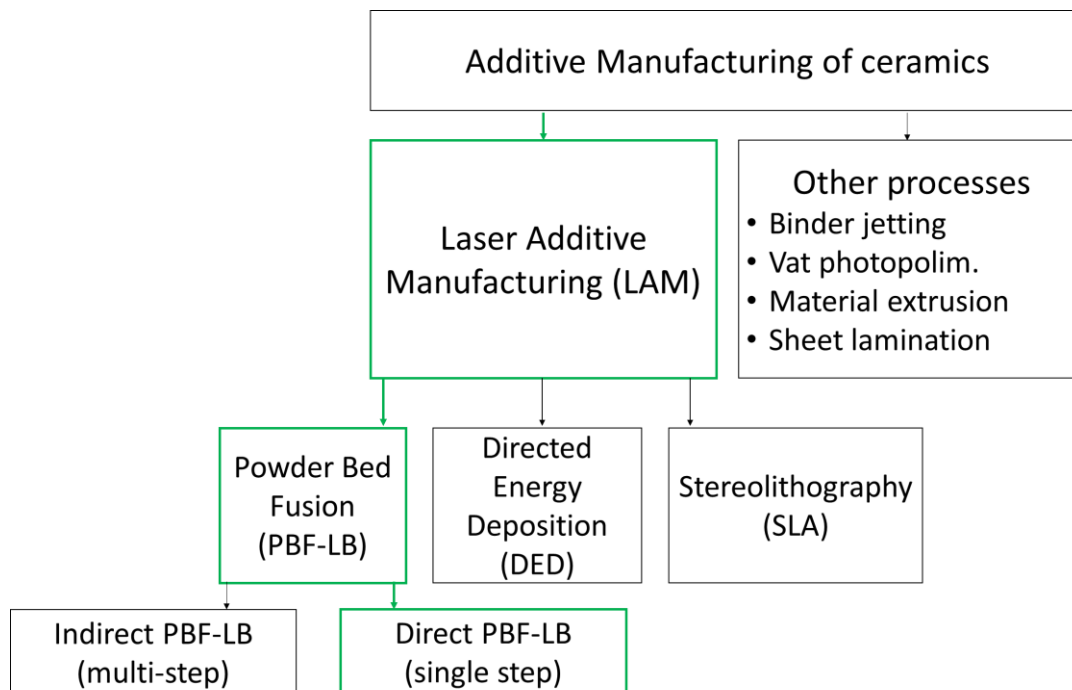


**Figure 1:** Current additive manufacturing methods for ceramics in accordance to ISO/ASTM 52900:2018 and [1, 21, 23]; process categories highlighted in green are the ones reviewed in this study

Laser-based Powder bed fusion (PBF-LB) was first developed for polymers in the 1980s by Carl R. Deckard and Joseph J. Beaman at the University of Texas [25]. In this process, polymer particles within a powder bed are selectively fused or sintered together by employing the focused energy of a laser beam based on selective sintering or melting the material based on cross-sectional slice information to produce complex 3D parts in a layer-wise manner (layer thickness typically below 100 microns) [1, 26].

**Figure 2** illustrates the schematic of PBF-LB. A typical PBF-LB-machine consist of two chambers. One is filled with the powder supply, which is spread by a powder recoater to a powder layer on the build chamber. To manufacture the part, the laser beam is guided across the powder bed of the build chamber by a scanning system, usually a galvano scanner, fusing the powder layer by layer. The requirements in terms of beam quality, absorption, wavelength and power for the used laser can vary for different materials [21]. In theory, this method could be a unique process, which could deliver complex ceramic parts directly produced in a ready-to-use state without any time consuming and cost-intensive post-processing.

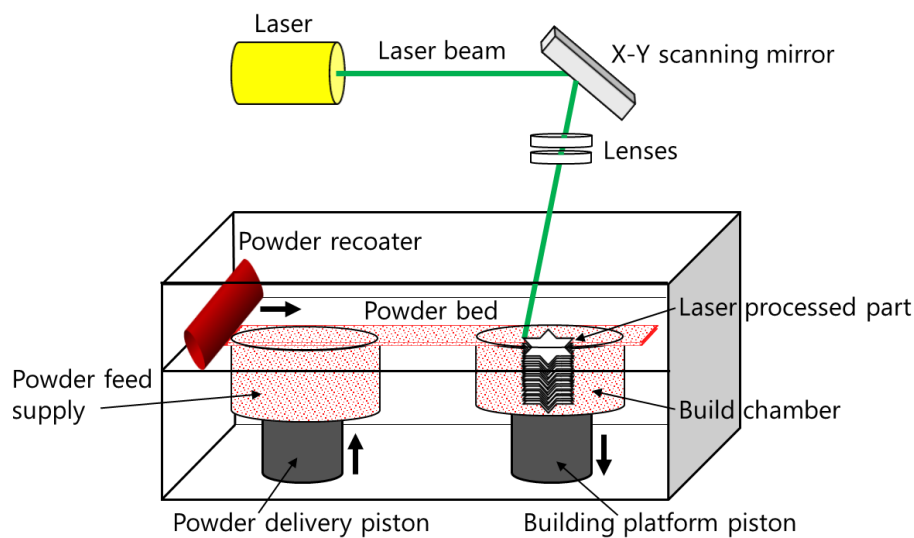


**Figure 2:** Schematic of powder bed fusion with a laser beam (PBF-LB).

For the FUORCLAM project of the "Strategic Focus Area Advanced Manufacturing" of the ETH Board, who funded the joint project between ETH, PSI and Empa, an experimental PBF-LB machine was specially developed and built in-house at ETH Zurich, Institute of Machine Tools and Manufacturing (**Figure 3**). With this PBF-LB box it is possible to work with different lasers and under different atmospheres, since the box can be relocated and closed gastight. Furthermore, the building axis of this box has a resolution of only 1.5  $\mu\text{m}$ , what allows an accurate testing of different thicknesses of the powder layer for the process.

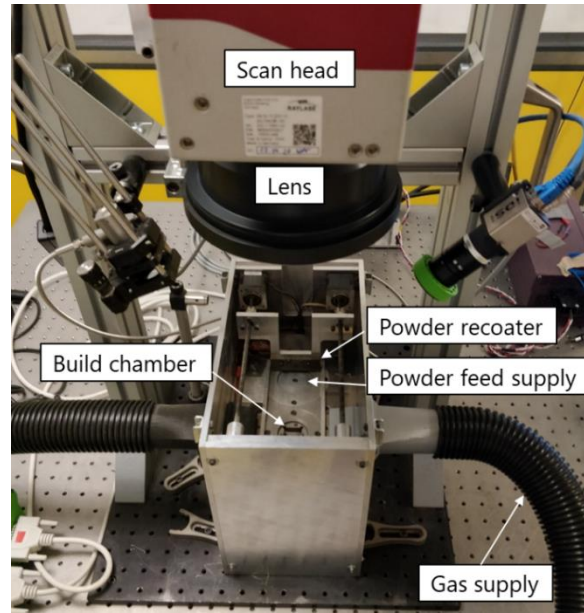


*Figure 3: Experimental PBF-LB machine developed and built in-house at ETH Zurich*

In PBF-LB, highly dense powder beds are required to achieve a part density by laser consolidation [19, 27]. Furthermore, traditionally only fine-grained ceramic parts show adequate mechanical properties at room temperature, particles with sizes in the range of tens of nanometers to a few micrometers are preferred. However, particles below 10 micron tend to agglomerate [28] reducing the flowability, causing poor powder bed density and inhomogeneity. The reason is that the gravitational force dominates for bigger particles, since it scales with the cube of the size, whereas adhesion forces depending on particle surface falls linear with the size with the result that spheres of 1  $\mu\text{m}$  in diameter dimensions experience an adhesion force more than a million times greater than the force of gravity [28].

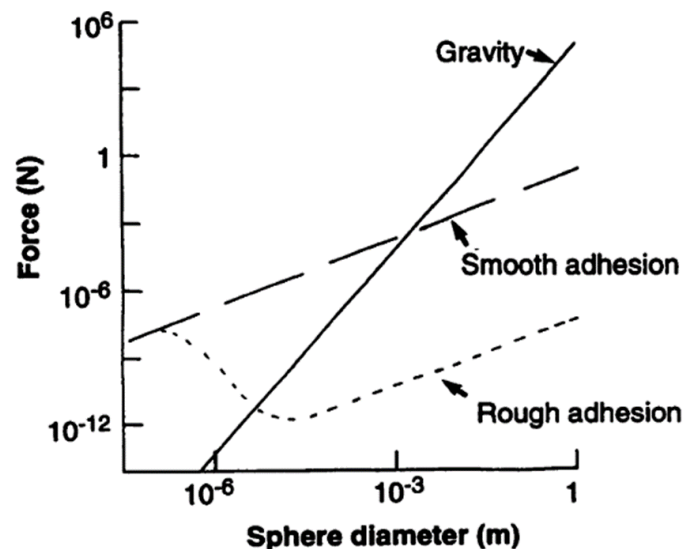


*Figure 4: Comparison of the adhesion force and gravity for very smooth and rough spheres of different diameters [28].*



**Figure 4** shows the adhesion force and gravity for very smooth and rough spheres of different diameters [28]. The adhesion forces can vary with geometry, material stiffness, molecular surface forces and the contact geometry. Rough surfaces have a by several orders of magnitude reduced adhesion (dotted line, **Figure 4**). A ball bearing is for example much rougher than the 1-nm range of the surface forces and therefore, only the roughness peaks are in contact with the other spheres on a microscopic level [28]. Since this adhesive interface can exist in metastable states, it is possible that the interface state can change as a function of time, temperature and applied force [29-31]. However, it is a fact that everything below 1  $\mu\text{m}$  sticks together in air. Fortunately, colloidal chemistry enables to reduce the adhesion work by introducing repulsive surface forces, so that small particles can move freely in fluid environments [28]. More information about the interaction of van der Waals attractions and ionic repulsions to provide colloidal stability of particles in aqueous suspensions can be found in chapter 2.3.

Instead of layering granules or powders, a ceramic slurry can be deposited in a similar manner by a doctor blade comparable to tape casting and dried subsequently. This technique was originally patented in the year 2004 [32] and it is called here slurry-based PBF-LB. As for the powder-based method, the laser beam is guided across the powder bed by a scanning system to consolidate a part based on CAD data. The main advantages are that thin layers (down to 10  $\mu\text{m}$ ) composed of nanoparticles can be deposited uniformly and with a high packing density. The formation is comparable to slip casting. Capillary forces (additional to gravitational and interparticle forces in the powder bed method) draw the liquid of the suspension into the pores of the previously deposited non-solidified powder bed [2, 26]. The highly dense powder bed formation is additionally assisted by the drying of the deposited slurry on a preheated building platform. For water-based slurries, this drying can be achieved in less than 10 s, which is also beneficial to prevent bubble formation [3]. The speed of the doctor blade is crucial for this process. When too slow, collision of the cast with the doctor blade can happen due to rapid solidification of the slurry in front of the blade. When the solidified cast grows higher than the tailing edge of the doctor blade, collision will happen, which is especially a problem for a high solids content and for slurries with fine particles ( $< 1 \mu\text{m}$ ). When speed is too high, inhomogeneous deposition occurs due to shear stresses.

### **2.1.2 Advantages against other AM processes**

LAM offers several possible advantages for the production of ceramic parts (as well as for polymeric and metallic parts) compared not only to traditional manufacturing processes, but also to other AM methods.

- Low unit cost in LAM for small series and prototypes (especially compared to the traditional shaping and sintering process)
- Expanded boundaries for design engineers
- Production on demand with short lead times
- Possibility of in-situ part shaping and therefore, avoidance of the time consuming thermal post-processing accompanied by problematic sinter shrinkage, crystalline phase change, cracking and delamination.
- Possibility of merging hard-machining or laser subtractive processes with AM as a hybrid technique

The unit cost of an LAM part depends on material cost, build time, energy consumption, labor and indirect costs [33], which can be in general related to production volume or the degree of complexity and customization of the part (**Figure 5**) [21, 34]. The advantage of low unit cost in LAM for small series and prototypes, will reduce the need to produce small lots of parts in low-wage countries in the future [35]. In general, LAM requires less workforce to produce parts [36] and low raw material costs will be reached, when it can be bought commercially and further processed with a minimum effort [26].

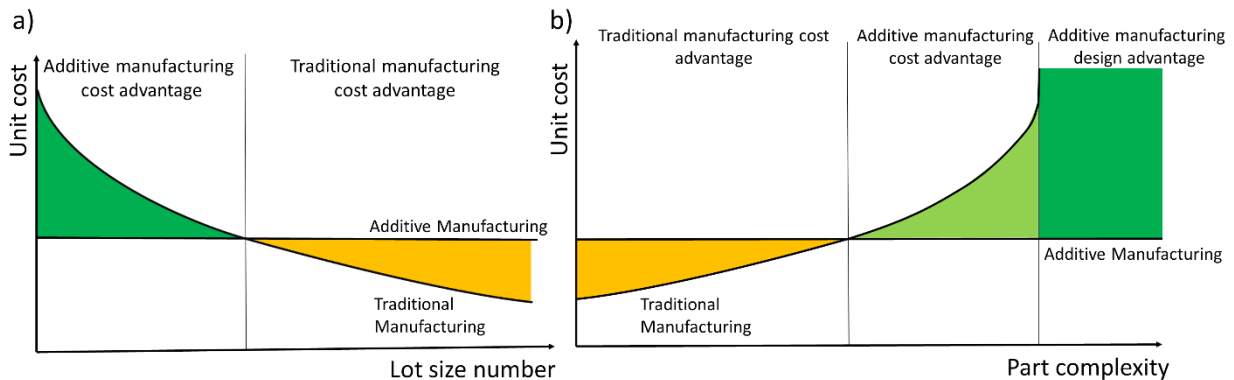


**Figure 5:** Unit cost for additive and traditional manufactured parts referred to a) production volume and b) complexity or customization of the parts according to Pinkerton [21] and influence of new design opportunities by additive manufacturing on unit cost referred to complexity of the parts compared to traditional processes according to Bain & Company, Inc. [37]. The green area shows the more favorable range for AM as manufacturing method.

For larger production volumes, the production via AM is favorable for complex parts (**Figure 5**). For LAM increasing part complexity does not correlate with higher manufacturing costs enabling a higher degree of customization [21, 26, 34]. This could be particularly beneficial for the medical industry, where low volume and personalized parts are required [38] such as dental crowns, artificial limbs and porous bone scaffolds [36].

The magnitude of the potential design benefits depends in general on the application and have still not been completely exploited [26, 37]. This includes the possibility to design multi-material systems [26], multifunctional components [23] and independently moving parts that are directly assembled after printing (e.g. fully functional ball bearings) [36]. In the case of multi-materials, thermal expansion coefficients and shrinkage behavior of the different materials should be taken into account to avoid cracking and delamination. Furthermore, complex shaped-porous structures can be produced with a precise control of dimension, shape and amount of pores [26], which could be beneficial for several ceramic applications such as bone scaffolding and filtration membranes [23].

LAM also allows the production on demand with short lead times, which can result in storage cost reduction, better customer services and savings on unnecessary transportation costs. A shorten time span between design, testing and implementation leads to short lead and setup times for tooling. This reduces the time to market costs, which was one of the initial motivations for the development of rapid prototyping technologies [21, 26, 37].

Besides the costs considerations, the main advantage of direct consolidation of the material via LAM in comparison to other AM technologies is that the manufacturing and material fusion are combined into one-step and a time consuming thermal treatment step is not needed. This offers the possibility of in-situ part shaping by PBF-LB and therefore, the problematic sinter shrinkage can be avoided. Debinding and sintering in indirect AM are often based on experience and can vary considerably between different material, crystalline phase, size of the powder and component geometries. The amount of organic binder used in indirect AM methods for ceramic processing can be for example up to 50 Vol% (VAT Photopolymerization) [39]. Cracking and delamination are possible problems generated by debinding of these high organic amounts. Parts with thin wall thicknesses can be problematic in terms of stability and thick wall thicknesses can lead to extremely long or even impossible debinding in indirect AM [40]. In addition, the avoidance of debinding and thermal treatment lead to less pollution and greenhouse emissions [41].

In contrast to other indirect AM methods, lasers offer also the possibility to merge hard machining and laser subtractive processes with AM processes as a hybrid, which presents a great chance to manufacture innovative components and broadens greatly the range of producible parts and geometries.

### 2.1.3 Challenges of laser powder bed fusion

Until now, several barriers prevent a broader application of LAM. Following disadvantages are specified in this chapter:

- Low production speed and throughput
- Poor surface quality and strength issues
- High production costs for small lots, prototypes or complex-shaped parts due to expensive starting materials and high investment prices.
- Lack of technical standards, quality assurance systems and guidelines

A drawback for LAM is the low production speed and low throughput, which limits the production of large sized objects due the long time required to build a part layer by layer [21, 36, 37, 41, 42]. The industrial usage of LAM depends on the possibility to produce parts as close as possible to the desired geometry [1], since machining can amount up to 80% of the overall traditional manufacturing costs [43]. The surface quality is not only important for aesthetical reasons, but also can influence the mechanical properties of the printed part in AM [26]. Since melting and rapid solidifications at high temperatures are always involved in LAM, surface quality and part accuracy are challenges due to melt-pool instabilities. Thermal stresses are generated due to the temperature gradients in LAM, which can lead to cracking [44]. Balling, porosity and other defects due to melt-pool physics combined with a low fracture toughness of the material are typical challenges of LAM [23]. The crack problem correlates also with an increased density, since dense parts lead to more volume contraction during cooling. For a successful integration of an AM process into an existing process chain in ceramics, the finally produced part properties should be equal or superior compared to those of traditionally manufactured parts. Processing failure have to be considered very strongly in ceramics, since each defect can cause a catastrophic failure of the ceramic component due to the brittle nature of the material.

The high production costs for specially customized raw materials will automatically reduce in the future by the economics of scale, when more competitors will enter the market [37, 45]. For laser technology, the high production costs should decrease in the future due to technological improvements such as increased laser power, adoption of multiple laser and lower machine investment costs [37].

The lack of technical standards, quality assurance systems, manufacturing guidelines (e.g. about support design [42]), design rules and the existing patent law results in long certification periods for critical parts [46, 47] and slows down a broader use of LAM for ceramic parts [21, 37].

**Table 1** summarizes advantages and disadvantages of laser additive manufacturing compared to other additive manufacturing processes specified in chapter 2.1.2 and 2.1.3.

***Table 1:** Advantages and disadvantages of laser additive manufacturing compared to other additive manufacturing processes specified in chapter 2.1.2 and 2.1.3.*

Advantages	Disadvantages
Low unit cost in LAM for small series and prototypes	Low production speed and throughput
Small workforce and low number of people required	Poor surface quality and strength issues
Expanded boundaries for design engineers in terms of multimaterial systems, multifunctional components and independently moving parts	High production costs for specially customized starting materials and high LAM machine prices
Production of complex shaped porous structures with a precise control of dimension, shape and amount of pores possible	Lack of technical standards, quality assurance systems, manufacturing guidelines and design rules
No need of thermal post-processing	
More environmental friendly due to less pollution and greenhouse emissions by the avoidance of thermal treatment	
Possibility to produce parts with thin and thick wall thicknesses, which are problematic in indirect AM in terms of stability and extremely long or even impossible debinding	
Possibility to merge subtractive machining and additive manufacturing processes	

## 2.1.4 State of the art of laser powder bed fusion of aluminum oxide based ceramics

### 2.1.4.1 Powder bed preparation and impact on the process

In general, high performance oxides ceramics are consolidated by solid state sintering, which is based on diffusion processes. It is stated that high powder bed densities are necessary to overcome the obstacle of weak densification and to achieve a high density of the final parts in

PBF-LB [18, 19] and it is well known that strength of ceramic parts decrease with increasing porosity [48].

Different approaches to overcome the low powder bed density are as follow:

- A. Use of spray dried granules and mechanical blending
- B. Mechanical powder bed compaction
- C. Slurry casting via doctor blade or rubber scrapper
- D. Application via spraying techniques
- E. Electrophoretic deposition of ceramic dispersions

A. Use of spray dried granules and mechanical blending

In traditional ceramic manufacturing (e.g. pressing) the voids between and within the granules are closed by compaction and sintering [49]. However, in PBF-LB, a partial melting or total melting of the granules during laser processing is necessary, to close the voids formed by the granules. A successful application was shown by Juste et al. [50]. Aluminum oxide was mixed with additional carbon to enhance the interaction between the laser light and the ceramic powder, since alumina shows almost no absorption at the emitted wavelength (1070 nm) of the fiber laser light. The resultant mixture was formed by spray granulation of fine alumina powder ( $d_{50}$  of 0.4 $\mu$ m) with a colloidal suspension containing graphite in the slurry to obtain highly flowable granules ensuring a dense powder bed. At a concentration of 0.1 and 1 Vol% graphite, the powder showed an absorbance in a 5 mm thick pellet of about 50% and 80%, respectively. Sieving of the granules to reduce the layer thickness of the powder bed improved the microstructure and increased the density of the final parts.

The present work shows that colored metal oxide nanoparticles can be used as an alternative to carbon to increase the powder absorptance of spray-dried aluminum oxide granules. The necessary doping amount for a successful alumina part consolidation was found to be below 1 Vol% due to a homogeneous distribution of the dopant nanoparticles within the granules. Furthermore, several approaches were conducted to increase the powder bed density and therefore, the final part density. These approaches were the use of multimodal particle distributions within the spray-dried granules, the addition of coarse aluminum oxide particles to the granules and a thermal pre-treatment of the granules before laser processing. The existing in-situ formation of ternary oxide phases during PBF-LB was identified as a possibility to reduce severe crack formation by the selection of suitable oxide ceramic additives.

Mapar et al. [51, 52] used spray dried granules made from the eutectic composition of micron  $\text{Al}_2\text{O}_3$  and nano yttria stabilized  $\text{ZrO}_2$  (37 mol%). In comparison to larger granules supplied from industry, the spray dried granules showed a lower flowability, and were therefore expected to be less suitable for the PBF-LB. It was also suggested to remove the organic of the granules (at 600°C) before the laser treatment. Furthermore, Liu et al [53] showed the possibility to use spray dried granules made from the eutectic mixture of  $\text{Al}_2\text{O}_3/\text{GdAlO}_3/\text{ZrO}_2$  (58/19/23 mol%).

Following the approach of filling voids with smaller particles, Liu et al. [54] showed the possibility for non-spray dried zirconia powder beds. A coarse powder fraction (22.5–45  $\mu\text{m}$ ) and a fine fraction (20 wt% with 9–22.5  $\mu\text{m}$ ) were mixed to get the advantages of higher laser light absorptance of the fine powder and better flowability of the coarse fraction. However, when the finer fraction increased, a homogeneous powder deposition was almost impossible due to electrostatic forces. Evaporation of residual moisture was found to increase the flowability in these powders [54, 55].

Verga et al. [56] suggested an alternative way of carbon distribution within alumina toughened zirconia spray dried granules. To achieve a higher homogeneity the organics in the spray dried granules were pyrolysed leaving an amount of carbon of ca. 0.4 wt%. The color of the granules changed from white prior to pyrolysis to black after pyrolysis and tapped powder densities of up to 41% of the theoretical densities were reached.

In contrary, Ferrage et al. [57] used a simple mechanical blending of micron-sized graphite and YSZ particles. Dense parts could be produced by increasing the powder absorptance from 2% to 57% with an addition of 0.75 wt% graphite. The flowability of the zirconia powder was not affected by this addition of micron-sized graphite. Furthermore, they applied a roller system to improve the powder packing prior to laser processing. Similarly, Moniz et al. [58] suggested to add nanometric carbon and  $\beta$ -SiC particles to alumina by mechanical blending. They found that the absorption steadily increases with the carbon content and for SiC addition a maximum absorption was reached for 0.5 wt%. Despite this absorption increase, the apparent as well as tapped density and the flowability worsened due to nanoparticles in the final powder blend. Nevertheless, stable parameter windows were found for optimal powder dopant quantities and regular scan tracks could be built. Gan et al. [59] were able to build dense ceramic-glass composites by mechanically blending of 50 Vol% spherical alumina and 50 Vol% irregular shaped spodumene powder. Notwithstanding a poor flowability of the powder (avalanche angle of 53.4°), the recoating process ensured a smooth and homogeneously distributed powder bed.

### B. Mechanical powder bed compaction

Exner et al. [6, 60, 61] and Regenfuss et al. [7, 62] used powder with grain sizes around 1  $\mu\text{m}$ . However, problems with the powder layering in terms of final powder bed density occurred due to the nature of the fine particles [6]. They solved this problem depositing the powder with a custom-built machine equipped with a circular coating blade, applying pressure on the powder layer to increase the packing density of the powder bed [61]. Compaction of the powder layer (up to 25% of TD) took place by elevating the substrate towards a stable lid (maximum compaction pressure 50 kPa) [63]. A higher final part density resulted from a more constant laser light absorption and increased heat conduction [61, 63].

### C. Slurry casting via doctor blade or rubber scraper

Slurry casting can give powder bed densities up to potentially more than 60% TD, nanoparticles can be used and the organic content can be minimized [26]. Highly solid loaded, stable slurries with a good fluidity contained for example as solids 25.5 wt% pure  $\alpha$ -alumina ( $d_{50} = 1.7 \mu\text{m}$ ), 6.0 wt% crystalline silica ( $d_{50} = 0.2 \mu\text{m}$ ) and 68.5 wt% amorphous silica ( $d_{50} = 11.1 \mu\text{m}$ ) and a water content of 34 wt% (56.4 Vol%), where the particles were dispersed in water by a pH adjustment to 10 [64]. These layers were homogenous and led to dense parts.

Zhang et al. [65] applied a similar approach in terms of a layerwise deposition of an alumina slurry. The ceramic slurry consisted of 50 wt% (79.9 Vol%) water and 50 wt% (20.1 Vol%) alumina particles with a mean size of 0.62  $\mu\text{m}$ . A rubber scraper was used to apply the dispersion on a preheated alumina substrate (110  $^{\circ}\text{C}$ ), which ensured total evaporation of the water. However, the solid load was even 36.3 Vol% less than in the work of Heinrich et al. [64]. This requires in consequence more time for the drying step and therefore, for layering prior to laser processing.

### D. Application via spraying techniques

Another approach to increase the density of the green compact was the deposition of highly solid loaded slurries of dispersed alumina and zirconia by airbrush spraying technique to achieve dense and homogenous layers [66]. However, by application of too much slurry disconnected planes and rough surfaces were achieved. Furthermore, insufficient wetting and the drying process by an infrared heater led to delamination during laser processing, which gave porous parts with a high roughness [66].

On the other hand, aerosol assisted spraying technique gave uniform smooth powder beds with a controllable microstructure and this resulted in complete consolidation after laser processing



[4]. An ethanol-based alumina (d50 of 0.45  $\mu\text{m}$ ) suspension (solid load 5 wt% (1 Vol%)) was deposited at temperatures close to and over the boiling point by creating droplets with an electrostatic atomizer. Addition of 0.2 wt% polyacrylic acid ensured a stable and homogeneous dispersion by electrosteric stabilization and ensured the lowest viscosity, since excessive dispersant chains can introduce a bridging effect between neighboring particles [4].

#### E. Electrophoretic deposition

Deckers et al. [5] deposited fine-grained alumina (d50 of 0.3  $\mu\text{m}$ ) by electrophoretic deposition (EPD). By friction, the EPD deposited powder layer was transferred from the deposition electrode onto the previous layers. The density of such layers was approximately 57% of the theoretical density.

### **2.1.4.2 Critical rating of the powder bed preparation techniques**

The different powder preparation techniques offer several advantages, but also disadvantages. This chapter gives a critical rating by comparison of the different techniques.

Mechanical blending of micron-sized (d50 of ca. 15  $\mu\text{m}$  [57, 58]) raw powders with different absorbers offers the fastest and easiest way to achieve a dense powder bed with a good absorbance in the visible or near-infrared range of the laser light. However, the addition of nano-sized absorbers decreases the powder flowability due to electrostatic forces and therefore, the final powder bed density [58]. Liu et al. [54] reported even problems to achieve a homogeneous powder bed, when increasing the fine fraction (9–22.5  $\mu\text{m}$ ) of the used oxide powders. Furthermore, a complete melting of the powders is necessary during PBF-LB, since the coarse starting powders offer a low sintering ability. A mechanical powder bed compaction by applying pressure via a coating blade [58] was only partly a solution for powders smaller than 1  $\mu\text{m}$ , since a powder bed density of only 25% of the theoretical density could be reached [60].

A powder bed density of potentially more than 60% of the TD can be reached by slurry casting. This powder preparation technique enables a uniform deposition of thin layers (down to 10  $\mu\text{m}$ ) composed of nanoparticles with a high packing density due to the use of highly solid loaded dispersions. Furthermore, the organic content within the powder bed for laser processing can be minimized. However, this layering process combines also several disadvantages. One disadvantage is the necessary removal of the parts after PBF-LB by a solvent (for water-based slurries water acts as a solvent), since the part it is in contrary to the powder-based method embedded into the densified slurry [26]. Furthermore, storage and stability is better with powders or granules, since slurries can undergo settling and agglomeration. In comparison to other PBF-

LB techniques, the drying step requires additional time for layering and process optimization. The speed of the doctor blade is crucial for the layering process, since collision of already solidified cast with the doctor blade (doctor blade moves too slow) and an inhomogeneous deposition due to shear stresses (doctor blade moves too fast) can occur. Furthermore, nanoparticles in multimodal powder combinations can tend to the top surface of the layer due to evaporation forces. This could be prevented by using alcohol with a lower evaporation point as solvent. However, the dielectric constant of alcohol is lower than that of water, what results in problems to reach a good and stable colloidal dispersion [49]. Finally, the risk for laser processing of flammable residual solvents cannot be totally excluded, when using organic solvents [2].

The application of the powder layer via spraying techniques shows similar advantages than slurry casting such as achieving dense powder layers composed of only nanoparticles. However, problems such as an essential drying step before laser processing, low dispersion stability and fire hazard by using organic solvents also exist. Furthermore, low slurry solid loads used for spraying lead to long times required to apply a certain layer thickness of tenth of microns. In addition, Waetjen et al. reported delamination problems by insufficient wetting [66]. The integration of the spraying apparatus directly within PBF-LB machine is also an engineering problem, which has to be solved. This is also the main challenge of the electrophoretic deposition technique. Up to now, the powder layer is transferred from the deposition electrode onto the previous layers by friction [5], which can finally lead to accuracy problems of the laser processed part.

In the present work, the use of spray-dried granules was chosen as the desired powder bed preparation technique, since it combines the advantages to add nano dopants and therefore, to increase the absorptance of aluminum oxide in the visible or near-infrared range of the laser light without decreasing the powder flowability and the final powder bed density. A big advantage of this technique is that most commercial PBF machines are powder-based systems. Spraying of granules consisting from only nanoparticles is possible. However, layering with these granules gives in general a lower powder bed density than layering by slurry casting. This problem is addressed in this work by spray drying of granules consisting of multimodal particle combinations. Furthermore, the layer thickness is limited by the size of the granules. A storage problem and a fire hazard risk is not given for spray-dried granules, since these are normally sprayed from a water-based slurry. The main disadvantage of using spray-dried granules for powder preparation is the time-consuming development and optimization of these granules.

The challenge to achieve highly flowable, dense, homogeneous and spherical granules has to be addressed.

### 2.1.4.3 Processing methods and properties

The following classification was drawn to classify the different approaches to consolidate powder beds to dense high performance oxides via PBF-LB. This section gives an overview of the approaches to improve properties by increase of absorptance, reduction of melting temperature, reduction of thermal stresses and crack formation and liquid phase formation. The limitations in terms of porosity, mechanical properties and accuracy are summarized in section 2.1.4.4. Subchapters are as following:

- A. Use of different dopants
- B. Use of eutectic material ratios
- C. Application of preheating
- D. Application of different lasers and scanning strategies
- E. Generation of ceramic-glass composites
- F. Addition of metals to the starting powders
- G. Combination of PBF-LB with self-propagating high temperature synthesis

The laser parameters used for the different works are summarized in **Table 2** at the end of this chapter.

#### A. Use of different dopants

Juste et al. [50] used 0.1 vol% graphite containing alumina granules to reach a maximum part density of 97.5% by increasing the powder absorptance of the laser light (**Figure 6**). Scanning Electron Microscopy (SEM) revealed cracks and pores. Verga et al. [56] showed also the possibility to use carbon doping for alumina toughened zirconia (ATZ) to increase the absorptance of the powder. The zirconia was stabilized with yttria to prevent the component to crack because of stresses generated by the strong expansion of the phase transition to monoclinic phase during cool-down. Upon laser processing with a continuous wave Nd-YAG fiber laser ATZ parts with a density of up to 96 % [56] were produced.

#### B. Use of eutectic material ratios

The use of a eutectic ratio offers the possibility to reduce the melting temperature of the system such as for a mixture of  $\text{Al}_2\text{O}_3$  and  $\text{ZrO}_2$  down to 1860 °C. This mixture should be slightly beneficial to avoid crack formation due to a reduced resolidification temperature and by the toughening of a second phase. Furthermore the bandgap of  $\text{ZrO}_2$  (5.8 eV) is slightly smaller

than the bandgap of  $\text{Al}_2\text{O}_3$  (8.8 eV) [67]. Mapar et al. [51, 52] produced parts made from  $\text{Al}_2\text{O}_3$  and YSZ with a continuous ytterbium fiber laser. By the use of high laser power and low scanning speed ceramic components could be manufactured. However, the parts showed a low density and were fragile and unstable. Zhao et al. [68] observed an oxygen reduction in this powder mixture during laser processing in argon atmosphere, which led to a color change from white to black. This was confirmed by peak shifts x-ray diffraction pattern. However, the samples also dealt with inhomogeneous leveling, delamination, balling and cracking effects.



**Figure 6:** Pure PBF-LB processed alumina parts manufactured by Juste et al. [50]

Liu et al [53] proofed the feasibility to produce ternary eutectic ceramics by laser melting. One powder layer composed of  $\text{Al}_2\text{O}_3/\text{GdAlO}_3/\text{ZrO}_2$  was processed with a  $\text{CO}_2$  laser under argon atmosphere to give a ceramic with a density of ca. 98%. Despite the big laser spot size and low scanning speed, which should be beneficial to reduce thermal stresses, micro-cracks were formed and hardness and fracture toughness were lower compared with traditional manufactured components [69]. Furthermore, the melting efficacy differed from the center to edge of the laser spot.

### C. Application of preheating

To achieve crack free parts, different laser strategies and preheating were applied. In theory, cracks due to thermal stresses are reduced by increasing the ambient temperature during processing and afterwards by controlling the cooling stage. Hagedorn and Wilkes [15, 16] processed the eutectic ratio of micron-sized  $\text{Al}_2\text{O}_3$  and YSZ powder by a dual laser system (**Figure 7**). Powder consolidation was achieved by a continuous wave Nd:YAG laser and preheating by a  $\text{CO}_2$  laser equipped with a diffractive optical element for homogenizing the power output and

to deliver temperatures close to the melting point. They found that a preheating temperature of at least 1600 °C was necessary to avoid crack formation. Although the processed parts were almost 100% dense and without cracks for small parts, they offered a poor surface quality and the size was limited to about 1-2 mm to avoid cracks. Bigger parts suffered crack formation in higher regions, since a homogenous preheating of the specimens could be not achieved due to heat losses by radiation, conduction and convection (even by using induction heating at the bottom). Therefore, thermal stresses were generated due to temperature differences between bottom and top areas of the parts [70].

Buls et al. [14] used microwaves to generate preheating temperatures of 1100 °C in aluminum oxide powder for processing of single tracks and layers with high densities and without any thermal cracks. For interaction with the microwave frequency of 2.45 GHz at room temperature a SiC susceptor was used, since alumina is not absorbing at this wavelength at room temperature. The temperature of the powder was raised by heat conduction and results in lowering of the required laser power for consolidation. However, the use of microwaves can also trigger a thermal runaway at the melt-pool (uncontrolled energy release that further increases temperature during processing), since the absorption of the microwave radiation changes for ceramics at higher temperatures.

Coulon and Aubry [71] developed a laser manufacturing process in closed oven that can heat up the powder up to 800 °C. Alumina parts with a maximum density of 65%, a maximum size of 50 mm (fabrication time 15 hours) and a minimum wall thickness of 0.3 mm were manufactured by this process.

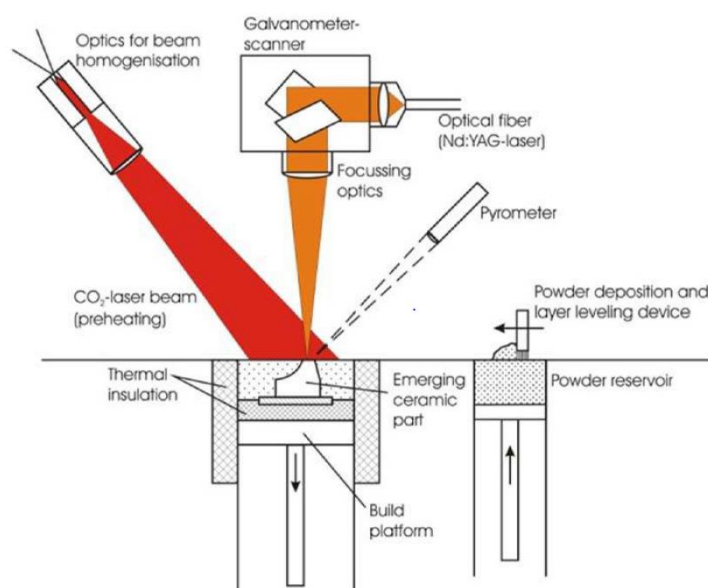


**Figure 7:** Schematic of laser preheating with second laser in PBF-LB [16]

Deckers et al. [5] produced alumina parts with 85% density with an applied furnace preheating temperature of 800 °C (homogeneously heated cylindrical zone), that reduced the necessary energy density of the used CO<sub>2</sub> laser required for fusion. Additionally to preheating, a post heat treatment at 1600 °C was performed. SEM of these parts revealed a partial melting, but cracking formation was not avoided.

### D. Application of different lasers and scanning strategies

Different lasers have been already tested to improve the properties of PBF-LB produced high performance oxide ceramics.

In general unmodified high performance oxide ceramics show an absorption of a CO<sub>2</sub> laser in comparison to Nd:YAG lasers, e.g. alumina powder bed had 96 % of absorption to CO<sub>2</sub> laser wavelength [20]. Wilkes and Wissenbach [72, 73] used a CO<sub>2</sub> laser for a possible processing by a powder bed based direct laser melting of pure aluminum oxide with a CO<sub>2</sub> laser. The final resolution with the CO<sub>2</sub> laser was down to 60 µm and the surface roughness down to 12 µm [72]. In comparison, the use of a Nd:YAG laser led to overheating due to the high intensities necessary to start the absorption process (avalanche effect).

Wu et al. [4] achieved a complete densification with very few pores in the triple grain boundary with a CO<sub>2</sub> laser (energy density of 8.5 J/mm<sup>2</sup>). However, the significantly large laser beam (2 mm) diverges considerably from typical PBF-LB processes, which aim at building small features and achieving accuracy in the order of at least 0.1 mm.

Zhang et al [65] optimized the energy density (889 - 911 J/mm<sup>3</sup>) to improve the surface quality of alumina parts. However, rough surfaces as well as cracks were still present, which came mainly from an insufficient overlap of the scan tracks, an unstable melt pool, a thermocapillary convection or an exaggerated energy input.

### E. Generation of alumina-glass composites

Crack-free selective laser melting of pure silica glass was already shown in literature for single tracks and single layers [74] and also for bioactive glasses [75]. Since pure silica and other glasses have low thermal expansion coefficient and a low glass-transition temperature, they are a promising candidate for LAM. Furthermore, a liquid phase during processing is generated and fuse the powders in short interaction time during the process. However, as described in Gahler et al. [3] only rearrangement occurs, and not the other stages of sintering like solution precipitation and solid-state sintering like typical in traditional liquid phase sintering.

Exner et al. [6, 60, 61] and Regenfuss et al. [7, 62] achieved highly dense parts made of an alumina-silica composite (density up to 98%) with a resolution of up to 40  $\mu\text{m}$  and an average surface roughness of circa 5  $\mu\text{m}$  by using a pulsed Nd:YAG laser. Manufacturing of parts with aspect ratios of 2 and a maximum height of 10 mm was possible. The created glass phase acted as matrix phase for the crystalline fillers [7]. Tests showed a decomposition of the silica phase due to overheating and thus evaporation [61], similarly to the loss of Si and O from the glass phase described in Manob et al. [76]. A lower intensity of the pulses caused a higher resolution in the parts and less material decomposition. A shrinkage of 0.7% due to crack annealing (1600  $^{\circ}\text{C}$ ) and due to decrease of the pore number was measured [61, 62], which led to final mechanical strength of 120 MPa in a 4-point bending test. XRD measurements showed low content of mullite after laser processing, which increased after thermal treatment.

By the use of a nanosecond laser operating with stochastic pulse distribution, it is possible to build parts with relative low stresses and to avoid an overheating due to short times of energy transfer (10-100ns) and temperature-dependent absorption [7, 62]. The stochastic distribution of pulses enabled the consolidation of micro-surfaces, which do not overlap at an initial stage and cross-link only towards the end of every layer. The high resolution and the stress-free fabrication results from this selective consolidation [6]. The higher photon energy of the green laser leads, according to [6, 7, 60-62], to higher laser absorption. In addition, the nanosecond pulses allow to process materials with a bandgap bigger than photon energies, since electrons in the valence band can be also excited due non-linear multi-photon absorption or excited state absorption [7, 62]. However, the use of too high intensities involves the risk of overheating (avalanche effect) [7].

The sintering model for the 200 ns pulse irradiation is described in [6, 7, 60-62] by evaporation and condensation during laser processing. The model contained 4 steps: a) formation of a gas bubble above the molten material, b) rapid bursting, c) formation of a slower jet, and d) dispersion of the jet into droplets and solidification [7, 62].

Already in the 90s, Lee et al [77-79] tried to implement alumina-glass composites made from aluminum oxide, boron oxide and zinc borosilicate glass powders by PBF-LB. The advantage of the chosen borosilicate glass was the low softening point of only 630  $^{\circ}\text{C}$ .

Bae et al. [80] reported for  $\text{Al}_2\text{O}_3$  mixed with a grinded glass powder based on a  $\text{SiO}_2\text{--B}_2\text{O}_3\text{--RO}$  ( $\text{R} = \text{Ba, Zn}$ ) ternary system similar results. a black pigment (up to 3 wt%) was added to increase the laser light absorption. A heat-treatment at 750  $^{\circ}\text{C}$  was necessary to achieve high densities after laser processing (glass softening point of 671  $^{\circ}\text{C}$ ). No secondary phase formation

by reactions between the amorphous glass and crystalline alumina was observed during the whole process chain.

Heinrich et al. [64], Mühler et al. [2] and Gahler et al. [3] manufactured ceramic parts with densities of up to 92% of the theoretical density with a continuous wave CO<sub>2</sub> laser light using Al<sub>2</sub>O<sub>3</sub> and SiO<sub>2</sub> (**Figure 8**). An alumina content smaller than 31 wt% could deliver stable parts. A larger amount of alumina resulted in cracks and delamination issues. An optimized range for the laser energy density to avoid vaporization, decomposition and still fuse the material was evaluated [3] (**Table 2**). The maximum roughness of the top surface was 4.5 µm. In contrary to the work of Exner et al. [6, 60], an increased mullite formation and re-crystallization controlled by dissolution of alumina was reported already after the laser process without thermal post-treatment [64]. A formation of mullite needles is especially interesting due to increase of mechanical stability by reinforcement. An inhomogeneous crystallization within one layer resulted from temperature gradients. A thermal post-treatment further increased the density of the parts to 96% [64] and led to a formation of cristobalite from the amorphous silica phase and further mullitization [3, 64].

Wang et al. [81, 82] also used this concept to produce bioceramics made from an alumina-based system containing zirconia and silica by a pulsed Nd:YAG laser (1064 nm). The final product was homogeneous and contained dendrite like-mullite, which is favorable in terms of fracture toughness. The starting YSZ was transformed during laser processing to monoclinic zirconia. By adjusting the alumina-zirconia ratio, the final grain growth of these two particles could be controlled. However, dense parts contained cracks.

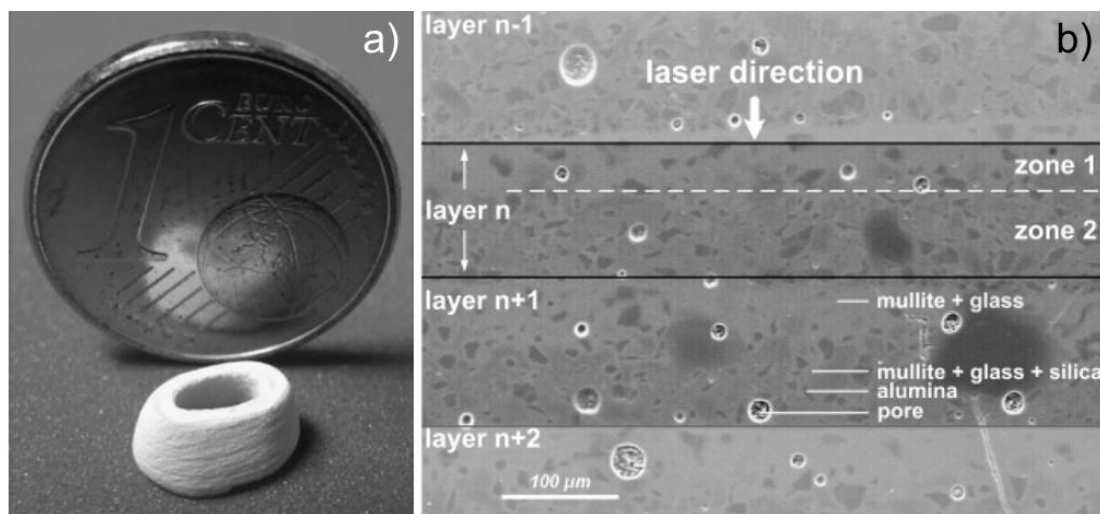


**Figure 8:** a) Tooth model consisting of 35 layers (Al<sub>2</sub>O<sub>3</sub>–SiO<sub>2</sub> ratio: 0.37) and b) typical microstructure of these composite shown in Gahler et al.



**Table 2:** Process parameters of relevant publications regarding powder bed fusion of high performance aluminum oxide ceramics

Publications	Material	Laser	Wavelength [μm]	Laser power [W]	Scanning speed	Spot diameter	Hatch space [μm]	Layer thickness [μm]	Energy Density [J/mm <sup>3</sup> ]
Juste et al.	Al <sub>2</sub> O <sub>3</sub> doped with carbon black	Cw fiber laser	1.064	125-150	ca. 109	ca. 30	50	50	332.4–398.9
Verga et al.	ATZ doped with carbon	Cw Nd:YAG la	1.064	34	86	N/A	175	40	109.8
Mapar et al.	Al <sub>2</sub> O <sub>3</sub> and Y <sub>2</sub> O <sub>3</sub> -stabilized ZrO <sub>2</sub> in eutectic ratio	Cw ytterbium fiber laser	1.07	700-900	400	760	400	500	4.6-5.9
Liu et al.	Al <sub>2</sub> O <sub>3</sub> /GdAlO <sub>3</sub> /ZrO <sub>2</sub> ternary eutectic ceramic	Cw CO <sub>2</sub> laser	10.6	200	0.1	8	N/A	500	500
Hagedorn and Wilkes	Al <sub>2</sub> O <sub>3</sub> and Y <sub>2</sub> O <sub>3</sub> -stabilized ZrO <sub>2</sub> in eutectic ratio	CO <sub>2</sub> laser for preheating and Cw Nd:YAG laser for consolidation	1.064	60	200	200	50	50	30
Coulon and Aubry	Al <sub>2</sub> O <sub>3</sub>	Cw ytterbium fiber laser	1.060 -1.100	100	N/A	60	N/A	60	N/A
Exner and Regenfuss et al.	Al <sub>2</sub> O <sub>3</sub> and SiO <sub>2</sub>	pulsed Nd:YAG laser (pulse duration: 200 ns or shorter; repetition	0.532 or 1.064	N/A	N/A	N/A	N/A	1-10	N/A
Lee et al	Al <sub>2</sub> O <sub>3</sub> , B <sub>2</sub> O <sub>3</sub> and Zinc-Borosilicate glass	N/A	N/A	15	560	N/A	125	200-250	0.9-1.1
Bae et al.	Al <sub>2</sub> O <sub>3</sub> and glass based on SiO <sub>2</sub> -B <sub>2</sub> O <sub>3</sub> -RO (R=Ba, Zn)	Fiber laser	1.06	20	N/A	50	N/A	1000	N/A
Wang et al.	Al <sub>2</sub> O <sub>3</sub> , ZrO <sub>2</sub> and SiO <sub>2</sub>	Pulsed Nd:YAG laser (repetition rate: 1400 Hz)	1.064	40	15	100	100	N/A	N/A
Gan et al.	Al <sub>2</sub> O <sub>3</sub> and spodumene	Cw ytterbium fiber laser	1.060 -1.100	Up to 400	10000	80-115	ca. 2	50	7.0-10.0
Subramanian et al.	Al <sub>2</sub> O <sub>3</sub> with aluminum addition	Pulsed Nd:YAG laser (repetition rate: 20 kHz)	1.06	43	46	N/A	N/A	N/A	N/A
Slocombe and Li	TiO <sub>2</sub> , Al and C to synthesize TiC-Al <sub>2</sub> O <sub>3</sub>	Pulsed Nd:YAG laser (pulse duration: 18 ns; repetition rate: 20 kHz)	N/A	60	2	200-600	100	180	277.8-833.3
Gahler and Heinrich et al.	Al <sub>2</sub> O <sub>3</sub> and SiO <sub>2</sub>	Cw CO <sub>2</sub> laser	10.6	17-24	35-65	100	40-80	100	26.2-68.6
Zhang et al.	Al <sub>2</sub> O <sub>3</sub>	Cw ytterbium	1.07	200-205	90	60	50	50	759.3
Wu et al.	Al <sub>2</sub> O <sub>3</sub>	Cw CO <sub>2</sub> laser	10.6	72	4	2000	N/A	2000	4.5
Deckers et al.	Al <sub>2</sub> O <sub>3</sub>	Cw CO <sub>2</sub> laser	10.6	2	5.2	400	200	50-200	19.2

Gan et al. [59] were able to build dense ceramic-glass composites composed of alumina and spodumene with an ytterbium fiber laser in nitrogen atmosphere. Despite of a pre-heating of

the substrate, delamination of the part could not be avoided. A layer thickness of 50  $\mu\text{m}$  was identified to achieve the highest density and flexural strength. The microstructure consisted of embedded alumina particles in a partially crystallized glass-ceramic. Despite partial melting of the glass phase, micro cracks were apparent due to difference in the thermal expansion. A heat treatment up to 950  $^{\circ}\text{C}$  led to further crystallization, but was not beneficial for increasing density and mechanical strength in contrast to pure spodumene.

### A. Addition of metals to the starting powders

Subramanian et al. [83] mixed alumina powders with 15, 25 or 35 wt% aluminum to use the metal phase as a binder during manufacturing with a Nd:YAG laser. Laser processing led to a partial oxidation of the aluminum, which could be further oxidized by a post heat treatment. Wetting of the alumina particles with the molten aluminum depended on the achieved temperature (contact angle decrease with temperature). Delamination and cracking were severe, and this limited significantly the mechanical properties.

### B. Combination of PBF-LB with self-propagating high temperature synthesis (SHS)

The generation of a high exothermic reaction (SHS) was another proposal to solve the densification issue in PBF-LB. The used laser energy activated the exothermic reaction of  $\text{TiO}_2$ , Al and C to synthesize a  $\text{TiC-Al}_2\text{O}_3$  ceramic. However, the synthesized part showed poor accuracy and high porosity after processing [84].

## 2.1.4.4 Part properties

There are still several open challenges for PBF-LB of high performance aluminum oxide ceramics, because several defects typical of LAM techniques affect the properties of the produced parts. In this chapter, the most relevant defects are reviewed and their effects on properties is thoroughly discussed, focusing on the physical causes and the solutions to the open challenges. The mostly affected properties could be categorized as follows:

- A. **Porosity** due to poor densification
- B. **Microstructural properties** involving grain size, grain boundaries and phase transformation.
- C. **Mechanical properties** affected by e.g. thermal-induced cracks and microstructure.
- D. **Geometrical accuracy and surface quality defects** due to instabilities and/or residual stresses.

**Table 3** at the end of this chapter shows a summary of the properties of all the reported works.

### A. Porosity

High part density, and therefore low porosity, is a necessary requirement for high performance ceramics in engineering applications with high mechanical requirements. In fact, the mechanical strength of ceramics typically decay exponentially with an increase of porosity according to the empirical law of Duckworth [85]. Furthermore, the Young's modulus of porous materials follows a similar empirical law, called the Spriggs' equation, and decreases also exponentially with the increase of the porosity [86]. However, not only the total porosity, but also the pore geometry, size and orientation are major factors affecting the mechanical strength [87]. Bigger pores and pores parallel to the applied stress reduce the strength of the part [87, 88]. More information on the impact of different pore geometries on the mechanical strength can be found in Brown et al. [87]. The same behavior LAM processes often lead to poor densification of the starting powder depending on process conditions and thermophysical properties of the material. For these reasons, density measurements are generally performed and reported in most publications about AM of ceramics.

The most common measurements of porosity are derived from Archimedes density measurements or density measurements based on the geometrical dimension and weight of the part. Challenges of these methods are that Archimedes measurements cannot take into account the open porosity, which can be relevant in case of small and porous parts, whereas on the other side measuring the size and the weight is often linked to large measurement errors in the dimensions.

A modified version of Archimedes test is described in the standard ASTM C20-00 (2015) [89] and applied by Verga et al. [56]. This version takes into account the open porosity of the sample. The parts are measured not only dry and under water, but also wet, so that the volume of water filling the open porosity can be estimated. However, the size of the measured sample, according to the standard, should be a cube of  $410 - 490 \text{ cm}^3$  quartered from a larger specimen, while generally smaller samples are built in PBF-LB.

Another measurement possibility for porosity consists in analyzing a cross-section of a sample after grinding and polishing. However, this method is extremely time consuming and provide information of only a single cross-section. Furthermore, the sample is destroyed by the preparation of the cross-section.

Finally, computer tomography (CT) allows to have a full 3D model, from which calculations of porosity can be accurately performed, as long as the size of the sample is small enough to allow x-ray penetration. Gan et al. [59] used it to analyze  $3 \times 4 \text{ mm}$  pillars. Furthermore, they

compared the Archimedes method with CT scan measurements: the density calculated was ca. 88% according to Archimedes principle and ca. 95% according to micro-CT for the same part [59]. The difference was probably due to the unknown theoretical density of the PBF-LB produced material. A clear advantage of computer tomography is also the possibility to analyze at the same time other defects, such as cracks as well as geometrical and surface defects, when the resolution is high enough.

Considering the variety of used measurement methods and the large deviation in the measurement results, it is difficult to compare results from different publications. However, for PBF-LB of high performance oxide ceramics it can be noticed that values of porosity lower than 10% could be achieved only by using high temperature preheating (above 1600 °C) [15, 16, 54] or by using dopants [50, 56]. This proves that poor laser light absorption at room temperature is the leading cause for high porosity in PBF-LB. Other proven causes for high porosity are irregular powder shape [16], insufficient laser energy density [9] and a too large layer thickness [18, 50, 59].

Furthermore, Exner et al. [6, 60, 61, 63], Regenfuss et al. [7, 62], Gahler et al. [3] and Heinrich et al. [64] could also achieved porosity lower than 10% by using composite materials including silica and alumina and a CO<sub>2</sub> laser, or by using spodumene and alumina in equal ratio as starting material [59].

In conclusion, porosity in PBF-LB is highly critical and it can be solved up to now only by using specific materials and process combinations.

### B. Microstructure

Typically for PBF-LB techniques, part shape and microstructure are generated simultaneously during the melting and resolidification process. This means that tailoring the microstructure, such as grain size and shape, is challenging, since the microstructure obtained is heavily dependent on the processing conditions and often only small parameter windows are available. Especially, the microstructure has hereby a large impact on mechanical or other desired physical properties.

In the case of PBF-LB of pure alumina, the low speed and high power, required to have dense parts and to reduce cracks, lead to large grains. Deckers et al. [5] could achieve grain diameters as low as 5 µm by PBF-LB, but density was limited to 85%. Zhang et al. [65] and Zheng et al. [11] noticed that lamellar structures of few microns in width and tens of microns in length were generated along the build direction by thermal capillary convection, influenced by Marangoni

effect, streak convection and flowing Bénard cells. Fan et al. observed that columnar dendrites transformed into equiaxed dendrite at high energy densities [8]. In addition, they found a correlation between energy density and grain size: higher energy density implies also higher cooling rate and therefore larger grains. Wu et al. achieved small spherical grains of about 1.5  $\mu\text{m}$  using a large beam (2 mm), because of liquid phase sintering with small amounts of impurities [4]. However, the study was limited to a single layer.

The situation is quite different for eutectic compositions or other composites. Mapar [52] observed for eutectic alumina-zirconia a flake-shaped microstructure. This was explained by the difference in surface tension between the two materials. Finer grains were obtained using a laser with a small spot size (80  $\mu\text{m}$ , instead of 760  $\mu\text{m}$ ) and higher scan speed (250 mm/s). This was explained by the higher cooling rate induced by the smaller spot and faster speed. Verga et al. [56] observed crystalline zirconia surrounded by alumina, which is supposedly amorphous before a post heat treatment. Liu et al. [53] used a ternary eutectic starting material and obtained different eutectic structures at different position in the samples. At the bottom, ultra-fine colony microstructures are evident, at the top rod-like eutectic structures are dominant and lamellar structures are seen in between. The spacing of the eutectic structure is varying from 0.92  $\mu\text{m}$  at the bottom to 0.48  $\mu\text{m}$  at the top.

Using a second laser for high temperature preheating, Hagedorn et al. obtained a nano-sized microstructure interrupted by coarser crystals in intervals of 50  $\mu\text{m}$  corresponding to the layer thickness [15]. Such a unique microstructure was explained by local evaporation of alumina, but its effect on mechanical properties is not yet well understood.

Gan et al performed PBF-LB on a composite of alumina-spodumene powder. Spodumene formed the matrix around the alumina particles. EDS analysis before and after heat treatment at 900°C showed that the matrix is changing from silicon rich to aluminum rich. In addition, alumina crystals are growing because of the heat treatment, which is explained by nucleation and crystal growth of spodumene around the alumina particles.

Wang et al. [82], Heinrich et al. [64], Mühler et al. [2] and Gahler et al. [3] found that both amorphous silica and mullite are produced when alumina and silica are laser processed. They mention that mullite needles could improve the fracture toughness of the parts. In [3], post heat treatment transformed the amorphous alumina in cristobalite and further enhanced the mullitization of silica in proximity of alumina. In addition, the same authors observed different microstructures within each layer, because of the different cooling rate at different depths.

### C. Mechanical properties

Common mechanical properties tests for LAM produced parts are:

- Bending strength with 3-point, 4-point or ball-on-3-balls (B3B) bending test
- Compressive strength
- Tensile strength
- Fracture toughness by indentation
- Hardness by indentation

Generally for ceramics, bending tests are the most appropriate, because tensile stresses are particularly critical for ceramics parts that therefore are usually designed with the criteria to avoid tensile stresses [48]. Indentation tests are proven to be a not reliable test for fracture toughness estimation since discrepancies were found with other standardized fracture toughness tests [90]. However, it may be used for comparison between different process parameters or materials as long as the microstructure is sufficiently homogeneous. Hardness by indentation is not a critical test for LAM-produced ceramics, because local hardness is high for large grains typically produced by these processes. This is especially the case for small indenters (nano- and micro-indenters), because they can involve small, local crack-free areas.

It is commonly agreed that cracks during LAM of ceramics are generated by the large thermal stresses that arise from rapid melting and re-solidification of the material. This limits considerably the mechanical strength of the produced parts and therefore also their applications in mechanically demanding applications.

Griffith explained the discrepancy between theoretical strength and actual strength of a material with existing flaws (e.g. cracks and pores) in the manufactured part [91]. Stresses are concentrated at these flaws. Griffith approached the critical crack length by an energy balance of the stored elastic energy and the additional created surface energy by a fracture [91, 92]. For a crack smaller than this critical crack length, the surface energy dominates and for a larger crack, the released strain energy dominates [92]. The Griffith equation shows that the fracture stress  $\sigma_f$  depends on the Young's modulus  $E$  and the surface energy  $\gamma$  of the material as well as the crack length  $c$  [91]:

$$\sigma_f = \sqrt{\frac{2E\gamma}{\pi c}} \quad (1)$$

The flaw morphology has to be also considered. Atomically sharp cracks with only elastic deformation ahead of the crack front are very detrimental to the strength of an ideal brittle material [92]. The stresses acting near the end of the crack were expressed in terms of two parameters by Irwin [93]. These are the adjustable uniform stress parallel to the crack extension direction and a second parameter direct proportional to the square root of the force causing crack extension (stress-intensity factor) [93]. Sih and Liebowitz [94] calculated that the critical stresses for a narrow ellipse and a sharp crack change only slightly, but the critical shear stress of a line crack (assumed by the Griffith-approach [91]) differs significantly from those. A comparable relationship between the pore geometry, size and orientation and the mechanical strength was already described in subchapter 2.1.4.4 A. [87]. Furthermore, the volume of the part has a major impact on the final strength, since the probability of having a crack and the size of the largest crack decreases with a decreasing sample volume and therefore, the strength of the parts increases [91, 92].

The facts, that ceramic parts produced by laser powder bed fusion offer a high amount of different flaw sizes and shapes in combination with typically small sample sizes and a low amount of test samples, make an evaluation of the failure probability by a Weibull plot unnecessary for laser processed oxide ceramic parts.

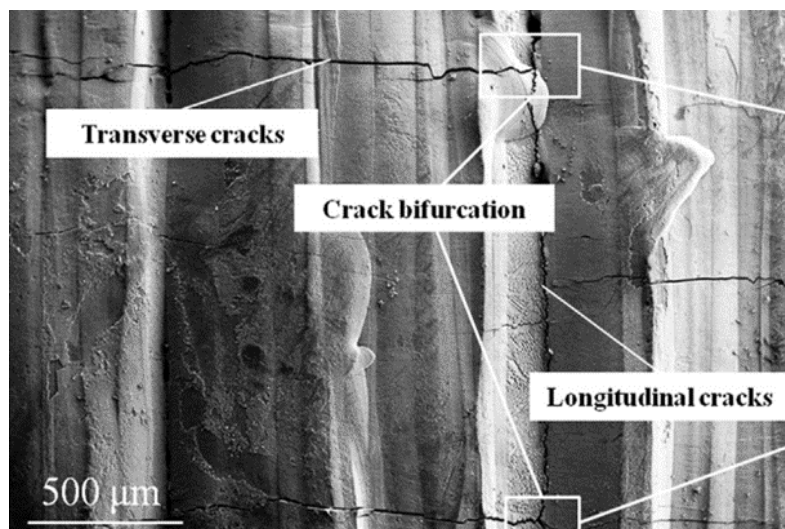


**Figure 9:** Classification of cracks in PBF-LB: longitudinal cracks run along scan track boundaries, while transverse cracks run across scan tracks [11]

Zhang et al. [65] and Zheng et al. [11] thoroughly analyzed cracks in PBF-LB of high performance ceramics and they both distinguished between transverse cracks, that are perpendicular to the scanning direction, and longitudinal cracks, that are parallel to the scanning direction as shown in **Figure 9**. Zhang et al. noticed that transverse cracks were the most common within

tracks and in the center of the specimen, while longitudinal cracks happened mainly between scan tracks [65]. Preliminary tests showed that the island scanning strategy could mitigate these problems. Zheng et al. noted that intergranular fractures along the columnar crystals are the most common, but transgranular cracks can also occur [11].

Verga et al. showed that ATZ processing under nitrogen was beneficial for crack formation on the top surface of the samples [56]. This was explained by the high-temperature reactions in air between oxygen and carbon, the dopant used to increase absorption. A 4-point bending strength was performed only for samples thermally post-treated at 1300°C, because parts without heat treatment failed during preloading. The achieved bending strength was 31 MPa.

Juste et al. reported thermal treatments of PBF-LB-produced alumina parts at 1550 °C were detrimental for mechanical properties: it generated additional cracks perpendicular to the building directions and did not reduce the porosity [50]. Possible reasons mentioned by the authors are related to residual stresses and gas evaporation resulting from reactions of the remaining graphite additive, used during the process for absorption enhancement. A beneficial effect was also not seen in [95] for alumina PBF-LB-produced parts heat treated at 1700°C. This proves that for alumina, differently than for ATZ, no shrinkage occurs because large cracks and pores cannot be removed with a post-treatment, since the distances are too big to be closed. The reason why ATZ may show a different behavior could be that phase transformation from tetragonal to monoclinic transition accompanied by volume expansion at crack tip occurs in zirconia.

The use of high temperature preheating by using a second laser and induction heating for alumina and zirconia ceramics in eutectic ratio is to date the only method that allowed to build parts of high mechanical strength [96] in PBF-LB. However, the required preheating temperature was above 1600°C and the non-uniformity of temperature caused cracks due to different volume changes between top and bottom of the sample, especially in the case of bigger samples [70]. Mechanical strength was tested with B3B method for parts of only 0.6 mm in height and the achieved values were above 500 MPa with an average of 814 MPa. This value was close to the strength of traditional manufactured zirconia ceramics with a strength of 1000 MPa or higher [97]. Another pre-heating option is offered by microwave. Buls et al. implemented a microwave-assisted PBF-LB process in a self-built machine made mainly in microwave-transparent quartz [14]. Crack-free parts were built but only for single tracks and single layers.

Exner et al. used a ceramic glass composite to avoid crack formations in PBF-LB and reported a flexural strength of 100 MPa and compressive strength of 800 MPa, which are similar to glass-



related values [7, 98]. The physical principle is that amorphous silica has a low thermal expansion coefficient: if partial melting of silica is achieved, then thermal stresses due to shrinkages during cooling are avoided [99]. By annealing of these parts, [61] the bending strength was increased to 120 MPa (4-point bending method) and compressive strength to circa 1150 MPa. The values are considerably lower compared to sintered high performance ceramic, but the ceramic and glass composite could still be an alternative to solid state sintering or melting of oxides for low demanding application. Bae et al. evaluated a hardness of 5.67 GPa for a composite made of 70 wt% glass based on  $\text{SiO}_2\text{--B}_2\text{O}_3\text{--RO}$  ( $\text{R} = \text{Ba, Zn}$ ) to 30 wt% alumina [80]. The hardness is close to the values of glass [100] and much lower than that of alumina [101].

Using metal phases as starting material, which oxidize in-situ during PBF-LB, is another alternative [83]. Mechanical properties were limited by delamination and the four-point bending strength of the parts was only  $3.6 \pm 0.7$  MPa. This was most likely due to the low part density (45%).

Mapar claimed to have achieved crack free melting and resolidification by using a large spot of 760  $\mu\text{m}$ , a high power of 900 W and speed of 400 mm/s, but the realized parts were extremely porous (about 30% of porosity), showing that a larger spot and a combination of a relatively high power and low speed may lead to crack-free parts [52].

#### D. Geometrical accuracy and surface quality

Achieving good accuracy and good surface quality is often problematic in PBF-LB, due to the highly dynamic behavior of the melting and solidification processes.

Wilkes et al. showed that melt often flowed out of intended contour during PBF-LB process at high temperatures, generating a very rough surface (roughness in the order of tens to few hundreds  $\mu\text{m}$ ), which was considered not suitable for the intended dental application [16]. Roughness values below 5  $\mu\text{m}$  were reported by Exner et al. [61] using a green pulsed laser and an experimental setup in which fine powder was compressed before the PBF-LB process.

Balling is also a typical problem in PBF-LB: it is caused by the relatively high surface tension of molten ceramics. Balling was avoided by reducing the scanning speed, increasing the power and reducing the hatch space, which means increasing the energy density [102].

Juste et al. noticed that PBF-LB processed parts with regular shapes had low density, while parts with higher density exhibited a concave upper surface [50]: the authors explained this with the high recoil pressure generated during the process.

## 2 Literature review

**Table 3: Properties of aluminum oxide parts processed by PBF-LB**

Publications	Material	Porosity	Cracks	Geometrical accuracy and surface quality	Microstructure	Mechanical properties (test method)
Gahler et al. [3] and Heinrich et al. [62]	Al <sub>2</sub> O <sub>3</sub> and SiO <sub>2</sub>	8%	N/A	N/A	Mullite needles	N/A
Wu et al. [4]	Al <sub>2</sub> O <sub>3</sub>	N/A	N/A	N/A	Relatively fine grains (1.5 µm)	N/A
Deckers et al. [5]	Al <sub>2</sub> O <sub>3</sub>	15%	Yes	High porosity and high inhomogeneities Not evident defects	Inhomogeneous, grains of tens of micrometer Generation of mullite.	N/A
Exner et al. [6, 58, 59] and Regenfuss et al. [7, 60]	Al <sub>2</sub> O <sub>3</sub> and SiO <sub>2</sub>	2%	No	High surface and geometrical accuracy. R <sub>a</sub> < 5 µm Resolution of 40 µm	Some porosity left even after post-heat treatment. Columnar dendrites Equiaxed dendrites for high energy densities	120 MPa (4-point bending) 15-20 GPa (Vickers microhardness)
Fan et al. [8]	Al <sub>2</sub> O <sub>3</sub>	N/A	Yes	N/A	N/A	N/A
Buls et al. [14]	Al <sub>2</sub> O <sub>3</sub> -ZrO <sub>2</sub>	N/A	No	Not evident in single layer	N/A	N/A
Hagedorn and Wilkes [15, 16]	Al <sub>2</sub> O <sub>3</sub> -ZrO <sub>2</sub> eutectic ratio	< 3 %	No	Poor surface	Fine eutectic structure	> 500 MPa (B3B)
Juste et al. [48]	Al <sub>2</sub> O <sub>3</sub> , carbon-doped	2.50%	Yes	Concave upper surface	Porous and irregular	N/A
Mapar et al. [49, 50]	Al <sub>2</sub> O <sub>3</sub> -ZrO <sub>2</sub> eutectic ratio	30.60%	No	High porosity and inhomogeneity	Porous and flake-shaped	N/A
Mapar et al. [49, 50]	Al <sub>2</sub> O <sub>3</sub> -ZrO <sub>2</sub> eutectic ratio	N/A	Yes	Delamination Slight balling	Fine eutectic structure	N/A
Liu et al. [51]	Al <sub>2</sub> O <sub>3</sub> /GdAlO <sub>3</sub> /ZrO <sub>2</sub>	< 2%	No	N/A	“Chinese script”, lamellae, rod-like microstructure varying with position	15.3 GPa (microhardness)
Verga et al. [54]	ATZ (Al <sub>2</sub> O <sub>3</sub> 20% - ZrO <sub>2</sub> 80%) Carbon-doped	4%	Yes	Not evident defects	Al <sub>2</sub> O <sub>3</sub> -ZrO <sub>2</sub> partially eutectic system	31 MPa (4-point bending)
Gan et al. [57]	Al <sub>2</sub> O <sub>3</sub> (50%) and spodumene (50%)	> 5%	Yes	Delamination at substrate	Composite – alumina included in spodumene matrix	< 12 MPa (3-point bending)
Zhang et al. [63]	Al <sub>2</sub> O <sub>3</sub>	N/A	Yes	N/A	Columnar crystals	N/A
Coulon and Aubry [68]	Al <sub>2</sub> O <sub>3</sub>	35%	N/A	N/A	N/A	15 MPa (tensile test)
Lee et al [74-76]	Al <sub>2</sub> O <sub>3</sub> , B <sub>2</sub> O <sub>3</sub> and zinc borosilicate glass	N/A	N/A	N/A	Formation of aluminum borate and gahnite. No formation of secondary phases.	70-110 MPa after Ceracon forging (4-point bending)
Bae et al. [77]	Al <sub>2</sub> O <sub>3</sub> and glass based on SiO <sub>2</sub> -B <sub>2</sub> O <sub>3</sub> -RO (R = Ba, Zn)	< 5%	No	Not evident defects	Molten glassmatrix for alumina content < 30wt%	7.57 GPa (Vickers microhardness)
Wang et al. [78, 79]	Al <sub>2</sub> O <sub>3</sub> -ZrO <sub>2</sub> -SiO <sub>2</sub> 3 different combinations	N/A	N/A	N/A	Mullite needles Silica-based matrix	N/A
Subramanian et al. [80]	Al <sub>2</sub> O <sub>3</sub> and Al	65%	Yes	Delamination	Agglomerations	N/A

Gan et al. experienced cracks and delaminations at the part-substrate interface, due to high thermal gradients [59]. This phenomenon was most evident for a layer thickness of 50  $\mu\text{m}$ , which is also the parameter value that delivered the highest density. Delamination was avoided by Verga et al. coating a thin layer of soldering alloy Sn60Pb40 on a steel plate resulting in a better head conduction of the substrate and improved interface strength between built part and substrate [56]. In addition, removal of parts from the substrates was relatively easier, since it is possible to heat the soldering alloy up to its melting temperature in order to remove the parts.

## 2.2 Theoretical and experimental considerations for powder bed preparation

### 2.2.1 Spray granulation

In spray drying of ceramics a water-based ceramic suspension is pumped to an atomizer, which forms a range of spherical droplets due to high surface tensions. The whole process takes part in a drying chamber with a hot air flow, what causes a fast evaporation of the water based on a large surface area to volume ratio. The final granules are agglomerates of many particles linked together by attractive forces, where the moisture has been evaporated [103].

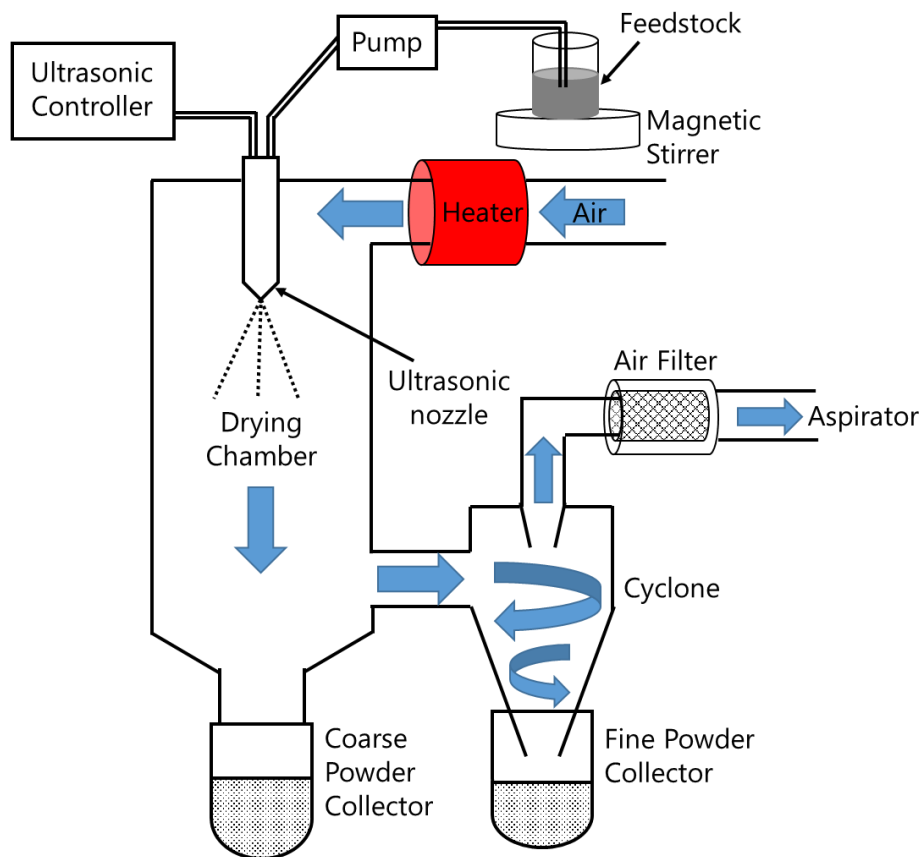


*Figure 10: Schematic of spray drying*

The spray drying process should be done in a chamber big enough to avoid collision of granules with the wall [104] and the nozzle blockage should be avoided [105] to achieve finally a high yield. **Figure 10** shows the schematic of the spray drying process in the current work.

The atomizer can use pressure (two-fluid nozzle), centrifugal (rotary disk) or ultrasonic energy (ultrasonic nebulizer) as a driving force. In the present work, the spray dryer B-290 (Büchi Labortechnik AG, Switzerland) offered the possibility to use an ultrasonic nozzle or a two-fluid nozzle. The ultrasonic nozzle was chosen for further experiments, since it was reported to have a better ability to form spherical granules with an increased size when comparable process conditions were used [106]. This was explained by the different way of the droplet generation. Furthermore, the generation of uniform droplet sizes with only a small variability due the change of the flow rate was reported for this nozzle [107].

The application determines in general the spray granulation process. Several morphologies including spherical, doughnut-shaped, raspberry-shaped, encapsulated, porous, hollow and "hairy" granules can be sprayed with a broad range of different materials. In general, spray drying is done to ensure a high flowability for a consistent and homogeneous die filling before compaction by pressing [23]. However, the great shape variety producible via spray drying leads to several different applications from catalytic applications [108] to drug delivery [109] or virus filtration [110].

In the case of PBF-LB, spray drying offers the advantages to produce appropriate small granules ( $< 100\ \mu\text{m}$ ) with a homogeneous particle distribution to manufacture a final part with a high accuracy. However, a hollow core can form in the center of the granules. The use of nano- and submicron particles for PBF-LB is also possible by the application of other powder bed preparation techniques than spray granulation, as already explained in chapter 2.1.4.1. Other granulation techniques like high shear granulation and fluidized bed granulation cannot produce granules small and homogeneous enough as required for the powder bed method. Freeze granulation could also give these fine granules as spray drying. However, these granules always contain porous channels arising from the processing method. A suitable granule densification to achieve dense powder beds does not occur, since capillary forces do not act during granulation by this method.

For spray granulation, several typical phenomena must be considered. The impact of different influencing factors on the following properties of spray-dried granules or the slurry for spray drying are specified in this chapter:

- A. Granule shape
- B. Granule size
- C. Final binder distribution within granules and slurry viscosity before spray drying

However, it has to be considered that the cited results were achieved by using different spraying nozzles, process parameters and material compositions. Therefore, the achieved results are difficult to compare with the achieved results using the Mini spray dryer B-290 (Büchi Labortechnik AG, Switzerland) with an ultrasonic atomizer in this work. **Table 40** in the conclusion (chapter 6) summarizes the results achieved in the present work regarding the impact of different influencing factors on the granule shape and size.

A. Influencing factors on granule shape

A rapid mass transfer during drying and different slurry additives can influence the granule shape (hollow, unshapely granules), what can result in a lower powder bed density. A higher solid load in the slurry will not only increase the yield but also the density of the granules [103, 111] and can improve the sphericity of the granules [112]. Voids inside the granules are often produced when the evaporation inside the granule is higher than the diffusion rate during drying of the solvent and explosion happens, when a certain pressure limit is reached [113]. Lukasiewicz gave a maximum solid load of approximately 50 vol%, that could be achieved for suspensions containing micron-sized ceramic particles. Higher solid loads cannot be processed by spray drying, since the viscosity of the slurry rises extremely. A reduction of the mean particle size, a non sphericity of the particles and the presence of organic binders will decline this value [103]. Lee et al. [114] used well dispersed  $\text{Si}_3\text{N}_4$  suspensions of ultrafine particles to give hollow granules. They claimed a limited liquid flow rate and an increased tortuosity due to fine capillaries to be responsible for this behavior. Naglieri et al. [115] produced donut-shaped and hollow granules from deflocculated  $\text{Al}_2\text{O}_3\text{-ZrO}_2$  suspensions. The flocculation of the slurry increased when the pH approached the PZC. However, in both works these irregular shaped high-dense granules yield a higher tapped density than the spherical granules without a central cavity made from flocculated suspensions. The same effect was reported by other groups [116-120]. Walker et al. [111] tested additionally the influence of other processing parameters (binder type, solid load, spray drier type) on spray drying of aqueous alumina slurries. The effect of solid loading on the granule density was in accordance to the results of Lukasiewicz. The binder type had also an influence on the density. Spray drying with the more highly adsorbed binder PEG Compound 20M resulted in a lower particle packing density than with PEG 8000. In addition, granules sprayed in co-current mode showed a higher density than in mixed-flow mode. The

granule shape wasn't depending on the spray dryer type (also reported in [119]), but from the exposed temperature. Shell thickness of the granules strongly depends on the state of the dispersion in the slurry. A better dispersion generates thinner shells [118]. Fully dispersed particles are very versatile without intergranular interactions and move together with the binder to pack densely at the shell [119]. The movement of smaller particles in multimodal particle combinations is enhanced, since they are more mobile within the droplet [121] and can build encapsulated granules. Despite having a lower buoyancy force, the Brownian motion effect is larger for small particles. The internal voids within the granules are created by a collapse due to a pressure difference with the ambient atmosphere [119]. Particle size distributions can be strongly influenced by the atomizing technique. On the one hand, a narrow, uniform distribution of the granules is favorable to achieve a good flowability; on the other hand, a wide distribution will render a high packing density due to filling of the interstices between the bigger granules by smaller ones.

### B. Influencing factors on granule size

Influencing factors for the particle size are the applied time for the process (size of the spray drying chamber) [122], the solid concentration, the viscosity of the slurry [111], the feeding rate, the feeding pressure, the drying temperature [113] and nozzle diameter [104]. The size of the granules increases with these factors. However, Elversson et al. found that size of lactose particles increase only up to a certain solid content and then stay constant [104]. A higher flow of the carrier gas was found to decrease the final granule size in this work [104]. Temperature can hereby have an influence on the surface tension of the droplet. However, the influence of surface tension on the particle size is contradictory in the literature. Lukasiewicz stated that surface tension is direct proportional to the granules size for many different nozzles [103] and Cao et al. even produced granules with a 57% larger mean size using water with a much a higher surface tension compared to ethanol [113]. In contrary, Schmid et al. stated that the change of surface tension of differently concentrated trehalose solutions with and without surfactant did not influence the final granule size after spray drying [105]. Iskandar et al. stated that droplet stability strongly depends on hydrodynamic effects during drying [121]. Airflow and temperature conditions can hereby play a major role. According to them, a droplet destabilization could be achieved by an increasing droplet size (e.g. by increasing the power of the nebulizer), an increasing droplet density (e.g. by increasing the solid content to consecutively increase the internal surface energy inside the droplet), an increasing air flow rate (aspirator) and decreasing

the surface tension of the droplet (e.g. by use of surfactants or by increasing the spraying temperature). All of these findings were proven by spray drying of nano-silica particles [121].

### C. Influence of binder choice on final distribution within granules and slurry viscosity

Another important factor for the spray-dried granules is the final binder distribution. Hidber et al. [123] showed a binder migration of PVA to the surface of green parts during drying, where the solvent vaporized and the remaining nonvolatile PVA formed a hard surface layer. The presence of citric acid strongly reduced the PVA adsorption on the particle surfaces. In contrary to PVA, Citric acid has a high affinity to the used  $\text{Al}_2\text{O}_3$  particles and occupied the most adsorption sites. This leads to a further increased segregation of PVA, since more non-bound binder remains mobile in the dispersion. Baklouti et al. [124] claimed also that a water-soluble binder usually migrates with the solvent flow to the granule surface during spray drying. Polyvinyl alcohol (PVA) was there finally distributed in a small surface layer due to solvent evaporation. PVA was in contrary to the used ammonium polymethacrylate not very affine to the alumina particle surfaces and only ca. 20% of binder were adsorbed. Other authors [125, 126] suggested polyacryl acid (PAA) as an alternative for PVA, which also behaves as a binder and as a dispersant by absorbing of ionized carboxylic groups on the particle sites (alumina) and shifting the IEP. However, despite a good flowability, the powder packing was quite loose [126]. Binder addition is also rather critical for de-stabilization of slurries already stabilized with a dispersant. Tsetsekou et al. [112] compared different binders regarding slurry rheological properties for spray-drying of single or mixed oxide systems ( $\text{Al}_2\text{O}_3$  and  $\text{TiO}_2$ ). They showed that carboxymethylcellulose (CMC) significantly increases the slurry viscosity and that acrylic based binders have furthermore a tendency for foaming. The best results in terms of viscosity were achieved by a combination of Darvan C (ammonium polymeric monomer dispersant) with polyethylene glycol (PEG), also better than with PVA. Another organic binder described in literature acting also as dispersant and reducing the viscosity was polyethyleneimine (PEI) [113]. Cellulose binders were described as not satisfying binders due to swelling effect and strong viscosity increase [113].

## 2.2.2 Particle packing theories

To achieve a highly dense PBF-LB processed part a certain density of the powder bed is essential, since sufficient material has to be delivered to the melt-pool. Several approaches were already tried to increase the powder packing. These models are usually based on spherical particles and on the implementation of different particle size fractions, since monomodal packing of uniform particles is always limited to a value of ca. 74% (cubic packing) without packing

failures. Other problematic factors in real-particle systems can be rough particle surfaces leading to bridging forces with the machining tools or a high particle aspect ratio leading to a higher porosity. Furthermore, absorbed polymeric additives (e.g. binder) can sterically hinder particle movement [127].

McGeary [128] achieved a packing density of 80% with bimodal distributions (volume fraction 0.726:0.274) and 89.8% with trimodal distributions (volume fraction 0.647:0.244:0.109) of spheres. Therefore, the ratio between the nearest particle sizes should be more than seven, so that the smaller spheres can enter the interstices of the coarse content. However, attractive van der Waals forces cause agglomeration, especially for the nano and submicron particles. The control of this agglomeration is from great importance to transfer the work of McGeary to spray-dried granules, since a homogenous distribution of all ceramic particles is desired. A dispersion of the powders and prevention of unwanted uncontrolled agglomeration can be achieved by means of a suitable dispersant and milling process. In theory, this will lead to denser spray-dried granules and in conclusion to a higher powder bed density.

Ceramic powders show in general a continuous particle size distribution with a broad range, which can also significantly influence the final packing density [127, 129]. The Andreasen equation for dense packing approximates the proportions of such a dense packing blend by particle size ( $a$ ), maximum particle size ( $a_{\max}$ ) and the distribution modulus ( $1/n$ ):

$$f_M(a) = \frac{n}{a} \left[ \frac{a}{a_{\max}} \right]^n \quad (2)$$

The proportion of fine particles increases, if particle size decreases in this model [127]. According to Andreasen a practical range of  $n$  was 0.33-0.5 for a particular  $a_{\max}$ . However, due to reasons described before, the Andreasen model is also difficult to be applied for submicron particles. Digger Funk identified that the finest particles in real powders are restricted in size. In contrary to Andreasen, who assumed that the finest particles would be infinitesimally small. For this reason, Dinger-Funk added this minimum size of the particle system ( $a_{\min}$ ) to the equation [127]:

$$F_M(a) = \frac{a^n - a_{\min}^n}{a_{\max}^n - a_{\min}^n} \quad (3)$$

Zou et al. applied the Andreasen model for example to increase the particle packing and thus the overall properties of indirect PBF-LB processed  $\text{Al}_2\text{O}_3$  ceramics green bodies and final parts [130]. Mixtures of monomodal distributed small ( $d_{50} = 5.7 \mu\text{m}$ ), medium ( $d_{50} = 22.4 \mu\text{m}$ ) and coarse ( $d_{50} = 112.8 \mu\text{m}$ ) particles were used to adapt the Andreasen model with  $q$ -values 0.3,



0.4, 0.5, 0.6, 0.7 and 0.8. These  $q$ -values depend on the desired properties of the final powder (good flowability ( $<0.25$ ), high packing density ( $<0.36$ )). A too high volume fraction of fine particles in a coarse particle dominated matrix or voids caused by introduction of coarse particles into a system of fine particles can decrease the packing density in those multi-component packing systems [131]. A  $q$ -value of 0.5 was found favorable for the apparent porosity, bulk density, geometric accuracy, mechanical strength and the surface flatness due to a more homogeneous powder dispersion and low amount of coarse powder with low sinter activity.

## 2.3 Mechanisms for particle dispersing

### 2.3.1 DLVO-theory

The DLVO theory (based on Derjaguin, Landau, Vervy and Overbeek) describes the balance of attractive and repulsive forces [132-134]. It takes into account interactions between colloidal particles under consideration of the polarity of the surrounding medium. The repulsive force formation in dispersions is usually due to chemical reactions and an electrical double layer formation due to the attraction of oppositely charged ion in solution. This double layer consist from a diffuse cloud of ions and surface charge of the particle. The attractive forces result from Van der Waals attraction in between the particles. These forces depend on the material, geometries and the media. The origin of the van der Waals forces lies in fluctuations of electrical dipoles or induced dipoles [135].

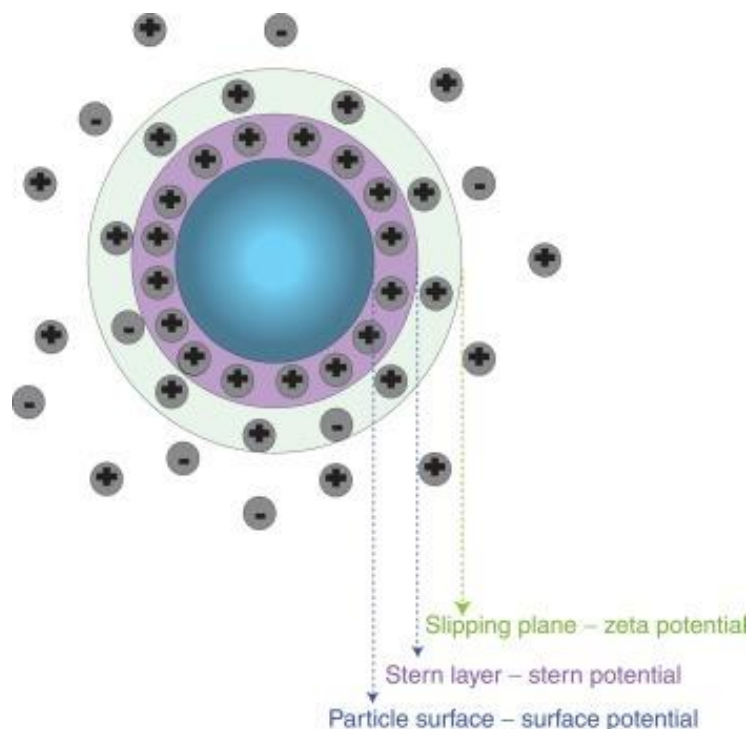


*Figure 11: Zeta potential at the slipping plane within counter ions in the double electrical diffuse layer [136]*

Repulsive forces are described by the Stern [137] and Grahame [138] model in the DLVO theory. An overlap of similar electrical double layers leads to repulsion. The shear plane (following the Stern layer) on the particle surface gives the value of the zeta potential (**Figure 11**). It is the voltage difference between shear plane and bulk electrolyte and measured by movement of charged particle in an electrical field (streaming potential, electrophoresis and electroacoustic). It is the measurable approximation of the surface potential. A higher zeta potential describes higher repulsive forces. It strongly depends from the ionic strength in solution.

The interaction of particles  $\Delta G_{total}$  is described by superposition of attractive forces  $\Delta G_A$  (e.g. Van der Waals forces) and repulsive forces  $\Delta G_R$  (e.g. double layer forces).

$$\Delta G_{total} = \Delta G_A + \Delta G_R \quad (4)$$

Moreover, for the repulsive forces follows with electrolyte concentration  $c_0$ , Boltzmann constant  $k$ , temperature  $T$  and the inverse Debye length  $1/\kappa$ , where the Stern potential has fallen to the value  $1/e$  (Euler's number) [139].

$$\Delta G_R = \frac{64c_0kTZ^2}{\kappa} e^{-\kappa D} \quad (5)$$

The quantity  $Z$  can be calculated by using the ion valency  $z$  and the elementary charge  $e$  [139, 140]:

$$Z = \tanh\left(\frac{ze\Phi_0}{4kT}\right) \quad (6)$$

This parameter is related to the surface potential  $\Phi_0$ . If the surface potential approaches zero,  $Z$  approaches zero. In contrary, a constant value is approached for high surface potentials. This indicates that a upper limit to the force exists independent from the surface charge [140].

Adhesion work, which is the energy needed to dissimilar surfaces from contact to infinite separation, can be described by the attractive van der Waals forces. For the interaction energy (between identical surfaces) follows [139]:

$$\Delta G_A = -\frac{A_H}{12\pi D^2} \quad (7)$$

$A_H$  represents the Hamaker constant, and  $D$  stands for the separation distance. Applying an oversimplification, the Hamaker constant is direct proportional to the square of the polarizability [135] (the tendency of matter to acquire an electric dipole moment in proportion to an applied electric field).

The attractive van der Waals forces can be minimized by the choice of a proper dispersion medium, since the Hamaker constant can differ for ceramic material up to a factor of 50 depending on material and solvent [141].

**Figure 12** shows an energy–distance curve described by the classical DLVO theory presented by Piacenza et al. [142]. The primary minimum indicates the lowest-energy condition. The particles should be preferably here. The primary maximum is an activation barrier, which has to be exceeded to overcome aggregation, preferably by collision with sufficient energy. The secondary minimum could be seen as a flocculated state, which can break by slight shearing. Adhesion is weak and easy reversible in this minimum [135].

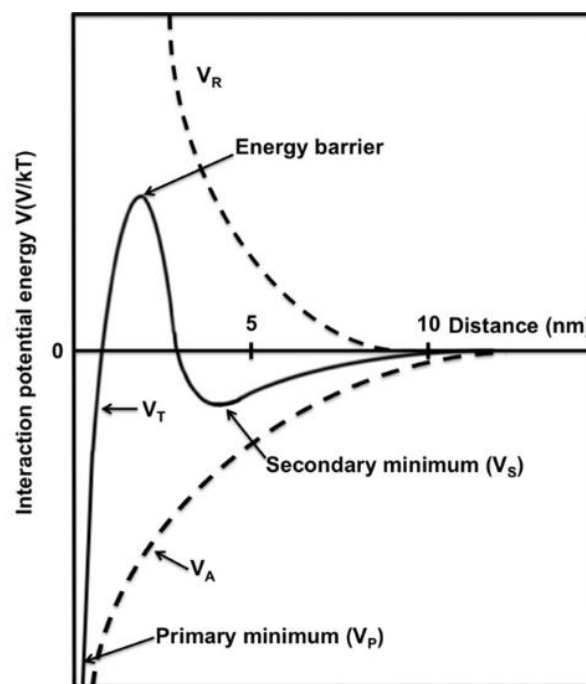


*Figure 12: Energy–distance curve described by the DLVO theory [142]*

### 2.3.2 Surface charge and electrical double layer

The particles in ceramic processing are generally below a few microns or in the submicron range. Smaller particles have an increased sintering activity and reduce furthermore the necessary sintering temperature. However, attractive van der Waals forces can increase strongly, especially, when working with nano dopants ( $< 100$  nm). Gravity forces dominate for particles bigger than  $10\text{ }\mu\text{m}$  with rough surfaces and thus only a few contact points exist [28]. However, in contrary to organic solvents, interparticle interactions can be very well controlled by electrostatic forces controlled by surface modification in water-based slurries [26] and thus, a homogeneous distribution of particles with different sizes can be reached. As an alternative steric

stabilization in nonpolar solvents and polar solvents can be done by comb-type block copolymers or hydrophobic surfactants.

Surface charges are formed by a direct ionization in water (polar medium). First hydroxide is formed at the particle surfaces. In a second step, these hydroxy groups are protonated or deprotonated at the surface. Depending on the pH-value of the solution, a positive, negative or neutral surface charge can be formed. The addition of acid or base can shift the zeta-potential values towards low and high pH values. A positively charged surface indicates an excess of surface protons, whereas a negatively charged surface indicates a proton deficiency [143]. At the point of zero charge, the surface potential is zero. This surface charge describes the force of the repulsive electrical double layer. Zeta potential measurements evaluate the charge of a shear plane close to the surface (**Figure 11**). Additionally, a final check by particle size distribution measurements can ensure the dispersion quality without appearing agglomerations. In general, the absolute value of the zeta potential should be bigger than 25 mV to avoid flocculation or coagulation.

Surface charge formation by molecular species, which is generated by complex formation, requires firstly a deprotonation and secondly chemical adsorption to the surface. Specific ion adsorption leads to a covered surface of the oxide with negative or positive charged complex forming ions and the zeta potential curve can be shifted to smaller or bigger values. Depending on the surfactant (magnitude of charge) and the added amount, different powders can be thus electrostatically modified and stabilized at different pH values in polar protic solvents with high dielectric constant and ionic strength. In the optimized case, the adsorption is limited to a monolayer coverage. However, it has to be taken into account that dispersions are not stable close to the isoelectric point (IEP) or at too high salt concentrations. At the IEP, the charge of the electrical double layer at the shear plane is balanced with counter ions and the repulsive forces are approximately zero. Known examples are polyelectrolytes, self-assembling organic molecules, citrates, acrylates, multivalent ions, aromatic carboxylic acids, aromatic phenols, combined phenols/acids, gallic acid and more [144]. However, they should be carefully chosen, since impurities are not desired in ceramics. Phosphates or silicates for example can be also used as stabilizers [145]. However, they can build residuals after sintering and build glass phase in the material. Adsorbed multivalent ions can change the properties, when adsorbed on the surface.

Hidber et al. [146] showed that citrate with a high affinity for aluminum oxide can be a convenient dispersing agent, since the adsorption of the citrate creates a negatively charged surface

by exchange of hydroxyl groups with carboxylate ions. This causes a change of the double layer repulsion (electrostatic stabilization). Because of this formation of a negatively charged citrate-alumina complex the point of zero charge of the amphoteric oxide can be adjusted at pH between 9 and 3. The molecular species connects with the particle by a hydrogen bridge bond. This combination of OH and COOH groups leads to an excellent adsorption and simultaneously a high influence on surface charge. With increasing addition of citric acid the absorbed percentage on the surface decreases and the excess remains in solution. The PZC can only be reduced until a specific amount, because of saturation on the particle surfaces. Hidber et al. claimed that only a citrate monolayer is formed on the surface [146]. Furthermore, the adsorption behaviour of the citrate depends on the pH of the dispersion. A pH increase causes a decrease of the citric acid adsorption, since the electrostatic attraction between the positively charged alumina and the citrate anion diminishes.

## 2.4 Conceptualization of new ideas for laser powder bed fusion of aluminum oxide

**Figure 13** summarizes the current challenges of laser powder bed fusion of high performance aluminum oxide ceramics targeted in this PhD study by different powder technology approaches.

### Challenge:

Low **thermal shock resistance** and **crack formation**

### Approach:

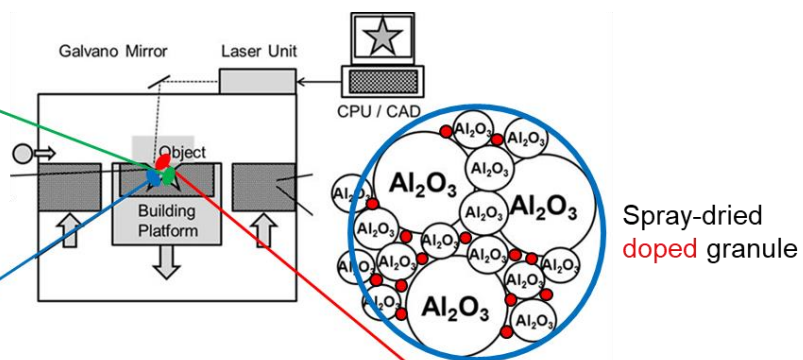
Reducing of thermals stresses by additives

### Challenge:

Weak densification and limited powder flowability

### Approach:

**Spray granulation of multimodal alumina combinations** to increase powder flowability and packing density



### Challenge:

Low laser light absorption of alumina

### Approach:

Addition of **colored nano oxides**

*Figure 13: Challenges of laser powder bed fusion of aluminum oxide ceramics and approaches to solve these.*

The challenges range from weak densification and limited powder flowability, to low powder absorptance of the visible and near infrared laser light as well as low thermal shock resistance and therefore, a severe cracking issue. The approaches conducted in this work are the use of spray granulation of multimodal aluminum oxide combinations to improve the flowability and powder bed density, the addition of colored metal oxide nanoparticles to the granules to improve the powder absorptance and the test of different additives to reduce the thermal stress generated during laser processing.

### **2.4.1 Densification, powder flowability and absorption issue**

A high density is a key factor for ceramic parts to achieve good mechanical properties. In chapter 2.1.4.4., it was noticed that porosity lower than 10% could be achieved only by using high temperature preheating [15, 16, 54] or by using dopants [56] in PBF-LB for different oxide ceramics. This is due to low absorption in the visible or near infrared range of alumina at room temperature [20]. With increasing temperature the absorption of alumina can increase. This was already shown for laser excitation [147, 148]. Other authors mixed carbon [50, 56-58, 149] and SiC [58] together with alumina particles to improve the interaction between laser light and the powder. In the present work, alumina granules are directly doped with  $\text{Fe}_2\text{O}_3$  and  $\text{MnO}_2/\text{Mn}_2\text{O}_3$  nanoparticles during spray drying, since these dopants are known as effective absorbers to improve the absorption of alumina granules in the visible and near infrared range [17, 95, 150-152].  $\text{Fe}_2\text{O}_3$  and  $\text{Mn}_2\text{O}_3$  have a bandgap of 2.19 eV [153] and 3.32 eV [154] respectively.

These dopants can have a significant influence on microstructure, phase composition and properties of sintered alumina, which has already been extensively studied in the past for conventional sintered alumina. For example, a complex series of oxides can arise by thermal treatment in manganese-doped alumina, since manganese shows a variable valency change. Thus, different manganese cations with different valency states can replace the aluminum cations in the lattice, which results in fast diffusion lowering the energy required for sintering [155, 156]. It is already established that up to 2% manganese oxide increases grain growth in  $\text{Al}_2\text{O}_3$  and promotes excessive irregular grain growth grain growth [157]. A density between 98-99% [155, 158] was reached for sintering temperatures between 1550 °C and 1650 °C independent of the amount of the dopant. Aluminum oxide doped with manganese showed increased hardness and flexural strength [155, 158].  $\text{Fe}_2\text{O}_3$  also enhances sintering by entering the lattice of alumina [156]. Preliminary studies on iron oxide doped alumina granules showed that thermal treatment in air leads to this homogeneous incorporation. At 1600 °C a single corundum type phase was created, where iron diffused in the alumina lattice [159]. With more than 1% of iron oxide the

grain growth is inhibited and results in equiaxed, spheroidal grains [157]. Ferric oxide doped alumina samples showed an almost consistent flexural strength value up to 0.1 wt%, a slight decrease up to 2 wt% and a following strong decrease as the ferric oxide amount was further increased [160]. By seeding the alumina with 4 wt% iron oxide the temperature to reach full density could be lowered to 1350 °C [161].

Spray drying creates preferably spherical granules, which contributed to a high flowability necessary for the PBF-LB process [127, 162]. Reed [127] stated that granules with smooth, non-sticky surfaces that are bigger than ca. 40 µm have good flow behavior. He described also that granule surfaces become smoother when composed of finer particles and at the same time, none of the finer particles stick to the coarser granules. Furthermore, irregular shaped granules may impede the flow by bridging and should be removed by sieving to achieve a high flowability [127]. Ramavath et al. reported that narrow particle size distributions and spherical shapes of alumina granules resulted in excellent flow characteristics and a reduced cohesion index in comparison to as received alumina powders. They stated that morphology of the granules plays a major role for the cohesion index and flowability, rather than the sizes of the granules [162]. A further advantage of spray-dried granules is the implementation of submicron- and nanopowders and thus the use of their high surface activity.

#### **2.4.2 Reduction of crack formation**

Crack formation is a main issue in PBF-LB of alumina due to low thermal shock resistance of the material and the high thermal stresses generated in the melting and resolidification process. Furthermore, microstructure properties as grain size and shape are generated simultaneously during this process and can have a large impact on mechanical or other desired physical properties. The main-focus of the works found in the literature was hereby on process parameter optimization and quality improvement to solve the crack formation issue.

In the present work, several additives are proposed to solve the problem of crack formation via customizing of material compositions. These additives range from mullite with a lower thermal expansion coefficient than alumina and a high silica content for a possible glass phase formation to rare earth oxide addition, which were seen in the literature to facilitate formation of amorphous aluminum oxide [163]. Other additives were mixed to aluminum oxide to create secondary phases with either a low thermal expansion (aluminum titanate from alumina and titania) or even a negative thermal expansion (zirconium tungstate from zirconia and tungsten oxide) and thus to compensate cracks formed by thermal stresses.

### A. Mullite addition

As described in chapter 2.1.4, Exner and Regenfuss et al. [6, 7, 60-62] achieved highly dense glass composites made of an alumina and silica composite. XRD measurements showed a partly mullitization after laser processing, which increased after thermal treatment. Heinrich and Gahler et al. [2, 3, 64] reported similar results for ceramic parts laser processed from  $\text{Al}_2\text{O}_3$  and  $\text{SiO}_2$ . In contrary to the work of Exner et al. [6, 60], an increased mullite formation and re-crystallization controlled by dissolution of alumina was reported already after the laser process without thermal post-treatment [64]. A formation of mullite needles was described to be beneficial for increasing the mechanical stability by reinforcement. Thermal post-treatment led to a formation of cristobalite as well as further mullitization [3, 64]. The idea was to use the low thermal expansion coefficient and the partial melting with a low glass transition temperature of silica to avoid thermal stresses due to shrinkages during cooling [99]. The creation of mullite made from a stoichiometric ratio of (crystalline) alumina (71.8 wt%) and (partly crystalline) silica (28.2 wt%) was also possible by directed energy deposition [164]. In this process, the melt-pool is formed by irradiation of the substrate and subsequent powder is added into the melt-pool by a powder nozzle coupled to the laser beam. Mullite has similar to silica a low thermal expansion coefficient, which is beneficial for reducing thermal stresses. Even though the density was higher than in traditional formed mullite ceramics with 97.8% [165], the mechanical properties were lower due to defects [166, 167] such as pores and cracks within the microstructure. Silicon was predominantly detected by EDS analysis at grain boundaries of the columnar shaped mullite crystals oriented parallel to the building direction, which may be a proof that a thin glass matrix was formed between the grains, explained by the fast cooling and the limited time for crystallization.

### B. Generation of amorphous alumina

Rosenflanz et al. [163] reported the possibility to form amorphous and transparent bulk glasses based on alumina and rare earth oxides without containing a conventional glass-forming component. By increasing the ionic size of the rare earth oxide, a depression of the glass transition temperature and the crystallization temperature happened. Moreover, the gap between these two temperatures also widened. Furthermore, the viscosity depended on the ionic size. With the same deformation temperature, the viscosity decreased and same temperature difference between glass transition temperature and deformation temperature a higher viscosity appeared with larger ions.



The low glass-transition temperature to generate amorphous alumina should be in theory beneficial to avoid crack formation, since cracks can only be formed in solid material and not within the molten condition of the material above the crystallization temperature. The eutectic ratio of rare earth oxides to alumina was given to be suitable to achieve amorphous phase. As suitable rare earth oxides, cerium oxide and yttria were chosen, since they offer a suitable ionic size (0.90 Å for  $\text{Y}_2\text{O}_3$  and 1.01 Å for  $\text{CeO}_2$  [168]), a smaller bandgap than alumina (6.08 eV for  $\text{Y}_2\text{O}_3$  [169], 3.19 eV for  $\text{CeO}_2$  [170] and 8.80 eV for  $\text{Al}_2\text{O}_3$  [171]) and they are not too exotic and thus too expensive.

The use of  $\text{Y}_2\text{O}_3$  is a quite common additive to  $\text{Al}_2\text{O}_3$  to in-situ generate eutectic ceramic matrix composites in DED. These show a refined interpenetrating microstructure and the mechanical properties in terms of fracture toughness or strength can be improved especially at high temperatures [172, 173]. Crack propagation is usually decreased in such materials. This was reported by several authors [174-177].

### C. Addition of reduced $\text{TiO}_{2-x}$

The potential of crack reduction or even total suppression in melt grown ceramics lies also in in-situ reactions. A possible starting combination can be for example alumina and titania powders to form aluminum titanate [178-180]. This phase has a low thermal expansion coefficient, low thermal conductivity and therefore excellent thermal shock behavior [181] and improves the poor fracture toughness of  $\text{Al}_2\text{O}_3$  through crack deflection and residual compressive stress regions [182, 183]. Furthermore, aluminum titanate based ceramics show also a low Young's modulus, what is also beneficial for the thermal shock resistance [184]. The local residual stresses and microcracks are usually generated by the difference of thermal expansion coefficients between  $\text{Al}_2\text{O}_3$  and  $\text{Al}_2\text{TiO}_5$  [182]. Furthermore, Abali et al. found that with an increasing amount of  $\text{TiO}_2$  (40 to 48 mol%) the hardness decreases and the thermal expansion increases in these alumina-titania composites [185]. Titania can also influence the sintering behavior of alumina. Sathiyakumar and Gnanam [158] reported that up to a doping amount of 0.2 wt%  $\text{TiO}_2$  is effective for grain growth promotion with the result of a high density and bending strength of 409 MPa already achieved at a maximum sintering temperatures of 1400 °C. This amount is close to the solubility limit of 0.25-0.3 mol% of titania in alumina given by Winkler et al. [186]. With higher additive amounts, the sintering rate started to decrease and grain size decreased with contents of up to 4.0 wt% [158]. However, a bending strength of 347 MPa was still given at this amount.  $\text{Al}_2\text{TiO}_5$  was preferably found at triple junctions and occasionally along the grain boundaries in these samples [158].

This secondary aluminum titanate phase is prone to decomposition into  $\text{Al}_2\text{O}_3$  and  $\text{TiO}_2$ , especially during thermal shock in a temperature range between 750 and 1300 °C [187]. This decomposed  $\text{Al}_2\text{TiO}_5$  can be recreated, when heated above 1300 °C [188]. Due to decomposition, the material loses the low thermal expansion coefficient and the excellent thermal shock behavior [189]. However, the decomposition was already proven to be suitable to increase the strength values after several thermal shock cycles compared to the as sintered samples [190], since it can generate areas with compressive stresses by the accompanied volume change of  $\text{Al}_2\text{TiO}_5$  located at the grain boundaries of an alumina ceramic [190, 191]. After five quenching cycles, no  $\text{Al}_2\text{TiO}_5$  was anymore found in these samples. Much work was done to improve the thermal durability of this material. The first approach was done by the formation of solid solutions with the additives  $\text{MgO}$ ,  $\text{Fe}_2\text{O}_3$ , or  $\text{TiO}_2$  in the aluminum titanate lattice [184]. Another approach was the limitation of microcracks, microcrack growth and grain growth by the addition of  $\text{SiO}_2$ ,  $\text{ZrO}_2$ ,  $\text{ZrTiO}_4$  or mullite, which can restrain the tendency of  $\text{Al}_2\text{TiO}_5$  to decompose [190].

Crack-free parts could be already manufactured by DED containing alumina and aluminum titanate [178]. The reaction formed phase was mainly found as a matrix at  $\alpha$ -alumina grain boundaries consisting of  $\text{Al}_2\text{TiO}_5$  and also the peritectic phase  $\text{Al}_6\text{Ti}_2\text{O}_{13}$  [180]. However, the difference in term of crystal structure and physical properties of these phases is not relevant. Cracks could be suppressed proportionally to the amount of additive used up to 50 wt% [178]. However, due to the low mechanical strength of aluminum titanate, the best flexural strength was achieved for amounts of additive below 10 wt% [179]. Higher amounts of aluminum titanate led to a strong decrease of flexural strength, hardness and fracture toughness accompanied by an increase of the porosity up to 5% [179]. A  $\text{TiO}_2$  addition of 5 wt% [180] was proven to be the most suitable amount in terms of fracture toughness [179]. Also in laser cladding,  $\text{Al}_2\text{O}_3$ - $\text{TiO}_2$  powders were already applied without cracks, low porosity and an excellent bonding behavior between ceramic layer and metallic substrate [192-194]. Wang et al. needed to apply a preheating of 500 °C to achieve these properties [194]. The substrates varied hereby from Ti-6Al-4V [192] to nickel based alloys [193, 194] and the amount of  $\text{TiO}_2$  to  $\text{Al}_2\text{O}_3$  was fixed in these works to 13 wt%. The powder was hereby given to melt pool in form of spray dried granules [192] or prior to laser processing by pressing with a pressure equipment [194]. All authors reported different solidification microstructures within the solidified layer depending on different cooling rates. An effect of substrate preheating resulted in fine equiaxed crystals at the upper region, columnar crystals in the middle region and very fine equiaxed crystals at the

bottom region [194]. The different microstructure evolved from a fully melting or partially liquid-phase-sintering [193]. The final stable phases were  $\alpha$ - $\text{Al}_2\text{O}_3$  as well as some brookite  $\text{TiO}_2$  and  $\text{Al}_2\text{TiO}_5$ . A formation of  $\gamma$ - $\text{Al}_2\text{O}_3$  was not detected [192-194].

In the present work, the titania dopant was reduced under argon/hydrogen atmosphere, which led in consequence to a blackish color of the granules. This enabled to use only titania as an effective dopant for laser processing, since the bandgap of non-treated titania is in general too big to be laser processed in the visible or near-infrared range of the light. Reduced  $\text{TiO}_{2-x}$  is normally used due to enhanced photocatalytic effect. It offers not only a smaller bandgap (depends on the reduction grade), but also shows electrical higher conductivity [195]. Other techniques were also already shown to be suitable to produce  $\text{TiO}_{2-x}$  (magneli phases) such as by pulsed UV laser irradiation in acetonitrile [196], using zirconium getter [195], at 950 °C with pure hydrogen [197] or  $\text{N}_2$  and  $\text{H}_2$  mixture [198], by the aid of molten reduced aluminum [199], by the use of a carbothermal reduction via carbon black powder under constant argon flow [200] or even with 35 bar at a hydrogen atmosphere [201] and others. The UV-Vis spectra of  $\text{TiO}_2$  treated under hydrogen for up to 20 days at room temperature is given in **Figure 14**. The dark color appeared after 15 days.

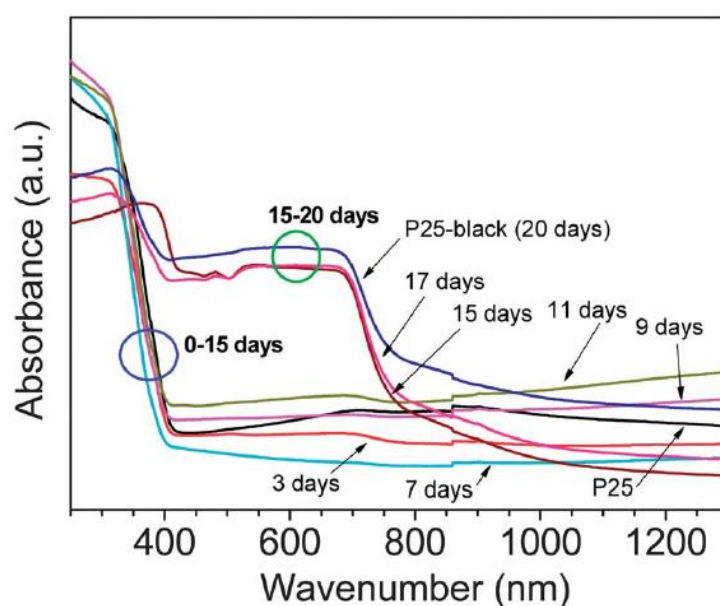


**Figure 14:** UV-Vis spectra of  $\text{TiO}_2$  treated under hydrogen for up to 20 days at room temperature [201]

Since titania particles are untreated only available as nano- or submicron particles, pre-treatment temperatures have to be carefully evaluated, since already at low temperatures sintering and rapid grain growth can appear. Dittmann et al. [202] measured for nano titania Aeroxide P25 (Evonik Degussa) a start of shrinkage at 500 °C in air atmosphere. At 780 °C, the whole

sample was transformed from anatase to pure rutile and at starting from 800 °C, rapid grain growth appeared (average grain size of 6  $\mu\text{m}$  at 1050 °C). At 900 °C, the whole sample was already completely sintered. The native titania had a rutile content of 14 wt%, BET specific surface area of 46  $\text{m}^2/\text{g}$  and BET equivalent particle diameter of 33 nm. Mazaheri et al. [203] described a similar phenomenon for the same material. Strong sintering and rapid grain growth was reported already at temperatures of 650 and 800 °C, respectively.

### D. Generation of zirconium-tungstate

By the generation of zirconium tungstate ( $\text{ZrW}_2\text{O}_8$ ) during processing, thermal stresses could be in theory minimized in the final PBF-LB aluminum oxide ceramic. The thermal expansion coefficient of zirconium tungstate is known to be negative [204, 205] and thus the generation of this phase could create expansion during cooling and this may result in compressive stresses. Furthermore, this would give in theory the chance to adjust the resultant thermal expansion in the oxide ceramic to near zero. The negative thermal expansion (NTE) effect of  $\text{ZrW}_2\text{O}_8$  is the largest known over an extended temperature range of 0.3 – 1050 K (coefficient of thermal expansions (CTE) of  $-8.7 \times 10^{-6} \text{ 1/K}$  for  $\alpha\text{-ZrW}_2\text{O}_8$  (20 – 430 K) and  $-4.9 \times 10^{-6} \text{ 1/K}$  for  $\beta\text{-ZrW}_2\text{O}_8$  (430 – 950 K)) [204, 205]. Zirconium tungstate is a metastable phase and can be achieved by rapid quenching, which is the case in the PBF-LB processes. By this rapid cooling a decomposition into  $\text{WO}_3$  and  $\text{ZrO}_2$  can be avoided [205, 206]. The thermodynamically stable temperature area is between 1105 and 1257 °C [207, 208]. Above 1257 °C  $\text{ZrW}_2\text{O}_8$  melts incongruently to  $\text{ZrO}_2$  and a liquid [148]. Chen et al. [206] sintered the material for 6 h between 1155 and 1200 °C with a subsequent quenching in liquid nitrogen. This appropriate heat treatment decreased the CTE of the parts even more to a mean value of  $-11 \times 10^{-6} \text{ 1/K}$ . De Buysser et al. [209] heated prior pressed spray dried granules made from  $\text{ZrO}_2$  and  $\text{WO}_3$  up to ca. 1177 °C. Air was shown by Sun et al. [210] as an alternative medium for quenching .

Since  $\text{ZrW}_2\text{O}_8$  is transparent throughout the visible spectrum [204], pure  $\text{WO}_3$  and  $\text{ZrO}_2$  powders (bandgaps of 2.6 eV [211] and 5.1 eV [212]) have to be used to increase sufficiently the powder absorptance for a successful PBF-LB process. To achieve only the pure  $\text{ZrW}_2\text{O}_8$  phase according to the phase diagram [207, 208], a mixture of a 76.4 Vol% (68 Mol%)  $\text{WO}_3$  and 23.6 Vol% (32 Mol%)  $\text{ZrO}_2$  has to be used.

The  $\text{ZrW}_2\text{O}_8$  structure consists of a  $\text{ZrO}_6$  octahedron centered at the origin and face center positions. These octahedra are surrounded by  $\text{WO}_4$  tetrahedra. Upon heating a phase transition from  $\alpha\text{-}$  to  $\beta\text{-ZrW}_2\text{O}_8$  occurs at about 150-155 °C. Furthermore, the high-pressure phase  $\gamma\text{-ZrW}_2\text{O}_8$  can be created at pressures of about 2 kbars [204]. All of these phases offer a negative

thermal expansion behavior with the highest value for  $\alpha$ -ZrW<sub>2</sub>O<sub>8</sub> [204]. The effect of volume contraction is based on an open network structure (so-called framework structure [209]) with oxygen in double coordination to the metal cations. The transverse thermal motion of oxygen in the threefold axis of two W atoms and one O atom can cause thermal contraction by a dynamical disorientation. These thermal motions of the various metal-oxygen-metal linkages are coupled by tilting of corner-sharing linked polyhedras [204], which can fulfill a three-dimensional rotation. A transverse vibration of a bridging O in a framework in which M-O bond distances remain unchanged will result in a contraction of the M-M distance and this in turn results in a negative coefficient of thermal expansion [205]. In other words, the stiff polyhedral in the rigid unit modes have strong M-O bonds and short O-O distances. In case of coupled rotations of these polyhedra and contemporaneous constant intrapolyhedra bond distances and intra-polyhedra, the material exhibits a decrease in volume [209]. These anisotropic thermal vibrations are usually also present in other materials, but expansion coefficients are mostly dominated by other forces, which lead to a positive thermal expansion [205].

To avoid the formation of other reaction products with alumina (e.g. Al<sub>2</sub>W<sub>3</sub>O<sub>12</sub>, AlWO<sub>4</sub>, and etc. [213]), which can have a low positive thermal expansion coefficient [214, 215], the use of coarse grained alumina with less tendency for melting or reaction was tested in the current work. However, this also increases the possibility of having undesired coarse alumina grains in the final laser processed part. Sun and Kwon reported also that a small addition (0.07 wt%) of nano Al<sub>2</sub>O<sub>3</sub> was helpful to increase the final relative density due liquid phase formation of Al<sub>2</sub>W<sub>3</sub>O<sub>12</sub> and did not change the CTE [210]. A further challenge of NTE materials is the low mechanical strength due to microcracking [204] and high porosity (11.0 – 17.3 % in [206]) after processing. Microcracks can develop below the consolidation temperature of the NTE materials, since thermal expansion often occurs anisotropic (strong expansion and contraction in different spatial directions within the material possible) [204]. Due to these features, De Buysser et al. measured for pure ZrW<sub>2</sub>O<sub>8</sub> a 3-point bending strength of only 14 MPa [209]. In terms of resistance to thermal shock, the microcracking can be also beneficial and increase the resistance [204]. Microcracking and porosity could be decreased after an annealing step [210]. Furthermore, ZrW<sub>2</sub>O<sub>8</sub> is in general unsuitable for high-temperature applications due to an instability from 600 to 1105 °C [204] and shows a rather big volume change at 155 °C due to the  $\alpha$ - to  $\beta$ -phase transformation, what can also cause stresses in the surrounding material. When working with this material, the rule of mixture for thermal expansion coefficient did not work in past studies [209, 213], because of the low stiffness of ZrW<sub>2</sub>O<sub>8</sub> [213] and the apparent voids and cracks due to thermal stresses [209, 216, 217]. Sun and Kwon [210, 218] suggested as

follows the Levin model for prediction of their  $\text{ZrO}_2/\text{ZrW}_2\text{O}_8$  composite CTEs using a compliance tensor. However, this compliance tensor has to be calculated before by the Mori-Tanaka approach [219]. Romao et al. [213] suggested to use the Turner model [220, 221] for prediction of the CTE for even more complex composites consisting of ATZ with incorporation of zirconium tungstate and aluminum tungstate:

$$\alpha_c = \frac{\alpha_1 K_1 V_1 + \alpha_2 K_2 V_2}{K_1 V_1 + K_2 V_2} \quad (8)$$

$\alpha$  is the CTE,  $V$  is the volume fraction and  $K$  is the bulk modulus in this formula. The subscripts  $c$ , 1 and 2 refers to the composite, the first phase ( $\text{ZrW}_2\text{O}_8$  in the present work) and the second phase ( $\text{Al}_2\text{O}_3$  in the present work), respectively. Bulk modulus (volumetric stress and strain) and thermal expansion values are 13 GPa [210] and  $-4.9 \times 10^{-6}$  1/K for  $\beta$ - $\text{ZrW}_2\text{O}_8$  [204] and 250 GPa [222] and  $8.1 \times 10^{-6}$  1/K [223] for  $\alpha$ - $\text{Al}_2\text{O}_3$ . The high importance of the bulk modulus leads to an optimized calculated ratio of 96.9/3.1 Vol% of  $\text{ZrW}_2\text{O}_8/\text{Al}_2\text{O}_3$  for an almost zero expansion (CTE =  $5.2 \times 10^{-8}$  1/K) according to the Turner model.

Zirconium tungstate could be already synthesized via rapid laser processing of densely pressed blocks of  $\text{WO}_3$  and  $\text{ZrO}_2$  by a  $\text{CO}_2$  laser (laser scan speed: 1-5 mm/s, laser power: 400-800 W) [224]. Both starting materials show a high absorption at the wavelength of the  $\text{CO}_2$  laser (10.6  $\mu\text{m}$ ) [225, 226]. The samples showed an oriented growth of nano-crystallites depending on the heat-transfer direction and mainly the high-pressure phase  $\gamma$ - $\text{ZrW}_2\text{O}_8$  was present after laser processing (scan speed  $> 2$  mm/s), indicating compressive stresses induction during solidification. This phase turned to  $\alpha$ - $\text{ZrW}_2\text{O}_8$  after annealing or with scan speeds  $< 2$  mm/s [224].

### **3 Doped spray-dried granules to solve densification and absorption issue in laser powder bed fusion of alumina**

Parts of this chapter were already published in *Advanced Engineering Materials*, Volume 21 (6), (2019) 1801351, in *Applied Surface Science*, Volume 520, (2020) 146304 and in *Open Ceramics*, Volume 2, (2020) 100007.

#### **3.1 Dispersing of aluminum oxide, iron oxide and manganese oxide**

##### **3.1.1 Experimental**

The work was accomplished with several alumina powders. Nano  $\gamma$ -/ $\delta$ -alumina Aeroxide AluC (Evonik Industries AG, Germany), submicron  $\alpha$ -alumina Taimicron TM-DAR (Taimei Chemicals Co. LTD, Japan), AA03 (Sumitomo Chemical Co. LTD, Japan) and spherical micro-sized  $\alpha$ -alumina AA3 (Sumitomo Chemical Co. LTD, Japan) were used to achieve bimodal or trimodal distributions within the spray dried granules. Additionally, spherical nano- $\alpha/\gamma$ -Fe<sub>2</sub>O<sub>3</sub> (L2715D, BASF SE, Germany), elongated  $\alpha$ -Fe<sub>2</sub>O<sub>3</sub> hematite particles [227] (L2818D, BASF SE, Germany) and nano-MnO<sub>2</sub> particles (US3319, US Research Nanomaterials, USA) were introduced during spray drying to improve the absorption of the green laser light. The use of

ammonium citrate dibasic p.a. 98% (Sigma Aldrich Corp., USA) as surfactant and PEG 35000 (Sigma Aldrich Corp., USA) as binder guaranteed a homogeneous dispersion of all particles in water as well as the formation of non-broken granules with high strength after spray granulation. For pH-value adjustment of the MnO<sub>2</sub> dispersion a 10% diluted ammonium hydroxide solution (Carl Roth GmbH + Co. KG, Germany) was utilized.

The absolute densities of all powders were measured by helium pycnometry (AccuPyc II 1340, Micromeritics, USA). The specific surface area (SSA) was evaluated by BET (Brunauer–Emmett–Teller) measurements (SA 3100, Beckman Coulter, Krefeld, Germany). Prior to the measurements, the raw powders were degassed with synthetic air for two hours at 180 °C to remove adsorbed water from the surfaces (SA-PREP Surface Area Outgaser, Beckman Coulter, Krefeld, Germany). For all these powders a BET average particle size was calculated from the absolute density and the corresponding SSA assuming monomodal spherical particles according to the Sauter mean diameter [228]. The surface area of AA18 was too small to evaluate an accurate value for the SSA. To determine the surface potential and the saturation amount of the dispersant on the particle surfaces, zeta potential measurements were carried out by an electroacoustic method with a ZetaProbe Analyzer (Colloidal Dynamics, USA). The saturation amount of the dispersant, which should guarantee high surface potential of the particles for homogeneous dispersion in Nanopure water and low residuals of dispersant in the spray dried granules, was found by evaluation of the change of PZC (point of zero charge) as a function of added amount. The zeta potential measurements were carried out at different pH-values with an equilibration delay of 30 seconds. To adjust the pH of the utilized 5 wt% suspensions a 0.1 molar solution of HCl (Carl Roth GmbH + Co. KG, Germany) and 0.1 molar NaOH (Sigma Aldrich Corp., USA) were added. Required dielectric constants were taken from literature [229]. After determination of the saturation amount, particles were mixed with the surfactant and dispersed in Millipore water by roll milling, vibration milling or a combination of both with ZrO<sub>2</sub> milling balls ranging from 0.4, 1 and 5 mm. A detailed attribution of the used milling ball size to the oxide particles is given for each material in chapter 3.1.4. Particle size distributions of the dispersed starting materials were measured in water by laser diffraction (LS 13320, Beckman Coulter GmbH, Germany) and dynamic light scattering (ZetaSizer Nano ZS, Malvern Panalytical Ltd, United Kingdom). The required refractive indexes and extinction coefficients for both size measurements were taken from [230] for Fe<sub>2</sub>O<sub>3</sub>, Al<sub>2</sub>O<sub>3</sub> and from [231] for MnO<sub>2</sub>.



Particle shapes were investigated with Scanning Electron Microscopy (VEGA3 Tescan, Tescan instruments, Brno, Czech Republic) for the micron sized particles and with Transmission Electron Microscopy (JEM-2200FS 200kV, Jeol USA, Peabody, USA) for the nano-particles. Before SEM analysis, the powder was distributed with compressed air on the adhesive carbon sample tabs and then sputtered (Sputter coater 108 auto, Tescan instruments, Brno, Czech Republic) with Au-Pd twice using angles of 45° and 90° (sample carrier to sputter direction). Secondary electron images were then taken with an accelerating voltage of 10 kV. TEM samples were prepared by adding a drop of isopropanol dispersed powder on a carbon film coated copper grid (Lacey Carbon Film/Cu 200 mesh, PLANO GmbH, Germany).

### 3.1.2 Particle characterization

The absolute densities, the specific surface area (SSA) and the resulting BET average particle size of the raw powders were determined before the dispersing step. The results are summarized in **Table 4** and **Table 5**.

**Table 4:** Absolute densities, specific surface area and BET average particle size of alumina powders

Raw material	Al <sub>2</sub> O <sub>3</sub> AA18	Al <sub>2</sub> O <sub>3</sub> AA3	Al <sub>2</sub> O <sub>3</sub> AA3	Al <sub>2</sub> O <sub>3</sub> Taimicron TM-DAR	Al <sub>2</sub> O <sub>3</sub> Aerioxide AluC
Absolute density [g/cm <sup>3</sup> ]	3.99	4.01	4.03	3.95	3.5 (company given value)
Specific surface area [m <sup>2</sup> /g]	< 0.1	0.4	5.5	11.8	95.3
BET average particle size [nm]		3700	269.9	128.8	18.0

**Table 5:** Absolute densities, specific surface area and BET average particle size of dopants

Raw material	Fe <sub>2</sub> O <sub>3</sub> L2715D	Fe <sub>2</sub> O <sub>3</sub> L2818D	MnO <sub>2</sub> /Mn <sub>2</sub> O <sub>3</sub> US3319
Absolute density [g/cm <sup>3</sup> ]	4.38	4.11	4.28
Specific surface area [m <sup>2</sup> /g]	69.7	126.1	22.7
BET average particle size [nm]	19.6	11.6	61.7

The densities measured by helium pycnometer for the single powders were 3.99 g/cm<sup>3</sup> for AA18, 4.01 g/cm<sup>3</sup> for AA3, 4.03 g/cm<sup>3</sup> for AA03 and 3.95 g/cm<sup>3</sup> for Taimicron TM-DAR. These values are in good accordance with the company given values. For the nano particle dopants, this was only the case for Fe<sub>2</sub>O<sub>3</sub> L2715D (company given values of 4.4 g/cm<sup>3</sup>). However, the density of 4.11 g/cm<sup>3</sup> for L2818D and 4.28 g/cm<sup>3</sup> for MnO<sub>2</sub> US3319 differ significantly from the company quoted density of 4.5 g/cm<sup>3</sup> and 5.03 g/cm<sup>3</sup>, respectively. In the case of manganese oxide, this can be explained by a significant amount of Mn<sub>2</sub>O<sub>3</sub> (68%) with a

theoretical density of  $4.5 \text{ g/cm}^3$ , as seen by XRD. By this method, L2715D was identified as 75%  $\alpha\text{-Fe}_2\text{O}_3$  and 25%  $\gamma\text{-Fe}_2\text{O}_3$ . The measured densities for the organic materials were  $1.23 \text{ g/cm}^3$  for PEG 35000 and  $1.60 \text{ g/cm}^3$  for ammonium citrate dibasic. In the case of Aerioxide AluC, the company given value of  $3.5 \text{ g/cm}^3$  was used to calculate the BET average particle size and the final relative density of the laser processed parts, since the powder could not be compacted sufficiently inside the measurement chamber of the pycnometer due to their low packing density.

SEM and TEM images verified the desired shape and size of the used powders (**Figure 15**).

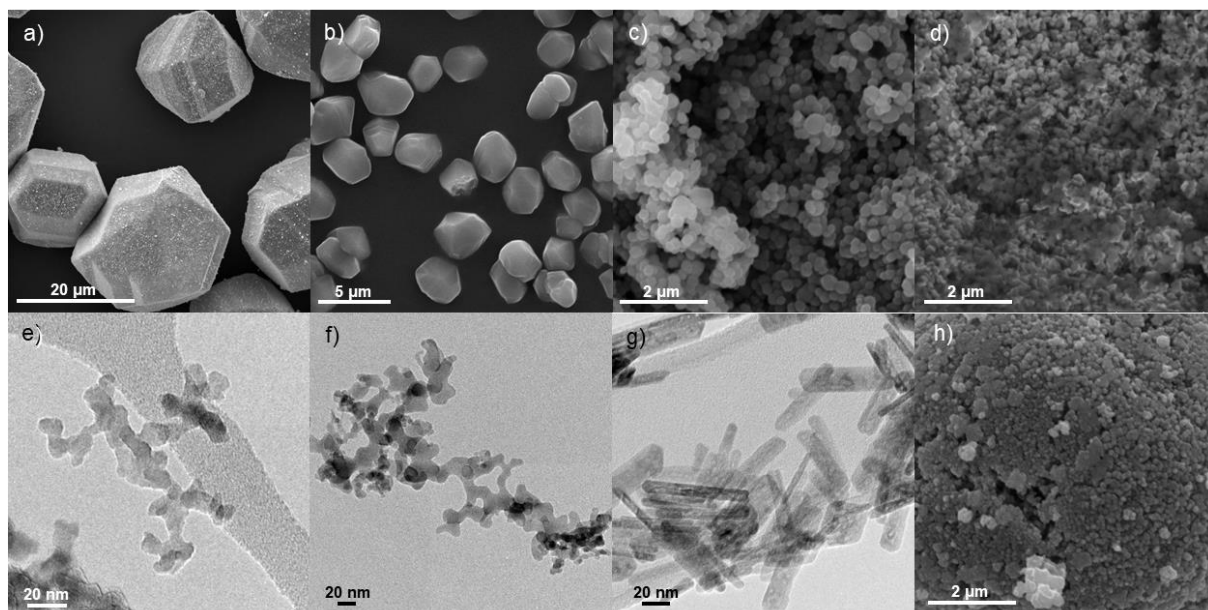


**Figure 15:** SEM images of a) AA18 ( $\text{Al}_2\text{O}_3$ ), b) AA3 ( $\text{Al}_2\text{O}_3$ ), c) AA03 ( $\text{Al}_2\text{O}_3$ ), d) Taimicron TM-DAR ( $\text{Al}_2\text{O}_3$ ), h) US3319 ( $\text{MnO}_2$ ) and TEM images of e) Aerioxide AluC ( $\text{Al}_2\text{O}_3$ ), f) L2715D ( $\text{Fe}_2\text{O}_3$ ), g) L2818D ( $\text{Fe}_2\text{O}_3$ ).

All particles exhibited a roundish spherical shape except for the elongated rod-shaped L2818D hematite nanoparticles (**Figure 15g**). Because of this shape, the specific surface areas (SSA) of the elongated  $\text{Fe}_2\text{O}_3$ -nanoparticles were distinctly higher than those of the spherical hematite ( $126.1 \text{ m}^2/\text{g}$  vs.  $69.7 \text{ m}^2/\text{g}$ ). The calculation of the BET average particle size revealed a theoretical size of  $11.6 \text{ nm}$  for the rod-shaped and  $19.6 \text{ nm}$  for the spherical nanoparticles. Furthermore, the calculated BET average size for the manganese oxide nanoparticles was  $61.7 \text{ nm}$ , what should be still small enough to achieve a homogeneous doping and in consequence a high absorption of the applied laser light. However, the calculated value for the rod-shaped particles is not very reliable, since it assumes a monomodal spherical particle shape and size distribution.

The measured SSA of the aluminum oxides were 0.4 m<sup>2</sup>/g for AA3, 5.5 m<sup>2</sup>/g for AA03, 11.8 m<sup>2</sup>/g for Taimicron TM-DAR and 95.3 m<sup>2</sup>/g for Aeroxide AluC. Consequently BET average particle sizes of 3.7 μm for AA3, 269.2 nm for AA03, 128.8 nm for Taimicron TM-DAR and 18.0 nm for Aeroxide AluC were calculated. These sizes should be adequate to achieve high packing densities in bimodal or trimodal distributions according to the results of McGeary [128], if agglomeration through attractive van der Waals forces can be prevented. The SSA of AA18 could not be evaluated, because of the small surface area of the coarse particles and the limitation of the BET instrument using nitrogen.

#### 3.1.3 Saturation amount evaluation of dispersant

As a suitable dispersant to prevent agglomeration of alumina in water, ammonium citrate dibasic was tested (**Figure 16**). It was previously found to be a suitable dispersant for alumina powder [146]. The citrate has a high affinity to aluminum oxide. By adsorption on the particle surfaces citrate causes an exchange of hydroxyl groups with carboxylate ions and the so created negative surface charge enables a homogeneous dispersion (electrostatic stabilization) (**Figure 16a, b, c, d**) [95, 146]. The point of zero charge could be adjusted at a pH saturation value of around 3 (**Figure 16e, f**). Beyond this saturation value, the surface of the particles should be already fully covered with a monolayer of citrate anions and the excess of remaining dispersant stays in the solution. This amount of citrate ions should guarantee a good dispersion of the alumina particles, since the absolute value of the zeta potential at the initial pH was higher than -60 mV for all alumina powders including the Aeroxide AluC nanoparticles. The optimized amounts of ammonium citrate dibasic for further dispersion of the alumina particles by means of different dispersing methods were 0.06 wt% for AA3, 0.4 wt% for AA03, 0.6 wt% for Taimicron TM-DAR and 3.6 wt% for Aeroxide AluC. These results are in accordance with the measured specific surface area. The relation of the zeta potential to citrate concentration was expected according to Hidber et al. [146] They found that the surface of an α-Al<sub>2</sub>O<sub>3</sub> powder with a specific surface area of 10 m<sup>2</sup>/g was saturated with an addition of 0.4 wt% citric acid. These results are consistent with our results, as AA03 (BET average particle sizes of 269.2 nm) was also saturated at this value.

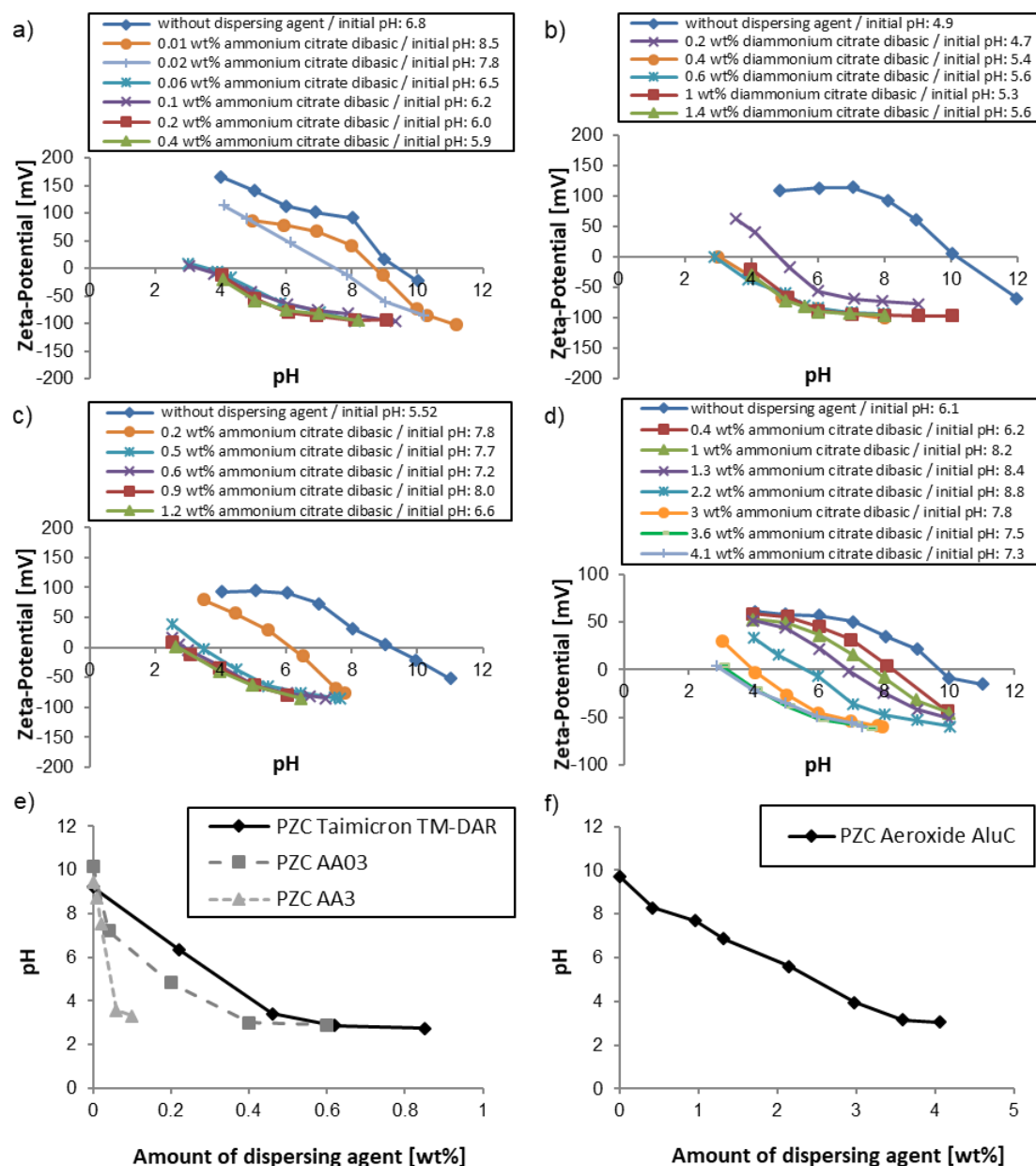


**Figure 16:** Zeta-potential of aluminas a) AA3, b) AA03, c) Taimicron TM-DAR, d) Aeroxide AluC as a function of pH value and citrate concentration.  $pH_{PZC}$  of e)  $\alpha$ -Al<sub>2</sub>O<sub>3</sub> and f)  $\gamma$ -Al<sub>2</sub>O<sub>3</sub> nanoparticle suspensions as function of ammonium citrate dibasic addition.

For iron oxide, a strong and similar effect to alumina was seen for the spherical L2715D (**Figure 17b**). For an amount of more than 3.1 wt% ammonium citrate dibasic, the pH value of the PZC tends to remain approximately 2 (**Figure 17d**). The zeta potential is also below -60 mV for the starting mixture. On the contrary, only a small shift of the zeta potential curve was recorded by use of this dispersant for the already negative charged L2818D (**Figure 17c**). The particle surface was saturated in citrate anions using an amount of 3.0 wt% dispersant. The zeta potential for this dispersion was only at around -30 mV at the initial pH, which means less electrostatic repulsion between the particles of this powder for further dispersing.

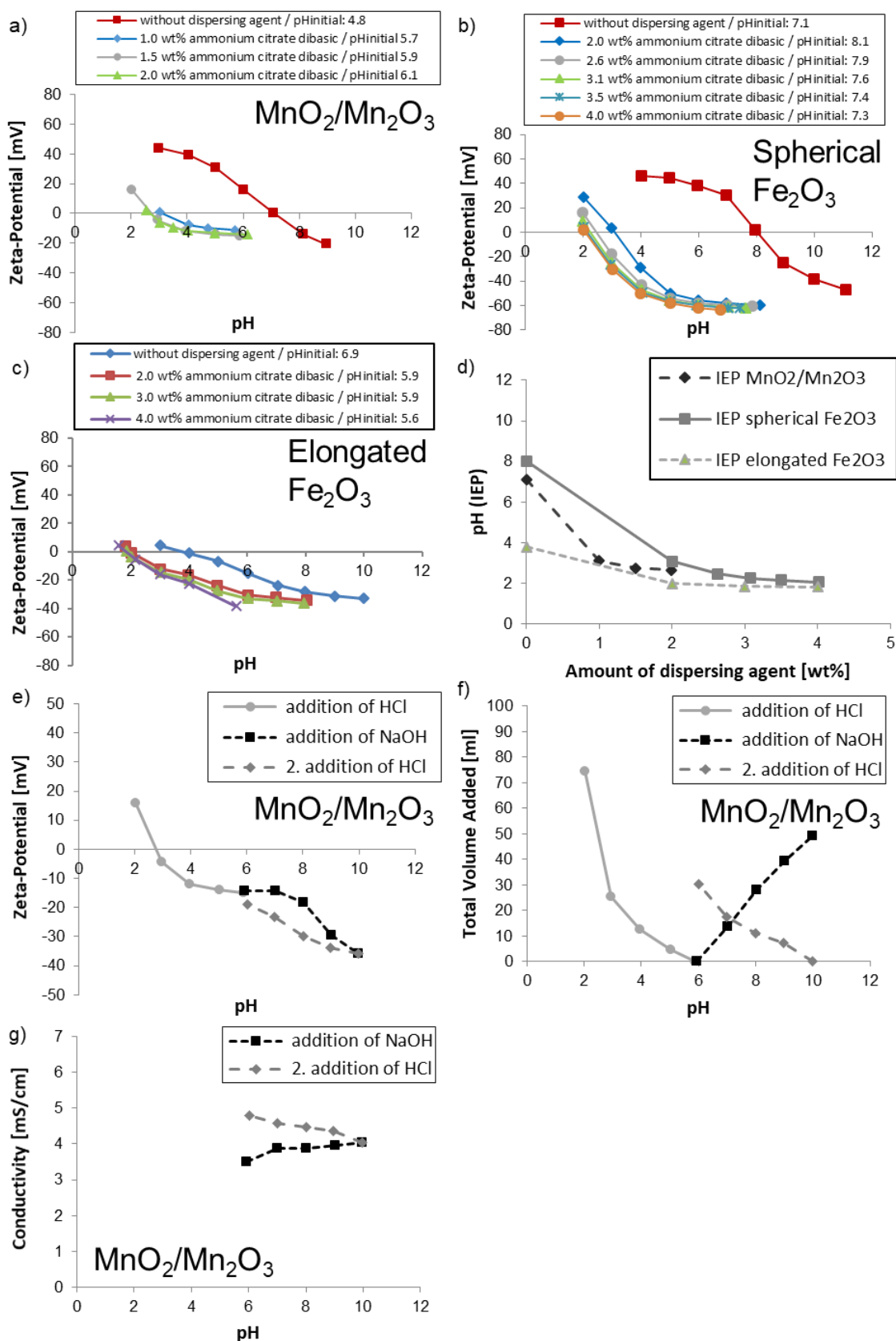


**Figure 17:** Zeta potential of **a)**  $\text{MnO}_2/\text{Mn}_2\text{O}_3$  and **b),c)**  $\text{Fe}_2\text{O}_3$  nanoparticles as a function of pH value and various citrate concentrations. **d)** pH<sub>IEP</sub> of  $\text{MnO}_2/\text{Mn}_2\text{O}_3$  and  $\text{Fe}_2\text{O}_3$  suspensions as function of ammonium citrate dibasic addition. **e)** Zeta potential of  $\text{MnO}_2/\text{Mn}_2\text{O}_3$  with 1.5 wt% (4.0 vol%) ammonium citrate dibasic as function of pH value and **f)** corresponding conductivity change by HCl and NaOH addition as function of pH value and **g)** added volume.

Since the  $\text{MnO}_2/\text{Mn}_2\text{O}_3$  nanoparticles were initially positively charged (39.9 mV) (**Figure 17a**), the dispersion by ammonium citrate dibasic was expected to be as efficient as for  $\text{Fe}_2\text{O}_3$  L2715D. The isoelectric point could be easily adjusted at a pH saturation value of 3 like for the L2715D  $\text{Fe}_2\text{O}_3$  nanoparticles. The evaluated saturation amounts of ammonium citrate dibasic on the nanoparticles surfaces for further dispersion were 1.5 wt% (4.0 vol%) for  $\text{MnO}_2/\text{Mn}_2\text{O}_3$  and 3.1 wt% (8.4 vol%) for  $\text{Fe}_2\text{O}_3$  (**Figure 17d**).

Since the surface of the  $\text{MnO}_2/\text{Mn}_2\text{O}_3$  nanoparticles was initially positively charged, a homogeneous dispersion of  $\text{MnO}_2/\text{Mn}_2\text{O}_3$  nanoparticles in water was not straight forward as for the  $\text{Fe}_2\text{O}_3$  and the  $\text{Al}_2\text{O}_3$  nanoparticles. By adding the saturation amount of ammonium citrate dibasic (**Figure 17a, e**) a negatively charged surface could be indeed created, though the zeta-potential was only around -15 mV for the starting mixture. A pH-adjustment with NaOH to a pH of 10 delivered a zeta potential shift to a higher value of -36 mV, but a consecutive acid titration (HCl) gave other zeta potential values than measured during base titration (**Figure 17e**). This could be due to  $\text{MnO}_2/\text{Mn}_2\text{O}_3$  dissolution at higher pH values. A steady increase of the conductivity during addition of NaOH and HCl (**Figure 17g**) confirms this assumption, since the increased particle amount could apparently result in a higher zeta potential due to peptisation. However, in the total volume change to achieve a certain pH value (**Figure 17f**) no extreme increase was apparent above a pH of 8, which does not totally confirm the assumption of  $\text{MnO}_2/\text{Mn}_2\text{O}_3$  dissolution.

### 3.1.4 Particle size distributions after dispersing

After evaluating the optimized amount of surfactant, the particles were dispersed in water. The volume-based particle size distributions determined by dynamic light scattering (DLS) and laser diffraction (LD) show a good dispersion of the submicron and nanoparticles without agglomeration.

#### 3.1.4.1 Particle size distributions of alumina powders

The results for  $d_{10}$ ,  $d_{50}$  and  $d_{90}$  in water by using an optimized dispersant amount and dispersing routine are summarized in **Table 6**. For the coarse alumina powders AA3 and AA18, the particle size distributions were only evaluated by laser diffraction, since the particle size was at the upper measurement limit of the dynamic light scattering device. In addition, AA03 was only evaluated by laser diffraction due to the broad particle size distribution. **Figure 18** shows the volume based particle size distributions of the alumina powders in water by using an optimized

dispersant amount and dispersing routine. The particle size distributions were determined by dynamic light scattering (DLS) and laser diffraction (LD), respectively.

**Table 6:**  $d_{10}$ ,  $d_{50}$  and  $d_{90}$  of volume based particle size distributions of alumina powders in water by optimized dispersant amount and dispersing routine determined by dynamic light scattering (DLS) and Laser diffraction (LD).

Powder	Al <sub>2</sub> O <sub>3</sub> AA18	Al <sub>2</sub> O <sub>3</sub> AA3	Al <sub>2</sub> O <sub>3</sub> AA03	Al <sub>2</sub> O <sub>3</sub> Taimicron TM-DAR	Al <sub>2</sub> O <sub>3</sub> Aeroxide AluC		
Measurement method	LD	LD	LD	LD	DLS	LD	DLS
$d_{10}$	10.9 $\mu\text{m}$	2.2 $\mu\text{m}$	81 nm	109 nm	133 nm	76 nm	28 nm
$d_{50}$	18.6 $\mu\text{m}$	3.0 $\mu\text{m}$	304 nm	148 nm	201 nm	95 nm	50 nm
$d_{90}$	26.1 $\mu\text{m}$	4.4 $\mu\text{m}$	670 nm	212 nm	295 nm	117 nm	90 nm

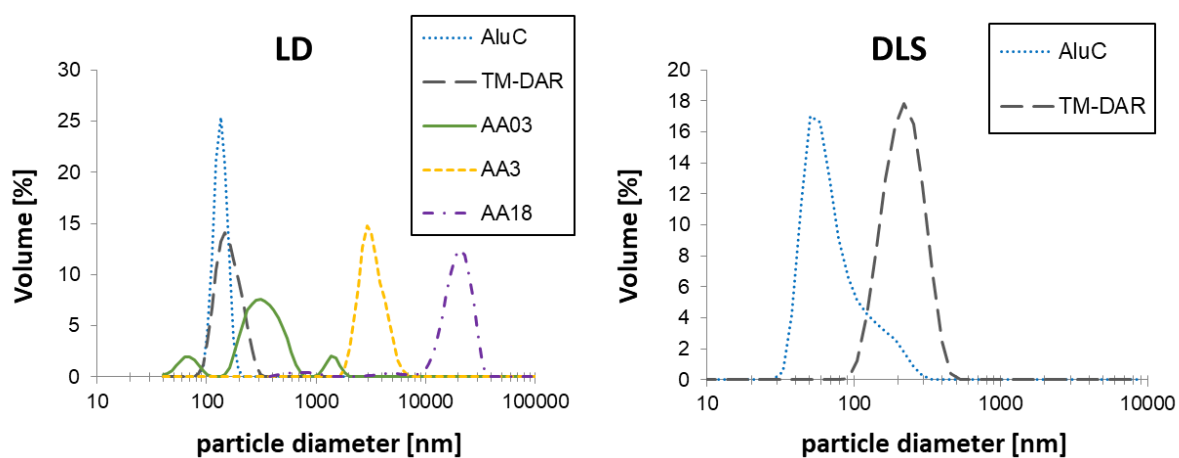


**Figure 18:** Volume based particle size distributions of alumina powders in water by optimized dispersant amount and dispersing routine determined by dynamic light scattering (DLS) and Laser diffraction (LD).

A  $d_{50}$  of 148.2 nm ( $d_{10}$  = 109.1 nm,  $d_{90}$  = 212.2 nm) was determined for Taimicron TM-DAR in the volume based LD measurement. This was confirmed by DLS and by a BET average particle size of 128.8 nm. The roll milled spherical submicron AA03 had a broader distribution ( $d_{10}$  = 80.8 nm,  $d_{50}$  = 303.9 nm,  $d_{90}$  = 670.2 nm) than the submicron Taimicron TM-DAR. 3 mm milling balls, a solid load of 35 Vol% and an ammonium citrate dibasic amount of 0.4 wt% (1.0 Vol%) referred to the inorganic particles were used for the dispersion of AA03 by roll milling (24 hours). Both the coarse AA18 ( $d_{10}$  = 10.9  $\mu\text{m}$ ,  $d_{50}$  = 18.6  $\mu\text{m}$ ,  $d_{90}$  = 26.1  $\mu\text{m}$ ), used for increasing the flowability and the packing bed density of the powders for laser treatment, and the roll milled AA3 ( $d_{10}$  = 2.2  $\mu\text{m}$ ,  $d_{50}$  = 3.0  $\mu\text{m}$ ,  $d_{90}$  = 4.4  $\mu\text{m}$ ) had uniform distributions. The used dispersant amount of ammonium citrate was 0.06 wt% (0.15 Vol%) for AA3 and 0 Vol% for AA18. The size of the milling balls and roll milling time were 5 mm and 24 hours in both cases. The micron-sized alumina powders and the nanopowders could be well dispersed by ammonium citrate dibasic with no agglomerates visible by DLS or LD.



Different sizes of milling balls, different solid contents of powders in water and dispersing methods were tested to achieve these results. The following discussion summarizes different dispersing steps for the nano-sized powders AluC Aerioxide and Taimicron TM-DAR in more detail, since gravity forces are smaller than attractive van der Waals forces below 10  $\mu\text{m}$  and decrease faster. Therefore, adhesive van der Waals forces dominate for nano particles and an intensive dispersing step with higher energy input is required for these particles [28]. In the case of the bigger particles (AA03, AA3 and AA18), gravity forces normally ease the dispersing [28].

In the case of the nano-sized alumina Aerioxide AluC milling balls from 0.4 mm up to 3 mm, solid loads up to 13.5 Vol% and roll milling, vibration milling, ultrasonication or different combinations of them were evaluated. As expected from the zeta-potential measurements, ammonium citrate dibasic acted as an effective dispersant for AluC Aerioxide (**Figure 16d**). **Figure 19** shows the volume based particle size distributions of AluC Aerioxide nanoparticles in water measured by dynamic light scattering or laser diffraction.

However, using only AluC and water led also to an agglomeration-free dispersion after 5 min ultrasonication (**Figure 19g**). This can be explained by a zeta-potential below -55 mV at a present pH of 6.1, which is high enough for a successful electrostatic stabilization of the dispersion (ca. >25mV). However, such a high zeta-potential is not present for all the used powders, especially the dopants, after the initial pH after adding to water. If citrate is considered to act as a dispersing agent, all the used powders in the final mixture should be dispersed by this dispersing agent, since it has a high affinity to aluminum oxide [146] and will tend to the surfaces of the particles, which were only added to water without dispersant. Ultrasonication with an optimized dispersant amount of 3.6 wt% (7.9 Vol%) ammonium citrate dibasic led only after 15 minutes to agglomeration-free dispersions. The smallest particles sizes and closest particle size distribution were reached after the maximum used time of 30 minutes.

The best results for roll milling for 24 hours, which were similar with the ultrasonication results, were achieved with 1 mm milling balls and a solid load in water of 5 Vol% according to the DLS measurements (**Figure 19a-d**). These measurements gave a  $d_{10}$  of 42.7 nm, a  $d_{50}$  of 72.4 nm and a  $d_{90}$  of 161.7 nm. LD measurements showed some agglomerates, when 0.4 mm and 3 mm milling balls were used instead of 1 mm balls. This could be due to too less impact of the 0.4 mm milling balls and due to too less collisions of the 3 mm milling balls with the particles despite having a higher energy input.



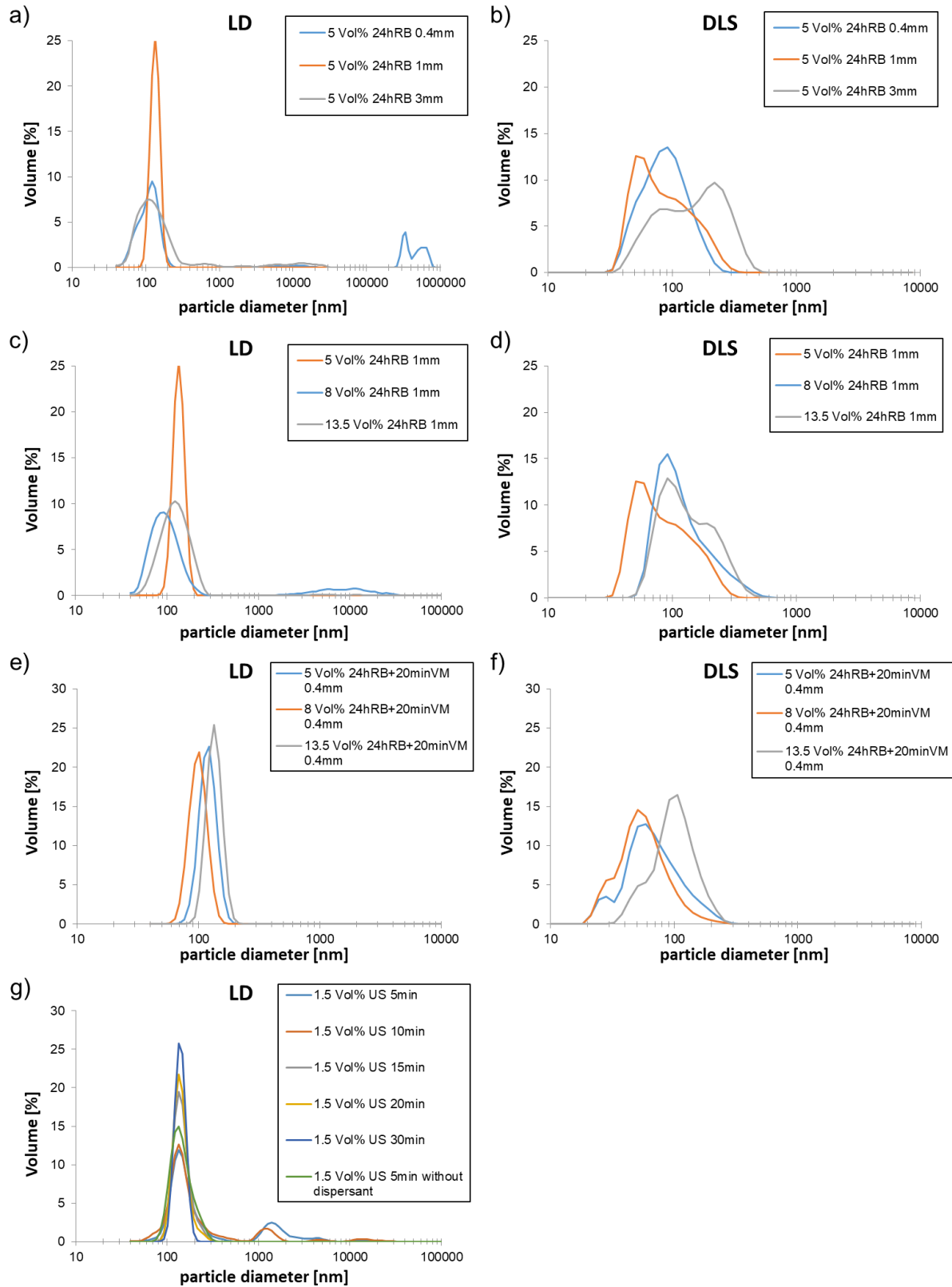


**Figure 19:** Volume based particle size distributions of AluC Aeroxide in water measured by dynamic light scattering (DLS) or Laser diffraction (LD) and dispersed roll milling (a, b) or a combination of roll milling and vibration milling (c, d, e, f) or ultrasonication (g) with an optimized dispersant amount of 3.6 wt% (7.9 Vol%) ammonium citrate dibasic.

An additional vibration milling step for 20 min before roll milling provided a further shift to smaller particles sizes (**Figure 19e, f**). This can be attributed to the higher energy input by this method. Furthermore, a higher solid load of 8 Vol% was proved as most suitable in this case. A d10 of 28.0 nm, a d50 of 50.0 nm and a d90 of 90.5 nm were achieved according to the DLS measurement. Only 0.4 mm milling balls provided agglomeration-free particle size distributions after vibration milling.

The highest solid load of 13.5 Vol% showed after both dispersing methods the worst milling results. This could be due to strongly raised viscosity of the nano-dispersion at this solid load, for which a higher energy input than provided by roll milling (and vibration milling) would be required.

The commercial dispersant Dolapix CE64 (Zschimmer & Schwarz GmbH Co., Germany) was also tested to disperse AluC Aeroxide. This alkali-free anionic polyelectrolyte should provide an electrosteric stabilization of the aluminum oxide particles [232, 233]. Despite the promising zeta-potential measurements with values below -50 mV at the initial pH, strong agglomeration was observed. One reason for this could be the dissolution of  $\text{Al}^{3+}$ , what could finally lead to a collapse of the electrical double layer of the particles and therefore, a reduction of the electrical double layer forces [234]. Another reason could be residual surface groups on the AluC particles, which could interfere with the electrostatic stabilization process. However, due the fact that the structure of Dolapix CE64 remains unknown, makes further conclusions impossible. The presumptions made before need further investigation to find the underlying cause of the unexpected particle agglomeration despite of promising zeta-potential measurements.

**Figure 20** illustrates the volume based particle size distributions of Taimicron TM-DAR particles dispersed in water with 0.6 wt% (1.5 Vol%) ammonium citrate dibasic. The particle size distributions were measured by laser diffraction (**Figure 20a**) or dynamic light scattering (**Figure 20b**).

The comparison between DLS and LD volume based particle size showed that in the case of alumina Taimicron TM-Dar the distribution was similar. The d50 values of the dispersed powder were in the range of the BET average particle size of 128.8 nm for the volume based LD measurement (148.2 nm) (**Figure 20a**) and for the volume-based DLS measurement (201.2 nm) (**Figure 20b**). An optimized saturation amount of 0.6 wt% (1.5 Vol%) of ammonium citrate dibasic and a total solid load of 30 Vol% was used to disperse the particles homogeneously in water by roll milling for 24 hours. The use of 5 mm milling balls led in contrary to the use of 1 mm milling balls to agglomerations in the size range of 1  $\mu\text{m}$  up to 2  $\mu\text{m}$ .

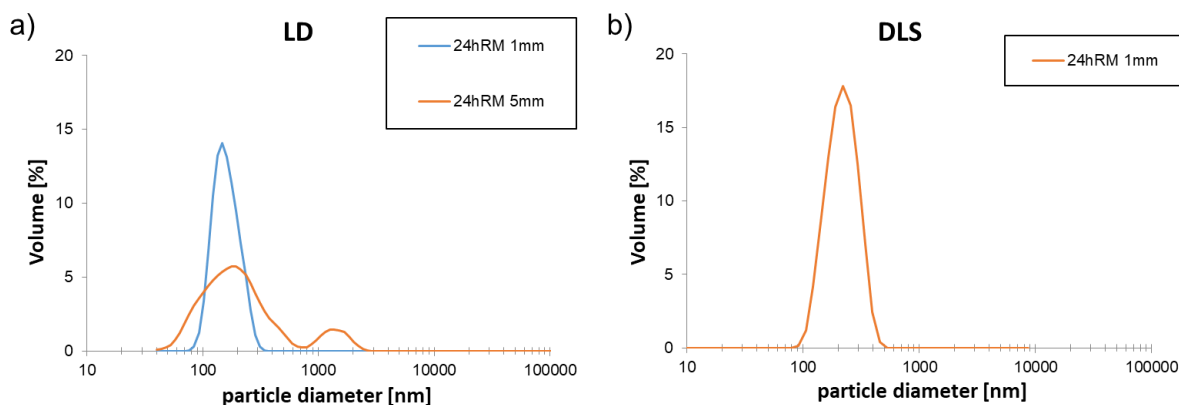


**Figure 20:** Volume based particle size distributions of Taimicron TM-DAR dispersed in water with 0.6 wt% (1.5 Vol%) ammonium citrate dibasic measured by **a)** laser diffraction (LD) or **b)** dynamic light scattering (DLS).

Ultrasonication led to similar particle sizes. However, it was limited to a solid loading of 5 Vol% Taimicron TM-DAR particles in Nanopure water due to an emerging high viscosity (similar to AluC Aerioxide). Since a high amount of these particles would be necessary to reach high packing densities in the bimodal or trimodal distribution within the spray-dried granules according to McGearry [128], this low solid loading would reduce the final density of the final granules for laser processing. Thus, ultrasonication was not considered as a suitable alternative to roll milling.

### 3.1.4.2 Particle size distribution of dopants

The results for  $d_{10}$ ,  $d_{50}$  and  $d_{90}$  of nanosized particles dispersed in water by using an optimized dispersant amount and dispersing routine are summarized in **Table 7**. The volume based particle size distributions of the used dopants by using an optimized dispersant amount and dispersing routine are illustrated in **Figure 21**. The particle size distributions were determined by dynamic light scattering (DLS) and Laser diffraction (LD)

**Table 7:**  $d_{10}$ ,  $d_{50}$  and  $d_{90}$  of volume based particle size distributions of dopants in water by optimized dispersant amount and dispersing routine determined by dynamic light scattering (DLS) and Laser diffraction (LD).

Powder	Fe <sub>2</sub> O <sub>3</sub> L2715D		Fe <sub>2</sub> O <sub>3</sub> L2818D		MnO <sub>2</sub> /Mn <sub>2</sub> O <sub>3</sub> US3319			
					pH = 8.1		pH = 8.6	
Measurement method	LD	DLS	LD	DLS	LD	DLS	LD	DLS
$d_{10}$	51 nm	37 nm	90 nm	64 nm	95 nm	116 nm	95 nm	102 nm
$d_{50}$	79 nm	53 nm	116 nm	146 nm	134 nm	172 nm	133 nm	172 nm
$d_{90}$	110 nm	82 nm	368 nm	228 nm	257 nm	248 nm	287 nm	250 nm

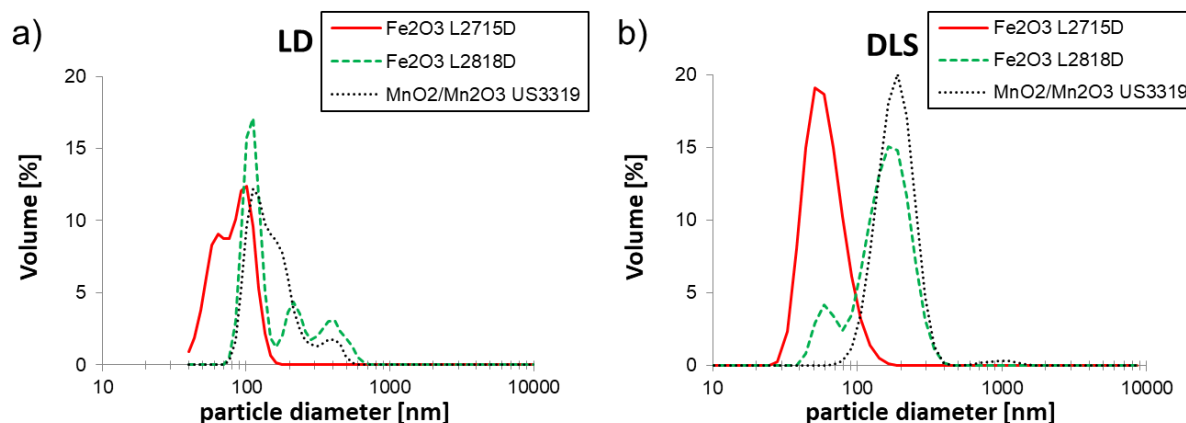


**Figure 21:** Volume based particle size distributions of dopants in water by using optimized ammonium citrate dibasic (dispersant) amount (1.5 wt% (4.0 vol%) for  $\text{MnO}_2/\text{Mn}_2\text{O}_3$ , 3.1 wt% (8.4 vol%) for  $\text{Fe}_2\text{O}_3$  L2715D and 3.0 wt% (8.4 Vol%) for  $\text{Fe}_2\text{O}_3$  L2818D) and dispersing routine determined by **a)** Laser diffraction (LD) and **b)** dynamic light scattering (DLS).

The size of the  $\text{Fe}_2\text{O}_3$  L2715D, dispersed by vibration milling for 20 minutes and additionally 24 hours roll milling, is mainly below 100 nm (volume based DLS measurement  $d_{50} = 53$  nm). Milling balls, solid load and ammonium citrate dibasic content were 0.4 mm, 7.5 Vol% and 3.1 wt% (8.5 Vol%) respectively. Roll milling for 24 hours (1 mm milling balls) generated the best results for the rod-shaped  $\text{Fe}_2\text{O}_3$  L2818D (volume based DLS measurement  $d_{50} = 146.4$  nm). A saturation amount of 3.0 wt% (8.4 Vol%) of ammonium citrate dibasic and a total solid load of 5 Vol% was used to disperse the particles homogeneously. In comparison, the volume based LD measurement gave a smaller  $d_{50}$  of 115.7 nm. The higher values compared to L2715D were already expected from the zeta potential measurement, but these results must be considered carefully, since the measurement assumes spherical particles for the calculation. Agglomerates below  $0.8 \mu\text{m}$  of the dispersed iron oxide dopants arose only for L2818D in this LD measurement. For the  $\text{Fe}_2\text{O}_3$  L2715D, the distribution measured by DLS was shifted to smaller values compared to LD measurements, since the size of the dispersed particles is partly below the resolution limit of the laser diffraction device.

The roll milled (24 hours) and vibration milled (20 min) manganese oxide US3319 was shifted to higher values ( $d_{10} = 116$  nm,  $d_{50} = 172.9$  nm,  $d_{90} = 248.2$  nm according to DLS measurements) as expected from visual analysis and BET measurements. However, an adjustment of the pH to higher values (pH = 8.1 - 8.6) was necessary due to initially positively charged surface of the particles. This is explained more in detail below. 0.4 mm milling balls, a solid load of 10 Vol% and an ammonium citrate dibasic amount of 1.5 wt% (4.0 Vol%) were used to disperse the manganese oxide particles.

For both iron oxides, the manganese oxide and the nano-alumina (Aeroxide AluC), the measured values are higher than the calculated BET average particle sizes (confirmed visually by TEM). This can be explained as hard agglomerates are still not being adequately dispersed by the aid of the surfactant and broken during the milling process.

The use of coarser iron oxide particles (Bayferrox 222 FM, Lanxess Deutschland GmbH, Germany) for laser additive manufacturing was also tested in first experiments. d10, d50 and d90 after roll milling in water were 157 nm, 588 nm and 963 nm according to LD measurements, respectively. However, no interaction with the green ns-pulsed laser light was noted and thus, the part consolidation was not successful with this dopant.

The volume based particle size distributions of dispersed  $\text{Fe}_2\text{O}_3$  L2715D particles was measured by DLS or LD after vibration milling (**Figure 22a, b**) or by vibration milling and additional roll milling (**Figure 22c, d**).

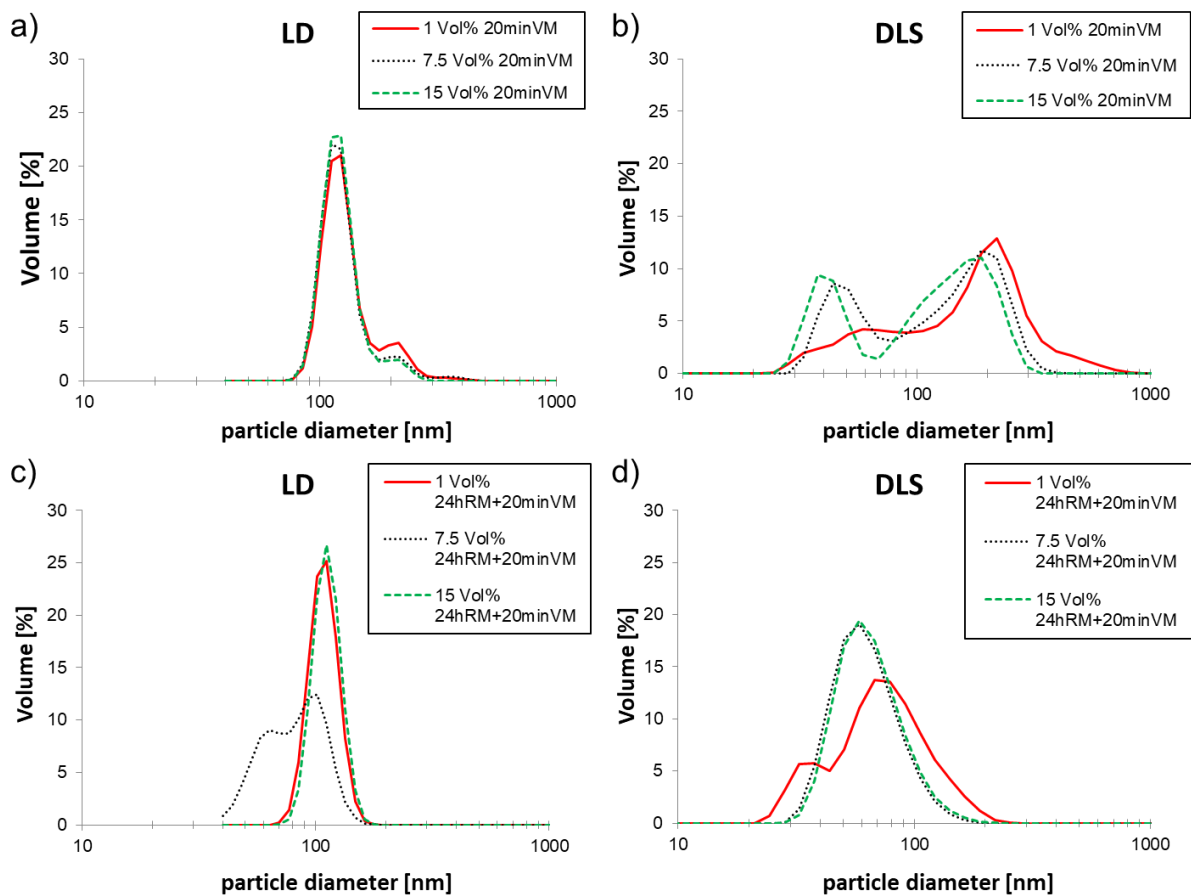


**Figure 22:** Volume based particle size distributions of  $\text{Fe}_2\text{O}_3$  L2715D measured by dynamic light scattering (DLS) or Laser diffraction (LD) and dispersed by only vibration milling (**a, b**) or by vibration milling and additional roll milling (**c, d**) with an optimized dispersant amount of 3.1 wt% (8.5 Vol%) ammonium citrate dibasic.

Solely vibration milling for 20 minutes provided already small particle without severe agglomeration (particle size below 400 nm according to LD and below 800 nm according to DLS) for the different solid loadings. The lowest solid loading of 1 Vol% showed the highest content of agglomerates according to both techniques. This could be due to the lower probability to hit agglomerates by the accelerated milling balls (0.4 mm) in the dispersion with the lowest solid content during the short time span of only 20 min. Furthermore, it could be that viscosity of the dispersion is getting too small and thus, the dispersion just splashes away before the milling balls can break the agglomerations at the walls of the vibration milling container or in between themselves.

In case of additional roll milling for 24 hours after vibration milling the agglomerates above 200 nm disappeared completely for a particle solid loading of 7.5 Vol% and 15 Vol% for DLS and LD (**Figure 22c, d**). The particle size distribution for 1 Vol% was similar, but the DLS measurement showed agglomerates of up to 250 nm. To measure even higher solid loads than 15 Vol% of the dispersion was not possible due to the fast increasing viscosity of the nano-dispersion with higher particle content. The d10, d50 and d90 after vibration and roll milling were 51 nm, 79 nm, 110 nm for a solid loading of 7.5 Vol% and 94 nm, 114 nm, 150 nm for a solid loading of 15 Vol% according to the LD measurements. DLS measurements gave a more similar result of a d10, d50 and d90 of 37 nm, 53 nm, 82 nm and 41 nm for a solid loading of 7.5 Vol% and 58 nm, 90 nm for 7.5 Vol% for a solid loading of 15 Vol%. The characteristic values are smaller for the DLS measurements due to the higher accuracy in the range below 100 nm of this method.

Long duration milling was performed to gain a better understanding of the effect of additional roll milling on the dispersion quality of the nano-Fe<sub>2</sub>O<sub>3</sub> (L2715D). A vibration milling step for 20 minutes was done at first and afterwards the volume based particle size distribution was measured by DLS within a time range of up to 72 hours (**Figure 23**). A significant influence after roll milling of up to 2 hours was not visible (**Figure 23a**). However, a constant shifting of the particle size distribution to lower values is measured after reaching a time of 4 hours of rolling (**Figure 23b**). There could be two reasons for this behavior. The adsorption of the citrate could be a kinetic driven effect to cover the complete surface area of the particles. This means that the formation of the negatively charged surface created by exchange of hydroxyl groups with carboxylate ions on the particles and thus, a quality stabilization of the dispersion by double layer repulsion, is a time-dependent process. Furthermore, it could be also that weak sinter bridges in between the particles could be only slowly dissolved due to dissolution reactions

caused by the low energy input of the roll milling process so called peptization. These sinter bridges are a result of the synthesizing process of these nanoparticles during the gas phase process in a hot wall flow reactor. The already agglomerated particles can sinter quickly during flight through the reactor.

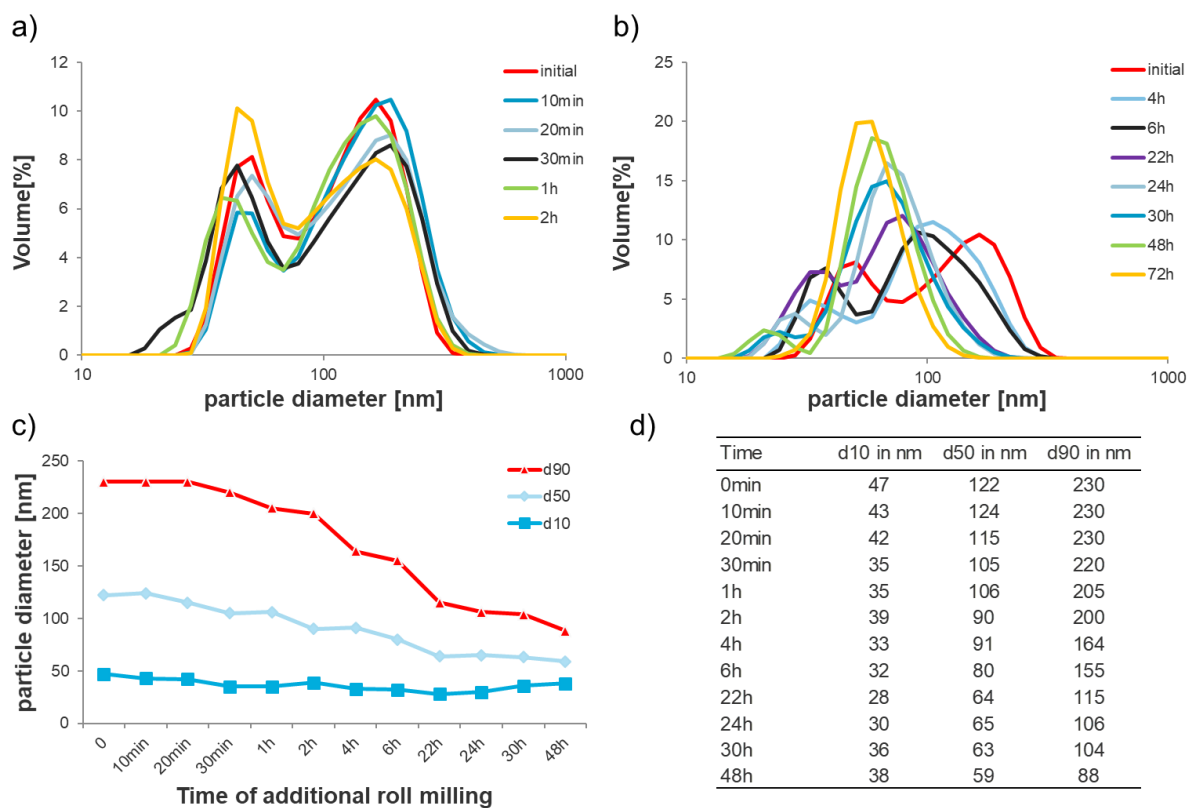


**Figure 23:** a, b) Volume based particle size distributions (DLS) of  $\text{Fe}_2\text{O}_3$  L2715D measured after different additional roll milling time ranges of up to 72 hours upon vibration milling. c, d) Temporal history of the characteristic particle size values of d10, d50 and 90 after additional roll milling.

The characteristic values of d10, d50 and 90 experience a different change during the additional roll milling (**Figure 23c, d**). To neglect a theoretical strong influence of dissolution after long time, only roll milling time up to 48 hours are listed. The particle size values for d10 show only a small decrease up to 22 hours (47 nm down to 28 nm) and at last a small increase to the final roll milling time of 48 hours (38 nm). The constant decrease of the other two characteristic values are more severe. d50 and d90 decrease from 122 nm down to 59 nm (48 hours) and from 230 nm down to 88 nm (48 hours).

To demonstrate the stability of the dispersion, several drops were given to ca. 300 ml Nanopure water after different roll milling times. After 3 days of waiting, these samples were visually analyzed (**Figure 24**).

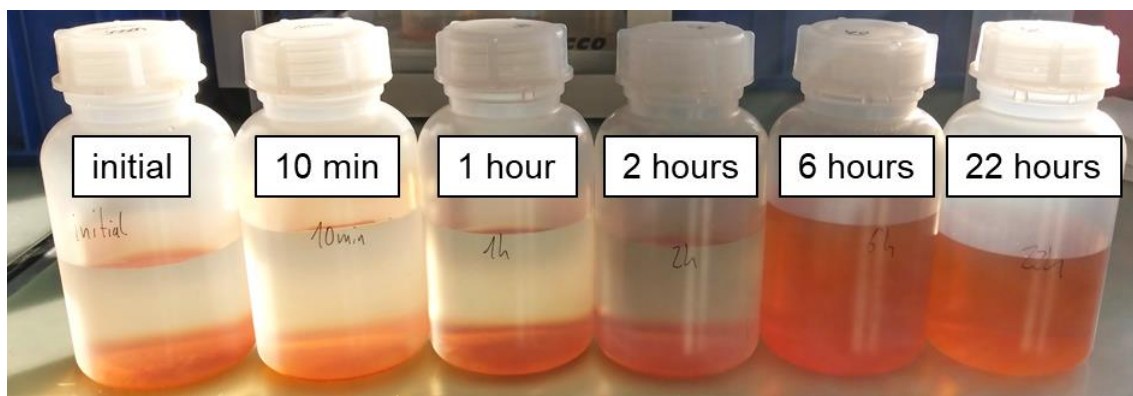


**Figure 24:** Sedimentation experiments with an idle time of 3 days for dispersions, which experienced a vibration milling of 20 minutes and an additional roll milling step for 0 minutes, 10 minutes, 1 hour, 2 hours, 6 hours and 22 hours.

Sediments were visible in the dispersions, which experienced only an additional roll milling process of up to 2 hours (**Figure 24**). Particles, which do not offer a completely covered surface by a surfactant after milling, can tend to re-agglomerate. However, well-dispersed particles can be still present in the upper part of the dispersion. These are just not visible due to low solid content in this part. The samples, which experience the additional treatment of 6 and 22 hours of roll milling, were still well dispersed after 3 days. This is in agreement with the stronger decrease of the bigger amount of agglomerates after 4 hours shown in **Figure 23**.

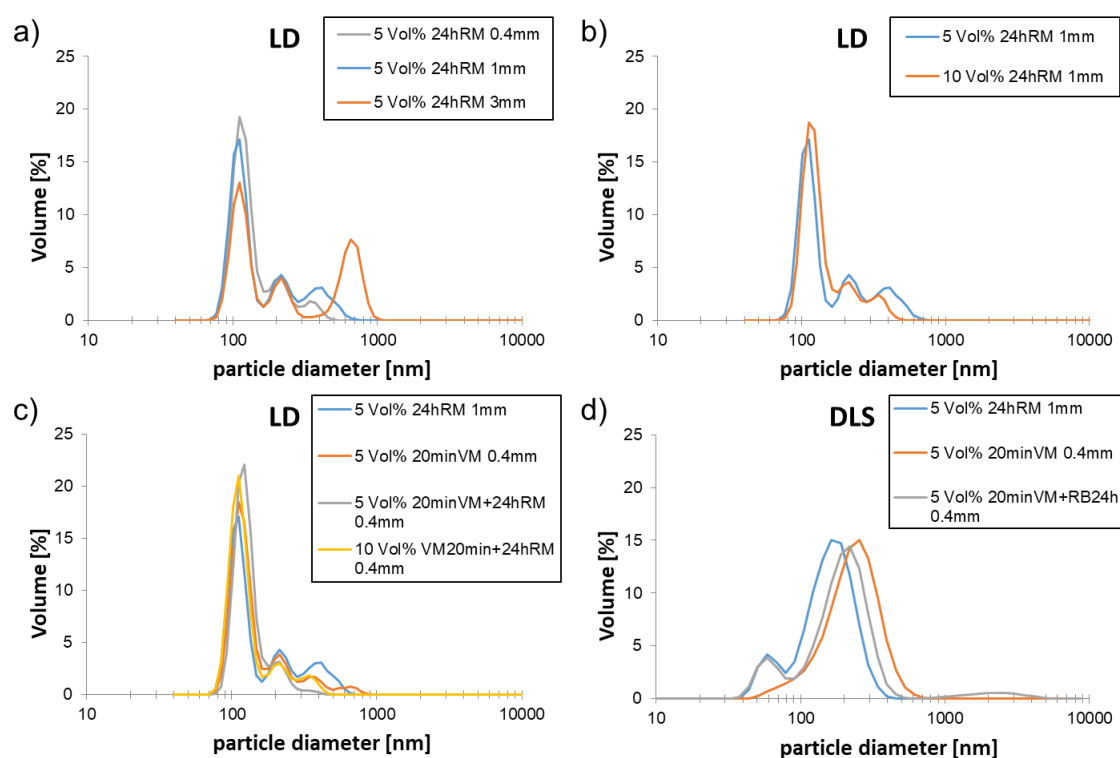


**Figure 25:** Volume based particle size distributions of  $\text{Fe}_2\text{O}_3$  L2818D measured Laser diffraction (LD) and dispersed by roll milling **a)** with different sizes of the milling balls or **b)** different solid loadings. Volume based particle size distributions of  $\text{Fe}_2\text{O}_3$  L2818D dispersed by roll milling, vibration milling or a combination of both and measured by **c)** Laser diffraction (LD) or **d)** dynamic light scattering (DLS)



Several combinations of milling ball sizes, solid loadings and milling methods were tested to disperse the  $\text{Fe}_2\text{O}_3$  L2818D (**Figure 25**). The influence on the dispersion quality of the milling ball sizes was bigger as the change of solid loading of the dispersion. The dispersion stirred with 3 mm milling balls for 24 hours on the rolling bench showed a bigger fraction of agglomerates up to  $1\ \mu\text{m}$  than the dispersions stirred with 0.4 mm and 1 mm milling balls (**Figure 25a**). As described before, this could be due to the lower probability to hit agglomerates by the low energy roll milling process. The lowest d10 and d50 was achieved with milling balls of 1 mm and a solid loading of 5 Vol%, even though the d90 was higher compared to the particle size distributions achieved with smaller milling balls (0.4 mm) and higher solid loadings (10 Vol%) (**Figure 25b**). The volume based particle size distributions achieved by roll milling (5 Vol% solid loading, 1 mm milling balls) were compared to vibration milling or a combination of both in **Figure 25c, d**. The particle size distributions measured by laser diffraction showed no big differences for the particle sizes below 300 nm. However, the only processing without almost no agglomerations above this value was the combination of vibration milling for 20 min and roll milling for 24 hours with milling balls of 0.4 mm and a solid loadings of 5 Vol% (laser diffraction: d10 = 96 nm, d50 = 118 nm, d90 = 186 nm). Dynamic light scattering gave a different result (**Figure 25d**). The smallest particle size distribution was achieved by the roll milling with milling balls of 1 mm and a solid loading of 5 Vol%. The characteristic values of d10, d50 and d90 measured by dynamic light scattering and laser diffraction are given in **Table 7**. For further processing this combination of roll milling was chosen, since dynamic light scattering showed the smallest particle sizes and furthermore, this combination offers an opportunity for an easy upscaling due to the simplicity of the process.

**Figure 26** depicts the volume-based differential particle size distribution of  $\text{MnO}_2/\text{Mn}_2\text{O}_3$  nanoparticles measured by dynamic light scattering and laser diffraction. The particles were dispersed in water by means of ammonium citrate at different pH values.

By adding ammonium citrate dibasic to  $\text{MnO}_2/\text{Mn}_2\text{O}_3$  nanoparticles, the zeta-potential was only around -15 mV for the starting mixture. A pH-adjustment with NaOH to a pH of 10 delivered a zeta potential shift to a higher value of -36 mV. However, a consecutive acid titration (HCl) gave other zeta potential values than measured during base titration, what led to the assumption that there could be a  $\text{MnO}_2/\text{Mn}_2\text{O}_3$  dissolution at higher pH values (**Figure 17**).

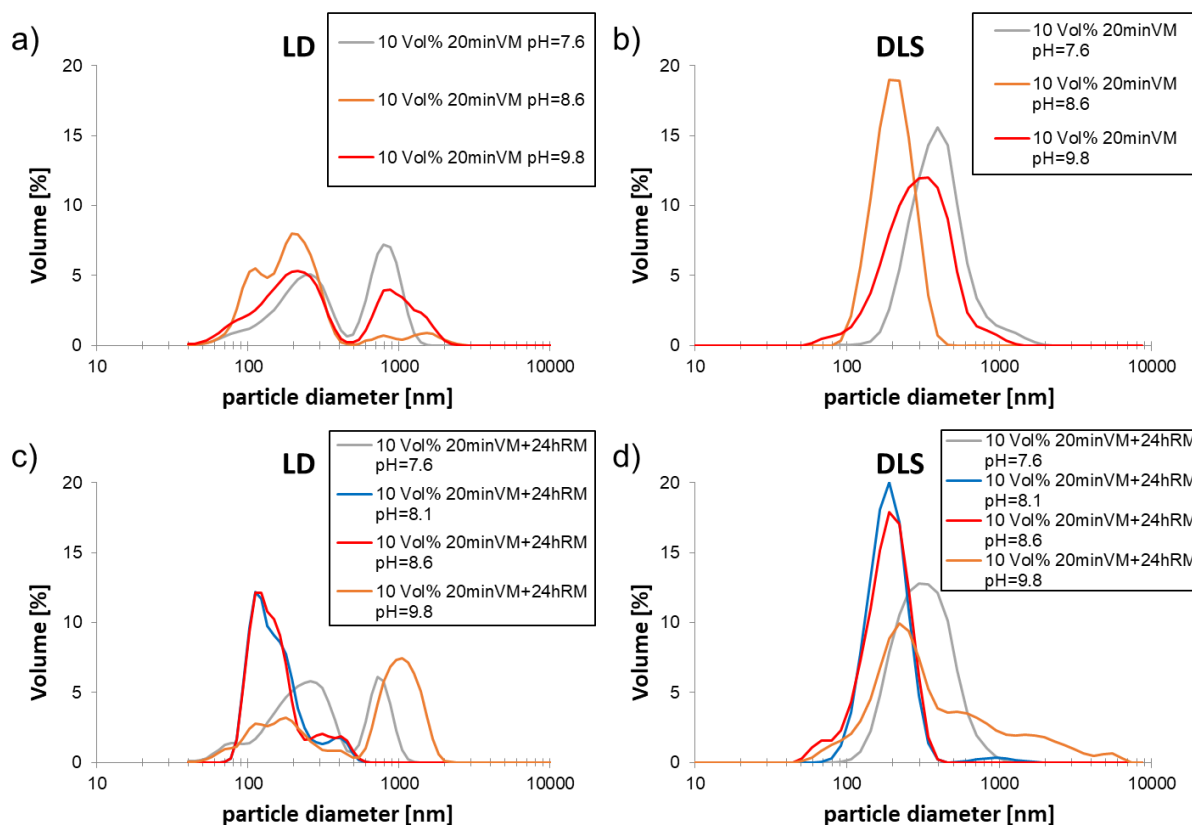


**Figure 26:** Volume-based differential DLS particle size distribution of  $\text{MnO}_2/\text{Mn}_2\text{O}_3$  and volume-based differential LD particle size distribution of  $\text{MnO}_2/\text{Mn}_2\text{O}_3$  in water dispersed by means of ammonium citrate at different pH values by a), b) roll milling and by c), d) a combination of vibration milling and roll milling.

To ensure an adequate dispersion of  $\text{MnO}_2/\text{Mn}_2\text{O}_3$  in water with the saturation amount of ammonium citrate dibasic, the pH of the solution was increased by the addition of ammonium hydroxide solution, with regard to the increasing zeta potential. Ammonium hydroxide solution was chosen to avoid impurities in the final granules. The volume based particle size distributions determined by dynamic light scattering (DLS) and laser diffraction (LD) revealed agglomerates for a pH of 7.6 and a pH of 9.8 (**Figure 26**). An explanation for this could be that for pH values lower than 8.1 the negative charge of the particle surfaces is too small for a proper electrostatic stabilization of the dispersion. The measured agglomerates confirmed the assumption of manganese dissolution at a pH 9.8, which was made due to a steady increase in the conductivity value.

**Figure 26a and b** show the volume based particle size distribution in water after 20 min of vibration milling. The smallest particle sizes and the lowest amount of agglomerates was given at a pH of 8.6, which was seen for the dynamic light scattering as well as the laser diffraction

measurements. An additional roll milling step for 24 hours improved the particle size distributions for both measurements (**Figure 26c, d**). The improvement was more pronounced in the laser diffraction measurement than for dynamic light scattering measurement. This could be due to kinetic effect of citrate adsorption to the surface or due to the slowly dissolving of weak sinter bridges in between the nanoparticles, as described more into detail for the  $\text{Fe}_2\text{O}_3$  L2715D.

The volume based DLS measurement as well as the volume based LD measurement showed a very similar distribution for  $\text{MnO}_2/\text{Mn}_2\text{O}_3$  nanoparticles dispersed at a pH of 8.1 and a pH of 8.6 by vibration milling and roll milling (**Figure 26c, d**). The values for  $d_{10}$ ,  $d_{50}$  and  $d_{90}$  at these two pH values are listed in **Table 7**. Although a zeta potential of only ca. -20mV was present at this pH value, the nanoparticles could be properly dispersed. However, the evaluated  $d_{50}$  by both particle size measurements were less than three times higher than the BET average particle size of 61.7 nm. This indicates still a suitable dispersion of the nanoparticles in water, despite being more than for other particles e.g.  $\text{Al}_2\text{O}_3$  Taimicron TM-DAR. However, the high refractive index (real part = 3.164, imaginary part = 0.316 [231]) (for LD) and the high absorptivity (for DLS) of the dark  $\text{MnO}_2/\text{Mn}_2\text{O}_3$  has to be considered in both measurement methods, since it can influence the evaluated particle size distributions significantly in terms of scattering and backscattering of the incident light.

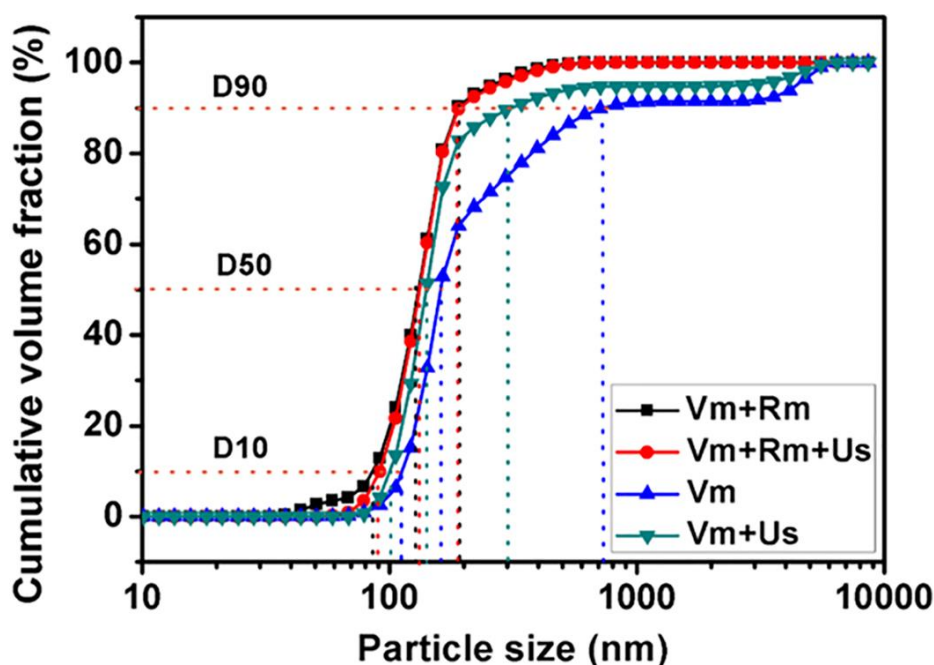


**Figure 27:** Volume-based differential DLS particle size distribution of  $\text{MnO}_2/\text{Mn}_2\text{O}_3$  particles dependent on different milling approaches. ("Vm" represents Vibration milling for 20 min with the frequency of  $30 \text{ s}^{-1}$ ; "Rm" represents Roll milling for 24 h; "Us" represents Ultrasonic treatment for 1.5 min.)

On the other side, various milling approaches have significant influence on the dispersion of  $\text{MnO}_2/\text{Mn}_2\text{O}_3$  nanoparticles, thus vibration milling, roll milling as well as ultrasonic treatment were studied at pH of ca. 8.1 (**Figure 27**). A combination of vibration milling and roll milling facilitated an improved dispersion of the  $\text{MnO}_2/\text{Mn}_2\text{O}_3$  particles, since their particle sizes were the lowest compared to the other techniques.

### 3.2 Packing density increase of spray-dried granules

**Table 8:** Impacts of different influencing factors on packing density and flowability of **a)** spray dried granules and **b)** granules mixed with additives.

<b>a) Spray dried granules</b>			
<b>Influencing factor</b>	<b>Chapter</b>	<b>Packing density</b>	<b>Flowability</b>
Solid load of slurry	3.2.2	Highest apparent and tapped density with a solid load of 50 vol%	Higher Hausner ratio for solid loads of 40 and 45 vol%; Flowability better (low Hausner ratio) for solid loads of 50, 55 and 60 vol%.
Particle ratio of raw powders (bimodal distribution)	3.2.2	Highest packing density with weight fraction of 0.726/0.274 coarse/fine particles confirming McGearry [118]	Lowest Hausner ratio (best flowability) for weight fraction of 0.726/0.274 coarse/fine particles
Dopant shape	3.2.3	No influence of dopant shape on packing density	No influence of dopant shape on flowability
Multimodal distribution of particles	3.2.3 3.2.6	Bimodal granules with higher apparent and tapped density than trimodal granules	Trimodal granules with better flowability (lower Hausner ratio) than bimodal granules
Thermal pre-treatment	3.2.8	Decrease of apparent density and constant tapped density, since formed granule agglomerations prevent a close packing	Strong increase of the Hausner ratio due to formed sintering necks in between the granules
Surface tension	3.2.9	No significant difference in apparent and tapped density with decreasing surface tension	No significant difference in flowability with decreasing surface tension
<b>b) Ceramic particle additions to spray dried granules</b>			
<b>Influencing factor</b>	<b>Chapter</b>	<b>Packing density</b>	<b>Flowability</b>
Addition of coarse alumina AA18 to spray-dried granules	3.2.6	Increase of Apparent and tapped density with addition of AA18 (high packing density)	Slight increase of Hausner ratio (decrease of flowability)
Addition of coarse alumina CB-P02 to spray-dried granules	3.2.6	Highest tapped density reached at ratio of granules/CB-P02 of 30/70 vol%. Steady decrease of apparent	Increase of Hausner ratio
Addition of coarse alumina CB-P10 to spray-dried granules	3.2.6	Tapped density increases constantly. Apparent density stays almost	Increase of Hausner ratio
Addition of different combinations of coarse alumina to spray-dried granules	3.2.6	Most favorable combination consisting of 50 Vol% pure granules, 45 Vol% AA18 and 5 Vol% CB-P10	Slight increase of Hausner ratio with 5 Vol% CB-P10. Higher amounts of CB-P10 lead to further flowability decrease
Application of Andreasen model	3.2.7	Packing theory can deliver a higher tapped density. However, the apparent density remains unchanged or	Formed agglomerations, especially when smaller particles are used, lead to lower flowability
Thermal pre-treatment and coarse alumina AA18 addition	3.2.8	Increase of apparent and tapped density due to densification of granules by sintering and separation of bonded granules by AA18	Minor effect on the Hausner ratio, when compared to as spray-dried granules

The results of the different strategies to increase the packing densities are summarized in **Table 8**. The impacts of the different influencing factors on packing density and flowability are listed for spray dried granules (**Table 8a**) and granules mixed with additives (**Table 8b**). More details can be found in the specific chapter.

#### 3.2.1 Experimental

Spray granulation was performed with the Mini spray dryer B-290 (Büchi Labortechnik AG, Switzerland) with an ultrasonic atomizer in co-current mode. The slurry was supplied by a peristaltic pump to the nozzle and left stirring to prevent a demixing. A maximum solid load in the slurry for spray drying of 50 vol% was chosen. Furthermore, an ultrasonic atomizer and a co-current droplet air mixing were used for spray drying. Process parameters were an inlet temperature of 140 °C, an outlet temperature of 100 °C, an air flow rate within the spraying apparatus of 25 m<sup>3</sup>/h, an ultrasonic nozzle power of around 9 W, a nozzle frequency of 60 kHz and a slurry feed rate of circa 1.2 ml/min. All parameters were kept constant during the process. The ultrasonic nozzle was prevented from overheating by a flow of compressed air. The Dehumidifier B-296 (Büchi Labortechnik AG, Switzerland) supplied constant and reproducible humidity conditions of around 90-95% relative humidity. The final granule separation was accomplished in a cyclonic collector and an additional screening step was performed with a 120 mesh (125 µm) sieve (Retsch GmbH, Germany), since only a fine fraction was suitable to achieve good resolution and to connect properly the different layers during laser processing.

Before spray drying, the separate powders were mixed with zirconia milling balls (Tosoh Corporation, Tokyo, Japan), dispersing agent and Nanopure water. Afterwards, the powders were dispersed by either roll milling in polyethylene bottles for 20 hours or a combination of vibration milling for 20 min with a vibrational frequency of 30 Hz (Retsch MM301, Retsch GmbH, Haan, Germany) with subsequent roll milling for 20 hours. For all the slurries the binder PEG 35000 was added to the coarse AA3 after rotating for 1 hour. The amount of binder was 2 wt% (6.2 vol%) referred to total amount of all powders in the slurries for spray drying. After dispersing, the individual slurry components were mixed and additionally homogenized for 4 hours on a rolling bench. After removing the milling balls, the slurry was continuously stirred to prevent demixing. To determine the change of pH-value during the single slurry preparation steps, the Five Easy Plus pH meter FP 20-Std-Kit (Mettler Toledo Schweiz GmbH, Switzerland) was used.

Thermal treatment of the spray dried granules was carried out in air in a high temperature furnace (LHT 04/17, Nabertherm GmbH, Germany). The granules were thermally treated to increase the densities of the single granules by sintering and, therefore, to achieve high packing densities in the powder beds for laser processing. The applied temperature varied from 1400 up to 1600 °C. Holding times of 2 and 4 hours were used with a heating rate of 2 K/min. After thermal treatment the powders were screened with a 120 mesh sieve and finally mixed with 30 vol% coarse alumina AA18 (Sumitomo, Chemical Co. LTD, Japan) on a rolling bench for 1 hour. The coarse alumina was added to the spray dried granules to break the sintering necks in between the granules by the constant movement on the rolling bench to maintain a high flowability of the powder. Additionally, coarse spherical alumina AA18 was also mixed to granules directly after spray drying to increase the powder bed density. The viscosity and shear stress in respect to shear rate were evaluated by the Modular Compact Rheometer MCR 302e (Anton Paar GmbH, Austria). The coaxial cylinder measuring system CC27-SN36412 were used to perform the measurements.

The quality of the as-prepared and thermal treated granules with and without AA18 was characterized by several techniques. Apparent density was measured with a setup (PTL Dr. Grabehorst GmbH, Germany) according to the standard DIN EN ISO 23145-2. A jolting volumeter (JEL STAVII, J. Engelsmann AG, Germany) was used to determine the tapped density by tapping the sample 1000 times with a displacement of 3 mm in compliance to EN ISO 787-11. Relative densities were calculated as fractions of the apparent and tapped density over the absolute powder density measured by a helium pycnometer (AccuPyc II 1340, Micromeritics, Norcross/GA, USA). The ratio of tapped density divided by apparent density (Hausner ratio) was used to grade the flowability of the powders. The Hausner ratio is a commonly used parameter in the field of selective laser melting of different metals [235-238] and ceramics such as alumina and zirconia [57, 58] and relates to frictional conditions in a moving powder [236, 238]. It gives a quantitative prediction of the powder deposition behavior by an easy measurement method [239]. In general, a Hausner ratio below 1.25 is considered as an indicator for a suitable flowability of powders for selective laser melting [57, 237]. Powder with a higher Hausner ratio and thus a poor flow behavior can result in localized porosity [238]. The residual moisture content of the different powders was measured at 140 °C for 1 hour with the moisture analyzer HR83 (Mettler Toledo GmbH, Switzerland). The influence of binder dissolution at this temperature on the measured moisture content should be very low, since PEG contains only a low amount of hydroxyl groups. The fraction of the received fine granules after spray drying and sieving to the weight of all solid contents in the slurry before spray drying revealed the total

yield of granules suitable for laser processing. Size distributions of the dry powders were monitored by laser diffraction (LS 13320, Beckman Coulter GmbH, Krefeld, Germany) including the characteristic values for d10, d50 and d90. Isopropanol is used to measure the size distributions of the spray-dried granules. In contrary to water the non-calcined granules are not destroyed in this solvent, since the used binder PEG 35000 is insoluble in isopropanol.

To evaluate continuous particle size distribution according to the Andreasen model in terms of final packing density, the EMMA (Elkem Materials-Mixture Analyzer) - Particle Packing Program (Elkem, Norway) was utilized.

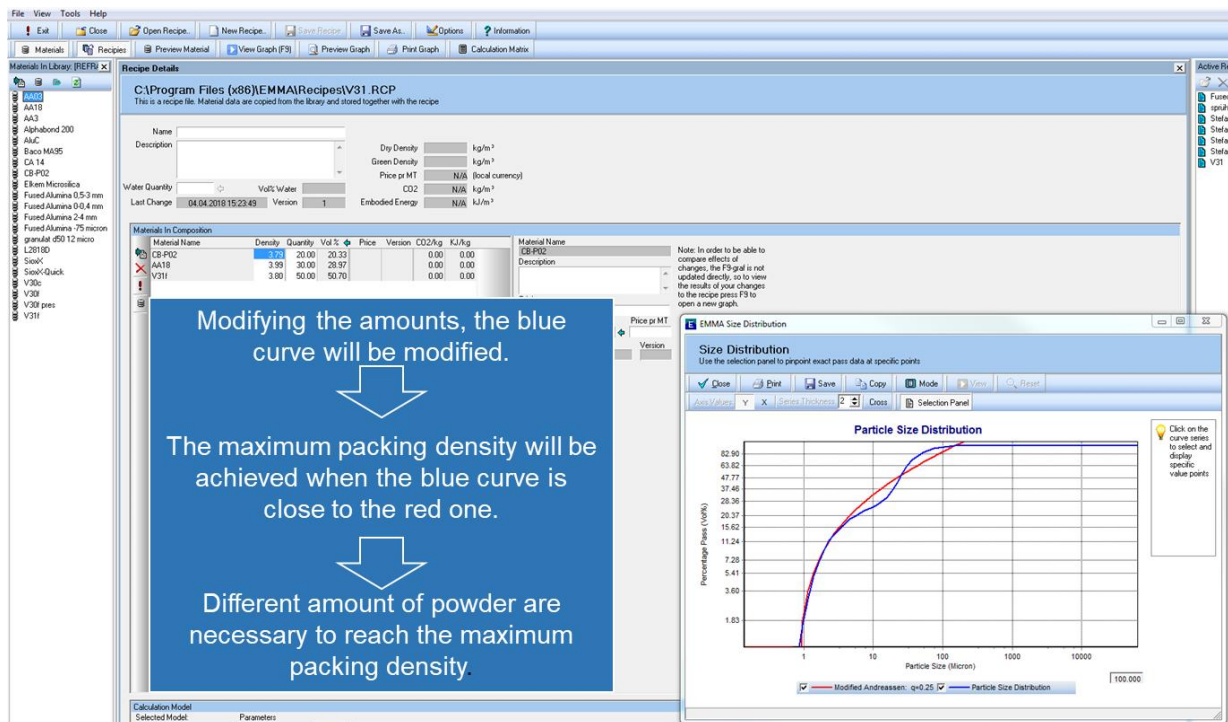


**Figure 28:** User interface of the EMMA (Elkem Materials-Mixture Analyzer) software.

**Figure 28** shows the user interface of the software. The total particle size distribution is calculated from mixtures of different powders (blue curve in particle size distribution in **Figure 28**) and can be directly compared to the optimal distribution according to the Andreasen model (red curve in particle size distribution in **Figure 28**). Before this step, it is necessary to record the characteristic particle size values of d10, d25, d50, d75 and d90 of all powders (granules and additional alumina powders) in the database of the software. The maximum packing density will be achieved when the blue curve is close to the red one. Different amount of powder are necessary to reach the maximum packing density.

**Figure 29** displays the parameter and model selection panel of the software.



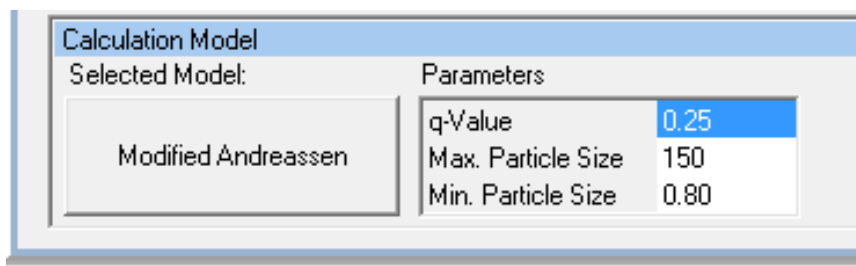


*Figure 29: Parameter and model selection panel of the EMMA software.*

A modified Andreasen equation (Dinger-Funk equation [127]) can be used within the software, which also considering a minimum particle size of the powder. Experimental data for sizes larger than about 1  $\mu\text{m}$  fall within the Andreasen bounds, as described in [127, 129]. Due to strong agglomeration, the Andreasen model is difficult to be applied for submicron particles. Furthermore, q-values, which determine the desired properties of the final powder: (good flowability ( $<0.25$ ), high packing density ( $<0.36$ )) can be chosen in this panel. The minimum and maximum particle size was set according to the particle size distributions of the used powders.

As spray-dried granules and thermal pre-treated granules (1400  $^{\circ}\text{C}$ ) were mixed with the different raw powders according to the calculation made by the EMMA software. Roll milling for 1 hour was applied to achieve a homogeneous mixture of the as spray-dried granules or the thermal pretreated granules with the additional aluminum oxides. Roll milling for 16 hours was performed to evaluate the effect of the mixing duration.

The influence of different temperatures and holding times on the microstructure of the doped granules was visualized and studied by Scanning Electron Microscopy (VEGA3 Tescan, Tescan instruments, Czech Republic). Prior to the SEM studies, the powder was attached to an adhesive carbon tab and distributed with compressed air. Sputtering with Au-Pd (Sputter coater 108 auto, Tescan instruments, Czech Republic) was performed twice using angles of  $45^{\circ}$  and  $90^{\circ}$  (sample carrier to sputter direction). For imaging of the granules morphologies, an accelerating voltage of 10 kV was employed.

The distribution of Fe and Mn dopant atoms in the granules was examined by  $\mu$ -beam scanning X-ray fluorescence ( $\mu\text{XRF}$ ) contrast tomography. The measurements were performed at the microXAS beamline at the Swiss Light Source synchrotron (Paul Scherrer Institut), using an X-ray beam focused down to  $1 \times 1 \mu\text{m}^2$  with an energy of 14.7 keV. Granules were placed in glass capillaries with internal diameter of 100  $\mu\text{m}$ , which were mounted on the rotational stage at the beamline. To visualize the dopant distribution in 3D, the tomography was performed by lateral scanning of the capillary in a continuous manner, at different orientations equally spaced



over 180°. The X-ray fluorescence signal was recorded simultaneously along with the incoming and transmitted intensity for every micrometer of the sample, using dwell time of 200 ms. The XRF signal was recorded using two silicon drift detectors, the transmitted intensity with a SiC diode and the incoming one with a mini ionization chamber. This procedure was performed at different positions along the axial direction of the cylindrical capillary, and afterwards the sample was analyzed slice by slice. Each analyzed slice in a volume was separately scanned, reconstructed and afterwards stitched together into a 3D volume. More information about the measurement method can be found in Sanchez et al. [240].

To identify major and minor crystallographic phases before and after thermal treatment, high resolution powder diffraction measurements were conducted at Material Science (MS) beamline at the Swiss Light Source (PSI) synchrotron [241]. The energy of the beam set for powder diffraction measurements was 12.398 keV and the wavelength was 1.0009 Å, which was evaluated based on the measurement of the SI standard from NIST. As-prepared and thermal treated granules as well as the starting powders were measured in glass capillaries (diameter 200 µm) in a transmission mode (Debye-Scherrer geometry). Rietveld refinement using TOPAS Bruker AXS software was used to quantify the crystallographic phases.

X-ray photo-electron spectroscopy (XPS) measurements were performed using a Quantum 2000 photoelectron spectrometer (Physical Electronics Inc., USA) with a monochromatic Al K $\alpha$  source (1486.6 eV) and a base chamber pressure below  $8 \times 10^{-9}$  mbar. Survey spectra were recorded with an energy step size of 0.4 eV and a pass energy of 93.90 eV. The detailed Mn 2p peak spectra were recorded with an energy step size of 0.125 eV and a pass energy of 29.35 eV. The use of the 2p peak for the valency state analysis of manganese was recommended in the Handbook of x-ray photoelectron spectroscopy by Moulder et al. [242]. After the measurements spectra were fit using the CasaXPS software package. The aim of the measurements was to identify the present elements and the valency states of the manganese atoms within thermal pre-treated manganese oxide doped granules. The method is based on the excitement of atoms by x-rays and subsequent release of photoelectrons. Prior to the measurements, the granular sample was attached on a glass substrate by an adhesive carbon tap to achieve a homogeneous powder layer.

The absorption of the powders for laser processing was quantified with an integrating sphere (Gigahertz-Optik UPB-150-ARTA, Gigahertz-Optik GmbH, Germany) equipped with a detector (power meter Ophir 10 A) and coated with barium sulfate in accordance to Florio et al. [17].

The layer thickness of 100  $\mu\text{m}$  and the green pulsed laser (IPG GLPM-5) were selected to recreate similar absorption conditions like in the SLS/SLM process. Temperatures during the measurement were assumed to be close to room temperature, since a laser power of only 1 W and a distance of focus to sample of 160 mm were used. The measurable power range was 15  $\mu\text{W}$  - 3 W. By measuring the reflectivity  $R$  and transmission  $T$  of the sample in two different positions, the absorption  $A$  in % was calculated as:

$$A = 1 - R - T \quad (9)$$

A qualitative absorption measurement of the powders for a wavelength range of 300 - 1500 nm (in 2 nm steps) was performed with the Shimadzu 3600 UV-VIS-NIR spectrophotometer (Shimadzu Corporation, Japan). Since powder induces complex scattering of light, the Kubelka-Munk method for measurements of diffuse reflectance was chosen. Assuming an infinite thickness of the powder layer (thick enough that a further thickness increase does not change the reflectance), a ratio of arbitrary constants of absorption (absorption coefficient  $K$ ) and scattering (scattering coefficient  $S$ ), can be calculated by measuring the reflectance of the sample [243, 244]:

$$\frac{K}{S} = \frac{(1 - R')^2}{2R'} \quad (10)$$

A requirement for the Kubelka-Munk theory is a significant stronger scattering in the medium than absorption and that the scattered radiation is isotropic so that the reflection at the surface is negligible, which is usually the case for bright and dull colors. To achieve these requirements a weight ratio of sample to  $\text{BaSO}_4$  powder (Nacalai Tesque Inc., Japan) of 1:9 was homogeneously mixed and compacted in a sample holder (depth: 6 mm; diameter: 25 mm) before the measurements.  $\text{BaSO}_4$  serves as a reference material, since it offers almost complete scattering of the used monochromatic light. To account for the reflectance and the residual absorption in the  $\text{BaSO}_4$  powder, the quantity  $R'$  was determined as the ratio of the reflectance of the compacted mixed powder  $R_p$  to that of the compacted, pure  $\text{BaSO}_4$  powder  $R_0$  [243, 244]:

$$R' = \frac{R_p}{R_0} \quad (11)$$

A qualitative absorption spectrum was finally given by plotting the  $K/S$  ratio over the wavelength. For the doped granules with and without coarse alumina AA18 the corresponding wavelength  $\lambda$  for calculation of the bandgap was evaluated by direct fitting from this absorption

spectrum. For a better comparison, both spectra were normalized. The bandgap energy was calculated from the following equation:

$$E_p = \frac{hc}{\lambda} \frac{1}{e} \quad (12)$$

using elementary charge  $e$ , Planck's constant  $h$  and the speed of light  $c$ .

### 3.2.2 Influence of solid load and particle ratio on granules

A bimodal powder combination consisting of coarse alumina AA3 and fine alumina AA03 was chosen, to confirm the results of McGeary [128] (**Figure 30b**) and the influence of the solid load on the packing bed density [103, 111] (**Figure 30a**) for spray dried granules. However, a homogeneous distribution of the individual powders within each other is a main requirement. These tests were also performed to estimate an appropriate solid load of the dispersion for the work with an ultrasonic nozzle.

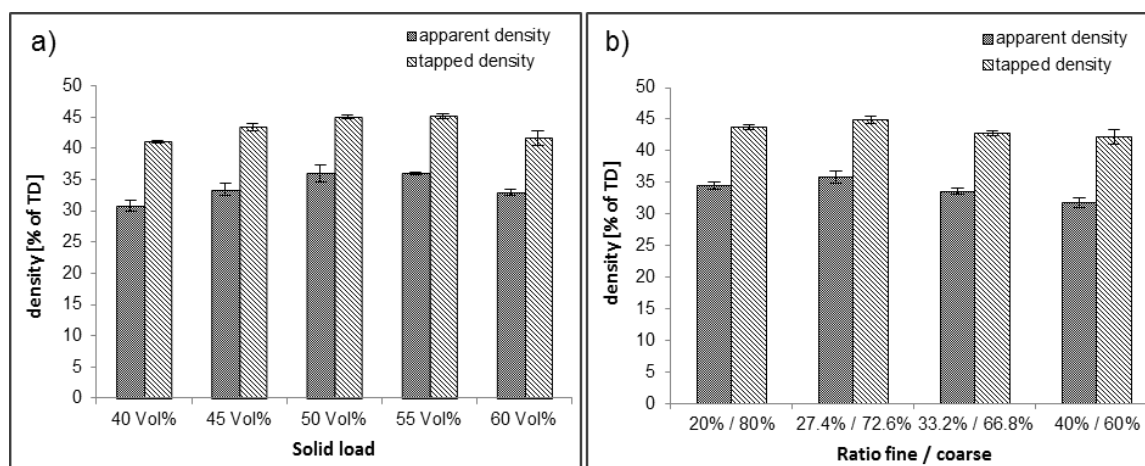


**Figure 30:** a) apparent and tapped density versus solid load and b) influence of ratio of fine to coarse starting powder on the apparent and tapped density of spray dried granules (powder combination A – bimodal distribution).

The highest apparent and tapped densities were reached with a solid load of 50 vol%. At higher solid loads more and more broken granules were found. This is a result of the lower flowability of the liquid medium and the denser shell, which prevents evaporation of the liquid. The yield of the spray drying process also increased up to this value and then declined abruptly. This behavior occurs due to the abrupt rise in slurry viscosity over 50 vol% solid load, which Lukasiewicz [103] already noted. The proposed thesis of McGeary [128] for spheres, that a weight fraction of 0.726/0.274 coarse to fine particles should feature the highest packing density

for bimodal distributions, could be confirmed in this work for spray dried granules. The difference between the worst distribution (40%/60%) and the best was 4.6% in apparent density and 2.8% in tapped density.

### 3.2.3 Influence of dopant shape and multimodal distributions on granules

Three different powder combinations of water based spray drying slurries were prepared for the various experiments. To achieve highly dense powder for the laser processing, powder combination A, B and C (**Table 9**) were spray dried. Two types of  $\text{Fe}_2\text{O}_3$  nanoparticles (rod-shaped and spherical) were chosen to study the effect of granule shape on laser light absorption (powder combination B and C). TEM images of both iron oxide particles are given in **Figure 15** (chapter 3.1.2).

**Table 9:** Powder combinations.

Powder combination	Composition $\text{Al}_2\text{O}_3$		$\text{Fe}_2\text{O}_3$
A	AA3 / AA03 / AluC	trimodal	rod-shaped L2818D
B	AA3 / TM-Dar	bimodal	spherical L2715D
C	AA3 / TM-Dar	bimodal	rod-shaped L2818D

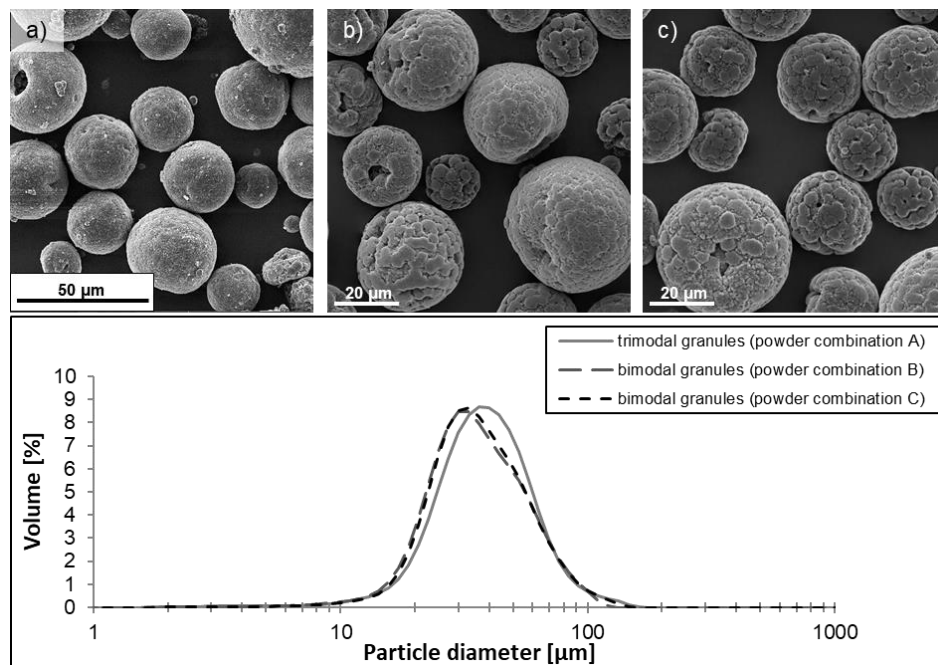


**Figure 31:** SEM images of granules spray dried from a) powder combination B – trimodal distribution, b) powder combination C – bimodal distribution, c) powder combination D – bimodal distribution d) volume-based LD particle size distribution of granules.

The spray drying process produced predominantly spherical, but also donut shaped granules (**Figure 31a, b, c**). This is likely due to the ultrasonic nozzle, since in other works deflocculated

slurries led to irregular shaped granules. Spherical particle shape is very beneficial, since it ensures a high flowability of the powder needed in the SLM/SLS process. Due to good dispersions of the suspensions, the granules had predominantly a small hollow core with a dense shell. In this state of dispersion the particles are more mobile without interparticle forces and can pack densely. Because of the high solid loads, these shells remained thick and the hollow cores of the processed granules small. It was also noted that the shell of the granules had a graded structure. More of the fine particles were gathered in the outer regions of the shell than in the inner regions. An explanation could be that the finer particles are moving easier than the coarse particles to the outside during evaporation of the liquid medium. An influence of the dopant (elongated or spherical  $\text{Fe}_2\text{O}_3$ ) on the shape was not recognizable. For all powder combinations, a binder content of 2 wt% PEG 35000 was needed to obtain non-broken granules.

Particle size distribution of the produced powders is represented in **Figure 31d**. The granules produced by spray drying have a uniform size distribution. The bimodal granules are slightly shifted to a smaller average size (powder combination B:  $d_{10} = 19.8 \mu\text{m}$ ,  $d_{50} = 33.3 \mu\text{m}$ ,  $d_{90} = 61.4 \mu\text{m}$ ; powder combination C:  $d_{10} = 20.2 \mu\text{m}$ ,  $d_{50} = 33.9 \mu\text{m}$ ,  $d_{90} = 62.1 \mu\text{m}$ ) compared to the trimodal granules (powder combination A:  $d_{10} = 20.9 \mu\text{m}$ ,  $d_{50} = 36.3 \mu\text{m}$ ,  $d_{90} = 62.3 \mu\text{m}$ ). Both bimodal granules have nearly the same distribution, which shows, that the shape of the hematite does not have an influence on the granule size and the spray drying process is reproducible. The maximum granule size is around  $150 \mu\text{m}$  due to the separation of fine and coarse granules within the spray dryer and the subsequent screening with a 120 mesh sieve.

#### **3.2.4 Evolution of pH-value during slurry preparation and slurry stability after mixing of all components**

The pH change of three different slurries for powder combination A, B and C was monitored to guarantee the long-term stability of the particle dispersions (**Figure 32**). By the addition of the binder PEG 35000 to the micron-sized AA3 aluminum oxide particles, the pH increases for all slurries from a value above 7 to a value of above 8. Measurements of PEG 35000 in water showed a slightly alkaline pH value, what could be due the used synthesizing method. The AA3 dispersion for powder combination A displayed lower pH values than the dispersions for the other two dispersions (with and without binder). This is due to the lower solid load of particles in water (41 Vol% compared to 45 Vol%). A higher solid load for the slurry of powder combination A led to a strong dropping effect during spray drying, as explained more in details in chapter 3.2.5. AA03 aluminum oxide particles showed as the only starting material a pH below

7 in combination with Nanopure water and the dispersant ammonium citrate dibasic. This atypical value could be due to residual surface groups or impurities of the material, which interfere in the negative charge formation. However, the final pH value of the slurry for powder combination A as well as the pH values for the other two slurries were above a value of at least 7 (powder combination A: 7.79, powder combination B: 8.20, powder combination C: 7.97).

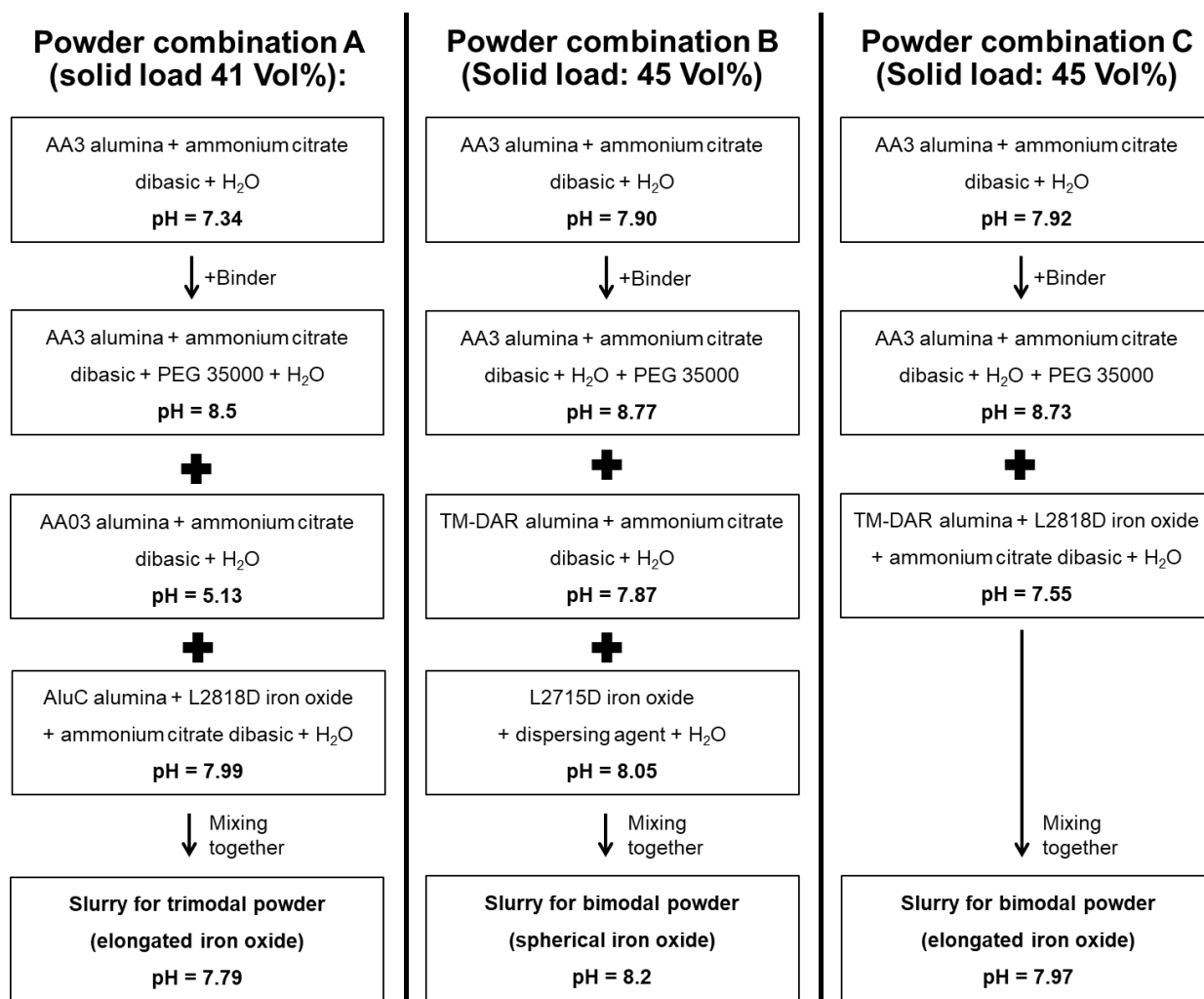


**Figure 32:** Evolution of pH-value of the three different dispersion for powder combination A, B and C during slurry preparation.

These values should ensure in theory a stable dispersion without formation of agglomeration during the mixing process according to the findings in chapter 3.1. The slurry for powder combination B showed a higher final value than the one for powder combination C. 1 Vol% of the elongated nano iron oxide (L2818D) was used instead of 1 Vol% spherical nano-iron oxide (L2715D). This could be expected due to the small shift of the zeta potential curve of L2818D

in water by using ammonium citrate dibasic. Since the surface charge of these particles is already negative in water without dispersant, and thus an adsorption of the dispersant on the surface is aggravated due to charge interferences (**Figure 17c**).

The slurry for powder combination C was left without agitation after the final mixing step for up to 60 hours to evaluate the sedimentation behavior and the dispersion stability (**Figure 33**).

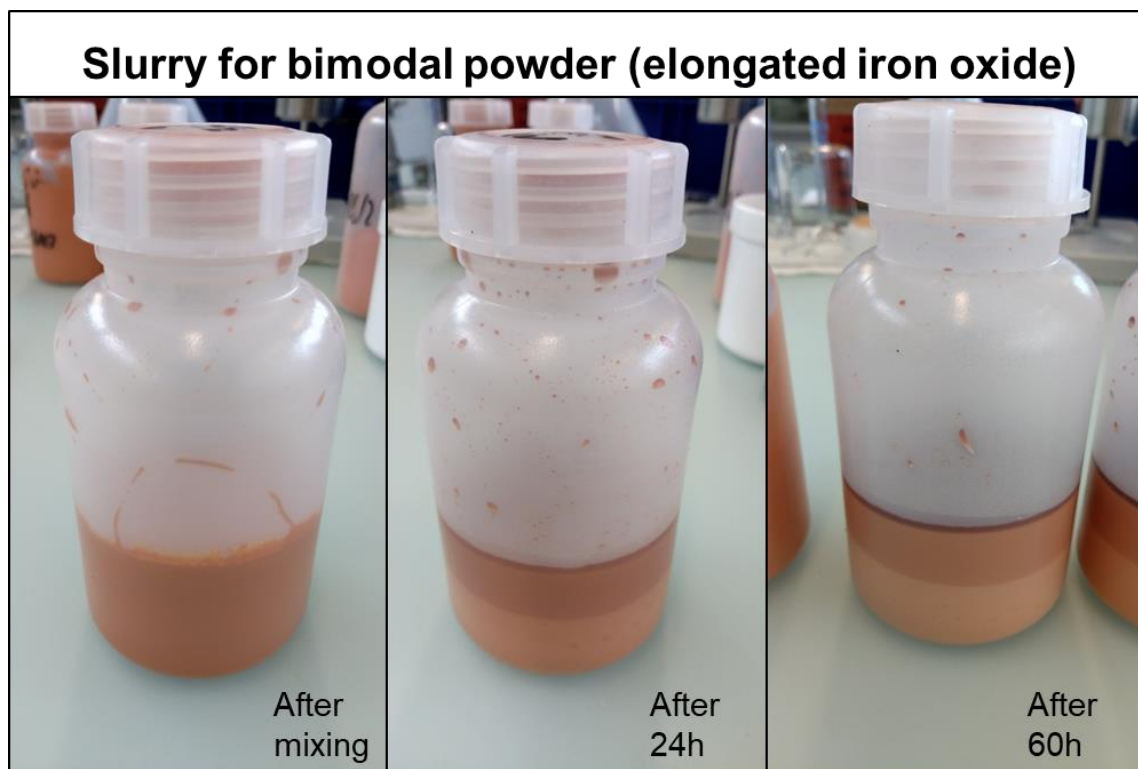


*Figure 33: Slurry for powder combination C directly after mixing and left without agitation for 24 hours and 60 hours.*

After mixing, the slurry is homogeneously dispersed. The orange color, which is a result of the red iron oxide and white alumina powder, is uniform within the whole slurry. After 24 hours, three regions with a different color are visible. The lowest region represents an excess of coarse AA3 aluminum oxide particles. However, a small fraction of both nanoparticles should be also present in this region, since the color was still slightly orange toned. For micron-sized particles the gravitational force of this particles, responsible for sedimentation, can overcome the adhesion forces in dependence on the adhesion mechanism and for particles bigger than 10 micron, the gravitational force dominates [28]. The middle region consisted mainly of TM-DAR aluminum oxide nanoparticles, which can also sediment when re-agglomeration of these particles occurs. The upper region featured the darkest color due to the highest amount of red nano- $\text{Fe}_2\text{O}_3$  particles. After 60 hours, these three regions were even more pronounced. To avoid a demixing during spray drying, which can last up to several hours, a magnetic stirrer was used



### 3.2.5 Influence of slurry viscosity on yield of granules

**Figure 34** shows viscosity as well as shear stress in relation to shear rate of the slurries used for the granulation with different bimodal and trimodal powder combinations (**Table 9**). The relevant shear rate for spray drying are usually in the range of  $10^4$ – $10^5$  1/s [245] for systems using atomizing air according to the estimation by mathematical modeling.

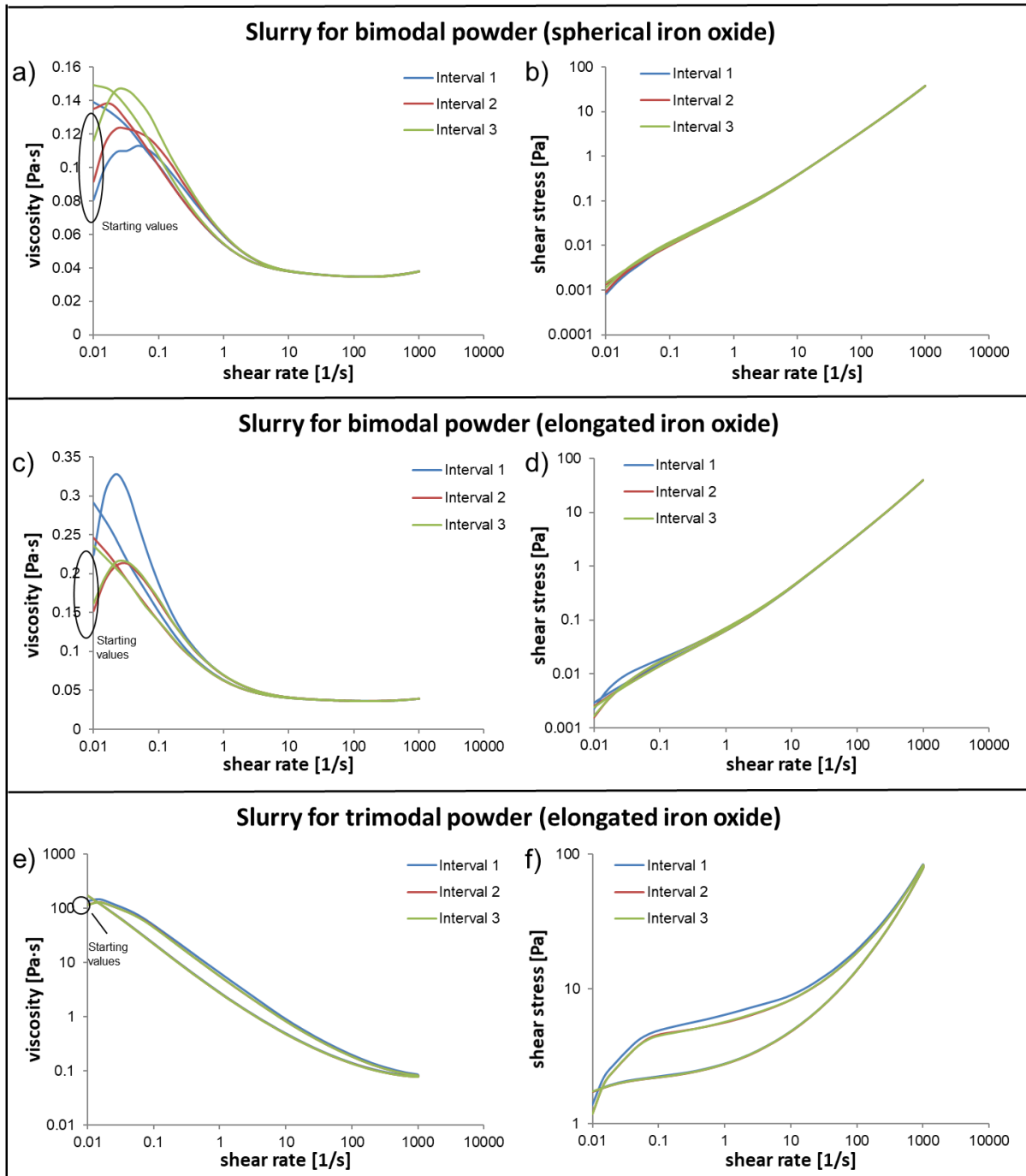


**Figure 34:** Measurements of viscosity respectively shear stress in relation to shear rate of the slurries for **a, b**) powder combination B, **c, d**) powder combination C, **e, f**) powder combination A.



The slurry for powder combination B (bimodal powder with spherical iron oxide dopant) (**Figure 34a, b**) showed very slight difference in the three tested intervals at the important shear rates for spray drying of around 1000 1/s. However, the starting values varied within the values 0.08 – 0.12 Pa·s, which most probably due to the low accuracy of the measurement device at low shear rates. The constant slope of the shear stress in the shear rate range from 10 1/s till 1000 1/s suggests the dispersion behaves almost as a Newtonian fluid.

The slurry for the bimodal powder with elongated iron oxide (powder combination C) revealed slightly higher starting values and end values of the viscosity than the slurry doped with spherical iron oxide. Otherwise, the values and behavior for shear stress over shear rate were very similar. At shear rates from 10 1/s until 1000 1/s the slurry behaved almost as a Newtonian fluid (**Figure 34c, d**).

The slurry for the trimodal powder (powder combination A) showed a shear thinning behavior, which is favorable behavior for spray granulation with high shear rates, since the viscosity decreases under higher shear strain (**Figure 34f**). However, the slurry had also the doubled values of viscosity in the shear rate range from 10 1/s until 1000 1/s in comparison to other two slurries (**Figure 34e**), which led due to strong dropping from the ultrasonic nozzle during spray drying.

In consequence, a lower yield of the granulation process for this slurry was expected. However, the yield of the granules from the three dispersions, taken from the powder collector and screened with a 125 µm sieve, was quite similar (powder combination A: 28.9 %, powder combination B: 26.9 %, powder combination C: 28.0 %). The similar yield of powder combination A, despite the strong visual dropping effect, could be due to the high amount of alumina nanoparticles, which show a strong tendency for agglomeration due to an increased impact of attractive van der Waals forces[28]. Kendall et al. showed for example that granulation with only nanoparticles and without a binder was possible only due to the strong attractive forces of nanoparticles [246]. However, an increase in solid load to 45 Vol% and 49 Vol% led to even stronger drop formation at the nozzle and gave yields of only 8.7 % and 7.3 %, respectively. Despite the slightly lower viscosity of the slurry for powder combination B compared to the slurry for powder combination C, the yield was higher for the later slurry. These small differences could be due the current uncertainty of both measurements.

#### **3.2.6 Addition of coarse alumina to spray-dried granules**

The coarse alumina AA18 could be homogenously distributed within the different granules (**Figure 35a, b, c**) and the granules were not destroyed during the mixing process. Particle size

distribution of the produced powders with the mixture of coarse AA18 alumina are imaged in **Figure 35**.

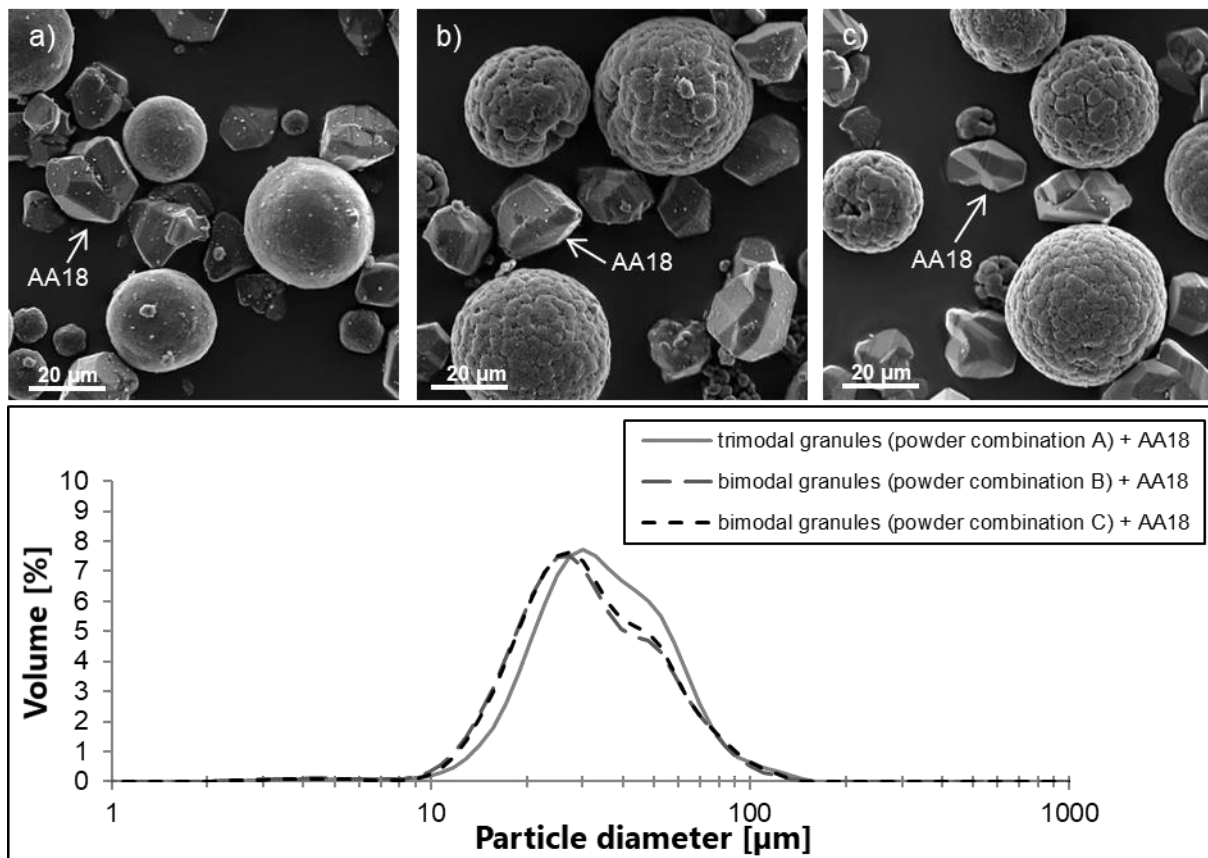


**Figure 35:** SEM images of granules spray dried from a) powder combination B – trimodal distribution, b) powder combination C – bimodal distribution, c) powder combination D – bimodal distribution, d),e),f) granules above mixed with coarse alumina AA18. Volume-based LD particle size distribution of granules with the mixture of coarse AA18 alumina (70 vol% granules / 30 Vol% AA18).

The characteristic size values are shifted to a smaller average sizes (powder combination A:  $d_{10} = 18.1 \mu\text{m}$ ,  $d_{50} = 32.2 \mu\text{m}$ ,  $d_{90} = 60.4 \mu\text{m}$ ; powder combination C:  $d_{10} = 15.1 \mu\text{m}$ ,  $d_{50} = 28.0 \mu\text{m}$ ,  $d_{90} = 57.5 \mu\text{m}$ ; powder combination A:  $d_{10} = 16.1 \mu\text{m}$ ,  $d_{50} = 28.8 \mu\text{m}$ ,  $d_{90} = 58.5 \mu\text{m}$ ) by mixing coarse alumina AA18 with the granules. Both bimodal granules have nearly the same distribution, which shows, that AA18 could be distributed in a similar manner within the spray-dried granules. The maximum granule size is slightly smaller (around  $140 \mu\text{m}$ ) than prior to mixing due to the 30 Vol% of AA18 with  $d_{90}$  of only  $26.1 \mu\text{m}$ . Mixing with coarse alumina AA18 led to smaller sizes and uneven distributions.

By adding this alumina with minor particle sizes, the portion of  $10 - 30 \mu\text{m}$  is increased, which also affected the flowability of the powders (**Figure 36**). The Hausner ratios for both bimodal and trimodal granules increased.

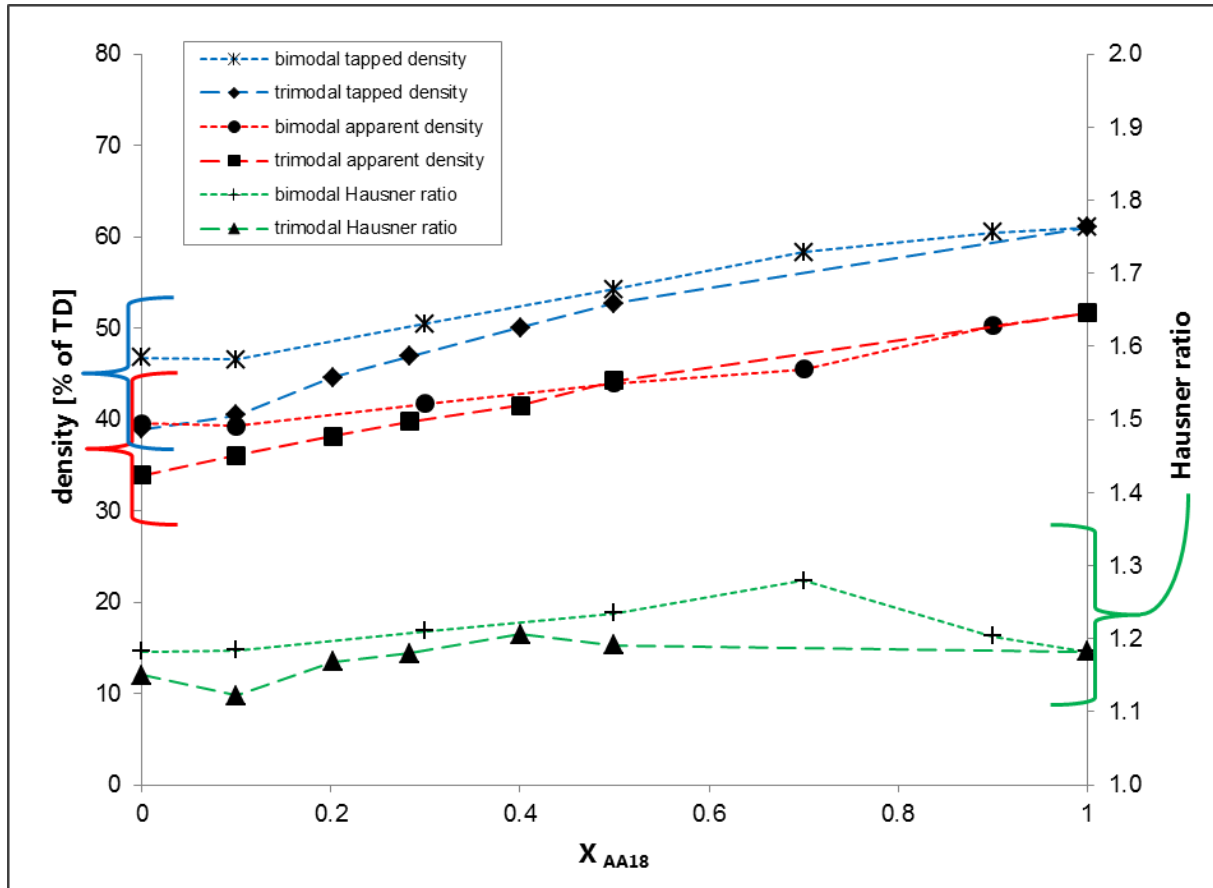


Figure 36: Apparent and tapped density as well as Hausner ratio dependent on amount of additional coarse AA18.

The higher values can be attributed to the more irregular size distribution, since the granules and the coarse AA18 have almost the same flowability. Apparent and tapped density of the powder increase with the addition of the coarse alumina. This effect can be explained by the high packing density of the AA18, which can be homogeneously mixed and packed densely together with the granules. However, the powder is too coarse to fill the interstices of the granules to achieve even higher densities. The bimodal granules have higher densities than the trimodal granules, but with increasing addition of coarse AA18, the densities become more similar. The dispersion of the particles for the trimodal granules was not sufficient, to reach a ratio between the nearest particle sizes of more than seven (in accordance to McGeary [128]). For higher densities, this ratio should be met so that the smaller particles can fill the interstices of the bigger ones.

Aluminum oxide powders with particle sizes in the range of 1-10  $\mu\text{m}$  were applied to achieve higher packing density by a bimodal distribution of granules and additional powder. The aim was to increase the ratio between the nearest particle sizes and consequently, further increase

the powder packing density according to McGeary [128]. The aluminum oxides CB-P02 and CB-10 (Showa Denko, Japan) were tested to achieve these goals.

**Figure 37** presents images of CB-P02 and CB-10 made by SEM. Both powders have a spherical appearance. However, submicron particles and consequently, agglomerations are also present in both images.

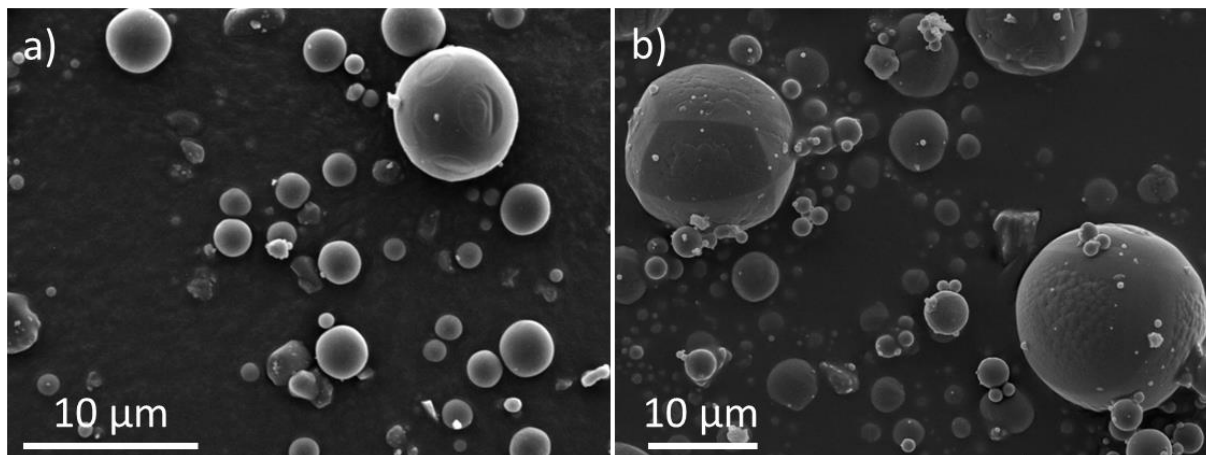


*Figure 37: SEM images of a) CB-P02 ( $Al_2O_3$ ) and b) CB-P10 ( $Al_2O_3$ ).*

The specific surface area (SSA) and the resulting BET average particle size of CB-P02 were  $0.9 \text{ m}^2/\text{g}$  and  $1.7 \text{ }\mu\text{m}$ , respectively. A BET analysis was not performed for CB-P10 due to the expected low SSA. A particle size measurement of CB-P10 with the dry powder system gave the characteristic values of  $d_{10}$  of  $0.86 \text{ }\mu\text{m}$ ,  $d_{50}$  of  $6.18 \text{ }\mu\text{m}$  and  $d_{90}$  of  $14.73 \text{ }\mu\text{m}$ .

The apparent and tapped density of CB-P10 were 43.3 % and 65.0 % of the theoretical density (TD), respectively. This tapped density was even higher than for AA18 (61.1 % of TD). However, the Hausner ratio of CB-P10 was also higher than AA18 (1.50 compared to 1.18). CB-P02 showed an even higher Hausner ratio of 1.79 due to apparent agglomerations. Furthermore, apparent and tapped density were lower compared to the other two powders (29.2 and 55.0 % of TD).

By adding the powder CB-P10, the tapped density of the bimodal powder mixtures increased constantly (**Figure 38b**), since the smaller aluminum oxide particles could fill the interstices of the bigger granules due to the suitable ratio between the nearest particle sizes according to McGeary [128]. In case of CB-P02, a maximum tapped density was reached at a ratio of granules to additional alumina of 30 to 70 Vol% (**Figure 38a**). A distinct increase of the tapped density was also recorded for the addition of this powder.

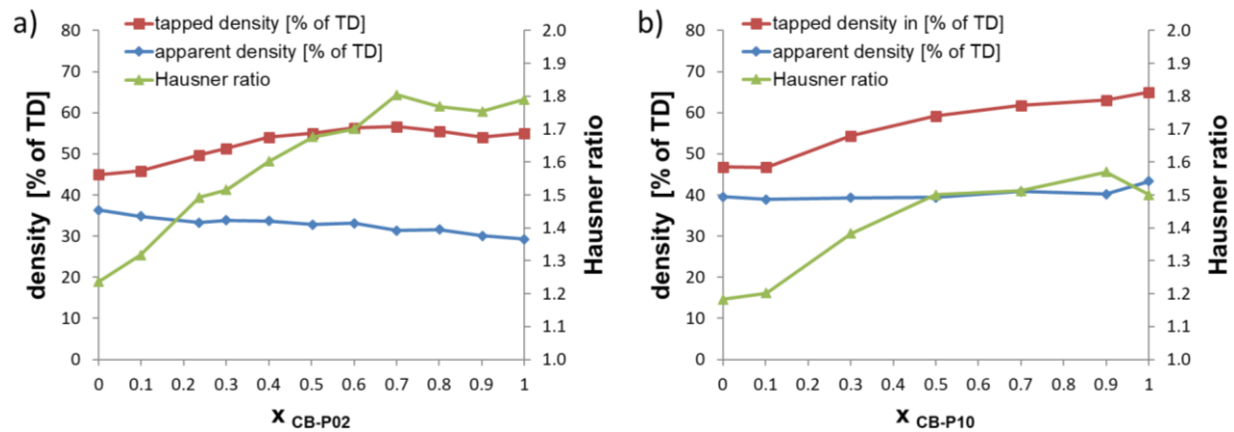


**Figure 38:** Apparent, tapped density and Hausner ratio dependent on amount of additional aluminum oxide **a)** CB-P02 and **b)** CB-P10.

However, the Hausner ratio increased by the addition of both types of alumina and thus the flowability of the mixed powders worsened. This effect was more distinct for the addition of CB-P02, which also showed a higher Hausner ratio for pure powders than CB-P10 (1.79 compared to 1.50). This flowability decrease had a strong effect on the apparent density of both powder mixtures. The apparent density stayed almost constant for powder mixtures with CB-P10 and experienced a steady decrease by the addition of CB-P02.

In contrary to these powders, the apparent as well as the tapped density increase with the addition of the coarse alumina AA18. This makes addition of AA18 more favorable for the laser processing, since the layering process creates a powder bed density, which should be between the values of apparent and tapped density.

Different combinations of 50 Vol% pure granules with additional aluminum oxides AA18 and CB-P10 were also tested (**Figure 39**). The aim was to combine a high apparent density achieved by addition of AA18 with a high tapped densities achieved by addition of CP-B10. The most favorable combination for laser processing consisted of 50 Vol% pure granules, 45 Vol% AA18 and 5 Vol% CB-P10. The apparent density, tapped density and Hausner ratio were 44.2 % of TD, 54.2 % of TD and 1.22, respectively. These values were better than the values achieved with the mixture of 50 Vol% granules and 50 Vol% AA18. However, only small differences were measured. Apparent and tapped density increased by 0.7 and 0.8 % of TD, and the Hausner ratio decreased by the less significant value of 0.01. The other powder combinations with a higher amount of CB-P10 led to a flowability decrease (increase of Hausner ratio). However, the use of the ratio 50 Vol% granules, 40 Vol% AA18 and 10 Vol% CB-P10 gave also a higher apparent and tapped density (44.0 and 56.2 % of TD) compared to 50 Vol% granules and 50

Vol% AA18. The Hausner ratio of 1.28 for this powder mixture was higher than the recommended value of 1.25 for laser powder bed fusion [57, 237].

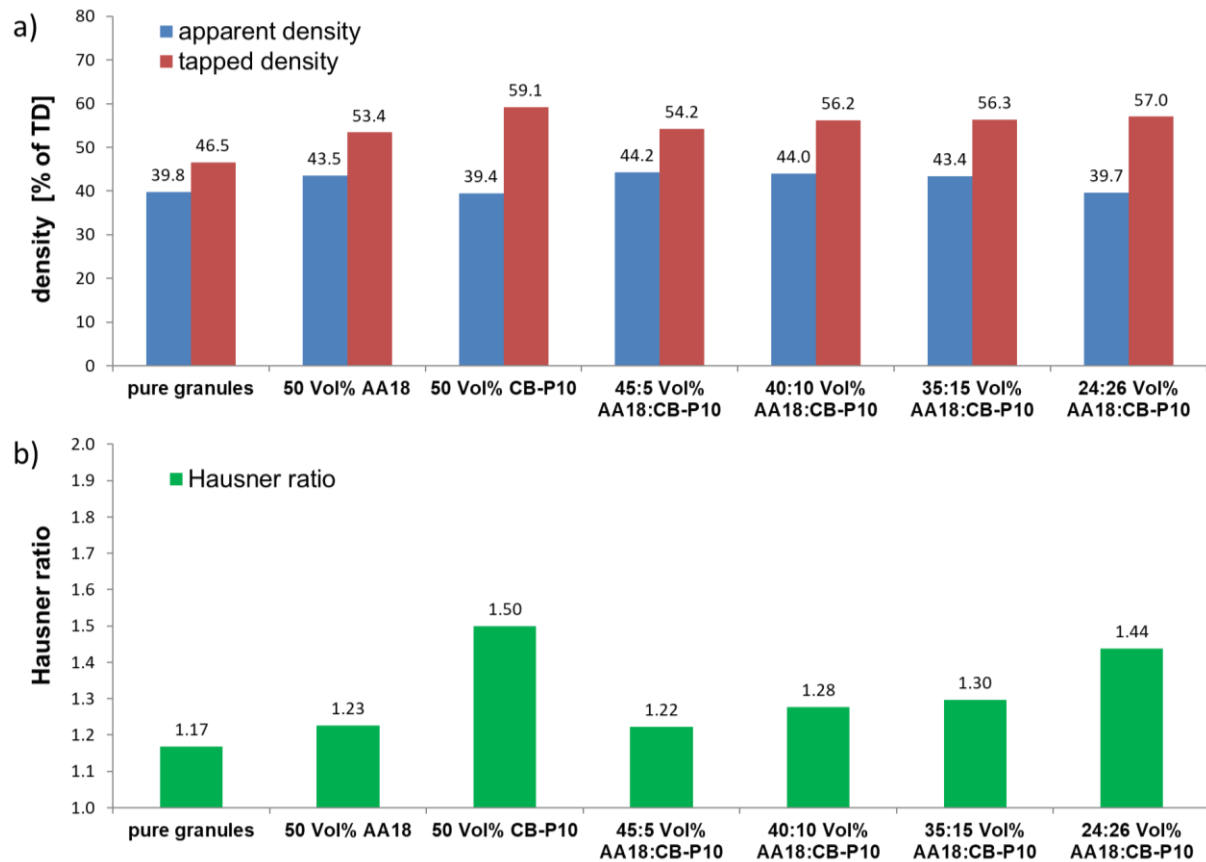


Figure 39: Different combinations of 50 Vol% pure granules with additional aluminum oxides AA18 and CB-P10.

### 3.2.7 Application of Andreasen model on mixtures of ceramic particles with spray-dried granules

The use of the Andreasen model [129] was considered to maximize powder packing by a continuous size distribution. The approximations of such a dense packing blend by using this model were done by the EMMA software. The powder properties of the used powders are described in the chapters before.

**Table 10** summarizes the calculated powder combinations by the EMMA software (Mixtures 2, 4, 6, 7, 9) for the addition amounts of 40 wt%, 50 wt% and 50 Vol%. Mixtures 1, 3, 5 and 8 consist of pure granules and the addition of the same amount of coarse alumina AA18. These mixtures were made for comparison of the results achieved by the powder combinations calculated by the EMMA software. Four different types of granules were used for these experiments: Spray-dried granules A (Mixtures 1 and 2), thermal pre-treated granules A (Mixtures 3 and 4), spray-dried granules B (Mixtures 5 and 6) and spray-dried granules C (Mixtures 7, 8 and 9).

### 3 Doped spray-dried granules to solve densification and absorption issue in PBF of alumina

**Table 10:** Powder combinations calculated by the EMMA software (Mixtures 2, 4, 6, 7, 9) and powder combinations with coarse alumina AA18 (Mixtures 1, 3, 5, 8) made for comparison of the achieved results.

	Pure granules	Thermal pre-treated granules	Aluminum oxide AA18	Aluminum oxide AA3	Aluminum oxide CB-P02	Aluminum oxide CB-P10
Mixture 1	60 wt%		40 wt%			
Mixture 2	60 wt%		19 wt%	9.5 wt%	11.5 wt%	
Mixture 3	60 wt%		40 wt%			
Mixture 4	60 wt%		19.25 wt%	3.5 wt%	19.25 wt%	
Mixture 5		50 wt%	50 wt%			
Mixture 6		50 wt%	30 wt%		20 wt%	
Mixture 7	70 wt%		7 wt%			23 wt%
Mixture 8	50 Vol%		50 Vol%			
Mixture 9	50 Vol%		10 Vol%			40 Vol%

**Figure 40** illustrates cut screen-shots of the EMMA interface after the calculation of mixture 2, 4 and 6.

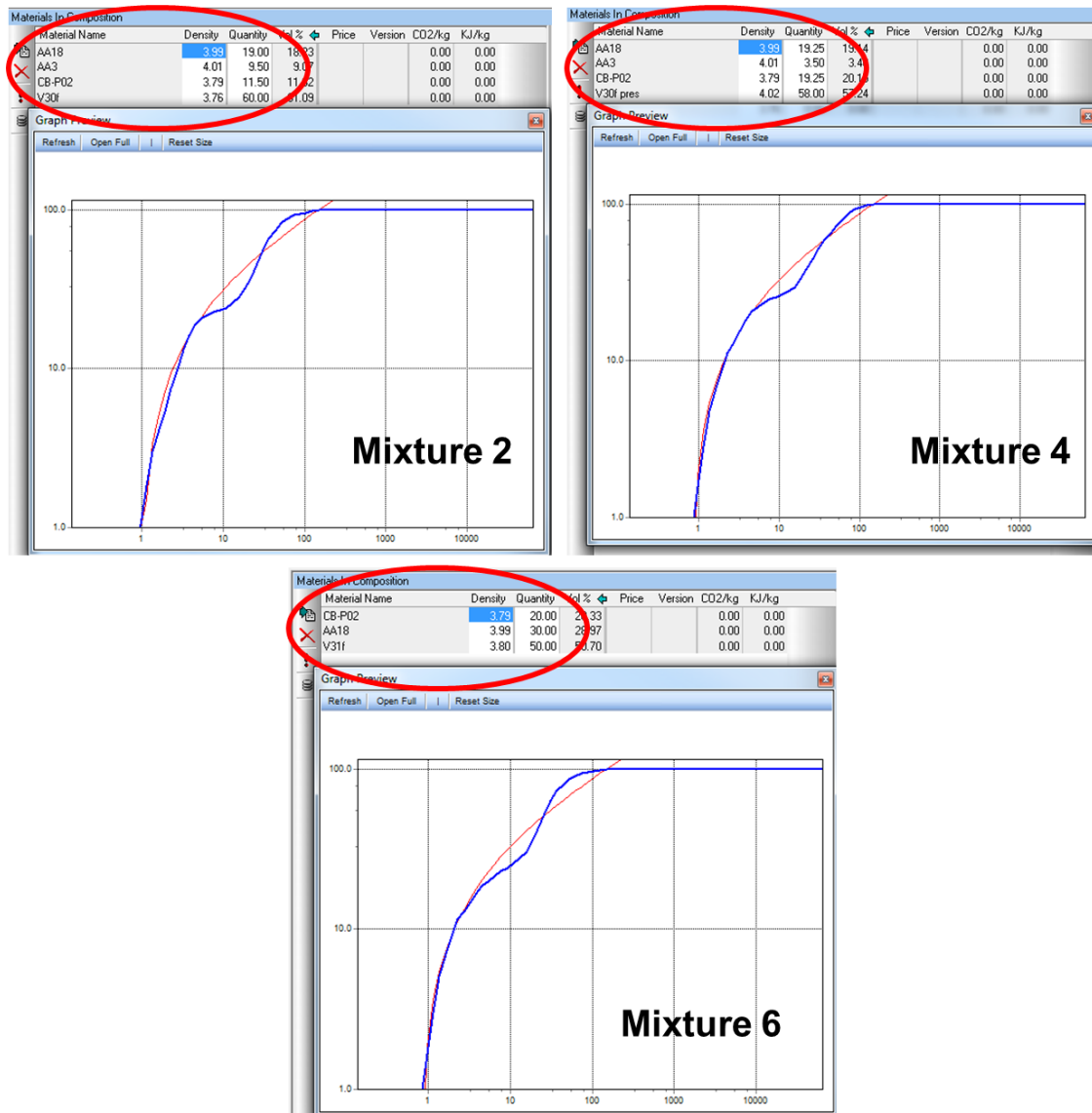


**Figure 40:** Cut screen-shots of the EMMA interface after the calculation of mixture 2, 4 and 6.



A maximum packing density given by the EMMA software (red curve) was not achieved for these mixtures, since the approximation of blue curve was close to the red curve, but still a certain difference compared to the optimal distribution according to the Andreasen model was visible. The best approximation was reached by mixture 4.

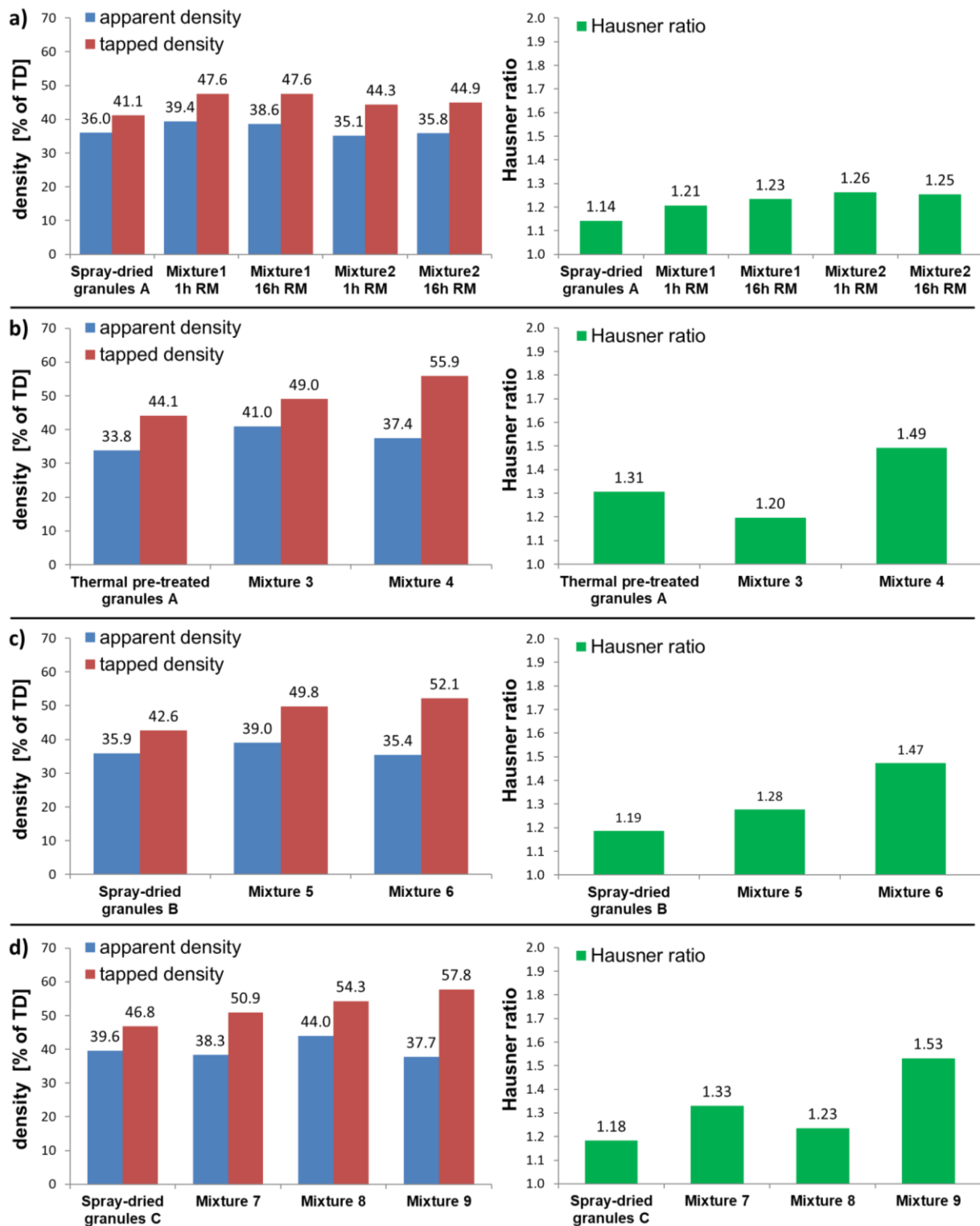


Figure 41: Measured apparent densities, tapped densities and Hausner ratios by using the powder combinations summarized in Table 9.



**Figure 41** shows the measured apparent densities, tapped densities and Hausner ratios by using the powder combinations summarized in **Table 9**.

**Figure 41a** evaluates the influence of the roll milling time (1 and 16 hours) on these properties. However, only small differences were noted due to the increase of the mixing time. A small decrease of the apparent density (0.8 % of TD) was measured for mixture 1 (40 wt% AA18). The apparent and tapped density of mixture 2 increased slightly by 0.7 and 0.6 % of TD, respectively. These slight changes of the values could be within the measurement error.

**Figure 41b, c, and d** show a similar behavior in terms of the change of apparent and tapped density as well as Hausner ratio despite of the change of the initial granules. The apparent density in the mixtures according to Emma Software remains similar to the apparent density of the granules. Only mixture 4, which was also the best approximation, shows an increase of the apparent density. However, the starting granules of this mixture were thermally pre-treated. This thermal treatment leads to an increase of the Hausner ratio (from 1.14 to 1.31) and thus, to a decrease of the apparent density by a worsened flowability. The Hausner ratio was in general higher for powder combinations calculated by the EMMA software compared to pure granules and powder combinations with merely coarse alumina AA18. The highest apparent densities were found in the mixtures containing only the additive alumina AA18. Higher tapped density were received by mixing powder combinations according to the EMMA software. To fulfil the packing theory according to the Andreasen model, the utilized particles were too small in size. Agglomerations, especially the smaller particles, lead to a lower flowability and thus, a lower apparent density. However, this packing theory delivers higher tapped density, since more voids of bigger particles can be filled by smaller particles and the flowability does not have a too large impact due to the nature of the powder consolidation method.

Zou et al. described similar results for increasing the particle packing using the Andreasen model [130]. Due to the powder bed density increase, the overall properties of indirect PBF-LB processed Al<sub>2</sub>O<sub>3</sub> ceramics improved for the green bodies and the final parts. However the smallest used particles had a d<sub>50</sub> of 5.7 µm, which should be more favorable to avoid agglomerations [28] than the smaller particles (CB-P02, AA3) applied in this work. The change of apparent density and Hausner ratio was not reported in the work of Zou et al [130].

### 3.2.8 Thermal pre-treatment of granules

The spray dried granules were thermally treated in air up to 1600 °C to increase the densities of the single granules by sintering and, therefore, to achieve high packing densities in the powder beds for PBF-LB. Furthermore, the thermally treated granules were mixed with coarser aluminum oxide to maintain a high flowability of the powder.

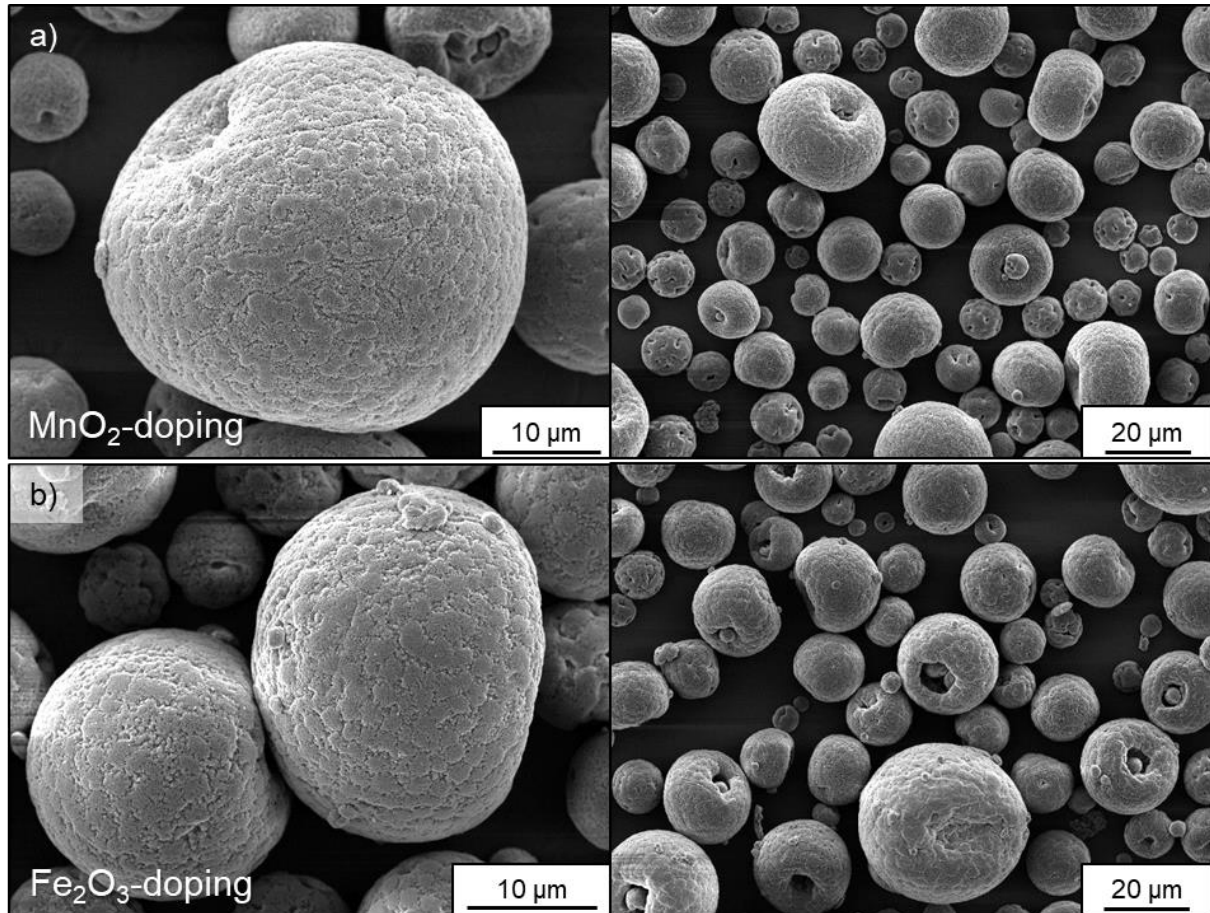


**Figure 42:** SEM images of as-prepared granules after spray drying of bimodal alumina with a)  $\text{Fe}_2\text{O}_3$  doping or b)  $\text{MnO}_2$  doping.

**Figure 42a and b** show alumina granules doped with iron oxide and manganese oxide directly after spray drying. The bimodal distributions of alumina were dispersed in water using an optimal concentration of ammonium citrate dibasic as dispersant (in accordance to chapter 3.1) and consecutively spray dried with addition of PEG 35000 as binder. The aluminum oxide granules are spherical and have a narrow size distribution with both dopants (**Figure 42**). Only a few donut shaped granules were present. The different dopants had no significant influence on the granule shape and granule sizes.

In the case of manganese oxide a slightly higher dopant concentration of 1.24 wt% (1.16 vol%) compared to 0.99 wt% (0.91 vol%) of iron oxide was added, since the particle sizes after dispersing were bigger and a worse distribution was expected. Spray drying led in both cases to preferably spherical granules, which contributed to a high flowability necessary for the SLM/SLS process [127, 162]. The size values of the granules with the different dopants ( $d_{10} = 21.8 \mu\text{m}$ ,  $d_{50} = 36.7 \mu\text{m}$  and  $d_{90} = 63.9 \mu\text{m}$  for  $\text{Fe}_2\text{O}_3$  doped granules and  $d_{10} = 22.0 \mu\text{m}$ ,  $d_{50} = 38.6 \mu\text{m}$  and  $d_{90} = 70.8 \mu\text{m}$  for  $\text{MnO}_2/\text{Mn}_2\text{O}_3$ -doped granules after spray drying) were quite similar. The spherical shape of the granules was most likely a result of the ultrasonic atomizer as discussed in the authors previous paper [95].

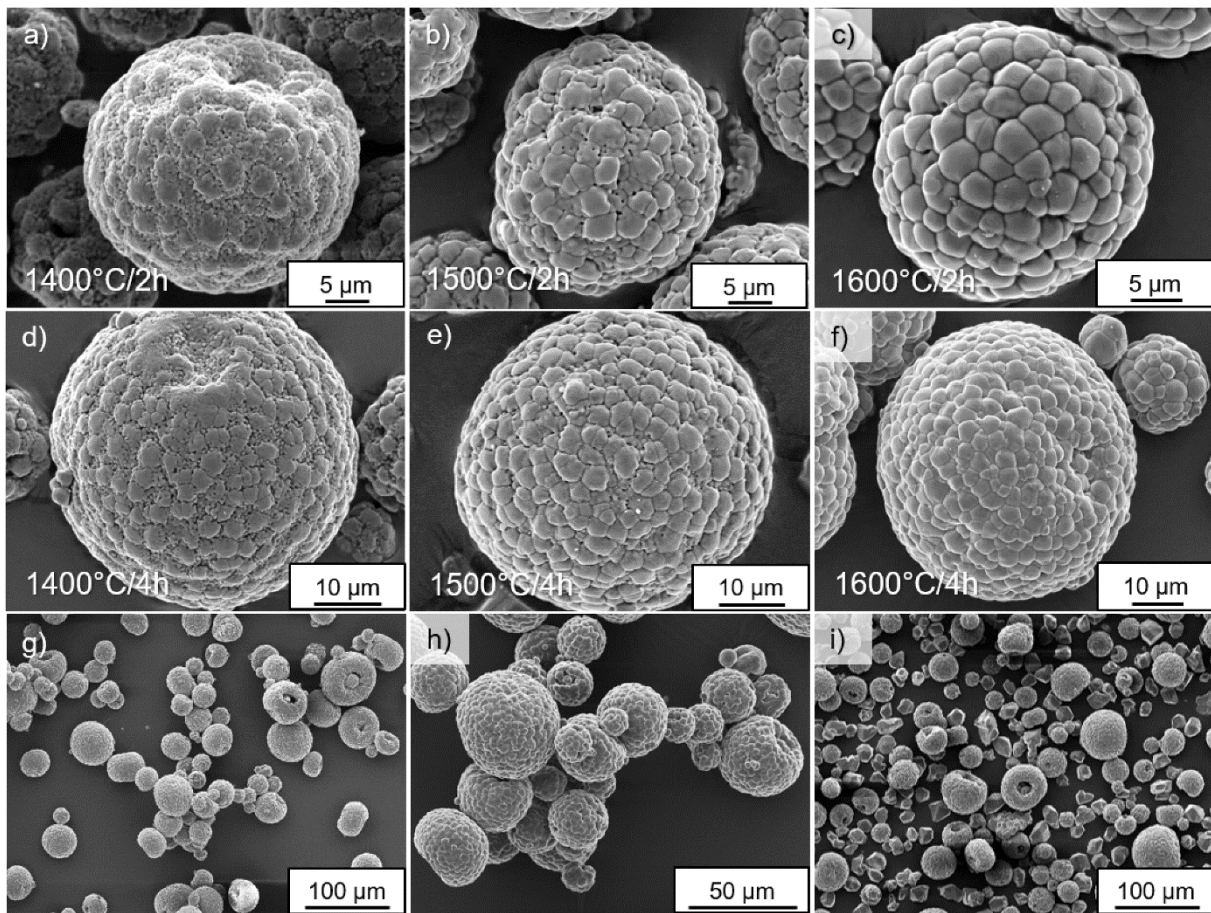


**Figure 43:** SEM images of spray dried granules thermally treated at a) maximum temperature: 1400 °C / holding time: 2 hours, b) 1500 °C/2 hours, c) 1600 °C/2 hours, d) 1400 °C/4 hours, e) 1500 °C/4 hours, f) 1600 °C/4 hours. Illustration by SEM of g), h) sintering necks between the granules and formed agglomerates after thermal treatment at 1600 °C and i) deagglomeration by mixing with AA18.

To increase the density,  $\text{Fe}_2\text{O}_3$ -doped  $\text{Al}_2\text{O}_3$  granules were heat-treated in air at temperatures in the range from 1400 up to 1600 °C. As described in the literature the grain growth within the granules was uniform and equiaxed [161] (**Figure 43a-d**). At a temperature of 1400 °C the sintering of the alumina was at an early stage, reaching an intermediating stage at 1500 °C and



a final sintering at 1600 °C after a idle time of two hours. Sintering necks between the granules, which formed during thermal treatment (**Figure 43g, h**), could be broken by the mixing with coarse alumina AA18 (**Figure 43i**).

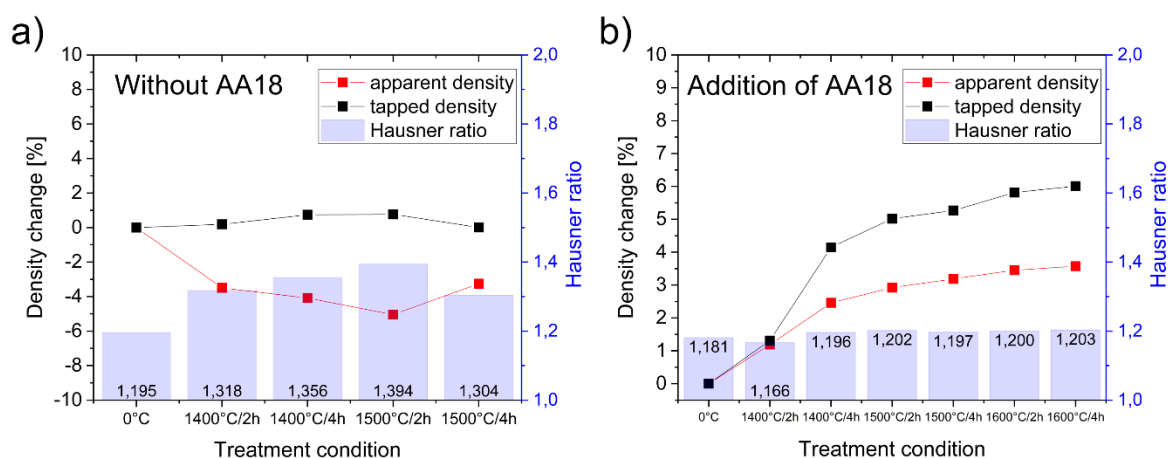


**Figure 44:** Apparent and tapped density change as well as Hausner ratio of thermal treated granules in respect to treatment conditions (temperature/holding time) a) without addition of AA18 and b) with addition of AA18.

Without the addition of AA18, the apparent density of the granules decreased up to 5.0 %, since the formed sintering necks worsened the flowability. This could be seen by the increase of the Hausner ratio up to the maximum of 1.394. The tapped density, which was expected to increase after thermal treatment, remained almost unchanged (less than 0.8 % change), since the formed granule agglomerations prevent a close packing of the powder (**Figure 44a**). By the addition of AA18 (30 Vol% in all mixtures), the apparent and tapped density of the thermal treated powders could be increased by +3.6 % and +6.0 %, respectively. Thermal treatment of the granules had only a minor effect on the Hausner ratio in this mixture. Addition of AA18 resulted in significantly better flowability of approximately 1.2 compared to the results without AA18. This could be due to the separation of bonded granules as well as coarse AA18 acting as flowable medium. Further experiments were conducted with a sintering temperature of 1600 °C and a holding time of 2 hours, since the difference between 2 and 4 hours was less than 0.2% in density change (**Figure 44b**).

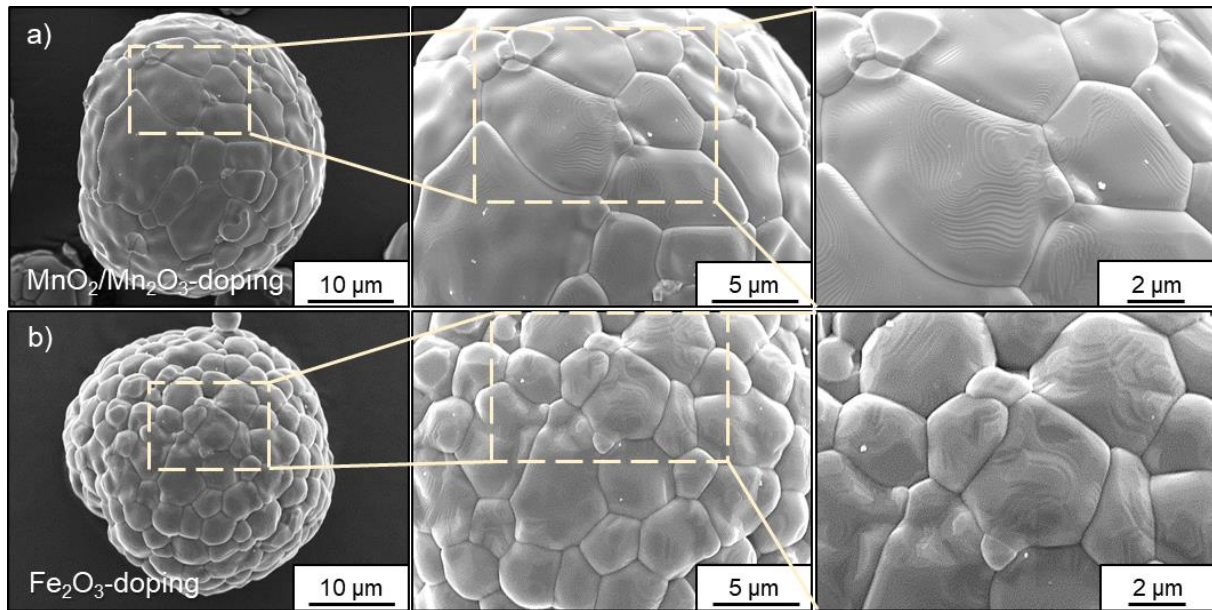


**Figure 45:** SEM Illustration of grain growth and microstructure evolution in alumina granules after sintering at 1600 °C depending on a)  $\text{MnO}_2/\text{Mn}_2\text{O}_3$  doping or b)  $\text{Fe}_2\text{O}_3$  doping.

The two different dopants had a different impact on the sintering behavior of the alumina granules. Whereas the iron oxide dopant triggered a uniform and equiaxed grain growth (**Figure 45b**), the alumina granules doped with manganese oxide exhibited irregular shaped grains after sintering at 1600 °C (**Figure 45a**). Furthermore, the grain growth was more excessive in the case of manganese oxide doping. In both cases the sintering at 1600 °C resulted in dense microstructures with no visible porosity. A promotion of an irregular grain growth by a manganese oxide doping was already described [155-158]. In contrast to promoting anisotropy and vermicular grain growth in  $\text{Fe}_2\text{O}_3$  doped alumina (up to a doping amount of 1% reported in [157] and 0.8 wt% reported in [247]), a uniform and equiaxed grain growth of the granules was observed for a doping amount of 1 wt% and even for 0.1 wt%. This could be due to the higher purity of the raw powders.

X-ray fluorescence contrast tomography was performed on manganese (**Figure 46a-d**) and iron oxide doped (**e-h**) granules. Manganese oxide doped granules are displayed in **Figure 46a and c** before thermal treatment and in **Figure 46b and d** after calcination at 1600°C. **Figure 456e and g** correspond to iron oxide doped granules before thermal treatment and **Figure 46f and h** to the granules after calcination. The corresponding scanned volumes are illustrated in the optical microscopy images of the capillaries (**Figure 46a, b, f**) by the pink rectangles. In case of non-calcinated iron oxide doped granules (**Figure 46e, g**), only one slice is presented.

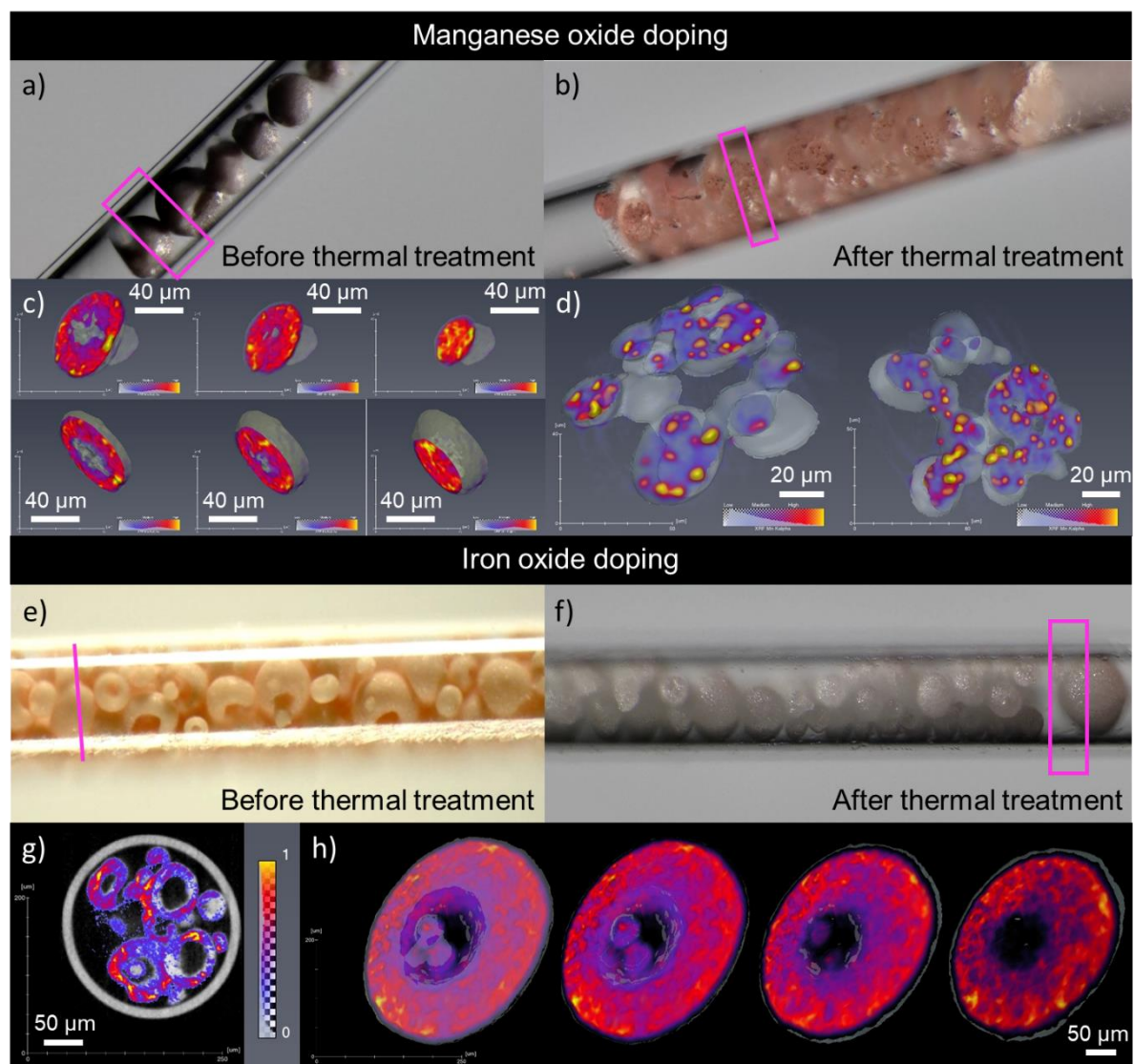


**Figure 46:** Optical microscopy images and X-ray fluorescence contrast tomography of the Mn- (a-d) and Fe-doped (e-h) granules before (a, c, e, g) and after thermal treatment at 1600 °C (b, d, f, h). The color scale indicates the intensity of X-ray fluorescence of Fe K $\alpha$  (yellow-high, red-medium, blue-low), which is a measure of Fe atoms concentration (lack of Fe atoms is indicated by gray color).

The images in the **Figures 46c, d, g and h** were obtained by combining volume reconstructions from  $\mu$ XRF tomography (illustrated by the normalized color scale) and from absorption tomography (illustrated by the gray scale). Therefore, the color scale corresponds to the distribution of Mn and Fe atoms, respectively, while the transparent gray scale corresponds to the whole material of the granules. Gray color is visible only in volume not occupied by dopant atoms, thus in cases of homogeneous distribution the gray material is hardly visible. These measurements clearly demonstrate the effect of calcination on the distribution of the dopants in the granules, showing that originally well dispersed and homogeneously distributed Mn atoms agglomerate by demixing upon calcination. In contrary, the distribution of Fe atoms becomes even

more homogeneous upon calcination at 1600 °C. This observation is in good agreement with the results of the powder diffraction studies presented in [159], where it was demonstrated that due to calcination at 1600 °C, Fe atoms from hematite nanoparticles are implemented in the corundum lattice and no other phases were formed.

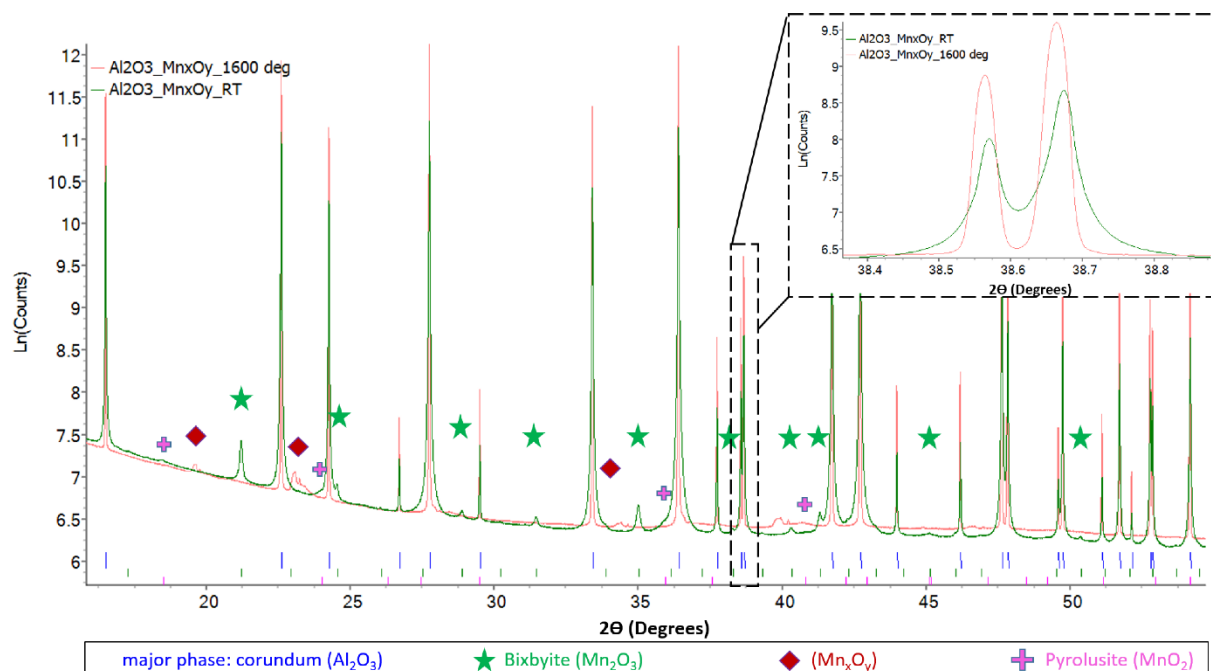


**Figure 47:** High resolution powder diffraction of the Mn-doped granules with peak enlargement to illustrate the implementation of Mn ions within corundum lattice.

The high resolution powder diffraction of the  $\text{MnO}_2/\text{Mn}_2\text{O}_3$ -doped granules presented in **Figure 47**, shows that calcination leads to disappearance of the  $\text{Mn}_2\text{O}_3$  (bixbyite phase), which was the major phase of the manganese oxide dopant particles, and to creation of a very small amount of a not identified manganese oxide phase. The quantification of this phase from refinement of the powder diffraction data is very challenging, as its amount is in the order of the uncertainty of the technique (below 0.1%), therefore it is expected that at least a part of the Mn atoms was implemented in the corundum lattice. This is in agreement with the pink color of the calcined granules. The implementation of Mn ions within corundum lattice is confirmed by the slight change of the lattice constant of corundum (a from 4.7573 Å to 4.7590 Å and c from 12.9870 Å to 12.9930 Å), which was evaluated by the Rietveld refinement and can be seen in the small shift of the corundum peaks (Inlet in **Figure 47**).

X-ray photoelectron spectroscopy (XPS) measurements (**Figure 48a, b and c**) were performed to clarify the oxidation state of manganese within the granules after thermal treatment and to further specify the undefined phase in **Figure 47**.

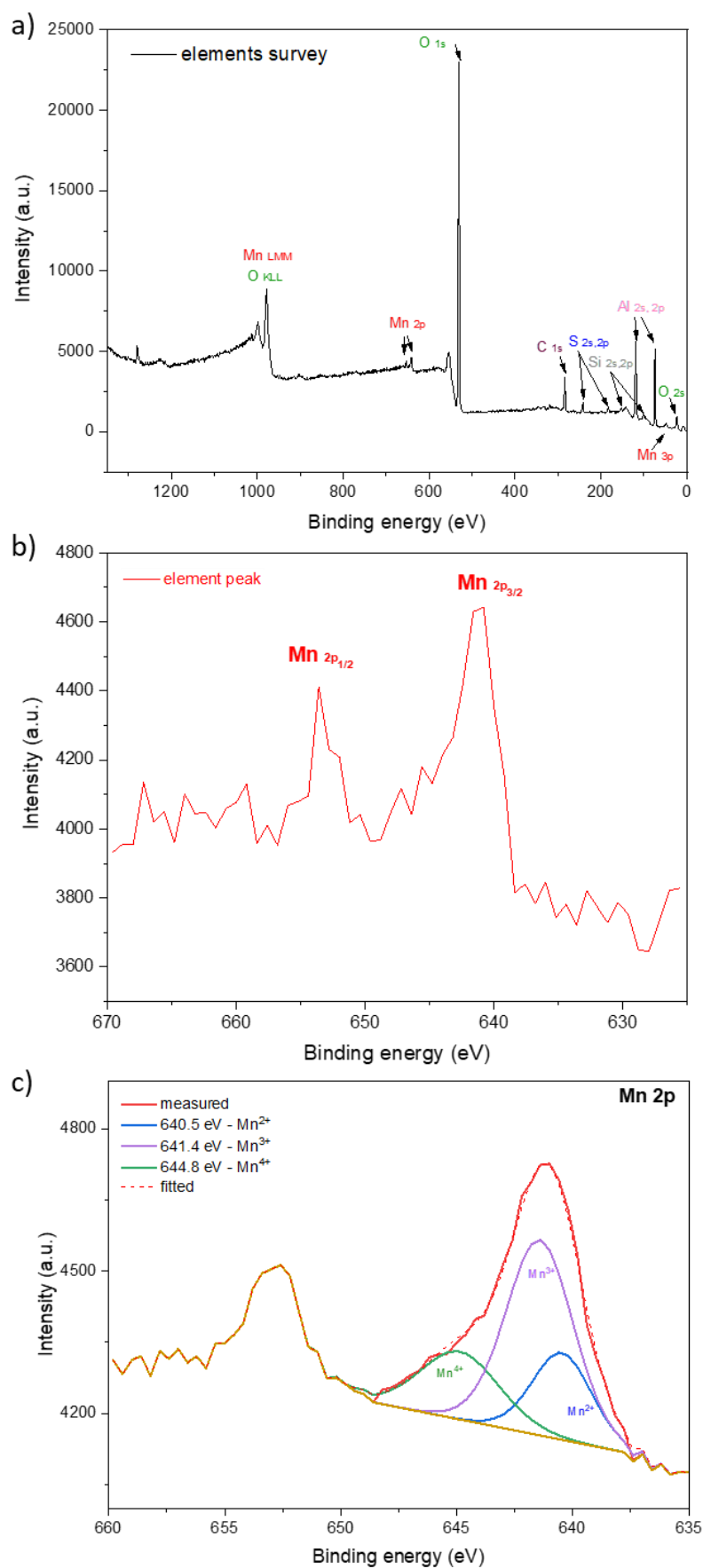


**Figure 48:** X-ray photo-electron spectroscopy measurement of thermal pre-treated manganese oxide doped granules: **a)** elements survey, **b)** enlarged 2p line containing the 2p<sub>1/2</sub> and 2p<sub>3/2</sub> line, **c)** detailed analysis of the Mn2p peak with fitting of the 2p<sub>3/2</sub> line by manganese cations with different valency states.



The XPS method is based on the photo effect. **Figure 48a** reveals the present elements in the thermal pre-treated granules. As expected from the used raw materials, aluminum, manganese and oxygen were present. The measured carbon, silicon and sulfur atoms originate most probably from the underlying glass substrate and from the used adhesive carbon tap, since only a thin powder layer was applied and the x-rays could penetrate to deeper layers. The  $2p_{3/2}$  line is recommended for the analysis of manganese atoms [242]. **Figure 48b** shows an enlarged illustration of the measured 2p line containing the  $2p_{1/2}$  and  $2p_{3/2}$  line.

**Figure 48c** shows a detailed analysis of the Mn2p peak with a higher resolution. According to the made fitting of the measured curve, manganese cations with different valency states ( $Mn^{2+}$ ,  $Mn^{3+}$  and  $Mn^{4+}$ ), which can replace aluminum cations in the lattice, were present after thermal treatment. This was in correlation with the literature [155, 248]. However, these measurements did not give an explanation for the undefined phase in the XRD pattern given in **Figure 47**.

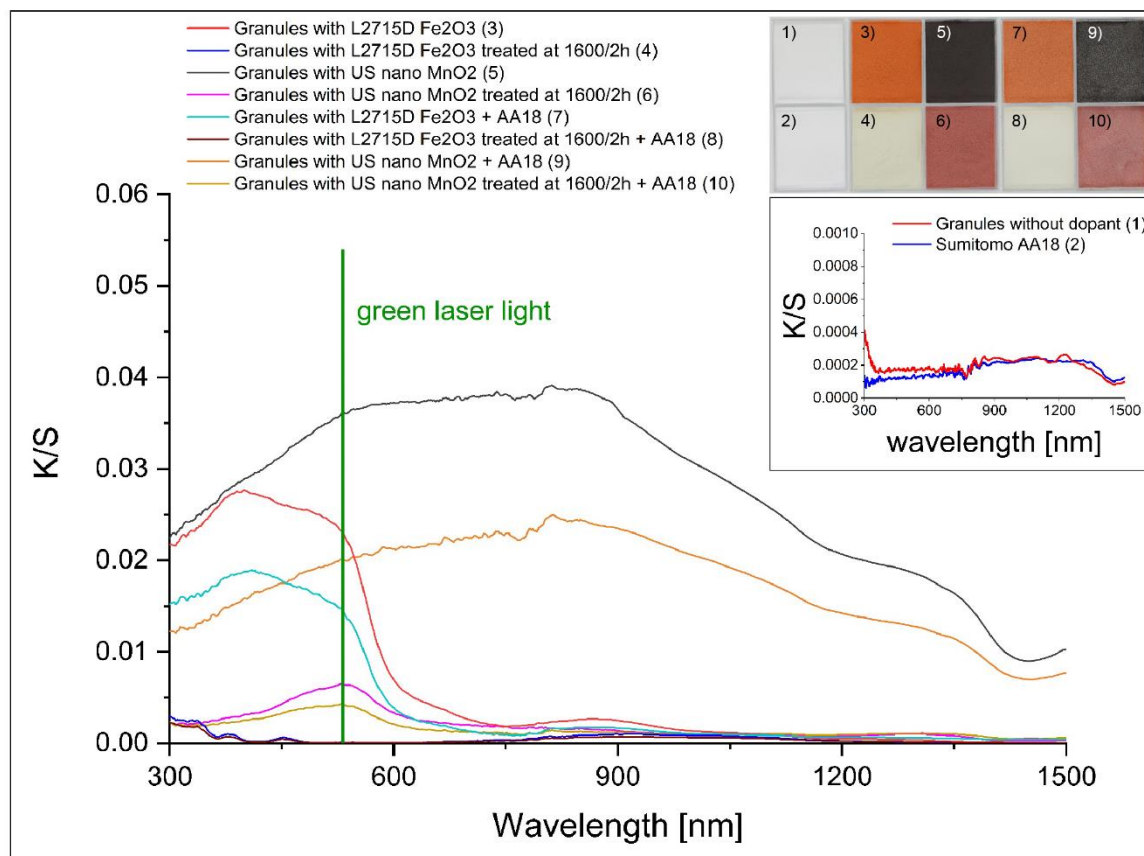


**Figure 49:** Qualitative absorption spectrum for spray dried powders evaluated by the Kubelka Munk method for measurements of diffuse reflectance given by plotting K/S ratio over wavelength.

The qualitative Kubelka Munk spectra revealed a higher absorbance over the whole wavelength range from 300 - 1500 nm for blackish MnO<sub>2</sub>/Mn<sub>2</sub>O<sub>3</sub>-doped granules (powder No. 5 in **Figure**

**49 and Table 11**) than for  $\text{Fe}_2\text{O}_3$ -doped granules (No. 3 in **Figure 49 and Table 11**). This could be mainly due to the higher concentration of manganese oxide (0.25 vol%). The manganese oxide doped granules absorbed better at 532 nm (wavelength of used green laser), while the absorption below ca. 400 nm was nearly the same for both dopants. A color change after thermal treatment at 1600 °C was observed for both doped powders. The orange iron oxide doped alumina changed its color to light beige (No. 4). As described in [159], the  $\text{Fe}^{3+}$  ions diffused first in the nanosized alumina particles at lower temperatures resulting first in two corundum type structures and finally in only one single corundum phase at 1600 °C. Calcination of manganese doped alumina produced magenta colored ceramic granules (No. 6), which was already observed in previous studies [249]. Non-stoichiometric compounds can easily occur during thermal treatment, since manganese cations show a valency change and replace the aluminum cations in the lattice [155, 156], as already shown for the manganese doped alumina granules by the shift of the alumina peak in **Figure 47**. The absorbance decreased for both dopants after thermal treatment. The addition of coarse alumina AA18 led in all cases to a decrease of the K/S ratio (No. 7-10), since pure alumina is a poor absorber in the range of 300-1500 nm, as presented for bimodal alumina granules without dopant (No. 1) and AA18 (No. 2) in the inset on top right side of **Figure 49**. The colors of the powders faded after the addition of alumina. Since a clear absorption edge could be only seen for the  $\text{Fe}_2\text{O}_3$  doped granules with and without AA18 (No. 3 and 7), the calculation of the bandgaps was only made for these two samples. The effective bandgap value of the as-prepared granules was 1.98 eV and only slightly smaller than the 2.00 eV for mixed granules indicating a minor effect of the addition of coarse alumina on the bandgap and the optical properties of the powder.

**Table 11:** Absorbance, reflectance and transmission values of the green laser light in the powder bed measured by an integrating sphere.

Powder	Reflectance [%]	Transmittance [%]	Absorbance [%]
Granules without dopant (1)	82.5	5.9	11.6
Sumitomo AA18 (2)	84.3	6.8	8.9
Granules with $\text{Fe}_2\text{O}_3$ (3)	13.6	0	86.4
Granules with $\text{Fe}_2\text{O}_3$ treated at 1600°C/2h (4)	79.9	3.8	16.3
Granules with $\text{MnO}_2/\text{Mn}_2\text{O}_3$ (5)	7.5	0	92.5
Granules with $\text{MnO}_2/\text{Mn}_2\text{O}_3$ treated at 1600°C/2h (6)	14.6	0	85.4
Granules with $\text{Fe}_2\text{O}_3$ + AA18 (7)	18.1	0	81.9
Granules with $\text{Fe}_2\text{O}_3$ treated at 1600°C/2h + AA18 (8)	82.2	5.2	12.6
Granules with $\text{MnO}_2/\text{Mn}_2\text{O}_3$ + AA18 (9)	11.9	0	88.1
Granules with $\text{MnO}_2/\text{Mn}_2\text{O}_3$ treated at 1600°C/2h + AA18 (10)	22	0	78

For comparison, the quantitative absorption of the green laser light in the powder bed was measured with an integrating sphere. The measured absorption values for various powders are summarized in **Table 11**. As for the other measurements,  $\text{MnO}_2/\text{Mn}_2\text{O}_3$  doped alumina granules (No. 5) showed the highest absorption of 92.5% (6.1% higher than for  $\text{Fe}_2\text{O}_3$  doped alumina granules (No. 3)). Thermal treatment of the powders led to lower absorption in both cases (No. 4 and 6). Whereas the absorption of the  $\text{MnO}_2/\text{Mn}_2\text{O}_3$  doped samples dropped only to 85.4%, the absorption of the  $\text{Fe}_2\text{O}_3$  doped alumina granules was only 16.3%, which is only 4.7% more than the value of the pure alumina granules (No. 1) and 7.4% more than measured for coarse AA18 powder (No. 2). In both cases, the thermal treatment initiates a lattice doping of the alumina and additionally, in the case of manganese doping a change of the band structure caused by an oxidation state change, leading to the decreased values in absorbance. By adding the coarse AA18 powder to all granules (No. 7-10), the measured absorptions by the integrating sphere showed the same decreasing effect like in the Kubelka Munk measurements. The values decreased within a range of 3.7 - 7.4%.

Both techniques gave similar results for all of the tested materials with only two exceptions. The K/S ratio of the as-prepared manganese doped granules mixed with coarse alumina (No. 9) was slightly below the value of iron oxide doped granules (No. 3) at 532 nm in the Kubelka Munk plot, whereas the quantitative measurement showed a higher absorption for the manganese oxide doped sample. Since it is only a small deviation, it could be within the error range of the measurements. Another inconsistency was between thermal treated  $\text{MnO}_2/\text{Mn}_2\text{O}_3$ -doped granules (No. 6) and  $\text{Fe}_2\text{O}_3$ -doped granules mixed with coarse alumina (No. 7), where the values had a bigger difference.

Even if in both measurements the absorption values for the thermal treated  $\text{Fe}_2\text{O}_3$  doped granules were low, both calcined and non-calcined powders could be successfully additively consolidated by the laser. Since the excitation energy of the laser photons is smaller than the bandgap, it could be possibly explained, that granules with homogeneously distributed color centers (Fe-atoms) within the  $\text{Al}_2\text{O}_3$  lattice after thermal treatment [159], can absorb the green laser light at lower temperatures by multiphoton absorption or by excited state absorption, where the high heat flux of the laser generates a constant intermediate energy level [250]. The absorption measurements in the present work evaluate only the absorptance of the powder bed at room temperature and this does not take into account the dynamics of the whole SLM process. However, it was already shown that optical powder properties at room temperature are also important in order to stabilize the process [17]. With increasing temperature the absorption

of alumina can increase. This was already shown for laser excitation [147, 148]. In the particular case of doped alumina, a change of the band structure caused by an oxidation state change of the dopant as well as a change of the substrate absorbance during processing has to be considered for absorption at higher temperatures.

Florio et al. studied the absorptance under PBF-LB process conditions for the given  $\text{Fe}_2\text{O}_3$ -doped and  $\text{MnO}_2/\text{Mn}_2\text{O}_3$  doped granules by in-situ absorptance measurement of the laser light using an integrating sphere [251, 252]. The absorptance was analyzed during PBF-LB of a single track (10-mm length) and full layers (4 x 4 mm). The absorption behavior in both experiments was proven as a non-linear and dynamic process. The  $\text{MnO}_2/\text{Mn}_2\text{O}_3$ -doped granules showed a higher and more stable absorptance during the single track experiments, whereas the  $\text{Fe}_2\text{O}_3$ -doped granules gave a higher absorptance in the full layer experiments. However, it was shown by in-situ high-speed video imaging using a high-speed camera and an external laser illumination that both dopants led to a stable melt-pool when using an infrared laser (wavelength of 1070 nm) [252]. The influence of the dopants on the melt pool stability was different. On the one hand, manganese oxide-doped powders revealed a larger and more stable melt pool in the single tracks experiments. On the other hand, iron oxide showed a better result in terms of melt pool size and stability during processing of full layers, despite having a lower absorptance at room temperature at the used wavelength of 1070 nm. The reversed results were explained by the change in crystalline phase by melting and re-solidification and the impact of this change on the subsequent tracks. Florio et al. concluded that the used powders should not only show a suitable absorptance at room temperature, but also after re-solidification due to the impact of previously scanned tracks and layers on the absorptance during processing. Furthermore, high-speed video imaging revealed convection flows around the melt-pool, which generate a denudation zone having a strong influence on the next laser scan track [252].

Quantitative absorption measurements via integrating sphere showed that the laser light absorption increased during processing under PBF-LB process conditions. Whereas the lowest absorption was present in unprocessed  $\text{Fe}_2\text{O}_3$ -doped aluminum oxide powder at room temperature, an increase of the absorption of 19.4% was measured during laser processing with 2 mm/s using the green pulsed laser [251]. This leads to the conclusion that most of the energy is absorbed by the melt pool. Petrov confirmed this abrupt absorption increase of molten alumina by laser processing [148]. However, a high powder bed absorptance is also needed to guarantee a stable process, since a consolidation of the alumina granules was not possible without the iron oxide dopants using the same laser [251]. These dopants absorb the laser light first and transfer

the absorbed energy to the other particles. At higher temperatures, the aluminum oxide particles show also a higher absorption, since their absorption increases with increasing temperature. Zhang and Modest already showed this temperature-dependent absorptance of  $\text{Al}_2\text{O}_3$  using an integrating sphere and an IR laser ( $\lambda=1,06 \mu\text{m}$ ) [147]. Furthermore, the impact of the previous layer or the substrate on the absorptance has to be considered during PBF-LB, since their optical properties, thermal properties and phase stability can significantly influence the process [251]. Florio et al noticed that the absorptance of the iron oxide doped powder bed increased after the first track, whereas the absorptance of the manganese oxide doped powder decreased [251, 252]. This could be explained by the formation of a black hercynite phase ( $\text{FeAl}_2\text{O}_4$ ) and an orange galaxite phase ( $\text{MnAl}_2\text{O}_4$ ) during laser processing, which changed the absorption of the previous consolidated tracks and layers [252]. More information on the ternary phase formations can be found in chapter 3.3.2 and 3.3.4.

**Figure 50** shows the qualitative absorption spectra of  $\text{Fe}_2\text{O}_3$  (L2818D)-doped trimodal granules thermally treated at different temperatures in air (heating and cooling rate of 2 K/min). The absorption at 532 nm (wavelength of used green laser) constantly decreases starting with the highest value measured for the as spray-dried granules to the lowest value measured for granules thermally pre-treated at 1600 °C. A change of the absorption curve course at a treatment temperature of 900 °C at low wavelengths is visible. This could be due to the change of  $\gamma$ -/ $\delta$ - $\text{Al}_2\text{O}_3$  to  $\alpha$ - $\text{Al}_2\text{O}_3$  (AluC aluminum oxide nanoparticles) and due to the starting incorporation of iron atoms into the aluminum oxide lattice in this temperature range as shown by Makowska et al. [159].

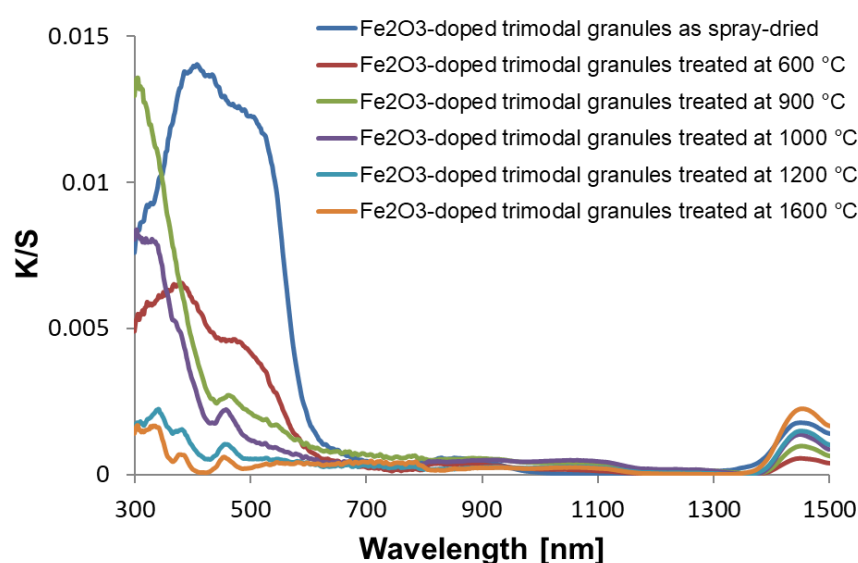


**Figure 50:** Qualitative absorption spectrum analyzed by the Kubelka Munk method for  $\text{Fe}_2\text{O}_3$  (L2818D)-doped trimodal granules thermally treated at different temperatures in air.

### 3.2.9 Influence of surface tension of slurry on granule size and density

Surface tension in the slurry for spray drying can be reduced by different surfactants. In this work, the hypothesis of a reduction of droplet size and thus granules size by addition of 1-octanol was followed. Therefore, a final minimization of the hollow core was expected. The influence of surface tension on the particle size is, as already described, contradictory in the literature. Surface tension was described to be directly proportional to granules size [103] and to produce bigger granules using a spraying medium with a higher surface tension [113], whereas other authors stated that the change of surface tension with and without surfactant did not influence the final granule size after spray drying [105]. However, information of the influence of the surface tension on granule size and density for the use of the ultrasonic atomization was not found in the literature.

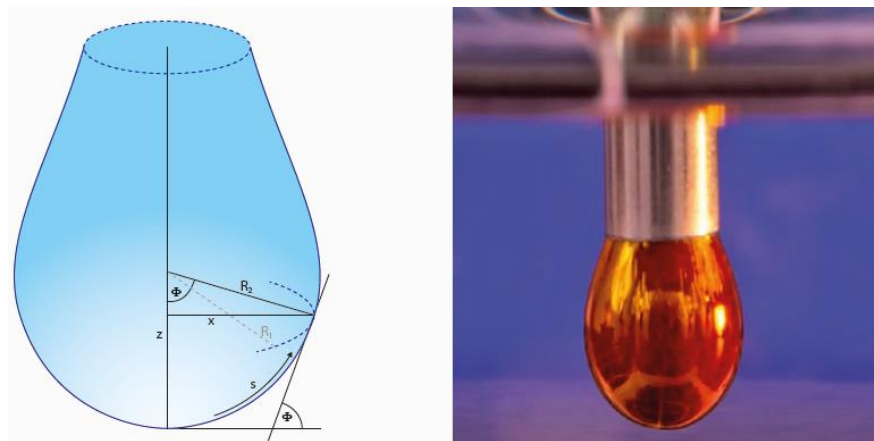


**Figure 51:** Drop schematic and measurement of interfacial tension [253]

Measurement of the surface tension  $\sigma_L$  of a  $\text{Fe}_2\text{O}_3/\text{Al}_2\text{O}_3$  dispersion (powder combination B with 1 Vol%  $\text{Fe}_2\text{O}_3$  dopant (**Table 9**)) was performed by the characteristic shape of a drop profile recognized by the Young-Laplace evaluation (**Figure 51**) [253]. The measurement device of the OCA - series (DataPhysics Instruments GmbH, Filderstadt, Germany) recorded 2.5 images/second and dosed  $0.3 \mu\text{l}/\text{second}$ . The total measurement volume was adjusted between 5 and  $10 \mu\text{l}$ . The typical drop shape forms due to elongation by gravity.

The surface tension of the droplets decreased from  $61.0 \text{ mN/m}$  to the lowest value of  $29.3 \text{ mN/m}$  with the addition of  $0.77 \text{ Vol}\%$  1-octanol. With the addition of  $0.14$ ,  $0.19$  and  $0.42 \text{ Vol}\%$ , the surface tension had values of  $36.6$ ,  $34.2$  and  $30.3 \text{ mN/m}$ , respectively (**Figure 52a**). The highest standard deviation of  $1.24$  was observed at the original slurry with  $0 \text{ Vol}\%$  octanol. Other measurements had a lower standard deviation of only  $0.76$ ,  $0.46$ ,  $0.51$  and  $0.22$  (**Figure 52b**). Octanol acts as suitable surfactant to decrease the surface tension of these slurries.

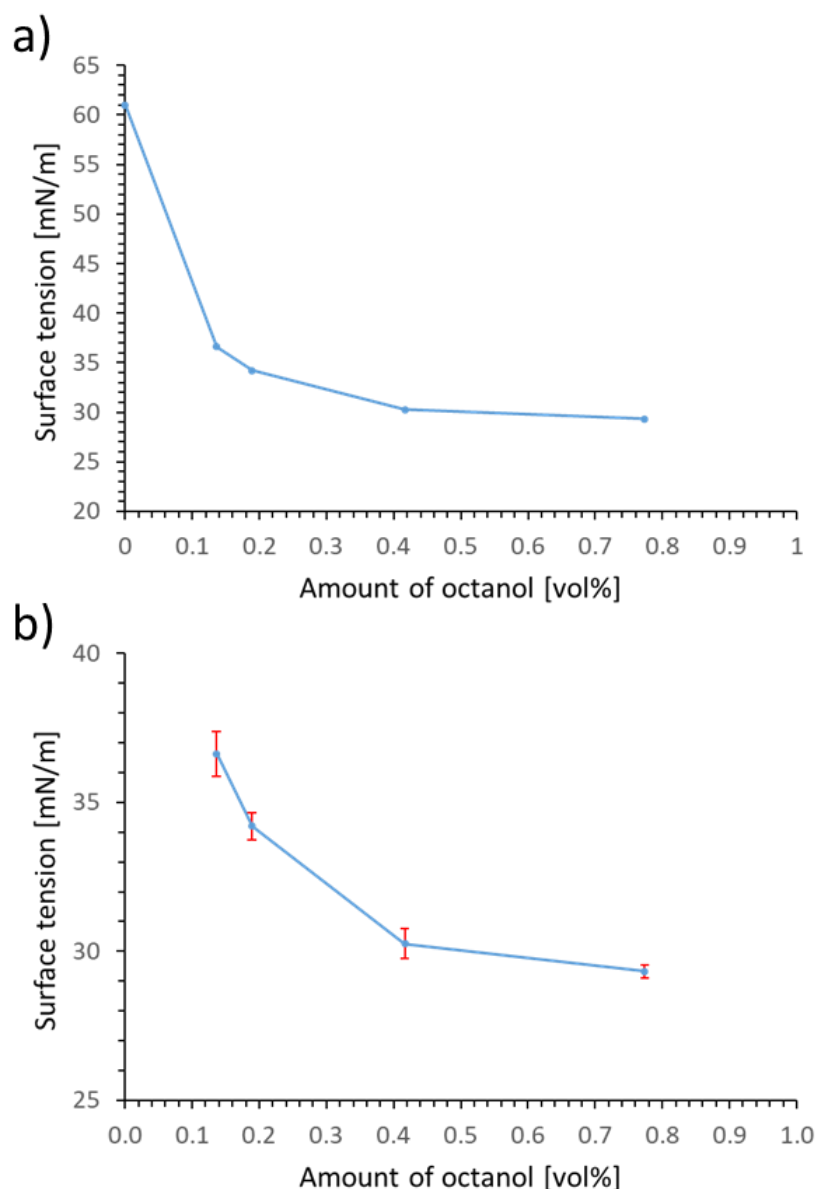


**Figure 52:** a) Surface tension of  $\text{Fe}_2\text{O}_3$  doped  $\text{Al}_2\text{O}_3$  slurry for spray drying in respect to amount of octanol. b) Consideration of standard deviation of measurement.

The granules from the fine powder collector (**Figure 10** in chapter 2.2.1) were imaged By SEM after screening with a 250  $\mu\text{m}$  sieve (**Figure 53**). No obvious shape distortions from a spherical shape of the granules were visible by the addition of the surfactant despite the decrease of the surface tension. This is contradictory to the results of Iskandar et al. [121], who reported a droplet destabilization by decreasing the surface tension of the droplet for spray drying of nano-silica particles, even though they used the same type of nebulizer (ultrasonic). Granule size differences were also not evident, even in bigger magnifications. **Figure 54** shows the volume-based LD particle size distribution of granules with addition of different amount of 1-octanol. The size of the granules does not change by addition of the surfactant.



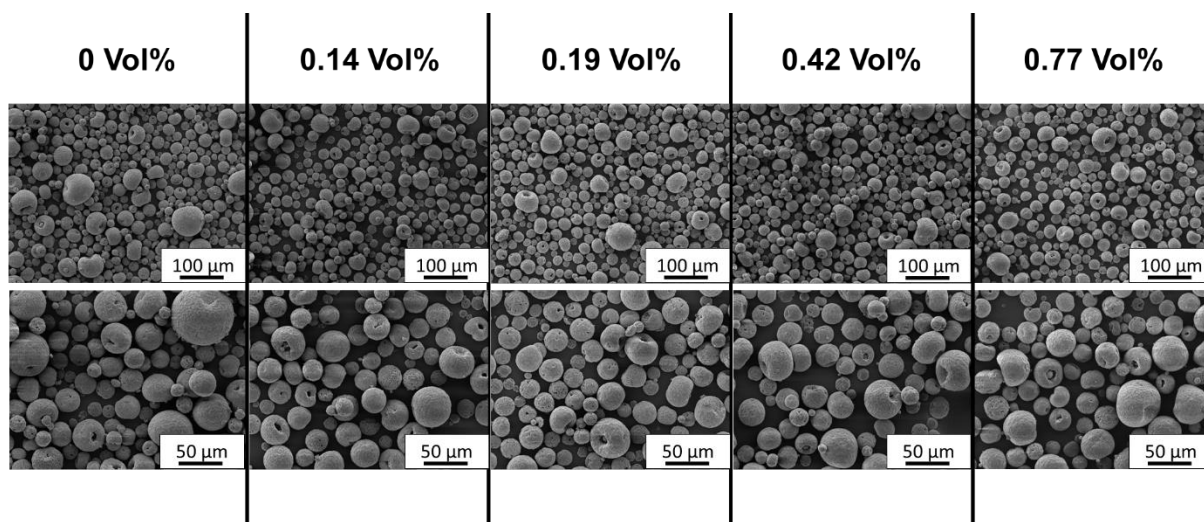


**Figure 53:** SEM images of fine fraction of spray dried granules with different amount of 1-octanol.

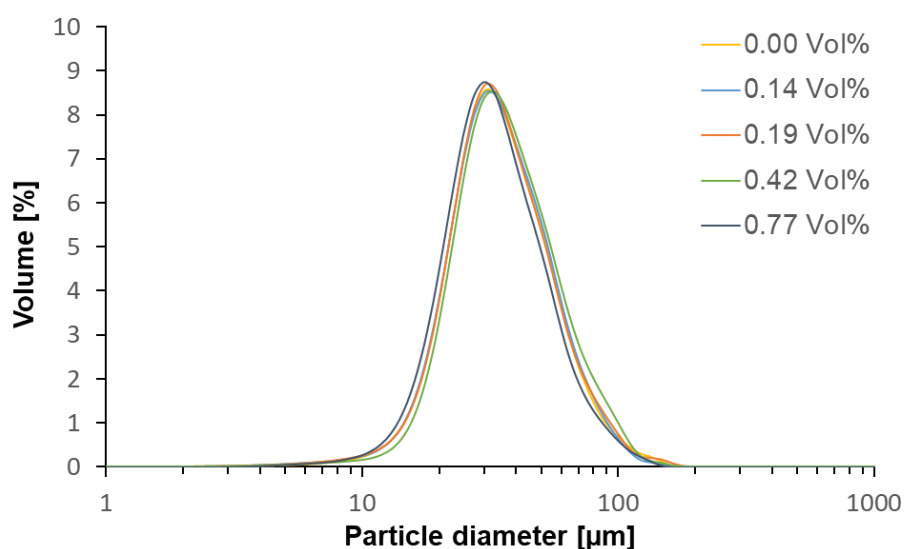


**Figure 54:** Volume-based LD particle size distribution of fine fraction of granules with addition of different amount of 1-octanol.

**Table 12:** Apparent and tapped density as well as Hausner ratio and yield of the granules with octanol amount.

Octanol amount	apparent density in % of TD	tapped density in % of TD	Hausner ratio	yield in %
0.00 Vol%	39.8	46.0	1.16	21.6
0.14 Vol%	40.3	46.4	1.15	21.7
0.19 Vol%	40.0	46.6	1.16	21.2
0.42 Vol%	40.5	46.9	1.16	18.1
0.77 Vol%	39.4	46.1	1.17	20.8

Further measurements showed that no significant difference in the apparent and tapped densities, Hausner ratio and yield of the fine granules was observed by addition of 1-octanol (**Table 12**). The difference within the apparent and tapped densities of the granules were within 1.1 %



and 0.9 % of the theoretical material density and not showing a clear trend. The Hausner ratio was relatively constant between 1.15 and 1.17 and the yield was between 18.1 and 21.6 %.

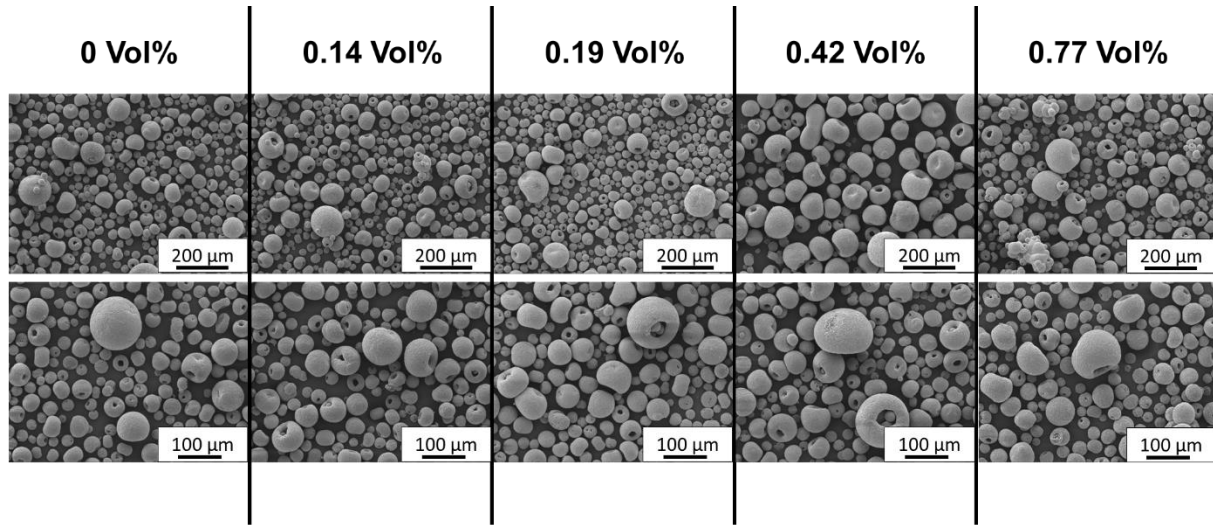


**Figure 55:** SEM images of coarse fraction of spray dried granules with different amount of 1-octanol.

In the case of the granules from the coarse powder collector (**Figure 10** in chapter 2.2.1) screened with a 250  $\mu\text{m}$  sieve, SEM images showed differences of the spray dried granules after addition of octanol (**Figure 55**). The granules with more octanol are more unshaped and appear bigger with the addition of octanol due to less stable droplets. The minimization of the hollow core of the granules was not achieved.

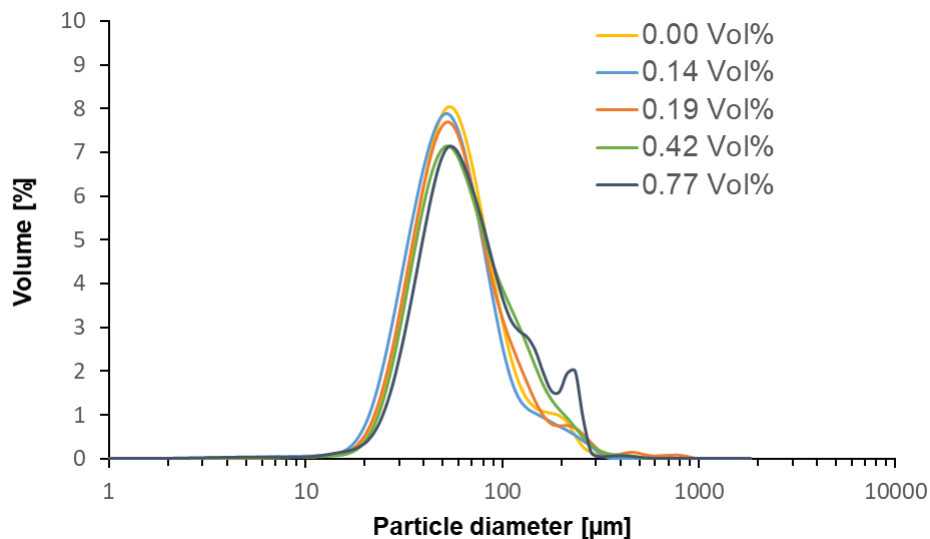


**Figure 56:** Volume-based LD particle size distribution of coarse fraction of granules with addition of different amount of 1-octanol.

**Table 13:** Characteristic values for d10, d50 and d90 of coarse fraction of granules with addition of different amount of 1-octanol.

Octanol amount	d10 in $\mu\text{m}$	d50 in $\mu\text{m}$	d90 in $\mu\text{m}$
0.00 Vol%	30.2	53.5	108.3
0.14 Vol%	27.8	50.4	100.4
0.19 Vol%	29.7	53.6	116.8
0.42 Vol%	31.1	57.1	130.0
0.77 Vol%	32.3	60.3	149.3

The granule sizes first decreased up to an addition of 0.14 vol%. However, this decrease was very small. The differences in d10, d50 and d90 were only 2.4  $\mu\text{m}$ , 3.1  $\mu\text{m}$  and 7.9  $\mu\text{m}$ , respectively (**Table 13**). With further addition of 1-octanol, the granule size increased in this fraction, which was the opposite effect than originally expected. At an addition of 0.77 vol% the maximum granule sizes of d10, d50 and d90 were present. Furthermore, agglomerates appeared in the volume-based LD particle size distribution in **Figure 56**, which are also counter-productive for flowability and powder bed density.

In contrary to other authors, which claimed that the granule size is direct proportional to the surface tension [103, 113], the fraction of the  $\text{Fe}_2\text{O}_3$  doped aluminum oxide granules from the fine powder collector sprayed by the ultrasonic nozzle are unchanged by the 1-octanol surfactant in the present work. This applies also on the flowability and powder density of these granules. A similar behavior was only shown in [105] where the change of surface tension did not influence the final granule size after spray drying. However, the results reported in the present work are achieved with an ultrasonic atomizer and may therefore differ due to the different types of droplet formation. Furthermore, different material compositions and process parameters were used.

In the case of the fraction from taken from the coarse powder collector, an increase of the granules sizes was seen in the present work. However, this fraction contained big and unshaped agglomerates in the powder bed. Furthermore, the addition of 1-octanol did not lead to a minimization of the hollow core within the granules, but increased the granule size. Thus, the granule density could not be increased by the addition of the surfactant.

### 3.3 Investigation of laser manufactured parts

The impacts of the different influencing factors on the properties of the laser-manufactured parts are summarized in **Table 14**. More details can be found in the specific chapter.

**Table 14:** Summary of the impacts of different influencing factors on the properties of the laser manufactured parts.

Properties of laser manufactured parts			
Influencing factor	Analyzed property	Chapter	Short summary of results
Different iron oxide dopants and multimodal particle distributions within granules	Part shape Density Microstructure	3.3.2	High accuracy of lateral areas and high roughness of top surfaces for all parts. Higher density of powder bed (bimodal particle distribution) caused higher density of final parts. Different nano iron oxides without influence on final parts. Various laser introduced cracks and some bigger pores containing unmolten granules within the microstructure of all samples.
Additive amount variation of coarse alumina AA18	Part shape Density Microstructure Compressive strength	3.3.3	Parts made from pure granules with lowest accuracy of top surface (strong balling effect) and parts made with 30/70 wt% iron oxide granules/AA18 with highest accuracy. Part densities in the same range (small standard deviation). Strong cracking visible for all used powder combinations. Highest compressive strength of $191.0 \pm 42.3$ MPa measured for parts made with 30/70 vol% manganese oxide doped granules/AA18. Compressive strengths of parts made by other AA18 variations within standard deviation of these parts. Consolidation problems of powder with addition amount of 90 vol% AA18 by PBF-LB most probably due to lower temperatures reached by a less homogeneous dopant distribution.
Thermal pre-treatment	Part shape Microstructure Phase content Pore distribution Density	3.3.4	Desired dimensions achieved for all parts by laser processing. Rough surfaces on the lateral and on the top areas present. SEM and tomographic microscopy show presence of pores and reveal various cracks within microstructure due to huge thermal gradients during laser processing. Significantly higher amount of cracks and pores at the bottom part of the samples. Coarse alumina particles as well as non-molten or partly molten granules present in some pores. Not all granules affected by laser beam. Black and orange color of parts processed from iron oxide or manganese oxide doped granules or due to formation of hercynite ( $\text{FeAl}_2\text{O}_4$ ) or galaxite ( $\text{MnAl}_2\text{O}_4$ ). Higher densities for samples manufactured with thermal pre-treated powders due to a higher powder bed density.
Laser scanning speeds	Grain structure	3.3.5	Irregular grain sizes due to melt pool instabilities. Grain orientation predominantly parallel to the building direction due to highest cooling rate in this direction. Bigger grain sizes for lower laser scanning speeds. Amount of grains due to smaller width of the grains perpendicular to the building direction for the faster speeds.
Post thermal treatment of parts processed with granules containing different dopants (manganese oxide and iron oxide)	Thermal expansion	3.3.6	Small length changes of below 0.1% (maximum temperature of 1480 °C) for both materials. Changes negligible in terms of densification.
Thermal pre-treatment of manganese oxide doped alumina granules	Manganese amount	3.3.7	Thermal treatment at 1600 °C resulted in a depletion of manganese. Laser processing resulted in a further depletion of the manganese amount

#### 3.3.1 Experimental

The powder was processed by the Institute of Machine Tools and Manufacturing at ETH Zurich in an experimental in house built SLM machine, where the layer thickness can be controlled by a recoater blade made of natural rubber. The size of the building chamber is 20 x 20 x 50 mm. A green pulsed laser (IPG GLPM-5) was used for the laser processing of the doped granules. The laser has the following characteristics: a wavelength of 532 nm, a pulse duration of 1.5 ns, a nominal average output power of 5 W and a pulse repetition rate of 300 kHz. The laser parameters used during processing were a spot diameter of circa 135  $\mu\text{m}$ , a hatch space of 135

μm, a laser power of 5.75W (measured by a power meter) and a laser speed of 2mm/s. More details are mentioned in Florio et al. [17].

The SLM printed cubic ceramic parts were representatively imaged by optical microscopy (StEIO Discovery.V20, Carl Zeiss Microscopy, Germany). To visualize the internal structure of the parts, optical microscopy, SEM and X-ray tomographic microscopy at the TOMCAT beamline of the Swiss Light Source were performed. Before the analysis of the microstructure by SEM and optical microscopy, the samples were cold embedded in a resin (CaldoFix-2, Struers GmbH, Switzerland). Afterwards the cross-sections were ground, polished (with a 1 μm diamond suspension) and coated with gold-palladium. Tomography scans were performed using a standard setup for full field tomography composed of a 100 micron-thick LuAG:Ce scintillator, an optical microscope with 4x magnification and a sCMOS camera, which provides a field of view of 4.2 mm x 3.5 mm with 1.625 μm pixel size. The used energy of the X-ray beam was 25 keV. 1501 projections were acquired over 180° with 280 ms exposure time per projection. 3D imaging of 3x3x3 mm<sup>3</sup> sized cubes allowed to visualize and quantify cracks and pores with a spatial resolution of about 3 μm. Density values of the laser processed parts were evaluated for the whole volume and for a selected inner region from the tomography visualizations. Accuracy of the density evaluation from tomographic microscopy was determined by obtained contrast and spatial resolution. The error estimated for these measurements was ca. 0.1%. Phase composition after laser printing was evaluated from high resolution powder diffraction measurements of crushed samples at Material Science (MS) beamline at the Swiss Light Source (PSI) synchrotron as described in chapter 3.2.1.

Furthermore, the density according to the Archimedes principle was determined using water as liquid medium. The relative density of the parts was calculated based on the measured densities of the used starting materials. The compressive strength was measured using cylinders with a part diameter *d* of ca. 3 mm and a length of ca. 6 mm to achieve a length to diameter ratio of ca. 2. The samples were polished up to a 5 μm finish prior to the compression tests. The compression tests were performed using the testing machine AllroundLine Z005 (Zwick Roell ZwickRoell GmbH & Co. KG, Germany). The uniaxial compressive strength  $\sigma$  was calculated using the applied force *F* and the cross sectional area *A* of the cylinders as follows:

$$\sigma = \frac{F}{A} = \frac{F}{\frac{1}{4}d^2\pi} \quad (13)$$

Electron Back-Scattered Diffraction (EBSD) was performed to illustrate the grain size and orientation of the remolten parts made from Fe<sub>2</sub>O<sub>3</sub>-doped granules. Prior to the EBSD measurements, the samples were ground and polished to minimize the apparent surface roughness. The EBSD measurements were performed by a FEI Quanta 200F SEM (FEI Company, USA) in low vacuum mode (pressure of 40 Pa). The samples were mounted under a 70° angle in respect to the electron beam. The software FEI maps was used for mapping.

The shrinkage behavior of the laser processed parts was measured by thermo-mechanical analysis with TMA 402 F3 Hyperion (Netzsch GmbH, Germany) in a temperature range from 0 – 1480°C in air atmosphere by using a heating rate of 2 K/min and a cooling rate of 5 K/min. The samples experienced a holding time of 2 hours at the maximum temperature. Before the measurement, the laser processed samples were ground on both sides to achieve a parallel top and bottom plane. The apparent length in build direction of the laser processed parts (length according to a certain point of the time-temperature profile) was calculated by utilization of the initial part length L<sub>0</sub> and the length change dL as:

$$\text{apparent length [\%]} = \frac{L_0 - dL}{L_0} \times 100 \quad (14)$$

For calculation, the initial part length of parts processed from iron oxide doped granules (4.494 mm) and manganese oxide doped granules (3.823 mm) were set as 100%.

The change of the manganese amount within the powders and the laser additive manufactured parts by thermal pre-treatment of the doped granules was evaluated by using an Orbis PC Micro-XRF Analyzer (Ametek Inc., USA) [254]. Line profiles were obtained by scanning samples with a focused X-ray beam with a 30 µm spot size. The final Mn content was evaluated from an integrated line scan measured over 1 mm. Prior to the measurements, as spray-dried and thermal pre-treated granules (heating and cooling rate: 2 K/min, max. temperature 1600 °C, holding time: 2 hours) were pressed with 114 MPa into cylindrical samples of 27 mm in diameter. Before pressing, the thermal pre-treated granules were mixed with water and PEG 35000 (ratio of 80.1/18.9/1.0 Vol% of granules, water and PEG, respectively) for 1 hour to assist the consolidation, since binder within the granules was removed during the previous heat treatment step. The manganese amount of laser processed parts was determined at the cross-sections ground and polished for SEM and optical microscopy. This measurement was performed for parts made from as spray-dried and thermal pre-treated granules. To achieve a better consolidation and a bigger area for the line scans after laser processing, two cylindrical samples were heated with 2 K/min to 700°C (Profitherm PY 12 H furnace, PYROTEC Brennofenbau GmbH,

Germany) and 1600 °C (LHT 04/17, Nabertherm GmbH, Germany) in air and consolidated for 2 hour at the maximum temperature. Afterwards, one layer of 10 mm x10 mm was processed on the top area of each sample by the green pulsed laser.

### 3.3.2 Influence of different iron oxide dopants and multimodal particle distributions within granules

The most important properties of the powders used for the laser processing to compare the influence of different iron oxide dopants and multimodal particle distributions are summarized in **Table 15**. The powder 1, 2, and 3 contain granules sprayed from powder combination A, B and C (**Table 9**, chapter 3.2.3), respectively, and additional 30 vol% of coarse alumina AA18.

**Table 15:** Properties of powders used for laser processing, which contain coarse alumina AA18 and spray dried granules (powder combination A, B and C).

Properties	Powder 1	Powder 2	Powder 3
Composition	70 vol% granules of powder combination A + 30 vol% coarse alumina AA18	70 vol% granules of powder combination B + 30 vol% coarse alumina AA18	70 vol% granules of powder combination C + 30 vol% coarse alumina AA18
Solid load in slurry [Vol%]	41.2	45.2	45.1
Apparent density [% of TD]	37.14 ± 0.03	40.85 ± 0.26	41.07 ± 0.98
Tapped density [% of TD]	44.30 ± 0.23	48.42 ± 0.67	49.52 ± 0.40
Absolute density [g/cm <sup>3</sup> ]	3.890	3.892	3.880
Hausner ratio	1.193 ± 0.005	1.185 ± 0.023	1.206 ± 0.036
Moisture content [wt%]	0.62	1.25	1.10
d <sub>10</sub> [μm]	18.1	15.1	16.1
d <sub>50</sub> [μm]	32.2	28.0	28.8
d <sub>90</sub> [μm]	60.4	57.5	58.5

The solid load in the slurry for spray drying was selected based on the yield of fine granules. The minimum yield should be at least 30 %. Highly dense granules were produced by spray drying. The well distributed particles in the slurry led to granules with uniform distribution of the finer and coarser content of the used alumina. Because of this, the smaller particles could enter the interstices of the larger ones. An additional portion of 30 vol% was chosen for AA18, since the density should be increased, but at the same time the absorption of the laser light should not be diminished too much. The relative tapped density of 50% is close to a theoretical density in the green body of a conventional ceramic (over 60%), which is necessary to achieve dense parts during solid state sintering. The residual moisture content of the non-calcined powder was only around 1 wt% and for powder 1 even lower.

Parts made from powder 1, 2, and 3 by green pulsed laser SLM are shown in **Figure 57a, c, e**. The parts are homogeneously consolidated except for a small amount of bigger pores. The accuracy of the lateral areas is very high, whereas the top surfaces show a high roughness. The relative density was  $93.7\% \pm 1.1\%$  for parts processed with powder 1. Both bimodal powders (powder 2 and 3) gave a higher relative density of the final parts ( $96.1\% \pm 0.6\%$  with spherical iron oxide and  $96.4\% \pm 0.4\%$  with elongated iron oxide). These differences are in accordance with the apparent and tapped densities of the utilized powders (**Table 15**). A higher density of the powder bed caused a higher density of the final alumina parts, which is in compliance with the literature [18]. The final densities were close to the density of 97.5%, which Juste et al. [50] reached for parts manufactured from graphite containing alumina granules. The different shapes of the iron oxides did not have an influence on the densities of the final parts, since the relative densities of the final parts as well as the apparent and tapped densities of powders were in both cases (with spherical and elongated iron oxide) the same.

Representative images of the whole ceramic part obtained by the laser process before and after heat treatment at 1650 °C are presented in **Figure 57g, h**. The black color of the parts was already explained in [17] by the formation of a hercynite phase ( $\text{FeAl}_2\text{O}_4$ ) during PBF-LB, which was not expected according to phase diagrams referring to the standard conditions [255]. The treatment temperature of 1650 °C was chosen for a whitening of the laser processed parts, since hercynite can transit into the liquid melt status between 1565 up to 1709 °C [255] and, therefore, iron can be slowly incorporated into the corundum structure.

There could be two reasons for the origin of the bigger pores within all samples. During laser manufacturing of the ceramic component, a melt pool cavity (keyhole) is usually formed by the melt pool dynamics induced by evaporation of the material [256]. The size of this keyhole is further increased by the use of a pulsed laser, since very high peak powers essential for keyhole creation are available [256], and therefore, not completely closed during processing. In addition, the flowability and the packing density of the powders are most likely too small to produce a completely closed and homogeneous layer on the uneven surface during the application of a layer. In general micron-sized (ca. 20-40  $\mu\text{m}$ ), highly flowable  $\text{Al}_2\text{O}_3$  particles (comparable to Tosoh  $\text{ZrO}_2$  milling balls with a size of 30 microns) would be perfect to reach a high powder bed density and to achieve dense parts in the PBF-LB process. However, these particles would need to be surface modified to achieve a suitable powder absorptance of visible or near infrared laser light. Furthermore, a total melting of the particles needs to be achieved, since the sinter activity of particles this big is very low.



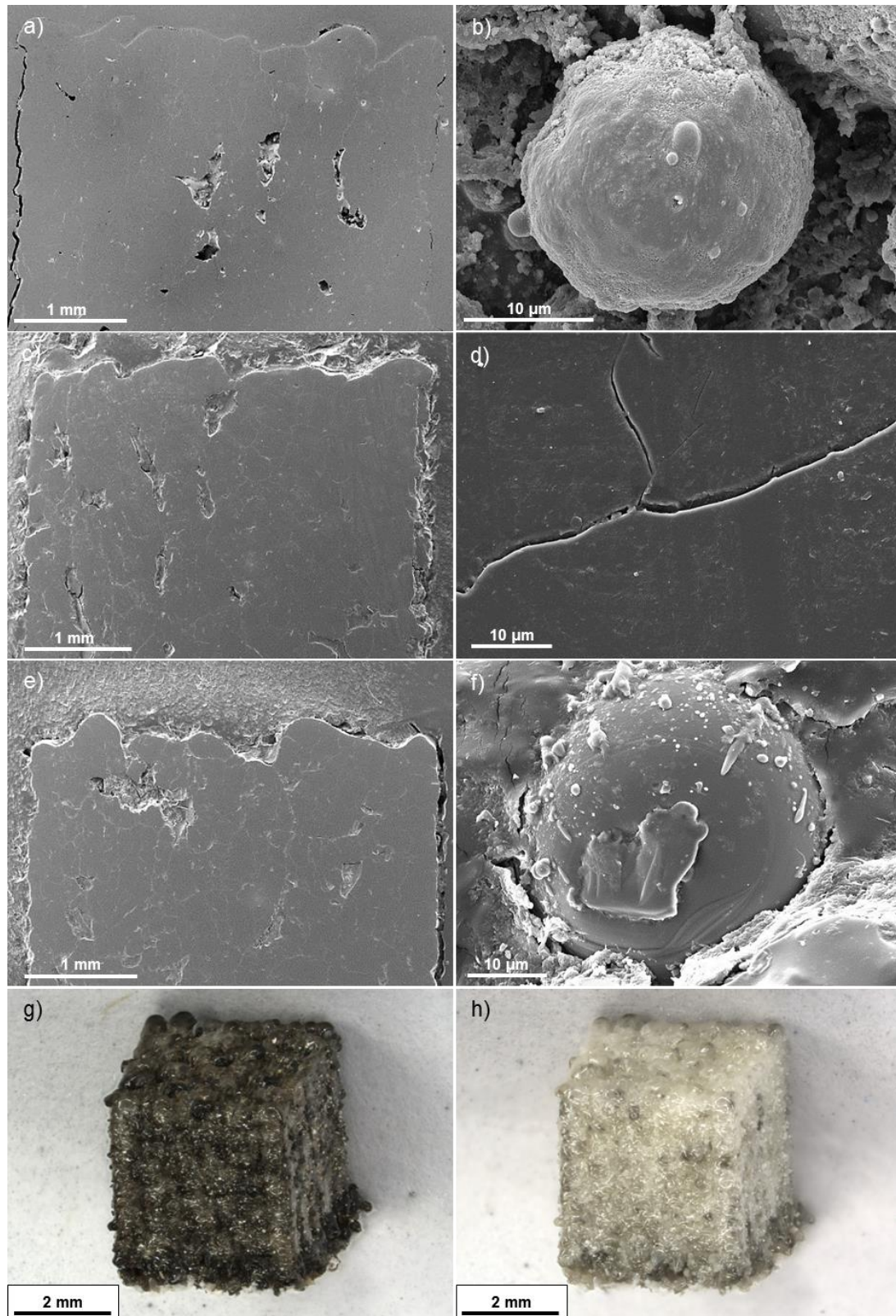


**Figure 57:** SEM images of laser manufactured parts with **a), b)** powder 1, **c), d)** powder 2, **e), f)** powder 3. Images of the ceramic part obtained by the laser process **g)** before and **h)** after heat treatment at 1650 °C

Several characteristic features of the laser manufactured samples were discovered at higher magnifications. Microstructure analysis revealed for example unmolten granules (**Figure 57b**),



which remained intact during processing. On the other hand, totally molten granules (**Figure 57f**) were also seen, which were not connected to their surroundings. Various laser-induced cracks (**Figure 57d**) could be seen within the microstructure of the parts. These were generated by thermal shock, which occur due to huge thermal gradients created by the laser irradiation during processing. A cooling rate of ca.  $2.9 \times 10^4$  K/s between the maximum temperature of ca. 3000 °C down to 1000 °C has been calculated for the given material and process parameters by modelling through finite volume method [251]. The reduction of thermal stresses and crack formation during laser-processing is the scope of the chapter 4.

#### 3.3.3 Influence of coarse alumina variation

##### A. Iron oxide doped aluminum oxide granules

Coarse alumina AA18 (30 wt% and 70 wt%) was mixed to pure Fe<sub>2</sub>O<sub>3</sub> doped granules to evaluate the influence of increasing apparent and tapped density as well as the change of the dopant distribution on the part formation during laser processing. **Figure 58** shows the powders after mixing of the spray-dried granules with the coarse aluminum oxide powder.

The color uniformity decreases by adding a higher amount of coarse aluminum oxide. The original Fe<sub>2</sub>O<sub>3</sub> content was higher in the spray dried granules to achieve the same dopant content of ca. 1.0 Vol% in the final powders (**Table 16**). This explains the darker colors of the granules mixed with 30 wt% and 70 wt% AA18 aluminum oxide. The added aluminum oxide particles are visible as white spots in **Figure 58**.



**Figure 58:** Powders to evaluate the influence of coarse alumina variation on the part formation by PBF-LB.

The granule properties (**Table 16**) behave like described in chapter 3.2.6. Apparent and tapped density as well as the Hausner ratio increase by the addition of the coarse alumina particles.

**Table 16:** Properties of powders used for laser processing, which contain spray dried granules doped with iron oxide and a different amount of coarse alumina AA18.

Powder	Pure granules	70 wt% Granules + 30 wt% AA18	30 wt% Granules + 70 wt% AA18
Fe <sub>2</sub> O <sub>3</sub> content in granules in wt%	0.99	1.42	3.33
Total Fe <sub>2</sub> O <sub>3</sub> content in wt%	0.99	0.99	0.99
Apparent density in % of TD	40	44.2	48.3
Tapped density in % of TD	46.6	53	57.9
Hausner ratio	1.17	1.2	1.2

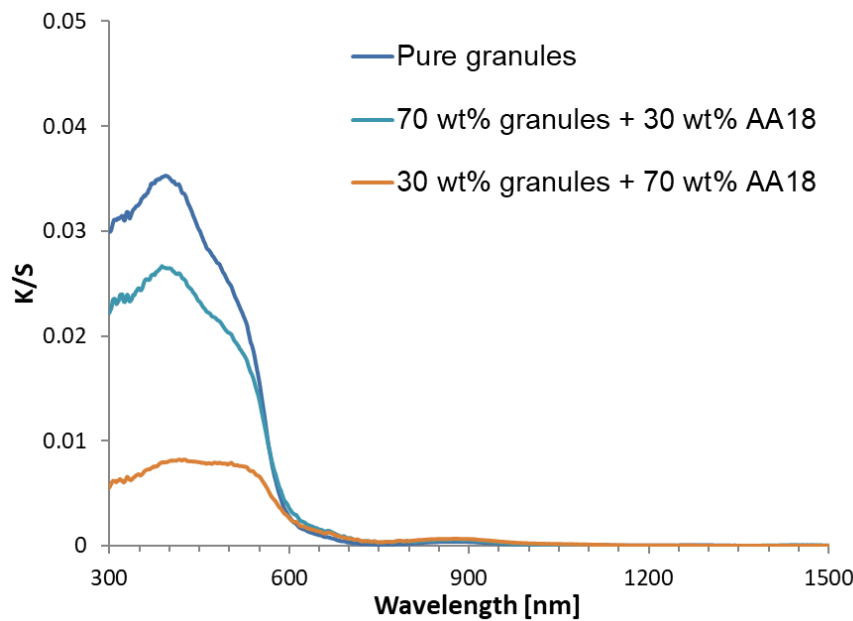


**Figure 59:** Qualitative absorption spectrum evaluated by the Kubelka Munk method of the three different combinations.

The qualitative absorption spectrum evaluated by the Kubelka Munk method (experimental explanation in chapter 3.2.1) showed a continuous decrease of the K/S ratio (absorption coefficient K divided by scattering coefficient S) at room temperature at the used laser wavelength of 532 nm (**Figure 59**). This could be due to higher scattering effect or less absorption of the initial beam by the increasing non-uniformity of the powder.

**Figure 60** images the shape and cross sections of the laser manufactured parts processed from the three different powder combinations. The shape of the parts was imaged by optical microscopy, whereas, the cross sections were imaged by SEM. The parts made from pure granules showed visually the highest pore volume of all samples. This would be in accordance to Bertrand et al. [18], who stated that higher density of the powder bed causes a higher density of the final parts. However, only three cross sections were evaluated. Furthermore, the lowest accuracy of the top surface was apparent due to a strong balling effect. The pore amount and volume

of the parts made from granules mixed with 30 wt% of the coarse aluminum oxide AA18 was similar, but slightly higher compared to the granules mixed with 70 wt% AA18. The top surface was produced with a medium accuracy and a moderate balling effect compared to the other powders. The highest accuracy of top surface was achieved for a mixture of 30 wt% granules and 70 wt% coarse aluminum oxide particles. The surface appears relatively flat. This could be due to the higher temperatures reached by a more homogeneous dopant distribution and thus, a more uniform powder absorptance. The higher temperature of the melt would consequently reduce the viscosity of the melt and thus promote the balling phenomena during laser processing.

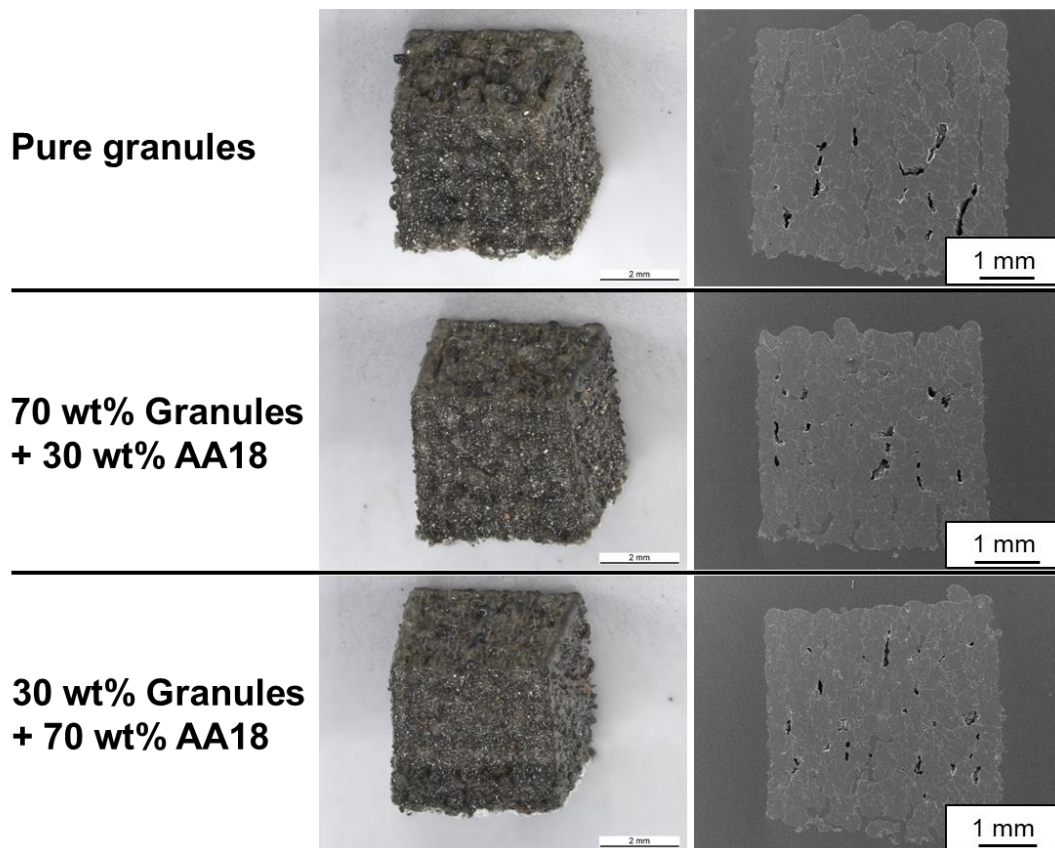


*Figure 60: Shape imaged by optical microscopy and cross sections imaged by SEM of laser manufactured parts*

Higher magnifications of the internal structure of the parts are imaged in **Figure 61**. A strong cracking is visible for all used powder combinations. The use of the pure granules showed the lowest amount of unmolten material in microstructure after laser processing. However, unmolten granules were also found in the pores of the additively produced part. The amount of unmolten material increased with increasing the additional added coarse aluminum oxide AA18. This indicates also that higher temperatures are reached by a more homogeneous dopant distribution and consequently, a reduced viscosity, as seen for the balling phenomena imaged in

**Figure 60.** A mixture of unmolten granules and AA18 in the pores was seen after laser processing of powder with 30 wt% AA18 and mostly unmolten AA18 was found in the pores the laser processed parts using powder with 70 wt% AA18.

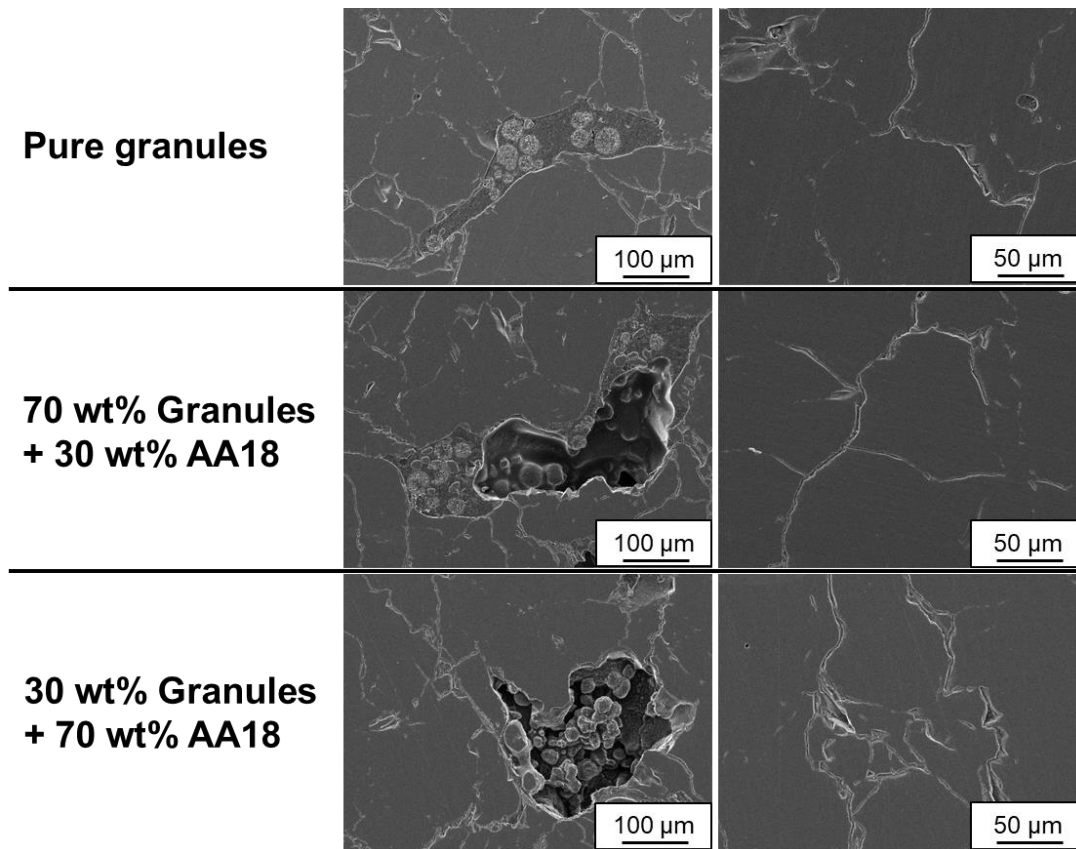


**Figure 61:** Higher magnifications of internal structure imaged by SEM of laser manufactured parts.

**Table 17:** Archimedes density in % of the theoretical density (TD) of laser processed parts.

AA18 Amount	Density in % of TD	Standard deviation in %
0 wt%	97.4	0.6
30 wt%	97	0.9
70 wt%	96.8	0.4

**Table 17** summarizes the density according to the Archimedes principle of the processed parts. A clear conclusion cannot be drawn by the density measurements in accordance with the Archimedes principles due to final densities of 96.8% – 97.4% and standard deviations in the range from 0.4% - 0.9%. The values must be considered as constant values of around 97%. The final densities of the laser processed parts are in a close range, despite the different trend visually seen by the decrease of the pore volume with increasing addition amount of coarse aluminum oxide in **Figure 60**. Explanations for these discrepancies could be that only three cross

sections were evaluated per laser processed parts of each powder, as already mentioned before and that the Archimedes measurements also offer several challenges, since open porosity is not taken into account and especially for small parts, measurements of the size and weight can lead to large measurement errors. Furthermore, a lower laser light absorptance was measured for higher AA18 amount, although the  $\text{Fe}_2\text{O}_3$  content was constant within the different powders. This worse absorptance could counteract the higher part density expected by the higher powder density.

### B. Manganese oxide doped aluminum oxide granules

The performance of manganese oxide doped granules with the addition of a different amount of coarse aluminum oxide AA18 was also tested. **Table 18** summarizes the properties of the used powders.

An AA18 content of up to 90 Vol% was tested. The manganese oxide content in the pure granules and the mixed powders was adjusted to ca. 2 Vol% (**Table 18**). The apparent and tapped density as well as the Hausner ratio increased by the addition of coarse alumina particles (chapter 3.2.6).

The visual appearance in terms of uniformity diminished from greyish-black to black with white spots by the addition of coarse aluminum oxide, as also seen for the  $\text{Fe}_2\text{O}_3$  doped granules (orange to red with white spots). Visible areas with localized light absorbing granules increased with increasing AA18 content. The darker colors of the granules mixed with a higher amount of coarse aluminum oxide can be explained by the higher doping content used for the initial granules (**Table 18**).

**Table 18:** Properties of powders used for laser processing, which contain spray-dried granules doped with manganese oxide and a different amount of coarse alumina AA18.

Powder	Pure granules	70 Vol% Granules + 30 Vol% AA18	30 Vol% Granules + 70 Vol% AA18	10 Vol% Granules + 90 Vol% AA18
$\text{MnO}_2/\text{Mn}_2\text{O}_3$ content in granules in Vol%	2.01	2.85	6.66	20
Total $\text{MnO}_2/\text{Mn}_2\text{O}_3$ content in Vol%	2.01	2	2	2
Apparent density in % of TD	39.5	41.1	45	46.2
Tapped density in % of TD	44.2	48.7	55.8	57.5
Hausner ratio	1.12	1.19	1.24	1.24

The qualitative absorption spectrum evaluated by the Kubelka Munk method (**Figure 62**) showed similar results compared to the  $\text{Fe}_2\text{O}_3$  doped granules. The highest room temperature



absorption was present for the pure granules and the K/S ratio decreased over the completely measured wavelengths (300 - 1500 nm). However, all powders, except of pure AA18 (coarse aluminum oxide), could be processed by the green ns-pulsed laser.

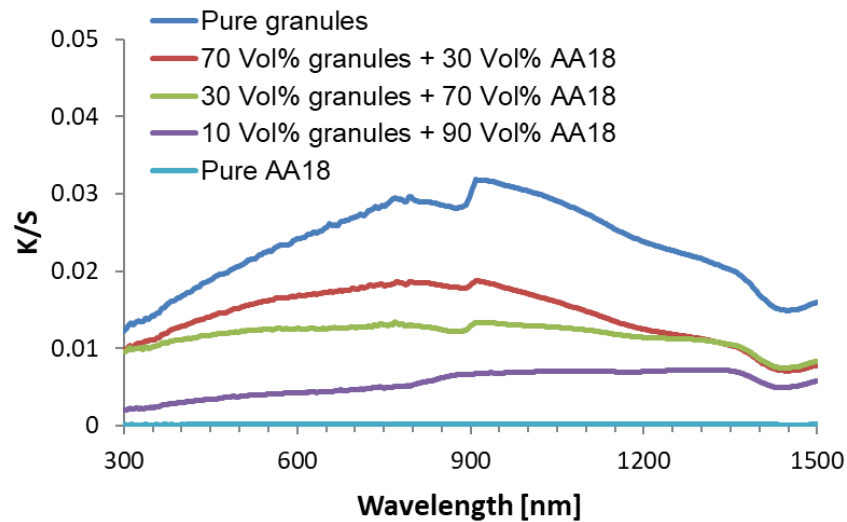


**Figure 62:** Qualitative absorption spectrum evaluated by the Kubelka Munk method of pure granules, granules mixed with coarse aluminum oxide and pure coarse aluminum oxide AA18.

**Figure 63** shows the compressive strength of the laser processed parts using the powders with a fixed manganese oxide amount of 2 Vol% and with a different amount of coarse aluminum oxide AA18.

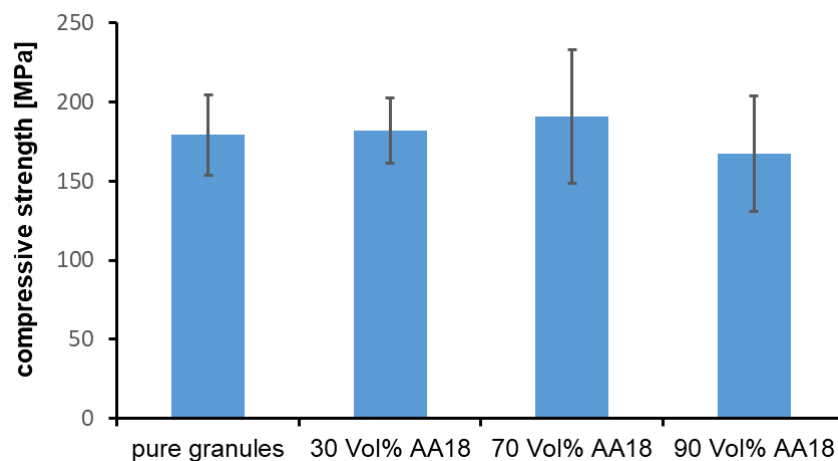


**Figure 63:** Compressive strength of parts produced with pure granules and granules mixed with different amount of coarse aluminum oxide AA18

The highest compressive strength of  $191.0 \pm 42.3$  MPa was measured for the parts made with 30 Vol% granules and 70 Vol% AA18. However, the compressive strengths of the parts made

by the other powders (pure granules:  $179.2 \pm 25.5$  MPa; 30 Vol% AA18:  $182.0 \pm 20.6$  MPa; 90 Vol% AA18:  $167.2 \pm 36.4$  MPa) were within the standard deviation of these parts. The powder with addition amount of 90 Vol% led to the parts with the lowest compressive strength. Only 5 measureable parts upon laser processing could be produced, because consolidation problems appeared during PBF-LB. The other parts of this series showed already severe geometrical deviations prior to the polishing step.

Compressive stresses of traditional processed aluminum oxide parts are ca. 4000 MPa for 99% pure alumina ceramics [257] (also depending on the used grain size and production method). This big difference originates from the severe crack formation due to thermal stresses and the formation of big grains (further specified in chapter 3.3.5) within the alumina part by PBF-LB. However, the strength values of the parts produced from the manganese oxide doped powders are also below the compressive strength value of 800 MPa after laser processing and 1150 MPa after annealing, which Exner et al. achieved using a glass-ceramic composite in PBF-LB [7, 61]. This is due to the low thermal expansion coefficient of the partly molten amorphous silica, what leads to avoidance of thermal stresses [99]. Furthermore, the green nanosecond laser was operated with a stochastic pulse distribution in Exner et al. [7, 61] in contrary to the steady grid scanning in the present work. They claimed that parts could be manufactured with relative low stresses and overheating could be avoided by the consolidation of micro-surfaces, which do not overlap at an initial stage and cross-link only towards the end of every layer [6]

### 3.3.4 Influence of thermal pre-treatment of powders

**Table 19:** Properties of powders used for laser processing, which contain coarse alumina AA18 and spray dried granules doped with either iron oxide or manganese oxide.

Powder	Powder 1	Powder 2	Powder 3	Powder 4
Composition	70 vol% Fe <sub>2</sub> O <sub>3</sub> -doped granules + 30 vol% coarse alumina AA18	70 vol% MnO <sub>2</sub> /Mn <sub>2</sub> O <sub>3</sub> -doped granules + 30 vol% coarse alumina AA18	70 vol% Fe <sub>2</sub> O <sub>3</sub> -doped granules treated at 1600°C/2h + 30 vol% coarse alumina AA18	70 vol% MnO <sub>2</sub> /Mn <sub>2</sub> O <sub>3</sub> -doped granules treated at 1600°C/2h + 30 vol% coarse alumina AA18
Solid load in slurry [Vol%]	49.8	49.6	49.8	49.6
Dopant amount [Vol%]	0.6	0.8	0.6	0.8
Apparent density [% of AD]	42.9	44.2	45.1	48.4
Tapped density [% of AD]	50.9	51.9	53.2	56.4
Absolute density [g/cm <sup>3</sup> ]	3.889	3.858	4.022	3.973
Hausner ratio	1.19	1.18	1.18	1.17
Moisture content [wt%]	1.26	0.72	0.12	0.10
d <sub>10</sub> [μm]	17.5	17.4	20.0	18.5
d <sub>50</sub> [μm]	32.1	30.5	43.8	40.5
d <sub>90</sub> [μm]	65.4	58.2	94.6	97.1

The properties of the powders used for laser processing to evaluate the influence of thermal pre-treatment are summarized in **Table 19**. 30 vol% of AA18 was added to manganese oxide and iron oxide doped granules, firstly following spray drying and secondly after spray drying and subsequent thermal pre-treatment, resulting in four powders in total.

The granules were thermally treated in air to increase the granule density by solid state sintering. The aim was to achieve a higher powder bed density for the PBF-LB process by densification of the single granules.

The highest apparent (48.4%) and tapped (56.4%) densities were obtained for thermal treated manganese oxide doped granules, which could be due to the larger grain growth as described in section 3.3. All powders showed a comparable flowability (Hausner ratio between 1.17 and 1.19) for comparable processing conditions with the laser. Thermal treatment resulted in an increase of granulate particle size, which can be explained that still bonded granules were present and not totally separated by the added AA18. Furthermore, the moisture content decreased from 1.26 wt% to 0.12 wt% for iron oxide doped granules and from 0.72 wt% to 0.10 wt% for manganese oxide doped granules. This reduction could be in theory beneficial to reduce crack formation, since sudden evaporation of water (possibly also bound as hydroxide) can lead to a strong volume expansion [258] during the fast heating by the laser. The moisture content values after the heat treatment at 1600 °C were expected to be zero or closer to zero. This variation could be within the measurement error of the device.

In **Figure 64** the geometries and the internal structure of parts manufactured by green pulsed SLM (parameters defined in chapter 2.4) are representatively illustrated by optical and scanning electron microscopy images. The shape of the desired item was a cube with an edge length of 4 mm. The same dimensions were achieved for all parts. A rough surface is apparent on the lateral and even more on the top areas. The reason for the top surface roughness could be the formation of a melt pool cavity (keyhole) by melt pool dynamics induced by evaporation of the material during laser manufacturing and the powder spattering effect, which are proportionally bigger for pulsed lasers compared to a continuous wave laser, or a high viscosity of the melt. Scanning electron microscopy revealed various cracks within the microstructure of all samples, which were caused by huge thermal gradients during laser processing (thermal shock). A crack reduction by the reduction of the moisture content could not be identified in these images. The AA18 alumina phase is totally molten during laser processing in the bulk part of the sample (**Figure 64e**). However, coarse AA18 particles can remain together with the spray dried granules in the pores of the sample (**Figure 64f**).



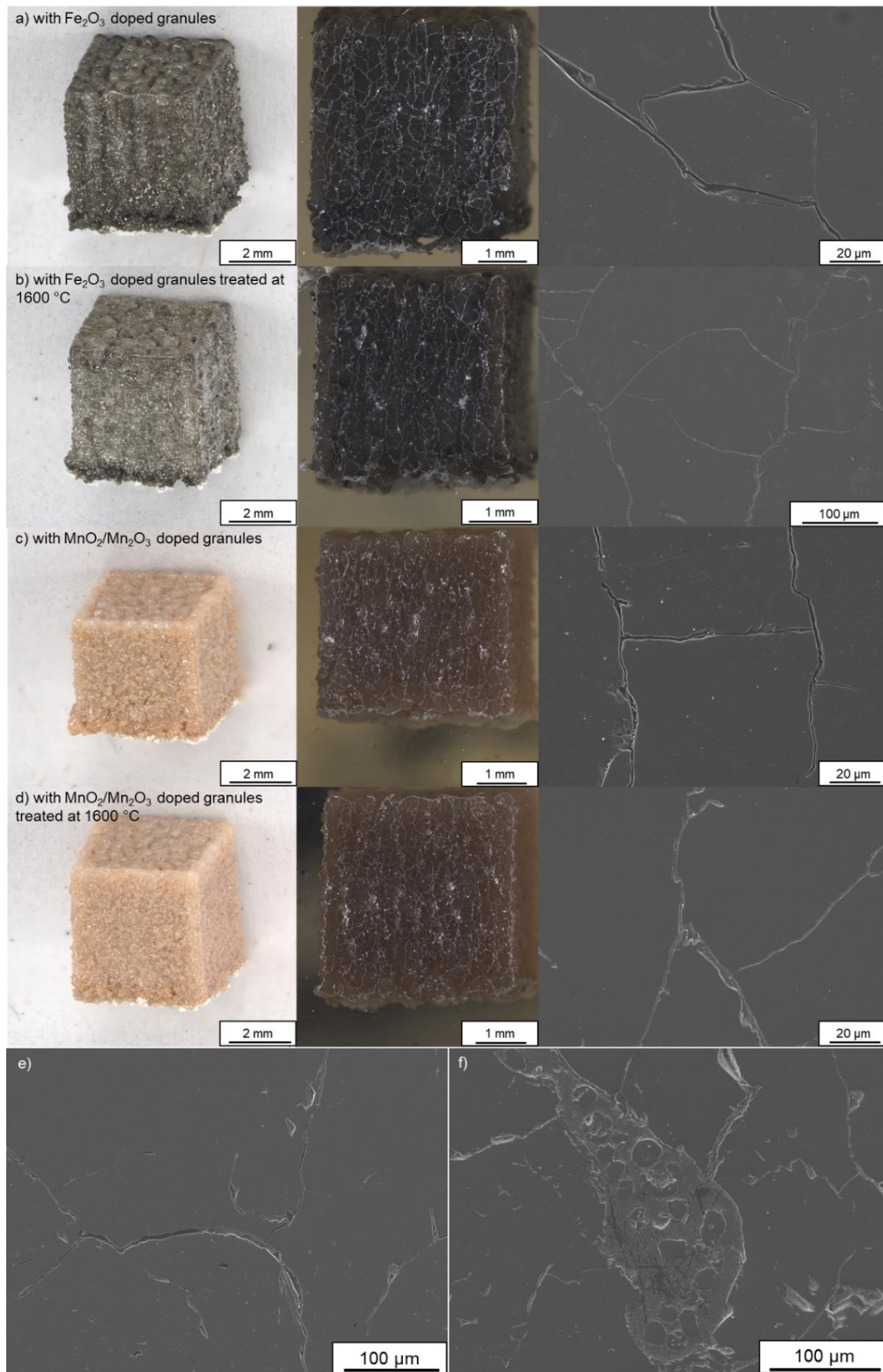


**Figure 64:** Shape (left column) and cross-sections (center column) imaged by optical microscopy as well as internal structure imaged by SEM (right column) of laser manufactured parts produced with Fe<sub>2</sub>O<sub>3</sub>-doped (a, b) and MnO<sub>2</sub>/Mn<sub>2</sub>O<sub>3</sub>-doped (a, c, e: untreated; b, d, f: thermally pre-treated) powders.

The black color of the parts processed from iron oxide doped granules, was already explained in [17] by the formation of hercynite phase ( $\text{FeAl}_2\text{O}_4$ ) during processing. First tests showed hereby that the amount of hercynite in the final part could be diminished by thermal treatment (**Figure 57g, h**), since iron can be incorporated into the alumina lattice [156, 159]. Hercynite can transit into the liquid melt status between 1565 up to 1709 °C, depending on the stoichiometry ratio (iron content) of the spinel [255]. Understanding of this spinel phase formation could be one aspect of further research. In the case of ceramic parts processed with manganese oxide doped granules, a combination of corundum lattice doping by manganese atoms (dopant atom occupies an interstitial region, but is not incorporated into the crystal lattice) and the formation of the galaxite phase ( $\text{MnAl}_2\text{O}_4$ ) was found to be the reason for the orange color.

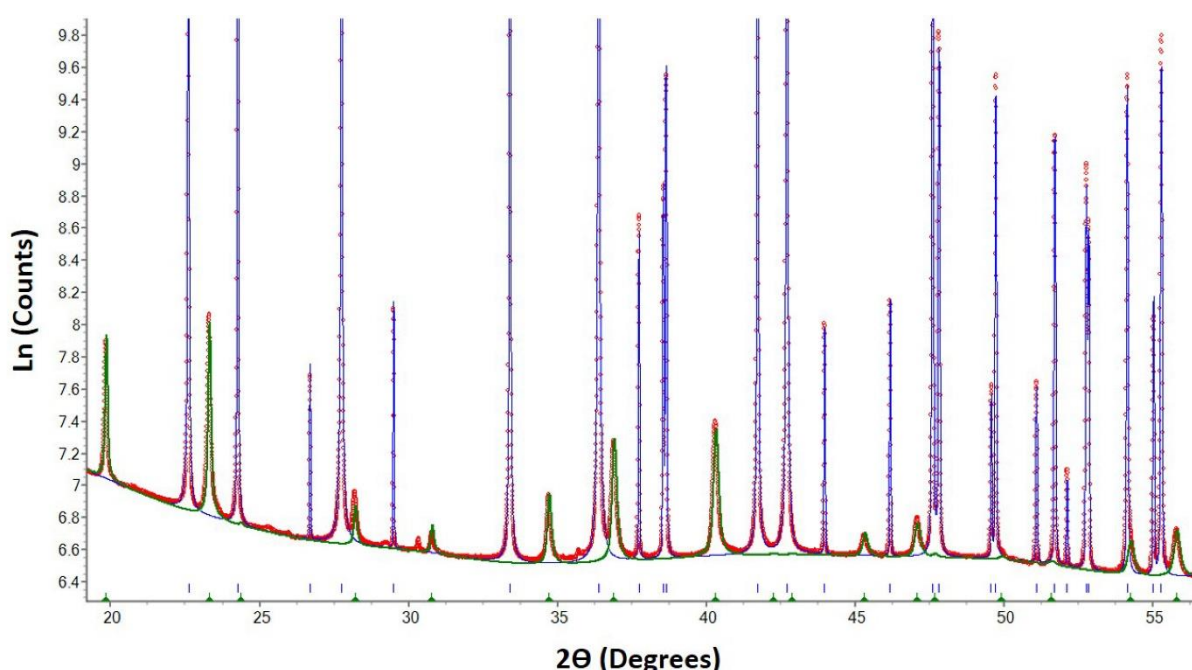


**Figure 65:** High resolution powder diffraction pattern of a laser manufactured part revealing presence of the phases corundum and galaxite. Red dots are the measured data, blue and green lines are calculated patterns of corundum and galaxite phases, respectively.

A high resolution powder diffractogram of the laser manufactured parts from manganese oxide doped granules with a peak enlargement to illustrate the formed galaxite phase is presented in **Figure 65**. The quantification of galaxite ( $\text{MnAl}_2\text{O}_4$ ) phase based on refinement of the powder diffraction data gave a value of 1.75%. The volume expansion, caused by the spinel formation from the well-dispersed dopants, can also lead to crack formation during this rapid process. The challenge of thermal stress reduction and thus a diminution of crack formation is still a major issue of the ongoing research.

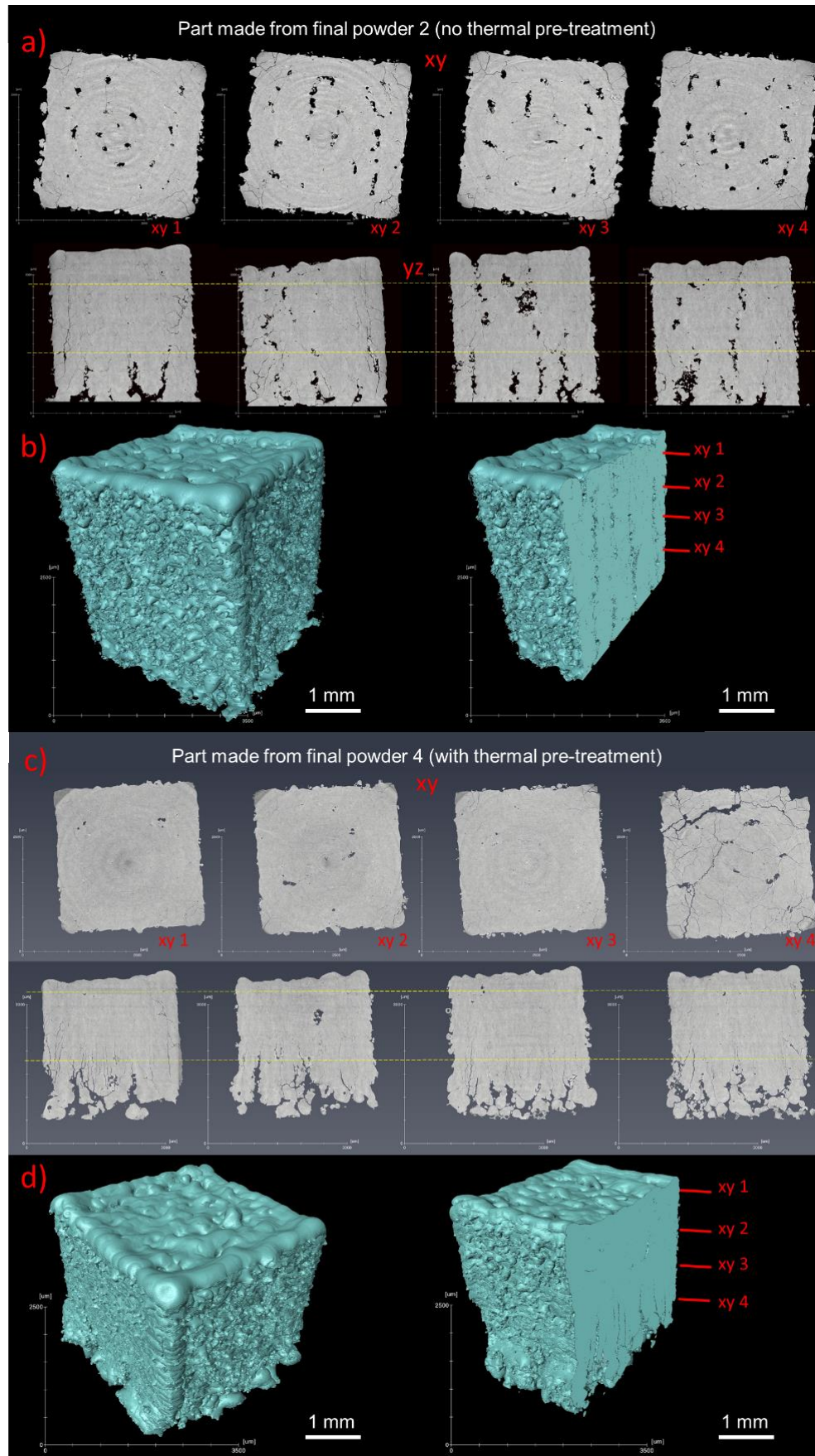


**Figure 66:** Tomographic microscopy imaging of two parts prepared with a), b) as-prepared (powder 2) and c), d) heat treated (powder 4) Mn-doped granules.



**Figure 66** presents the results of tomographic microscopy experiments of two parts prepared with manganese oxide doped non-calcined powder 2 (**Figure 66a, b**) and calcined powder 4 (**Figure 66c, d**). Two laser-manufactured samples were imaged for each powder using tomographic microscopy. The reconstructed 3D volumes clearly show the presence of cracks and pores in the samples. **Figure 66a and c** show virtual tomographic slices perpendicular to the build and scanning directions, respectively. By segmentation of the phases (alumina, pores) in the reconstructed volumes, the density of the parts was evaluated.

From the visualization of the structure, it is apparent that the bottom of the samples has a significantly higher amount of cracks and pores. It was observed that the roughness of the top surface and the cracks at the bottom part strongly affect the evaluated density values. Therefore, the density was evaluated for the whole volume and for a region selected inside the samples, where the effects of the substrate and of the top roughness were avoided (the region limited by the dashed yellow lines in **Figure 66a and c**).

The density values evaluated for the whole volume were 96.2% for parts from calcined and 94.6% from non-calcined powder. In comparison, the densities evaluated for the selected inner region were 98.6% and 96.2%, respectively. The sample manufactured from pre-treated powder exhibits noticeably higher density, which is clearly seen in **Figure 66**. This is most likely due to the higher powder bed density of the thermal pre-treated powder. Furthermore, a porosity arising by trapped CO<sub>2</sub> (binder and dispersant act as carbon source), which could not easily evaporate during laser processing, could lead to a density decrease in parts from non-calcined powder 2. In addition, the higher residual moisture content in this powder (0.72 wt%) in combination with the strong volume expansion of water [258] during the fast heating process could be a reason for the increased porosity. Since the residual organic used for spray drying (ca. 4.6 vol% binder and dispersant) within the pre-treated granules was totally burned out during thermal treatment, the influence of CO<sub>2</sub> formation on porosity could be excluded in these samples. In the present work, a higher density of the powder bed caused a higher density of the final alumina parts, which is in agreement with the literature [18, 19]. This confirms the findings in the authors previous work, in which laser processing of iron oxide doped powders with a tapped powder density of 48.4% led to a density of the ceramic sample of 96.1% and a tapped density of 44.3% to a part density of only 93.7% [95]. In comparison to this, Verga et al. [56] reported a density of 96% with a tapped density of 41% for alumina toughened zirconia parts produced with a continuous wave 200W Nd-YAG fiber laser operating at 1064 nm. The final densities of parts made from pre-treated powder are similar to the density of 97.5%, which Juste et al. [50]

measured according to the Archimedes principle. These parts manufactured with a continuous wave fiber laser from graphite containing alumina granules. However, the achieved part density values of Verga et al [56] and Juste et al. [50] are difficult to compare with the values achieved in this work; since the used laser, the process parameters and the material were different.

The relative densities measured by the Archimedes method for parts processed with the different powders were similar and within the standard deviation (**Table 20**).

**Table 20:** Relative densities for parts processed by green-pulsed laser SLM with different powders

Parts made from	Powder 1	Powder 2	Powder 3	Powder 4
	70 vol% Fe <sub>2</sub> O <sub>3</sub> -doped granules + 30 vol% coarse alumina AA18	70 vol% MnO <sub>2</sub> /Mn <sub>2</sub> O <sub>3</sub> -doped granules + 30 vol% coarse alumina AA18	70 vol% Fe <sub>2</sub> O <sub>3</sub> -doped granules treated at 1600°C/2h + 30 vol% coarse alumina AA18	70 vol% MnO <sub>2</sub> /Mn <sub>2</sub> O <sub>3</sub> -doped granules treated at 1600°C/2h + 30 vol% coarse alumina AA18
Density [%]	96.3 ± 1.3	95.8 ± 0.9	96.0 ± 0.5	95.3 ± 0.4

The different dopants did not have a significant influence on the final part density. The density of parts manufactured with manganese oxide doped granules was slightly lower, but still within the standard deviation of the density measurement.

However, in contrary to the density measurements made by tomographic microscopy, where an increase of the powder density resulted in an increase of the final part density, no clear trend was seen. To ensure comparable processing conditions with the laser, the Hausner ratio was fixed to constant flowability values of the different powders (1.17 – 1.19).

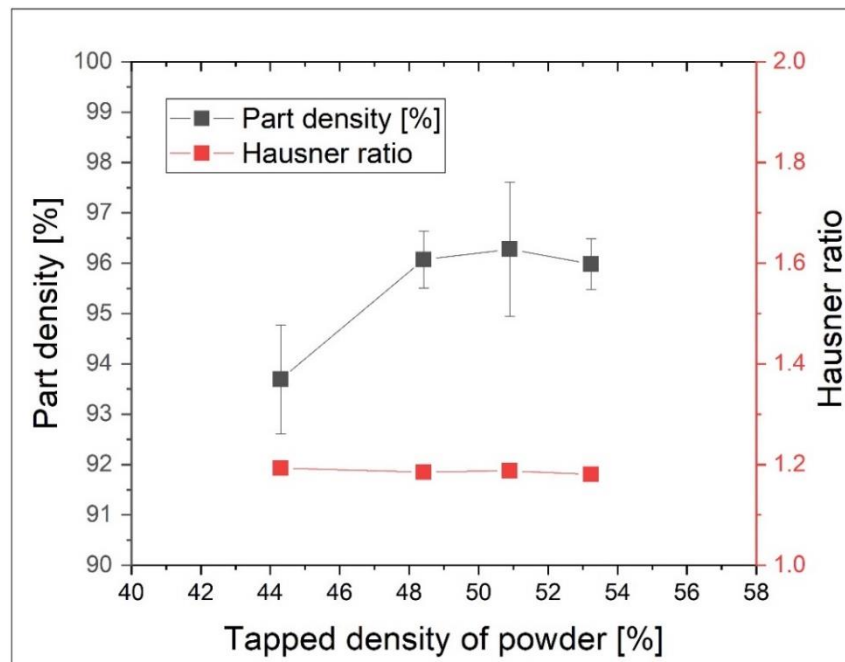


**Figure 67:** Laser processed part density and Hausner ratio as function of tapped powder density.

Up to a tapped density of 48.4% of the theoretical powder density, a higher density of the powder bed (doped with iron oxide) caused a higher density of the final alumina parts (**Figure 67**), which is in agreement with the tomographic microscopy measurements. By laser processing of the iron oxide doped powder with a tapped density of 48.4%, parts with density of 96.1% were produced. With a tapped powder density of 44.3% a density of the ceramic sample of only 93.7% was reached [95]. For a tapped density above 48.4% the values remained at a constant value of around 96% (**Table 20**), which is in contrast to the tomographic measurements (**Figure 66**) and to Bertrand et al. [18], who stated that a higher powder bed density is necessary to achieve a higher density of the final parts. However, Bertrand et al. [18] did not state a certain value of necessary powder bed density. Furthermore, the Archimedes method has to be treated carefully parts, since open porosity is not taken into account and measurements of size and weight can vary strongly for small parts. This can in consequence lead to measurement errors.

**Figure 68** illustrates electron microscopy and tomography images of laser processed parts from manganese oxide doped as-prepared (left) and thermal treated (right) granules. Non-molten or partly molten granules were found in the pores of these parts

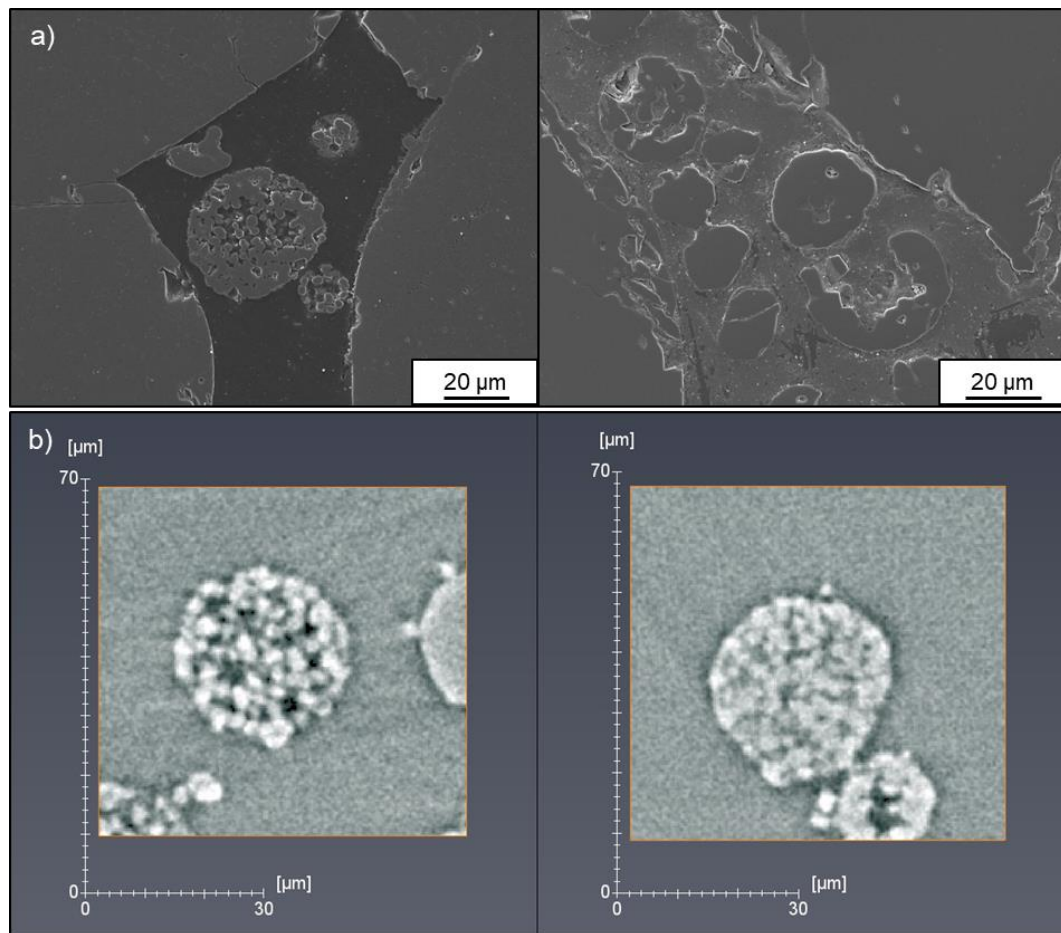


**Figure 68:** a) Electron microscopy and b) tomography images of the parts processed from Mn-doped as-prepared (left) and thermal treated (right) granules presenting non-molten granules found in pores of the parts.

The electron microscopy images in **Figure 68a** present cross sections, showing non-molten as prepared granules (left) and thermal treated granules (right) present within the bigger pores of the laser printed ceramic cubes. It is worth noting that this structure can be distorted during grinding and polishing for SEM cross-section analysis and provide misleading information. **Figure 68b** presents selected areas of the volume obtained by tomographic microscopy showing also non-molten granules that can be found in pores in the printed parts. This image shows the structural difference of the granules before (left) and after sintering (right), that can be compared with the microscopy image above. The resolution of the tomograms is not as good as that of SEM, but as a nondestructive technique, the microstructure is unaffected, as is the case for microscopy images of the cross section. Furthermore, a 3D information is given by the tomograms, which allows a more detailed analysis. Thus, these two techniques provide complementary information. Both techniques show that heat treatment of the granules leads to densification of granules, and thus densification of the powder bed. Not all granules are affected by the laser beam (not sintered or molten) and thus remain unchanged within the microstructure of the laser manufactured parts.

### 3.3.5 Grain structure of laser additive manufactured parts

Electron backscatter diffraction (EBSD) was used to characterize the grain structure and orientation within the microstructure of the polycrystalline materials. **Figure 69a, b and c** show EBSD mapped results for laser scanning speeds of 2, 5 and 10 mm/s. Parts made from iron oxide doped samples were chosen for these measurements.

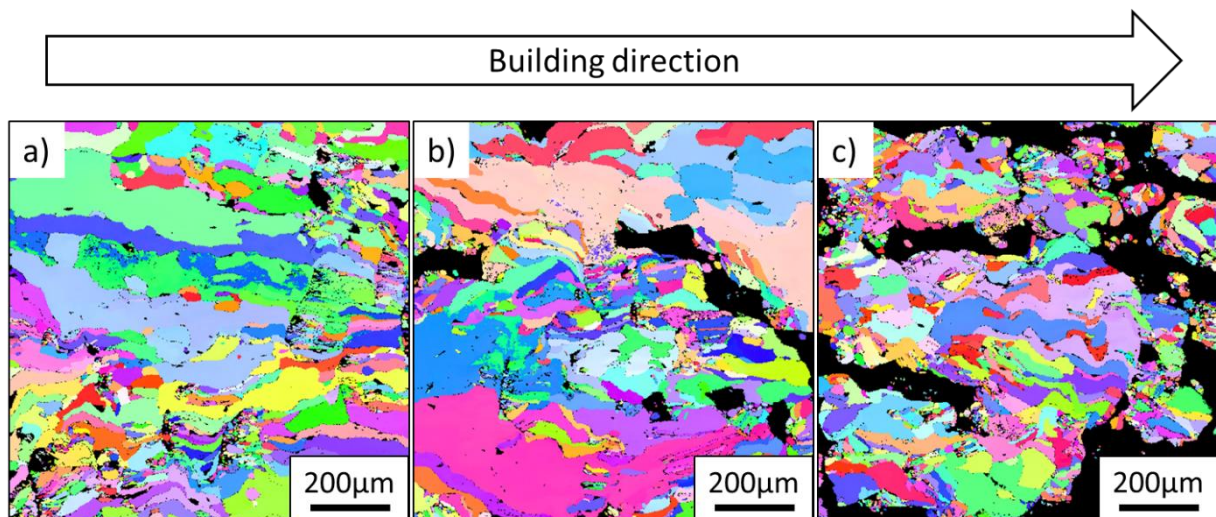


**Figure 69:** EBSD mapped results of parts made from iron oxide doped granules with the laser scanning speeds of **a)** 2 mm/s, **b)** 5 mm/s and **c)** 10 mm/s (Colored areas represent grains with different crystal orientation; black areas represent the porosity within the laser processed parts).

At a first glance, an irregular grain orientation and grain sizes can be noted. This could be due to slight melt pool instabilities described by Florio et al. [252], which can cause temperature variations during laser processing of the iron oxide doped aluminum oxide granules. However, a deeper look reveals that crystal grains are growing predominantly parallel to the building direction. This was also seen by Wu et al [164], who ascribed this growth along the building direction to an unstable solid/liquid interface caused by constitutional supercooling. The growth rate is the highest in this direction during PBF-LB, since the heat dissipation of the molten pool is principally conducted through the substrate or the previous consolidated layers below.

Furthermore, a difference in the grain size is present for the different speeds. The grains sizes are up to length of 1 mm for a speed of 2 mm/s, whereas the grains lengths are only up to a maximum of 400  $\mu\text{m}$  for a speed of 10 mm/s. The amount of grains in the same measurement area increases also due to smaller width of the grains perpendicular to the building direction for the faster speed of 10 mm/s. The samples experience a higher cooling rate due to a higher laser scanning speed and thus, smaller grains are formed. The same behavior was observed by Mapar [52]. A reduction of the grain size in a eutectic alumina-zirconia mixture was achieved by using a smaller laser spot size and a higher scanning speed, what induced a higher cooling rate. Similarly, Fan et al. reported that a higher laser energy density caused a smaller cooling rate for solidification and therefore larger grains [8]. Zhang et al. [65] and Zheng et al. [11] ascribed lamellar structures of few microns in width and tens of microns in length along the build direction due to thermal capillary convection, influenced by Marangoni effect, streak convection and flowing Bénard cells. The achieved size of the crystals in these laser-processed  $\text{Al}_2\text{O}_3$  parts [11, 65] was much smaller than the size of the crystals shown in **Figure 69**. This should be due to a higher cooling rate caused by higher laser scanning speeds (60-120 mm/s) and by the use of a dense aluminum oxide substrate, which offers a higher heat conductivity than the porous aluminum oxide foam substrates used in the present work.

In contrary to the present work, Deckers et al. reported a more regular grain orientation and grain sizes of only 5  $\mu\text{m}$  by PBF-LB [5]. Hagedorn et al. achieved  $\text{Al}_2\text{O}_3\text{-ZrO}_2$  ceramics with a regular nano-structured microstructure interrupted by intervals of coarser crystals corresponding to the layer thickness [15]. They explained this unique microstructure by local evaporation of alumina, which could be caused by using a second laser for high temperature preheating. Gahler et al. noticed the influence of the different cooling rates at different layer depths on the grain size and orientation during PBF-LB of alumina-silica composites [3]. However, this influence was not seen in this work for doped alumina.



To improve the irregular grain orientation and the coarse grain structure for parts made from metal oxide granules by PBF-LB will be challenging, since the microstructure depends on the processing conditions. These are limited by a small parameter window for a successful consolidation [17], since part shape and microstructure are generated simultaneously during the melting and resolidification process. Low speed and high power, required in general to have dense alumina parts by PBF-LB, lead to large grains. As seen in **Figure 69**, a laser scanning speed of 10 mm/s generates a higher porosity compared to scanning with 2 or 5 mm/s. A solution could be to search for other suitable dopants, which restrict extensive grain growth even more than iron oxide. However, in contrary to the big impact of dopants in sinter processes [157], it is not proven that this can have also an impact for melt processes.

### 3.3.6 Thermal expansion of laser processed parts

**Figure 70** plots the thermomechanical analysis of laser additive manufactured parts made from  $\text{Fe}_2\text{O}_3$  or  $\text{MnO}_2/\text{Mn}_2\text{O}_3$  doped aluminum oxide granules. The aim of this study was to evaluate the changes of further densification by post-thermal treatment. The apparent length changes only slightly during the chosen temperature profile (maximum temperature of 1480 °C, idle time of 2 hours, heating rate of 2 K/min and cooling rate of 5 K/min) for both materials. The maximum changes of the measured length (build direction) for parts made from  $\text{Fe}_2\text{O}_3$  doped granules were below 0.1%. These changes were similar for parts made from manganese oxide doped granules (below 0.1%). The measured values are difficult to evaluate, since the accuracy of the analysis is also limited. However, it is clear that the small length changes in build direction are negligible in terms of a densification, which is not given by this thermal post treatment.

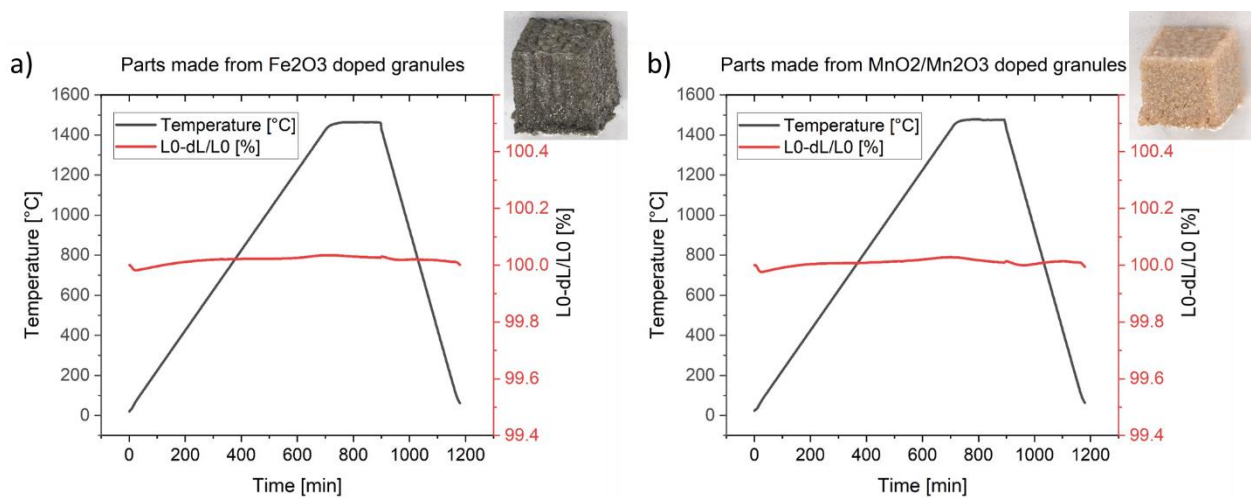


**Figure 70:** Thermomechanical analysis illustrating the length change in respect to time and temperature of laser additive manufactured parts made from **a)** iron oxide or **b)** manganese oxide doped granules.

Gilshtein et al. stated that in a conventional furnace sintering process with a heating rate of 2 K/min, the shrinkage for compressed iron-oxide doped granules started at a temperature of 875 °C [259]. The determined apparent activation energy of this powder-based system was 680 kJ/mol, which was slightly higher than the activation energy of 520 kJ/mol evaluated for nano-sized alumina by Brosnan et al. [260]. This shows that a shrinkage should be present for the initial granular powder system used before laser sintering based on the given thermal history.

However, the sinter activity after laser processing is low due to large grains formed during the process (chapter 3.3.5), which increase the activation energy for sintering due to a low surface area. Furthermore, distances in between cracks or pores are too big to be closed by solid state sintering via diffusion process.

Lee et al [78] reported a strength increase of 3-5 MPa due to porosity reduction by thermal annealing of laser manufactured parts infiltrated with colloidal silica. A similar method to hot isostatic pressing, Ceracon forging was also applied to further densify laser processed parts [77]. Instead of a gaseous medium to apply pressure, solid ceramic particles are used as a pressure transmitting medium [261]. An increase of the 4-point bending strength of up to 110 MPa after full densification was reported in their work. However, both works dealt with alumina glass composites, where the glass phase with a low melting temperature and low melt viscosity could support the densification process.

#### **3.3.7 Influence of thermal pre-treatment and laser processing on manganese amount within granules and laser additive manufactured parts**

**Table 21a and b** summarizes the average manganese content measured by XRF line scans of spray-dried and thermal pre-treated granules and of the laser manufactured parts from these two types of granules. Due to the high temperatures involved in the process of thermal treatment (1600 °C) and PBF-LB (at least 2054 °C (melting point of  $\text{Al}_2\text{O}_3$ ) [255]), a manganese depletion was assumed.

The XRF line scans confirmed a significant difference in the concentration distribution of Mn within different samples. Thermal treatment at 1600 °C resulted in a depletion of 0.64 wt% (0.32 at%) of manganese compared to the untreated spray-dried granules. Laser processing resulted in a further depletion. The final manganese amount was 1.32 wt% (0.65 at%), what represents a significant reduction of 1.02 wt% (0.51 at%) compared to the as spray dried granules. In the case of laser processing of the as spray-dried granules, the reduction was only 0.18 wt% (0.08 at%). In conclusions, it can be stated that the thermal treatment by the oven or the laser

results in a manganese depletion. The long-lasting thermal treatment in the furnace (in the range of several hours) is hereby more detrimental for the manganese amount than the short processing times used for PBF-LB, even if the temperature is significantly higher during laser processing. This could be due to the rapid cooling in laser processing of the already consolidated material. However, the results have to be interpreted carefully, since the standard deviations of the measurements made at the laser-manufactured parts are rather high (1.91 wt% for parts made from as spray-dried granules and 0.72 wt% for parts made from thermal pre-treated granules). This is a result of the inhomogeneous distribution of the galaxite phase, which could be caused by the demixing of Mn atoms [159, 262].

**Table 21:** Average manganese content measured by XRF line scans of **a)** spray-dried and thermal pre-treated granules and of **b)** laser processed parts made from spray-dried and thermal pre-treated granules

**a) Granules**

	As spray-dried granules		Thermal pre-treated granules	
	wt%	at%	wt%	at%
Position 1	2.27	1.13	1.81	0.90
Position 2	2.27	1.13	2.18	1.08
Position 3	2.06	1.02	1.77	0.88
Position 4	2.35	1.17	1.46	0.72
Position 5	2.74	1.36	1.28	0.63
Average	2.34	1.16	1.70	0.84
standard deviation	0.25	0.12	0.35	0.17

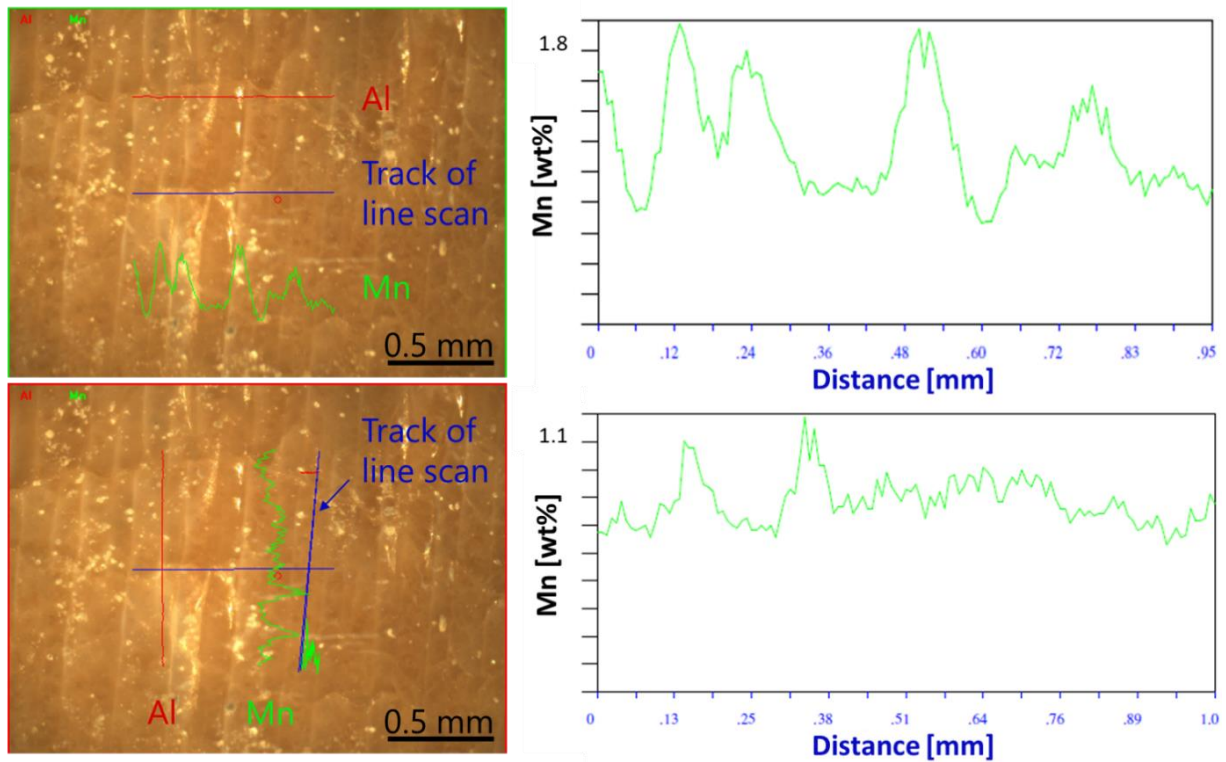
**b) Laser processed parts**

	As spray-dried granules		Thermal pre-treated granules	
	wt%	at%	wt%	at%
Position 1	0.16	0.08	1.39	0.69
Position 2	0.54	0.26	2.00	0.99
Position 3	4.50	2.26	0.56	0.28
Position 4	3.56	1.78		
Position 5	0.66	0.32		
Position 6	3.56	1.78		
Average	2.16	1.08	1.32	0.65
standard deviation	1.91	0.96	0.72	0.36

Two laser processed layers located on thermally pre-treated cylindrical substrates (700°C (**Figure 71a**) and 1600 °C (**Figure 71b**)) were consolidated to give larger areas for the line scans

and thus, to improve the statistics of the measurement. Furthermore, the corresponding manganese content in wt% measured at the marked tracks (blue lines in optical microscopy images) is depicted in **Figure 71**. The red and green line within the microscopy images represent the measured aluminum and manganese content, respectively. The aluminum content is constantly high and was not examined more closely.

a) Laser processed layer (compressed granules thermally pre-treated at 700 °C)



b) Laser processed layer (compressed granules thermally pre-treated at 1600 °C)

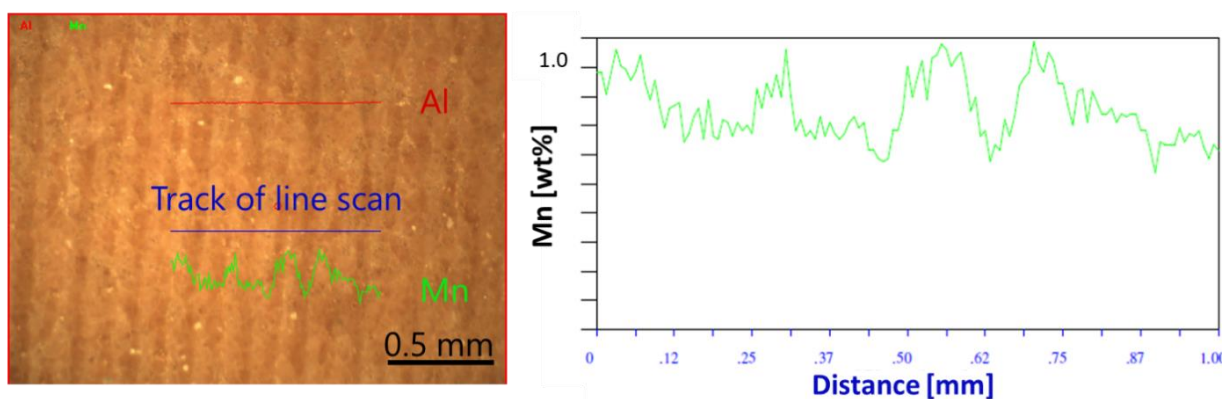


**Figure 71:** Optical microscopy images of laser processed layers located on thermally pre-treated circular substrates **a)** 700°C and **b)** 1600 °C and corresponding manganese content in wt% measured at the marked line scans (blue lines in the optical microscopy images). The red and green line within the optical microscopy represent the measured aluminum and manganese amount, respectively.

**Figure 71a** shows that a higher concentration of Mn is predominately located at the edges of the laser beam track. The peaks of the manganese concentration of the line scan perpendicular to laser beam track are more pronounced than that of the parallel scan in the center of the laser beam track. The manganese content measured for the perpendicular scan varies from 0.6 – 2.0 wt%, whereas the manganese variation for the parallel scan is only between 0.7 and 1.2 wt%. The peaks of Mn in the transition area of two laser scans could result from the thermal capillary convection (Bernard-Marangoni convection) generated by temperature variations within the melt pool [11, 65]. The maximum temperatures during processing is in general in the center of the processed laser line. The manganese amount measured on the laser processed layers located on the substrate thermal pre-treated at 1600 °C was in between 0.6 and 1.1 wt% for a perpendicular scan (**Figure 71b**).

**Table 22** summarizes the average manganese content measured by XRF line scans made on the two laser processed layers presented in **Figure 71**. The thermal pre-treatment at 1600 °C results in Mn depletion as also seen for the laser processed parts summarized in **Table 21**. The laser processed layer on the substrate thermal pre-treated with 700°C exhibits a higher content of 1.26 wt% (0.62 at%) compared to content of 0.81 wt% (0.40 at%) measured on the layer on the substrate pre-treated with 1600 °C.

**Table 22:** Average manganese content measured by XRF line scans of laser-processed layers consolidated on thermal pre-treated substrates (700 and 1600 °C).

<b>Laser processed layers</b>				
	Substrate thermally pre-treated at 700 °C		Substrate thermally pre-treated at 1600 °C	
	wt%	at%	wt%	at%
Average	1.26	0.62	0.81	0.40

Manganese depletion by evaporation is a well-known phenomenon. You et al. recognized an increasing manganese loss with temperature (1450 - 1700 °C) during oxygen refining of high-carbon ferromanganese melts [263]. The influence of the temperature could be clearly indicated, but this was not as significant as for example the slag basicity. The depletion was explained by an oxidation and evaporation processes. Chu and Bao reported a similar behavior of manganese depletion of high-carbon ferromanganese and silicon manganese alloys at 1600 °C in vacuum [264]. They reported a severe manganese volatilization from the molten steels depending from the partial vapor pressure of the manganese component.



## 4 Additives to reduce crack formation in selective laser melting and sintering of alumina

The impact on crack formation of several additive powders was tested in this work. **Table 23** summarizes briefly the theoretical principle of crack reduction in the PBF-LB processed aluminum oxide parts by the use of these additives.

***Table 23:** theoretical principle of crack reduction in the PBF-LB processed aluminum oxide parts by the use of these additives*

<b>Additives within powders</b>	<b>Theoretical principle of crack reduction</b>
Mullite	<ul style="list-style-type: none"><li>• Glass phase formation (partial melting) due to high silica content</li><li>• Low thermal expansion coefficient</li></ul>
Rare earth oxide (ceria and yttria)	<ul style="list-style-type: none"><li>• Decrease of solidification temperature by formation of amorphous bulk glasses based on alumina and rare earth oxides</li></ul>
Reduced titanium oxide	<ul style="list-style-type: none"><li>• In-situ formation of aluminum titanate with low thermal expansion coefficient, low thermal conductivity, low young's modulus and therefore, excellent thermal shock behavior</li></ul>
Zirconia and tungsten oxide	<ul style="list-style-type: none"><li>• Generation of zirconium tungstate with a negative thermal expansion coefficient during laser processing</li></ul>

## 4.1 Experimental

Mullite WFM 0-10 (Imerys Fused Minerals Zschornowitz GmbH, Gräfenhainichen, Germany), a not commercially available submicron mullite (extra milled for project) (Mullite d<sub>50</sub> < 1 μm, Imerys Fused Minerals Laufenburg GmbH, Laufenburg, Germany), CeO<sub>2</sub> nanoparticles (Nanografi Nanotechnology Co. Ltd., Turkey), submicron-sized Y<sub>2</sub>O<sub>3</sub> (Auer-Remy GmbH, Hamburg, Germany) or Aeroxide TiO<sub>2</sub> P25 nanoparticles (Evonik Industries AG, Essen, Germany) were incorporated within the spray dried granules. Furthermore, spray-dried granules made from ZrO<sub>2</sub> nanoparticles TZ-0 (Tosoh Corporation, Tokyo, Japan) and WO<sub>3</sub> nanoparticles (ALB Materials Inc, Henderson, USA) were mixed with coarse aluminum oxide AA18 (Sumitomo, Chemical Co. LTD, Tokyo, Japan). Ammonium citrate dibasic p.a. 98% (Sigma Aldrich Corp., USA) was utilized as surfactant. A 10% diluted ammonium hydroxide solution (Carl Roth GmbH + Co. KG, Germany) was used for pH-value adjustment of the WO<sub>3</sub> nanoparticle dispersions. The change of the pH-value was measured by the Five Easy Plus pH meter FP 20-Std-Kit (Mettler Toledo Schweiz GmbH, Switzerland).

The absolute densities of the additive powders were evaluated by helium pycnometry (AccuPyc II 1340, Micromeritics, USA). BET (Brunauer–Emmett–Teller) measurements (SA 3100, Beckman Coulter, Krefeld, Germany) gave the specific surface area (SSA). The powders were degassed with synthetic air for two hours at 180 °C (SA-PREP Surface Area Outgasser, Beckman Coulter, Krefeld, Germany) before performing the SSA measurement. The corresponding BET average particle size was calculated from the measured absolute density and SSA according to the Sauter mean diameter [228].

The surface potential of the particles was determined by zeta potential measurements by an electroacoustic method with a ZetaProbe Analyzer (Colloidal Dynamics, USA). The zeta potential measurements were performed at different pH-values with an equilibration delay of 30 seconds. A 0.1 molar solution of HCl (Carl Roth GmbH + Co. KG, Germany) and 0.1 molar NaOH (Sigma Aldrich Corp., USA) were titrated to adjust the pH of the utilized 5 wt% suspensions. Dielectric constants were taken from literature [229]. A saturation amount of surfactant on the particle surfaces was evaluated for each powder by these measurements. This amount of dispersant was mixed with the additive powders to conduct a proper dispersion in Nanopure water. The dispersion was either made by roll milling for 24 hours or vibration milling for 20 min with a vibrational frequency of 30 Hz (Retsch MM301, Retsch GmbH, Haan, Germany) or a combination of both using ZrO<sub>2</sub> milling balls (Tosoh Corporation, Tokyo, Japan). The used sizes (0.4 – 3 mm) are stated in the specific chapter, since they vary for the different powders.



Volume based particle size distributions of the dispersed starting materials were measured in water by laser diffraction (LS 13320, Beckman Coulter GmbH, Germany) and dynamic light scattering (ZetaSizer Nano ZS, Malvern Panalytical Ltd, United Kingdom). The required refractive indexes and extinction coefficients for the size measurements were taken from [265] for mullite, [266] for  $\text{Y}_2\text{O}_3$ , [267] for  $\text{CeO}_2$ , [268] for  $\text{TiO}_2$ , [269] for  $\text{WO}_3$  and [270] for  $\text{ZrO}_2$ . Particle shapes were imaged by Scanning Electron Microscopy (VEGA3 Tescan, Tescan instruments, Brno, Czech Republic) Prior to the SEM analysis, the powder was distributed with compressed air on an adhesive carbon tab and then sputtered with Au-Pd

Spray granulation was performed in the Mini spray dryer B-290 (Büchi Labortechnik AG, Switzerland) with an ultrasonic atomizer in co-current mode. The slurry was delivered by a peristaltic pump to the nozzle and left stirring to prevent a demixing. An ultrasonic atomizer and a co-current droplet air mixing were used for spray drying. Process parameters for the aluminum oxide based granules were an inlet temperature of 140 °C, an outlet temperature of 100 °C, an air flow rate within the spraying apparatus of 25 m<sup>3</sup>/h, a nozzle frequency of 60 kHz and a slurry feed rate of circa 1.1 ml/min. The used ultrasonic power is stated in the specific chapter, since the value can vary for different powder combinations. The ultrasonic nozzle was prevented from overheating by a flow of compressed air. A detailed process parameter study for the  $\text{ZrO}_2/\text{WO}_3$  granules is given in chapter 4.2.4. The Dehumidifier B-296 (Büchi Labortechnik AG, Switzerland) supplied constant and reproducible humidity conditions. The process parameters were kept constant during spray drying. The final granule separation was accomplished in a cyclonic collector and an additional screening step with a 230 mesh (63  $\mu\text{m}$ ) sieve (Retsch GmbH, Germany). In the case of the aluminum oxide based granules, the binder PEG 35000 (Sigma Aldrich Corp., USA) was added to the coarse AA3 after rotating for 1 hour prior to spray drying. The amount of binder was 2 wt% (6.2 Vol%) referred to total amount of all powders in the slurries for spray drying. After dispersing, the individual slurry components were mixed and homogenized for 4 hours on a rolling bench. In the case of the  $\text{ZrO}_2/\text{WO}_3$  granules, only 1 wt% (5Vol%) PEG 35000 was added after 20 hours to the dispersed  $\text{ZrO}_2$  particles. After a homogenization step of the two hours, the two slurry components were finally mixed for two hours. The slurry was continuously stirred during spray drying to prevent a demixing.

Thermal treatment in Ar/H<sub>2</sub> (98/2%) atmosphere of the granules containing titanium oxide was performed in the tube furnaces Carbolite STF 16/610 and Carbolite CTF 17/300 (Carbolite Gero GmbH & Co. KG, Neuhausen, Germany). The applied temperature varied from 1000 up to 1600 °C. Holding times of 2 hours were used with a heating rate of 2 K/min. After thermal

treatment the powders were screened with a 120 mesh sieve and finally mixed with 30 vol% coarse alumina AA18 on a rolling bench for 1 hour to achieve powders with a final  $\text{TiO}_{2-x}$  content of 0.7 Vol%, 10 Vol% and 50 Mol% (43.4 Vol%). The amount of 50 Mol% of aluminum oxide and titanium oxide was used to achieve pure aluminum titanate in the case of a fully completed reaction. The coarse alumina was added to the granules to break the sintering necks in between the granules and act as an easy flowable medium. Prior to the thermal treatment in the tube furnaces, a thermal gravimetric analysis (Netzsch STA 449F3 Jupiter, Netzsch Gerätebau GmbH, Selb, Germany) in argon/hydrogen (2%) atmosphere was performed to evaluate the minimum temperature necessary to reduce the  $\text{TiO}_2$  particles. The measurement was conducted with a heating rate of 2 K/min up to a temperature of 1470 °C.

The quality of the powders for PBF-LB was evaluated by apparent density measurements (PTL Dr. Grabehorst GmbH, Germany) according to the standard DIN EN ISO 23145-2 and tapped density measurements by applying a jolting volumeter (JEL STAVII, J. Engelsmann AG, Germany). The sample was tapped 1000 times with a displacement of 3 mm in compliance to EN ISO 787-11. Relative densities were calculated as fractions of the apparent and tapped density over the absolute powder density measured by. The ratio of tapped density divided by apparent density (Hausner ratio) enabled a flowability grading of the powders (Hausner ratios below 1.25 are considered as suitable for powders used for selective laser melting [57, 237]). The fraction of the received granules to the weight of all solid contents in the spray drying slurry revealed the total yield of the process. Particles size distributions of the powders were monitored by laser diffraction (LS 13320, Beckman Coulter GmbH, Krefeld, Germany) in isopropanol including the characteristic values for  $d_{10}$ ,  $d_{50}$  and  $d_{90}$ . The shape of the granules and the impact of thermal treatment in Ar/ $\text{H}_2$  on the microstructure was visualized by the SEM VEGA3 Tescan (Tescan instruments, Czech Republic). Element distributions within the granules were examined by energy-dispersive X-ray spectroscopy by Bruker XFlash 6-10 detector (Bruker Corporation, Billerica, USA). Qualitative absorption measurements for a wavelength range of 300 - 1500 nm (in 2 nm steps) employing the Kubelka-Munk method were performed with the Shimadzu 3600 UV-VIS-NIR spectrophotometer (Shimadzu Corporation, Japan). More details to the Kubelka Munk method can be found in chapter 3.2.1.

Laser powder bed fusion of the customized powders was done by the Institute of Machine Tools and Manufacturing at ETH Zurich in an experimental in house built SLM machine. Two types of lasers were used. Based on the results for  $\text{Fe}_2\text{O}_3$  doped  $\text{Al}_2\text{O}_3$  granules, a green pulsed laser (IPG GLPM-5) was used for the laser processing of the granules containing additional mullite.

The laser used the following characteristics: a wavelength of 532 nm, a pulse duration of 1.5 ns, a nominal average output power of 5 W and a pulse repetition rate of 300 kHz. The laser parameters used during processing were a spot diameter of circa 135  $\mu\text{m}$ , a hatch space of 100  $\mu\text{m}$ , a laser power of 5.75W (measured by a power meter) and a laser speed of 2mm/s. For the processing of the powders containing the other additives a continuous wave IR fiber laser (redPOWER R4 200W, SPI lasers, UK) was used. The laser features following characteristics: a wavelength of 1070 nm and a maximum output power of 200 W. A spot size of 90  $\mu\text{m}$ , a hatch distance of 175  $\mu\text{m}$  and a layer thickness of 40  $\mu\text{m}$  was used for laser processing. This laser combines several advantages. YAG laser light is usually used by most commercial PBF machines because of the reliability. In comparison to a CO<sub>2</sub> laser, the spot size can be smaller, since the spot size is dependent of the used wavelength. Furthermore, the size of the melt pool cavities (keyholes) formed by the melt pool dynamics induced by evaporation of the material should be prevented by the avoidance of a pulsed laser with high peak intensities. Additional, a higher absorptance was measured for ZrO<sub>2</sub>/WO<sub>3</sub> granules and granules containing reduced TiO<sub>2-x</sub> at a wavelength of 1070 nm compared to absorptance at the wavelength of 532 nm of the green laser.

The shape of the PBF-LB printed ceramic parts was imaged by optical microscopy (SteREO Discovery.V20, Carl Zeiss Microscopy, Germany). The internal structure of the parts was illustrated by optical microscopy (Keyence VHX 5000 microscope, Keyence Corporation, Japan) and SEM (VEGA3 Tescan, Tescan instruments, Czech Republic). Before the microstructure imaging, the samples were cold embedded in a resin (CaldoFix-2, Struers GmbH, Switzerland) and the cross-sections were ground and polished (with a 1  $\mu\text{m}$  diamond suspension).

The density according to the Archimedes principle was determined using water as liquid medium. The relative density of the parts was calculated based on the absolute densities of crushed PBF-LB printed parts. The compressive strength was measured using cylinders with a part diameter of ca. 5 mm and a length of ca. 8 mm. The samples were polished up to a 5  $\mu\text{m}$  finish prior to the compression tests. The compression tests were performed using the Instron 8801 servohydraulic testing systems (Illinois Tool Works Inc., USA). The uniaxial compressive strength was calculated according to formula 12.

The young's modulus of the laser processed samples was measured using the ultrasonic method. Each sample was ground plane-parallel to enable a good coupling. The sound velocity of longitudinal ( $c_L$ ) and transverse ( $c_T$ ) waves were created by the ultrasonic measuring device Panametrics 5900 PR (Olympus K.K., Japan) by the use of 4 and 0,5 MHz, respectively, and

calculated from material thickness measurements and time of flight measurements evaluated by the equipped software Ultrasound Imaging System Version 2.2.c. The young's modulus  $E$  can be determined evaluating the material density  $\rho$  as follows:

$$E = 4\rho c_T^2 \frac{\frac{3}{4} - \left(\frac{c_T}{c_L}\right)^2}{1 - \left(\frac{c_T}{c_L}\right)^2} \quad (15)$$

X-ray tomographic microscopy was performed at the TOMCAT beamline of the Swiss Light Source. Tomography scans were performed using a standard setup for full field tomography composed of a 100 micron-thick LuAG:Ce scintillator, an optical microscope with 4x magnification and a sCMOS camera, which provides a field of view of 4.2 mm x 3.5 mm with 1.625  $\mu\text{m}$  pixel size. The energy of the X-ray beam was 25 keV. 1501 projections were acquired over 180° with 280 ms exposure time per projection. 3D imaging of 2x2x2 mm<sup>3</sup> sized cubes allowed to visualize the microstructure with a spatial resolution of about 3  $\mu\text{m}$ . Part density and crack density values were evaluated for the laser processed parts from the tomography visualizations. Accuracy of the density evaluation from tomographic microscopy was determined based on the obtained contrast and spatial resolution. The relative error estimated for these measurements was ca. 0.1%.

The distribution of the crystallographic phases in 3D in the Ti doped alumina samples was obtained by diffraction (XRD) contrast tomographic microscopy (**Figure 72**) performed at the microXAS beamline (SLS, PSI). The laser processed samples with 1x1mm<sup>2</sup> dimensions were cut with a diamond wire saw into pieces with cross-sections of 0.25x0.25 mm<sup>2</sup>. The as-prepared sample was mounted on the sample manipulator with a high precision air-bearing rotational stage at the beamline. Several tomographic slices were obtained by scanning the samples in x direction in a continuous manner at different orientations equally spaced over 180 ° to visualize the phase distribution over cross sections of the sample. Diffraction signal was recorded with a dwell time of 200 ms. The X-ray beam was focused down to 1x1  $\mu\text{m}^2$  using Kirkpatrick-Baez (KB) mirrors, which also defines the limit of the spatial resolution. The diffraction patterns in form of Debye–Scherrer rings were measured with a Eiger4M 2D area detector, the transmitted intensity with a mini SiC diode mounted in the beamstopper and the incoming beam with a mini ionization chamber mounted in the exit window KB box (maintained under helium atmosphere). The relative positions of XRD detector – sample – X-ray beam direction were calibrated based on measurement of a LaB<sub>6</sub> standard from NIST. Measurements were performed using an X-ray beam at an energy of 17.2 keV, which corresponds to a wavelength of 0.7208 Å.

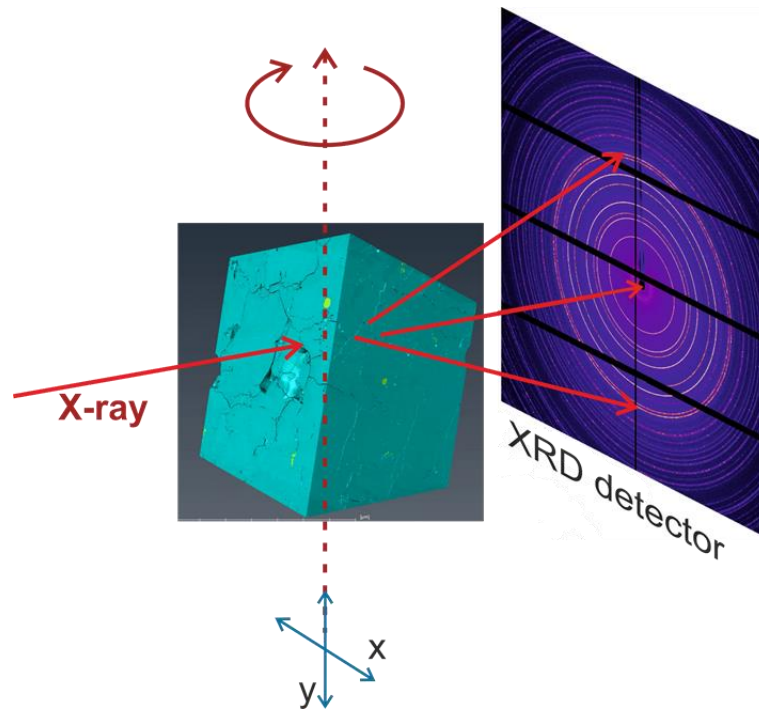


**Figure 72:** Schematics of the setup for the XRD-contrast microscopy experiments

Crystalline phases were identified for raw powders and printed parts respectively layers by X-ray diffraction measurements. The raw powder mullite WFM 0-10 was characterized in the  $2\theta$  range of  $10\text{--}80^\circ$  with a step size of  $0.016^\circ$  and a scanning speed of  $0.021^\circ$  by the Bruker D8 (Bruker Corporation, Billerica, USA) using Cu  $K\alpha_1$  radiation ( $1.5406 \text{ \AA}$ ). A consequent Rietveld refinement using TOPAS Bruker AXS revealed the crystalline composition. The raw powders  $\text{Y}_2\text{O}_3$  and  $\text{CeO}_2$  were characterized using the PANalytical X'Pert PROh-2h (PANalytical, Netherlands) scan system equipped with a Johansson monochromator (Cu  $K\alpha_1$  radiation,  $1.5406 \text{ \AA}$ ) and a X'Celerator linear detector. The scans were collected in the  $2\theta$  range of  $5\text{--}80^\circ$  with a step size of  $0.016^\circ$  and a scanning speed of  $0.021^\circ \text{ s}^{-1}$ . Phase compositions were evaluated by using HighScore Plus Software.

Crystalline phases of PBF-LB printed parts were evaluated by high resolution powder diffraction measurements conducted at Material Science (MS) beamline at the Swiss Light Source (PSI) synchrotron [241]. The energy of the beam set for powder diffraction measurements was  $12.398 \text{ keV}$  and the wavelength was  $1.0009 \text{ \AA}$ . Prior to the measurements the printed parts were ground to powder and measured in glass capillaries (diameter  $200 \text{ }\mu\text{m}$ ) in a transmission mode (Debye-Scherrer geometry).

To evaluate the influence of the laser parameters on the crystallographic composition of granules doped with rare earth oxides as well as the  $\text{ZrO}_2/\text{WO}_3$  granules, eight layers of 10 mm x 10 mm were directly consolidated on the top surface by the IR laser on cylindrical samples of 43 mm in diameter (uniaxial pressed with 70 MPa). Diffraction measurements were performed either on the processed layers or on ground powder. Rietveld refinement using TOPAS Bruker AXS software enabled the quantification of the crystallographic phases.

## 4.2 Additives to reduce thermal stresses

### 4.2.1 Selective laser melting with mullite additives

**Figure 73** shows the particle shape of the used mullite powders. The custom-made submicron mullite features particles with similar size and shape (mainly below 1  $\mu\text{m}$ ), whereas the SEM images reveal a broad size distribution (up to 10  $\mu\text{m}$  in size) with irregular formed particles for the mullite WFM 0-10. The inset in **Figure 73a** shows the white optical appearance of WFM 0-10.

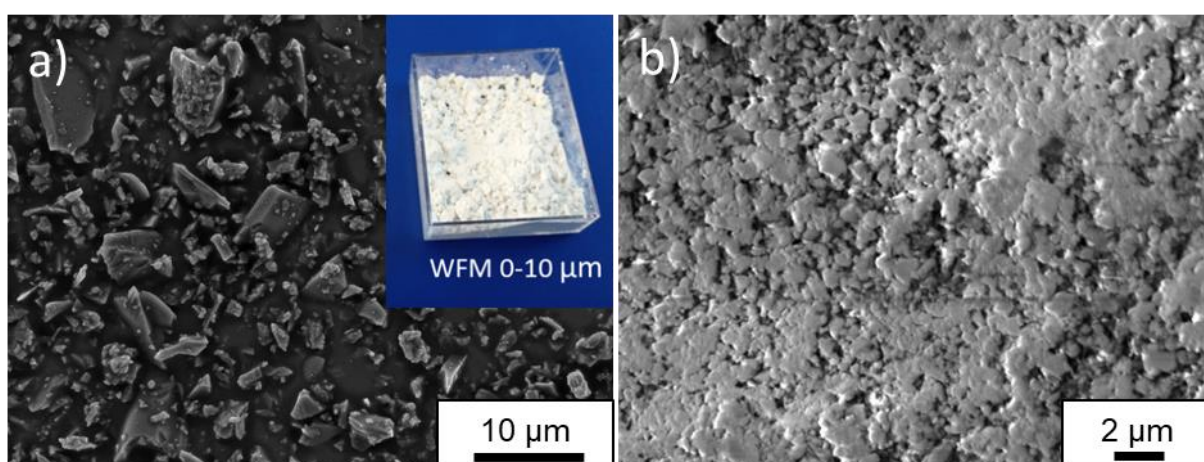


**Figure 73:** SEM images of a) mullite WFM 0-10 and b) submicron mullite. Inlet in a) shows the optical appearance of WFM 0-10.

An absolute density of 3.14  $\text{g}/\text{cm}^3$  and a specific surface area of 2.7  $\text{m}^2/\text{g}$  was determined for WFM 0-10, which gave a corresponding BET average particle size of 718.5 nm. Submicron mullite had an absolute density of 3.05  $\text{g}/\text{cm}^3$ . However, the specific surface area of 20.2  $\text{m}^2/\text{g}$  was significantly higher due to the small particle sizes. A BET average particle size of 97.4 nm was calculated. However, the BET average particle size had to be evaluated carefully, since the particle shapes were nonspherical. The crystalline phases of the mullite WFM 0-10 were identified as 98.4  $\text{Al}_2\text{O}_3$  (corundum) and 1.6% mullite by X-ray diffraction and Rietveld refinement (**Figure 74**).

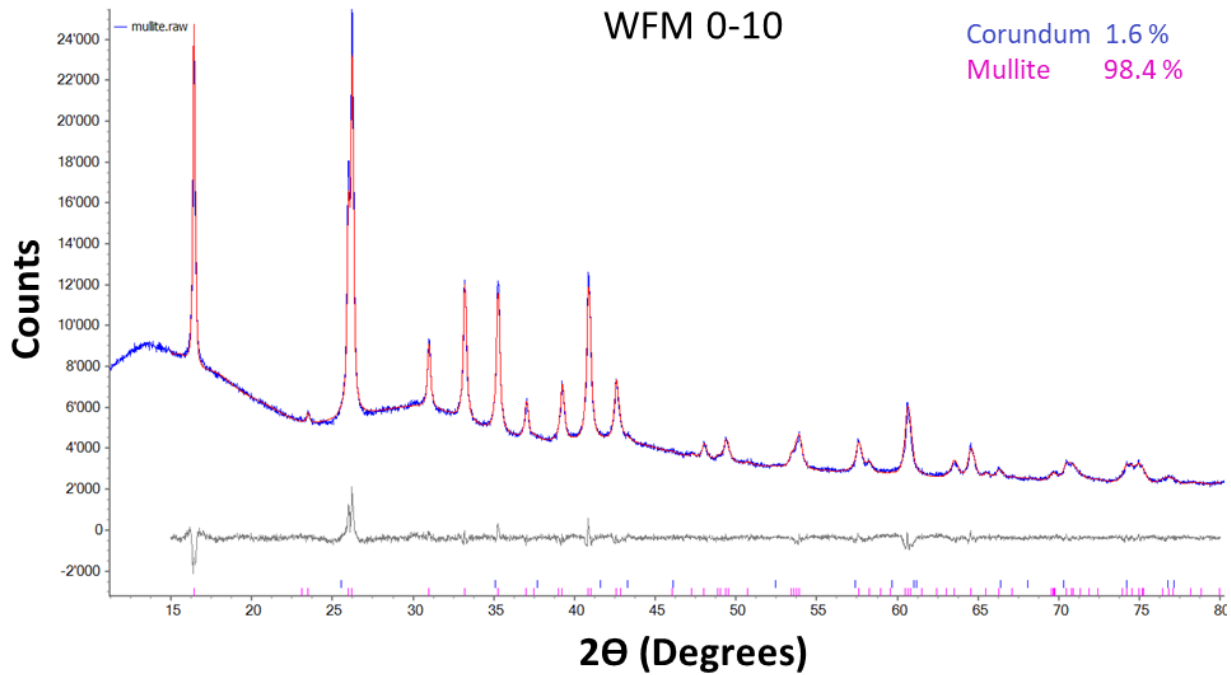


*Figure 74: X-ray diffraction pattern of mullite WFM 0-10.*

**Figure 75** summarizes the zeta potential of mullite WFM 0-10 (**Figure 75a**) and submicron mullite particles (**Figure 75d**) in water as a function of the pH value and various citrate concentrations. Addition of ammonium citrate dibasic shifts the isoelectric point of mullite WFM 0-10 from 7.6 to 2.5 (**Figure 75c**) and of submicron mullite particles from 7.3 to 3.2 (**Figure 75f**). A saturation amount, where the surface of the particles should be already fully covered with a monolayer of citrate anions, of ca. 0.2-0.4 wt% (0.4-0.8 Vol%) for micron-sized mullite WFM 0-10 and 1.2 wt% (2.3 Vol%) for submicron mullite was found. Additionally a zeta potential below -60 mV (pH values bigger than 7) is created for both powders using these saturation amounts. The created negative surface charge should result in a successful electrostatic stabilization of the powders, since the zeta potential should be bigger than 25 mV to avoid flocculation or coagulation. This confirms that citrate acts as a suitable dispersant to prevent agglomeration by adsorption on the particle surfaces. As expected, a higher amount of citrate (up to 5 times higher) is necessary to cover the surface of the submicron mullite. These results are reasonable, since the measured specific surface area of the submicron-sized mullite (20.2 m<sup>2</sup>/g) was ca. 7.5 times bigger than of the micron-sized mullite (2.7 m<sup>2</sup>/g). A possible dissolution of the particles starting at pH values of ca. 3-4 was seen for both powders, since the total volume of added HCl increased intensively in this pH range. A dissolution generates more and smaller particles, which in terms offers a more surface area of the particles for an interaction



with the anion and cations. However, it is also a fact that the titration from pH 4 to 3 requires 10 times more HCl than the titration from pH 5 to 4. This undermines the assumption of mullite dissolution.

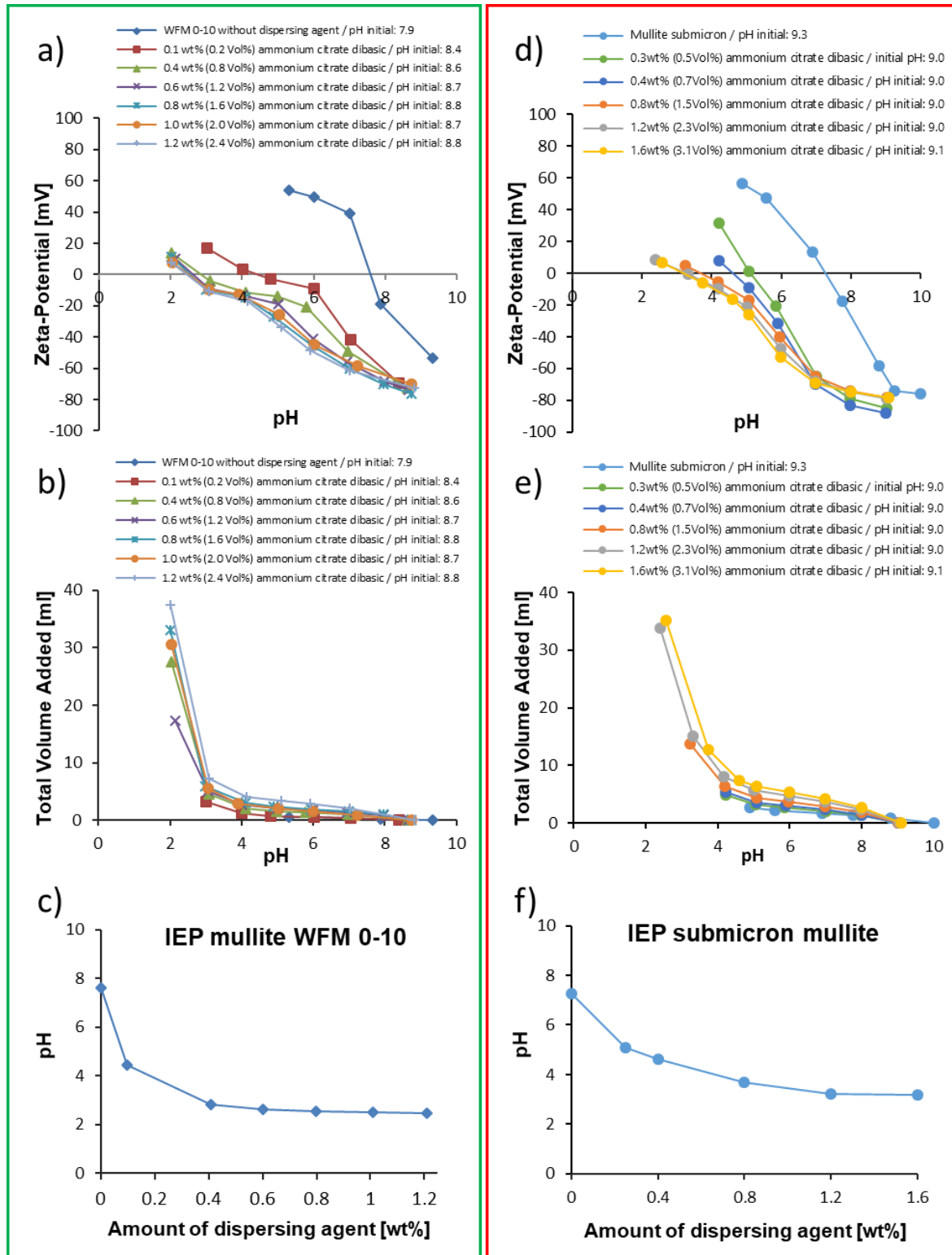


**Figure 75:** Zeta potential of **a)** mullite WFM 0-10 and **d)** submicron mullite particles as a function of pH value and various citrate concentrations with corresponding **b), e)** volume change by HCl and NaOH addition as function of pH value.  $pH_{IEP}$  of **c)** mullite WFM 0-10 and **f)** submicron mullite suspensions as function of ammonium citrate dibasic addition.



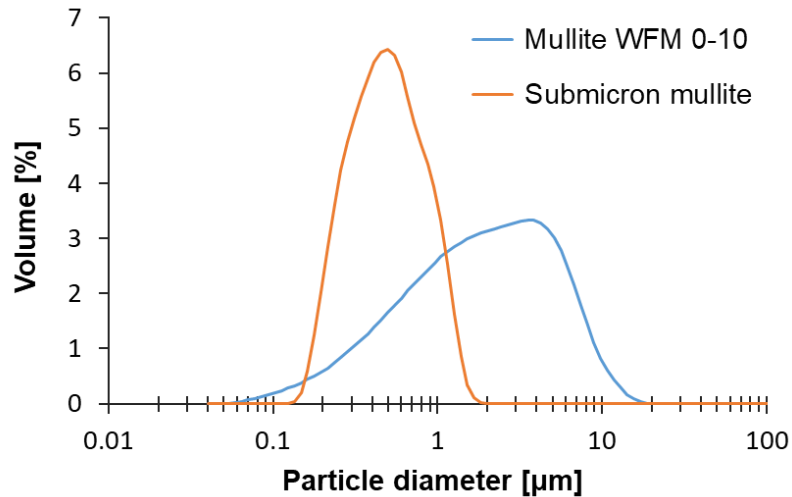


**Figure 76:** Volume based particle size distributions of mullite powders in water by optimized (ammonium citrate dibasic) dispersant amount (0.8 wt% (1.6 Vol%) for micron-sized mullite WFM 0-10 and 1.2 wt% (2.3 Vol%) for submicron mullite) and dispersing routine determined by Laser diffraction (LD).

It was straight forward to achieve a proper dispersion of the two mullite particles in water using the dispersant amounts of 0.8 wt% (1.6 Vol%) for micron-sized mullite WFM 0-10 and 1.2 wt% (2.3 Vol%) for submicron mullite. **Figure 76** shows the volume based particle size distributions determined by laser diffraction of both mullite powders in water by using 24 hours of roll milling (submicron mullite: milling balls of 1 mm and solid load of 30 Vol%; WFM 0-10: milling balls of 5 mm and solid load of 30 Vol%). The characteristic values of  $d_{10}$ ,  $d_{50}$  and  $d_{90}$  were 0.38, 0.46 and 0.93  $\mu\text{m}$  for submicron mullite and 0.23, 1.75 and 6.08  $\mu\text{m}$  for WFM 0-10. A proper dispersion of the particles can be assumed, since the observations made by SEM (**Figure 73**) that submicron mullite features particles sizes mainly below 1  $\mu\text{m}$  and mullite WFM 0-10 has a broad size distribution with particles up to 10  $\mu\text{m}$ , agree with the measured particle size distribution.

**Table 24 and 25** outline the way of mullite incorporation of both mullites on the basis of  $\text{Fe}_2\text{O}_3$  doped  $\text{Al}_2\text{O}_3$  granules (powder combination B) described in more details in chapter 3.2.3. The coarser mullite was incorporated instead of a part of the micron-sized aluminum oxide AA3 or instead of all other aluminum oxide particles. The submicron mullite replaced a part of the submicron-sized aluminum oxide Taimicron TM-DAR. An iron oxide doping amount of 0.9 Vol% was still used to guarantee a suitable powder absorptance, when using the green laser light.

**Table 24:** Way of incorporation of mullite WFM 0-10 on the basis of  $\text{Fe}_2\text{O}_3$  doped  $\text{Al}_2\text{O}_3$  granules.

<b>Way of incorporation in relation to bimodal <math>\text{Fe}_2\text{O}_3</math> doped <math>\text{Al}_2\text{O}_3</math> granules (powder combination B in chapter 3.2.3)</b>	
Granules A	30 Vol% mullite WFM 0-10 particles instead of micron-sized aluminum oxide AA3
Granules B	30 Vol% mullite WFM 0-10 particles instead of all other particles (submicron-sized aluminum oxide Taimicron TM-DAR and micron-sized aluminum oxide AA3)
Granules C	30 Vol% mullite WFM 0-10 particles instead of micron-sized aluminum oxide AA3

**Table 25:** Way of incorporation of submicron mullite on the basis of  $\text{Fe}_2\text{O}_3$  doped  $\text{Al}_2\text{O}_3$  granules.

<b>Way of incorporation in relation to bimodal <math>\text{Fe}_2\text{O}_3</math> doped <math>\text{Al}_2\text{O}_3</math> granules (powder combination B in chapter 3.2.3)</b>	
Granules D	30 Vol% submicron mullite particles instead of submicron-sized aluminum oxide Taimicron TM-DAR
Granules E	30 Vol% submicron mullite particles instead of submicron-sized aluminum oxide Taimicron TM-DAR

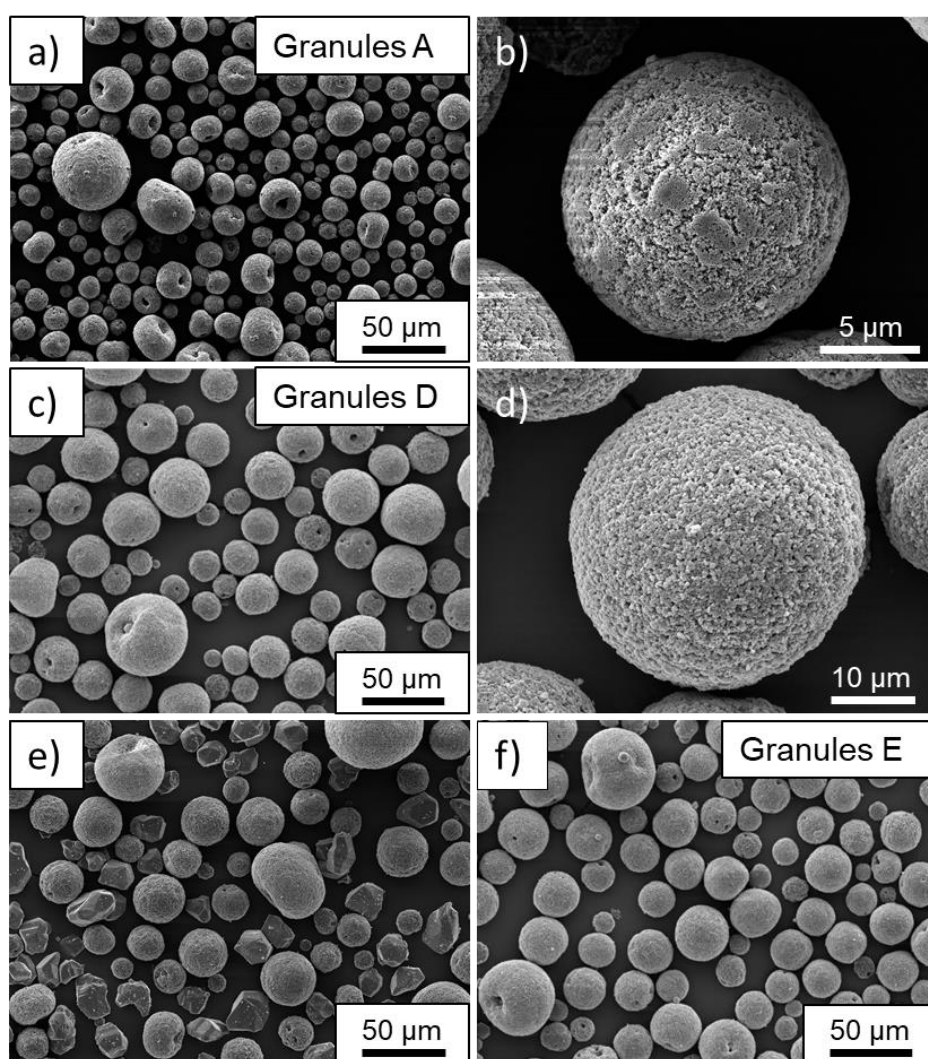


**Figure 77:** SEM images of spray-dried a), b) granules A, c), d) granules D, e) granules D mixed with coarse aluminum oxide AA18 and f) granules E.

The spray-dried granules are depicted in **Figure 77**. The granules D and E appear denser and smoother compared to the granules A, as a consequence of the higher amount of submicron powder. Furthermore, granules D and E appear more spherical than the granules made with micron-sized mullite. An enhanced movement of smaller particles in multimodal particle and thus the formation of encapsulated granules was already reported by Iskandar et al. [121]. Less donut shaped and hollow granules were spray dried by using higher solid load in the slurry used for spray drying (solid load granules D: 45.0 Vol%, solid load granules E: 48.9 Vol%), since the droplets created by the atomizer contained more particles. However, despite having less open pores, the same apparent and tapped density was measured for these granules (**Table 26**). Furthermore, the yield of spray drying decreased from 21.4 to 15.2 %, which could be due to the increased slurry viscosity and thus a stronger slurry dropping effect from the ultrasonic nozzle during spray drying. This was also seen by the ultrasonic power necessary to spray-dry the slurries with a higher solid load. The granules A, B and D with a used slurry solid load of ca. 45 Vol% were spray-dried with a ultrasonic power 9-9.5 W, whereas a ultrasonic power of 12-12.5 W was used in the case of granules C and granules E (solid load: 48.9-49.8 Vol%). Walker et al [111] and Lukasiewicz [103] reported a different result of increasing the slurry solid load. A higher solid load led not only to an increased yield but also to a higher density of the granules in their case. A mixing of the granules with the coarse aluminum oxide AA18 does not destroy the granules (**Figure 77e**), as also seen for Fe<sub>2</sub>O<sub>3</sub> doped Al<sub>2</sub>O<sub>3</sub> granules (chapter 3).

**Table 26 and 27** summarize the properties of the spray-dried powders containing micron-sized mullite WFM 0-10 or submicron-sized mullite.

**Table 26:** Properties of spray-dried powders containing micron-sized mullite WFM 0-10.

	Granules A	Granules B	Granules C	Granules A + 30 Vol% AA18
Solid load of slurry for spray drying [Vol%]	45.3	45.1	49.8	45.3
Apparent density [% of TD]	39.9	37.2	38.7	42.0
Tapped density [% of TD]	44.4	42.5	43.0	50.1
Hausner ratio	1.11	1.14	1.11	1.19
d10 [μm]	21.3	18.4	19.2	16.4
d50 [μm]	36.6	32.7	32.9	31.8
d90 [μm]	63.1	62.0	62.2	57.5
Yield [%]	29.0	24.8	8.1	N/A

**Table 27:** Properties of spray-dried powders containing submicron-sized mullite.

	Granules D	Granules E	Granules D + 30 Vol% AA18
Solid load of slurry for spray drying [Vol%]	45.0	48.9	45.0
Apparent density [% of TD]	37.5	37.5	41.4
Tapped density [% of TD]	42.4	42.5	47.5
Hausner ratio	1.13	1.13	1.15
d10 [ $\mu\text{m}$ ]	18.6	18.1	15.7
d50 [ $\mu\text{m}$ ]	31.3	29.9	27.3
d90 [ $\mu\text{m}$ ]	51.0	50.3	48.4
Yield [%]	21.4	15.2	N/A

For granules with mullite WFM 0-10, the apparent and tapped density was higher when the micron-sized mullite was incorporated instead of a part of the micron-sized aluminum oxide AA3. In this case, however, these granules have a lower apparent and tapped density than  $\text{Fe}_2\text{O}_3$  doped  $\text{Al}_2\text{O}_3$  granules (chapter 3), since the mullite WFM 0-10 has a broader size distribution than aluminum oxide AA3 and thus the optimized ratio between the nearest particle sizes in bimodal particles distributions according to McGeary [128] cannot be matched. The incorporation way of the micron sized mullite was the same for granules A and C, but the solid load was increased from 45.3 to 49.8 Vol%. Granules A gave a higher apparent density, tapped density and yield compared to the granules C. For granules made with submicron mullite, granules D were considered as more suitable for further processing than granules E, since the yield of spray drying was higher, although the properties were almost similar. 30 Vol% coarse aluminum oxide AA18 particles were mixed to the granules with the best properties after spray drying (granules A and granules D). The apparent and tapped density increase by the addition of 30 Vol% AA18 particles due the high packing density of the coarse alumina as seen in chapter 3.2.6. However, the Hausner ratio decreases for both powders due to the more irregular size distribution. The increase of the apparent and tapped density is bigger for the granules A. This could be due to the bigger granule sizes, which therefore also offers more interstices to be filled by the smaller aluminum oxide. The final mullite content after addition of AA18 was ca. 20 Vol% within the powders.

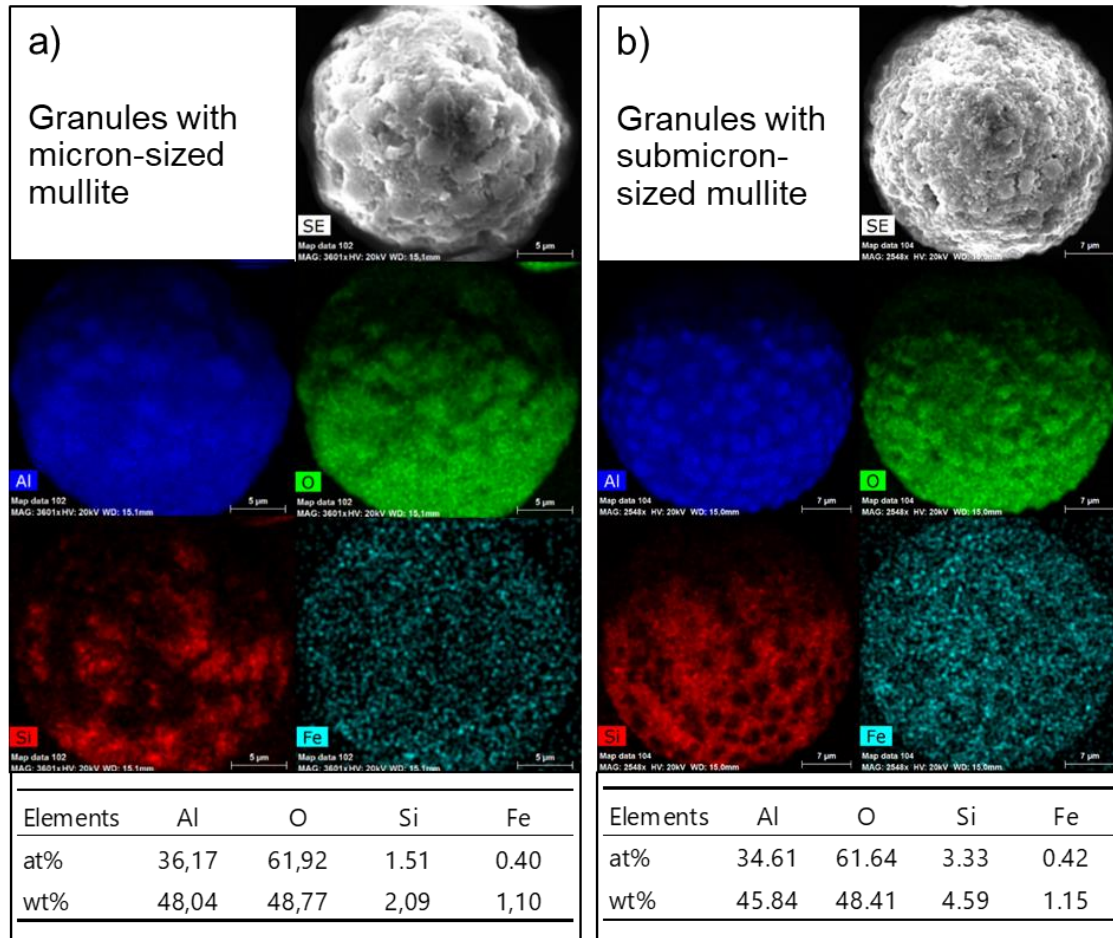


**Figure 78:** Element distributions within granules **a)** with micron sized and **b)** submicron sized mullite examined by energy-dispersive X-ray spectroscopy

**Figure 78** shows the element distribution within granules with micron-sized and submicron-sized mullite investigated by energy-dispersive X-ray spectroscopy. All elements are well distributed within the granules. The black areas visible on top of the granules do not show a lack of the measured elements, but rather points out problems with focus of the electron beam and thus with the x-ray signal. The distribution of Si in granules with submicron-sized mullite was more homogeneous than in granules with micron-sized mullite. The more uniform distribution is a result of the smaller particles sizes. The measured content of Si fits well with the theoretically calculated content of  $\text{SiO}_2$ . 5.7 wt%  $\text{SiO}_2$  should be the granules containing micron-sized mullite, using the company given values evaluated by a chemical analysis. The calculation for granules containing micron-sized mullite gave a  $\text{SiO}_2$  content of 7.1wt%, using the theoretical ratio of 60/40 mol%  $\text{Al}_2\text{O}_3/\text{SiO}_2$  in mullite ( $\text{Al}_6\text{Si}_2\text{O}_{13}$ ).



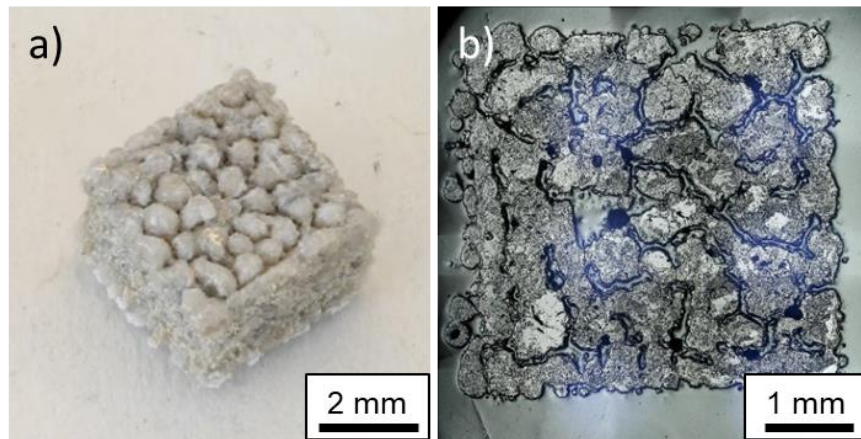


**Figure 79:** a) Shape and b) cross-section of laser manufactured parts produced with granules A and 30 Vol% AA18 imaged by optical microscopy.

It was also possible to build parts with granules containing mullite (**Figure 79a**). The used powder contained in this case 70 Vol% of granules A and 30 Vol% of AA18. Even though, these parts were not as dense as with pure alumina granules, which follows due to a lower powder bed density, a changed absorption behavior and different melt pool dynamics. Optical microscopy of the cross section revealed a severe amount of microporosity (**Figure 79b**).

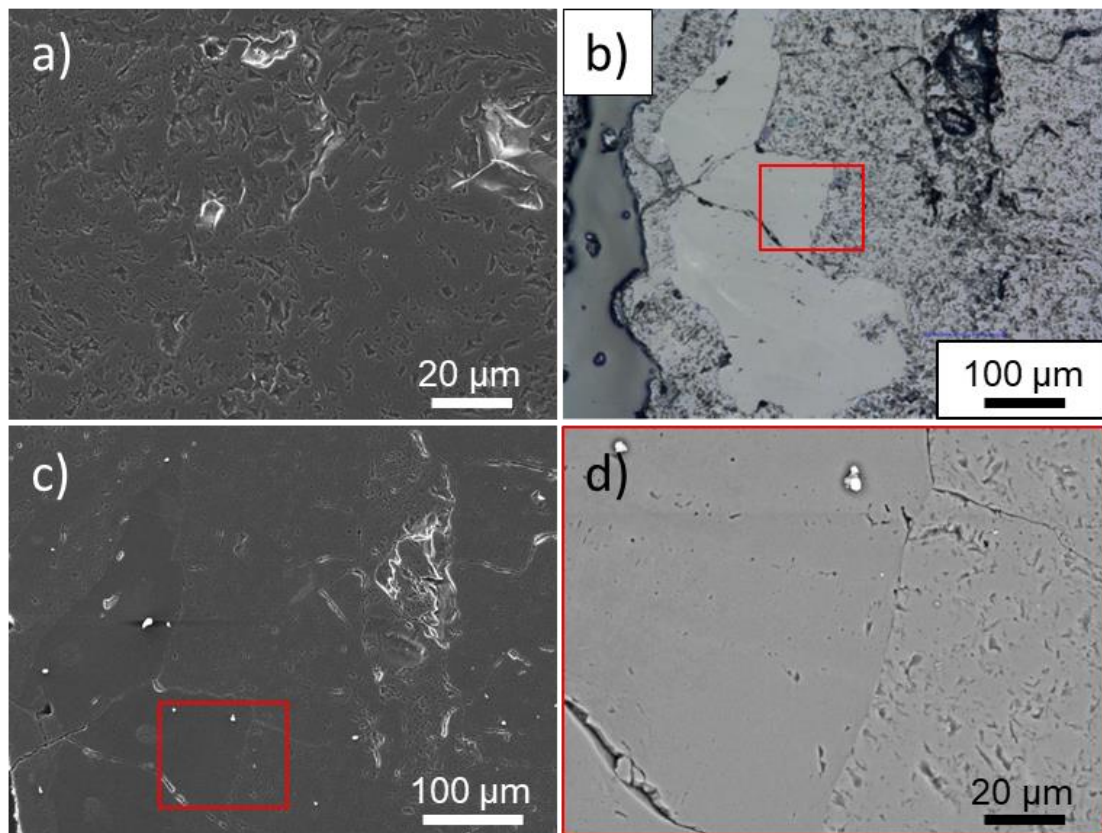


**Figure 80:** Internal structure of laser manufactured parts produced with granules A and 30 Vol% AA18 imaged by a) SEM (secondary electrons), b) optical microscopy d) SEM (backscattered electrons).

Higher magnifications showed that two types of microstructures were present within the laser manufactured parts (**Figure 80**). One microstructure contained vertical macro-cracks and random distributed micro-cracks, but was rather dense. The other microstructure showed a high amount of micron-sized pores. The analysis via backscattered electrons did not reveal a different contrast between these areas and thus no difference of the chemical compositions could be observed (**Figure 80d**).

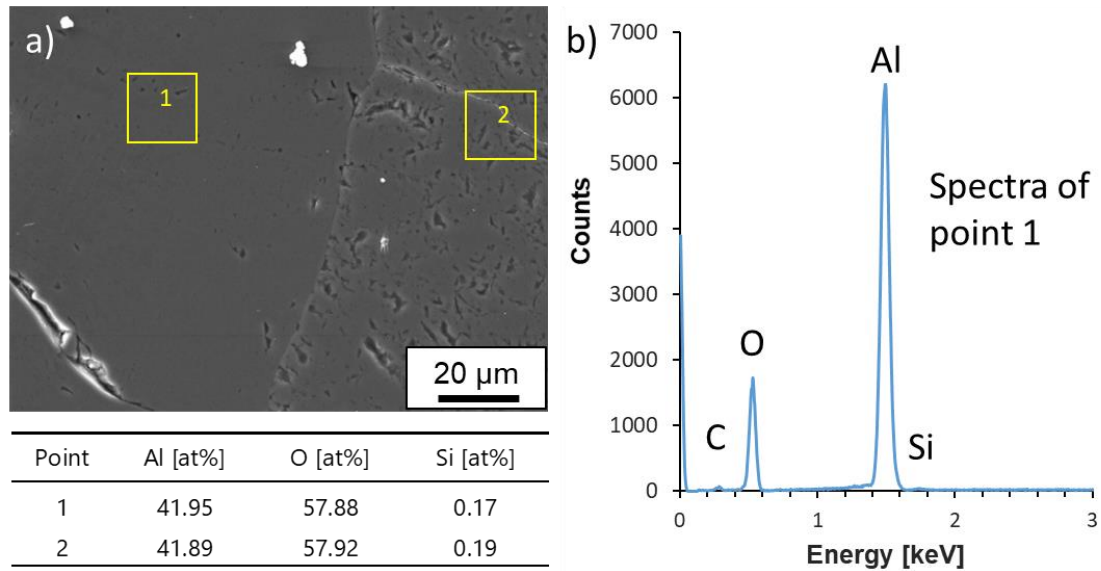


**Figure 81:** a) Evaluated positions and corresponding element content as well as b) corresponding spectra of point 1 examined by energy-dispersive X-ray spectroscopy.

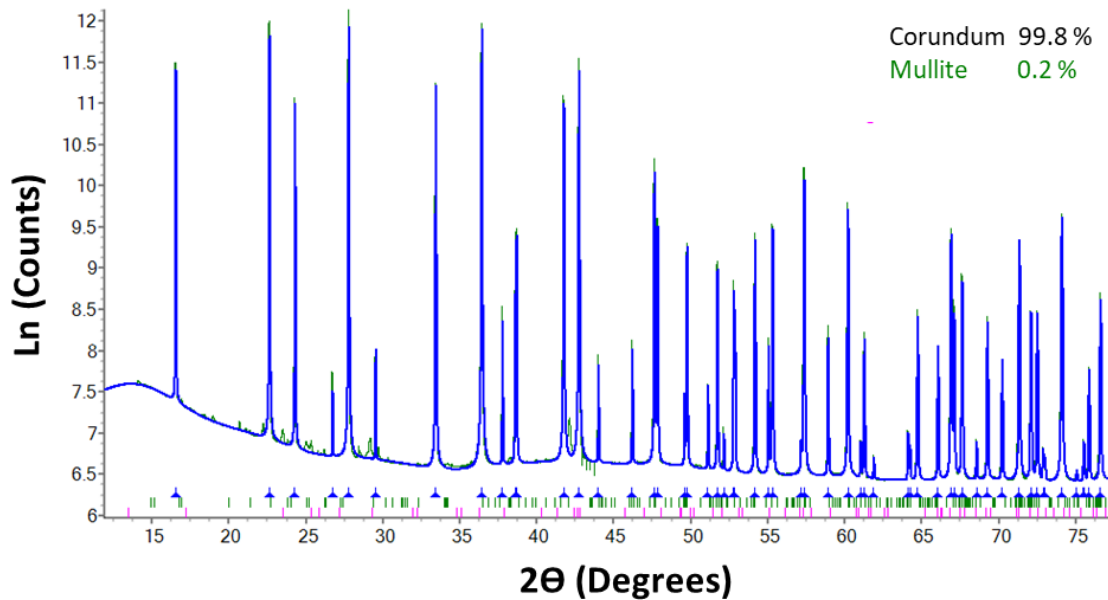


**Figure 82:** High resolution powder diffraction pattern of laser manufactured parts.

An investigation of the two microstructures by energy-dispersive X-ray spectroscopy (**Figure 81**) and by high resolution powder diffraction (**Figure 82**) showed that the final Si content was

very low after laser processing. According to energy-dispersive X-ray spectroscopy, the content of Si was only 0.17-0.19 at%. A difference in the elemental composition was not seen for the two microstructures. Furthermore, a content of mullite of only 0.2% was evaluated by Rietveld refinement. The low content of  $\text{SiO}_2$  could not be evaluated by this method. The lack of Si in the final parts could be due to evaporation of Si during processing. Modelling through finite volume method made by Florio gave a maximum temperature of ca. 3000 °C for the process parameters ( $\text{Fe}_2\text{O}_3$  doped aluminum oxide granules) [251]. Boiling point of Si and  $\text{SiO}_2$  are 3265 and 2230 °C, respectively.

The concept of using mullite with a lower thermal expansion coefficient and a high silica content for a possible glass phase formation to reduce crack formation was not successful in this work. The low glass transition temperature of a glass phase was described as beneficial in the literature to avoid thermal stresses during cooling [99]. Other researchers, which did not use a dopant to increase absorption, achieved highly dense glass composites made of an alumina and silica composite by using this approach [2, 3, 6, 7, 60-62, 64]. They described also a formation of mullite needles beneficial for increasing the mechanical stability by reinforcement [64]. This needle formation was also not observed in this work. This could be due to the high maximum temperatures of up to 3000 °C reached for the given process parameters and absorbance increased material (calculated by modelling through finite volume method [251]), which favor an evaporation of Si in the melt pool, before the mullite needles can form during the cooling stage.

#### 4.2.2 Amorphous alumina formation by rare earth oxide doping

**Figure 83a** shows the particle shape and optical appearance of the  $\text{CeO}_2$  nanopowders. The powder features particles with a uniform size distribution in the nano range. The  $\text{CeO}_2$  powder appeared in a yellow color. A BET average particle size of 22.4 nm was calculated from the measured absolute density of 6.34 g/cm<sup>3</sup> and a specific surface area of 42.3 m<sup>2</sup>/g. X-ray diffraction confirmed that the powder consisted principally of  $\text{CeO}_2$  (**Figure 83b**).

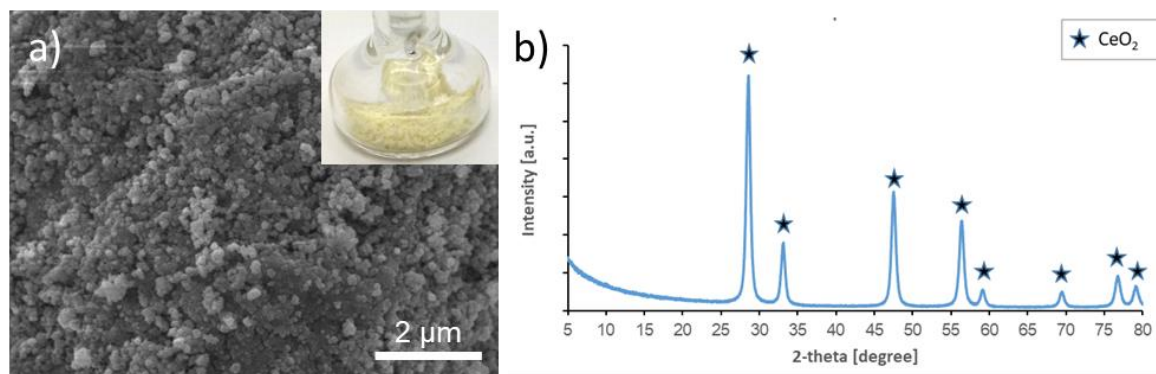


**Figure 83:** a) SEM images and optical appearance as well as b) x-ray diffraction pattern of  $\text{CeO}_2$  nanoparticles.



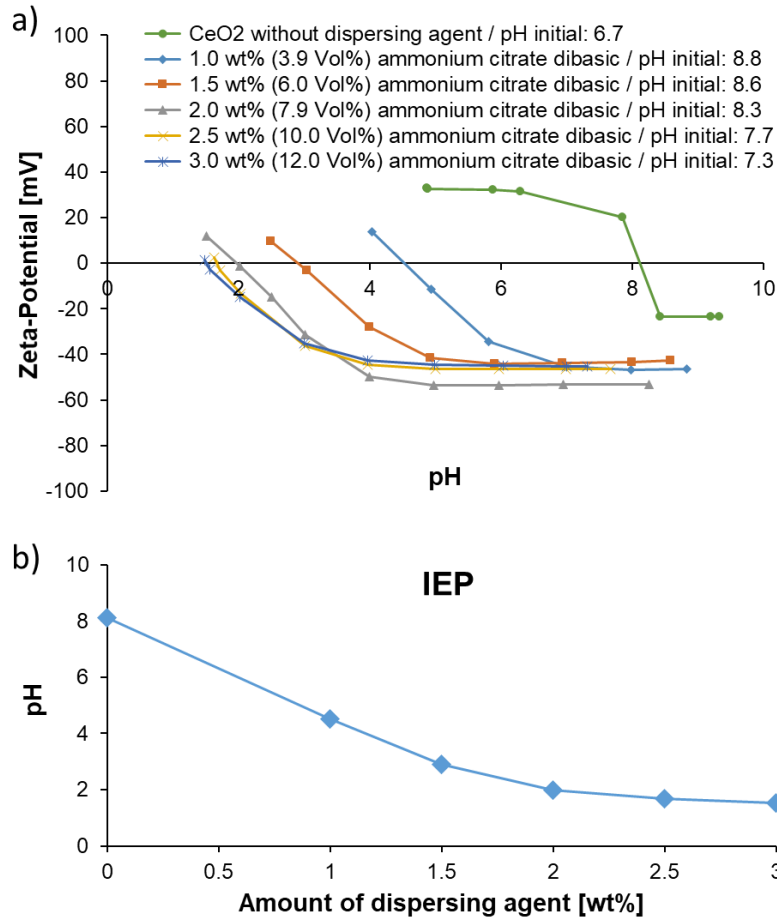


**Figure 84:** a) Zeta potential of CeO<sub>2</sub> nanoparticles as a function of pH value and various citrate concentrations. b) pH<sub>IEP</sub> of CeO<sub>2</sub> nanoparticles as function of ammonium citrate dibasic addition.

The zeta potential of CeO<sub>2</sub> nanoparticles in water as a function of pH value and various citrate concentrations is depicted in **Figure 84a**. The addition of ammonium citrate dibasic shifts the isoelectric point of from 8.1 to 1.6 (**Figure 84b**). The saturation amount of ammonium citrate dibasic was 2.5 wt% (10 Vol%). When adding this amount of dispersant, the zeta potential was below -45 mV in a pH range of 5-8, this should guarantee a successful electrostatic stabilization of the particles and can be used in bimodal dispersions containing aluminum oxide.

**Figure 85** shows the volume based particle size distributions determined by laser diffraction (LD) and dynamic light scattering (DLS) of the CeO<sub>2</sub> nanoparticles in water. Three different solid loadings were tested. Whereas dispersions with a solid load of 7.5 and 15 Vol% could be dispersed by using only 24 hours of roll milling (milling balls of 1 mm) or 20 minutes of vibration milling (milling balls of 0.4 mm), a combination of both was necessary to process dispersions with a solid load of 25 Vol%.

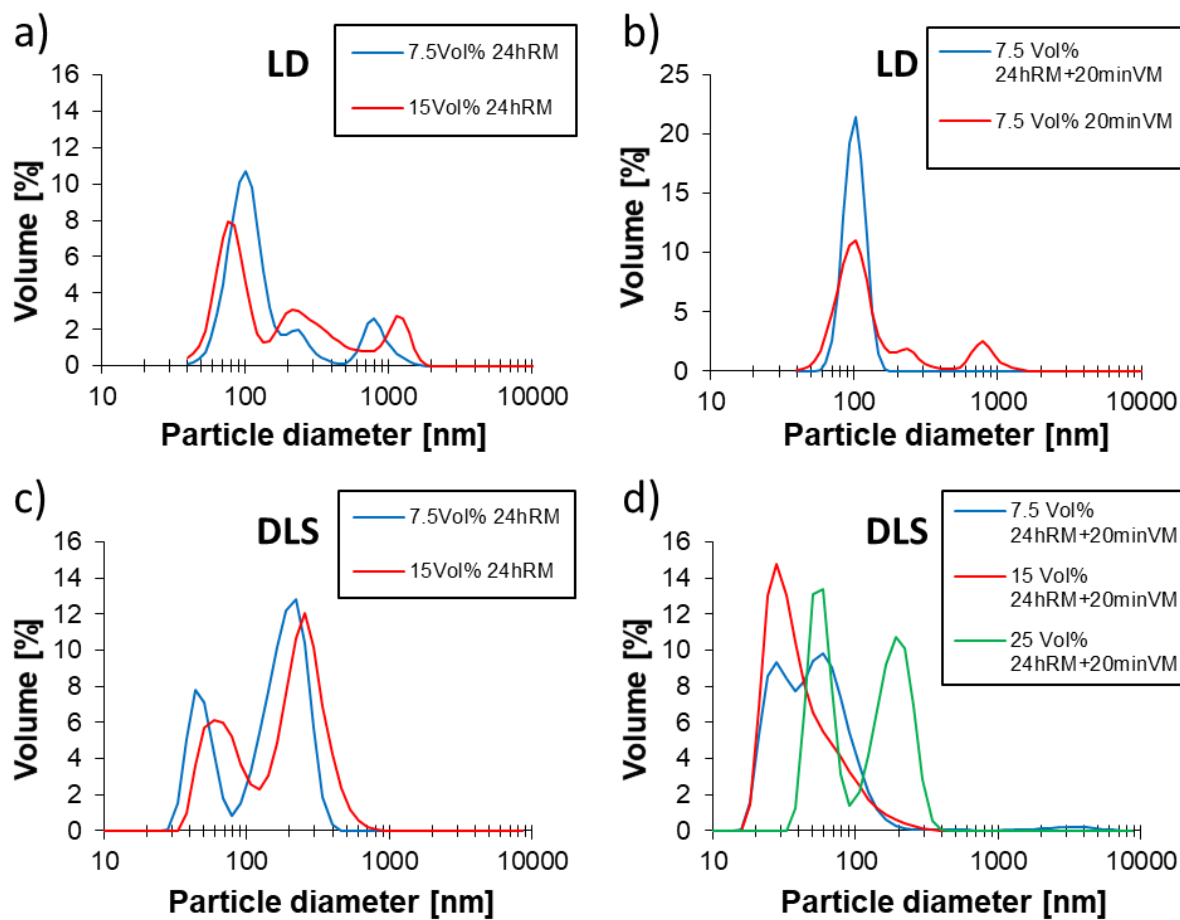


**Figure 85:** Volume based particle size distributions of  $\text{CeO}_2$  nanoparticles in water by optimized dispersant amount (2.5 wt% (10 Vol%) of ammonium citrate dibasic) and dispersing routine determined by **a), b)** laser diffraction (LD) and **c), d)** dynamic light scattering (DLS).

Agglomerates up to  $1\mu\text{m}$  were observed in the LD (**Figure 85a**) and DLS (**Figure 85c**) when using only roll milling for 24 hours. A similar behavior was seen by LD (**Figure 85b**), when using only 20 minutes of vibration milling. The combination of both led to a strong decrease of the agglomerates (**Figure 85b and d**). The smallest particle sizes were achieved using a solid load of 15 Vol%. The characteristic values of  $d_{10}$ ,  $d_{50}$  and  $d_{90}$  according to dynamic light scattering measurements were 21.4, 33.1 and 83.3 nm, which were very close to the calculated BET average particle size of 22.4 nm. It confirms a proper dispersion with small agglomerates. The quality of the dispersion was the worst for a solid load of 25 Vol%, which follows due to extremely raised viscosity of the slurry.

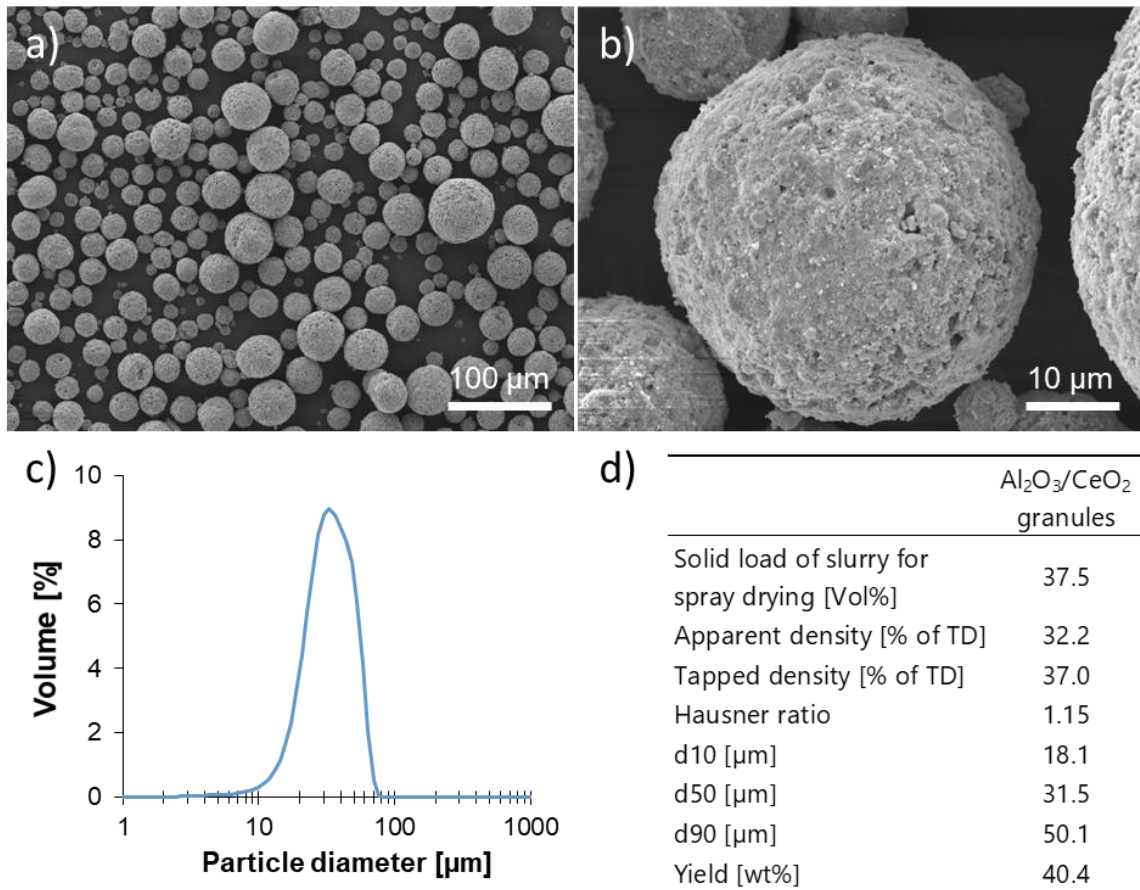
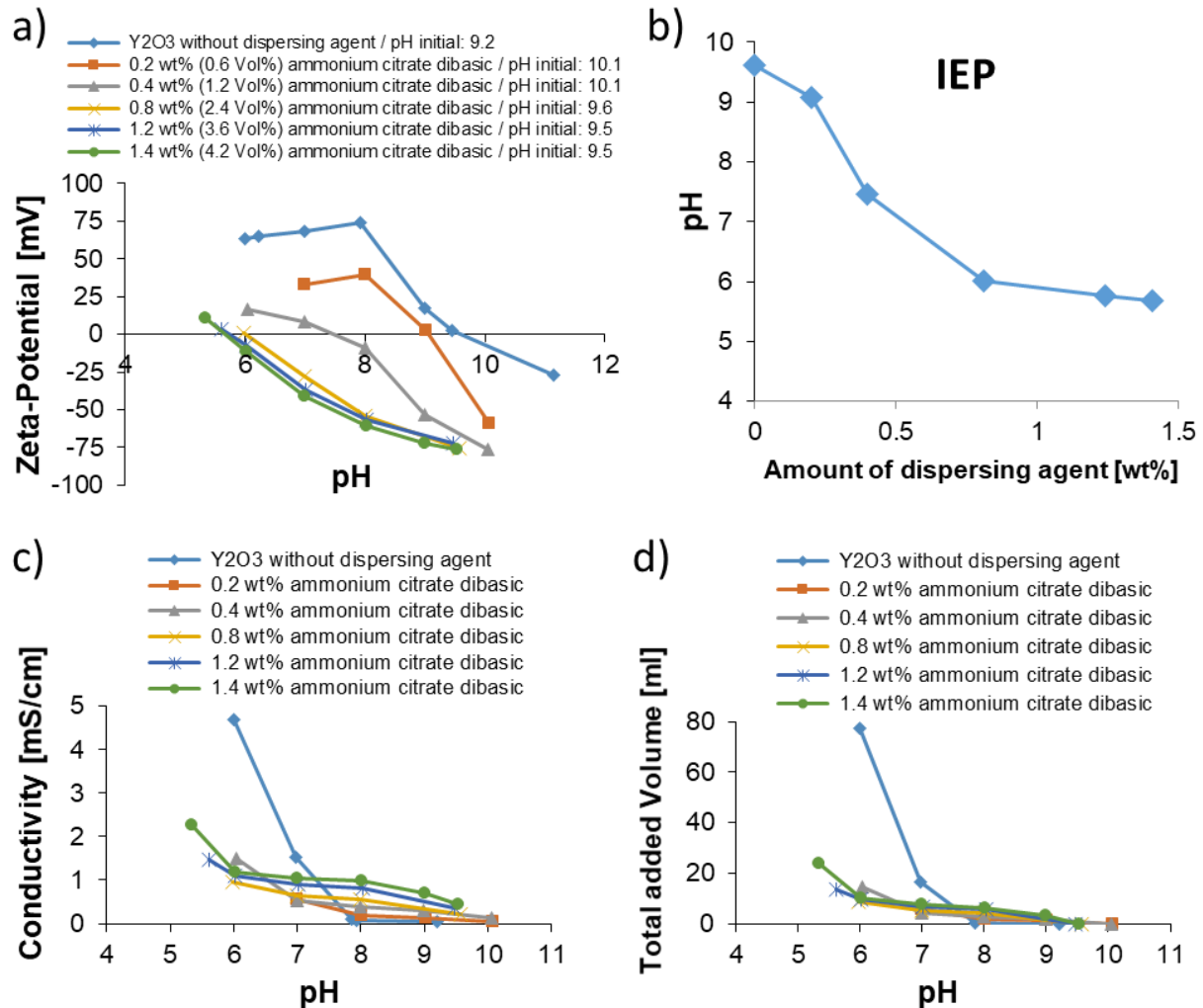


Figure 86: a), b) SEM images, c) volume based particle size distribution and d) properties of Al<sub>2</sub>O<sub>3</sub>/CeO<sub>2</sub> granules.

**Figure 86a and b** show SEM images of the spray-dried Al<sub>2</sub>O<sub>3</sub>/CeO<sub>2</sub> granules. The granules were spray-dried in the eutectic ratio of 50.6 Vol% micron-sized Al<sub>2</sub>O<sub>3</sub> AA3 and 49.4 Vol% CeO<sub>2</sub> nanoparticles with an ultrasonic power of 8 W. The eutectic ratio was chosen in accordance to Rosenflanz et al. [163], who reported the possibility to form amorphous and transparent bulk glasses based on the eutectic ratio of alumina to rare earth oxides. The granules have a spherical appearance. There are no granules with a hollow core or a donut shape visible. The high amount of CeO<sub>2</sub> nanoparticles leads to a high agglomeration tendency, since van der Waals attractions have more impact on smaller particles due to decreasing gravitation forces [28]. Due to enhanced movement of nanoparticles [121] and a dense granule shell was formed by the CeO<sub>2</sub> nanoparticles. However, the granules had a low apparent and tapped density on only 32.2% and 37.0% of the theoretical density, respectively (**Figure 86d**). These low density can be explained by the high amount of nanopowders (49.4 Vol%), which does not match with the optimized ratio for bimodal distributions (72.6/27.4 Vol%) found by McGeary [128]. Furthermore, only a low solid load could be used due to the high amount of nanopowders in the slurry for spray drying.

The other used rare oxide was submicron  $Y_2O_3$  powder with a white appearance. The BET average particle size of this particles (143.1 nm) was bigger than for  $CeO_2$  particles (22.4 nm). An absolute density of 4.71 g/cm<sup>3</sup> and a specific surface area of 8.9 m<sup>2</sup>/g was measured for this powder. Other crystalline phases than  $Y_2O_3$  were not found by x-ray diffraction.



**Figure 87:** a) Zeta potential of  $Y_2O_3$  particles as a function of pH value and various citrate concentrations with corresponding c) conductivity and d) volume change by HCl and NaOH addition as function of pH value. b) pH<sub>IEP</sub> of  $Y_2O_3$  suspensions as function of ammonium citrate dibasic addition.

Zeta potential measurements in water gave a saturation amount of 0.8 wt% (2.4 Vol%) of ammonium citrate dibasic (**Figure 87a and b**). Using this amount, the IEP was shifted from 9.6 to 6.0. Furthermore, a zeta-potential of < -25 mV was generated for pH values above 7, which should guarantee a suitable electrostatic dispersion for alumina and yttria particles. The citrate showed also a positive effect on the dissolution of the  $Y_2O_3$  particles at lower pH-values. A steady increase of the conductivity during addition of HCl (**Figure 87c**) and of the total volume of added HCl (**Figure 87d**) was already seen starting at a pH value of 8 when measuring  $Y_2O_3$

particles without citrate in water. This increase was shifted to values below 6 when citrate was added to the dispersion, which changes the surface charge of the strongly positive charge particles by exchange with carboxylate ions.

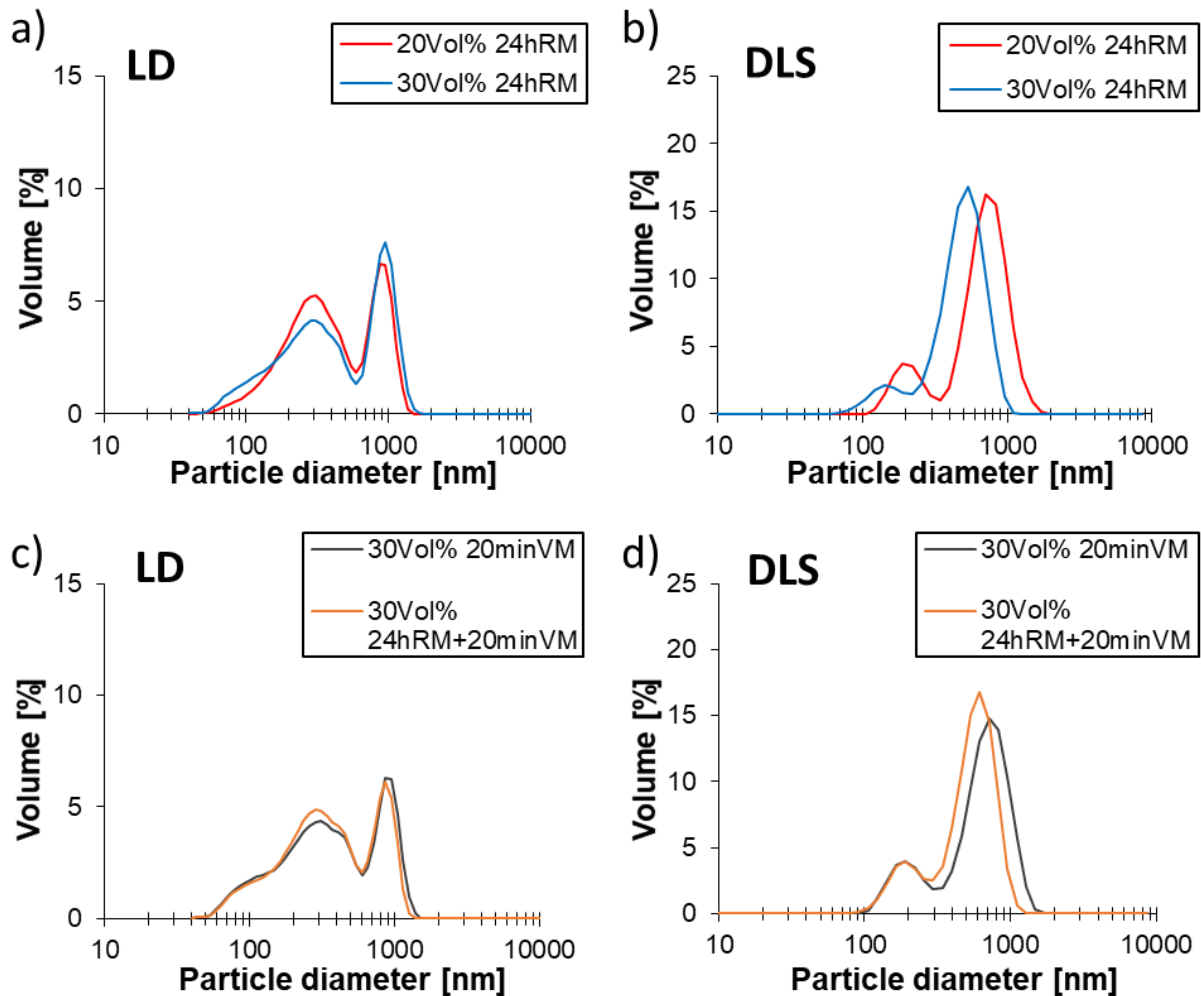


**Figure 88:** Volume based particle size distributions of  $Y_2O_3$  submicron particles in water by optimized dispersant amount (0.8 wt% (2.4 Vol%) of ammonium citrate dibasic) and dispersing routine determined by **a), c)** laser diffraction (LD) and **b), d)** dynamic light scattering (DLS).

**Figure 88** shows the volume based particle size distributions of  $Y_2O_3$  submicron particles in water. Laser diffraction and dynamic light scattering coincided that roll milling for 24 hours with a solid loading of 30 Vol% gave the lowest particles sizes compared to vibration milling or a combination of both milling options. The characteristic values  $d_{10}$ ,  $d_{50}$  and  $d_{90}$  of 121.8, 385.5 and 1019.7 nm according to laser diffraction and of 195.5, 450.1 and 677.1 nm according to dynamic light scattering were measured.



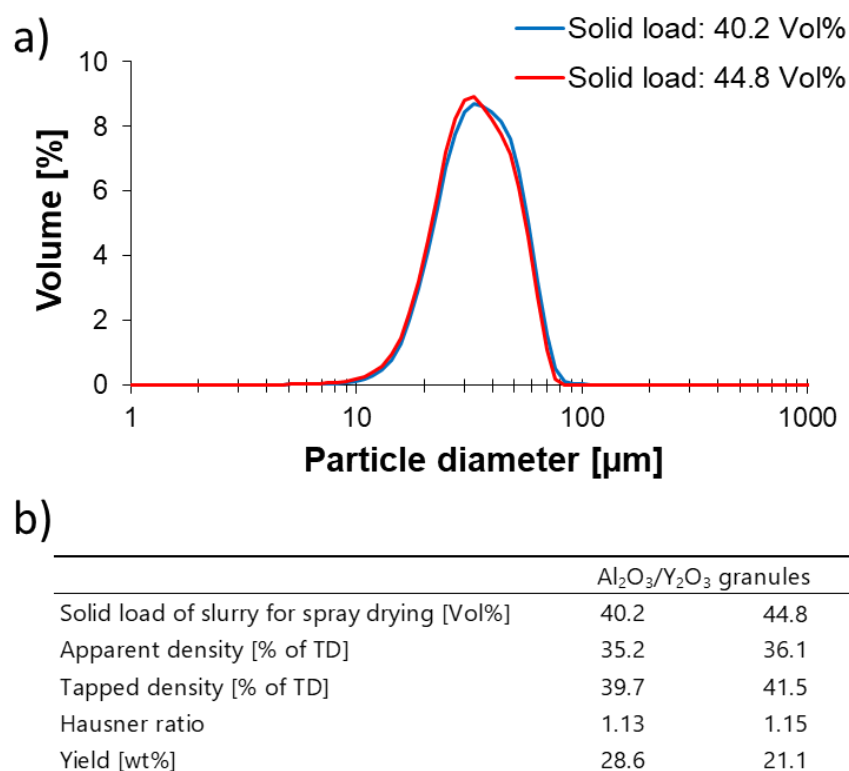


**Figure 89:** a) Volume based particle size distributions of  $\text{Fe}_2\text{O}_3$  doped  $\text{Al}_2\text{O}_3/\text{Y}_2\text{O}_3$  granules in isopropanol determined by laser diffraction (LD). d) properties of  $\text{Al}_2\text{O}_3/\text{Y}_2\text{O}_3$  granules.

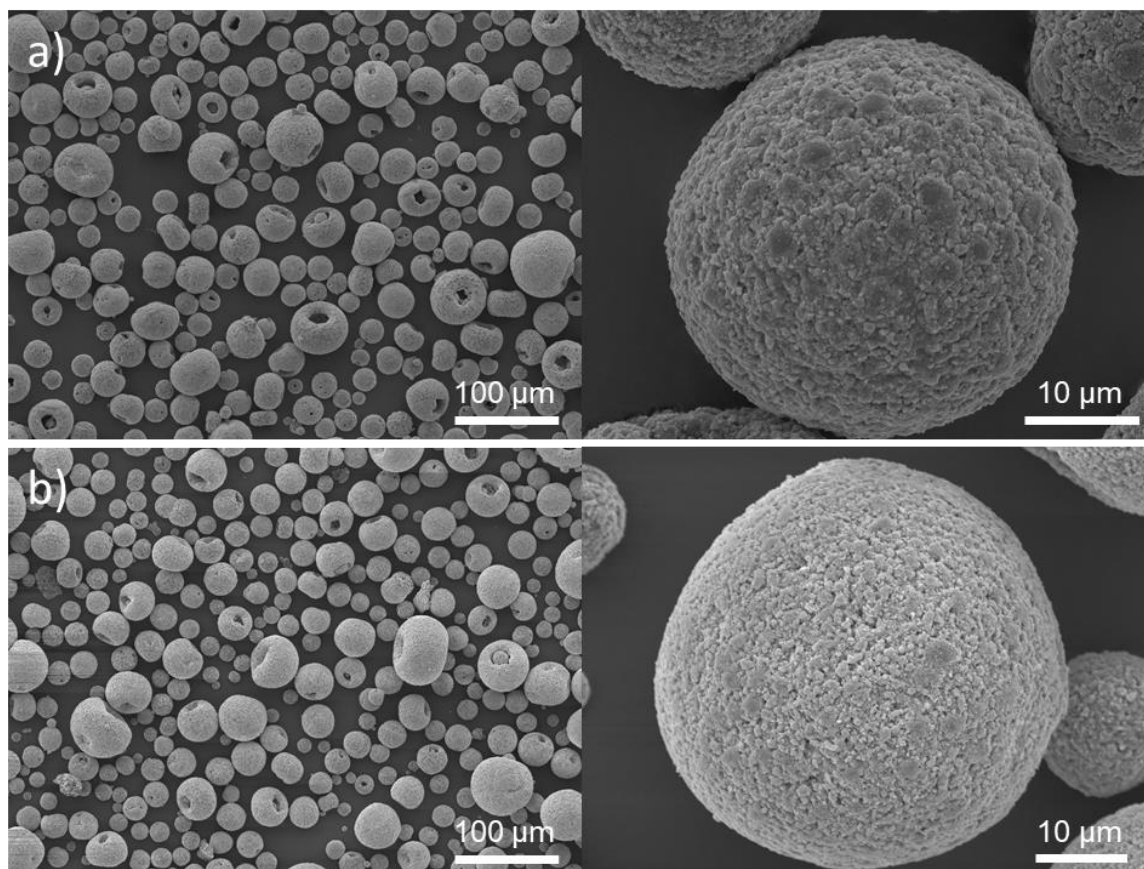


**Figure 90:** SEM images of  $\text{Fe}_2\text{O}_3$  doped  $\text{Al}_2\text{O}_3/\text{Y}_2\text{O}_3$  granules spray-dried with a) 40.2 Vol% and b) 44.8 Vol% solid load.

The properties and optical appearance are demonstrated in **Figure 89 and 90**. An amount of 1 Vol% iron oxide dopant had to be used, since first tests with pure  $\text{Al}_2\text{O}_3/\text{Y}_2\text{O}_3$  granules showed that a laser consolidation was not possible at wavelength of 1070 nm using solely  $\text{Y}_2\text{O}_3$  as an additive, despite having a smaller bandgap than alumina (6.08 eV for  $\text{Y}_2\text{O}_3$  [169], 3.19 eV for  $\text{CeO}_2$  [170] and 8.80 eV for  $\text{Al}_2\text{O}_3$  [171]). An iron oxide doping of 1 Vol% was added in the same way as for powder combination B described in chapter 3. Granules spray dried with a higher solid load of 44.8 Vol% showed a higher apparent and tapped density of 36.1 and 41.5% of the theoretical density (**Figure 89b**). However, the yield of spray drying decreased most probably due to the higher slurry viscosity from 28.6 to 21.1 % and the Hausner ratio slightly increased from 1.13 to 1.15. The volume based size distribution of the two granules was similar (**Figure 89a**). The granules spray dried with the higher solid load possessed less hollow cores and donut shaped granules. The sphericity of the two different granules was similar (**Figure 90a and b**). The granules with a solid load of 40.2 and 44.8 Vol% were spray-dried with an ultrasonic power of 12 and 14.5 W, respectively.

**Figure 91** shows uniaxial pressed cylindrical substrates containing both rare earth oxide/aluminum oxide granules. Eight layers were directly consolidated by the IR laser on the top surface of each substrate to evaluate the influence of the laser parameters on the crystallographic composition and possible amorphous phase by diffraction measurements and Rietveld refinement.

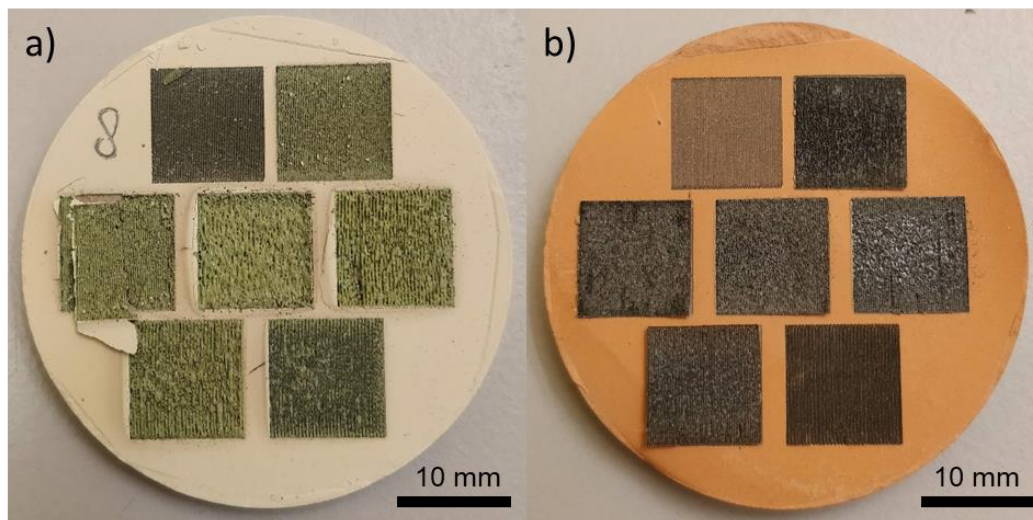


**Figure 91:** Laser consolidated layers on uniaxial pressed cylindrical substrates containing both rare earth oxide/aluminum oxide granules

X-ray diffraction confirmed a crystalline phase structure after laser processing of both rare earth oxide containing substrates (**Table 28 and 29**), which is especially clear in the laser-processed alumina-yttria pattern (**Figure 92a**). However, this measurement cannot exclude the presence

of a very small amount of amorphous phase. This is especially the case for laser-processed alumina-ceria pattern (**Figure 92b**), where a higher background between 65 and 110° was observed, which could be caused by the presence of an amorphous phase. It would be theoretically possible to measure the content of this amorphous phase using Transmission Electron Microscopy based selected area electron diffraction [271]. However, it would be extremely challenging as it would be difficult to find the location of the small amount of amorphous phase using this TEM-based analysis.

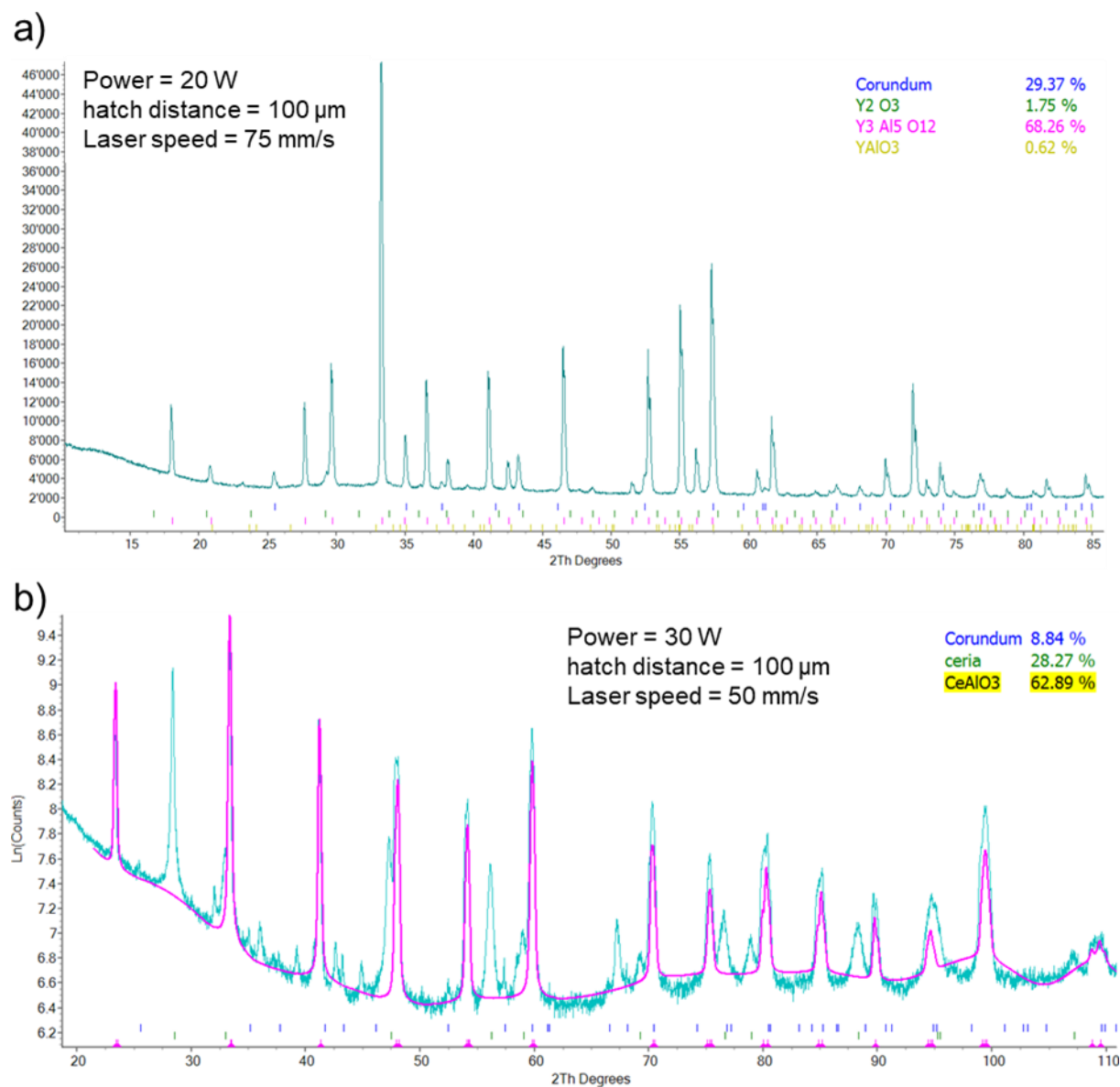


**Figure 92:** X-ray diffraction measurements of **a)** the laser-processed alumina-yttria (power = 20 W, hatch distance = 100  $\mu\text{m}$ , laser speed = 75 mm/s) and of **b)** laser processed alumina-ceria (power = 30 W, hatch distance = 100  $\mu\text{m}$ , laser speed = 50 mm/s).



**Table 28:** Evaluation of crystalline phases after laser processing of  $Al_2O_3/CeO_2$  substrates with different power, hatch distance, laser speed.

Alumina – Ceria							
Power [W]	hatch distance [ $\mu m$ ]	laser speed [mm/s]	Power/speed [J/mm]	Energy density [J/mm <sup>2</sup> ]	Crystalline phases [%]		
					Corundum ( $Al_2O_3$ )	$CeO_2$	$CeAlO_3$
30	100	450	0.067	0.866	41	47	11
30	100	100	0.300	3.896	20	38	42
7.6	150	25	0.304	3.948	41	45	14
30	100	50	0.600	7.792	8	28	63
15	150	25	0.600	7.792	9	26	63

**Table 29:** Evaluation of crystalline phases after laser processing of  $Al_2O_3/Y_2O_3/Fe_2O_3$  substrates with different power, hatch distance, laser speed.

Alumina – Yttria – Iron oxide								
Power [W]	hatch distance [ $\mu m$ ]	laser speed [mm/s]	Power/speed [J/mm]	Energy density [J/mm <sup>2</sup> ]	Crystalline phases [%]			
					Corundum ( $Al_2O_3$ )	$Y_2O_3$	YAG ( $Y_3Al_5O_{12}$ )	$YAlO_3$
100	100	1500	0.067	0.866	60	33	0	7
80	100	1200	0.067	0.866	62	18	1	18
40	100	250	0.160	2.078	23	2	74	1
10	100	62.5	0.160	2.078	16	1	81	2
200	100	1250	0.160	2.078	29	3	46	21
200	150	1250	0.160	2.078	60	25	0	15
200	100	750	0.267	3.463	30	2	66	2
80	100	300	0.267	3.463	26	10	63	1
20	100	75	0.267	3.463	29	2	68	1
200	150	750	0.267	3.463	33	5	47	16
200	100	375	0.533	6.926	31	2	64	3

In contrary to the results achieved in this work, the formation of amorphous and transparent bulk glasses based on alumina and rare earth oxides was clearly seen by Rosenflanz et al. [163]. It could be that the high quenching rates between ca. 1000 °C and room temperature reported in Rosenflanz et al. (estimated rate of ca. 10<sup>3</sup> K/s quenched in water [163]) were not reached by laser processing due to low thermal conductivity given by the powder bed. Therefore, a beneficial effect on the crack formation by exploiting the low glass-transition temperature of amorphous alumina was not observed. However, it was clearly seen that higher energy densities led to a preferred  $CeAlO_3$  (Table 28) or YAG formation (Table 29) by laser processing, which could be also interesting for other applications.

### 4.2.3 Formation of aluminum titanate by use of reduced titanium oxide

Parts of this chapter were already published in the Journal of European Ceramic Society, Volume 42 (8), (2022) 3515-3529.

### 4.2.3.1 Dispersing of titanium oxide nanoparticles in water

**Figure 93a** shows the zeta potential of the Aeroxide TiO<sub>2</sub> P25 nanoparticles in water as a function of pH value and various citrate concentrations. A shift of the isoelectric point from 6.7 to 2.7 occurs by the addition of ammonium citrate dibasic (**Figure 93b**). The saturation amount of ammonium citrate dibasic was 2.6 wt% (6.4 Vol%). By addition of the saturation amount of dispersant, the zeta potential was below -50 mV for a pH values bigger than five. For higher pH values a successful electrostatic stabilization of the particles by a strongly negative charged surface should be given, which makes the particles suitable for bimodal or trimodal dispersions containing aluminum oxide. Citrate causes an exchange of hydroxyl groups with carboxylate ions by adsorption on the TiO<sub>2</sub> particle surfaces. The saturation amount represents the amount, for which a monolayer of citrate anions fully covers the surface of the particles.

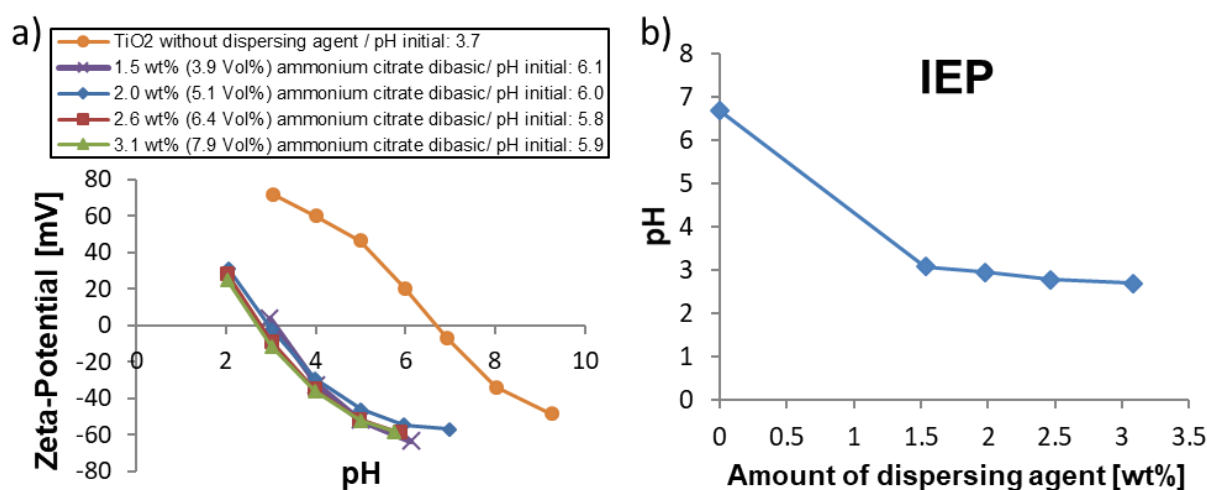


**Figure 93:** a) Zeta potential of TiO<sub>2</sub> particles as a function of pH value and various citrate concentrations. b) pH<sub>IEP</sub> of TiO<sub>2</sub> suspensions as function of ammonium citrate dibasic addition

The optical appearance of the TiO<sub>2</sub> powder was pure white. BET measurements gave a specific surface area of 50.0 m<sup>2</sup>/g of the particles. The company given value of 4.1 g/cm<sup>3</sup> was taken as the absolute density of the Aeroxide TiO<sub>2</sub> P25 nanoparticles. Therefore, a BET average particle size of 29.3 nm could be calculated.

**Figure 94** illustrates volume based particle size distributions of TiO<sub>2</sub> nanoparticles in water using the saturation amount of ammonium citrate dibasic of 2.6 wt%. Vibration milling led to agglomerations of up to ca. 850 nm measured by laser diffraction (**Figure 94a**) and up to ca. 600 nm measured by dynamic light scattering (**Figure 94b**). The higher energy input by an additional roll milling step for 24 hours diminished the amount of bigger agglomerates (**Figure 94d, e**). Attractive van der Waals forces dominate for small nano particles due to the faster

decreasing gravitation forces. In the case of bigger particles, these gravity forces ease the dispersing [28]. However, this additional dispersing step was less successful for the high solid loading of 10 Vol% than for 1 and 5 Vol% due to the extremely raised viscosity. Dispersing experiments with a solid loading of 5 Vol%  $\text{TiO}_2$  nanoparticles in water and 0.4 mm milling balls gave the best results. The characteristic values of  $d_{10}$ ,  $d_{50}$  and  $d_{90}$  were 86.0, 102.1 and 121.3 nm according to laser diffraction and 28.0, 56.0 and 106.4 nm according to dynamic light scattering. Klimkevicius et al., who synthesized cationic surfactants, have achieved even smaller particle sizes with this powder (unimodal size distribution curves with average value of about 18–22 nm measured by dynamic light scattering) [272]. Laser diffraction shows in general slightly bigger values to the given diffraction limit. However, the measured characteristic values of both methods were close to the calculated BET average particle size of 29.3 nm.

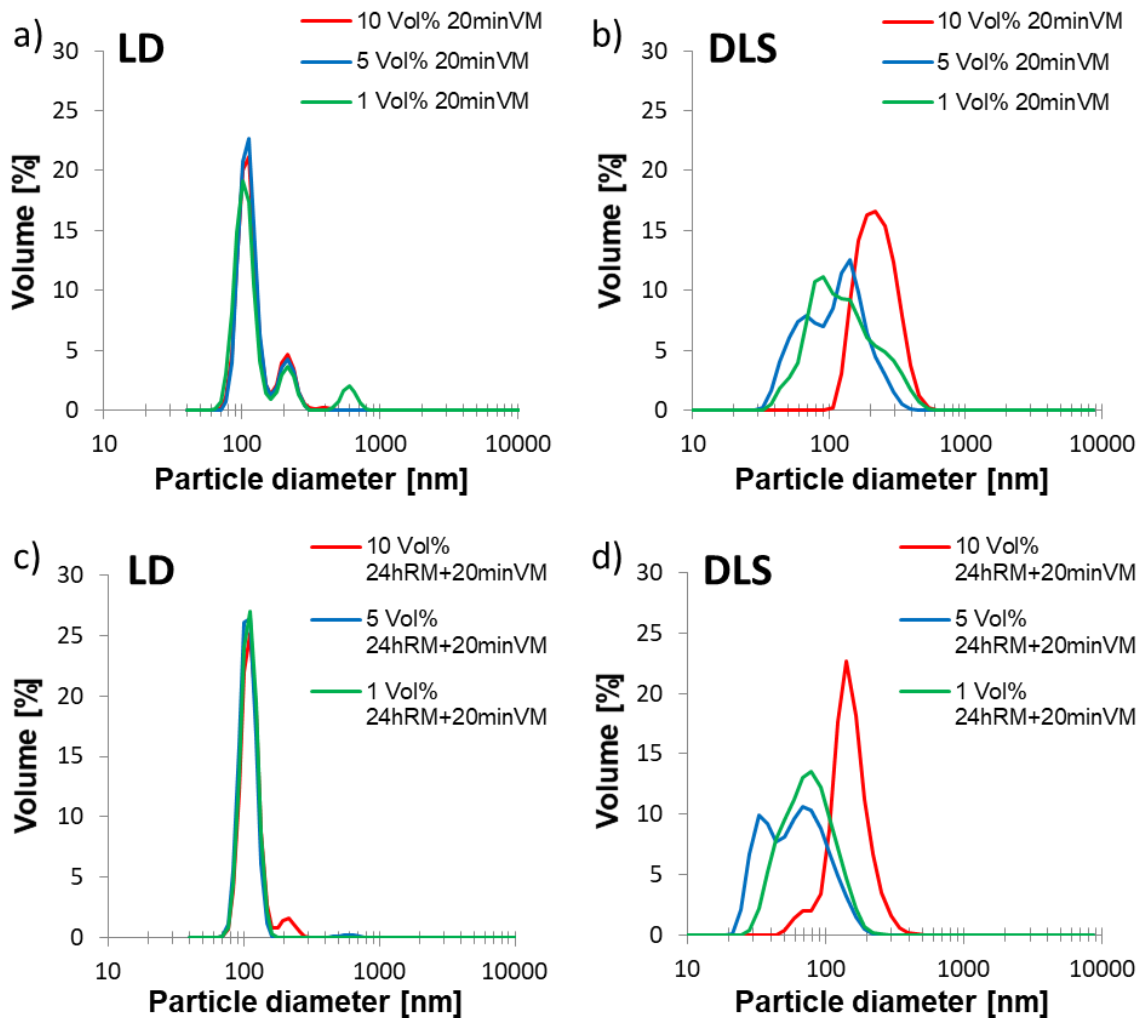


**Figure 94:** Volume based particle size distributions of  $\text{TiO}_2$  nanoparticles in water determined by **a), c)** laser diffraction (LD) and **b), d)** dynamic light scattering (DLS) and dispersed by optimized dispersant amount (2.6 wt%) and by vibration milling or a combination of roll milling and vibration milling.

#### 4.2.3.2 Thermal treatment of $\text{Al}_2\text{O}_3/\text{TiO}_2$ granules under argon/hydrogen atmosphere

**Figure 95a** depicts the thermal gravimetric analysis to evaluate the minimum temperature necessary to reduce the  $\text{TiO}_2$  nanoparticles to  $\text{TiO}_{2-x}$  in argon/hydrogen atmosphere. The derivation of the mass loss was calculated to facilitate the evaluation of the critical temperature for reduction, when using a heating rate of 2 K/min (**Figure 95b**). Furthermore, average values of 50 values were calculated to flatten the curve and therefore, to simplify the valuation of the reduction behavior changes. There was a significant mass loss as a result of  $\text{TiO}_2$  to  $\text{TiO}_{2-x}$  reduction after 980 °C. The measured mass loss between 200 and 980 °C was only 0.67 wt%, whereas the total mass loss up to the maximum temperature of 1470 °C was ca. 4.79 wt%. Above 980 °C the titanium oxide dopant shows a blackish color due to reduction, which enables the use of reduced titanium oxide as an effective dopant for laser processing in the visible or near-infrared range of the light.

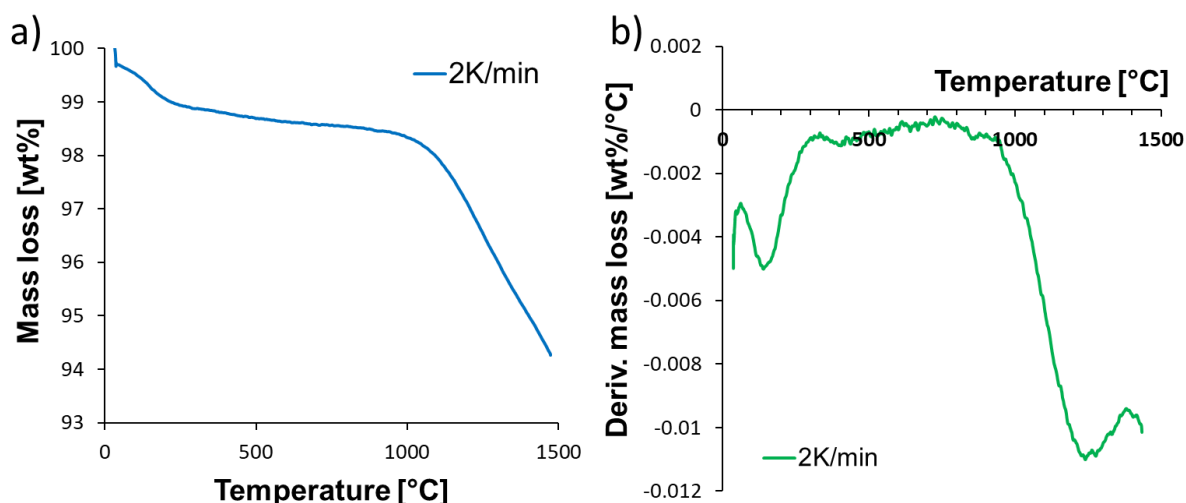


**Figure 95:** Thermal gravimetric analysis to evaluate the minimum temperature necessary to reduce the  $\text{TiO}_2$  nanoparticles to  $\text{TiO}_{2-x}$  in argon/hydrogen atmosphere by a) mass loss and b) derivation of the mass loss.

**Figure 96** features the optical appearance (maximum temperature: 1400 °C for 2 hours) and SEM images of spray dried granules containing 1 Vol% of  $\text{TiO}_{2-x}$  before and after thermal treatment in Ar/ $\text{H}_2$ . The powder changes the color from pure white to greyish-black even for the low doping amount. The microstructure is presented more into details for the maximum temperatures of 1400 °C and 1600 °C (holding times: 2 hours).

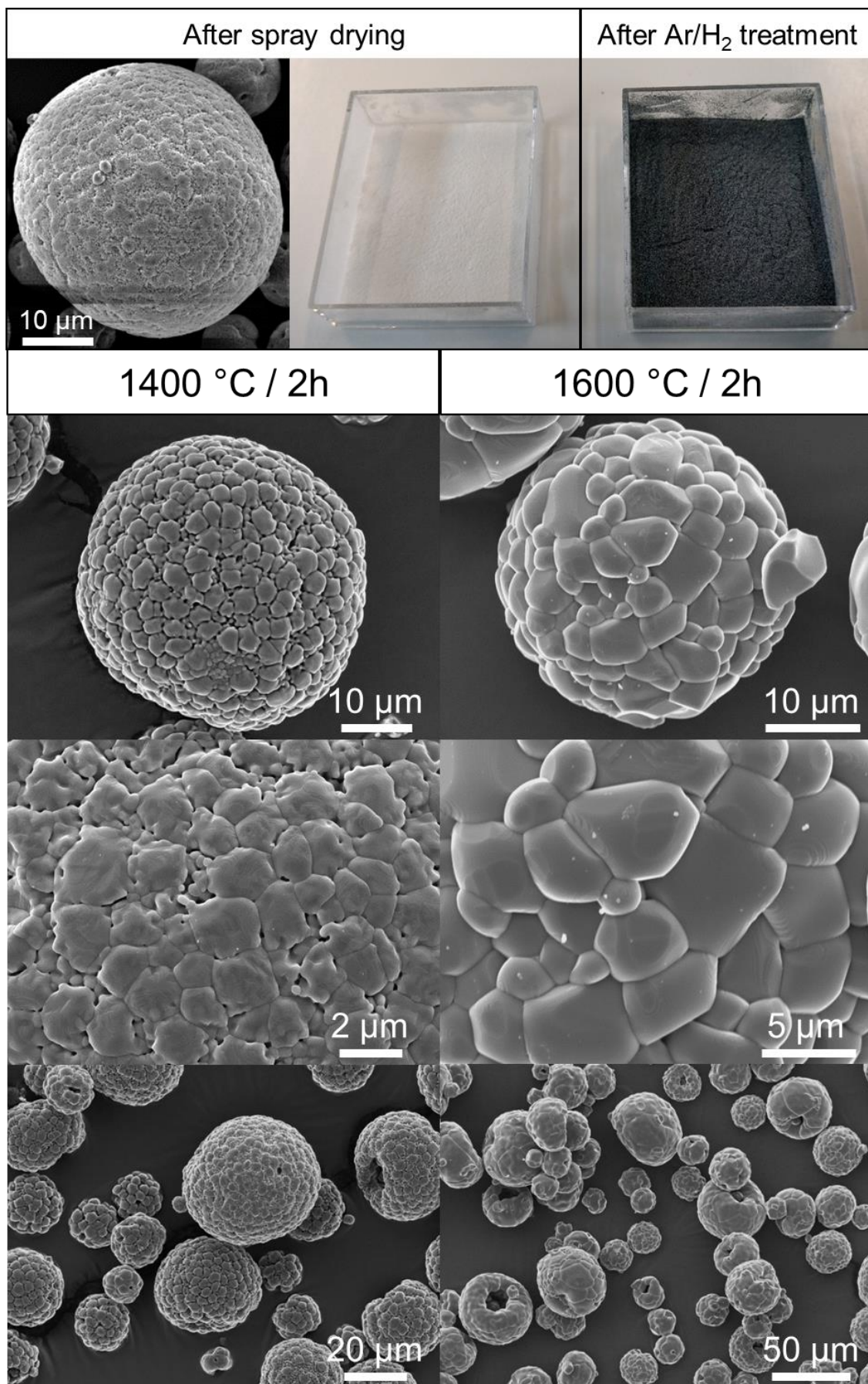


**Figure 96:** Optical appearance and SEM images of spray dried granules containing 1 Vol% of TiO<sub>2-x</sub> before and after thermal treatment in Ar/H<sub>2</sub> at maximum temperatures of 1400 °C and 1600 °C (idle times: 2 hours).



The spray-dried granules without thermal treatment have a spherical appearance. Only a few donut shaped granules were present in the powders. At a temperature of 1400 °C the sintering of the predominately alumina was at an early stage. A final complete sintering of the granules was reached at 1600 °C after a holding time of two hours in Ar/H<sub>2</sub>. This sintering resulted in dense microstructures with no visible porosity. However, the higher treatment temperature of 1600 °C led also to more sintering necks between the granules (satellite formation) than the lower treatment temperature of 1400 °C. The TiO<sub>2</sub> dopant triggered a uniform grain growth within the alumina granules. Such an impact on the sintering behavior on alumina was also reported by Sathiyakumar and Gnanam in air atmosphere [158]. They found that TiO<sub>2</sub> is effective for grain growth promotion in Al<sub>2</sub>O<sub>3</sub> up to a doping amount of 0.2 wt%. With higher additive amounts (contents of up to 4.0 wt%), the sintering rate and the grain sizes decreased in their work.

**Figure 97** represents SEM images of spray dried granules containing 14.2 Vol% of TiO<sub>2-x</sub> before and after thermal treatment in Ar/H<sub>2</sub>. The spray-dried granules without thermal treatment are less spherical than the granules sprayed with lower doping amount of 1 Vol%. However, also these powder offered a low amount of donut-shaped granules. Sintering of the particles was not visible after a thermal treatment with a maximum temperature of 1000 °C. The treatment at 1200 °C led to an early stage sintering, which was enhanced at 1300 °C and 1400 °C. The depletion of oxygen by reduction was visible by micron-size porosity appearing on the surface of the granules at the higher treatment temperatures. Another reason for this micron-sized porosity could be the sintering with the presence of residual carbon from the binder and dispersant in Ar/H<sub>2</sub> atmosphere. Michálek et al. [273] showed that sintering in argon atmosphere of carbon coated alumina samples led to areas with grain growth suppression with a high level of porosity. Their explanation was that the densification process controlled by transport along the grain boundaries was influenced by the presence of carbon at the alumina surfaces.

**Figure 98** illustrates SEM images of spray dried granules containing 68 Mol% of TiO<sub>2-x</sub> before and after thermal treatment in Ar/H<sub>2</sub> at maximum temperatures of 1000 °C, 1100 °C, 1200 °C, 1300 °C and 1400 °C. The spray-dried granules without thermal treatment showed a lower sphericity than the other granules. The movement of the nano-sized TiO<sub>2</sub> particles in multimodal particle combinations is enhanced [121]. The fully dispersed particles are very versatile without intergranular interactions within the droplets and to pack densely at the shell [119], which has in combination of the high amount of TiO<sub>2</sub> used for spray drying a detrimental effect on the particle shape. Furthermore, the sintering of the particles was enhanced for these granules. A thermal treatment with a maximum temperature of 1000 °C and 1100 °C showed an

early stage sintering. Higher temperatures rapid grain growth, which was enhanced at temperatures of 1300 °C and 1400 °C. In comparison, pure TiO<sub>2</sub> systems showed already at lower temperatures sintering and rapid grain growth. Dittmann et al. [202] evaluated a start of sintering and rapid grain growth in air atmosphere at temperatures of 500 °C and 800 °C, respectively. Mazaheri et al. [203] described a comparable sintering and rapid grain growth start at temperatures of 650 and 800 °C, respectively. The reduction of oxygen was also visible by micron-size porosity, as seen already for an addition amount of 14.2 Vol% of TiO<sub>2</sub>.

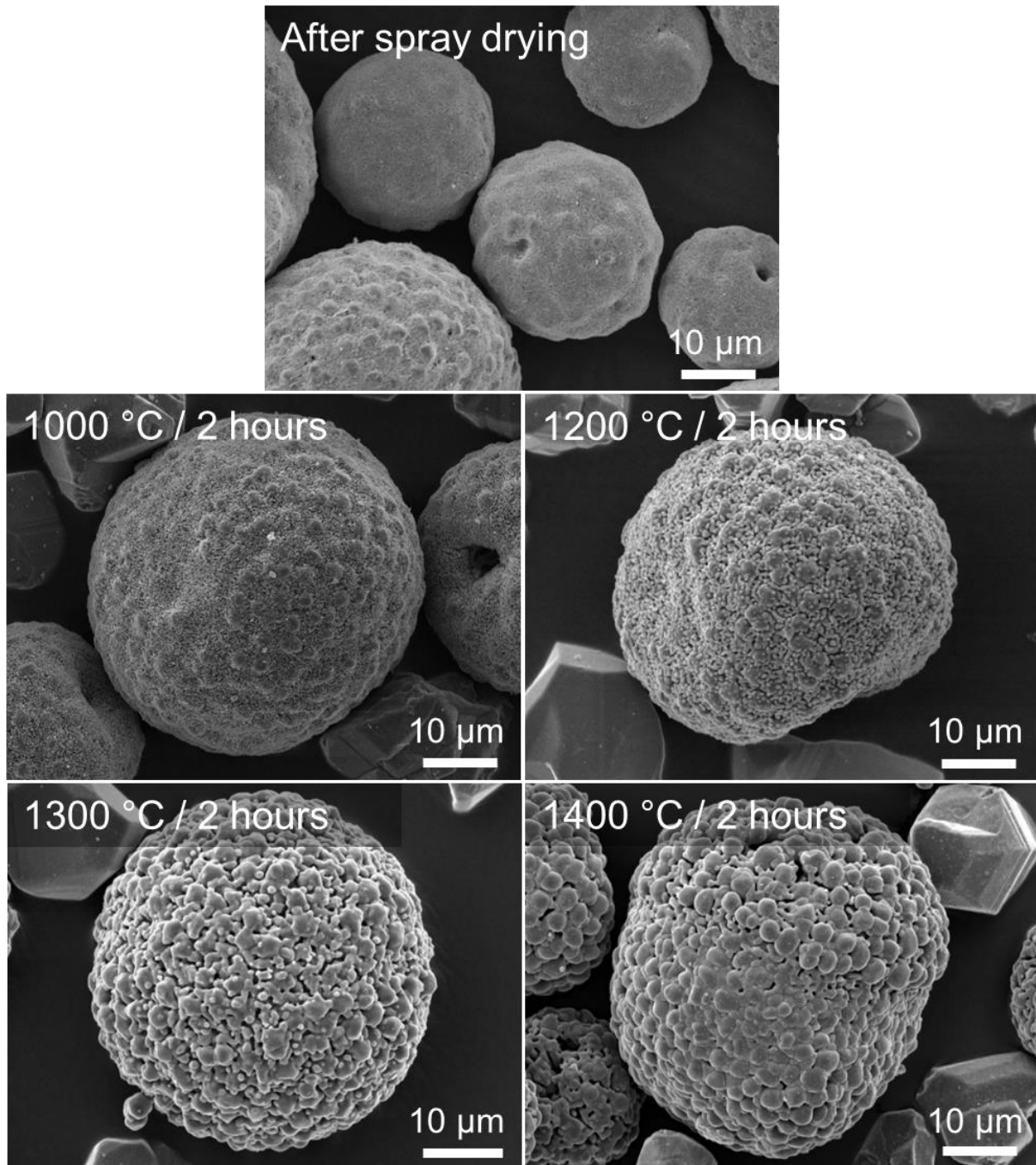


**Figure 97:** SEM images of spray dried granules containing 14.2 Vol% of TiO<sub>2-x</sub> before and after thermal treatment in Ar/H<sub>2</sub> at maximum temperatures of 1000 °C, 1200 °C, 1300 °C and 1400 °C (idle times: 2 hours).



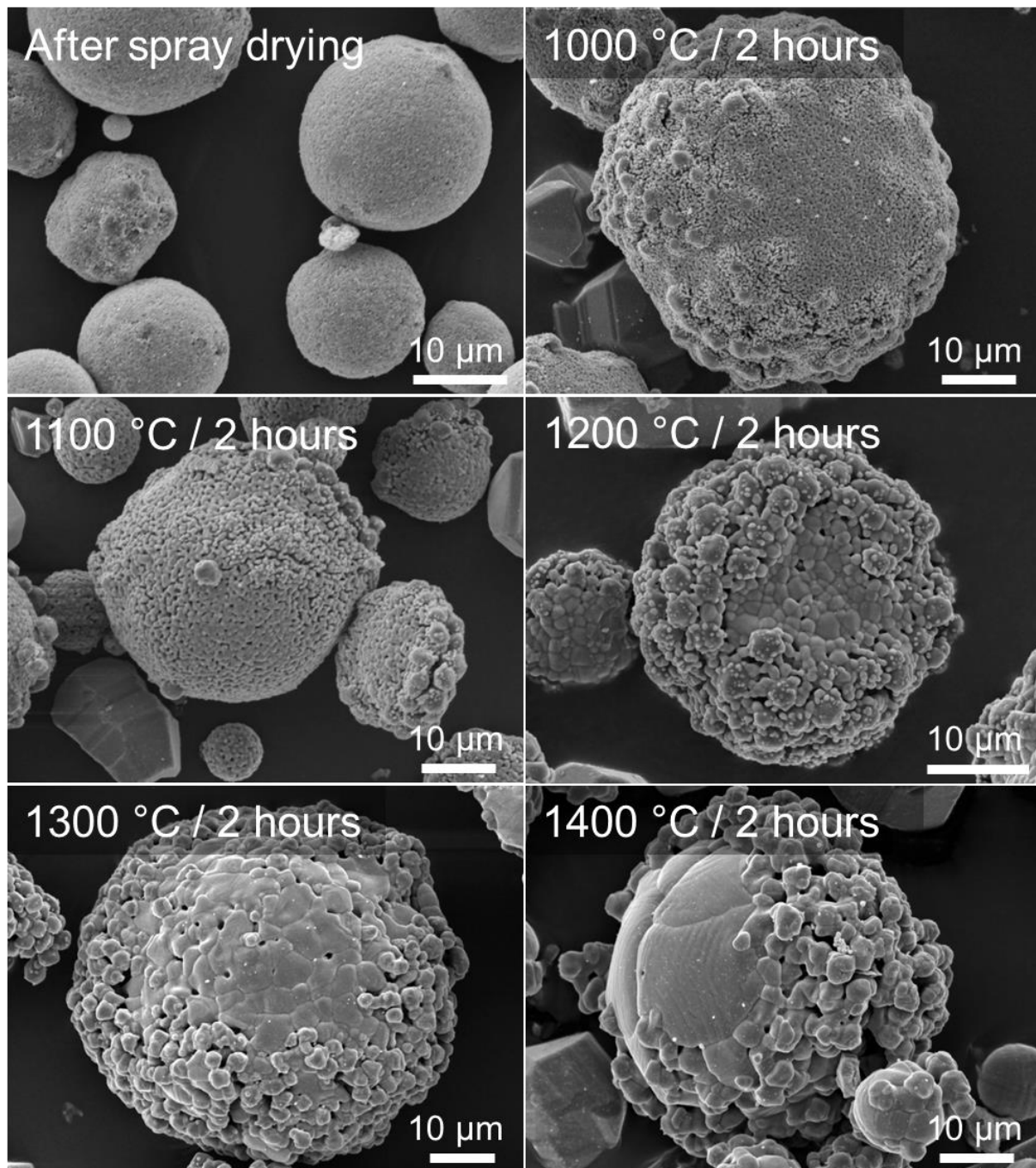


**Figure 98:** SEM images of spray dried granules containing 68 Mol% of  $\text{TiO}_{2-x}$  before and after thermal treatment in  $\text{Ar}/\text{H}_2$  at maximum temperatures of 1000 °C, 1100 °C, 1200 °C, 1300 °C and 1400 °C (idle times: 2 hours).

**Table 30** summarizes the apparent density, tapped density and Hausner ratio of spray dried granules as well as thermal treated granules with 1 Vol%, 14.2 Vol% and 68 Mol%  $\text{TiO}_{2-x}$  mixed with 30 Vol% coarse aluminum oxide AA18. Apparent and tapped density are lower before the thermal treatment and the consecutive mixing with the coarse aluminum oxide particles AA18. However, the flowability (Hausner ratio) of these granules were in general better. This increase of the densities and Hausner ratio by thermal treatment and consecutive mixing

with the coarse alumina was already described in chapter 3.2.8. The trends of the apparent densities, tapped densities and Hausner ratios followed the sintering behavior described in the SEM images. Rapid grain growth led to powders with a lower apparent and tapped density. Furthermore, this over-sintering worsened the flowability of the granules by formation of satellite like structures or by deterioration of the sphericity.

For further experiments, the thermal treatment temperatures of 1300 °C and 1200 °C were used for granules with 14.2 Vol% and 68 Mol% TiO<sub>2</sub> due the optimized ratio of apparent and tapped density as well as Hausner ratio. For 1 Vol% of TiO<sub>2</sub> a treatment temperature of 1400 °C was chosen due to the accessibility of the high temperature furnace. The granules with 1 Vol%, 14.2 Vol% and 68 Mol% TiO<sub>2</sub> were sprayed with an ultrasonic power of 11, 7 and 8 W. respectively.

**Table 30:** Properties of spray dried granules and thermal treated granules with 1 Vol%, 14.2 Vol% and 68 Mol% TiO<sub>2-x</sub> mixed with 30 Vol% coarse aluminum oxide AA18.

a) Spray-dried granules

Content of TiO <sub>2-x</sub>	Apparent density [% of TD]	Tapped density [% of TD]	Hausner ratio
1 Vol%	40.1	45.5	1.14
14.2 Vol%	35.5	39.7	1.12
68 Mol%	23.6	27.2	1.15

b) Thermal treated granules with 1 Vol% TiO<sub>2-x</sub> mixed with 30 Vol% coarse alumina AA18

Maximum temperature / holding time of treatment in in Ar/H <sub>2</sub>	Apparent density [% of TD]	Tapped density [% of TD]	Hausner ratio
1400 °C / 2h	44.3	53.6	1.21
1600 °C / 2h	47.9	54.9	1.15

c) Thermal treated granules with 14.2 Vol% TiO<sub>2-x</sub> mixed with 30 Vol% coarse alumina AA18

Maximum temperature / holding time of treatment in in Ar/H <sub>2</sub>	Apparent density [% of TD]	Tapped density [% of TD]	Hausner ratio
1000 °C / 2h	37.4	44.5	1.19
1200 °C / 2h	38.4	46.6	1.21
1300 °C / 2h	41.0	49.2	1.20
1400 °C / 2h	40.3	49.4	1.23

d) Thermal treated granules with 68 Mol% TiO<sub>2-x</sub> mixed with 30 Vol% coarse alumina AA18

Maximum temperature / holding time of treatment in in Ar/H <sub>2</sub>	Apparent density [% of TD]	Tapped density [% of TD]	Hausner ratio
1000 °C / 2h	35.0	42.8	1.22
1100 °C / 2h	33.7	41.9	1.24
1200 °C / 2h	37.1	45.6	1.23
1300 °C / 2h	37.3	44.8	1.20
1400 °C / 2h	34.5	43.5	1.26

The qualitative absorption spectrum of untreated and reduced granules is shown in **Figure 99a and b**. The spectrum was analyzed at room temperature by the Kubelka Munk method. The absorption spectrum of pure aluminum oxide AA18 is also depicted as a comparison.

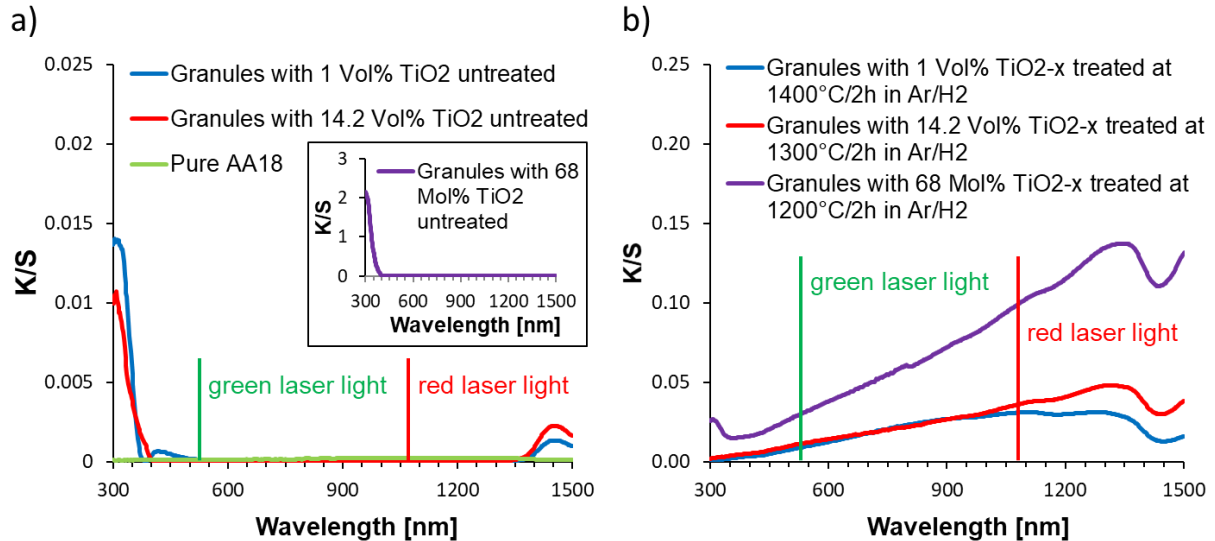


**Figure 99:** Qualitative absorption spectrum at room temperature measured by the Kubelka Munk method of **a)** untreated and pure AA18 as well as of **b)** reduced granules.

Granules after spray drying as well as pure aluminum oxide AA18 offer no absorption at the relevant wavelength of 532 nm (green laser) and 1070 nm (IR laser). However, the reduced TiO<sub>2-x</sub>-doped alumina granules showed an increased absorptance after reduction in Ar/H<sub>2</sub>, which makes them suitable for laser processing at these wavelengths. The highest absorption was measured for reduced granules containing 68 Mol% of titanium oxide, which is due to the high amount of blackish TiO<sub>2-x</sub> within the granules. The K/S ratio decreased over the completely measured wavelengths (300 - 1500 nm) for granules containing less reduced titanium oxide.

#### 4.2.3.3 Laser manufacturing of parts

**Table 31** summarizes the powder combinations used for laser processing. All of the powders contain 70 Vol% of granules and 30 Vol% of coarse aluminum oxide AA18. The optimized temperatures for reduction were taken from the results evaluated in chapter 4.2.3.2. The amount of titanium oxide in the different granules were 1 Vol%, 14.2 Vol% and 68 Mol%, which gives a final content of TiO<sub>2-x</sub> in the powder combinations A, B and C after mixing of 0.7 Vol%, 10 Vol% and 50 Mol%, respectively.

**Table 31:** Powder combinations used for laser processing

Powder combination	Content	Total Content of $\text{TiO}_{2-x}$ in powders for laser processing
A	70 Vol% Granules with 1 Vol% $\text{TiO}_{2-x}$ thermally treated at 1400 °C for 2h in Ar/ $\text{H}_2$	30 Vol% Coarse aluminum oxide AA18 0.7 Vol%
B	70 Vol% Granules with 14.2 Vol% $\text{TiO}_{2-x}$ thermally treated at 1300 °C for 2h in Ar/ $\text{H}_2$	30 Vol% Coarse aluminum oxide AA18 10 Vol%
C	70 Vol% Granules with 68 Mol% $\text{TiO}_{2-x}$ thermally treated at 1200 °C for 2h in Ar/ $\text{H}_2$	30 Vol% Coarse aluminum oxide AA18 50 Mol%

**Table 32** summarizes the properties of used powders for laser processing in terms of solid loading of the slurries for spray drying, of the yield of spray drying and the size distribution including the characteristic size values of d10, d50 and d90. Only small solid loadings in the slurries could be used when the content of nano-sized  $\text{TiO}_2$  increased. The highest yield of spray drying of 66.9 % was achieved for the spray-dried granules for powder combination B, which follows most probably due to the lowest slurry viscosity. The characteristic size values of d10 and d90 are similar for all powder combination. However, d90 of powder combination A is more than 15  $\mu\text{m}$  bigger than for the other powder combinations. This could be due the higher thermal treatment temperatures of 1400 °C leading to more sintering of granules to an unwanted satellite formation as well as due to the lower amount of nano-sized  $\text{TiO}_2$  in the slurry for spray drying leading to bigger granules after spray drying.

**Table 32:** Properties of powder combinations A, B and C.

Powder combination	A	B	C
Solid load in slurry [Vol%]	49.4	30.0	10.4
Yield of spray drying [%]	22.0	66.9	32.5
Apparent density [% of TD]	44.3	41.0	37.1
Tapped density [% of TD]	53.6	49.2	45.6
Hausner ratio	1.21	1.20	1.23
d10 [ $\mu\text{m}$ ]	16.8	17.5	15.5
d50 [ $\mu\text{m}$ ]	33.2	34.8	32.2
d90 [ $\mu\text{m}$ ]	73.0	56.4	57.6

#### A. Powder combination A

**Figure 100** shows attenuation contrast tomographic microscopy images of laser-manufactured parts made from powder combination A. The used processing parameter of the green ns-pulsed



laser were a hatch distance of 135  $\mu\text{m}$ , a laser spot diameter of 135  $\mu\text{m}$ , a layer thickness of 40  $\mu\text{m}$ , a laser power of 5.75 W and the two different processing speeds of 2 mm/s (**Figure 100a**) and 10 mm/s (**Figure 100b**).

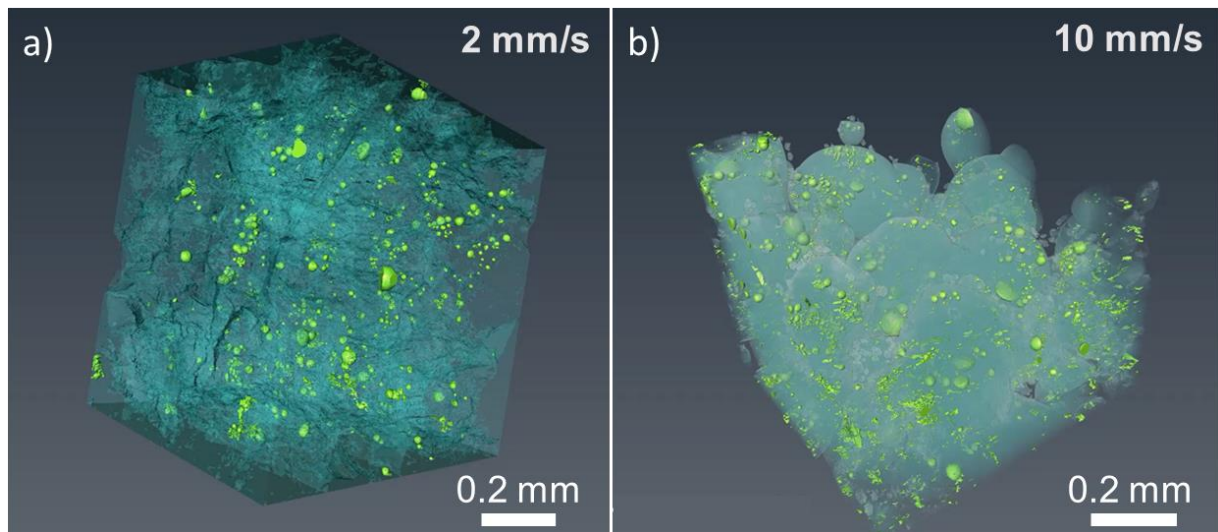


**Figure 100:** Attenuation contrast tomographic microscopy of laser-manufactured parts made from powder combination A and with different processing speeds **a)** 2 mm/s and **b)** 10 mm/s.

The laser manufactured parts showed a development of micropores during processing (light green bubbles in **Figure 100a and b**). The amount of pores was significantly higher by using the higher speed of 10 mm/s. However, an explanation for these relation of pore amount on the processing speed cannot given by just using these data. Furthermore, a clear dependency of the porosity from the laser speed was noticeable. The higher speed of 10 mm/s led to a lower density of the laser-processed parts (51.9% (10 mm/s) compared to 95.3% (2mm/s) evaluated by tomographic microscopy). This could be due to lower temperatures within the melt-pool, which were not sufficient for a complete consolidation of the used powder.

XRD-contrast tomography was conducted to analyze and to get more insides of the surroundings of the bubbles in terms of phase composition (**Figure 101**). At the angles of 17.8° and 20.5° strong intensities were visible next to the bubbles in the cross sections. However, the peak intensities of these extra phases were smaller than 0.3. These appoints to very small amount of these phases, since the main peaks showed intensities of up to 18000. Furthermore, a clear conclusion cannot be drawn by these measurements due to even smaller amounts than the amount of the  $\text{TiO}_2$  dopant.

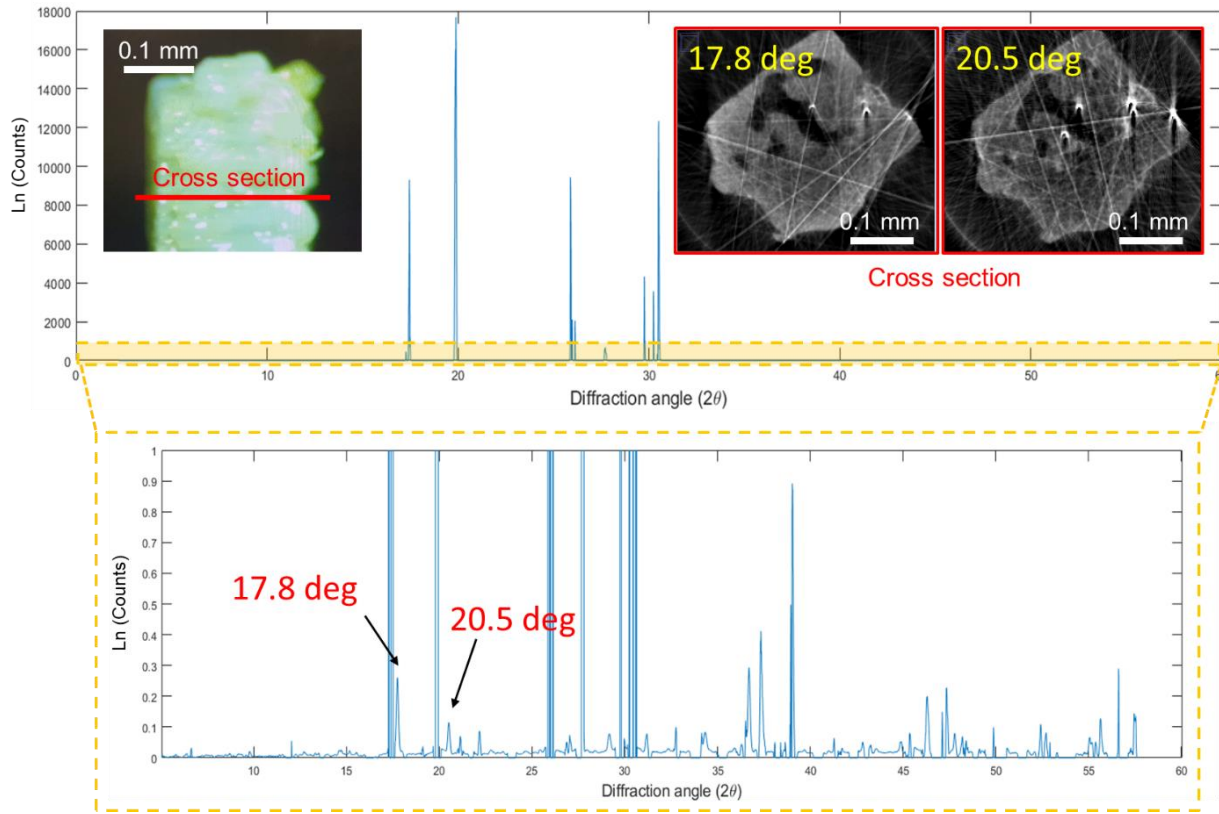


**Figure 101:** XRD-contrast tomography of laser-manufactured parts made from powder combination A. The insets show the laser manufactured part with the position of the analyzed cross section (left side) as well as the acquired intensities with the cross section at angles of 17.8° and 20.5° (right side).

**Figure 102** shows the evaluated parts density and cracks density as well as crack distribution in a cross section of laser printed alumina parts from tomographic microscopy. Three different dopants ( $\text{Fe}_2\text{O}_3$ ,  $\text{TiO}_{2-x}$ ,  $\text{Mn}_x\text{O}_y$ ) and three different laser scanning speeds (2 mm/s, 5 mm/s, 10 mm/s) were tested. The amount of dopant was smaller than 1 Vol% for all material systems. The crack density was calculated using following equation:

$$\text{Cracks density} = \frac{SA_{\text{cracks}}}{V\rho} \quad (16)$$

$SA_{\text{cracks}}$ ,  $V$  and  $\rho$  represent the total crack surface area in the measured volume in  $\mu\text{m}^2$ , the measured part volume in  $\mu\text{m}^3$  and the density of the part in % of the theoretical density, respectively.

An increasing scanning speed led for all of the three dopants to a decreased cracks density and a decreased part density (**Figure 102a, b and c**). However, no clear trend was seen for the influence of the three different dopants on the cracks density, when comparing them at different laser scanning speeds. Furthermore, the difference between the densities of the parts processed with different dopants were rather small (maximum differences of 3%) by using scanning

speeds of 2 mm/s and 5 mm/s. These observations are illustrated in the cross sections of the laser printed parts in **Figure 100d**. The conclusion can be drawn that a low dopant amount of below 1 Vol% is not effective to reduce the crack formation in PBF-LB of alumina and that the dopant choice plays no major role in terms of crack reduction for laser-manufactured parts with over 99 % pure alumina, since all crack densities were in a similar order of magnitude.

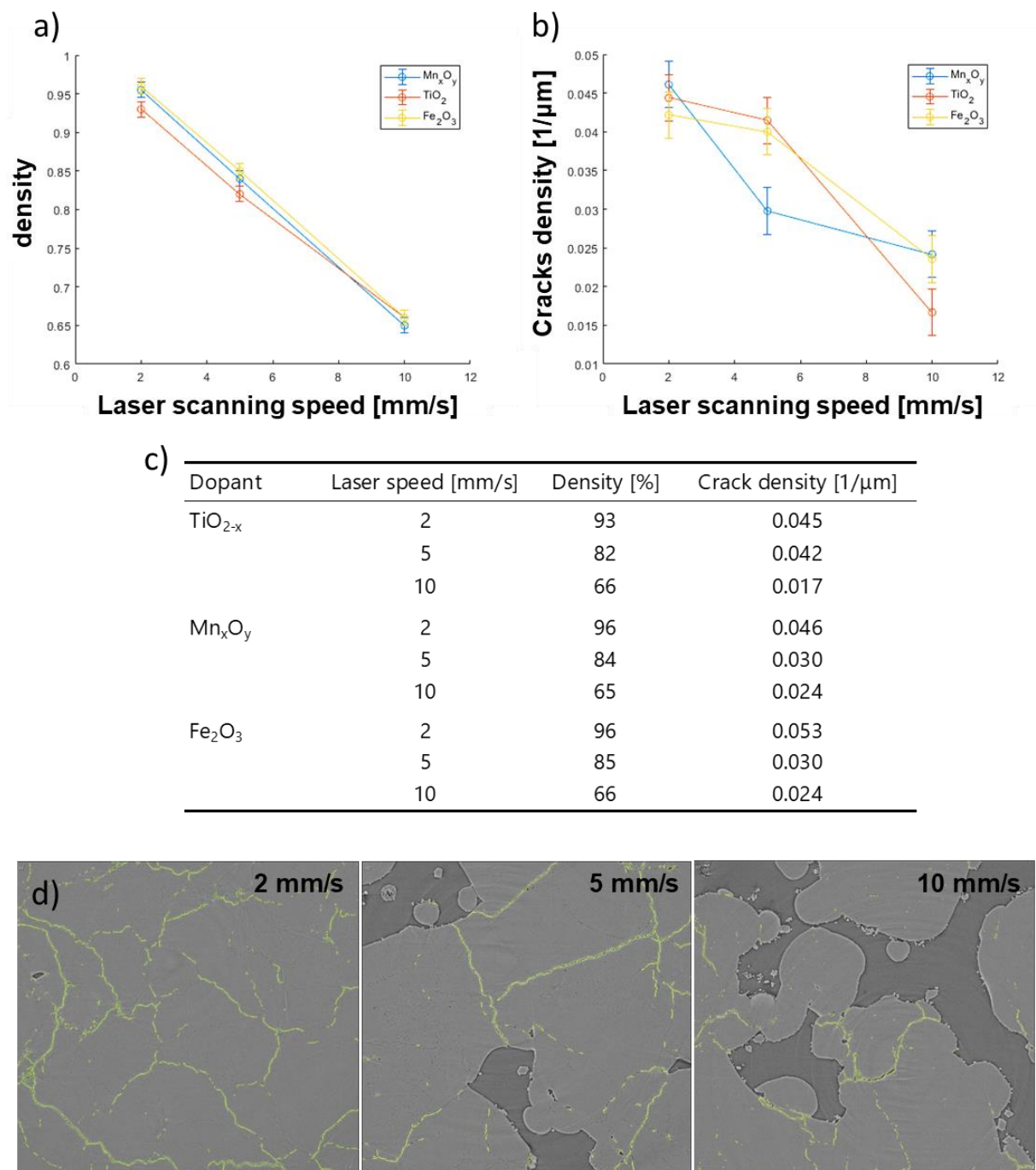


**Figure 102:** Evaluation of a), b), c) parts density and cracks density as well as d) crack distribution in a cross section of laser printed doped alumina parts for three different dopants (Fe<sub>2</sub>O<sub>3</sub>, TiO<sub>2-x</sub>, Mn<sub>x</sub>O<sub>y</sub>) at different laser scanning speed (2 mm/s, 5 mm/s, 10 mm/s) from tomographic microscopy.



B. Powder combination B and C

**Figure 103** shows the internal structure of laser manufactured parts produced with powder combination B.

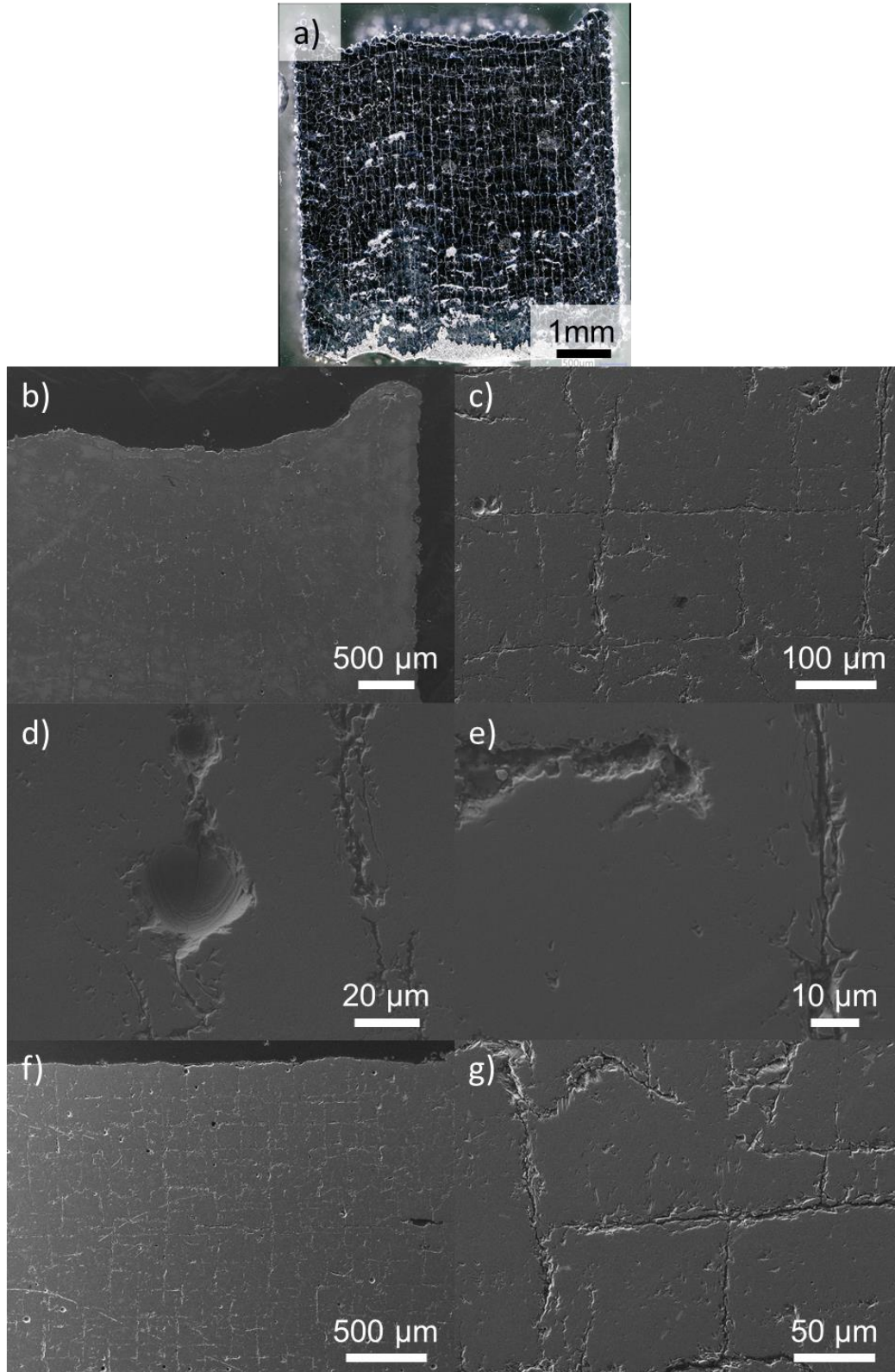


**Figure 103:** Internal structure imaged by optical microscopy and SEM of cross-sections (a-e) view in build direction and f), g) top view) of laser manufactured parts produced with powder combination B.

The parts were homogeneously consolidated by the IR laser (laser power: 40 W, scan speed: 80 mm/s). The part density evaluated by the Archimedes principle was 94.0%. Various laser-induced cracks generated by thermal shock due to huge thermal gradients during cooling were seen in the cross-sections (view of build direction **Figure 103a-e** and top view **Figure 103f and g**). A crack reduction by the formation of the ternary phase aluminum titanate was not successful in this case, except for a small amount of bigger pores. The microstructure revealed a small amount of circular pores (**Figure 103d**). Furthermore, unmolten particles were found within pores of the sample (**Figure 103e**).

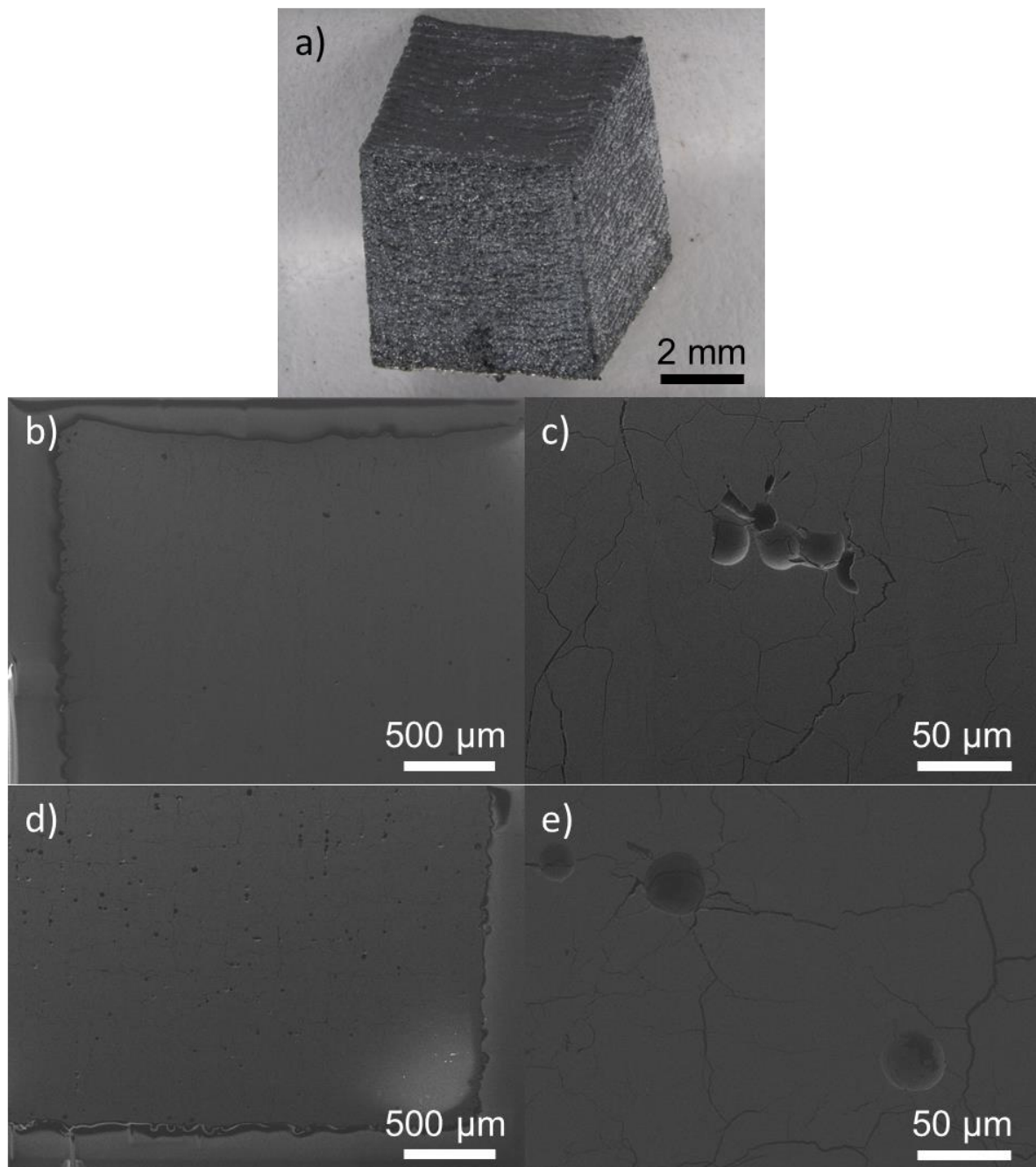


**Figure 104:** a) Shape imaged by optical microscopy. Internal structure imaged by SEM of cross-sections (b), c) view in build direction and d), e) top view) of laser manufactured parts produced with powder combination C.

The internal structure of laser-manufactured parts produced with powder combination C is presented in **Figure 104b, c** (view in build direction) and **Figure 104d, e** (top view). The parts were uniformly consolidated by the IR laser (laser power: 30 W, scan speed 70 mm/s) with a low amount of micron-sized pores. The part density was 96.5%. Laser-induced cracks were strongly reduced in these parts (visual impression) and could be only found in higher magnifications of the cross-sections. Furthermore, the shape of a part is imaged by optical microscopy (**Figure 104a**). The accuracy of the lateral areas is high, whereas the top surfaces has a wavy appearance.

The total content of 50 Mol%  $\text{TiO}_{2-x}$  in powder combination C leads to improved parts in terms of crack reduction compared to power combination A (0.7 Vol%  $\text{TiO}_{2-x}$ ) and power combination B (10 Vol%  $\text{TiO}_{2-x}$ ). This crack reduction follows most probably due to the in-situ reaction of aluminum oxide and titanium oxide to the ternary phase aluminum titanate, which has a low Young's modulus, a low thermal expansion coefficient, low thermal conductivity and therefore excellent thermal shock behavior [181, 184]. Crack-free parts were already manufactured by directed energy deposition (DED) using aluminum oxide and titanium oxide powders. The amount of cracks was reduced proportionally to the amount of dopant used [178], similar to the results of this work. However, the amount of 50 Mol% titanium oxide exceeds by far the amount of 10.5 Mol% (13 wt%), which was stated in several references about laser cladding of  $\text{Al}_2\text{O}_3$ - $\text{TiO}_2$  powders to achieve layers without cracks and with low porosity [192-194]. This could be due to a different process of the melt pool formation in DED and laser cladding, which is usually done by irradiation of the substrate and a subsequent powder addition into the melt pool. This method requires in general a laser spot diameter, which is ca. one order of magnitude larger than in PBF-LB and therefore, bigger and more homogenous temperature areas can be consolidated simultaneously compared to traditional PBF-LB leading to less thermal stresses.

X-ray diffraction confirmed the formation of reduced titanium oxide within the granules of powder combination C containing 50 Mol%  $\text{TiO}_{2-x}$  (**Figure 105a**). The titanium oxide changed from predominantly anatase and partially rutile to reduced  $\text{TiO}_{2-x}$  and rutile already for a maximum Ar/ $\text{H}_2$  treatment temperature of 1000 °C. A treatment with a maximum temperature of 1400 °C further transformed a significant part of the reduced titanium oxide and aluminum oxide to aluminum titanate ( $\text{Al}_2\text{TiO}_5$ ). **Figure 105b** shows that also the desired  $\text{Al}_2\text{TiO}_5$  formation was achieved in the PBF-LB printed parts made from powders containing 10 Vol% of  $\text{TiO}_{2-x}$  and 50 Mol%  $\text{TiO}_{2-x}$ . The parts made from powder combination C featured the majority

of  $\text{Al}_2\text{TiO}_5$  in the crystalline phase. However, a complete transformation of aluminum oxide and titanium oxide to aluminum titanate did not occur during laser processing.

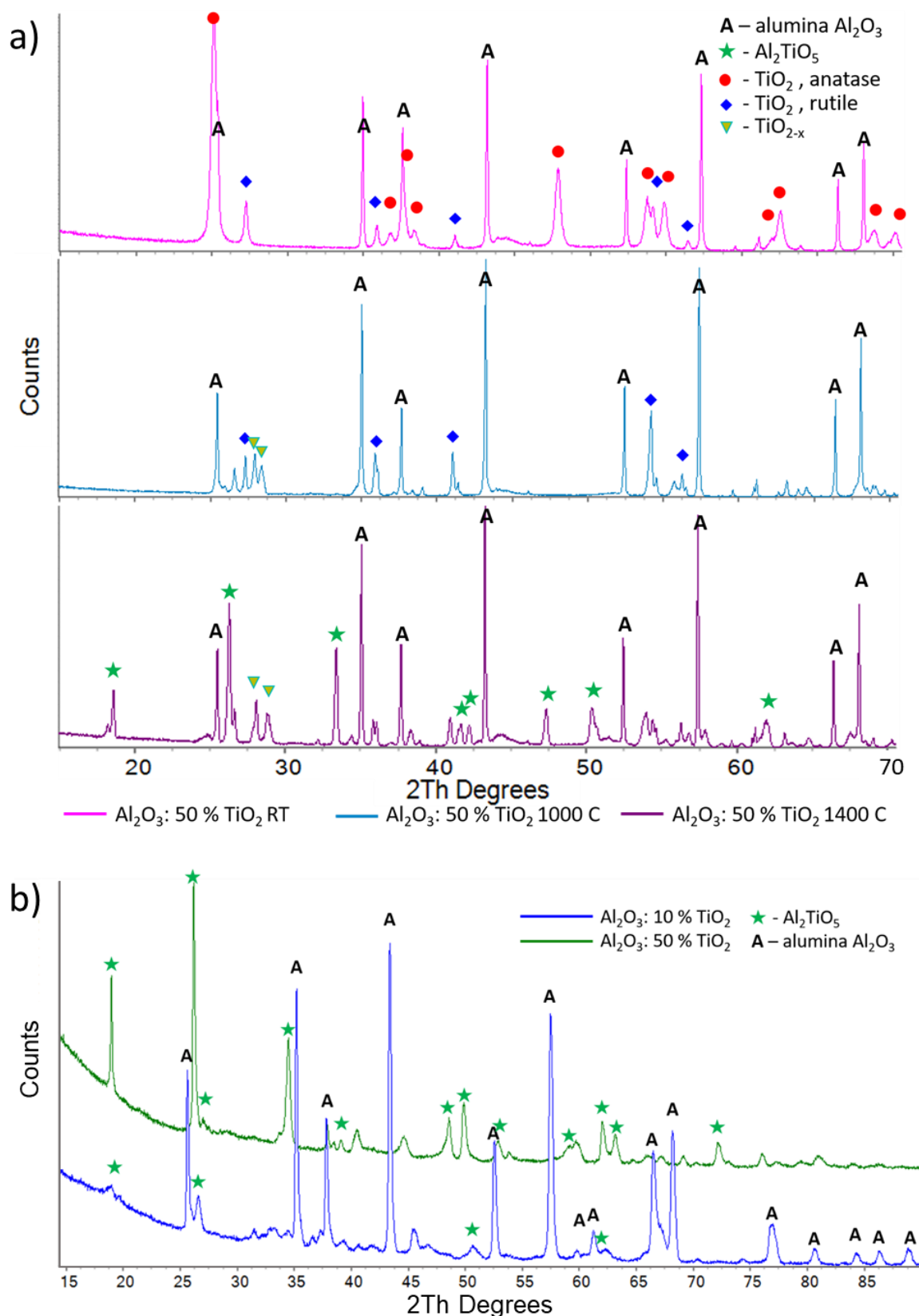


**Figure 105:** X-ray diffraction measurements of **a)** powder combination C (50 Mol% of  $\text{TiO}_{2-x}$ ) before and after thermal treatment in  $\text{Ar}/\text{H}_2$  at maximum temperatures (idle time: 2 hours) of 1000 °C and 1400 °C and of **b)** laser processed parts made from powder combination B (10 Vol% of  $\text{TiO}_{2-x}$ ) and powder combination C.

## 4.2.4 In-situ formation of negative thermal expansion materials

### 4.2.4.1 Dispersing of zirconia and tungsten oxide nanoparticles

A solution to minimize thermal stresses in PBF-LB of aluminum oxide ceramics could be the generation of zirconium tungstate ( $\text{ZrW}_2\text{O}_8$ ), which exhibits a negative thermal expansion coefficient over an extended temperature range (0.3-1050 K) [204, 205]. Zirconium tungstate is a metastable phase and can be achieved by rapid cooling to avoid a decomposition into  $\text{WO}_3$  and  $\text{ZrO}_2$ , which is the case in the PBF-LB processes [205, 206]. The formation of this negative thermal expansion phase will create compressive stresses by expansion during cooling, which gives the possibility to counterbalance the shrinkage of alumina and therefore, to adjust the resultant thermal expansion in the oxide ceramic to near zero. More information can be found in chapter 2.4.2.

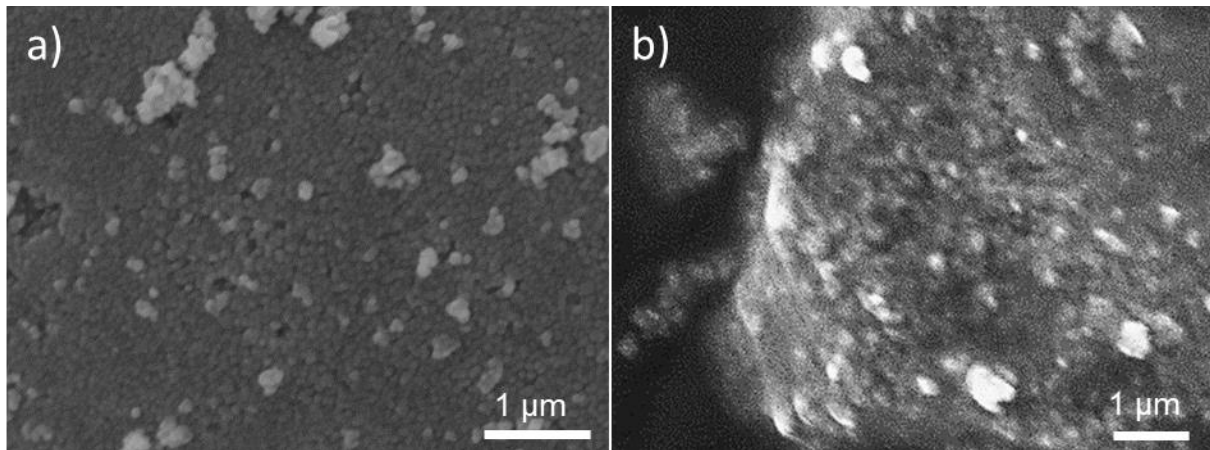


*Figure 106: SEM images of a)  $\text{ZrO}_2$  and b)  $\text{WO}_3$  nanoparticles.*

**Figure 106a** and **Figure 106b** show the optical appearance of the  $\text{ZrO}_2$  and  $\text{WO}_3$  nanoparticles, respectively. The powders feature particles with a uniform size distribution in the nano range. The  $\text{WO}_3$  powder had a yellow color, whereas the  $\text{ZrO}_2$  powder appeared in a pure white color. The measured absolute densities and specific surface areas were  $5.62 \text{ g/cm}^3$  and  $14.4 \text{ m}^2/\text{g}$  for the  $\text{ZrO}_2$  powder and  $6.93 \text{ g/cm}^3$  and  $7.9 \text{ m}^2/\text{g}$  for the  $\text{WO}_3$  powder. These results gave calculated BET average particle sizes of  $74.2 \text{ nm}$  for the  $\text{ZrO}_2$  particles and  $109.7 \text{ nm}$  for the  $\text{WO}_3$  particles. The  $\text{ZrO}_2$  powder consisted entirely of the monoclinic phase (Baddeleyite) according to x-ray diffraction. A phase content of 100% Krasnogorite was found for the  $\text{WO}_3$  powders. Other phases were not present in the powders.



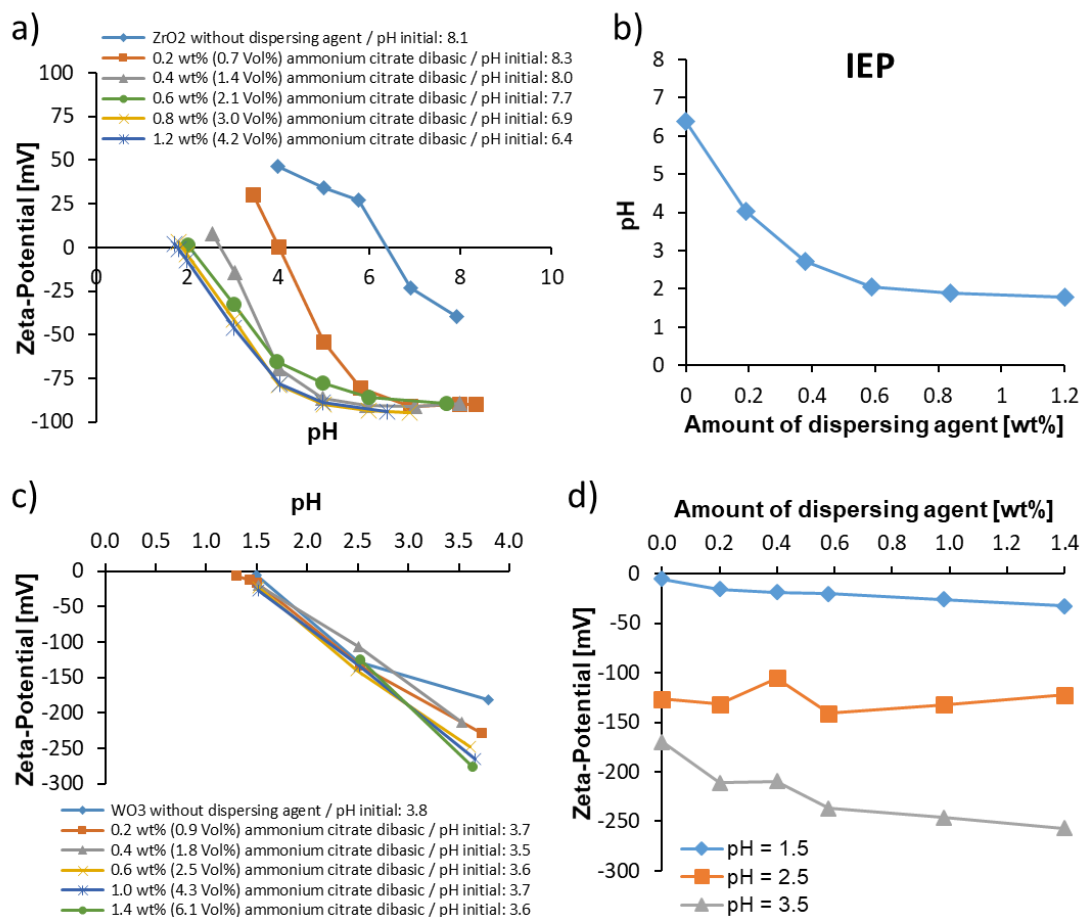


**Figure 107:** a) Zeta potential of ZrO<sub>2</sub> particles as a function of pH value and various citrate concentrations. b)  $pH_{IEP}$  of ZrO<sub>2</sub> suspensions as function of ammonium citrate dibasic addition. c) Zeta potential of WO<sub>3</sub> particles as a function of pH value and various citrate concentrations. d) Zeta potential of WO<sub>3</sub> suspensions as function of ammonium citrate dibasic addition at constant pH values of 1.5, 2.5 and 3.5.

The zeta potential of the ZrO<sub>2</sub> nanoparticles in water as a function of the pH value and various citrate concentrations is illustrated in **Figure 107a**. The addition of ammonium citrate dibasic shifts the isoelectric point from 6.4 to 1.8 (**Figure 107b**). Using the saturation amount of ammonium citrate dibasic (0.6 wt%/2.1 Vol%), a zeta potential below -77 mV is created for pH values bigger than 5, what should guarantee a successful electrostatic stabilization of these particles in this pH range. By adsorption on the particle surfaces, the citrate causes an exchange of hydroxyl groups with carboxylate ions and creates a strongly negative charged surface, which enables a homogeneous dispersion. At the evaluated saturation amount, the surface of the particles should be already fully covered with a monolayer of citrate anions. **Figure 107c** shows the Zeta potential of the WO<sub>3</sub> particles as a function of the pH value and the ammonium citrate addition. Since a dependency of the zeta was not clearly seen in this depiction, the zeta potential was represented as function of ammonium citrate dibasic addition at constant pH values of 1.5, 2.5 and 3.5 (**Figure 107d**). This depiction showed a decrease of the zeta-potential by addition

of ammonium citrate dibasic, especially for pH-values of 1.5 and 3.5. However, this decrease was only slight. Both powders are already negative charged without using citrate, but zirconia has a much smaller zeta potential at the initial pH values (-40 mV to -180 mV). This means less repulsion of the carboxylate ions. However, this also explains the small shift of the zeta potential by use of this dispersant for  $\text{WO}_3$ . For further dispersing experiments with  $\text{WO}_3$ , an amount of 0.2 wt% (0.9 Vol%) ammonium citrate dibasic was chosen, since a high zeta potential below -100mV was already present at pH values bigger than 2.5 and the change of the zeta potential was only small for bigger concentrations of the dispersing agent.

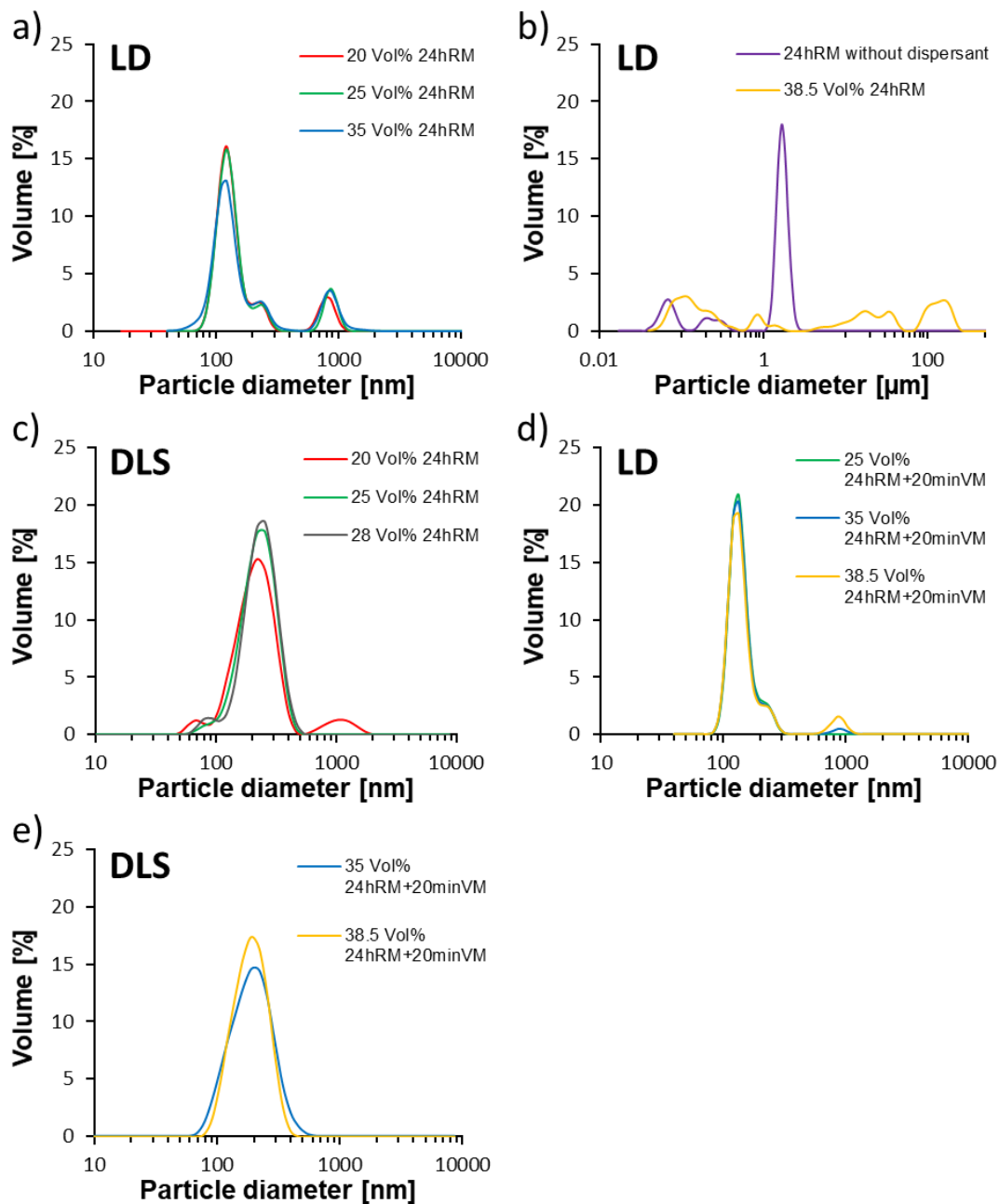


**Figure 108:** Volume based particle size distributions of  $\text{ZrO}_2$  particles in water dispersed by optimized dispersant amount (0.6 wt% (2.1 Vol%) of ammonium citrate dibasic) and roll milling for 24 hours or a combination of vibration milling (20 minutes) and roll milling (24 hours) and determined by **a), b), d)** laser diffraction (LD) and **c), e)** dynamic light scattering (DLS).



**Figure 108** summarizes volume based particle size distributions of  $\text{ZrO}_2$  nanoparticles in water. The used dispersant amount of ammonium citrate dibasic was 0.6 wt%. Laser diffraction and dynamic light scattering confirmed agglomerations up to  $2\ \mu\text{m}$  for different solid loadings when using only roll milling for 24 hours as dispersing method (**Figure 108a and c**). However, the sizes decreased by far when comparing to roll milling without a dispersant and when a too high solid loading of 38.5 Vol% was chosen (**Figure 108b**) due to a strongly increased viscosity. Since the attractive van der Waals forces have more impact on the small nano particles due to decreasing gravitation forces, these particles require an intensive dispersing step with a higher energy input. In the case of the bigger particles, gravity forces ease the dispersing [28]. An additional vibration milling step for 20 min before roll milling shifted particles sizes to smaller sizes and destroyed bigger agglomerates, which was attributed to the higher energy input (**Figure 108d, e**). Furthermore, this enabled the dispersion of suspensions with a high solid loading of 38.5 Vol%. The lowest particles sizes with the characteristic values of  $d_{10}$ ,  $d_{50}$  and  $d_{90}$  of 103.9, 129.0 and 190.3 nm according to laser diffraction and of 104.7, 176.9 and 283.7 nm according to dynamic light scattering were measured for a solid load of 35 Vol% close to the BET average particle size of 74.2 nm.

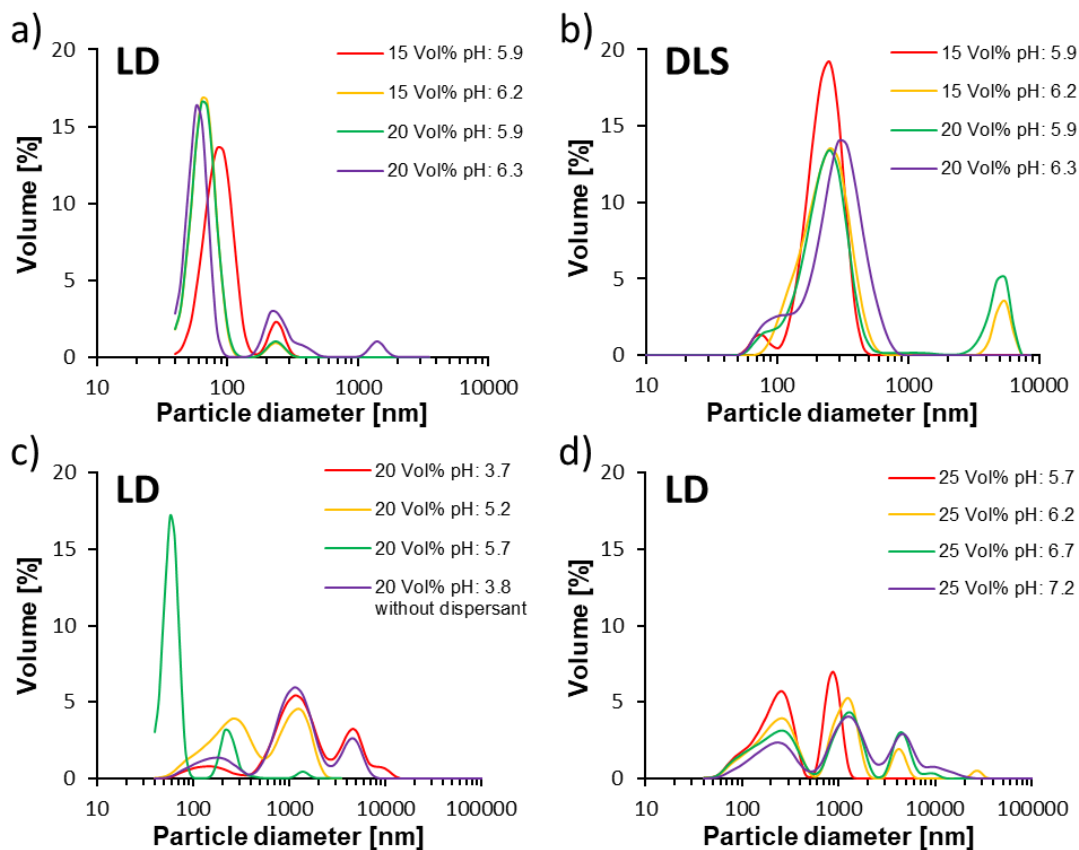


**Figure 109:** Volume based particle size distributions of  $\text{WO}_3$  particles in water by optimized dispersant amount (0.2 wt% (0.9 Vol%) of ammonium citrate dibasic) dispersed by roll milling for 24 hours and determined by **a), c), d)** laser diffraction (LD) and **b)** dynamic light scattering (DLS).

To achieve a proper dispersion was not straight forward in the case of the  $\text{WO}_3$  particles (**Figure 109**). Without adjusting the pH value, several agglomerations were measured at the initial pH values of 3.7 (0.2 wt% of ammonium citrate dibasic) and of 3.8 (no dispersant used) (**Figure 109c**), which could be due to complete deprotonation of citrate at pH values of 3.5 – 4. This impedes the exchange of hydroxyl groups with carboxylate ions on the particle surface and hinders a successful electrostatic stabilization. Furthermore, additional charges in the form of anions are not provided, but only neutral citric acid. Whereas the pH adjustment to 5.2 only decreased the sizes slightly, a promising refinement was seen for using a pH value of 5.7. Furthermore, a strong increase in the viscosity of the dispersions was observed, when ammonium citrate dibasic was used as a dispersant. However, the viscosity decreased again at higher pH values. This could be due to a change of a hydrophobic to a hydrophilic behavior of citrate on the particle surfaces in regards to the pH of the dispersion.

A pH-value adjustment by a diluted ammonium hydroxide solution slowly improved the distribution to smaller sizes. At a pH range of 5.9 – 6.3 almost agglomeration free dispersions are shown in **Figure 109a and b**. The characteristic values of d10, d50 and d90 of 59.1, 83.2 and 129.1 nm according to laser diffraction and of 138.9, 216.3 and 309.2 nm according to dynamic light scattering were achieved using a solid load of 15 Vol% and adjusting the pH to 5.9.

#### 4.2.4.2 Influence of spray drying process parameters

A detailed spray drying process parameter study was performed for the  $\text{ZrO}_2/\text{WO}_3$  granules. The influence of the parameters were evaluated for solid load of the slurry, slurry feed rate (pump rate), power output of the ultrasonic atomizer and the inlet temperature of the spraying chamber. The process parameters nozzle frequency and air flow rate within the spraying apparatus were kept constant at 60 kHz and 25 m<sup>3</sup>/h, respectively. The experiments were conducted by keeping three of the four variable parameters constant.

**Table 33 and Figure 110** summarize the influence of the process parameters on the properties and volume based particle size distribution of the spray-dried  $\text{ZrO}_2/\text{WO}_3$  granules. These impacts of the following process parameters will be discussed in details in the following:

- A. Solid load of slurry for spray drying
- B. Slurry pump rate (feed rate)
- C. Power output of ultrasonic nozzle
- D. Inlet temperature in spraying chamber

**Table 33:** Influence of **a)** solid load, **b)** pump rate, **c)** power output of ultrasonic nozzle and **d)** inlet temperature on properties of spray-dried  $\text{ZrO}_2/\text{WO}_3$  granules

a)

Solid load	12.5 Vol%	18 Vol%	23 Vol%
Apparent density in % of TD	30.8	30.0	30.9
Tapped density in % of TD	34.7	33.3	34.4
Hausner ratio	1.13	1.11	1.11
Yield in %	76.0	81.2	51.8
d10 in $\mu\text{m}$	15.4	16.8	18.4
d50 in $\mu\text{m}$	27.8	33.0	36.4
d90 in $\mu\text{m}$	42.9	50.6	52.9

b)

Pump rate	3%	4%	5%
Apparent density in % of TD	31.2	30.7	30.9
Tapped density in % of TD	34.7	34.1	34.4
Hausner ratio	1.11	1.11	1.11
Yield in %	50.8	57.8	51.8
d10 in $\mu\text{m}$	16.1	16.7	18.4
d50 in $\mu\text{m}$	29.8	32.2	36.4
d90 in $\mu\text{m}$	47.9	50.7	52.9

c)

Power ultrasonic nozzle	4 Watt	6 Watt	8 Watt	20 Watt
Apparent density in % of TD	31.2	30.2	29.9	N/A
Tapped density in % of TD	34.7	34.2	34.0	N/A
Hausner ratio	1.11	1.13	1.14	1.14
Yield in %	50.8	55.7	54.8	N/A
d10 in $\mu\text{m}$	16.1	16.1	15.5	13.1
d50 in $\mu\text{m}$	29.8	31.9	30.6	26.7
d90 in $\mu\text{m}$	47.9	50.3	49.1	50.3

d)

Temperature	150 °C	140 °C	130 °C
Apparent density in % of TD	31.0	31.2	29.9
Tapped density in % of TD	34.0	34.7	33.6
Hausner ratio	1.10	1.11	1.12
Yield in %	43.2	50.8	N/A
d10 in $\mu\text{m}$	16.0	16.1	16.9
d50 in $\mu\text{m}$	30.8	29.8	32.6
d90 in $\mu\text{m}$	50.0	47.9	51.0

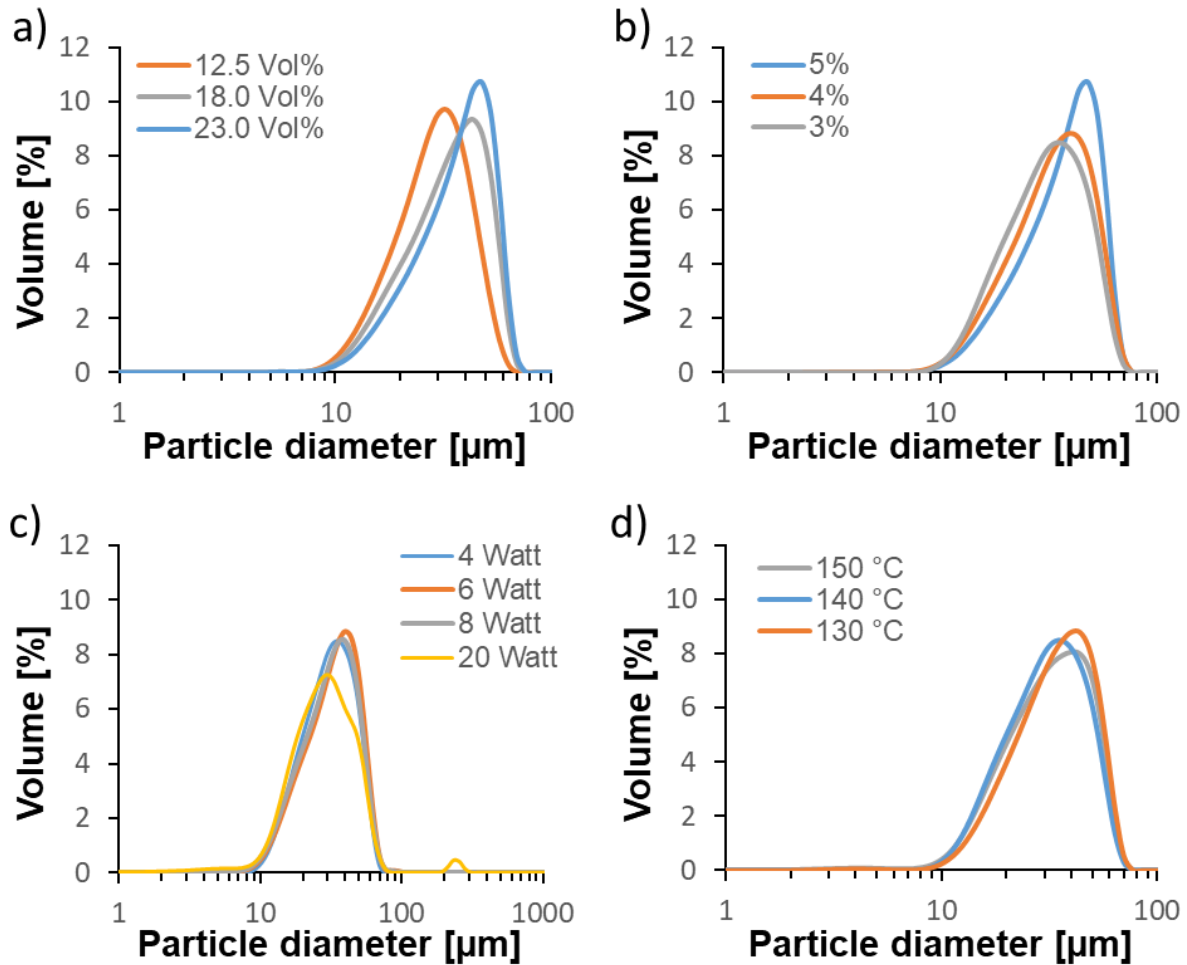


**Figure 110:** Influence of **a)** solid load, **b)** pump rate, **c)** power output of ultrasonic nozzle and **d)** inlet temperature on volume based particle size distribution of spray-dried  $\text{ZrO}_2/\text{WO}_3$  granules determined by laser diffraction (LD).

#### A. Influence of solid load

The inlet temperature, ultrasonic power output and pump rate were fixed at 140 °C, 4W and 5% for these experiments. A steady increase of the granule size by increasing the solid load used for the slurry for spray drying was observed (**Figure 110a**). The characteristic values of  $d_{10}$ ,  $d_{50}$  and  $d_{90}$  increased from 15.4, 27.8 and 42.9  $\mu\text{m}$  for a solid load of 12.5 Vol% up to 18.4, 36.4 and 52.9  $\mu\text{m}$  for a solid load of 23.0 Vol%. The droplets created by the atomizer contain more solid content and thus, bigger granules are formed. This was also seen by Walker et al. [111].

**Figure 111** illustrates the  $\text{ZrO}_2/\text{WO}_3$  granules spray-dried with different solid loads. The granules have a high sphericity with a homogeneous surface. Big differences are not visible between the granules made from the different solid loads. Granules with a hollow cores and a donut shape were not spray-dried. The solid load of 23 Vol% was evaluated as the most suitable, since

it combined a high apparent and tapped density with the lowest Hausner ratio. Even so the tapped density was the same for spray drying with a solid load of 12.5 Vol% (34.7% compared to 34.4% of the theoretical density), the flowability was poorer for this solid load (Hausner ratio of 1.13 compared to 1.11). However, the yield of 51.8 % was lower for a solid load of 23 Vol% than for 12.5 and 18 Vol% due to a higher viscosity and therefore, a stronger unwanted dropping effect from the nozzle.

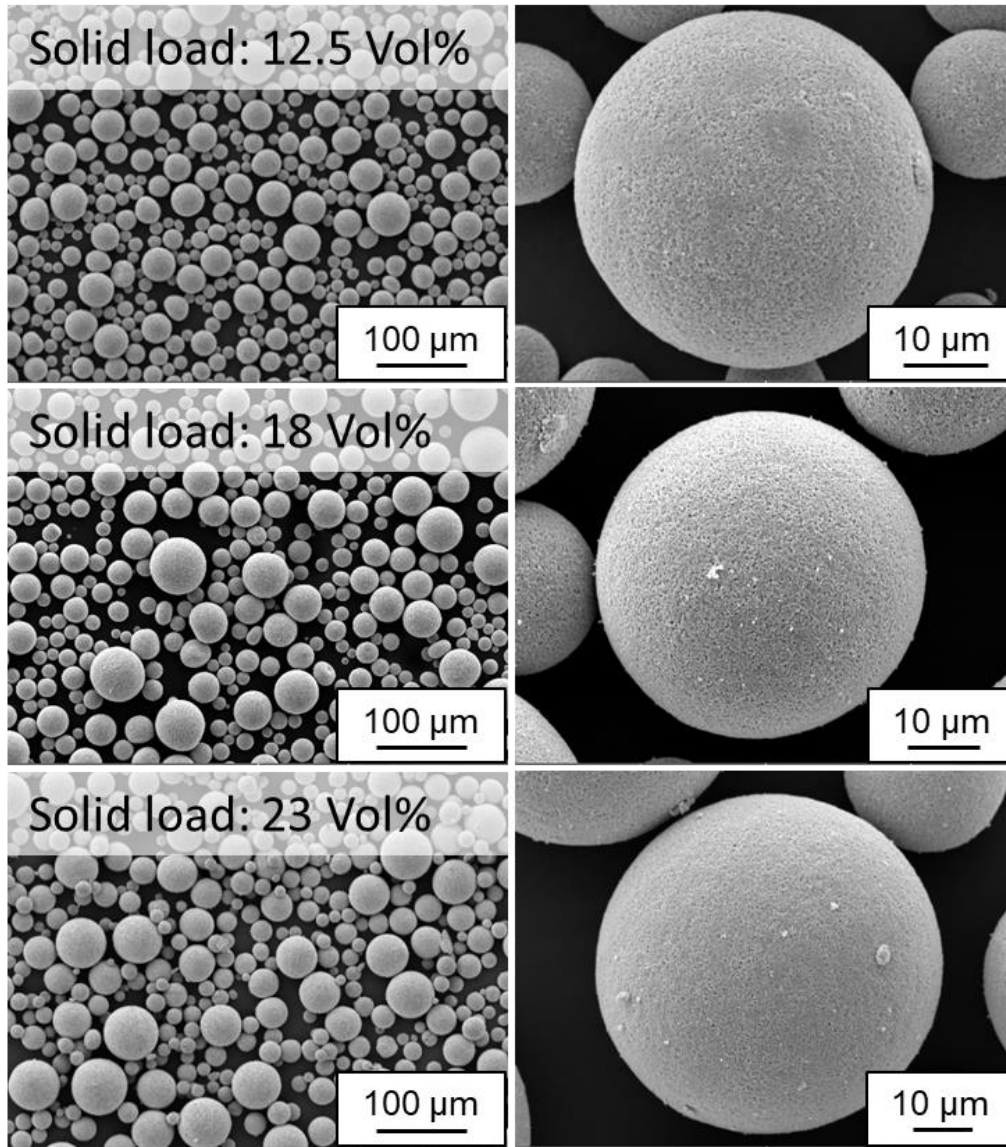


**Figure 111:** SEM images of  $\text{ZrO}_2/\text{WO}_3$  granules spray-dried with different solid loads.

#### B. Influence of slurry pump rate

**Figure 112** shows the relation of the controllable pump rate to the actual slurry feed flow during spray drying. The feed flow was estimated by weighing and recalculating the volume (using the absolute densities of the slurry ingredients) of the slurry amount, which was pumped for one

minute. The feed flow was evaluated for water and a  $\text{ZrO}_2/\text{WO}_3$  dispersion (solid load 23 Vol%) and compared to the values for water stated by Büchi in the operation manual of the Mini spray-dryer B-290. The measured flow rates in this work were significantly smaller than claimed by Büchi (differences of 22.4% - 29.5% depending from pump rate and liquid medium). The evaluated values in this work were slightly higher for water (3%: 0.681 ml/min; 4%: 0.902 ml/min; 5%: 1.118 ml/min) than for the  $\text{ZrO}_2/\text{WO}_3$  dispersion (3%: 0.705 ml/min; 4%: 0.953 ml/min; 5%: 1.207 ml/min) and the differences between the values became slowly bigger for higher pump rates. This follows from the higher viscosity of the nanoparticle dispersion compared to water, which generates in addition an aggravated feed flow for bigger pump rates.

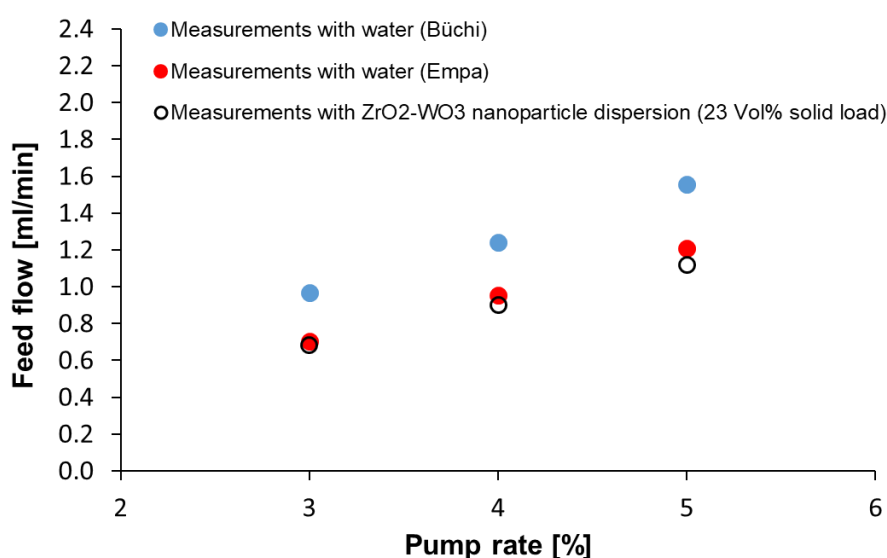


*Figure 112: Correlation of pump rate to actual slurry feed flow during spray drying.*

The inlet temperature, ultrasonic power output and solid load were fixed as 140 °C, 4W and 23 Vol% to evaluate the influence of the pump rate on the granule sizes and properties (**Table 33b and Figure 110b**). A steady increase of the granule size was seen by increasing the pump rate as already seen for increasing the solid load. The characteristic values of  $d_{10}$ ,  $d_{50}$  and  $d_{90}$  increased from 16.1, 29.8 and 47.9  $\mu\text{m}$  for a pump rate of 3% up to 18.4, 36.4 and 52.9  $\mu\text{m}$  for pump rate of 5%. When more slurry is present at the ultrasonic nozzle tip, the volume of the formed droplets can be bigger and in consequence, bigger granules are formed by evaporation of the solvent. This increase was also reported by Cao et al. [113]. The yield of spray drying was for all three pump rates in a comparable range of 50.8 – 57.8 %. The same Hausner ratio for all three granules implied the same flowability for the different granules. However, the highest apparent and tapped density (31.2% and 34.7% of the theoretical density) were measured for a pump rate of 3%.



### C. Influence of power output of ultrasonic nozzle

The inlet temperature, pump rate and solid load were fixed as 140 °C, 3% and 23 Vol% for these experiments. **Figure 113** illustrates the  $\text{ZrO}_2/\text{WO}_3$  granules spray-dried with a different ultrasonic power output. The sphericity of the granules decreases with the increase of the nozzle power output. While there are almost no differences visible for the use of 6W and only some slightly elongated granules appear for the use of 8 W (compared to 4W), several broken and malformed granules with a non-uniform appearance were seen for 20W. This loss of the sphericity led to a decrease of the flowability (decrease of Hausner ratio) and in consequence, a strong decrease of the apparent density (31.2% compared to 29.9% of the theoretical density) (**Table 33c**). Furthermore, a decrease of the tapped density was noticed. Whereas the yield for 4, 6 and 8 W was in a comparable range of 50.8 – 55.7 %, a very small yield was achieved by using a ultrasonic power output of 20 W. A severe nozzle heating and strong pollution of the spray drying chamber walls were the reasons, why not enough granules were available to measure the yield, the apparent and the tapped density. The characteristic values of  $d_{10}$ ,  $d_{50}$  and  $d_{90}$  increased first from 4 to 6 W and afterwards decreased again for 8 and 20 W. However, agglomerations were also generated by using an ultrasonic power of 20 W (small peak between 200 and 300  $\mu\text{m}$  in **Figure 110c**). These agglomerations are most probably the non-uniform granule satellites seen already in **Figure 113**.

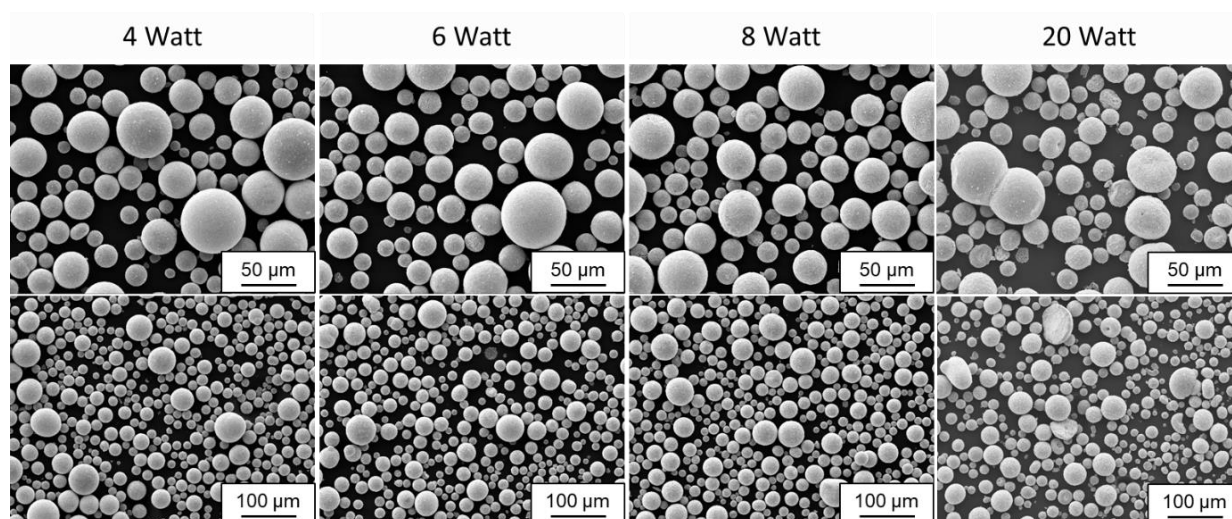


**Figure 113:** SEM images of  $\text{ZrO}_2/\text{WO}_3$  granules spray-dried with a different ultrasonic power output.

### D. Influence of inlet temperature

The ultrasonic power output, pump rate and solid load were fixed as 4W, 3% and 23 Vol% for these experiments. An inlet temperature of 140 °C was found as most favorable for apparent



and tapped density of the granules (31.2% and 34.7% of the theoretical density). Furthermore, a good flowability (Hausner ratio of 1.11) and the highest yield (50.8 %) was given for these granules. A clear trend for the volume based size distribution (**Figure 110d**) and the characteristic values of d10, d50 and d90 (**Table 33d**) was not identifiable in respect to the change of the inlet temperature. In contrary, Cao et al reported an increase of the granule size with an increasing drying temperature due to a lower surface tension of the droplet and a larger droplet ballooning [113]. However, they reported also that drying temperature is less effective on granule size than feeding rate and feeding pressure [113].

#### 4.2.4.3 Preparation of final powders for laser powder bed fusion

The process parameters for spray drying chosen to produce the final granules for laser powder bed fusion were a ultrasonic power output of 4 W, a pump rate of 3%, a solid load of 23 Vol% and an inlet temperature of 140 °C based on the findings explained in chapter 4.2.4.2.

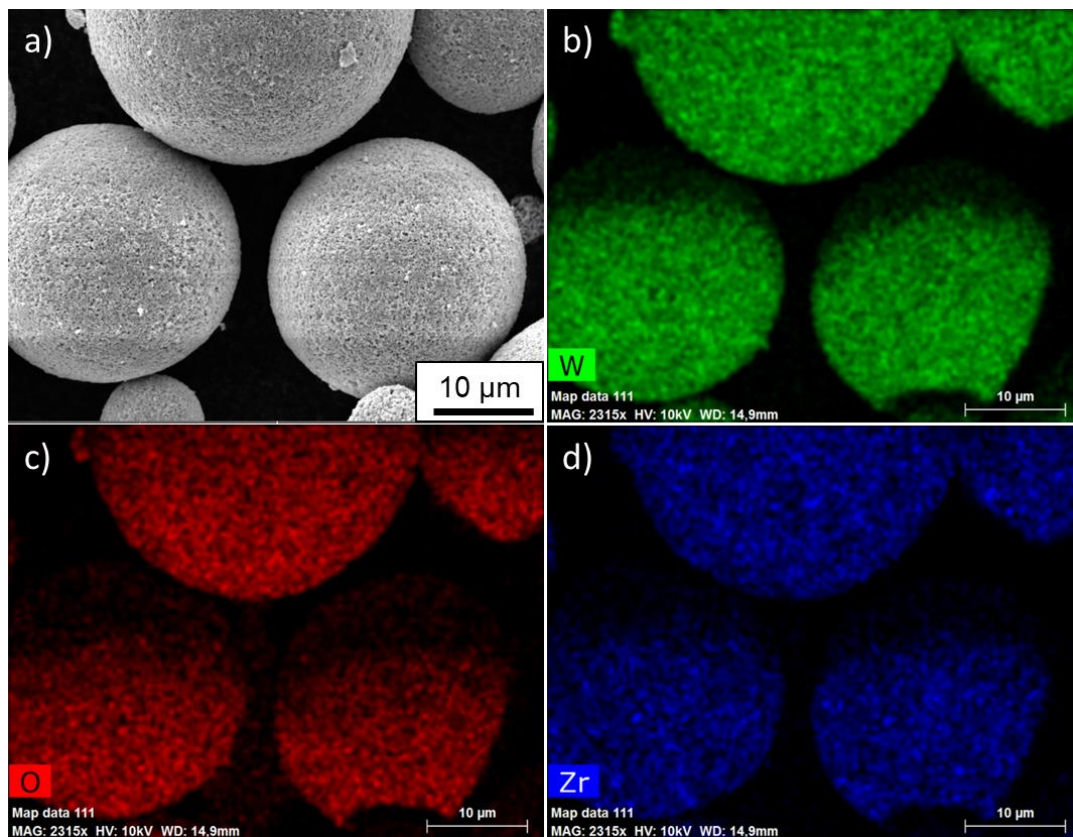


**Figure 114:** a) SEM image and b), c), d) corresponding element distributions of W, O and Zr examined by energy-dispersive X-ray spectroscopy of  $\text{ZrO}_2/\text{WO}_3$  granules

**Figure 114** shows the element distribution within  $\text{ZrO}_2/\text{WO}_3$  granules determined by energy-dispersive X-ray spectroscopy. The elements tungsten, oxygen and zirconium are uniform distributed within the granules. This indicates a homogeneous distribution of the  $\text{WO}_3$  and  $\text{ZrO}_2$

particles. The automatically calculated content of  $\text{ZrO}_2$  and  $\text{WO}_3$  was 22.1 wt% and 77.9 wt%, respectively, which is close to the desired eutectic ratio of 20 wt%  $\text{ZrO}_2$  to 80 wt%  $\text{WO}_3$  (23.6/76.4 Vol%).

Two different ratios of aluminum oxide powder to  $\text{ZrO}_2/\text{WO}_3$  granules were chosen in this work. Applying the Turner model, an optimized ratio of 96.9/3.1 Vol% of  $\text{ZrW}_2\text{O}_8$  to  $\text{Al}_2\text{O}_3$  ( $\text{CTE} = 5.2 \times 10^{-8} \text{ 1/K}$ ) was calculated. Furthermore, the ratio of 50 Vol%  $\text{Al}_2\text{O}_3$  and 50 Vol%  $\text{ZrO}_2/\text{WO}_3$  granules was evaluated in this work. The coarse aluminum oxide AA18 was chosen as raw powder, since it should not melt or react with the  $\text{ZrO}_2$  or  $\text{WO}_3$  due to the big size and therefore, formation of e.g.  $\text{Al}_2\text{W}_3\text{O}_{12}$ ,  $\text{AlWO}_4$  or other unwanted phases should be avoided. The different contents of coarse alumina AA18 could be homogeneously distributed within the  $\text{ZrO}_2/\text{WO}_3$  granules (**Figure 115a, b**). Furthermore, the granules were not destroyed during the mixing process.

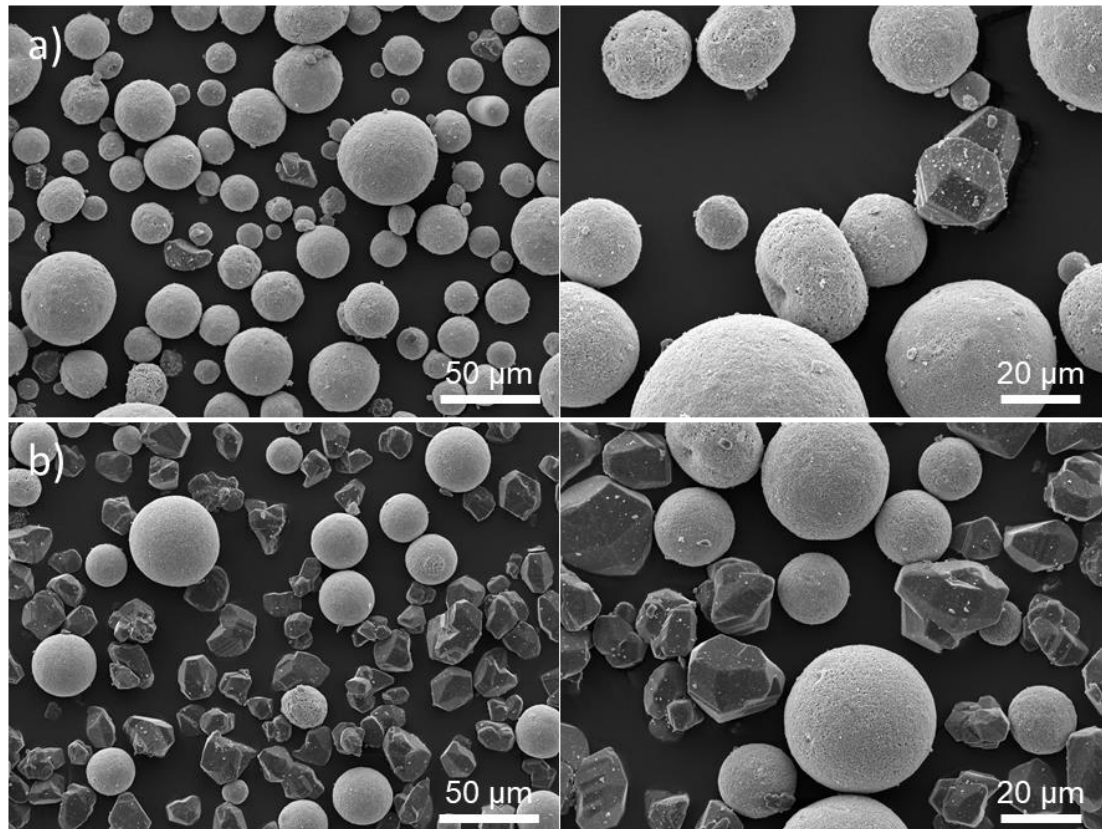


**Figure 115:** SEM images of  $\text{ZrO}_2/\text{WO}_3$  granules mixed with **a)** 3.1 Vol% and **b)** 50 Vol% coarse aluminum oxide AA18.

**Table 34** summarizes the properties of the powders used for laser processing. Apparent and tapped density first slightly decreased with the addition of the 3.1 Vol% coarse alumina and then strongly increased again after adding 50 Vol% coarse alumina (apparent and tapped density of pure granules are 31.2 and 34.7 % of TD). In contrary, the Hausner ratio of the powders

increased by increasing the amount of coarse aluminum oxide, which indicates a flowability worsening. A similar behavior was also seen by the mixing of bimodal  $\text{Fe}_2\text{O}_3$  doped  $\text{Al}_2\text{O}_3$  granules with the coarse aluminum oxide AA18 (chapter 3.2.6). The higher values of the Hausner ratio can be attributed to the more irregular size distribution, since adding of the alumina with minor particle sizes increases the portion of 10 - 30  $\mu\text{m}$ , as seen for the characteristic values of d10, d50 and d90 of the mixed powders. This more uneven size distribution impairs the flow behavior. This impaired flowability hinders a direct effect of density increase of the homogenously mixed AA18 with a high packing density for a small addition amount of 3.1 Vol%. However, the decreased flowability does not have such a big impact for an addition of 50 Vol% AA18 and the homogeneously distributed AA18 increases the apparent and tapped density in this case.

**Table 34:** Properties of powders used for laser processing containing coarse alumina AA18 and spray dried  $\text{ZrO}_2/\text{WO}_3$  granules.

Composition	96.9 Vol% granules + 3.1 Vol% alumina AA18	50 Vol% granules + 50 Vol% alumina AA18
Apparent density in % of TD	30.6	38.3
Tapped density in % of TD	34.4	44.3
Hausner ratio	1.13	1.16
d10 in $\mu\text{m}$	16.8	11.6
d50 in $\mu\text{m}$	33.5	21.0
d90 in $\mu\text{m}$	53.0	42.2

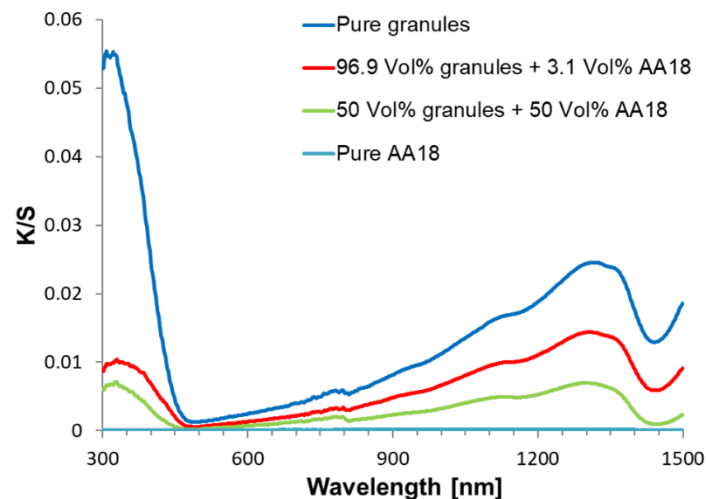


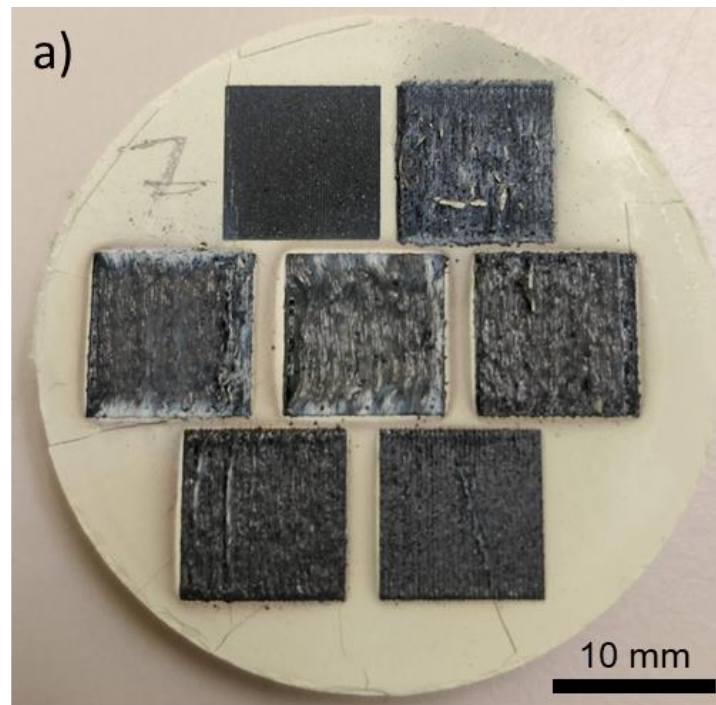
**Figure 116:** Qualitative absorption spectrum evaluated by the Kubelka Munk method of pure granules, granules mixed with coarse aluminum oxide and pure coarse aluminum oxide AA18.

The absorptance of the granules at room temperature was evaluated by the Kubelka Munk method (**Figure 116**). The qualitative absorption showed the highest absorption for the pure  $\text{ZrO}_2/\text{WO}_3$  granules. The K/S ratio decreased over the completely measured wavelengths (300

- 1500 nm) for the addition of coarse aluminum oxide AA18. Furthermore, an increased absorptance was measured at the featured wavelength of the used continuous wave IR fiber laser (1070 nm). Using this laser all presented powders could be processed, except of pure AA18.

#### 4.2.4.4 Laser manufacturing of layers and parts

**Figure 117a** shows uniaxial pressed cylindrical substrates containing pure  $\text{ZrO}_2/\text{WO}_3$  granules. Prior to PBF-LB, layers were directly consolidated by the IR laser on the top surface of these uniaxial pressed cylindrical substrates containing pure  $\text{ZrO}_2/\text{WO}_3$  granules to evaluate the influence of the laser parameters on the  $\text{ZrW}_2\text{O}_8$  formation by diffraction measurements.



b)

Zirconia – Tungsten Oxide					
Power [W]	hatch distance [μm]	laser speed [mm/s]	Power/speed [J/mm]	Energy density [J/mm <sup>2</sup> ]	Zr(WO <sub>4</sub> ) <sub>2</sub>
200	100	3000	0.067	0.87	no
200	100	2000	0.100	1.30	no
200	100	1500	0.130	1.73	no
30	100	450	0.067	0.87	yes
15	150	25	0.600	7.79	yes
7.6	150	25	0.304	3.95	yes

**Figure 117:** a) Laser consolidated layers on uniaxial pressed cylindrical substrates containing pure  $\text{ZrO}_2/\text{WO}_3$  granules. b) Evaluation of  $\text{Zr(WO}_4)_2$  phase after laser processing of  $\text{ZrO}_2/\text{WO}_3$  substrates with different power, hatch distance, laser speed.



X-ray diffraction measurements confirmed a  $\text{ZrW}_2\text{O}_8$  phase formation of this phase in various amounts for selected laser processing parameters (**Figure 117b**). It was observed that a low power to speed ratio as well as higher energy densities due to a low laser speed or power result in a preferred  $\text{ZrW}_2\text{O}_8$  formation by laser processing. This leads to the conclusion that low cooling rates are favorable for the formation of this negative thermal expansion phase. Similar to these results, Liang et al. reported also a formation of  $\text{ZrW}_2\text{O}_8$  for low speeds [224]. However, a  $\text{CO}_2$  laser was used for those experiments and therefore, a different laser absorption of the  $\text{ZrO}_2$  and  $\text{WO}_3$  starting material was given. Furthermore, higher laser powers of 400-800W, lower laser scan speeds of 1-5 mm/s and a bigger laser spot size of 10.4 mm were applied. Thus, the power/speed ratios (80 - 800 J/mm) and energy densities (7.69 – 76.92 J/mm<sup>2</sup>) of laser processing were both in a higher range. This fits with the observation of this PhD study that high energy densities are favorable for a  $\text{ZrW}_2\text{O}_8$  formation by laser processing, but it does not fit with the observation that the power to speed ratios should be low. Laser scanning speeds below 2 mm/s gave the cubic structure ( $\alpha$  phase). With laser scan speed of 2 mm/s or above, an orthorhombic structure ( $\gamma$  phase) was produced.

**Figure 118** shows optical microscope and SEM images of cross-sections (view of build direction) of laser-manufactured parts produced with powders containing 50 Vol% coarse alumina AA18 and 50 Vol%  $\text{ZrO}_2/\text{WO}_3$  granules. The shape of the parts had a high accuracy of the lateral areas as well as the top surface. The parts offered a high part density of 95.7% with a low amount of micron-sized circular pores, which confirms a suitable absorptance of the powders at the wavelength (1070 nm) of the used IR laser (power: 30 W, scan speed: 70 mm/s). Laser-induced cracks were hardly visible in the internal structure of these cross sections. Furthermore, the microstructure contained different lamellar structures after laser processing (**Figure 118d-f**). These structures were also seen by other researchers in material systems with more components. Zhang et al. [65] and Zheng et al. [11] noticed that lamellar structures were generated along the build direction by thermal capillary convection, influenced by Marangoni effect, streak convection and flowing Bénard cells. Liu et al. [53] obtained different eutectic structures with rod-like eutectic structures and lamellar structures using a ternary eutectic starting material.

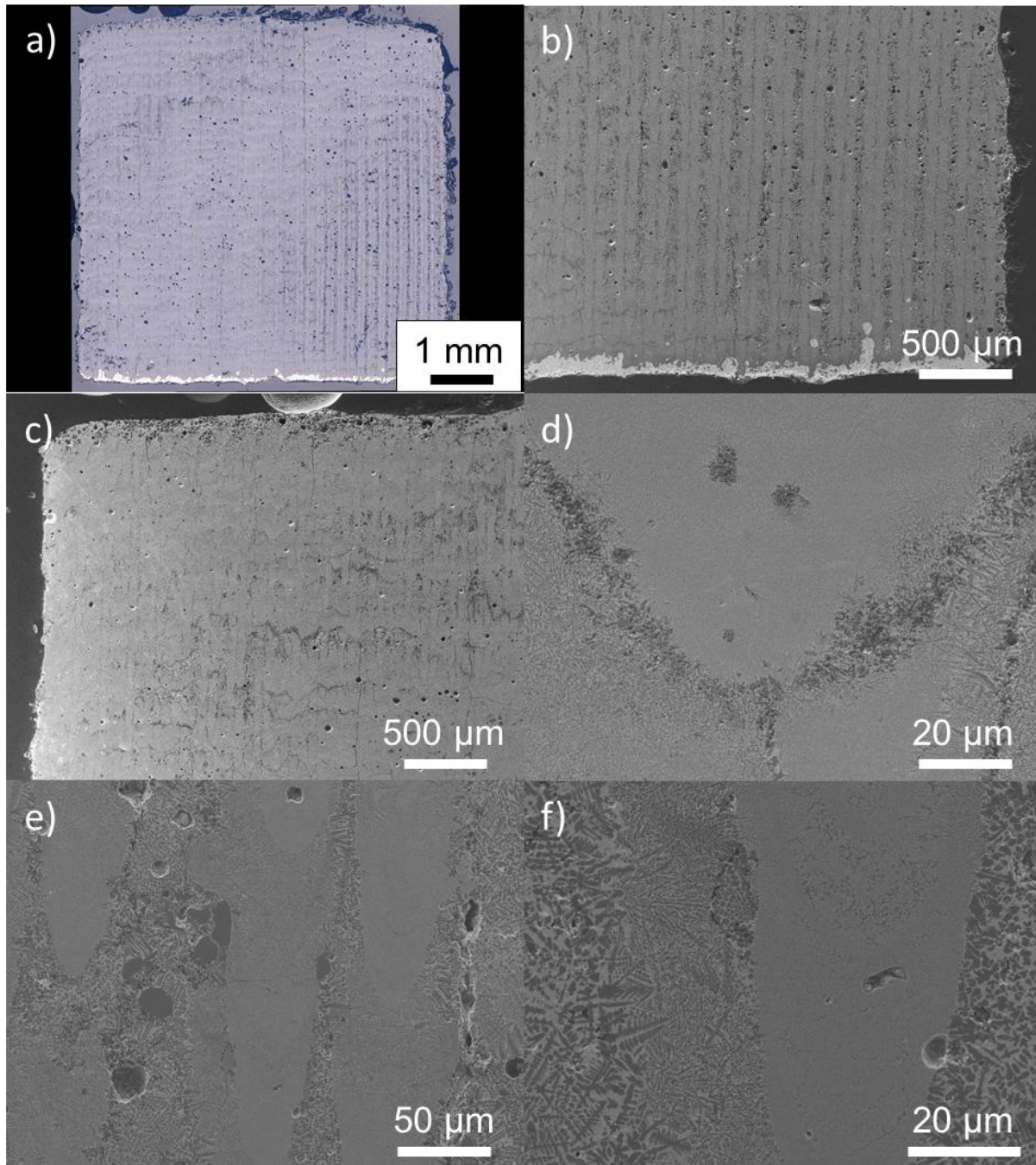


**Figure 118:** *a)* Optical microscope and *b-f)* SEM images of cross-sections (view of build direction) of laser-manufactured parts produced with powders containing 50 Vol% coarse alumina AA18 and 50 Vol% spray dried  $\text{ZrO}_2/\text{WO}_3$  granules.

**Figure 119** shows the top view cross-sections of the same samples presented in **Figure 119**. A small amount of laser-induced cracks was visible in these images. The cross-sections reveal uniform consolidated laser scanning tracks of ca. 50  $\mu\text{m}$ , which are by far smaller than the used laser spot size of 90  $\mu\text{m}$  (**Figure 119b-d**). These scanning tracks are surrounded by squares consisting of the already described lamellar structure. The origin of this special and unique microstructure could be due to the temperature differences within the melt pool, where the

higher temperatures are located in the center of the laser spot. This was already calculated by Florio using the finite volume method [251]. The bright and dark phases within the lamellar structure were further analyzed by energy-dispersive X-ray spectroscopy (**Figure 119e, f**). The Element distributions within the dark phase (position 1) points strongly to an aluminum oxide phase. This phase could be an unmolten AA18 particle considering the size of ca. 20  $\mu\text{m}$ . The surrounding bright phase (position 2) contains a high amount of Zr, W and O and could be an in-situ during laser processing formed  $\text{ZrW}_2\text{O}_8$  phase.

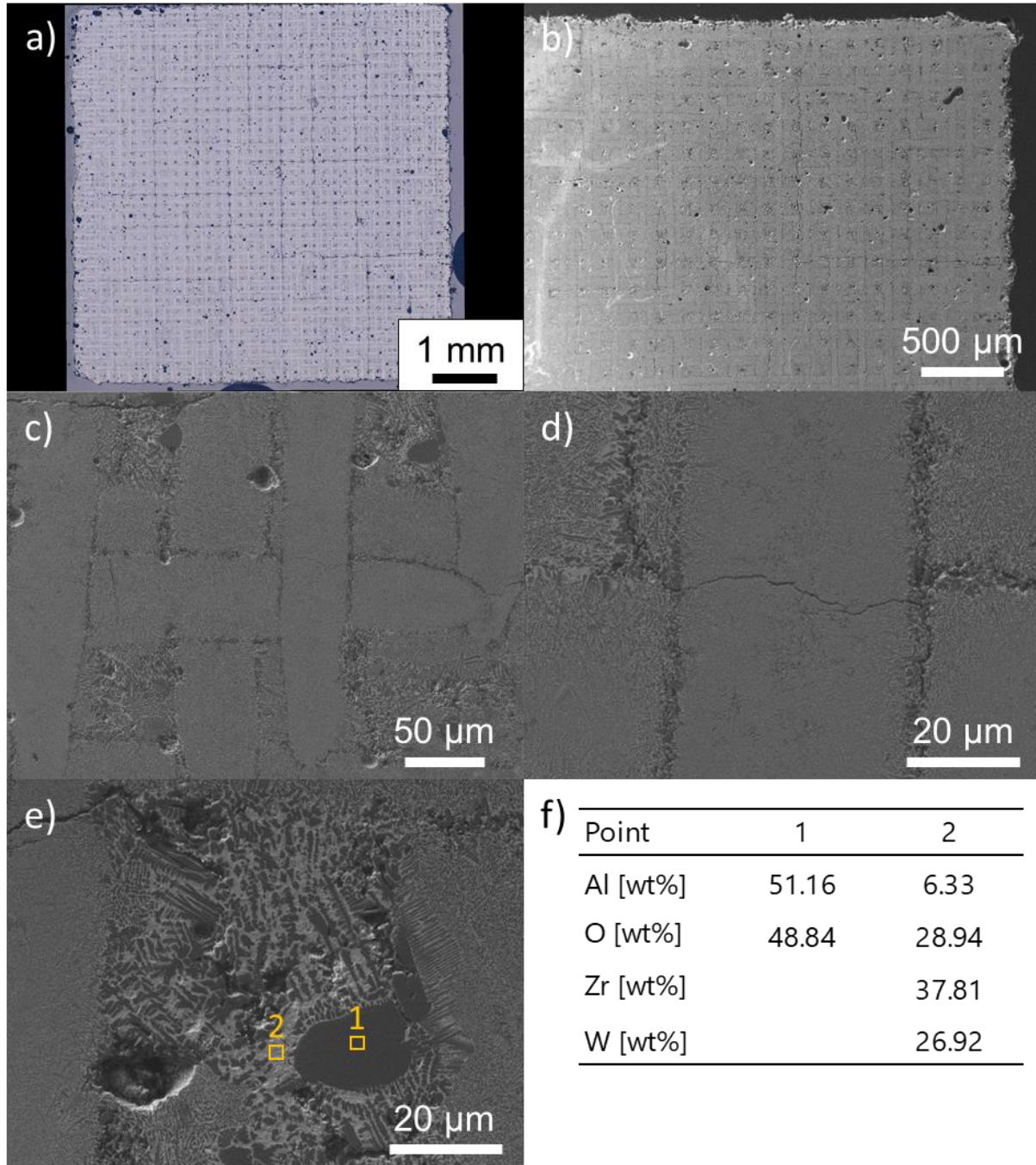


**Figure 119:** a) Optical microscope and b-e) SEM images of cross-sections (top view) of laser-manufactured parts produced with powders containing 50 Vol% coarse alumina AA18 and 50 Vol% spray dried  $\text{ZrO}_2/\text{WO}_3$  granules. f) Element content of evaluated position (marked in orange) in Figure 119e.



**Figure 120** shows laser-manufactured parts produced with powders containing 3.1 Vol% coarse alumina AA18 and 96.9 Vol% spray dried  $\text{ZrO}_2/\text{WO}_3$  granules (laser power of 15 W and scan speed of 30 mm/s). The shape of the parts shows a low accuracy of the lateral areas and the top surfaces (**Figure 120a**). A further adjustment of the laser parameters could help in this case, since many sparks were observed during laser processing. The part density measured in accordance to the Archimedes principle was 95.7%. Laser-induced cracks were not visible in low magnifications of the microstructure (**Figure 120b and c**). Only higher magnifications revealed very few cracks.

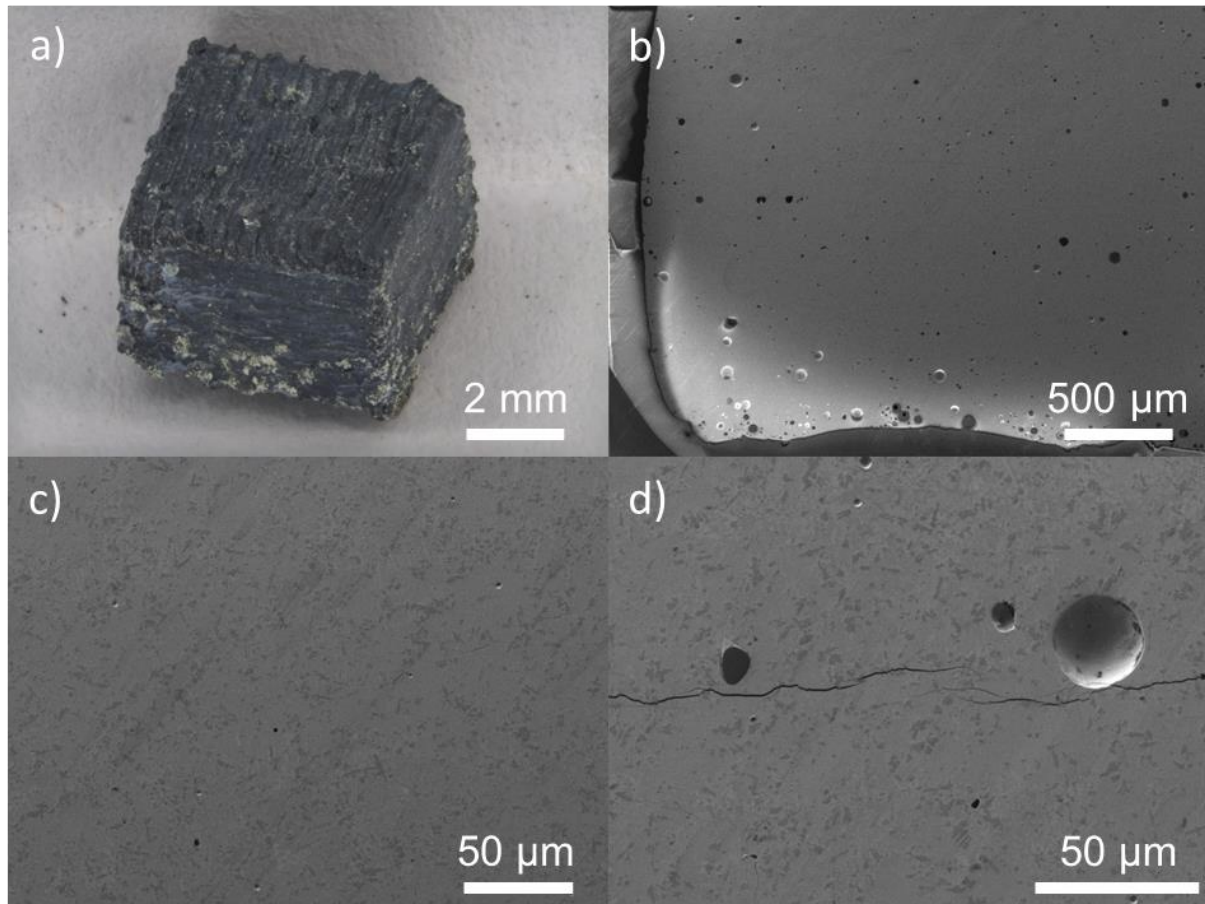


**Figure 120:** **a)** Shape imaged by optical microscopy and **a-d)** SEM images of cross-sections (top view) of laser-manufactured parts produced with powders containing 3.1 Vol% coarse alumina AA18 and 96.9 Vol% spray dried  $\text{ZrO}_2/\text{WO}_3$  granules

These observations point to the generation of zirconium tungstate ( $\text{ZrW}_2\text{O}_8$ ) during laser processing by rapid cooling. Furthermore, the rapid quenching prevented a decomposition of  $\text{ZrW}_2\text{O}_8$  into  $\text{WO}_3$  and  $\text{ZrO}_2$  [205, 206]. Thermal stresses during rapid cooling were minimized due to the negative thermal expansion of this phase [204, 205], which expands during cooling and generates compressive stresses. A resultant thermal expansion in the oxide ceramic close to near zero would be most beneficial in this case. The optimized calculated ratio of 96.9/3.1

Vol% of  $\text{ZrW}_2\text{O}_8/\text{Al}_2\text{O}_3$  according to the Turner model ( $\text{CTE} = 5.2 \times 10^{-8} \text{ 1/K}$ ) led to the lowest amount of cracks in this work, as suggested by Romao et al. [213].

### 4.3 Mechanical properties of laser processed parts

**Table 35** and **Figure 121** summarize the compressive strength values and corresponding standard deviations of laser-manufactured parts produced with specially developed powders for crack reduction in aluminum oxide. Furthermore, the achieved values are compared to the compressive strength values of laser processed parts made from  $\text{Fe}_2\text{O}_3$  or  $\text{MnO}_2/\text{Mn}_2\text{O}_3$  doped aluminum oxide granules (chapter 3).

**Table 35:** Compressive strength and standard deviations of laser-manufactured parts produced with powders containing a different additive content to aluminum oxide.

Additive content	Compressive strength [MPa]	Standard deviation
0.6 Vol% $\text{Fe}_2\text{O}_3$	219.3	45.7
50 Vol% $\text{ZrO}_2/\text{WO}_3$	498.9	89.3
96.9 Vol% $\text{ZrO}_2/\text{WO}_3$	327.9	52.1
50 Mol% $\text{TiO}_{2-x}$	346.6	47.9
10 Vol% $\text{TiO}_{2-x}$	138.0	31.2

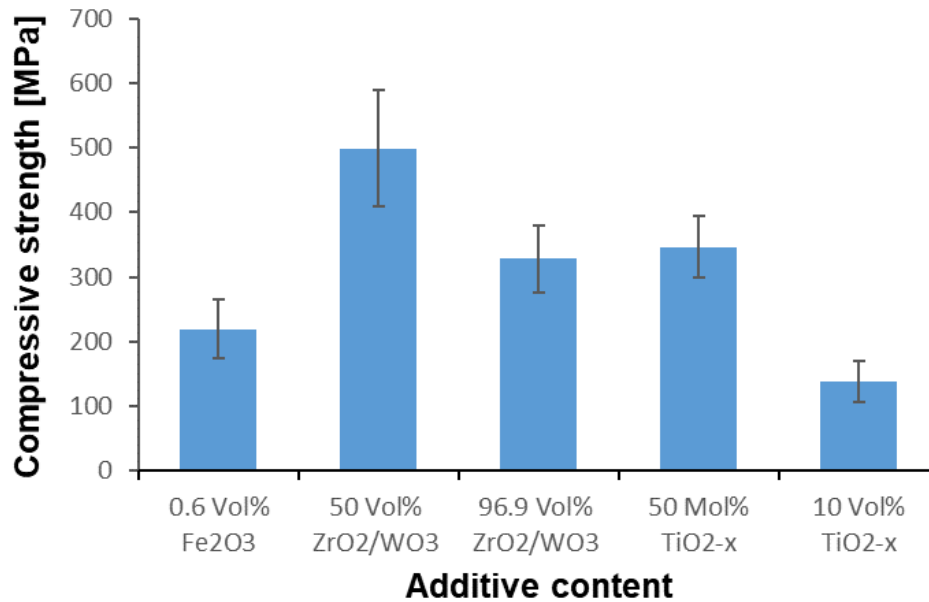


**Figure 121:** Compressive strength of laser-manufactured parts produced with powders containing a different additive content to aluminum oxide.

The highest compressive strength of  $498.9 \pm 89.3 \text{ MPa}$  was achieved by using powders consisting of 50 Vol% spray-dried  $\text{ZrO}_2/\text{WO}_3$  granules and 50 Vol% aluminum oxide AA18. The

compressive strength was higher than for the powder mixture of 96.9 Vol%  $\text{ZrO}_2/\text{WO}_3$  granules and 3.1 Vol% aluminum oxide AA18, despite possessing more cracks after laser processing. This low compressive strength is a consequence of the higher amount of the  $\text{ZrW}_2\text{O}_8$  phase with a low mechanical strength. De Buysser et al. measured already for pure  $\text{ZrW}_2\text{O}_8$  a 3-point bending strength of only 14 MPa [209]. However, these parts showed still an improved compressive strength than laser-processed parts made from  $\text{Fe}_2\text{O}_3$  or  $\text{MnO}_2/\text{Mn}_2\text{O}_3$  doped aluminum oxide granules. The highest compressive strength of laser processed parts using powders with a fixed manganese oxide amount of 2 Vol% was only  $191.0 \pm 42.3$  MPa (chapter 3.3.3). Parts made with a doping amount of 0.6 Vol% iron oxide gave a slightly higher compressive strength of  $219.3 \pm 45.7$  MPa. Florio et al. tested the mechanical strength of laser manufactured samples made from these iron oxide doped aluminum oxide granules by B3B method [17]. The achieved average bi-axial flexural strength was 25 MPa.

Laser processing with powders containing 10 Vol% and 50 Mol% of reduced titanium oxide gave parts with compressive strength values of  $138.0 \pm 31.2$  MPa and  $346.6 \pm 47.9$  MPa, respectively. The reduction of crack formation due to the in-situ formation of aluminum titanate has also a great impact on the strength improvement. The strength of the parts increases with the amount of used titanium oxide additive and therefore, with a higher amount of formed aluminum titanate, even so having a low compressive strength. The compressive strength of pure aluminum titanate parts was reported as only 200 MPa [274].

Compressive stresses of traditional processed aluminum oxide parts can be more than 4000 MPa [257] (depending on the used grain size, purity of the raw material and the production method). Severe crack formation due to thermal stresses during the rapid cooling in laser processing reduces this strength. The addition of titanium oxide as well as the combination of zirconia and tungsten oxide to in-situ form ternary oxides was shown in this work as effective way to reduce the crack formation. However, these ternary oxides offer in general a lower strength than aluminum oxide, which reduces the final strength of the parts. Comparable compressive strength values of laser-manufactured parts were found in Exner et al. [7, 61]. A compressive strength of 800 MPa directly after laser processing and of 1150 MPa after annealing was achieved using glass-ceramic composite materials. The low thermal expansion coefficient of partly molten amorphous silica leads to avoidance of crack formation [99]. However, these parts were also limited to the strength of the glass phase.

The measured Young's moduli of the parts made from powders containing 10 Vol% and 50 Mol% of reduced titanium oxide were 21.4 and 90.2 GPa, respectively. These low Young's

moduli follow due to the appearance of  $\text{Al}_2\text{TiO}_5$  with a Young's modulus of only 14 GPa [184], which is by far lower than the Young's modulus of  $\text{Al}_2\text{O}_3$  (410 GPa) [48]. Contrary to the expected values, the parts made with powder combination C showed a higher Young's modulus than the parts processed with powders combination B, despite having a higher phase content of aluminum titanate. This can be explained by the higher amount of porosity [48] and apparent cracks in the microstructure [275, 276], which strongly reduce the Young's modulus.

In addition, a low Young's modulus of 99.7 GPa was also achieved by using powders consisting of 50 Vol% spray-dried  $\text{ZrO}_2/\text{WO}_3$  granules and 50 Vol% aluminum oxide AA18. This Young's modulus was unexpected higher than the 51.3 GPa for the powder mixture of 96.9 Vol%  $\text{ZrO}_2/\text{WO}_3$  granules and 3.1 Vol% aluminum oxide, despite containing a slightly higher crack amount in the PBF-LB processed parts (**Figure 118-120**). The lower value follows to the higher amount of the  $\text{ZrW}_2\text{O}_8$  phase, which has a lower young's modulus (single crystal value of 88.3GPa [277]) than the aluminum oxide phase (410 GPa [48]). Furthermore, apparent porosity within the laser-processed parts has a major influence on the young's modulus. Effective values for the Young's modulus of traditional manufactured  $\text{ZrW}_2\text{O}_8$  were 4.31 GPa evaluated by Sun and Kwon [210] and 4.22 GPa evaluated by Chen et al. [206]. (affected by porosity within the bulk  $\text{ZrW}_2\text{O}_8$ ). Furthermore, an addition of submicron  $\text{Al}_2\text{O}_3$  (0.07 wt%) did not change the CTEs of the sample [210]. However, the decreasing sample porosity due to this addition was beneficial for the Young's moduli of the samples (increase up to 15.22 GPa) [210].



## **5 Flowability and inner structure of customized granules**

### **5.1 Experimental**

The dynamic flow behavior of different granules was evaluated using a Revolution Powder Analyzer (PS Prozesstechnik GmbH, Switzerland) located at the inspire AG, St.Gallen. Prior to the measurement, the powders were filled into a 25 ml drum equipped with two glass windows to guarantee a direct capture of the flow behavior by a CCD camera (15 Images/s). The final flowability measurement was performed using a powder amount of 10 ml (with regards to the tapped density). The drum was brought into rotation (0.6 rounds/minute) and the characteristic values of avalanche angle and surface fractal were automatically calculated by the integrated software. Three measurements were performed for each powder evaluating at least 127 avalanches within each run to ensure a repeatability of the results. A preparation time of 30 seconds was used. The avalanche angle is the angle.

The avalanche angle is defined as the angle of a linear regression of the free powder surface just before an avalanche starts to occur in a rotating drum, measured to a horizontal line [278]. The value of the avalanche angle is indirect proportional to the powder flowability. A low Avalanche angle implements a good powder flowability. The surface fractal describes the ability

of the powder to rearrange itself. The fractal is measured after each avalanche to determine the rearrangement. Furthermore, high values of the surface fractal represent a rougher powder surface. The results are normalized within a range of 1 to 11 stated by PS Prozesstechnik GmbH in the operation manual of the Revolution Powder Analyzer. Amado described the avalanche angle as a good indicator for the flowing behavior and the surface fractal as a helpful parameter to define small flowability differences between powders showing similar avalanche angles [279].

The dynamic characterization method by the Revolution Powder Analyzer offers the chance to investigate the powder behavior in terms of flowability (avalanche angle) and surface homogeneity (surface fractal) during agitation, which is close to stress conditions in the recoating process (blade or roll spreading) used in PBF-LB. Amado et al. [280] compared different flow behavior characterization methods for polymer powders. They aimed to evaluate the impact of particle size distribution, particle shape and inter-particle forces on the powder flowability in the selective laser sintering process. It was stated that the dynamic measurement with the Revolution Powder Analyzer is an appropriate way to get insides into to the conditions during recoating for selective laser sintering. However, for a complete characterization other techniques, such as angle of repose measurements (static under free external load) [280], Hausner ratio / Carr index measurements (static under effect of powder weight) [280, 281], ring shear cell measurements to evaluate the shear force in relation to compression rate (quasi-static under pressure) [280], powder bed expansion ratio measurements to evaluate the fluidized height in relation to the upstream fluid flow (dynamic under vertical fluid drag load) [280] or flow rate measurements by Hall or Gustavsson flowmeters (dynamic under effect of powder weight) [281], are also needed to supplement each other [280].

The measured avalanche angles were compared with the calculated Hausner ratios (static measurement by use of the powder gravity [280]) in terms of the impact on the flowability by composition change, doping content or thermal treatment of the different powders. The Hausner ratio can be calculated by tapped density divided by apparent density. The parameter relates to frictional conditions in a moving powder [236, 238] and can be found for metal powders [235-238] as well as ceramic powders [57, 58] used for PBF-LB. In general, a Hausner ratio below 1.25 should guarantee a suitable flowability to achieve a high powder bed density and avoid localized porosity by a poor flowing behavior [57, 237, 238].



The granule shapes were visualized by Scanning Electron Microscopy (VEGA3 Tescan, Tescan instruments, Czech Republic) by using an accelerating voltage of 10 kV: More information regarding the sample preparation prior to SEM can be found in chapter 3.2.1.

Prior to imaging of the microstructure and internal structure of the granules by SEM (VEGA3 Tescan, Tescan instruments, Czech Republic), the granular material were cold embedded in a resin (CaldoFix-2, Struers GmbH, Switzerland). A thin powder layer was placed on the bottom of the embedding die and the resin was poured on top. Afterwards, the powder layer was ground, polished (with a 3  $\mu\text{m}$  diamond suspension) and finally sputtered with gold-palladium. Secondary electron imaging was also performed with an accelerating voltage of 10 kV.

## **5.2 Comparison of flowability in terms of Hausner ratio, Avalanche angle and surface fractal measurements**

### **5.2.1 Influence of coarse alumina AA18 variation**

**Figure 122** shows the avalanche angles and surface fractals measured for iron oxide doped alumina granules as spray-dried or mixed with different amounts of coarse aluminum oxide AA18 (more details to these powders can be found in chapter 3). The avalanche angle increases from  $33.8^\circ$  up to  $51.6^\circ$  by adding these coarse aluminum oxide particles (**Figure 122a**), which have a sharp-edged morphology (chapter 3.1.2), to the spray-dried granules. The sharp-edged particle shape has a detrimental effect on the flowability of the mixtures. This was also seen by Reed, who reported that irregular shaped granules hamper the flow by bridging [127]. Amado et al. compared the avalanche angles of mechanical fused and spray-dried nano-silica [280]. The edged morphology of the mechanical fused particles gave a high avalanche angle of ca.  $60^\circ$  with a broad distribution of the measured values, whereas the spherical shape achieved by spray drying resulted in a low mean avalanche angle of ca.  $40^\circ$  with narrow value distribution [280]. Vetterli showed that spherical and stiff particles flow better than soft and irregular particles [282]. The increasing standard deviation of the measured values for the  $\text{Fe}_2\text{O}_3$  doped powders (**Figure 122a**) correlates well with the increasing avalanche angle values and confirms the worsening of the flowability.

Furthermore, an increase of the Avalanche angle could be due to the more uneven particle size distribution. This would also explain the avalanche angle decrease from  $51.6^\circ$  of the mixture of 30 Vol% granules and 70 Vol% AA18 down to  $44.6^\circ$  of pure coarse aluminum oxide AA18 with a more narrow particle size distribution. The results of Ramavath et al. confirm these observations [162]. Narrow particle size distributions and spherical shapes of alumina granules

gave an excellent flowability and a reduced cohesion index in comparison to as received alumina powders [162]. Vetterli reported also a size effect on the flowability [282]. He tested milling balls with a d50 of 27.4  $\mu\text{m}$  (Tosoh30, Tosoh Corporation, Tokyo, Japan) and d50 of 48.2  $\mu\text{m}$  (Tosoh50, Tosoh Corporation, Tokyo, Japan) with a spherical shape. The bigger milling balls offered a lower avalanche angle (ca. 28.4° compared to 36.5°) with slightly smaller distribution span, but the surface fractal did not change (1.76 compared to 1.75) [282]. This size effect could be a further explanation for the higher avalanche angles of pure AA18 with smaller particles sizes compared to the pure spray-dried granules.

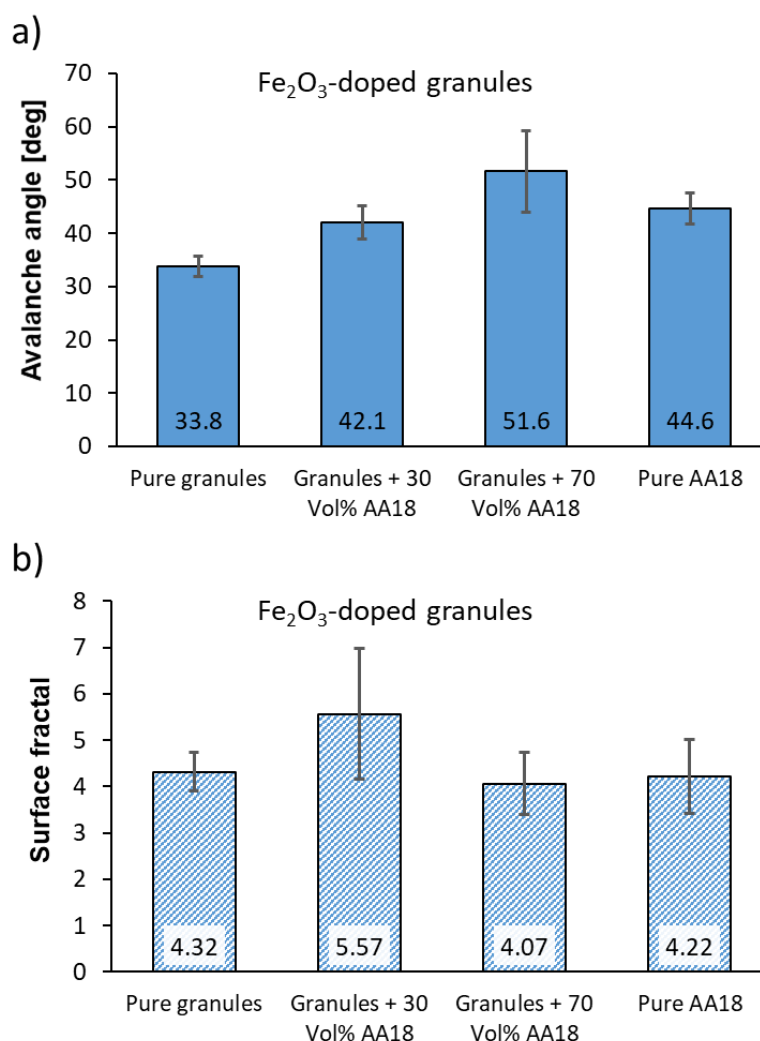


**Figure 122:** a) Avalanche angle and b) surface fractal of  $\text{Fe}_2\text{O}_3$  doped granules mixed with different amounts of coarse aluminum oxide AA18 (standard deviations calculated from three measurements for each powder evaluating at least 127 avalanches per measurement).

The surface fractals presented in **Figure 122b** are in a range of 4.07-5.57. The pure coarse aluminum oxide particles ( $4.22 \pm 0.80$ ) and the granules mixed with 70 Vol% AA18 ( $4.07 \pm$

0.67) had very similar values compared to pure  $\text{Fe}_2\text{O}_3$ -doped granules ( $4.32 \pm 0.42$ ). The addition of 30 Vol% coarse aluminum oxide led at a first glance to a fractal increase (5.57). However, this surface fractal shows also no significant difference to the other fractals given the high standard deviation of 1.40. Comparable measurements of spray-dried nano-silica granules given by Amado et al. [280] gave a lower average surface fractal of 1.72, which implements a better ability of the powder to rearrange itself and a smoother powder surface. It was reported, that distorted particle shapes lead to higher values and thus, a decrease in the powder bed packing density [280]. This could be confirmed in this work by the addition of up to 30 Vol% coarse sharp-edged aluminum oxide particles. However, a higher addition did not lead to a further increase of the surface fractal.

The Hausner ratio was almost direct proportional to the measured avalanche angles (**Table 36**). Powders with a higher avalanche angle also showed a higher Hausner ratio, except for pure AA18 particles (avalanche angle:  $44.6^\circ \pm 2.9^\circ$ , Hausner ratio: 1.18) compared to  $\text{Fe}_2\text{O}_3$ -doped granules mixed with 30 Vol% AA18 (avalanche angle:  $42.1^\circ \pm 3.1^\circ$ , Hausner ratio: 1.19). This deviation can be explained by the close values within the standard deviations for both measurements.

**Table 36:** Comparison of the avalanche angles and Hausner ratios of  $\text{Fe}_2\text{O}_3$  doped granules in terms of the impact on the flowability by addition of coarse aluminum oxide AA18.

	Avalanche angle [deg]	Hausner ratio
Pure $\text{Fe}_2\text{O}_3$ -doped granules	33.8	1.16
$\text{Fe}_2\text{O}_3$ -doped granules + 30 Vol% AA18	42.1	1.19
$\text{Fe}_2\text{O}_3$ -doped granules + 70 Vol% AA18	51.6	1.22
Pure AA18	44.6	1.18

### 5.2.2 Influence of thermal pre-treatment of powders

**Figure 123** represents the impact of thermal pre-treatment and additional mixing with 30 Vol% of coarse aluminum oxide AA18 on the avalanche angle and surface fractal of  $\text{Fe}_2\text{O}_3$  doped granules and  $\text{MnO}_2/\text{Mn}_2\text{O}_3$  doped granules. The addition of 30 Vol% AA18 leads for both granules to an increase of the avalanche angles (**Figure 123a, c**) as explained in chapter 5.2.1. Granules treated at a maximum temperature of 1600 °C for 2 hours show a similar increase of up to  $>60^\circ$  ( $60.5^\circ \pm 10.7^\circ$  for  $\text{Fe}_2\text{O}_3$  doped granules and  $61.4^\circ \pm 9.5^\circ$   $\text{MnO}_2/\text{Mn}_2\text{O}_3$  doped granules). These two powders offered a very poor flowability, which confirms the findings of Vetterli, who stated that powders with an avalanche angle  $>60^\circ$  or standard deviation  $>15\%$  behave very

cohesive with an inhomogeneous flowability [282]. Vetterli found this for polymer particles, which showed in general higher avalanche angles values due to lower “repulsive” gravitational forces limiting attractive interaction forces. Even so spherical polymer powders were flowing as homogeneous as spherical ceramic particles [282]. The standard deviations followed the same dependency as seen in **Figure 122**. The standard deviation increased with an increasing avalanche angle showing the decline of the flowability. An addition of the coarse aluminum oxide AA18 to the thermal pre-treated granules decreased the avalanche angles in both cases ( $47.5^\circ \pm 3.5^\circ$  for  $\text{Fe}_2\text{O}_3$  doped granules and  $46.8^\circ \pm 3.8^\circ$   $\text{MnO}_2/\text{Mn}_2\text{O}_3$  doped granules). The flowability improves by the separation of granules, which are slightly sintered together, as well as the coarse AA18 acting as flowable medium for the thermal pre-treated granules, what was shown in chapter 3.2.8 by SEM and an improving apparent density. The avalanche angle values of  $\text{Fe}_2\text{O}_3$  doped granules and  $\text{MnO}_2/\text{Mn}_2\text{O}_3$  doped granules were only slightly different (**Figure 123a, c**), despite a different sintering behavior triggered by the different dopants (chapter 3.2.8) and smaller BET average particle size of the  $\text{Fe}_2\text{O}_3$  dopant (19.6 nm) compared to the  $\text{MnO}_2/\text{Mn}_2\text{O}_3$  dopant (61.7 nm).

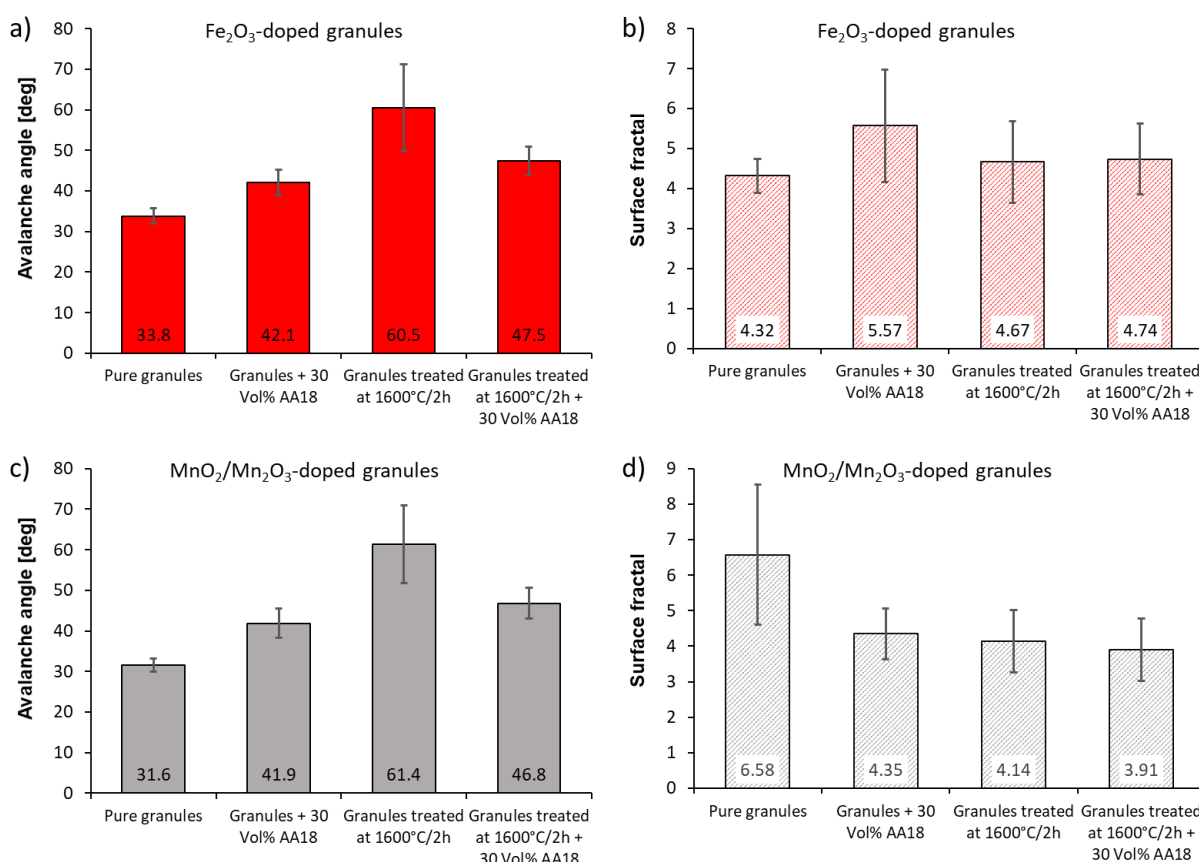


**Figure 123:** Impact of thermal pre-treatment and mixing with 30 Vol% coarse aluminum oxide AA18 on avalanche angle and surface fractal of **a), b)**  $\text{Fe}_2\text{O}_3$  doped granules and **c), d)**  $\text{MnO}_2/\text{Mn}_2\text{O}_3$  doped granules (standard deviations calculated from three measurements for each powder evaluating at least 127 avalanches per measurement).

The highest surface fractals were measured for the as spray-dried  $\text{MnO}_2/\text{Mn}_2\text{O}_3$  doped granules (6.58) and the  $\text{Fe}_2\text{O}_3$  doped granules mixed with 30 Vol% AA18 (5.57), despite having low avalanche angles and thus a good flowability. This was not expected, since distorted particle shapes (in this work satellite formation by sintering together of granules) should lead to higher surface fractal values [280]. Furthermore, the standard distributions of the surface fractals do not show a clear tendency for all the measured powders. Powders with a low avalanche angle and low surface fractal can show a higher standard distribution of the surface fractal value. This is contrary to the work of Vetterli [282], where the measured distributions of the surface fractals were directly proportional to the avalanche angle distributions.

The  $\text{Fe}_2\text{O}_3$  doped granules show an almost constant Hausner ratio (1.16 - 1.19) for all measured powders even after thermal pre-treatment or mixing with coarse aluminum oxide AA18 (**Table 37**). In contrary to this, the Hausner ratios of the  $\text{MnO}_2/\text{Mn}_2\text{O}_3$  doped granules follow clearly the trend of the evaluated avalanche angles. In the cases of these measurements, the avalanche angles should be weighted more in terms of flowability. A higher amount of test repetitions of at least three measurements for each powder evaluating at least 127 avalanches per measurement was made in comparison to only three apparent and tapped density measurements to calculate the Hausner ratios. Furthermore, a similarity between the avalanche angles obtained for granules doped with  $\text{Fe}_2\text{O}_3$  or  $\text{MnO}_2/\text{Mn}_2\text{O}_3$  is given.

The  $\text{MnO}_2/\text{Mn}_2\text{O}_3$  doped granules treated at 1600 °C for 2 hours with a measured avalanche angle of 61.4° and Hausner ratio of 1.23 offer a poor flowability, which was not suitable for the PBF-LB process. This is in a good agreement with the recommended values of below 1.25 (Hausner ratio) [57, 237, 238] and <60° [282], which should guarantee a suitable homogeneous flowability to achieve a high powder bed density.

**Table 37:** Comparison of the avalanche angles and Hausner ratios of  $\text{Fe}_2\text{O}_3$ - and  $\text{MnO}_2/\text{Mn}_2\text{O}_3$ - doped granules in terms of the impact on the flowability by thermal pre-treatment and mixing with 30 Vol% coarse aluminum oxide AA18.

	Avalanche angle [deg]	Hausner ratio
Pure $\text{Fe}_2\text{O}_3$ -doped granules	33.8	1.16
$\text{Fe}_2\text{O}_3$ -doped granules + 30 Vol% AA18	42.1	1.19
$\text{Fe}_2\text{O}_3$ -doped granules treated at 1600 °C/2h	60.5	1.17
$\text{Fe}_2\text{O}_3$ -doped granules treated at 1600 °C/2h+ 30 Vol% AA18	47.5	1.18
Pure $\text{MnO}_2/\text{Mn}_2\text{O}_3$ -doped granules	31.6	1.15
$\text{MnO}_2/\text{Mn}_2\text{O}_3$ -doped granules + 30 Vol% AA18	41.9	1.18
$\text{MnO}_2/\text{Mn}_2\text{O}_3$ -doped granules treated at 1600 °C/2h	61.4	1.23
$\text{MnO}_2/\text{Mn}_2\text{O}_3$ -doped granules treated at 1600 °C/2h+ 30 Vol% AA18	46.8	1.17

### 5.2.3 Influence of dopant content within granules

The influence of the dopant content within the granules on the avalanche angle and the surface fractal of  $\text{Fe}_2\text{O}_3$ - and  $\text{MnO}_2/\text{Mn}_2\text{O}_3$ -doped aluminum oxide granules is illustrated in **Figure 124**. The granules were sprayed with the different dopant amounts of 1 and 5 Vol%. The avalanche angles of the granules increased by  $2.9^\circ$  and  $4.8^\circ$  by raising the doping amount of  $\text{Fe}_2\text{O}_3$  and  $\text{MnO}_2/\text{Mn}_2\text{O}_3$  amount, respectively. The avalanche angles were similar for the same doping amount despite using a different dopant. The increase of the avalanche angles could be explained by emerging agglomerations of fine particles reducing the flowability. However, SEM images and particle size distributions did not reveal the presence of these unwanted agglomerations (**Figure 125**). A more likely explanation arises by the shape of the granules doped with 5 Vol%  $\text{Fe}_2\text{O}_3$  (**Figure 125a**) and 5 Vol%  $\text{MnO}_2/\text{Mn}_2\text{O}_3$  (**Figure 125b**). The SEM images reveal a high amount of donut-shaped granules. Lee et al. [114] reported that well dispersed  $\text{Si}_3\text{N}_4$  suspensions of ultrafine particles gave predominately hollow granules due to a limited liquid flow rate and an increased tortuosity due to fine capillaries. Reed already stated that irregular shaped granules may impede the flow by bridging and should be removed by sieving to achieve a high flowability [8]. Furthermore, Ramavath et al. reported that the morphology of spray-dried granules plays a major role for the cohesion index and flowability, rather than the sizes of the granules [9]. The influence of the granule shape on surface fractal and avalanche angle was also already reported by Vetterli [282]. Spherical granules containing nanosized alumina and zirconia particles were analyzed. The coarse fraction was composed of homogeneous granules. The fine fraction contained additional fragments of broken granules and showed inhomogeneous and broader size distribution. The avalanche angle of the fine and coarse fraction were ca.  $40.5^\circ$  and ca.  $31.4^\circ$ . Furthermore, the fine fraction showed a higher distribution span of the avalanche angle values. The difference between the surface fractals was even more distinct (fine fraction: 6.09; coarse fraction: 1.74). This was explained by the different shape, size and composition of each powder. The free movement of these particles was impeded by the irregular shaped particles and a stronger impact of the attractive Van der Waals forces within the fine fraction [282].

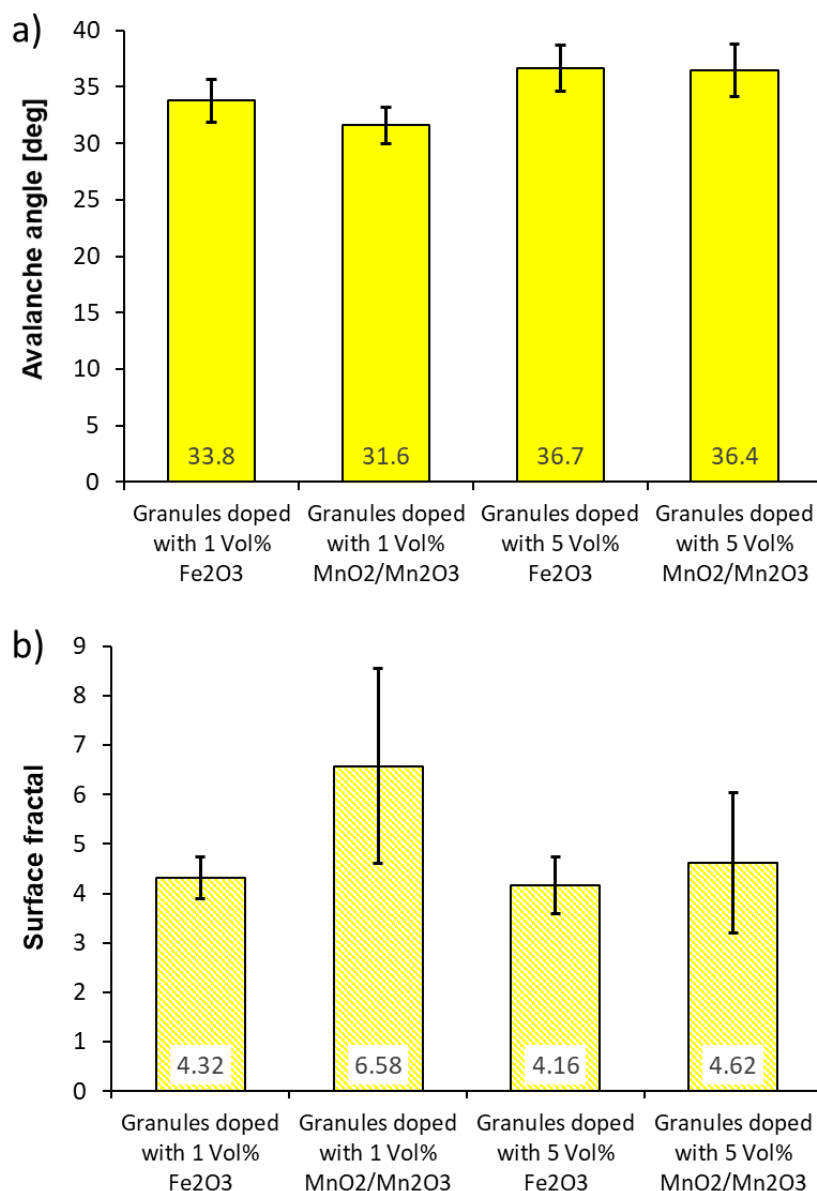


**Figure 124:** a) Avalanche angle and b) surface fractal of Fe<sub>2</sub>O<sub>3</sub>- and MnO<sub>2</sub>/Mn<sub>2</sub>O<sub>3</sub>-doped aluminum oxide granules containing different dopant amounts of 1 and 5 Vol% (standard deviations calculated from three measurements for each powder evaluating at least 127 avalanches per measurement).

The increase of the dopant amount to 5 Vol% also increased the granule sizes (**Figure 125c**). This change in size distribution should in theory improve the flowability, as already reported by Vetterli [282], who tested milling balls with a d<sub>50</sub> of 27.4 μm and 48.2 μm (chapter 5.2.1). Furthermore, Mapar et al. compared the flowability of spray-dried alumina-zirconia granules (1-30 μm) with that of the raw alumina particles before spray granulation (1-5 μm) by evaluating avalanche angle and surface linearity of these powders [51]. Before spray granulation an avalanche angle of ca. 35° was measured, whereas after spray granulation the avalanche angles improved to 20°. These avalanche angles cannot be directly compared to the values measured



in this work, since a higher drum rotation speed of 65 rounds/minute was used. Amado ascertained that avalanche angle results are only good estimators of the powder flowability at low rotational speeds, since the index failed to present suitable results at higher rotational speeds [279]. At low rotational speeds, the avalanche angle correlated linearly quite well with the normalized bulk density of the material [279]. However, higher rotational speeds are typical for the L-PBF process. In general, it can be stated that drum rotation speed and avalanche angle are inversely proportional, since the rest time between avalanches decreases with an increase in the rotational speed of the drum [283]. The raw alumina particles showed a high tendency for agglomeration and thus, a rough powder bed surface (high surface fractal) was present, what is detrimental for the layer deposition. However, the differences in size of the measured granules in this work was only small (**Figure 125c**) and thus the effect of flowability improvement became insignificant.

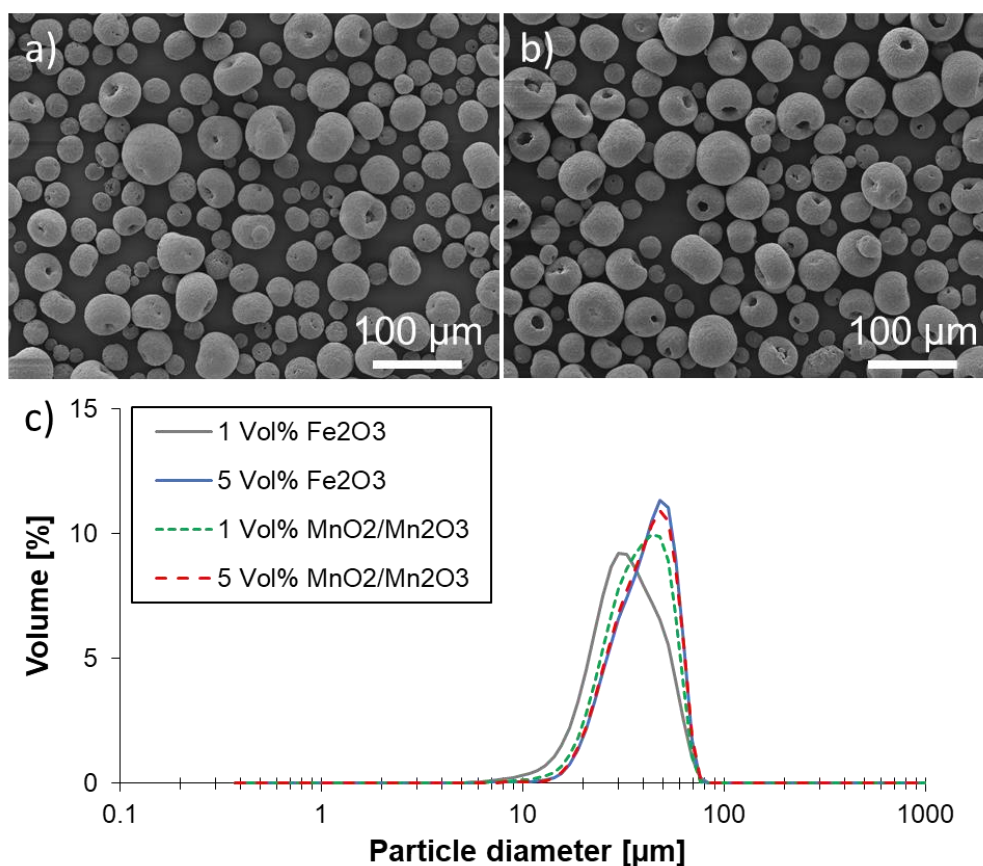


**Figure 125:** SEM images of **a)** 5 Vol%  $\text{Fe}_2\text{O}_3$ - and **b)** 5 Vol%  $\text{MnO}_2/\text{Mn}_2\text{O}_3$ -doped aluminum oxide granules as well as particle size distributions of the granules measured in Figure 124.

**Figure 124b** displays the influence of the dopant content on the surface fractals of  $\text{Fe}_2\text{O}_3$ - and  $\text{MnO}_2/\text{Mn}_2\text{O}_3$ -doped granules. The granules doped with 1 Vol%  $\text{MnO}_2/\text{Mn}_2\text{O}_3$  revealed a rather high surface fractal of 6.58, whereas the granules doped with 1 Vol%  $\text{Fe}_2\text{O}_3$ , 5 Vol%  $\text{Fe}_2\text{O}_3$ -

and 5 Vol%  $\text{MnO}_2/\text{Mn}_2\text{O}_3$  showed a similar surface fractal of 4.32, 4.16 and 4.62, respectively. This high surface fractal 1 Vol%  $\text{MnO}_2/\text{Mn}_2\text{O}_3$  doped granules was already discussed in chapter 5.2.2.

The Hausner ratio fits very well with the measured avalanche angles except for the aluminum oxide granules doped with 5 Vol%  $\text{MnO}_2/\text{Mn}_2\text{O}_3$ . (**Table 38**). In this case, the avalanche angles should be more trustworthy in terms of the flowability due the higher amount of test repetitions, as already discussed in chapter 5.2.2.

**Table 38:** Comparison of the avalanche angles and Hausner ratios of  $\text{Fe}_2\text{O}_3$ - and  $\text{MnO}_2/\text{Mn}_2\text{O}_3$ - doped granules in terms of the impact on the flowability by changing the dopant amount.

	Avalanche angle [deg]	Hausner ratio
Granules doped with 1 Vol% $\text{Fe}_2\text{O}_3$	33.8	1.16
Granules doped with 1 Vol% $\text{MnO}_2/\text{Mn}_2\text{O}_3$	31.6	1.15
Granules doped with 5 Vol% $\text{Fe}_2\text{O}_3$	36.7	1.14
Granules doped with 5 Vol% $\text{MnO}_2/\text{Mn}_2\text{O}_3$	36.4	1.24

#### 5.2.4 Flowability of zirconia-tungsten oxide granules and alumina granules with mullite or rare earth oxide addition

**Figure 126** images the avalanche angles and surface fractals of the granules containing the additives to reduce crack formation in selective laser melting and sintering of alumina. The avalanche angles of the measured granules are in a similar range between  $32.5^\circ$  and  $36.3^\circ$ . Furthermore, the granules containing the different additives have a similar flowability to  $\text{Fe}_2\text{O}_3$ - and  $\text{MnO}_2/\text{Mn}_2\text{O}_3$ -doped aluminum oxide granules. The avalanche angle decreased, when micron-sized particles ( $\text{Y}_2\text{O}_3$  and micron-mullite) were used instead of nano- or submicron-sized additives. This could be due to lower “repulsive” gravitational forces for nano- and submicron particles leading to prevalence of attractive van der Waals forces [28].

The surface fractals are also in a similar range of 5.28 - 6.33. The  $\text{ZrO}_2/\text{WO}_3$  granules showed the lowest surface fractal of  $5.28 \pm 1.15$ . This could be due to the nearly spherical shape of the spray-dried granules, which led to a good rearrangement of the powder and thus, an even powder bed surface.

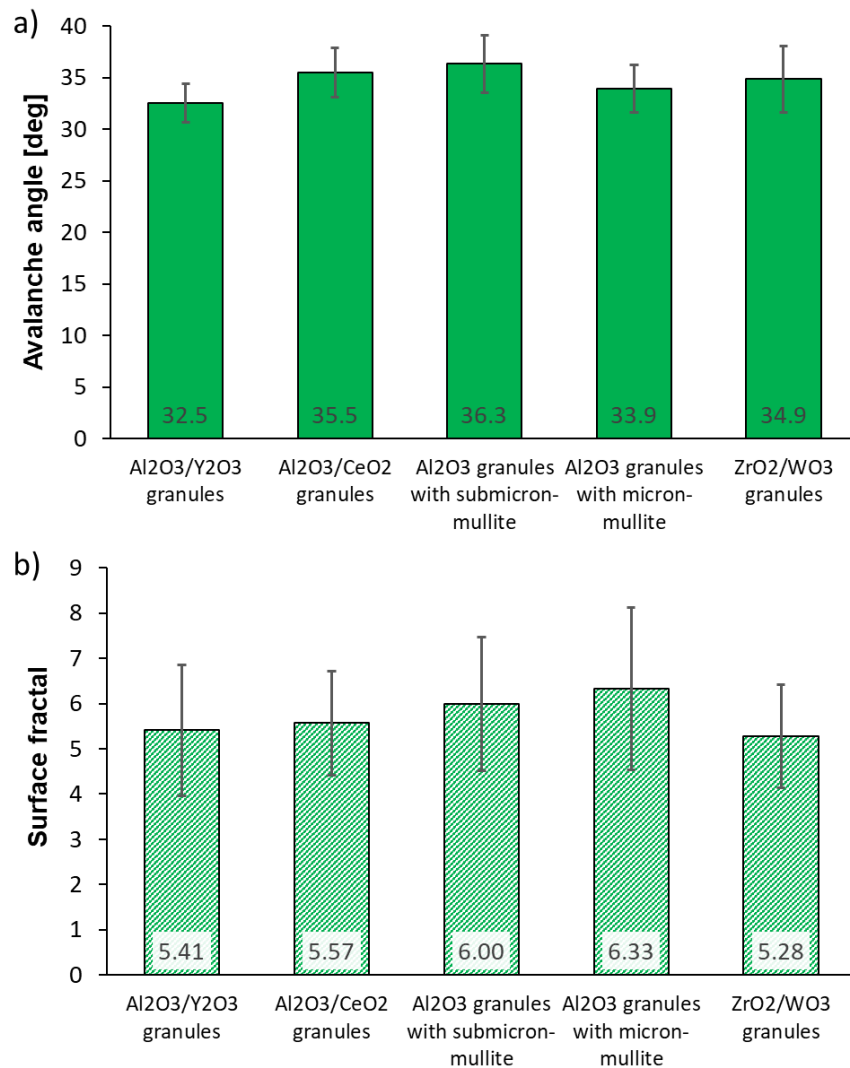


**Figure 126:** *a)* Avalanche angle and *b)* surface fractal of zirconia-tungsten oxide granules and alumina granules with mullite or rare earth oxide addition (standard deviations calculated from three measurements for each powder evaluating at least 127 avalanches per measurement).

The Hausner ratio followed more or less the trend of the avalanche angles (**Table 39**). Also, the measured Hausner ratios indicated a good flowability for the PBF-LB process with values far below the critical value of 1.25 [57, 237, 238].

**Table 39:** Comparison of the avalanche angles and Hausner ratios of zirconia-tungsten oxide granules and alumina granules with mullite or rare earth oxide addition in terms of the impact on the flowability.

	Avalanche angle [deg]	Hausner ratio
Al <sub>2</sub> O <sub>3</sub> /Y <sub>2</sub> O <sub>3</sub> granules	32.5	1.14
Al <sub>2</sub> O <sub>3</sub> /CeO <sub>2</sub> granules	35.5	1.15
Al <sub>2</sub> O <sub>3</sub> granules with submicron-mullite	36.3	1.13
Al <sub>2</sub> O <sub>3</sub> granules with micron-mullite	33.9	1.11
ZrO <sub>2</sub> /WO <sub>3</sub> granules	34.9	1.14

### 5.2.5 Flowability of titanium oxide doped alumina powders

**Figure 127** summarizes the impact of thermal treatment in Ar/H<sub>2</sub> and consecutive mixing with 30 Vol% coarse aluminum oxide AA18 on the avalanche angle and surface fractal of powders with a final TiO<sub>2-x</sub> content of 0.7 Vol%, 10Vol% and 50 Mol%. The spray-dried granules with the lowest amount of TiO<sub>2</sub> addition (1 Vol%) showed the smallest avalanche angle of  $32.9^\circ \pm 1.8^\circ$ . Pure granules with amount of 14.2 Vol% and 68 Mol% (61.9 Vol%) TiO<sub>2</sub> (amount before mixing with coarse aluminum oxide particles) gave an avalanche angle of  $37.7 \pm 2.3^\circ$  and  $37.3 \pm 2.9^\circ$ . A similar increase of the avalanche angles was also seen in chapter 5.2.4, when changing nano- or submicron-sized particles to micron-sized particles and in chapter 5.2.3, when increasing the dopant amount of nano-Fe<sub>2</sub>O<sub>3</sub> and nano MnO<sub>2</sub>/Mn<sub>2</sub>O<sub>3</sub> from 1 Vol% to 5 Vol%. However, the increase of titanium oxide within the granules from 14.2 Vol% to 61.9 Vol% did not significantly change the avalanche angle.

The thermal treatment in Ar/H<sub>2</sub> had different consequences for the three compositions. The avalanche angle of the granules containing 14.2 Vol% of TiO<sub>2-x</sub> only increased up to  $45.2^\circ$  following a thermal treatment at a maximum temperature of 1300°C for 2 hours (**Figure 127b**). This granules sinter only slightly at this temperature with almost no change in shape. In comparison, the avalanche angles of the granules containing 1 Vol% and 61.9 Vol% of TiO<sub>2-x</sub> were ca.  $60^\circ$  after the thermal treatments presented in **Figure 127a and b**. The reason for this big increase is the strong sintering phenomena forming irregular shaped granules and satellite-shaped constructions (sintered granules), which the granules containing 1 Vol% of TiO<sub>2-x</sub> experience at maximum temperatures of 1400 and 1600 °C and granules containing 61.9 Vol% of TiO<sub>2-x</sub> experience at maximum temperatures of 1200 and 1400 °C. It was also stated in the literature, that irregular and distorted particle shapes impede the flowability [127, 280, 282]. More details to the different sintering impacts are described in chapter 4.2.3.

The addition of 30 Vol% coarse aluminum oxide has a contrary effect for the avalanche angles of the different granules. The avalanche angle of the granules containing 14.2 Vol% of TiO<sub>2-x</sub> increased by  $3.1^\circ$ , whereas the avalanche angles of the granules containing 1 Vol% of TiO<sub>2-x</sub> decreased to  $48.0^\circ$  (1400 °C) and to  $49.2^\circ$  (1600 °C). The avalanche angles decreased to  $54.5^\circ$  (1200 °C) and  $53.2^\circ$  (1400 °C) for powders containing 61.9 Vol% of TiO<sub>2-x</sub>. The coarse aluminum oxide AA18 acts as flowable medium for the granules having a high avalanche angle after the thermal treatment in Ar/H<sub>2</sub>. Furthermore, the separation of slightly sintered satellite-shaped granule constructions improves the flowability. This was also seen for the Fe<sub>2</sub>O<sub>3</sub>- and MnO<sub>2</sub>/Mn<sub>2</sub>O<sub>3</sub>-doped aluminum oxide granules sintered in air (chapter 5.2.2). However, the

sharp-edged aluminum oxide AA18 already showed an avalanche angle of  $44.6^\circ$  (chapter 5.2.1) and thus the flowability improvement is limited for the granules containing 1 Vol% and 61.9 Vol% of  $\text{TiO}_{2-x}$ . The slight worsening of the avalanche angle of the granules containing 14.2 Vol% of  $\text{TiO}_{2-x}$  confirms the findings in chapter 5.2.1. Also Reed [127], Amado et al. [280] and Vetterli [282] reported such a detrimental effect on the flowability by irregular shaped granules.

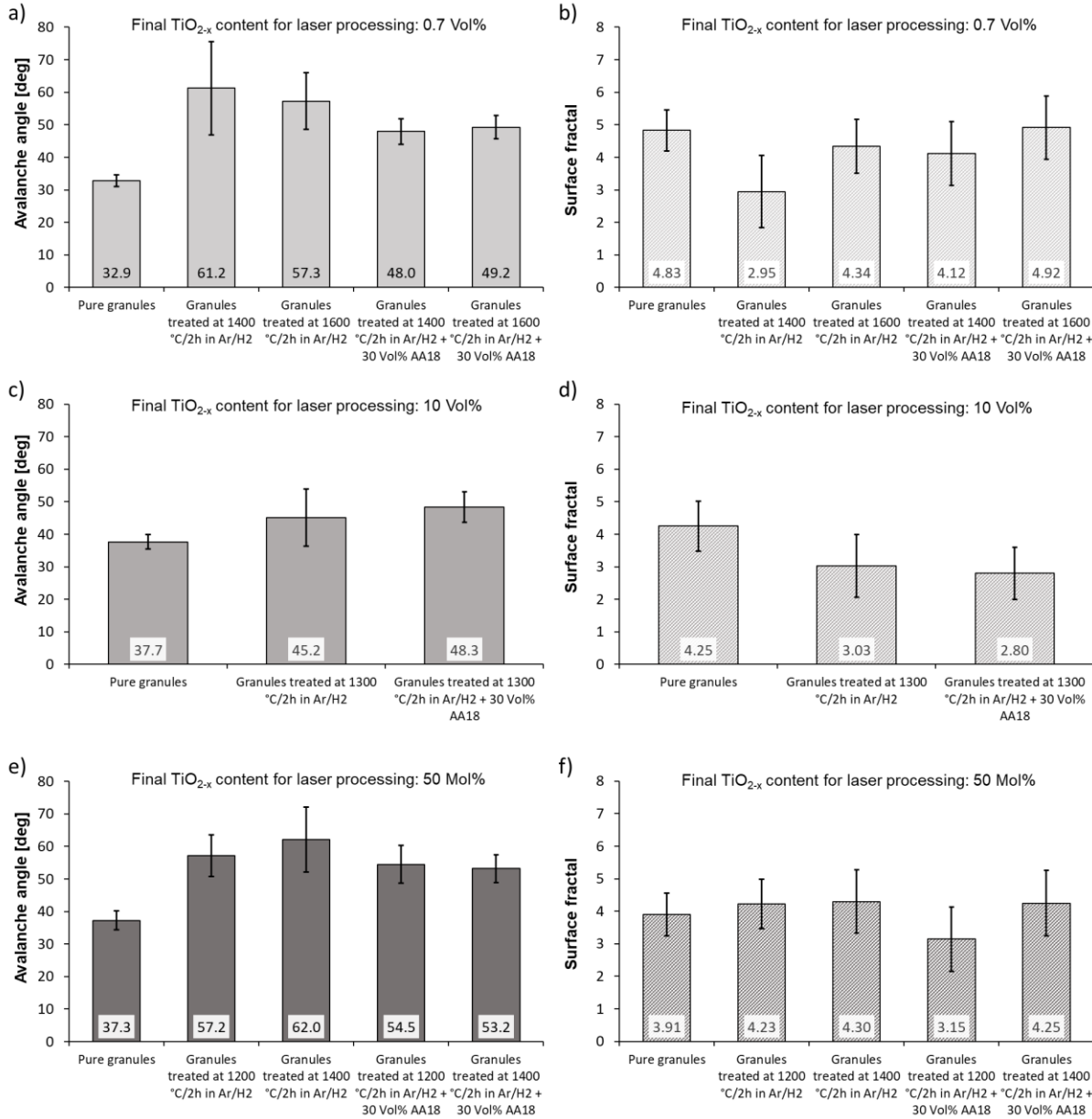


**Figure 127:** Impact of thermal treatment in  $\text{Ar}/\text{H}_2$  and mixing with 30 Vol% coarse aluminum oxide AA18 on avalanche angle and surface fractal of powders with a final  $\text{TiO}_{2-x}$  content of a), b) 0.7 Vol%, c), d) 10 Vol% and e), f) 50 Mol% (standard deviations calculated from three measurements for each powder evaluating at least 127 avalanches per measurement).

All of the measured surface fractals are below value of five (**Figure 127b, d, f**). This implicates a smooth powder surface and good rearrangement of the powder surfaces for all the measured

powders. A clear trend of the surface fractal values could not be seen. The lowest surface fractal ( $2.95 \pm 1.11$ ) for granules containing 1 Vol% of  $\text{TiO}_{2-x}$  was measured after a thermal treatment with a maximum temperature of 1400 °C (**Figure 127b**). However, the avalanche angle after this treatment was the highest measured for this powder due to the formation of irregular shaped granules, as described before. Granules containing 14.2 Vol% of  $\text{TiO}_{2-x}$  showed even an indirect proportional relation of surface fractal and avalanche angle (**Figure 127d**). The surface fractal decreased from  $4.25 \pm 0.76$  down to  $2.80 \pm 0.80$ , whereas the avalanche angle increased from  $37.7^\circ \pm 2.3$  up to  $48.3 \pm 4.7$  after application of thermal treatment in Ar/H<sub>2</sub> and the addition of coarse aluminum oxide AA18. The granules containing 61.9 Vol% of  $\text{TiO}_{2-x}$  showed a surface fractal within a range of  $3.15 \pm 0.99$  to  $4.30 \pm 0.98$  with no clear trend regardless of an increase or decrease of the avalanche angles for the different treatment steps. These results are contrary to the results of Amado et al., who reported, that distorted particle shapes (shape distortions and formation of granules-satellites by sintering) gave higher values of the surface fractal [280]. **However, an evaluation of the surface fractal is extremely difficult, since the large standard deviations make it difficult to examine the given values in this work precisely.**

**Table 40:** Comparison of the avalanche angles and Hausner ratios of powders with a final  $\text{TiO}_{2-x}$  content of **a)** 0.7 Vol%, **b)** 10Vol% and **c)** 50 Mol% in terms of the impact on the flowability by thermal treatment in Ar/H<sub>2</sub> and mixing with 30 Vol% coarse aluminum oxide AA18.

a)		Avalanche angle [deg]	Hausner ratio
	Granules doped with 1 Vol% $\text{TiO}_2$	32.9	1.14
	Granules doped with 1 Vol% $\text{TiO}_{2-x}$ treated at 1400 °C/2h in Ar/H <sub>2</sub>	61.2	1.25
	Granules doped with 1 Vol% $\text{TiO}_{2-x}$ treated at 1600 °C/2h in Ar/H <sub>2</sub>	57.3	1.18
	Granules doped with 1 Vol% $\text{TiO}_{2-x}$ treated at 1400 °C/2h in Ar/H <sub>2</sub> + 30 Vol% AA18	48.0	1.21
	Granules doped with 1 Vol% $\text{TiO}_{2-x}$ treated at 1600 °C/2h in Ar/H <sub>2</sub> + 30 Vol% AA18	49.2	1.15
b)		Avalanche angle [deg]	Hausner ratio
	Granules doped with 14.2 Vol% $\text{TiO}_2$	37.7	1.12
	Granules doped with 14.2 Vol% $\text{TiO}_{2-x}$ treated at 1300 °C/2h in Ar/H <sub>2</sub>	45.2	1.19
	Granules doped with 14.2 Vol% $\text{TiO}_{2-x}$ treated at 1300 °C/2h in Ar/H <sub>2</sub> + 30 Vol% AA18	48.3	1.21
c)		Avalanche angle [deg]	Hausner ratio
	Granules doped with 62 Vol% $\text{TiO}_2$	37.3	1.15
	Granules doped with 62 Vol% $\text{TiO}_{2-x}$ treated at 1200 °C/2h in Ar/H <sub>2</sub>	57.2	1.13
	Granules doped with 62 Vol% $\text{TiO}_{2-x}$ treated at 1400 °C/2h in Ar/H <sub>2</sub>	62.0	1.38
	Granules doped with 62 Vol% $\text{TiO}_{2-x}$ treated at 1200 °C/2h in Ar/H <sub>2</sub> + 30 Vol% AA18	54.5	1.23
	Granules doped with 62 Vol% $\text{TiO}_{2-x}$ treated at 1400 °C/2h in Ar/H <sub>2</sub> + 30 Vol% AA18	53.2	1.26

The Hausner ratios of the granules containing  $\text{TiO}_{2-x}$  follow only for an addition amount of 14.2 Vol% the trend of the avalanche angles (**Table 40b**). In the case of the granules with 1 Vol% of  $\text{TiO}_{2-x}$  (**Table 40a**) and the granules with 61.9 Vol% of  $\text{TiO}_{2-x}$  (**Table 40c**), the powders with a high avalanche angle had for some powders low Hausner ratios. A good example for this are the granules doped with 61.9 Vol% of  $\text{TiO}_{2-x}$  treated at 1200 °C in Ar/H<sub>2</sub>, which had a high avalanche angle of 57.2°, but also a low Hausner ratio of 1.13. **It shows that the dynamic characterization method by the Revolution Powder Analyzer and the static measurements to calculate the Hausner ratio are hardly comparable for these powders. However, the avalanche angles should be weighted more in terms of the flowability due the higher amount of test repetitions.**

In the case of the avalanche angles, only two granules with 1 Vol% of  $\text{TiO}_{2-x}$  (**Table 40a**) and the granules with 61.9 Vol% of  $\text{TiO}_{2-x}$  (**Table 40c**) treated at 1400 °C in Ar/H<sub>2</sub> gave a bigger angle than the critical value of 60° [282] to achieve a flowability suitable for the PBF-LB process. In case of the Hausner ratio, these two granules and additionally the granules with 61.9 Vol% of  $\text{TiO}_{2-x}$  treated at 1400 °C in Ar/H<sub>2</sub> and mixed with 30 Vol% aluminum oxide AA18 had a ratio of  $\geq 1.25$ , which was stated as an insufficient flowability to achieve a high powder bed density [57, 237, 238].

### 5.3 Cross sections of customized granules to image inner structure

The granule morphology and subsurface morphology of as spray-dried  $\text{Fe}_2\text{O}_3$  doped granules are illustrated in **Figure 128**. The granules have a spherical appearance, which follows due to the process of spherical droplet formation due to high surface tensions and the consecutive fast evaporation of water based on a large surface area to volume ratio during spray drying [103]. Furthermore, the ultrasonic nozzle is known to produce predominantly spherical granules. It is also reported that a higher solid load can improve the sphericity of the granules [112], what can in conclusion improve the powder bed density for laser processing due to an increased flowability. The maximum solid load processed in this work was up to ca. 50 Vol%. Afterwards, the viscosity of the slurry used for spray drying rises extremely, also seen by Lukasiewicz [103].

Hollow cores were found only within the bigger granules (**Figure 128b, c, d**). These voids within the granules can result when the solvent evaporation is higher than the diffusion rate during drying [113]. A collapse due to a pressure difference with the ambient atmosphere creates finally the hollow core [119]. In the worst case, the pressure limit is exceeded and an explosion occurs, what leads to doughnut shaped granules or a total destruction of the granule [113]. The droplet stability is related to the hydrodynamic effects during drying according to



Iskandar et al. [121]. Different factors play a major role, if solid dense granules or doughnut shaped granules are produced by spray drying. A droplet destabilization leading to doughnut-shaped granules was already reported for spray drying of nano-silica particles after an increase in droplet size (e.g. by increasing the power of the nebulizer), a decrease of smaller and an increase of larger particles and a decrease of the surface tension of the droplet (e.g. by use of surfactants). [121]. The  $\text{Fe}_2\text{O}_3$ -doped granules presented in **Figure 128** meet all these process conditions.

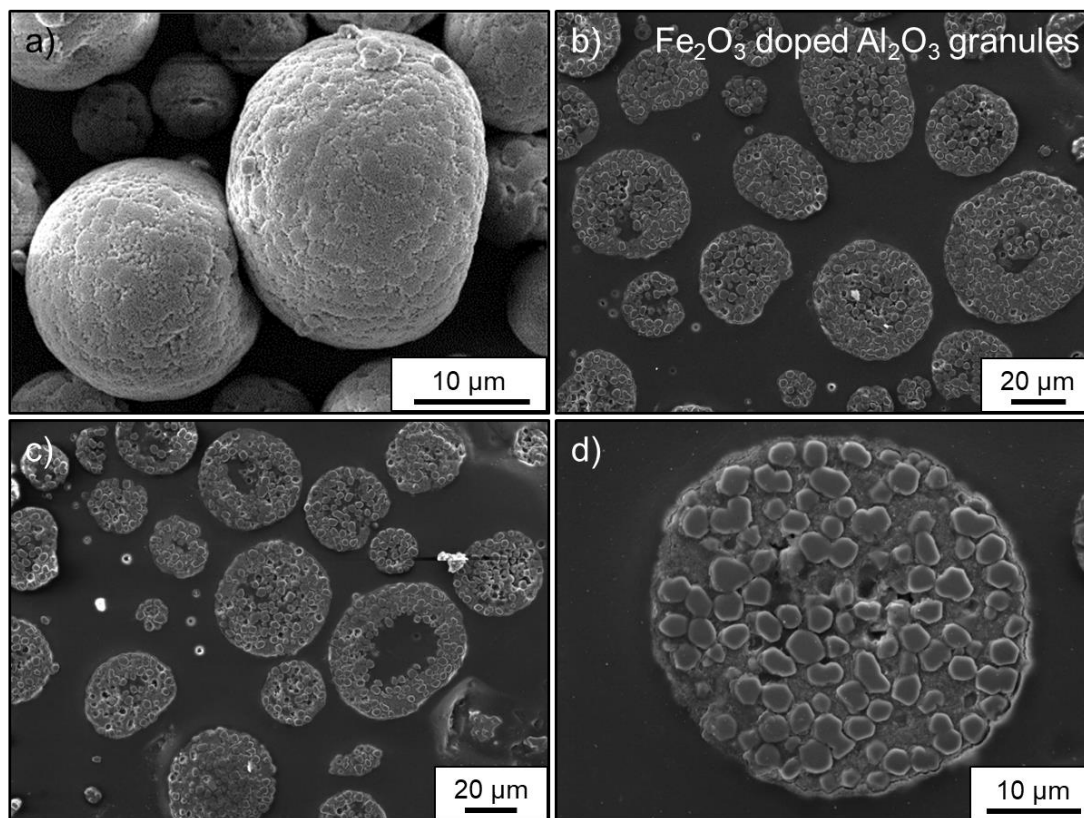


**Figure 128:** SEM images of as spray-dried  $\text{Fe}_2\text{O}_3$  doped granules illustrating **a)** the morphology and **b), c), d)** the subsurface morphology of the granules.

Furthermore, a gradient structure with a higher content of nanoparticles at the outer shell and more micron-sized aluminum oxide particles in the granule center was visible (**Figure 128d**). Lee et al. [114] reported the tendency of well dispersed ultrafine  $\text{Si}_3\text{N}_4$  particles to form a shell-morphology and to give hollow granules. Dispersed particles experience a high versatility without intergranular interactions within the spray-dried droplet and are moving into the direction of the shell due the forces generate by the solvent evaporation [119]. In multimodal particle combinations smaller particles show an enhanced movement due to a higher mobility within the droplet [121]. The fast evaporation of water at the already solidified outer granule shell during the drying process enables a directed movement of the smaller particles by occurring

capillary forces, which stops at the granule surface. Wegmann et al. [284] reported a similar behavior of colloidal zirconia nanoparticles during the modification of a commercial ceramic microfilter. They measured an increased zirconium concentration near the outer surface due to a forced directional flow of water during drying, which pushed the  $\text{Zr}(\text{OH})_x$  nanoparticles towards this surface.

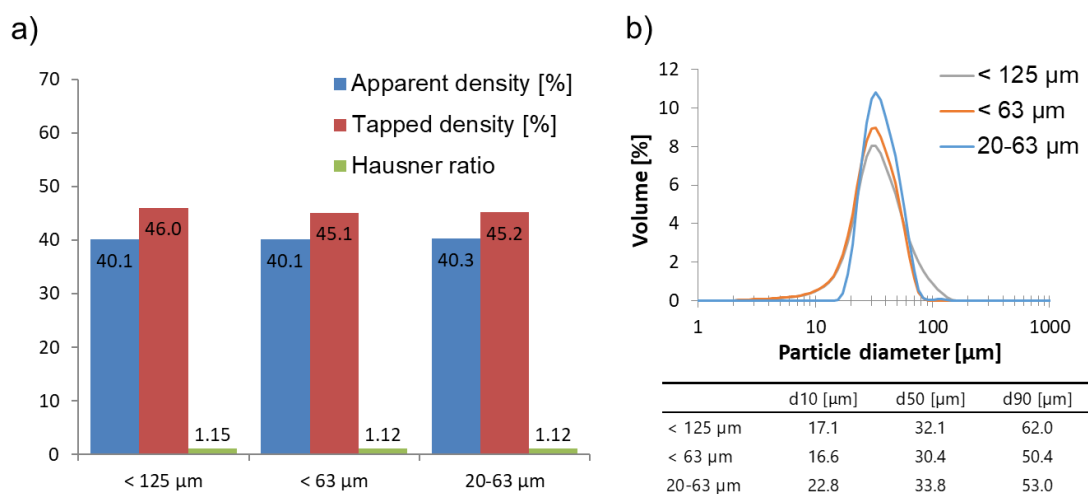


**Figure 129:** Impact of screening on a) apparent, tapped density and Hausner ratio and on b) the particle size distribution.

A screening of the granules (20 and 63  $\mu\text{m}$  sieves) was performed to eliminate the bigger granules containing an internal void and thus, potentially improve the packing density of the powders due to a smaller content of these hollow granules. Furthermore, a narrow and uniform distribution of the granules should be favorable for the flowability and a wide distribution should render a high packing density due to filling of the interstices between the bigger granules by smaller ones. The impact on the apparent, the tapped density, the Hausner ratio and the particle size distribution is depicted in **Figure 129**. By screening with a 63  $\mu\text{m}$  sieve, the tapped density decreased from 46.0% to 45.1%. This small difference is within the error limits of the measurement method. Consecutively, the Hausner ratio was reduced (1.15 to 1.12). The more narrow particle size distribution (**Figure 129b**) could be responsible for this improvement of the flowability and the decrease of the tapped density. A further screening with a 20  $\mu\text{m}$  sieve increased the apparent and tapped density slightly. However, the procentual changes are only 0.2% and 0.1%, respectively. The impact of screening on the density values was only small and within the error limits of the measurement method.

The as spray-dried granules doped with manganese oxide (**Figure 130a-d**) have a similar appearance compared to the iron oxide doped aluminum oxide doped granules.

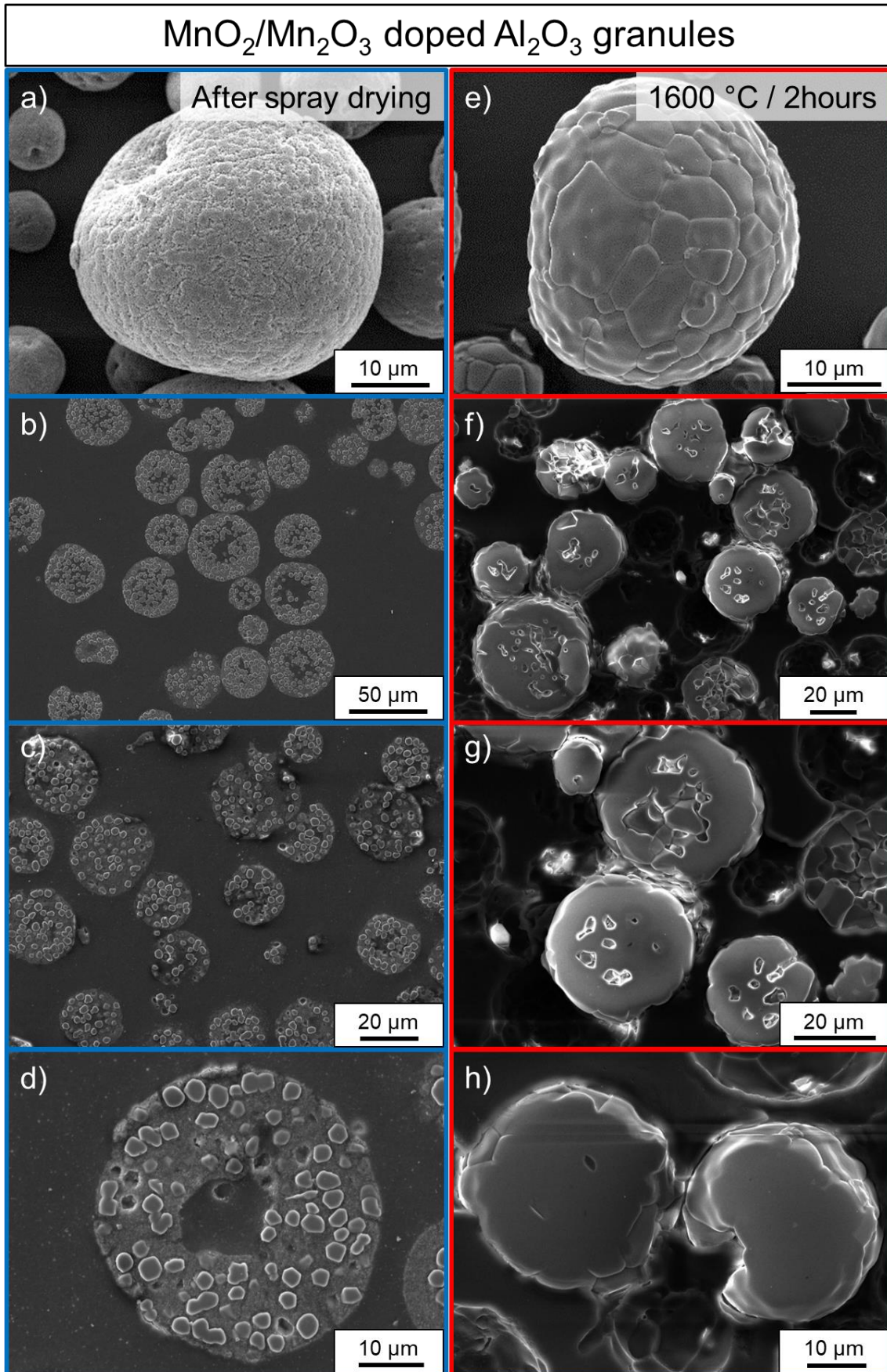


**Figure 130:** SEM images illustrating the morphology and the subsurface morphology of a), b), c), d) as spray-dried MnO<sub>2</sub>/Mn<sub>2</sub>O<sub>3</sub>-doped granules and e), f) g), h) thermal pre-treated granules in air (maximum temperature 1600  $^{\circ}\text{C}$ , heating and cooling rate: 2 K/min, idle time: 2 hours)



The thermal pre-treatment in air results in a dense microstructure with no visible porosity from the outside view (**Figure 130e**). The granules are strongly sintered and show an increased density (**Figure 130e-h**). This increase in density after adjusting the flowability was experimentally proven in chapter 3.2.8. However, the cross sections reveal a porosity with micron-sized pores within the inner structure. Compared to the as spray-dried granules these pores are smaller, which follows due to the occurring sintering at the used high temperatures (up to 1600 °C). Large grains are visible within the microstructure of the thermal pre-treated granules. This phenomenon was already described in chapter 3.2.8. The samples exhibit irregular shaped grains after sintering at 1600 °C (**Figure 130a**). An extensive grain growth by the manganese oxide doping can be seen in **Figure 130a, b**. Other researchers also saw this promotion of an irregular grain growth by this oxide doping within aluminum oxide [155-158]. To achieve better visibility results of the grain structures in the microscope, an etching step during sample preparation of the cross sections would be necessary.

**Figure 131** shows the morphology and the subsurface morphology of as spray-dried  $\text{Al}_2\text{O}_3/\text{CeO}_2$  granules imaged by SEM. The dark phase represents the micron-sized  $\text{Al}_2\text{O}_3$  particles and the bright phase represents the nano- $\text{CeO}_2$ , since elements with a larger atomic nucleus appear brighter in secondary electron microscopy.

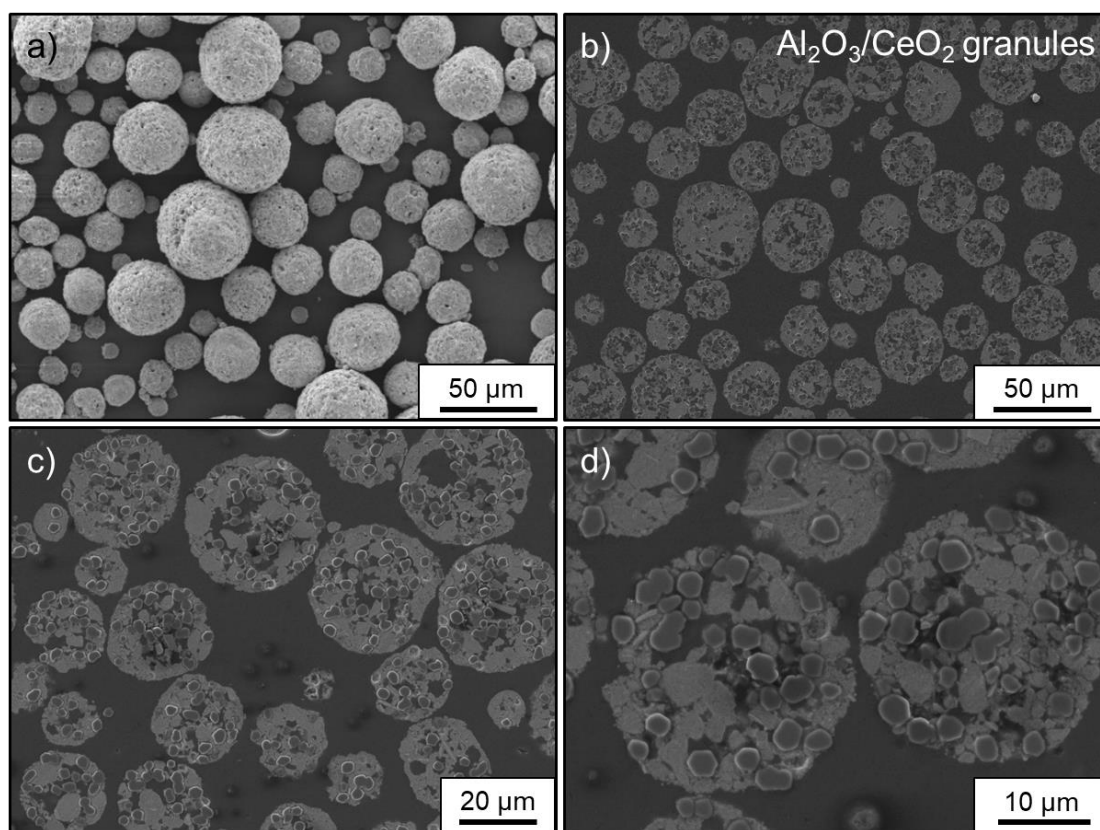


**Figure 131:** SEM images of as spray-dried  $\text{Al}_2\text{O}_3/\text{CeO}_2$  granules illustrating **a)** the morphology and **b), c), d)** the subsurface morphology of the granules.

The distribution of the  $\text{CeO}_2$  and  $\text{Al}_2\text{O}_3$  particles is less homogeneous than for the particles within the  $\text{Fe}_2\text{O}_3$ - and  $\text{MnO}_2/\text{Mn}_2\text{O}_3$ -doped  $\text{Al}_2\text{O}_3$  granules, despite successful dispersions without agglomerations achieved for the single powders (chapter 4.2.2). Big areas of agglomerated  $\text{CeO}_2$  particles (bright phases) are visible within the granules. The slight change of the pH value by mixing of the single components of the slurry for spray drying cannot be a reasonable explanation for this, since the pH values of the single components dispersed in water are 7.7 for  $\text{CeO}_2$ , 6.5 for  $\text{Al}_2\text{O}_3$  and 7.2 for PEG 35000. The mixing should not shift the pH-value in a pH-range, where the  $\text{CeO}_2$  particles tend to agglomerate due to a low zeta-potential. A more logical explanation could be given by the high content (eutectic ratio of 49.4/50.6 Vol%  $\text{CeO}_2/\text{Al}_2\text{O}_3$  for spray drying) of the nanoscale  $\text{CeO}_2$  particles (calculated BET average particle size of 22.4 nm), which could first lead to a colloidal coagulation with a resulting agglomeration of the particles during droplet drying. Van der Waals attractions have more impact on smaller particles due to decreasing gravitation forces [28] and can therefore lead to a destabilization of the colloidal dispersion, especially in droplets with a high concentration of nano-sized  $\text{CeO}_2$  particles. This coagulation and agglomeration behavior was more pronounced compared to the  $\text{Fe}_2\text{O}_3$ - and  $\text{MnO}_2/\text{Mn}_2\text{O}_3$ -doped  $\text{Al}_2\text{O}_3$  granules, since only ca. 1 Vol% of the nanoscale dopants and only ca. 27.1 Vol% of the submicron alumina Taimicron TM-DAR was used in these granules (related to the total inorganic solid load). Furthermore, Taimicron TM-DAR should also show a lower tendency for agglomeration according to larger particle sizes (BET average particle size of 128.8 nm) [28]. However, during processing of the  $\text{Al}_2\text{O}_3/\text{CeO}_2$  granules by laser powder bed fusion, a further homogenization is also given by thermal capillary convection (Bernard-Marangoni convection) within the melt pool [11, 65] and thus the effect of a lower granule homogeneity is less detrimental for achieving the desired phases in the final parts.

The  $\text{Al}_2\text{O}_3/\text{CeO}_2$  granules contain micron-sized pores and show rarely hollow cores in the granule center. However, some granules show a higher porosity in the center, which reveals a beginning void formation. This could be also due to the high content of nano-sized  $\text{CeO}_2$ , since the eutectic ratio of 49.4/50.6 Vol%  $\text{CeO}_2/\text{Al}_2\text{O}_3$  was used to prepare the dispersion for spray drying. This high amount of nanoparticles is beneficial to avoid the hollow core formation as also described by Iskandar et al. [121].

**Figure 132** shows the inner structure of spray-dried  $\text{ZrO}_2/\text{WO}_3$  granules. The granules have a very uniform microstructure, what was already assumed considering the EDX measurements illustrated in chapter 4.2.4. In contrary to the  $\text{Fe}_2\text{O}_3$ -doped  $\text{Al}_2\text{O}_3$  granules presented in **Figure 128**, the  $\text{ZrO}_2/\text{WO}_3$  granules are solid dense granules, which do not show a hollow core. Only

nano-pores are present within the microstructure. These observations confirm the results reported from Iskandar et al. [121]. Solid dense granules made from nano-silica were produced by using a high solid concentration, a high content of small particles and a small droplet size [121]. The  $\text{ZrO}_2/\text{WO}_3$  were spray-dried by using only nano-sized particles, whereas the major particle content of the  $\text{Fe}_2\text{O}_3$ -doped granules consisted of micron-sized particles. Furthermore, the maximum possible slurry solid load before achieving an extreme rise in the viscosity was used for spray drying of the  $\text{ZrO}_2/\text{WO}_3$  granules.

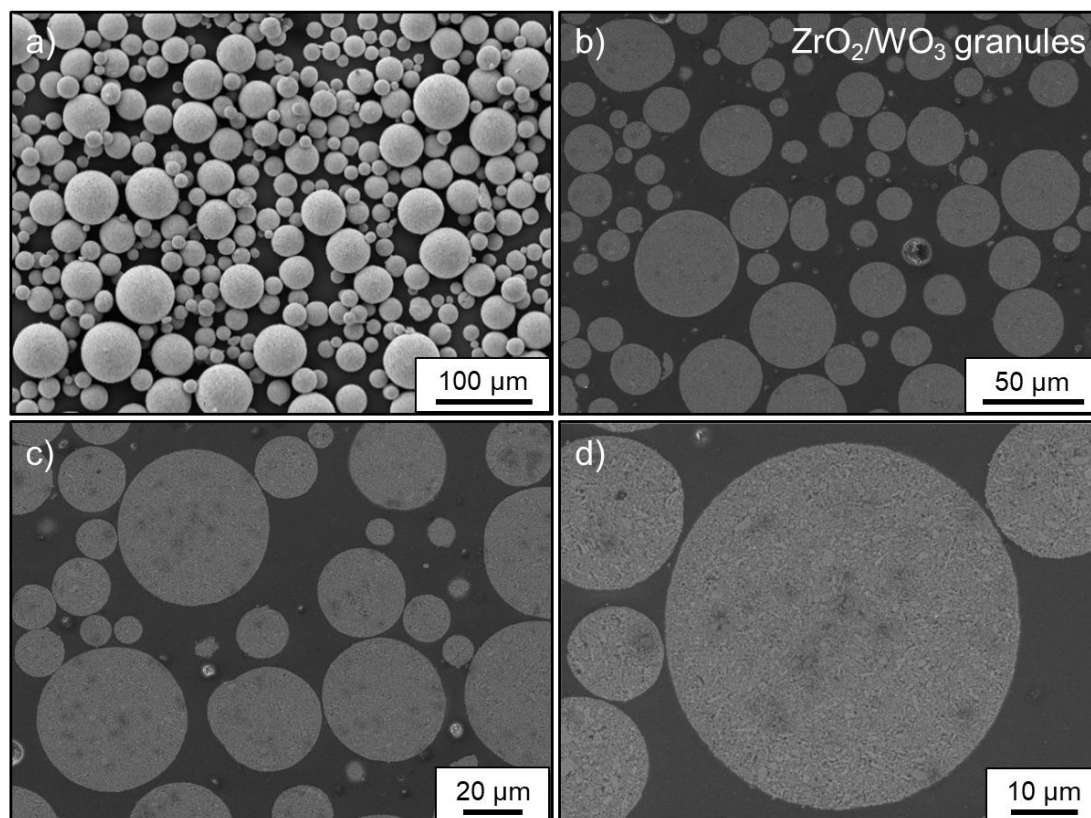


**Figure 132:** SEM images of as spray-dried  $\text{ZrO}_2/\text{WO}_3$  granules illustrating **a)** the morphology and **b), c), d)** the subsurface morphology of the granules

The apparent and tapped density of the  $\text{ZrO}_2/\text{WO}_3$  (chapter 4) was lower than that achieved by using bimodal or trimodal particle size distributions (chapter 3) for spray drying, even so the granule density appears higher due to the missing hollow core and micron-sized pores. This confirms the results of McGeary [128], that a higher packing density can be achieved when using homogeneous bimodal or trimodal particle size distributions with adequate size differences of the particles, for spray-dried granules (experimentally shown in chapter 3). In these multi-modal distributions, smaller particles can fill the interstices of the coarse content. However, agglomeration due to attractive van der Waals forces has to be avoided to guarantee a homogenous distribution of the particles, what allows a transfer of the work of McGeary to



nano- and micron-sized particle systems. The homogenous dispersions were achieved in this work by means of a suitable dispersant (ammonium citrate in this work), pH adjustment or milling process.

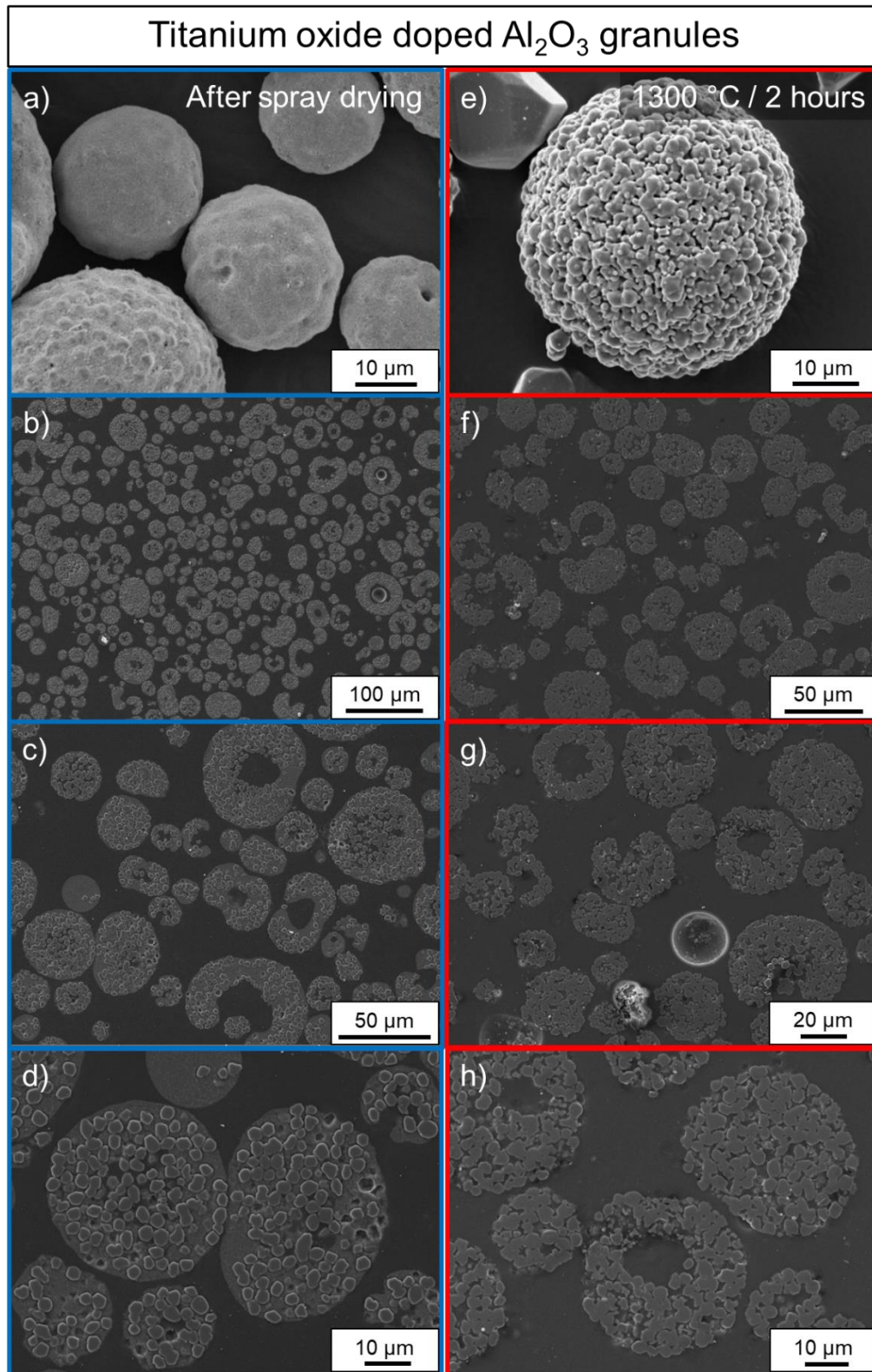


**Figure 133:** SEM images illustrating the morphology and the subsurface morphology of **a), b), c), d)** as spray-dried  $\text{Al}_2\text{O}_3/\text{TiO}_2$  granules and **e), f) g), h)** thermally reduced  $\text{Al}_2\text{O}_3/\text{TiO}_{2-x}$  granules in  $\text{Ar}/\text{H}_2$  atmosphere (maximum temperature 1300 °C, heating and cooling rate: 2 K/min, holding time: 2 hours)



**Figure 133** illustrates the impact of titanium oxide reduction in argon/hydrogen (2%) atmosphere within the alumina granules at 1300 °C. The TiO<sub>2</sub> content in the slurry for spray drying was 14.2 Vol%.

Hollow cores within the bigger granules and donut-shaped granules are present after spray drying and thermal treatment. Furthermore, these spray-dried granules showed a gradient structure with a higher content of nanoparticles at the outer shell and more micron-sized particles in the center. These phenomena were also seen for the Fe<sub>2</sub>O<sub>3</sub>- and MnO<sub>2</sub>/Mn<sub>2</sub>O<sub>3</sub>- doped Al<sub>2</sub>O<sub>3</sub> granules and their origin was already explained for these granules (chapter 2.2.1 and 3.2.3). **Figure 133b, c and d** reveals a uniform distribution of aluminum oxide and titanium oxide particles after spray drying.

The thermal treatment in Ar/H<sub>2</sub> atmosphere causes a grain growth of the particles in the granules (**Figure 133e-h**). The reduced titanium oxide nanoparticles disappear visually due to sintering with the aluminum oxide particles. However, micron-sized pores are created by the thermal treatment step, which could be formed due to oxygen reduction in this atmosphere (TiO<sub>2</sub> to TiO<sub>2-x</sub>). The sintering effect is not as strong as seen for the MnO<sub>2</sub>/Mn<sub>2</sub>O<sub>3</sub> doped Al<sub>2</sub>O<sub>3</sub> granules, what follows to the smaller energy input of the applied temperature profile with a maximum temperature of 1300 °C (compared to 1600 °C). Furthermore, it is well known, that different atmospheres can also have an impact on the sintering behavior. Whereas it was stated that manganese oxide doping promotes an extensive, irregular grain growth within aluminum oxide [155-158], no publication was found stating the grain growth for an addition of 14.2 Vol% titanium oxide in aluminum oxide thermally treated in Argon/hydrogen atmosphere. A content of 4 wt% TiO<sub>2</sub> reduced the sintering rate and the final grain size, when thermally treated in air [158]. For pure nano-titanium oxide, a rapid grain growth starting already from 800 °C was reported by Dittmann et al. [202] and Mazaheri et al. [203].

## 6 Summary, conclusions and outlook

Parts of this chapter were already published in the Journal of European Ceramic Society, Volume 41 (13), (2021) 6087-6114.

### 6.1 Summary and conclusions







Several customized ceramic granules were developed and analyzed in this PhD work to overcome the low thermal shock resistance, weak densification and low light absorptance at room temperature in the visible or near-infrared range in laser powder bed fusion of aluminum oxide. Powder properties such as powder flowability, packing density and laser light absorption have a strong impact on the quality and performance of the laser manufactured aluminum oxide ceramic parts. This has been addressed by spray drying of granules with different material compositions. Dibasic ammonium citrate was found to be a suitable dispersant for all oxides used in this work. An appropriate amount of dispersant for consecutive water-based spray granulation was determined by Zeta Potential measurements. The following conclusions regarding powders and final parts can be drawn:

#### A. Doped spray-dried granules for densification and absorption issue

The strategies to solve the densification and absorption issue in laser powder bed fusion aluminum oxide are summarized in **Table 41**. The red (unsuccessful) and green signals (successful)

display the success of these strategies. Further conclusions of these experiments are given in details in the following.

**Table 41:** Strategies to solve the densification and absorption issue in laser powder bed fusion aluminum oxide and visualization of the success by red signal (unsuccessful) and green signal (successful).

Strategies to solve the densification and absorption issue	Success of strategy
<b>Increase of powder bed absorption</b>	
Nano iron oxide and manganese oxide dopants (ca.1 Vol%) to improve absorption of alumina granules	
<b>Increase of powder bed density</b>	
Bimodal and trimodal distributions of coarse and fine alumina particles according to results of McGeary to increase packing density of granules	
Increase of slurry solid load to increase packing density of granules	Increase only up to 50 Vol% solid load
Influence of slurry surface tension on granule properties using an ultrasonic nozzle	
Addition of 0, 30, 70 and 90 Vol% of coarse alumina particles AA18 maintaining a constant doping amount	Comparable results up to 70 Vol% Part consolidation problems with 90 Vol%.
Application of Andreasen model (packing theory) on mixtures of spray-dried granules with ceramic particles	Tapped densities 
	Apparent densities 
Thermal treatment of granules and consecutive mixing of coarse alumina particles	





Nano iron oxide and nano manganese oxide dopants (ca.1 Vol%) improved the laser absorption of the alumina granules by up to 80.9%. This enabled a processing with a green pulsed laser, which was not possible with commercial available undoped powders, and led to ceramic parts with relative densities up to 98.6% (evaluated by tomographic microscopy) with a laser power of 5.75W. It was shown that bimodal or trimodal distributions of coarse and fine aluminum oxide particles according to results of McGeary are beneficial to increase the apparent and tapped density of the granules and to achieve a good flowability. The proposed weight fraction

by McGeary of 0.726/0.274 coarse to fine particles (bimodal distributions) could be confirmed as also appropriate for spray-dried granules. Higher solid loads led to higher apparent and tapped densities of the spray-dried granules. An influence of the dopant shape on the granules shape was not recognizable. Furthermore, contrary to the literature an influence of the slurry surface tension on the granule size was not seen by spray drying using an ultrasonic nozzle and the surfactant 1-octanol. Addition of coarse alumina particles to the granules only increased the apparent and tapped density, if the different additives had a good flowability. Laser processing was performed with amounts of 0, 30, 70 and 90 Vol% of coarse alumina particles AA18 (constant doping amount of 2 Vol%). The compressive strength values of the produced parts with these different mixing ratios were in a comparable range. However, part consolidation problems appeared during PBF-LB of the powder with an addition amount of 90 Vol%. The application of the Andreasen model (packing theory) on mixtures of spray-dried granules with ceramic particles did not lead to an increase of both packing densities, since agglomerations lowered the flowability. However, high tapped densities were reached using this model. Thermal treatment of the granules further increased the powder bed densities up to a maximum tapped density of 56.4% of the theoretical density, but coarse alumina particles had to be added to break sintering necks and therefore, maintain a good powder flowability. It was shown, that an increase in powder density also increased the final laser-processed parts density. However, the thermal treatment of the granules affected also microstructure and dopant distribution within the granules.  $\mu$ -beam X-ray fluorescence tomography confirmed a uniform distribution of both dopants after spray drying, but also revealed, that originally well distributed Mn atoms demix upon thermal treatment. High resolution powder diffraction revealed a partial incorporation of Mn-atoms and a total incorporation of Fe-atoms within the corundum lattice. Furthermore, the dopants had an impact on the sintering behavior of the alumina granules. Iron oxide dopant triggered a uniform, equiaxed grain growth, whereas manganese oxide resulted in an irregular, more excessive growth of the grains. Electron backscatter diffraction revealed large crystal grains growing predominantly parallel to the building direction. Thermomechanical analysis showed that the sinter activity of the laser-processed part was low due to large grains formed and the huge distances in between cracks or pores. XRF line scans confirmed a manganese depletion due to the high temperatures involved in the process of thermal treatment of the granules and PBF-LB. The long-lasting thermal treatment with lower temperatures in the furnace was hereby more detrimental for the manganese amount than the short processing times used for PBF-LB.

### B. Additives to reduce crack formation

Several additives were added to aluminum oxide to reduce crack formation caused by thermal stresses. **Table 42** summarizes the theoretical principle of crack reduction in the PBF-LB processed aluminum oxide parts by the use of them. The red (unsuccessful) and green signals (successful) display the success of crack reduction of the different additives. Further conclusions of these experiments are given in details in the following.

**Table 42:** Theoretical principle of crack reduction in PBF-LB processed aluminum oxide parts by the use of different additives and visualization of the success by red signal (unsuccessful) and green signal (successful).

Additives within powders	Theoretical principle of crack reduction	Success of crack reduction
Mullite	<ul style="list-style-type: none"> <li>Glass phase formation (partial melting) due to high silica content</li> <li>Low thermal expansion coefficient</li> </ul>	
Rare earth oxide (ceria and yttria)	<ul style="list-style-type: none"> <li>Decrease of solidification temperature by formation of amorphous bulk glasses based on alumina and rare earth oxides</li> </ul>	
Reduced titanium oxide	<ul style="list-style-type: none"> <li>In-situ formation of aluminum titanate with low thermal expansion coefficient, low thermal conductivity, low young's modulus and therefore, excellent thermal shock behavior</li> </ul>	
Zirconia and tungsten oxide	<ul style="list-style-type: none"> <li>Generation of zirconium tungstate with a negative thermal expansion coefficient during laser processing</li> </ul>	

Using mullite with a low thermal expansion coefficient and a high silica content for a possible glass phase formation was not successful in this work. Despite of a successful incorporation of 30 Vol% submicron or micron-sized mullite into the  $\text{Fe}_2\text{O}_3$  doped  $\text{Al}_2\text{O}_3$  granules, only traces of Si (according to energy-dispersive X-ray spectroscopy) and mullite (according to high resolution powder diffraction) were found in the final laser processed part. This could be due to high temperatures generated by the absorption of the laser light and therefore, an evaporation of Si or  $\text{SiO}$  during processing. Laser processing in an oxygen atmosphere would have been an option to avoid this evaporation given the reducing conditions [285] at high temperatures.

Furthermore, the incorporation of rare earth oxides ( $\text{CeO}_2$  and  $\text{Y}_2\text{O}_3$  particles) within the spray-dried granules did not lead to amorphous and transparent alumina bulk glasses as stated by Rosenflanz et al. [163], even though the quenching rates should be relatively high by the laser process. X-ray diffraction confirmed a crystalline phase structure after laser processing ( $\text{Al}_2\text{O}_3$ ,  $\text{CeO}_2$  and  $\text{CeAlO}_3$  for  $\text{CeO}_2$  addition and  $\text{Al}_2\text{O}_3$ ,  $\text{Y}_2\text{O}_3$ , YAG and  $\text{YAlO}_3$  for  $\text{Y}_2\text{O}_3$  addition). Therefore, a beneficial effect on the crack formation by the low glass-transition temperature of amorphous alumina was not observed.

To produce aluminum titanate with a low Young's modulus, a low thermal expansion coefficient, low thermal conductivity, titanium oxide was proposed as suitable additive. Thermal gravimetric analysis gave a minimum temperature necessary of 980 °C to reduce the  $\text{TiO}_2$  nanoparticles to  $\text{TiO}_{2-x}$  in argon/hydrogen atmosphere. The titanium oxide changed the color from white to blackish upon reduction, which enables its use as dopant for laser processing in the visible or near-infrared range of the light. Thermal treatment temperatures of 1400 °C, 1300 °C and 1200 °C were found as most suitable for granules with 1 Vol%, 14.2 Vol% and 68 Mol%  $\text{TiO}_2$ . These granules needed to be mixed with coarse alumina to increase the apparent density, tapped density and decrease the Hausner ratio, since sintering worsened the flowability of the granules by formation of satellite like structures or by deterioration of the sphericity. The final powder contained 0.7 Vol%, 10 Vol% and 50 Mol% titanium oxide after mixing with 30 Vol% coarse alumina particles. Tomographic microscopy revealed a similar crack formation by laser processing for the low dopant amount of 0.7 Vol%  $\text{TiO}_{2-x}$  as seen for the dopants  $\text{Fe}_2\text{O}_3$  and  $\text{MnO}_2/\text{Mn}_2\text{O}_3$ . Also the higher amount of 10 Vol%  $\text{TiO}_{2-x}$  was not effective to reduce the crack formation upon PBF-LB. The total content of 50 Mol%  $\text{TiO}_{2-x}$  led to improved part properties in terms of crack reduction, which follows the in-situ reaction of aluminum oxide and titanium oxide to aluminum titanate with excellent thermal shock behavior. Laser processing with this powder gave parts with a high density of 96.5% (evaluated by the Archimedes principle), a compressive strength of  $346.6 \pm 47.9$  MPa and Young's modulus of 90.2 GPa.

Since the negative thermal expansion phase  $\text{ZrW}_2\text{O}_8$  was desired to balance the thermal expansion of aluminum oxide and therefore, to achieve a total zero thermal expansion in the final laser processed parts, a powder consisting of  $\text{ZrO}_2/\text{WO}_3$  granules and coarse alumina particles (less prone to melting) was developed. A detailed spray drying process parameter study was performed for these granules. The influence of the parameters was evaluated for solid load of the slurry, feed rate (pump rate), power output of the ultrasonic atomizer and inlet temperature of the spraying chamber. A steady increase of the granule size by increasing the solid load and

the pump rate was observed. The sphericity of the granules decreased with an increase of the nozzle power output. This loss of the sphericity led to a decrease of the flowability and therefore, a strong decrease of the apparent density and a smaller decrease of the tapped density was observed. The inlet temperature of 140 °C was found as most favorable for apparent and tapped density of the granules. The final process parameters for spray drying were a ultrasonic power output of 4 W, a pump rate of 3%, a solid load of 23 Vol% and an inlet temperature of 140 °C. Energy-dispersive X-ray spectroscopy confirmed a uniform distribution of tungsten, oxygen and zirconium in these granules. The final powders were mixed according to the Turner model with the ratio of 96.9/3.1 Vol% of  $\text{ZrW}_2\text{O}_8$  to  $\text{Al}_2\text{O}_3$  (to achieve lowest CTE of  $5.2 \times 10^{-8} \text{ 1/K}$ ) and with a ratio of 50 Vol%  $\text{Al}_2\text{O}_3$  and 50 Vol%  $\text{ZrO}_2/\text{WO}_3$ . An increased absorptance at room temperature was measured at 1070 nm (wavelength of the used cw IR fiber laser) by the Kubelka Munk method. X-ray diffraction on laser-processed layers confirmed the formation of a  $\text{ZrW}_2\text{O}_8$  phase, when low power to speed ratios as well as high energy densities were used. Laser-processed parts made from 50 Vol% coarse alumina and 50 Vol%  $\text{ZrO}_2/\text{WO}_3$  granules showed a strong crack reduction. A lamellar structure due to the temperature differences within the melt pool was noticed in the microstructure. The optimized calculated ratio according to the Turner model revealed the lowest amount of cracks. Laser-induced cracks were not visible in low magnifications of the microstructure. Only higher magnifications showed a small amount of cracks. A high compressive strength of  $498.9 \pm 89.3 \text{ MPa}$  and a low young's modulus of 99.7 GPa was achieved by using powders consisting of 50 Vol%  $\text{ZrO}_2/\text{WO}_3$  granules and 50 Vol% coarse aluminum oxide. The compressive strength was higher than for the powder mixture of 96.9 Vol%  $\text{ZrO}_2/\text{WO}_3$  granules and 3.1 Vol% coarse aluminum oxide, despite possessing more cracks after laser processing.

The formation of ternary oxides was shown in this work as effective way to reduce the crack formation. However, a too high amount of  $\text{Al}_2\text{TiO}_5$  or  $\text{ZrW}_2\text{O}_8$  with a low mechanical strength reduced the final strength of the parts.

### C. Flowability and inner structure of customized granules

Avalanche angles and surface fractal measurements were performed to evaluate the flow behavior of the spray-dried granules. The avalanche angles of the powders followed in general the same trend like the Hausner ratios. However, the avalanche angles could be weighted more due to the higher reliability of the measurements, which follows due to a higher number of test repetitions. The addition of coarse aluminum oxide AA18 and an increase of the dopant amount increased the avalanche angles of the colored oxide doped granules. Granules treated at 1600



°C offered a poor flowability, which was not suitable for the PBF-LB process. Similar high avalanche angles and Hausner ratios were achieved for granules containing 68 Mol% TiO<sub>2</sub> treated in argon/hydrogen atmosphere at 1400 °C. The results were in good agreement with the recommended values of below 1.25 (Hausner ratio) [55, 213, 214] and <60° (avalanche angle) [249] to achieve a homogeneous flowability for a high powder bed density in laser processing. A further addition of AA18 decreased the avalanche angles by separation of sintered granules and by acting as flowable medium. The trend of the surface fractals was not clear. Higher additions of AA18, thermal treatment of the granules or the change of the granule composition did not lead to a further increase of the surface fractal.

The granule morphology and subsurface morphology were studied by granules cross sections. TiO<sub>2</sub>, Fe<sub>2</sub>O<sub>3</sub> or MnO<sub>2</sub>/Mn<sub>2</sub>O<sub>3</sub> doped Al<sub>2</sub>O<sub>3</sub> granules had a spherical appearance. However, hollow cores were found within the bigger granules. Furthermore, a gradient structure with a higher content of nanoparticles at the outer shell was visible. A screening of the granules to eliminate the bigger granules containing hollow cores did not improve the packing density or flowability of the powders. Thermal treatment in air or Ar/H<sub>2</sub> atmosphere revealed micron-sized pores within the inner structure. However, they appeared dense from the outside. Spray-dried Al<sub>2</sub>O<sub>3</sub>/CeO<sub>2</sub> granules showed a less homogeneous particle distribution within the granules, which is most probably a result of a colloidal coagulation with a resulting agglomeration of the nano-particles. The sub-morphology of ZrO<sub>2</sub>/WO<sub>3</sub> granules was solid and dense with no hollow cores.













#### D. Impact of slurry and spray drying parameters on granule size and shape

**Table 43** summarizes the results achieved in the present work regarding the impact of a slurry and spray drying parameter study on the granule shape and size for different material compositions. These results were achieved using the Mini spray dryer B-290 with an ultrasonic atomizer.

The spray drying parameters involve the solid load of the slurry, the surface tension of the dispersion and the fraction of nanoparticles. The increase of the solid load led not only for a multimodal aluminum oxide combination (micron- and submicron-sized particles), but also for a combination of zirconium oxide and tungsten oxide nanoparticles to an increase of the granule size. No shape change was visible in SEM images of the zirconia/tungsten oxide granules. However, an increasing amount of broken granules was found in such granules made from the highly concentrated aluminum oxide dispersion (up to 60 Vol%). A decrease of the surface tension (adding 1-octanol) had a different effect on the granules taken from the fine and coarse

powder collector. No size and shape effect was seen for the finer powder. However, the coarser powder increased strongly in size and showed severe shape distortions, as expected for both fractions due to the decreasing surface tension of the slurry for spray drying. Other authors, claimed that the granule size is direct proportional to the surface tension [103, 113] and that a droplet destabilization by decreasing the surface tension of the droplet occurs [121]. The increase of the nanoparticle fraction within the granules showed contrary results for different compositions. A small dopant increase from 1 to 5 Vol% led to an increase in size with no visible shape changes. However, a bigger addition (up to 61.9 Vol%) of nanoparticles (titanium oxide) resulted in severe shape distortions of the granules. This could be also caused due to a strongly increasing slurry viscosity.

**Table 43:** Impact of slurry and spray drying parameters on granule size and shape for different material compositions.

	Process parameter	Material composition	Chapter	Additional information	Dependency	
					Granule size	Granule shape
Slurry parameters	Solid load / Concentration	 Multimodal aluminum oxide combination	3.2.2	Micron- and submicron-sized particles		Increase of broken granules
			4.2.4.2	Nanoparticles		(=)
	Surface tension	 Multimodal aluminum oxide combination	3.2.9	Granules from fine powder collector	(=)	(=)
				Granules from coarse powder collector		Shape distortions
	Amount of nanoparticles	 Aluminum oxide and titanium oxide	4.2.3.2	Nano-sized titanium oxide amount from 1 to 14.2 and 61.9 Vol%	N/A	Shape distortions
			5.2.3	Nano-dopant amount from 1 to 5 Vol%		(=)
Spray drying parameters	Pump rate	 Zirconium oxide and tungsten oxide	4.2.4.2	Nanoparticles		(=)
	Power output of ultrasonic nozzle	 Zirconium oxide and tungsten oxide	4.2.4.2	Nanoparticles / Changes only at high powers		Shape distortions
	Inlet temperature	 Zirconium oxide and tungsten oxide	4.2.4.2	Nanoparticles	(=)	(=)

The impact of the spray drying parameters (pump rate, power output of the atomizer and inlet temperature) was evaluated using a dispersion consisting of zirconium oxide and tungsten oxide

nanoparticles. The increase of the pump rate from 0.7 to 1.2 ml/min led to a distinct increase in the granule size. The change of the power output has to be evaluated different for a power of 4 up to 8 W and for a power of 20 W. A strong decrease of the granule size and severe shape distortion were observed for a power of 20 W, whereas no changes in size and shape were seen for a power up to 8 W. The change of the inlet temperature (130 – 150 °C) did not show a clear impact on the granule size and shape.

## 6.2 Outlook

New approaches are necessary to expand the possibilities of PBF-LB of high performance aluminum oxide ceramics to combine high mechanical strength with good part accuracy in complex parts.

Currently, the only approach to have dense and crack-free parts with high mechanical strength are the combination of PBF-LB with high temperature preheating (above 1600°C) [15, 16, 54]. However, the feasible geometries are extremely limited. The uniformity of the extreme high temperature preheating is the main challenge, which must be improved to allow the build of larger and more complex structures. EBM could offer a possibility to generate a high temperature preheating, but the electrical charging of powder should be taken into account, in case non-electrically conductive materials are used. Klimov et al. showed the possibility to additively manufacture oxide ceramics by an electron beam reaching a temperature of 1350 °C [286]. However, they dealt with apparent porosity in the samples. Implementation of dopants could be a solution to improve the electrical conductivity and thus, finally improve the part properties.

Another suitable approach to avoid cracking could be the use of laser beam shapers instead of the standard scanning approach. The processing principle would be comparable to vat photopolymerization using the Lithography-based Ceramic Manufacturing-Digital light processing (LCM-DLP) technology [39]. In this technology, a digital micromirror device coupled with a projection system creates the layer image in a photopolymer resin. The image projection could be done for the laser beam by e.g. a top hat, a spatial light modulator or also a digital micromirror device. The advantage of using powerful lasers would be that no time-intensive debinding and sintering step would be necessary as for VAT Photopolymerization processed ceramic parts. Furthermore, thermal stresses in x-y plane would be reduced. Crack formation would be aggravated by bigger, in temperature more homogenous areas compared to the traditional PBF-LB processing with a small laser spot size. However, the complexity range of the structures would be limited, since processing of small recesses would also create peaks of thermal stresses. First tests of Florio with an continuous wave infrared laser (wavelength: 1070 nm; power 60

W; scanning speed: 1.5 mm/s) out of focus (laser spot size of 5 mm moving in a circle of 2 mm) showed the feasibility of this laser to deliver enough energy to consolidate pure  $\text{ZrO}_2/\text{WO}_3$  granules by using a beam shaper [251]. Dense cylindrically shaped parts (50 layers of 100  $\mu\text{m}$ ) with a few microcracks were processed by this way. Other powders ( $\text{Fe}_2\text{O}_3$ -doped  $\text{Al}_2\text{O}_3$ ,  $\text{Al}_2\text{O}_3$  with 10 Vol%  $\text{TiO}_{2-x}$  and  $\text{ZrO}_2/\text{WO}_3$  granules mixed with 50 Vol% coarse  $\text{Al}_2\text{O}_3$  particles) gave a higher amount of pores or cracks (power 60-160 W, layer thickness 100-400  $\mu\text{m}$ ). Furthermore, a non-uniform consolidation was observed due to the Gaussian distribution of the laser light [251]. However, this problem should be avoided by the use of beam shapers having focusing optics.

The need to avoid cracks reducing thermal stresses is often in contrast with the need for a fine microstructure. As seen in the authors work and by other authors, PBF-LB can increase the crystallite size if pure alumina is used and if the cooling rate is relatively low [57]. This phenomenon will in consequence weaken the mechanical properties of the laser-processed parts due to decreased fracture toughness even when micro-cracks can be avoided. A solution for the problem could be the addition of different oxide dopants, which are known to decrease the grain growth for certain materials (e.g. cobalt oxide, nickel oxide, magnesium oxide, barium oxide etc. for aluminum oxide [157]) or to adjust the laser parameter to achieve a high cooling rate. On the other hand, big grains are beneficial for high temperature applications due to reduced creep behavior, which could be a chance for LAM to find a future application field in this sector. Furthermore, dopants to generate nucleation from the melt during solidification to achieve precipitation hardening could be used. However, the use of dopants also changes the physics of the process completely and lead thus to difficult process adjustments.

Post processing of the parts could be another possibility. Wilkes and Wissenbach suggested an infiltration of the cracks by molten glass and the use of hot isostatic pressing for crack healing of selective laser melted samples [72]. However, to infiltrate cracks by glass the glass melt needs to have a low viscosity (adjustable by temperature or additives) and the part needs to have a reasonable amount of open porosity for full infiltration. Lee et al. [78] infiltrated laser manufactured alumina-glass composites with colloidal silica and thermally annealed the parts. The strength increase was 3-5 MPa due to porosity reduction. Hot isostatic pressing is promising, but its efficacy in closing relatively large cracks should be proven. Furthermore, it is a time-intensive and thus an expensive option. Similar to this method, Ceracon forging was applied to further densify laser processed parts [77]. Instead of the gaseous medium in hot isostatic pressing, solid ceramic particles are used to transmit pressures up to 1400 MPa [261]. The 4-

point strength of the alumina glass composites reached values up to 110 MPa after full densification. However, the shrinkage due to strong densification in this process was up to 59 % [77], which is counter-productive for a near net-shape fabrication aimed in LAM.

Another option for improving the current processes is to develop materials that are better suitable for LAM processes. Other materials with low or negative thermal expansion coefficient, high tensile strength and high fracture toughness are desirable for withstanding thermal stresses. These properties could be achieved also through the realization of composites, as for instance done by Wu et al. adding SiC particles [287]. Inclusion of nanofibers or whiskers could be another solution to improve this properties, as already shown for oxide matrices with addition of oxide fibers [288, 289]. Furthermore, Carbide or nitride fibers could be interesting in the case of PBF-LB. However, issues with powder handling have to be expected.

Suitable methods to reduce cracks, which was proven in this work, are the in-situ formation of  $\text{Al}_2\text{T}_1\text{O}_5$  and  $\text{ZrW}_2\text{O}_8$  by the addition of either reduced  $\text{TiO}_{2-x}$  or  $\text{ZrO}_2/\text{WO}_3$  granules to aluminum oxide. Aluminum titanate shows a low Young's modulus [184], a low thermal expansion coefficient and a low thermal conductivity excellent for thermal shock resistance [181]. The use of powder technology could give a better distribution of this phase in the final  $\text{Al}_2\text{O}_3/\text{Al}_2\text{TiO}_5$  parts and thus potentially an even more effective resistance against cracking. For example, a higher amount of coarse aluminum AA18 and more  $\text{TiO}_2$  in the spray-dried granules would lead to this distribution improve within the powder bed and consequently in the PBF-LB processed part. However, the aluminum titanate phase is also prone to decomposition into  $\text{Al}_2\text{O}_3$  and  $\text{TiO}_2$  in a temperature range between 750 and 1300 °C [187]. This decomposition tendency of the PBF-LB produced parts could be further evaluated in a future work. Possible additions to restrain this decomposition given for traditional processing are  $\text{MgO}$  or  $\text{Fe}_2\text{O}_3$  to form solid solutions in the aluminum titanate lattice [184] and additions of  $\text{SiO}_2$ ,  $\text{ZrO}_2$ ,  $\text{ZrTiO}_4$  or mullite to limit the microcrack growth and grain growth [190]. These additives could be also added to powders used for laser processing, what could be done by mechanical blending of raw powders or by direct addition within the granules by spray drying. Ammonium citrate dibasic was already proven as suitable dispersant for  $\text{Fe}_2\text{O}_3$ ,  $\text{ZrO}_2$  and mullite. A drawback of adding additional materials to the powder could be the generation of unwanted phases during laser processing. In the case of  $\text{ZrW}_2\text{O}_8$ , thermal expansion during rapid cooling due to negative thermal expansion [204, 205] and thus creation of compressive stresses result in crack reduction in the aluminum oxide based materials. This could be further optimized by testing more ratios of  $\text{ZrO}_2/\text{WO}_3$  granules to  $\text{Al}_2\text{O}_3$  coarse powder to adjust the resultant thermal expansion in the

oxide ceramic to near zero. The rule of mixture was already reported to be unsuitable to estimate the thermal expansion [209, 213]. Furthermore, it was shown in this work that the suggested ratio according to the Turner model [213] (96.9/3.1 Vol% of  $\text{ZrW}_2\text{O}_8/\text{Al}_2\text{O}_3$ ) gave worse results in terms of crack formation than the also tested ratio of 50/50 Vol%. It could be also interesting to analyze the high temperature behavior of the PBF-LB processed parts, since  $\text{ZrW}_2\text{O}_8$  was reported as unsuitable for high-temperature applications due to an instability from 600 to 1105 °C [204].

The formation of the ternary spinel phase  $\text{FeAl}_2\text{O}_4$  (hercynite) in the final parts processed from the  $\text{Fe}_2\text{O}_3$ -doped  $\text{Al}_2\text{O}_3$  granules was not expected according to phase diagrams referring to the standard conditions [255]. Volume expansion of the spinel formation from the well-dispersed dopants lead to additional crack formation by thermal stresses during this rapid process. Sodium could be added to the granules to potentially avoid this hercynite formation. Liu et al. reported hercynite formation in  $\text{Fe}_2\text{O}_3$ -based  $\text{Al}_2\text{O}_3$  supported oxygen carriers at temperatures above 800 °C [290]. They suggested using a  $\text{Na}_2\text{O}$  doping to inhibit the formation of  $\text{FeAl}_2\text{O}_4$  through formation of a thermomechanically stable sodium aluminate ( $\text{NaAlO}_2$ ) phase. First experiments showed that sodium citrate is a suitable dispersant for both materials. Using this dispersant, sodium could be already homogeneously dispersed within the powder bed prior to the laser fusion.

Finally, fractioning of raw powders or granules (e.g. by air classification or sieve screening) could improve the powder bed density in the PBF-LB process. The ratio between the nearest particle sizes should be more than seven in bimodal or trimodal powder distributions to achieve a high packing density by entering the given interstices of the big particles by smaller particles according to McGeary [128]. Furthermore, the optimal particle size distribution for a high packing density according to the Andreasen model could be closer reached by powder mixing using the calculations of the EMMA Software. Particles sizes below 10 micron should be excluded by the fractioning techniques, since these tend to agglomerate [28] and therefore reducing the flowability, causing poor powder bed density and inhomogeneity. Especially, when employing the Andreasen model, the smaller particles, led to a low apparent density due to a low flowability. However, the stability of spray-dried granules during fractioning in terms of breaking has to be considered, since critical forces given by the methods could destroy the weakly bonded granules. Pre-sintering at low temperatures could be a solution for this. Furthermore, an evaluation of commercially available spherical aluminum oxide powders with bigger particle sizes than the AA18 aluminum oxide will be an option.

---

## References

- [1] N. Travitzky, A. Bonet, B. Dermeik, T. Fey, I. Filbert-Demut, L. Schlier, T. Schlördt, P. Greil, Additive Manufacturing of Ceramic-Based Materials, *Adv. Eng. Mater.* 16(6) (2014) 729-754.
- [2] T. Mühler, C.M. Gomes, J. Heinrich, J. Günster, Slurry-based additive manufacturing of ceramics, *Int. J. Appl. Ceram. Technol.* 12(1) (2015) 18-25.
- [3] A. Gahler, J.G. Heinrich, J. Günster, Direct laser sintering of Al<sub>2</sub>O<sub>3</sub>-SiO<sub>2</sub> dental ceramic components by layer-wise slurry deposition, *J. Am. Ceram. Soc.* 89(10) (2006) 3076-3080.
- [4] Y. Wu, J. Du, K.-L. Choy, L.L. Hench, Laser densification of alumina powder beds generated using aerosol assisted spray deposition, *Journal of the European Ceramic Society* 27(16) (2007) 4727-4735.
- [5] J. Deckers, S. Meyers, J.P. Kruth, J. Vleugels, Direct selective laser sintering/melting of high density alumina powder layers at elevated temperatures, *Phys. Procedia* 56 (2014) 117-124.
- [6] H. Exner, P. Regenfuß, R. Ebert, L. Hartwig, A. Streek, S. Klötzer, M. Horn, Lasermikrosintern von keramischen Materialien, *RTeJournal* 3(3) (2006).
- [7] P. Regenfuss, A. Streek, L. Hartwig, S. Klötzer, T. Brabant, M. Horn, R. Ebert, H. Exner, Principles of laser micro sintering, *Rapid Prototyp. J.* 13(4) (2007) 204-212.
- [8] Z. Fan, M. Lu, H. Huang, Selective laser melting of alumina: A single track study, *Ceram. Int.* 44(8) (2018) 9484-9493.
- [9] J. Liu, S. Bai, Femtosecond laser additive manufacturing of YSZ, *Applied Physics A* 123(4) (2017).
- [10] F. Niu, D. Wu, F. Lu, G. Liu, G. Ma, Z. Jia, Microstructure and macro properties of Al<sub>2</sub>O<sub>3</sub> ceramics prepared by laser engineered net shaping, *Ceram. Int.* 44(12) (2018) 14303-14310.
- [11] Y. Zheng, K. Zhang, T.T. Liu, W.H. Liao, C.D. Zhang, H. Shao, Cracks of alumina ceramics by selective laser melting, *Ceram. Int.* 45(1) (2019) 175-184.
- [12] Z. Fan, Y. Zhao, Q. Tan, N. Mo, M.-X. Zhang, M. Lu, H. Huang, Nanostructured Al<sub>2</sub>O<sub>3</sub>-YAG-ZrO<sub>2</sub> ternary eutectic components prepared by laser engineered net shaping, *Acta Mater.* 170 (2019) 24-37.
- [13] V.K. Balla, S. Bose, A. Bandyopadhyay, Processing of bulk alumina ceramics using laser engineered net shaping, *Int. J. Appl. Ceram. Technol.* 5(3) (2008) 234-242.
- [14] S. Buls, J. Vleugels, B. Van Hooreweder, Microwave assisted selective laser melting of technical ceramics, *Annual international solid freeform fabrication symposium - an additive manufacturing conference* 29 (2018) 2349-2357.
- [15] Y.-C. Hagedorn, J. Wilkes, W. Meiners, K. Wissenbach, R. Poprawe, Net shaped high performance oxide ceramic parts by selective laser melting, *Phys. Procedia* 5 (2010) 587-594.
- [16] J. Wilkes, Y.C. Hagedorn, W. Meiners, K. Wissenbach, Additive manufacturing of ZrO<sub>2</sub>-Al<sub>2</sub>O<sub>3</sub> ceramic components by selective laser melting, *Rapid Prototyp. J.* 19(1) (2013) 51-57.
- [17] K. Florio, S. Pfeiffer, M. Makowska, N. Casati, F. Verga, T. Graule, H. Van Swygenhoven, K. Wegener, An innovative selective laser melting process for hematite-doped aluminum oxide, *Adv. Eng. Mater.* 21(6) (2019).
- [18] P. Bertrand, F. Bayle, C. Combe, P. Goeuriot, I. Smurov, Ceramic components manufacturing by selective laser sintering, *Appl. Surf. Sci.* 254(4) (2007) 989-992.
- [19] B. Qian, Z. Shen, Laser sintering of ceramics, *Journal of Asian Ceramic Societies* 1(4) (2013) 315-321.
- [20] N.K. Tolochko, Y.V. Khlopkov, S.E. Mozzharov, M.B. Ignatiev, T. Laoui, V.I. Titov, Absorptance of powder materials suitable for laser sintering, *Rapid Prototyp. J.* 6(3) (2000) 155-161.



- 
- [21] A.J. Pinkerton, Lasers in additive manufacturing, *Optics & Laser Technology* 78 (2016) 25-32.
- [22] T. Wohlers, R.I. Campbell, O. Diegel, R. Huff, J. Kowen, Wohlers Report 2020: 3D Printing and Additive Manufacturing State of the Industry Wohlers Associates Fort Collins, CO, 2020.
- [23] T. Moritz, S. Maleksaeedi, Additive manufacturing of ceramic components, in: J. Zhang, Y.-G. Jung (Eds.), *Addit. Manuf.*, Butterworth-Heinemann, 2018, 105-161.
- [24] I. Astm, ASTM52900-15 Standard Terminology for Additive Manufacturing—General Principles—Terminology, ASTM International, West Conshohocken, PA, 2015.
- [25] J.J. Beaman, C.R. Deckard, United States Patent 4938816, United States Patent 4938816 (1990).
- [26] A. Zocca, P. Colombo, C.M. Gomes, J. Günster, D.J. Green, Additive Manufacturing of Ceramics: Issues, Potentialities, and Opportunities, *J. Am. Ceram. Soc.* 98(7) (2015) 1983-2001.
- [27] S. Vock, B. Klöden, A. Kirchner, T. Weißgärber, B. Kieback, Powders for powder bed fusion: a review, *Progress in Additive Manufacturing* 4(4) (2019) 383-397.
- [28] K. Kendall, Adhesion: Molecules and Mechanics, *Science* 263(5154) (1994) 1720-1725.
- [29] K. Kendall, Peel Adhesion of Solid Films-The Surface and Bulk Effects, *The Journal of Adhesion* 5(3) (1973) 179-202.
- [30] K. Kendall, Kinetics of Contact between Smooth Solids, *The Journal of Adhesion* 7(1) (1975) 55-72.
- [31] K. Kendall, The dynamics of slow peeling, *International Journal of Fracture* 11(1) (1975) 3-12.
- [32] T. Krause, S. Engler, J. Gunster, J.G. Heinrich, Process and a device for producing ceramic molds, Google Patents, 2004.
- [33] D.S. Thomas, S.W. Gilbert, Costs and cost effectiveness of additive manufacturing, 2014.
- [34] B.P. Conner, G.P. Manogharan, A.N. Martof, L.M. Rodomsky, C.M. Rodomsky, D.C. Jordan, J.W. Limperos, Making sense of 3-D printing: Creating a map of additive manufacturing products and services, *Addit. Manuf.* 1-4 (2014) 64-76.
- [35] Print me a Stradivarius - How a new manufacturing technology will change the world, *The Economist*. 2011 (accessed 17.07.2020.).
- [36] B. Berman, 3-D printing: The new industrial revolution, *Business Horizons* 55(2) (2012) 155-162.
- [37] P. Serlenga, F. Montaville, Five Questions to Shape a Winning 3-D Printing Strategy, Bain & Company, Inc. <https://www.bain.com/insights/five-questions-to-shape-a-winning-3d-printing-strategy/>, 2015 (accessed 02.06.2020.).
- [38] V. Petrovic, J. Vicente Haro Gonzalez, O. Jordá Ferrando, J. Delgado Gordillo, J. Ramón Blasco Puchades, L. Portolés Griñan, Additive layered manufacturing: sectors of industrial application shown through case studies, *International Journal of Production Research* 49(4) (2011) 1061-1079.
- [39] M. Borlaf, A. Serra-Capdevila, C. Colominas, T. Graule, Development of UV-curable ZrO<sub>2</sub> slurries for additive manufacturing (LCM-DLP) technology, *Journal of the European Ceramic Society* 39(13) (2019) 3797-3803.
- [40] M. Pfaffinger, G. Mitteramskogler, R. Gmeiner, J. Stampfl, Thermal Debinding of Ceramic-Filled Photopolymers, *Mater. Sci. Forum* 825-826 (2015) 75-81.
- [41] S.H. Huang, P. Liu, A. Mokasdar, L. Hou, Additive manufacturing and its societal impact: a literature review, *Int. J. Adv. Manuf. Technol.* 67(5) (2013) 1191-1203.
- [42] N. Gladstone, Disadvantages of 3D Printers. <https://ourpastimes.com/disadvantages-of-3d-printers-12438915.html>, (accessed 17.07.2020.).
- [43] F. Klocke, Modern approaches for the production of ceramic components, *Journal of the European Ceramic Society* 17(2) (1997) 457-465.
-

- 
- [44] J.F. Li, L. Li, F.H. Stott, Thermal stresses and their implication on cracking during laser melting of ceramic materials, *Acta Mater.* 52(14) (2004) 4385-4398.
- [45] P. Stoneman, *The economics of technological diffusion*, Wiley-Blackwell, 2001.
- [46] S. Mellor, L. Hao, D. Zhang, Additive manufacturing: A framework for implementation, *International Journal of Production Economics* 149 (2014) 194-201.
- [47] D. Doherty, Downloading infringement: patent law as a roadblock to the 3D printing revolution, *Harv. JL & Tech.* 26 (2012) 353.
- [48] H. Salmang, H. Scholze, *Keramik*, Springer-Verlag Berlin Heidelberg Berlin Heidelberg 2007.
- [49] J.D. Cawley, Solid freeform fabrication of ceramics, *Current Opinion in Solid State and Materials Science* 4(5) (1999) 483-489.
- [50] E. Juste, F. Petit, V. Lardot, F. Cambier, Shaping of ceramic parts by selective laser melting of powder bed, *J. Mater. Res.* 29(17) (2014) 2086-2094.
- [51] M. Mapar, D.Q. Zhang, Z.H. Liu, W.Y. Yeong, C.K. Chua, B.Y. Tay, O. Geramifard, S. Maleksaeedi, F.E. Wiria, Preparation and flowability characterization of ceramic powders for selective laser melting, *High value manufacturing: Advanced research in virtual and rapid prototyping*, Leiria, PT, 2014, 267-271.
- [52] M. Mapar, *Selective laser melting of ceramic-based materials for dental applications*, Nanyang Technological University, 2014.
- [53] H. Liu, H. Su, Z. Shen, E. Wang, D. Zhao, M. Guo, J. Zhang, L. Liu, H. Fu, Direct formation of  $\text{Al}_2\text{O}_3/\text{GdAlO}_3/\text{ZrO}_2$  ternary eutectic ceramics by selective laser melting: Microstructure evolutions, *Journal of the European Ceramic Society* 38(15) (2018) 5144-5152.
- [54] Q. Liu, Y. Danlos, B. Song, B. Zhang, S. Yin, H. Liao, Effect of high-temperature preheating on the selective laser melting of yttria-stabilized zirconia ceramic, *J. Mater. Process. Tech.* 222 (2015) 61-74.
- [55] Q. Liu, B. Song, H. Liao, Microstructure study on selective laser melting yttria stabilized zirconia ceramic with near IR fiber laser, *Rapid Prototyp. J.* (2014).
- [56] F. Verga, M. Borlaf, L. Conti, K. Florio, M. Vetterli, T. Graule, M. Schmid, K. Wegener, Laser-based powder bed fusion of alumina toughened zirconia, *Addit. Manuf.* 31 (2020).
- [57] L. Ferrage, G. Bertrand, P. Lenormand, Dense yttria-stabilized zirconia obtained by direct selective laser sintering, *Addit. Manuf.* 21 (2018) 472-478.
- [58] L. Moniz, C. Colin, J.-D. Bartout, K. Terki, M.-H. Berger, Laser beam melting of alumina: Effect of absorber additions, *Jom* 70(3) (2018) 328-335.
- [59] M. Gan, C. Wong, Experimental studies on the properties of selectively laser melted alumina-spodumene composite, *Ceram. Int.* 44(15) (2018) 19008-19015.
- [60] H. Exner, M. Horn, A. Streek, L. Hartwig, R. Ebert, First results in laser micro sintering of ceramic materials, *European Congress on Advanced Materials and Processes*, Prague, 2005.
- [61] H. Exner, M. Horn, A. Streek, F. Ullmann, L. Hartwig, P. Regenfuß, R. Ebert, Laser micro sintering: A new method to generate metal and ceramic parts of high resolution with sub-micrometer powder, *Virt. Phys. Prototyping* 3(1) (2008) 3-11.
- [62] P. Regenfuss, A. Streek, L. Hartwig, M. Horn, S. Klötzer, R. Ebert, H. Exner, Laser micro sintering of ceramics—reaction models and results, *Ceramic Forum International/Ber. DKG*, 2008, 65-72.
- [63] H. Exner, A. Streek, High resolution laser micro sintering/melting using q-switched and high brilliant laser radiation, *Laser 3D Manufacturing II*, International Society for Optics and Photonics, 2015, 93530P.
- [64] J.G. Heinrich, A. Gahler, J. Günster, M. Schmücker, J. Zhang, D. Jiang, M. Ruan, Microstructural evolution during direct laser sintering in the  $\text{Al}_2\text{O}_3\text{--SiO}_2$  system, *J. Mater. Sci.* 42(14) (2007) 5307-5311.
-

- 
- [65] K. Zhang, T. Liu, W. Liao, C. Zhang, Y. Yan, D. Du, Influence of laser parameters on the surface morphology of slurry-based Al<sub>2</sub>O<sub>3</sub> parts produced through selective laser melting, *Rapid Prototyp. J.* 24(2) (2018) 333-341.
- [66] A.M. Waetjen, D.A. Polsakiewicz, I. Kuhl, R. Telle, H. Fischer, Slurry deposition by airbrush for selective laser sintering of ceramic components, *Journal of the European Ceramic Society* 29(1) (2009) 1-6.
- [67] J. Robertson, Band offsets of wide-band-gap oxides and implications for future electronic devices, *Journal of Vacuum Science & Technology B: Microelectronics and Nanometer Structures Processing, Measurement, and Phenomena* 18(3) (2000) 1785-1791.
- [68] Z. Zhao, M. Mapar, W.Y. Yeong, S. Zhang, D. Zhao, Initial Study of Selective Laser Melting of ZrO<sub>2</sub>/Al<sub>2</sub>O<sub>3</sub> Ceramic, *Proceedings of the 1st International Conference on Progress in Additive Manufacturing*, 2014.
- [69] A. Henniche, J. Ouyang, Y. Ma, Z. Wang, Z. Liu, Y. Wang, M. Derradji, X. Liu, Microstructure, mechanical and thermo-physical properties of hot-pressed Al<sub>2</sub>O<sub>3</sub>-GdAlO<sub>3</sub>-ZrO<sub>2</sub> ceramics with eutectic composition, *Progress in Natural Science: Materials International* 27(4) (2017) 491-497.
- [70] Y.-C. Hagedorn, Additive manufacturing of high performance oxide ceramics via selective laser melting, RWTH Aachen, 2013.
- [71] N. Coulon, P. Aubry, Results on laser sintering system for direct manufacturing of metallic or ceramic components, *International Congress on Applications of Lasers & Electro-Optics* 2004(1) (2004) P543.
- [72] J. Wilkes, K. Wissenbach, Rapid manufacturing of ceramic components by selective laser melting, *Lasers in Manufacturing*, Munich, 2007, 207-211.
- [73] J. Wilkes, K. Wissenbach, Rapid manufacturing of ceramic components for medical and technical applications via selective laser melting, *Conferences Euro-uRapid*, Frankfurt, 2006.
- [74] R.S. Khmyrov, C.E. Protasov, S.N. Grigoriev, A.V. Gusarov, Crack-free selective laser melting of silica glass: single beads and monolayers on the substrate of the same material, *Int. J. Adv. Manuf. Technol.* 85(5) (2016) 1461-1469.
- [75] R. Gmeiner, U. Deisinger, J. Schönherr, B. Lechner, R. Detsch, A. Boccaccini, J. Stampfl, Additive manufacturing of bioactive glasses and silicate bioceramics, *J. Ceram. Sci. Technol* 6(2) (2015) 75-86.
- [76] G. Manob, L. Lu, J. Fuh, Y. Cheng, Porous Li<sub>2</sub>O Al<sub>2</sub>O<sub>3</sub>SiO<sub>2</sub> (LAS) Glass-Ceramics Prepared by Selective Laser Melting and Annealing, *27th Annual Cocoa Beach Conference on Advanced Ceramics and Composites: B: Ceramic Engineering and Science Proceedings*, Wiley Online Library, 2003, 523-528.
- [77] I.S. Lee, Rapid full densification of alumina-glass composites fabricated by a selective laser sintering process, *J. Mater. Sci. Lett.* 17(22) (1998) 1907-1911.
- [78] I. Lee, A. Manthiram, H. Marcus, Selective laser sintering of alumina-zinc borosilicate glass composites using monoclinic HB02 as a binder, *1995 International Solid Freeform Fabrication Symposium*, 1995.
- [79] I. Lee, A. Manthiram, H. Marcus, Selective Laser Sintering of Alumina-Boron Oxide Composites, *1994 International Solid Freeform Fabrication Symposium*, 1994.
- [80] B.H. Bae, J.W. Lee, J.M. Cha, I.-W. Kim, H.-D. Jung, C.-B. Yoon, Preliminary Characterization of Glass/Alumina Composite Using Laser Powder Bed Fusion (L-PBF) Additive Manufacturing, *Materials* 13(9) (2020) 2156.
- [81] W. Wang, Y.X. Liu, J.Y.H. Fuh, P.J. Wang, Alumina-Zirconia-Silica Ceramics Synthesis by Selective Laser Sintering/Melting, *Applied Mechanics and Materials* 121-126 (2011) 2487-2491.
- [82] W. Wang, S. Ma, J. Fuh, L. Lu, Y. Liu, Processing and characterization of laser-sintered Al<sub>2</sub>O<sub>3</sub>/ZrO<sub>2</sub>/SiO<sub>2</sub>, *Int. J. Adv. Manuf. Technol.* 68(9-12) (2013) 2565-2569.
-

- 
- [83] K. Subramanian, G. Zong, H. Marcus, Selective laser sintering and reaction sintering of ceramic composites, 1992 International Solid Freeform Fabrication Symposium, 1992.
- [84] A. Slocombe, L. Li, Selective laser sintering of TiC–Al<sub>2</sub>O<sub>3</sub> composite with self-propagating high-temperature synthesis, *J. Mater. Process. Tech.* 118(1) (2001) 173-178.
- [85] W. Duckworth, Discussion of ryshkewitch paper by winston duckworth, *J. Am. Ceram. Soc.* 36 (1953) 68.
- [86] R. Spriggs, T. Vasilos, Effect of grain size and porosity on the transverse bend strength and elastic modulus of hot pressed alumina and magnesia, *J. Am. Ceram. Soc.* 40(4) (1961) 187.
- [87] S. Brown, R. Biddulph, P. Wilcox, A strength–porosity relation involving different pore geometry and orientation, *J. Am. Ceram. Soc.* 47(7) (1964) 320-322.
- [88] D. Hasselman, Griffith flaws and the effect of porosity on tensile strength of brittle ceramics, *J. Am. Ceram. Soc.* 52(8) (1969) 457-457.
- [89] A. Standard, Standard test methods for apparent porosity, water absorption, apparent specific gravity, and bulk density of burned refractory brick and shapes by boiling water, West Conshohocken, PA.: ASTM C20-00 (2015).
- [90] G.D. Quinn, R.C. Bradt, On the Vickers Indentation Fracture Toughness Test, *J. Am. Ceram. Soc.* 90(3) (2007) 673-680.
- [91] A.A. Griffith, VI. The phenomena of rupture and flow in solids, *Philosophical transactions of the royal society of london. Series A, containing papers of a mathematical or physical character* 221(582-593) (1921) 163-198.
- [92] C.B. Carter, M.G. Norton, *Ceramic materials* Springer Verlag, New York, 2013.
- [93] G.R. Irwin, Analysis of stresses and strains near the end of a crack traversing a plate, (1957).
- [94] G. Sih, H. Liebowitz, On the Griffith energy criterion for brittle fracture, *International Journal of Solids and Structures* 3(1) (1967) 1-22.
- [95] S. Pfeiffer, K. Florio, M. Makowska, D. Ferreira Sanchez, H. Van Swygenhoven, C.G. Aneziris, K. Wegener, T. Graule, Iron oxide doped spray dried aluminum oxide granules for selective laser sintering and melting of ceramic parts, *Adv. Eng. Mater.* 21(6) (2019).
- [96] J.I. Wilkes, *Selektives Laserschmelzen zur generativen Herstellung von Bauteilen aus hochfester Oxidkeramik*, RWTH Aachen, 2009.
- [97] K. Shimizu, M. Oka, P. Kumar, Y. Kotoura, T. Yamamuro, K. Makinouchi, T. Nakamura, Time-dependent changes in the mechanical properties of zirconia ceramic, *J. Biomed. Mater. Res.* 27(6) (1993) 729-734.
- [98] A.V. Gusarov, I.S. Malakhova-Ziablova, M.D. Pavlov, Thermoelastic Residual Stresses and Deformations at Laser Treatment, *Phys. Procedia* 41 (2013) 896-903.
- [99] A.V. Gusarov, M. Pavlov, I. Smurov, Residual Stresses at Laser Surface Remelting and Additive Manufacturing, *Phys. Procedia* 12 (2011) 248-254.
- [100] M. Yamane, J.D. Mackenzie, Vicker's Hardness of glass, *J. Non-Cryst. Solids* 15(2) (1974) 153-164.
- [101] A. Krell, P. Blank, Grain Size Dependence of Hardness in Dense Submicrometer Alumina, *J. Am. Ceram. Soc.* 78(4) (1995) 1118-1120.
- [102] Y.-D. Qiu, J.-M. Wu, A.-N. Chen, P. Chen, Y. Yang, R.-Z. Liu, G. Chen, S. Chen, Y.-S. Shi, C.-H. Li, Balling phenomenon and cracks in alumina ceramics prepared by direct selective laser melting assisted with pressure treatment, *Ceram. Int.* 46(9) (2020) 13854-13861.
- [103] S.J. Lukasiewicz, Spray-Drying Ceramic Powders, *J. Am. Ceram. Soc.* 72(4) (1989) 617-624.
- [104] J. Elversson, A. Millqvist-Fureby, G. Alderborn, U. Elofsson, Droplet and particle size relationship and shell thickness of inhalable lactose particles during spray drying, *J. Pharm. Sci.* 92(4) (2003) 900-910.
- [105] K. Schmid, C. Arpagaus, W. Friess, Evaluation of the Nano Spray Dryer B-90 for pharmaceutical applications, *Pharm. Dev. Technol.* 16(4) (2011) 287-294.
-

- 
- [106] A. Marie, M. Tourbin, A.-C. Robisson, C. Ablitzer, C. Frances, Wet size measurements for the evaluation of the deagglomeration behaviour of spray-dried alumina powders in suspension, *Ceram. Int.* 48(6) (2022) 7926-7936.
- [107] M.O. Panão, A.L.N. Moreira, J. Vicente, E. Costa, Assessment of ultrasonic sprays for spray drying, *Assessment* 7(10) (2014).
- [108] F. Iskandar, A.B.D. Nandiyanto, K.M. Yun, C.J. Hogan Jr, K. Okuyama, P. Biswas, Enhanced photocatalytic performance of brookite TiO<sub>2</sub> macroporous particles prepared by spray drying with colloidal templating, *Adv. Mater.* 19(10) (2007) 1408-1412.
- [109] N. Tsapis, D. Bennett, B. Jackson, D.A. Weitz, D. Edwards, Trojan particles: large porous carriers of nanoparticles for drug delivery, *Proceedings of the National Academy of Sciences* 99(19) (2002) 12001-12005.
- [110] J.M. Mazurkow, N.S. Yüzbaşı, K.W. Domagala, S. Pfeiffer, D. Kata, T. Graule, Nano-Sized Copper (Oxide) on Alumina Granules for Water Filtration: Effect of Copper Oxidation State on Virus Removal Performance, *Environ. Sci. Technol.* 54(2) (2020) 1214-1222.
- [111] W.J. Walker, J.S. Reed, S.K. Verma, Influence of Slurry Parameters on the Characteristics of Spray-Dried Granules, *J. Am. Ceram. Soc.* 82(7) (1999) 1711-1719.
- [112] A. Tsetsekou, C. Agrafiotis, I. Leon, A. Miliadis, Optimization of the rheological properties of alumina slurries for ceramic processing applications Part II: Spray-drying, *Journal of the European Ceramic Society* 21(4) (2001) 493-506.
- [113] X. Cao, R. Vassen, S. Schwartz, W. Jungen, F. Tietz, D. Stöver, Spray-drying of ceramics for plasma-spray coating, *Journal of the European Ceramic Society* 20(14-15) (2000) 2433-2439.
- [114] H.-W. Lee, G. Song, I.-S. Suk, S.-R. Oh, S.-G. Choi, Conference: 96. annual meeting of the American Ceramic Society (ACS), Indianapolis, IN (United States), American Ceramic Society, 1995.
- [115] V. Naglieri, D. Gutknecht, V. Garnier, P. Palmero, J. Chevalier, L. Montanaro, Optimized Slurries for Spray Drying: Different Approaches to Obtain Homogeneous and Deformable Alumina-Zirconia Granules, *Materials* 6(11) (2013) 5382-5397.
- [116] H. Takahashi, N. Shinohara, M. Okumiya, K. Uematsu, T. Junichi, Y. Iwamoto, H. Kamiya, Influence of Slurry Flocculation on the Character and Compaction of Spray-Dried Silicon Nitride Granules, *J. Am. Ceram. Soc.* 78(4) (1995) 903-908.
- [117] J. Tsubaki, H. Yamakawa, T. Mori, H. Mori, Optimization of Granules and Slurries for Press Forming, *J. Ceram. Soc. Jpn.* 110(1286) (2002) 894-898.
- [118] G. Bertrand, P. Roy, C. Filiatre, C. Coddet, Spray-dried ceramic powders: A quantitative correlation between slurry characteristics and shapes of the granules, *Chem. Eng. Sci.* 60(1) (2005) 95-102.
- [119] G. Bertrand, C. Filiatre, H. Mahdjoub, A. Foissy, C. Coddet, Influence of slurry characteristics on the morphology of spray-dried alumina powders, *Journal of the European Ceramic Society* 23(2) (2003) 263-271.
- [120] P. Höhne, B. Mieller, T. Rabe, Slurry development for spray granulation of ceramic multicomponent batches, (2018).
- [121] F. Iskandar, L. Gradon, K. Okuyama, Control of the morphology of nanostructured particles prepared by the spray drying of a nanoparticle sol, *J. Colloid Interface Sci.* 265(2) (2003) 296-303.
- [122] J.M. Phelps, O. Ratsep, Spray Drying Ceramics, 86th Annual Meeting, and the 1984 Fall Meeting of the Materials & Equipment and Whitewares Divisions: Ceramic Engineering and Science Proceedings, 1984.
- [123] P.C. Hidber, T.J. Graule, L.J. Gauckler, Competitive adsorption of citric acid and poly (vinyl alcohol) onto alumina and its influence on the binder migration during drying, *J. Am. Ceram. Soc.* 78(7) (1995) 1775-1780.

- 
- [124] S. Baklouti, T. Chartier, J. Baumard, Binder distribution in spray-dried alumina agglomerates, *Journal of the European Ceramic Society* 18(14) (1998) 2117-2121.
- [125] S. Tanaka, C. Chia-Pin, Z. Kato, K. Uematsu, Effect of internal binder on microstructure in compacts made from granules, *Journal of the European Ceramic Society* 27(2-3) (2007) 873-877.
- [126] M. Vicent, E. Sánchez, G. Mallol, R. Moreno, Study of colloidal behaviour and rheology of Al<sub>2</sub>O<sub>3</sub>-TiO<sub>2</sub> nanosuspensions to obtain free-flowing spray-dried granules for atmospheric plasma spraying, *Ceram. Int.* 39(7) (2013) 8103-8111.
- [127] J.S. Reed, *Introduction to the Principles of Ceramic Processing*, first ed., John Wiley & Sons, Inc., 1988.
- [128] R.K. McGeary, Mechanical packing of spherical particles, *J. Am. Ceram. Soc.* 44(10) (1961) 513-522.
- [129] A.H.M. Andreassen, J. Andersen, The relationship between grain gradation and the clearance in products from loosening grains (with some experiments), *Z. Kolloid* 50 (1930) 217-228.
- [130] Y. Zou, C.-H. Li, J.-A. Liu, J.-M. Wu, L. Hu, R.-F. Gui, Y.-S. Shi, Towards fabrication of high-performance Al<sub>2</sub>O<sub>3</sub> ceramics by indirect selective laser sintering based on particle packing optimization, *Ceram. Int.* 45(10) (2019) 12654-12662.
- [131] T. Stovall, F. de Larrard, M. Buil, Linear packing density model of grain mixtures, *Powder Technol.* 48(1) (1986) 1-12.
- [132] B. Derjaguin, L. Landau, Theory of the stability of strongly charged lyophobic sols and of the adhesion of strongly charged particles in solution of electrolytes, *Acta Physicochim: USSR* 14 (1941) 633-662.
- [133] B. Derjaguin, Untersuchungen über die Reibung und Adhäsion, IV, *Kolloid-Zeitschrift* 69(2) (1934) 155-164.
- [134] E.J.W. Verwey, J.T.G. Overbeek, K. Van Nes, *Theory of the stability of lyophobic colloids: the interaction of sol particles having an electric double layer*, Elsevier Publishing Company, 1948.
- [135] J. Israelachvili, *Intermolecular and Surface Forces (Second Edition)*, Elsevier Academic Press, 1991.
- [136] J. Moore, E. Cerasoli, *Particle light scattering methods and applications*, (2017).
- [137] O. Stern, The theory of the electric double layer, *Z. Electrochem* 30(508) (1924) 40.
- [138] D.C. Grahame, Diffuse Double Layer Theory for Electrolytes of Unsymmetrical Valence Types, *The Journal of Chemical Physics* 21(6) (1953) 1054-1060.
- [139] R.J. Hunter, *Foundations of colloid science*, second ed., Oxford University Press, 2001.
- [140] D.F. Evans, H. Wennerström, *The colloidal domain: where physics, chemistry, biology, and technology meet*, second ed., Wiley-VCH, 1999.
- [141] L. Bergström, Hamaker constants of inorganic materials, *Adv. Colloid Interface Sci.* 70 (1997) 125-169.
- [142] E. Piacenza, A. Presentato, R.J. Turner, Stability of biogenic metal(loid) nanomaterials related to the colloidal stabilization theory of chemical nanostructures, *Critical Reviews in Biotechnology* 38(8) (2018) 1137-1156.
- [143] G.E. Brown, V.E. Henrich, W.H. Casey, D.L. Clark, C. Eggleston, A. Felmy, D.W. Goodman, M. Grätzel, G. Maciel, M.I. McCarthy, Metal oxide surfaces and their interactions with aqueous solutions and microbial organisms, *Chem. Rev.* 99(1) (1999) 77-174.
- [144] P.C. Hidber, T.J. Graule, L.J. Gauckler, Influence of the dispersant structure on properties of electrostatically stabilized aqueous alumina suspensions, *Journal of the European Ceramic Society* 17(2) (1997) 239-249.
- [145] G.V. Chilingar, Study of the dispersing agents, *Journal of Sedimentary Research* 22(4) (1952) 229-233.
-

- 
- [146] P.C. Hidber, T.J. Graule, L.J. Gauckler, Citric acid—A dispersant for aqueous alumina suspensions, *J. Am. Ceram. Soc.* 79(7) (1996) 1857-1867.
- [147] Z. Zhang, M.F. Modest, Temperature-dependent absorptances of ceramics for Nd:YAG and CO<sub>2</sub> laser processing applications, *J. Heat Transfer* 120(2) (1998) 322-327.
- [148] V.A. Petrov, Abrupt increase of the absorption coefficient of alumina at melting by laser radiation and its decrease at solidification, *Int. J. Thermophys.* 30(6) (2009) 1938-1959.
- [149] S. Chang, L. Li, L. Lu, J.Y.H. Fuh, Selective laser sintering of porous silica enabled by carbon additive, *Materials* 10(11) (2017).
- [150] H. Feng, Y. Wang, C. Wang, F. Diao, W. Zhu, P. Mu, L. Yuan, G. Zhou, F. Rosei, Defect-induced enhanced photocatalytic activities of reduced  $\alpha$ -Fe<sub>2</sub>O<sub>3</sub> nanoblades, *Nanotechnology* 27(29) (2016).
- [151] M. Sharrouf, R. Awad, M. Roumié, S. Marhaba, Structural, optical and room temperature magnetic study of Mn<sub>2</sub>O<sub>3</sub> nanoparticles, *Mater. Sci. Appl.* 06(10) (2015) 850-859.
- [152] X. Zhang, S. Pfeiffer, P. Rutkowski, M. Makowska, D. Kata, J. Yang, T. Graule, Laser cladding of manganese oxide doped aluminum oxide granules on titanium alloy for biomedical applications, *Appl. Surf. Sci.* 520 (2020) 146304.
- [153] S. Piccinin, The band structure and optical absorption of hematite ( $\alpha$ -Fe<sub>2</sub>O<sub>3</sub>): a first-principles GW-BSE study, *Phys. Chem. Chem. Phys.* 21(6) (2019) 2957-2967.
- [154] D. Duc Dung, D. Van Thiet, D. Anh Tuan, S. Cho, Strain effects in epitaxial Mn<sub>2</sub>O<sub>3</sub> thin film grown on MgO (100), *J. Appl. Phys.* 113(17) (2013) 17A314.
- [155] H. Erkalfa, Z. Misirli, M. Demirci, C. Toy, T. Baykara, The densification and microstructural development of Al<sub>2</sub>O<sub>3</sub> with manganese oxide addition, *Journal of the European Ceramic Society* 15(2) (1995) 165-171.
- [156] I.B. Cutler, Nucleation and nuclei growth in sintered alumina, *Kinetics of high temperature process part III*, Technology Press of M. I. T. and John Wiley & Sons, 1959, 120-127.
- [157] H.P. Cahoon, C.J. Christensen, Sintering and grain growth of alpha-alumina, *J. Am. Ceram. Soc.* 39(10) (1956) 337-344.
- [158] M. Sathiyakumar, F.D. Gnanam, Influence of MnO and TiO<sub>2</sub> additives on density, microstructure and mechanical properties of Al<sub>2</sub>O<sub>3</sub>, *Ceram. Int.* 28(2) (2002) 195-200.
- [159] M. Makowska, S. Pfeiffer, N. Casati, K. Florio, M. Vetterli, K. Wegener, T. Graule, H. van Swygenhoven, Pre-processing of hematite-doped alumina granules for selective laser melting, *Ceram. Int.* 45(14) (2019) 17014-17022.
- [160] J.J. Rasmussen, G.B. Stringfellow, I.B. Cutler, S.D. Brown, Effect of impurities on the strength of polycrystalline magnesia and alumina, *J. Am. Ceram. Soc.* 48(3) (1965) 146-150.
- [161] P. Tartaj, J. Tartaj, Preparation, characterization and sintering behavior of spherical iron oxide doped alumina particles, *Acta Mater.* 50(1) (2002) 5-12.
- [162] P. Ramavath, M. Swathi, M. Buchi Suresh, R. Johnson, Flow properties of spray dried alumina granules using powder flow analysis technique, *Advanced Powder Technology* 24(3) (2013) 667-673.
- [163] A. Rosenflanz, M. Frey, B. Endres, T. Anderson, E. Richards, C. Schardt, Bulk glasses and ultrahard nanoceramics based on alumina and rare-earth oxides, *Nature* 430(7001) (2004) 761-764.
- [164] D. Wu, D. Zhao, F. Niu, Y. Huang, J. Zhu, G. Ma, In situ synthesis of melt-grown mullite ceramics using directed laser deposition, *J. Mater. Sci.* 55(27) (2020) 12761-12775.
- [165] S. Kanzaki, H. Tabata, T. Kumazawa, S. Ohta, Sintering and mechanical properties of stoichiometric mullite, *J. Am. Ceram. Soc.* 68(1) (1985) C-6-C-7.
- [166] W.E. Cameron, Mullite; a substituted alumina, *Am. Mineral.* 62(7-8) (1977) 747-755.
- [167] H. Schneider, R.X. Fischer, J. Schreuer, Mullite: Crystal Structure and Related Properties, *J. Am. Ceram. Soc.* 98(10) (2015) 2948-2967.
-



- 
- [168] R.D. Shannon, Revised effective ionic radii and systematic studies of interatomic distances in halides and chalcogenides, *Acta crystallographica section A: crystal physics, diffraction, theoretical and general crystallography* 32(5) (1976) 751-767.
- [169] T. Tomiki, J. Tamashiro, Y. Tanahara, A. Yamada, H. Fukutani, T. Miyahara, H. Kato, S. Shin, M. Ishigame, Optical spectra of Y<sub>2</sub>O<sub>3</sub> single crystals in VUV, *J. Phys. Soc. Jpn.* 55(12) (1986) 4543-4549.
- [170] S.A. Ansari, M.M. Khan, M.O. Ansari, S. Kalathil, J. Lee, M.H. Cho, Band gap engineering of CeO<sub>2</sub> nanostructure using an electrochemically active biofilm for visible light applications, *Rsc Advances* 4(32) (2014) 16782-16791.
- [171] R.H. French, Electronic band structure of Al<sub>2</sub>O<sub>3</sub>, with comparison to Alon and AlN, *J. Am. Ceram. Soc.* 73(3) (1990) 477-489.
- [172] Y. Waku, N. Nakagawa, T. Wakamoto, H. Ohtsubo, K. Shimizu, Y. Kohtoku, A ductile ceramic eutectic composite with high strength at 1,873 K, *Nature* 389(6646) (1997) 49-52.
- [173] T. Mah, T.A. Parthasarathy, L.E. Matson, Processing and Mechanical Properties of Al<sub>2</sub>O<sub>3</sub>/Y<sub>3</sub>Al<sub>5</sub>O<sub>12</sub> (YAG) Eutectic Composite, 14th Annual Conference on Composites and Advanced Ceramic Materials: Ceramic Engineering and Science Proceedings, 1990, 1617-1627.
- [174] D. Wu, H. Liu, F. Lu, G. Ma, S. Yan, F. Niu, D. Guo, Al<sub>2</sub>O<sub>3</sub>-YAG eutectic ceramic prepared by laser additive manufacturing with water-cooled substrate, *Ceram. Int.* 45(3) (2019) 4119-4122.
- [175] F. Niu, D. Wu, G. Ma, J. Wang, J. Zhuang, Z. Jin, Rapid fabrication of eutectic ceramic structures by laser engineered net shaping, *Procedia Cirp* 42 (2016) 91-95.
- [176] H. Su, J. Zhang, L. Liu, J. Eckert, H. Fu, Rapid growth and formation mechanism of ultrafine structural oxide eutectic ceramics by laser direct forming, *Appl. Phys. Lett.* 99(22) (2011) 221913.
- [177] Z. Fan, Y. Zhao, Q. Tan, B. Yu, M.-X. Zhang, H. Huang, New insights into the growth mechanism of 3D-printed Al<sub>2</sub>O<sub>3</sub>-Y<sub>3</sub>Al<sub>5</sub>O<sub>12</sub> binary eutectic composites, *Scr. Mater.* 178 (2020) 274-280.
- [178] F. Niu, D. Wu, Y. Huang, S. Yan, G. Ma, C. Li, J. Ding, Direct additive manufacturing of large-sized crack-free alumina/aluminum titanate composite ceramics by directed laser deposition, *Rapid Prototyp. J.* (2019).
- [179] D. Wu, Y. Huang, F. Niu, G. Ma, S. Yan, C. Li, J. Ding, Effects of TiO<sub>2</sub> doping on microstructure and properties of directed laser deposition alumina/aluminum titanate composites, *Virt. Phys. Prototyping* 14(4) (2019) 371-381.
- [180] Y. Huang, D. Wu, D. Zhao, F. Niu, H. Zhang, S. Yan, G. Ma, Process Optimization of Melt Growth Alumina/Aluminum Titanate Composites Directed Energy Deposition: Effects of Scanning Speed, *Addit. Manuf.* (2020) 101210.
- [181] Y. Ohya, S. Yamamoto, T. Ban, M. Tanaka, S. Kitaoka, Thermal expansion and mechanical properties of self-reinforced aluminum titanate ceramics with elongated grains, *Journal of the European Ceramic Society* 37(4) (2017) 1673-1680.
- [182] N.P. Padture, S.J. Bennison, H.M. Chan, Flaw-tolerance and crack-resistance properties of alumina-aluminum titanate composites with tailored microstructures, *J. Am. Ceram. Soc.* 76(9) (1993) 2312-2320.
- [183] S. Bueno, M.-H. Berger, R. Moreno, C. Baudín, Fracture behaviour of microcrack-free alumina-aluminium titanate ceramics with second phase nanoparticles at alumina grain boundaries, *Journal of the European Ceramic Society* 28(10) (2008) 1961-1971.
- [184] I.J. Kim, H. Supkwak, Thermal shock resistance and thermal expansion behaviour with composition and microstructure of Al<sub>2</sub>TiO<sub>5</sub> ceramics, *Can. Metall. Q.* 39(4) (2000) 387-396.
- [185] S. Abali, Effect of TiO<sub>2</sub> doping on microstructural properties of Al<sub>2</sub>O<sub>3</sub>-based single crystal ceramics, *J Ceram Process Res* 12(1) (2011) 21-25.
-

- 
- [186] E. Winkler, J. Sarver, I.B. Cutler, Solid solution of titanium dioxide in aluminum oxide, *J. Am. Ceram. Soc.* 49(12) (1966) 634-637.
- [187] G. Bayer, Thermal expansion characteristics and stability of pseudobrookite-type compounds, *Me<sub>3</sub>O<sub>5</sub>*, *Journal of the Less Common Metals* 24(2) (1971) 129-138.
- [188] I.M. Low, Z. Oo, Reformation of phase composition in decomposed aluminium titanate, *Mater. Chem. Phys.* 111(1) (2008) 9-12.
- [189] V. Buscaglia, P. Nanni, Decomposition of Al<sub>2</sub>TiO<sub>5</sub> and Al<sub>2</sub> (1-x) Mg<sub>x</sub>Ti (1+ x) O<sub>5</sub> ceramics, *J. Am. Ceram. Soc.* 81(10) (1998) 2645-2653.
- [190] C.G. Aneziris, S. Dudczig, N. Gerlach, H. Berek, D. Veres, Thermal shock performance of fine grained Al<sub>2</sub>O<sub>3</sub> ceramics with TiO<sub>2</sub> and ZrO<sub>2</sub> additions for refractory applications, *Adv. Eng. Mater.* 12(6) (2010) 478-485.
- [191] T. Kratschmer, C.G. Aneziris, Improved Thermal Shock Performance of Sintered Mg-Partially Stabilized Zirconia with Alumina and Titania Additions, *Int. J. Appl. Ceram. Technol.* 8(2) (2011) 398-410.
- [192] Y. Chen, D. Wu, G. Ma, W. Lu, D. Guo, Coaxial laser cladding of Al<sub>2</sub>O<sub>3</sub>-13%TiO<sub>2</sub> powders on Ti-6Al-4V alloy, *Surf. Coat. Technol.* 228 (2013) S452-S455.
- [193] X.-s. Gao, Z.-j. Tian, Z.-d. Liu, L.-d. Shen, Interface characteristics of Al<sub>2</sub>O<sub>3</sub>-13%TiO<sub>2</sub> ceramic coatings prepared by laser cladding, *Transactions of Nonferrous Metals Society of China* 22(10) (2012) 2498-2503.
- [194] D. Wang, Z. Tian, S. Wang, L. Shen, Z. Liu, Microstructural characterization of Al<sub>2</sub>O<sub>3</sub>-13wt.% TiO<sub>2</sub> ceramic coatings prepared by squash presetting laser cladding on GH4169 superalloy, *Surf. Coat. Technol.* 254 (2014) 195-201.
- [195] A. Kitada, G. Hasegawa, Y. Kobayashi, K. Kanamori, K. Nakanishi, H. Kageyama, Selective Preparation of Macroporous Monoliths of Conductive Titanium Oxides Ti<sub>n</sub>O<sub>2n-1</sub> (n= 2, 3, 4, 6), *J. Am. Chem. Soc.* 134(26) (2012) 10894-10898.
- [196] T. Ioroi, H. Kageyama, T. Akita, K. Yasuda, Formation of electro-conductive titanium oxide fine particles by pulsed UV laser irradiation, *Phys. Chem. Chem. Phys.* 12(27) (2010) 7529-7535.
- [197] X. Li, A.L. Zhu, W. Qu, H. Wang, R. Hui, L. Zhang, J. Zhang, Magnéli phase Ti<sub>4</sub>O<sub>7</sub> electrode for oxygen reduction reaction and its implication for zinc-air rechargeable batteries, *Electrochim. Acta* 55(20) (2010) 5891-5898.
- [198] I. Tsuyumoto, H. Uchikawa, New orthorhombic titanium oxide, TiO<sub>1.94</sub>, *J. Mater. Sci. Lett.* 19(23) (2000) 2075-2076.
- [199] T. Lin, C. Yang, Z. Wang, H. Yin, X. Lü, F. Huang, J. Lin, X. Xie, M. Jiang, Effective nonmetal incorporation in black titania with enhanced solar energy utilization, *Energy & Environmental Science* 7(3) (2014).
- [200] V. Adamaki, F. Clemens, P. Ragulis, S.R. Pennock, J. Taylor, C.R. Bowen, Manufacturing and characterization of Magnéli phase conductive fibres, *J. Mater. Chem. A* 2(22) (2014) 8328-8333.
- [201] H. Lu, B. Zhao, R. Pan, J. Yao, J. Qiu, L. Luo, Y. Liu, Safe and facile hydrogenation of commercial Degussa P25 at room temperature with enhanced photocatalytic activity, *RSC Adv.* 4(3) (2014) 1128-1132.
- [202] R. Dittmann, E. Wintermantel, T. Graule, Sintering of nano-sized titania particles and the effect of chlorine impurities, *Journal of the European Ceramic Society* 33(15-16) (2013) 3257-3264.
- [203] M. Mazaheri, A. Zahedi, M. Haghighatzadeh, S. Sadrnezhad, Sintering of titania nanoceramic: densification and grain growth, *Ceram. Int.* 35(2) (2009) 685-691.
- [204] A.W. Sleight, Isotropic negative thermal expansion, *Annual review of materials science* 28(1) (1998) 29-43.
- [205] T. Mary, J. Evans, T. Vogt, A. Sleight, Negative thermal expansion from 0.3 to 1050 Kelvin in ZrW<sub>2</sub>O<sub>8</sub>, *Science* 272(5258) (1996) 90-92.
-

- 
- [206] J.-C. Chen, G.-C. Huang, C. Hu, J.-P. Weng, Synthesis of negative-thermal-expansion ZrW<sub>2</sub>O<sub>8</sub> substrates, *Scr. Mater.* 49(3) (2003) 261-266.
- [207] L.L.Y. CHANG, M.G. SCROGER, B. PHILLIPS, Condensed Phase Relations in the Systems ZrO<sub>2</sub>-WO<sub>2</sub>-WO<sub>3</sub> and HfO<sub>2</sub>-WO<sub>2</sub>-WO<sub>3</sub>, *J. Am. Ceram. Soc.* 50(4) (1967) 211-215.
- [208] S. Jacob, J. Javornizky, G.H. Wolf, C.A. Angell, Oxide ion conducting glasses: synthetic strategies based on liquid state and solid state routes, *International Journal of Inorganic Materials* 3(3) (2001) 241-251.
- [209] K. De Buysser, P. Lommens, C. De Meyer, E. Bruneel, S. Hoste, I. Van Driessche, ZrO<sub>2</sub>-ZrW<sub>2</sub>O<sub>8</sub> composites with tailor-made thermal expansion, *Ceram.-Silik.* 48(4) (2004) 139-144.
- [210] L. Sun, P. Kwon, ZrW<sub>2</sub>O<sub>8</sub>/ZrO<sub>2</sub> composites by in situ synthesis of ZrO<sub>2</sub>+ WO<sub>3</sub>: Processing, coefficient of thermal expansion, and theoretical model prediction, *Mater. Sci. Eng., A* 527(1-2) (2009) 93-97.
- [211] S. Bandi, D. Vidyasagar, S. Adil, M.K. Singh, J. Basu, A.K. Srivastav, Crystallite size induced bandgap tuning in WO<sub>3</sub> derived from nanocrystalline tungsten, *Scr. Mater.* 176 (2020) 47-52.
- [212] A. Sinhamahapatra, J.-P. Jeon, J. Kang, B. Han, J.-S. Yu, Oxygen-Deficient Zirconia (ZrO<sub>2-x</sub>): A New Material for Solar Light Absorption, *Scientific Reports* 6(1) (2016) 27218.
- [213] C.P. Romao, B.A. Marinkovic, U. Werner-Zwanziger, M.A. White, Thermal Expansion Reduction in Alumina-Toughened Zirconia by Incorporation of Zirconium Tungstate and Aluminum Tungstate, *J. Am. Ceram. Soc.* 98(9) (2015) 2858-2865.
- [214] P. Jardim, E. Garcia, B. Marinkovic, Young's modulus, hardness and thermal expansion of sintered Al<sub>2</sub>W<sub>3</sub>O<sub>12</sub> with different porosity fractions, *Ceram. Int.* 42(4) (2016) 5211-5217.
- [215] L.P. Prisco, P.I. Pontón, M.V. Guamán, R.R. Avillez, C.P. Romao, M.B. Johnson, M.A. White, B.A. Marinkovic, Assessment of the thermal shock resistance figures of merit of Al<sub>2</sub>W<sub>3</sub>O<sub>12</sub>, a low thermal expansion ceramic, *J. Am. Ceram. Soc.* 99(5) (2016) 1742-1748.
- [216] C.Y. Ho, R.E. Taylor, Thermal expansion of solids, ASM international, 1998.
- [217] K.K. Chawla, Ceramic matrix composites, Springer Science & Business Media, 2013.
- [218] V. Levin, Thermal expansion coefficients of heterogeneous materials, 1992.
- [219] T. Mori, K. Tanaka, Average stress in matrix and average elastic energy of materials with misfitting inclusions, *Acta metallurgica* 21(5) (1973) 571-574.
- [220] N.K. Sharma, R.K. Misra, S. Sharma, Modeling of thermal expansion behavior of densely packed Al/SiC composites, *International Journal of Solids and Structures* 102-103 (2016) 77-88.
- [221] C. Karch, Micromechanical analysis of thermal expansion coefficients, *Modeling and Numerical Simulation of Material Science* 2014 (2014).
- [222] D. de Faoite, D.J. Browne, F.R. Chang-Díaz, K.T. Stanton, A review of the processing, composition, and temperature-dependent mechanical and thermal properties of dielectric technical ceramics, *J. Mater. Sci.* 47(10) (2012) 4211-4235.
- [223] Aluminum Oxide, Al<sub>2</sub>O<sub>3</sub> Ceramic Properties; <https://accuratus.com/alumox.html>. (accessed 11.06.2021.).
- [224] E. Liang, T. Wu, B. Yuan, M. Chao, W. Zhang, Synthesis, microstructure and phase control of zirconium tungstate with a CO<sub>2</sub> laser, *J. Phys. D: Appl. Phys.* 40(10) (2007) 3219.
- [225] H. Najafi-Ashtiani, A. Bahari, S. Gholipour, S. Hoseinzadeh, Structural, optical and electrical properties of WO<sub>3</sub>-Ag nanocomposites for the electro-optical devices, *Applied Physics A* 124(1) (2017) 24.
- [226] C.M. PHILLIPPI, K.S. MAZDIYASNI, Infrared and Raman Spectra of Zirconia Polymorphs, *J. Am. Ceram. Soc.* 54(5) (1971) 254-258.
- [227] R.D.C. Tavares Andre, N.F. Fischer, P. Hubach, C. Walsdorff, C. Schwidetzky, United States Patent 0121534, United States Patent 0121534 (2017).
- [228] J. Sauter, Die Größenbestimmung der im Gemischnebel von Verbrennungskraftmaschinen vorhandenen Brennstoffteilchen: (Mitteilung aus dem
-

- 
- Laboratorium für Technische Physik der Technischen Hochschule München), VDI-Verlag, 1926.
- [229] K.F. Young, H.P.R. Frederikse, Compilation of the Static Dielectric Constant of Inorganic Solids, *J. Phys. Chem. Ref. Data* 2(2) (1973) 313-410.
- [230] M.R. Querry, Optical constants, Missouri Univ-Kansas City, 1985.
- [231] M.M. Makhlof, Preparation and optical characterization of  $\beta$ -MnO<sub>2</sub> nano thin films for application in heterojunction photodiodes, *Sensors and Actuators A: Physical* 279 (2018) 145-156.
- [232] H. Sarraf, Z. Qian, L. Škarpová, B. Wang, R. Herbig, M. Maryška, L. Bartovska, J. Havrda, B. Anvari, Direct Probing of Dispersion Quality of ZrO<sub>2</sub> Nanoparticles Coated by Polyelectrolyte at Different Concentrated Suspensions, *Nanoscale Research Letters* 10(1) (2015) 456.
- [233] S. Gaydardzhiev, P. Ay, Characterisation of aqueous suspensions of fumed aluminium oxide in presence of two Dolapix dispersants, *J. Mater. Sci.* 41(16) (2006) 5257-5262.
- [234] P. Hidber, F. Baader, T. Graule, L.J. Gauckler, Sintering of wet-milled centrifugal cast alumina, *Journal of the European Ceramic Society* 13(3) (1994) 211-219.
- [235] G. Yablokova, M. Speirs, J. Van Humbeeck, J.P. Kruth, J. Schrooten, R. Cloots, F. Boschini, G. Lumay, J. Luyten, Rheological behavior of  $\beta$ -Ti and NiTi powders produced by atomization for SLM production of open porous orthopedic implants, *Powder Technol.* 283 (2015) 199-209.
- [236] J.-P. Choi, G.-H. Shin, H.-S. Lee, D.-Y. Yang, S. Yang, C.-W. Lee, M. Brochu, J.-H. Yu, Evaluation of Powder Layer Density for the Selective Laser Melting (SLM) Process, *Mater. Trans.* 58(2) (2017) 294-297.
- [237] J.-P. Choi, G.-H. Shin, S. Yang, D.-Y. Yang, J.-S. Lee, M. Brochu, J.-H. Yu, Densification and microstructural investigation of Inconel 718 parts fabricated by selective laser melting, *Powder Technol.* 310 (2017) 60-66.
- [238] R. Engeli, T. Etter, S. Hövel, K. Wegener, Processability of different IN738LC powder batches by selective laser melting, *J. Mater. Process. Tech.* 229 (2016) 484-491.
- [239] L. Sing Swee, Y. Yeong Wai, E. Wiria Florencia, Y. Tay Bee, Z. Zhao, L. Zhao, Z. Tian, S. Yang, Direct selective laser sintering and melting of ceramics: a review, *Rapid Prototyp. J.* 23(3) (2017) 611-623.
- [240] D.F. Sanchez, D. Grolimund, M. Hubert, P. Bleuet, J. Laurencin, A 2D and 3D X-ray  $\mu$ -diffraction and  $\mu$ -fluorescence study of a mixed ionic electronic conductor, *Int. J. Hydrogen Energy* 42(2) (2017) 1203-1211.
- [241] P.R. Willmott, D. Meister, S.J. Leake, M. Lange, A. Bergamaschi, M. Boge, M. Calvi, C. Cancellieri, N. Casati, A. Cervellino, Q. Chen, C. David, U. Flechsig, F. Gozzo, B. Henrich, S. Jaggi-Spielmann, B. Jakob, I. Kalichava, P. Karvinen, J. Krempasky, A. Ludeke, R. Luscher, S. Maag, C. Quitmann, M.L. Reinle-Schmitt, T. Schmidt, B. Schmitt, A. Streun, I. Vartiainen, M. Vitins, X. Wang, R. Wulschleger, The materials science beamline upgrade at the swiss light source, *J Synchrotron Radiat* 20(Pt 5) (2013) 667-82.
- [242] J. Moulder, W. Stickle, P. Sobol, K. Bomben, Handbook of X-ray photoelectron spectroscopy; Chastain, J, Perkin-Elmer Corp., Eden Prairie, MN (1992).
- [243] J.M. Olinger, P.R. Griffiths, Quantitative effects of an absorbing matrix on near-infrared diffuse reflectance spectra, *Anal. Chem.* 60(21) (1988) 2427-2435.
- [244] P. Kubelka, F. Munk, Ein Beitrag zur Optik der Farbanstriche (Contribution to the optic of paint), *Z. Techn. Phys.* 12 (1931) 593-601.
- [245] M. Ameri, Y.-F. Maa, Spray Drying of Biopharmaceuticals: Stability and Process Considerations, *Drying Technol.* 24(6) (2006) 763-768.
- [246] K. Kendall, T.P. Weihs, Adhesion of nanoparticles within spray dried agglomerates, *J. Phys. D: Appl. Phys.* 25(1A) (1992) A3-A8.
-

- 
- [247] J. Tartaj, G.L. Messing, Anisotropic grain growth in  $\alpha$ -Fe<sub>2</sub>O<sub>3</sub>-doped alumina, *Journal of the European Ceramic Society* 17(5) (1997) 719-725.
- [248] F. Lin, Z. Wang, Q. Ma, Y. Yang, R. Whiddon, Y. Zhu, K. Cen, Catalytic deep oxidation of NO by ozone over MnO<sub>x</sub> loaded spherical alumina catalyst, *Applied Catalysis B: Environmental* 198 (2016) 100-111.
- [249] S.X. Wang, J. Yang, X.Q. Ouyang, D.H. Han, Synthesis and properties of Mn-doped alumina red pigment prepared by low-temperature combustion-calcination process, *Adv. Mater. Res.* 250-253 (2011) 769-772.
- [250] Y. Deng, Y.L. Du, M.S. Zhang, J.H. Han, Z. Yin, Nonlinear optical properties in SrTiO<sub>3</sub> thin films by pulsed laser deposition, *Solid State Commun.* 135(4) (2005) 221-225.
- [251] K. Florio, personal communication, 2021.
- [252] K. Florio, D. Puccio, G. Vigano, S. Pfeiffer, F. Verga, M. Grasso, B.M. Colosimo, T. Graule, K. Wegener, Process characterization and analysis of ceramic powder bed fusion, submitted to *Int. J. Adv. Manuf. Technol.* (2021).
- [253] dataphysics, OCA product series; [https://www.dataphysics-instruments.com/Downloads/OCA\\_V1.3\\_EN.pdf](https://www.dataphysics-instruments.com/Downloads/OCA_V1.3_EN.pdf) (accessed 14.01.2021.).
- [254] Orbis PC Micro-XRF Analyzer; <https://www.edax.com/products/micro-xrf/orbis-pc-analyzer> (accessed 10 October 2018.).
- [255] L. Dreval, T. Zienert, O. Fabrichnaya, Calculated phase diagrams and thermodynamic properties of the Al<sub>2</sub>O<sub>3</sub>-Fe<sub>2</sub>O<sub>3</sub>-FeO system, *J. Alloys Compd.* 657 (2016) 192-214.
- [256] M.J. Torkamany, M.J. Hamed, F. Malek, J. Sabbaghzadeh, The effect of process parameters on keyhole welding with a 400 W Nd : YAG pulsed laser, *J. Phys. D: Appl. Phys.* 39(21) (2006) 4563-4567.
- [257] P. Auerkari, Mechanical and physical properties of engineering alumina ceramics, 1996.
- [258] U. Grigull, J. Straub, P. Schiebener, Steam Tables in SI-Units/Wasserdampftafeln: Concise Steam Tables in SI-Units (Student's Tables) Properties of Ordinary Water Substance up to 1000° C and 100 Megapascal/Kurzgefaßte Dampftafeln in SI-Einheiten (Studententafeln) Zustandsgrößen von gewöhnlichem Wasser und Dampf bis 1000° C und 1000 bar, Springer Science & Business Media, 2012.
- [259] E. Gilshtein, S. Pfeiffer, M.D. Rossell, J. Sastre, L. Gorjan, R. Erni, A.N. Tiwari, T. Graule, Y.E. Romanyuk, Millisecond photonic sintering of iron oxide doped alumina ceramic coatings, *Scientific Reports* 11(1) (2021) 3536.
- [260] K.H. Brosnan, G.L. Messing, D.K. Agrawal, Microwave Sintering of Alumina at 2.45 GHz, *J. Am. Ceram. Soc.* 86(8) (2003) 1307-1312.
- [261] R. Raman, S. Rele, R. Anderson, Potential Application of Solid Free-Form Fabrication (SFF) Process in Ceracon P/M Forging, 1993 International Solid Freeform Fabrication Symposium, 1993.
- [262] S. Pfeiffer, M. Makowska, F. Kevin, D.F. Sanchez, F. Marone, X. Zhang, C.G. Aneziris, H. Van Swygenhoven, K. Wegener, T. Graule, Selective laser melting of thermal pre-treated metal oxide doped aluminum oxide granules, *Open Ceramics* (2020) 100007.
- [263] B.-D. You, B.-W. Lee, J.-J. Pak, Manganese loss during the oxygen refining of high-carbon ferromanganese melts, *Met. Mater.* 5(5) (1999) 497.
- [264] J. Chu, Y. Bao, Volatilization Behavior of Manganese from Molten Steel with Different Alloying Methods in Vacuum, *Metals* 10(10) (2020) 1348.
- [265] J. Chen, V.M. Wheeler, B. Liu, A. Kumar, J. Coventry, W. Lipiński, Optical characterisation of alumina-mullite materials for solar particle receiver applications, *Sol. Energy Mater. Sol. Cells* 230 (2021) 111170.
- [266] Y. Nigara, Measurement of the optical constants of yttrium oxide, *Japanese Journal of Applied Physics* 7(4) (1968) 404.
- [267] R. Bueno, J. Martinez-Duart, M. Hernandez-Velez, L. Vazquez, Optical and structural characterization of rf sputtered CeO<sub>2</sub> thin films, *J. Mater. Sci.* 32(7) (1997) 1861-1865.
-

- 
- [268] J.R. DeVore, Refractive indices of rutile and sphalerite, *JOSA* 41(6) (1951) 416-419.
- [269] K.M. Karuppasamy, A. Subrahmanyam, Results on the electrochromic and photocatalytic properties of vanadium doped tungsten oxide thin films prepared by reactive dc magnetron sputtering technique, *J. Phys. D: Appl. Phys.* 41(3) (2008) 035302.
- [270] D.L. Wood, K. Nassau, Refractive index of cubic zirconia stabilized with yttria, *Appl. Opt.* 21(16) (1982) 2978-2981.
- [271] Z. Wang, W. Wu, X. Bian, Y. Wu, Synthesis and characterization of amorphous Al<sub>2</sub>O<sub>3</sub> and  $\gamma$ -Al<sub>2</sub>O<sub>3</sub> by spray pyrolysis, *Green Processing and Synthesis* 5(3) (2016) 305-310.
- [272] V. Klimkevicius, T. Graule, R. Makuska, Effect of structure of cationic comb copolymers on their adsorption and stabilization of titania nanoparticles, *Langmuir* 31(7) (2015) 2074-83.
- [273] M. Michálek, M. Micháľková, G. Blugan, J. Kuebler, Effect of carbon contamination on the sintering of alumina ceramics, *Journal of the European Ceramic Society* 38(1) (2018) 193-199.
- [274] Keranova AB [http://www.keranova.se/Engelsk/Exceltabell\\_E.htm](http://www.keranova.se/Engelsk/Exceltabell_E.htm). 2006 (accessed 13.07.2021).
- [275] Y. Ohya, Z.e. Nakagawa, K. Hamano, Crack healing and bending strength of aluminum titanate ceramics at high temperature, *J. Am. Ceram. Soc.* 71(5) (1988) C-232-C-233.
- [276] K. Hamano, Y. Ohya, Z.-e. Nakagawa, Crack propagation resistance of aluminium titanate ceramics, *International Journal of High Technology Ceramics* 1(2) (1985) 129-137.
- [277] F.R. Drymiotis, H. Ledbetter, J.B. Betts, T. Kimura, J.C. Lashley, A. Migliori, A.P. Ramirez, G.R. Kowach, J. Van Duijn, Monocrystal Elastic Constants of the Negative-Thermal-Expansion Compound Zirconium Tungstate (ZrW<sub>2</sub>O<sub>8</sub>), *Phys. Rev. Lett.* 93(2) (2004) 025502.
- [278] A.B. Spierings, M. Voegtlin, T. Bauer, K. Wegener, Powder flowability characterisation methodology for powder-bed-based metal additive manufacturing, *Progress in Additive Manufacturing* 1(1) (2016) 9-20.
- [279] A.F. Amado Becker, Characterization and prediction of SLS processability of polymer powders with respect to powder flow and part warpage, ETH zurich, Zurich, 2016.
- [280] A. Amado, M. Schmid, G. Levy, K. Wegener, Advances in SLS powder characterization, Proceedings of the 22th Solid Freeform Fabrication Symposium, Austin, Texas, USA, 2011, 438-452.
- [281] S.E. Brika, M. Letenneur, C.A. Dion, V. Brailovski, Influence of particle morphology and size distribution on the powder flowability and laser powder bed fusion manufacturability of Ti-6Al-4V alloy, *Addit. Manuf.* 31 (2020) 100929.
- [282] M. Vetterli, Powder optimization for laser sintering: An insight in powder intrinsic and extrinsic properties, ETH Zurich, Zurich, 2019.
- [283] H. Yang, R. Li, P. Kong, Q. Sun, M.J. Biggs, V. Zivkovic, Avalanche dynamics of granular materials under the slumping regime in a rotating drum as revealed by speckle visibility spectroscopy, *Physical Review E* 91(4) (2015) 042206.
- [284] M. Wegmann, B. Michen, T. Luxbacher, J. Fritsch, T. Graule, Modification of ceramic microfilters with colloidal zirconia to promote the adsorption of viruses from water, *Water Res.* 42(6) (2008) 1726-1734.
- [285] M. Makowska, personal communication, 2021.
- [286] A. Klimov, I.Y. Bakeev, E. Dvilis, E. Oks, A. Zenin, Electron beam sintering of ceramics for additive manufacturing, *Vacuum* 169 (2019) 108933.
- [287] D. Wu, F. Lu, D. Zhao, G. Ma, C. Li, J. Ding, F. Niu, Effect of doping SiC particles on cracks and pores of Al<sub>2</sub>O<sub>3</sub>-ZrO<sub>2</sub> eutectic ceramics fabricated by directed laser deposition, *J. Mater. Sci.* 54(13) (2019) 9321-9330.
- [288] M. Schmücker, P. Mechnich, All-oxide ceramic matrix composites with porous matrices, in: W. Krenkel (Ed.), *Ceramic Matrix Composites: Fiber Reinforced Ceramics and their Applications*, WILEY-VCH Verlag GmbH & Co., Weinheim, 2008.

- 
- [289] G. Jefferson, K.A. Keller, R.S. Hay, R.J. Kerans, Oxide/oxide composites with fiber coatings, in: W. Krenkel (Ed.), *Ceramic Matrix Composites: Fiber Reinforced Ceramics and their Applications*, WILEY-VCH Verlag GmbH & Co, Weinheim, 2008.
- [290] W. Liu, M. Ismail, M.T. Dunstan, W. Hu, Z. Zhang, P.S. Fennell, S.A. Scott, J. Dennis, Inhibiting the interaction between FeO and Al<sub>2</sub>O<sub>3</sub> during chemical looping production of hydrogen, *Rsc Advances* 5(3) (2015) 1759-1771.



## List of Figures

<b>Figure 1:</b> Current additive manufacturing methods for ceramics in accordance to ISO/ASTM 52900:2018 and [1, 21, 23]; process categories highlighted in green are the ones reviewed in this study .....	6
<b>Figure 2:</b> Schematic of powder bed fusion with a laser beam (PBF-LB). .....	7
<b>Figure 3:</b> Experimental PBF-LB machine developed and built in-house at ETH Zurich .....	8
<b>Figure 4:</b> Comparison of the adhesion force and gravity for very smooth and rough spheres of different diameters [28]. .....	8
<b>Figure 5:</b> Unit cost for additive and traditional manufactured parts referred to a) production volume and b) com-plexity or customization of the parts according to Pinkerton [21] and influence of new design opportunities by additive manufacturing on unit cost referred to complexity of the parts compared to traditional processes according to Bain & Company, Inc. [37]. The green area shows the more favorable range for AM as manufacturing method .....	10
<b>Figure 6:</b> Pure PBF-LB processed alumina parts manufactured by Juste et al. [50] .....	20
<b>Figure 7:</b> Schematic of laser preheating with second laser in PBF-LB [16] .....	21
<b>Figure 8:</b> a) Tooth model consisting of 35 layers ( $\text{Al}_2\text{O}_3$ – $\text{SiO}_2$ ratio: 0.37) and b) typical microstructure of these composite shown in Gahler et al. ....	24
<b>Figure 9:</b> Classification of cracks in PBF-LB: longitudinal cracks run along scan track boundaries, while transverse cracks run across scan tracks [11] .....	31
<b>Figure 10:</b> Schematic of spray drying .....	35
<b>Figure 11:</b> Zeta potential at the slipping plane within counter ions in the double electrical diffuse layer [136] .....	41
<b>Figure 12:</b> Energy–distance curve described by the DLVO theory [142] .....	43
<b>Figure 13:</b> Challenges of laser powder bed fusion of aluminum oxide ceramics and approaches to solve these. ....	45
<b>Figure 14:</b> UV-Vis spectra of $\text{TiO}_2$ treated under hydrogen for up to 20 days at room temperature [201] .....	51
<b>Figure 15:</b> SEM images of a) AA18 ( $\text{Al}_2\text{O}_3$ ), b) AA3 ( $\text{Al}_2\text{O}_3$ ), c) AA03 ( $\text{Al}_2\text{O}_3$ ), d) Taimicron TM-DAR ( $\text{Al}_2\text{O}_3$ ), h) US3319 ( $\text{MnO}_2$ ) and TEM images of e) Aeroxide AluC ( $\text{Al}_2\text{O}_3$ ), f) L2715D ( $\text{Fe}_2\text{O}_3$ ), g) L2818D ( $\text{Fe}_2\text{O}_3$ ). ....	58
<b>Figure 16:</b> Zeta-potential of aluminas a) AA3, b) AA03, c) Taimicron TM-DAR, d) Aeroxide AluC as a function of pH value and citrate concentration. $\text{pH}_{\text{PZC}}$ of e) $\alpha$ - $\text{Al}_2\text{O}_3$ and f) $\gamma$ - $\alpha$ - $\text{Al}_2\text{O}_3$ nanoparticle suspensions as function of ammonium citrate dibasic addition. ....	60
<b>Figure 17:</b> Zeta potential of a) $\text{MnO}_2/\text{Mn}_2\text{O}_3$ and b),c) $\text{Fe}_2\text{O}_3$ nanoparticles as a function of pH value and various citrate concentrations. d) $\text{pH}_{\text{IEP}}$ of $\text{MnO}_2/\text{Mn}_2\text{O}_3$ and $\text{Fe}_2\text{O}_3$ suspensions as function of ammonium citrate dibasic addition. e) Zeta potential of $\text{MnO}_2/\text{Mn}_2\text{O}_3$ with 1.5 wt% (4.0 vol%) ammonium citrate dibasic as function of pH value and f) corresponding conductivity change by HCl and NaOH addition as function of pH value and g) added volume. ....	61
<b>Figure 18:</b> Volume based particle size distributions of alumina powders in water by optimized dispersant amount and dispersing routine determined by dynamic light scattering (DLS) and Laser diffraction (LD). ....	63

<b>Figure 19:</b> Volume based particle size distributions of AluC Aeroxide in water measured by dynamic light scattering (DLS) or Laser diffraction (LD) and dispersed roll milling ( <b>a, b</b> ) or a combination of roll milling and vibration milling ( <b>c, d, e, f</b> ) or ultrasonication ( <b>g</b> ) with an optimized dispersant amount of 3.6 wt% (7.9 Vol%) ammonium citrate dibasic. ....	65
<b>Figure 20:</b> Volume based particle size distributions of Taimicron TM-DAR dispersed in water with 0.6 wt% (1.5 Vol%) ammonium citrate dibasic measured by <b>a</b> ) laser diffraction (LD) or <b>b</b> ) dynamic light scattering (DLS). ....	67
<b>Figure 21:</b> Volume based particle size distributions of dopants in water by using optimized ammonium citrate dibasic (dispersant) amount (1.5 wt% (4.0 vol%) for MnO <sub>2</sub> /Mn <sub>2</sub> O <sub>3</sub> , 3.1 wt% (8.4 vol%) for Fe <sub>2</sub> O <sub>3</sub> L2715D and 3.0 wt% (8.4 Vol%) for Fe <sub>2</sub> O <sub>3</sub> L2818D) and dispersing routine determined by <b>a</b> ) Laser diffraction (LD) and <b>b</b> ) dynamic light scattering (DLS). ....	68
<b>Figure 22:</b> Volume based particle size distributions of Fe <sub>2</sub> O <sub>3</sub> L2715D measured by dynamic light scattering (DLS) or Laser diffraction (LD) and dispersed by only vibration milling ( <b>a, b</b> ) or by vibration milling and additional roll milling ( <b>c, d</b> ) with an optimized dispersant amount of 3.1 wt% (8.5 Vol%) ammonium citrate dibasic. ....	69
<b>Figure 23: a, b</b> ) Volume based particle size distributions (DLS) of Fe <sub>2</sub> O <sub>3</sub> L2715D measured after different additional roll milling time ranges of up to 72 hours upon vibration milling. <b>c), d)</b> Temporal history of the characteristic particle size values of d10, d50 and 90 after additional roll milling. ....	71
<b>Figure 24:</b> Sedimentation experiments with an idle time of 3 days for dispersions, which experienced a vibration milling of 20 minutes and an additional roll milling step for 0 minutes, 10 minutes, 1 hour, 2 hours, 6 hours and 22 hours. ....	72
<b>Figure 25:</b> Volume based particle size distributions of Fe <sub>2</sub> O <sub>3</sub> L2818D measured Laser diffraction (LD) and dispersed by roll milling <b>a</b> ) with different sizes of the milling balls or <b>b</b> ) different solid loadings. Volume based particle size distributions of Fe <sub>2</sub> O <sub>3</sub> L2818D dispersed by roll milling, vibration milling or a combination of both and measured by <b>c</b> ) Laser diffraction (LD) or <b>d</b> ) dynamic light scattering (DLS) ....	72
<b>Figure 26:</b> Volume-based differential DLS particle size distribution of MnO <sub>2</sub> /Mn <sub>2</sub> O <sub>3</sub> and volume-based differential LD particle size distribution of MnO <sub>2</sub> /Mn <sub>2</sub> O <sub>3</sub> in water dispersed by means of ammonium citrate at different pH values by <b>a), b</b> ) roll milling and by <b>c), d</b> ) a combination of vibration milling and roll milling. ....	74
<b>Figure 27:</b> Volume-based differential DLS particle size distribution of MnO <sub>2</sub> /Mn <sub>2</sub> O <sub>3</sub> particles dependent on different milling approaches. (“Vm” represents Vibration milling for 20 min with the frequency of 30 s <sup>-1</sup> ; “Rm” represents Roll milling for 24 h; “Us” represents Ultrasonic treatment for 1.5 min.) ....	75
<b>Figure 28:</b> User interface of the EMMA (Elkem Materials-Mixture Analyzer) software. ....	79
<b>Figure 29:</b> Parameter and model selection panel of the EMMA software. ....	80
<b>Figure 30:</b> a) apparent and tapped density versus solid load and b) influence of ratio of fine to coarse starting powder on the apparent and tapped density of spray dried granules (powder combination A – bimodal distribution). ....	83
<b>Figure 31:</b> SEM images of granules spray dried from a) powder combination B – trimodal distribution, b) powder combination C– bimodal distribution, c) powder combination D – bimodal distribution d) volume-based LD particle size distribution of granules. ....	84
<b>Figure 32:</b> Evolution of pH-value of the three different dispersion for powder combination A, B and C during slurry preparation. ....	86

<b>Figure 33:</b> Slurry for powder combination C directly after mixing and left without agitation for 24 hours and 60 hours. ....	87
<b>Figure 34:</b> Measurements of viscosity respectively shear stress in relation to shear rate of the slurries for <b>a, b)</b> powder combination B, <b>c, d)</b> powder combination C, <b>e, f)</b> powder combination A. ....	88
<b>Figure 35:</b> SEM images of granules spray dried from a) powder combination B – trimodal distribution, b) powder combination C– bimodal distribution, c) powder combination D – bimodal distribution, d),e),f) granules above mixed with coarse alumina AA18. Volume-based LD particle size distribution of granules with the mixture of coarse AA18 alumina (70 vol% granules / 30 Vol% AA18). ....	90
<b>Figure 36:</b> Apparent and tapped density as well as Hausner ratio dependent on amount of additional coarse AA18. ....	91
<b>Figure 37:</b> SEM images of a) CB-P02 ( $\text{Al}_2\text{O}_3$ ) and b) CB-P10 ( $\text{Al}_2\text{O}_3$ ). ....	92
<b>Figure 38:</b> Apparent, tapped density and Hausner ratio dependent on amount of additional aluminum oxide <b>a)</b> CB-P02 and <b>b)</b> CB-P10. ....	93
<b>Figure 39:</b> Different combinations of 50 Vol% pure granules with additional aluminum oxides AA18 and CB-P10. ....	94
<b>Figure 40:</b> Cut screen-shots of the EMMA interface after the calculation of mixture 2, 4 and 6. ....	95
<b>Figure 41:</b> Measured apparent densities, tapped densities and Hausner ratios by using the powder combinations summarized in Table 9. ....	96
<b>Figure 42:</b> SEM images of as-prepared granules after spray drying of bimodal alumina with a) $\text{Fe}_2\text{O}_3$ doping or b) $\text{MnO}_2$ doping. ....	98
<b>Figure 43:</b> SEM images of spray dried granules thermally treated at a) maximum temperature: 1400 °C / holding time: 2 hours, b) 1500 °C/2 hours, c) 1600 °C/2 hours, d) 1400 °C/4 hours, e) 1500 °C/4 hours, f) 1600 °C/4 hours. Illustration by SEM of g), h) sintering necks between the granules and formed agglomerates after thermal treatment at 1600 °C and i) de-agglomeration by mixing with AA18. ....	99
<b>Figure 44:</b> Apparent and tapped density change as well as Hausner ratio of thermal treated granules in respect to treatment conditions (temperature/holding time) a) without addition of AA18 and b) with addition of AA18. ....	100
<b>Figure 45:</b> SEM Illustration of grain growth and microstructure evolution in alumina granules after sintering at 1600 °C depending on a) $\text{MnO}_2/\text{Mn}_2\text{O}_3$ doping or b) $\text{Fe}_2\text{O}_3$ doping. ....	101
<b>Figure 46:</b> Optical microscopy images and X-ray fluorescence contrast tomography of the Mn- <b>(a-d)</b> and Fe-doped <b>(e-h)</b> granules before <b>(a, c, e, g)</b> and after thermal treatment at 1600 °C <b>(b, d, f, h)</b> . The color scale indicates the intensity of X-ray fluorescence of Fe K $\alpha$ (yellow-high, red-medium, blue-low), which is a measure of Fe atoms concentration (lack of Fe atoms is indicated by gray color). ....	102
<b>Figure 47:</b> High resolution powder diffraction of the Mn-doped granules with peak enlargement to illustrate the implementation of Mn ions within corundum lattice. ....	103
<b>Figure 48:</b> X-ray photo-electron spectroscopy measurement of thermal pre-treated manganese oxide doped granules: <b>a)</b> elements survey, <b>b)</b> enlarged 2p line containing the 2p $_{1/2}$ and 2p $_{3/2}$ line, <b>c)</b> detailed analysis of the Mn2p peak with fitting of the 2p $_{3/2}$ line by manganese cations with different valency states. ....	104

<b>Figure 49:</b> Qualitative absorption spectrum for spray dried powders evaluated by the Kubelka Munk method for measurements of diffuse reflectance given by plotting K/S ratio over wavelength. ....	105
<b>Figure 50:</b> Qualitative absorption spectrum analyzed by the Kubelka Munk method for Fe <sub>2</sub> O <sub>3</sub> (L2818D)-doped trimodal granules thermally treated at different temperatures in air. ....	109
<b>Figure 51:</b> Drop schematic and measurement of interfacial tension [253] .....	110
<b>Figure 52:</b> a) Surface tension of Fe <sub>2</sub> O <sub>3</sub> doped Al <sub>2</sub> O <sub>3</sub> slurry for spray drying in respect to amount of octanol. b) Consideration of standard deviation of measurement. ....	111
<b>Figure 53:</b> SEM images of fine fraction of spray dried granules with different amount of 1-octanol. ....	112
<b>Figure 54:</b> Volume-based LD particle size distribution of fine fraction of granules with addition of different amount of 1-octanol. ....	112
<b>Figure 55:</b> SEM images of coarse fraction of spray dried granules with different amount of 1-octanol. ....	113
<b>Figure 56:</b> Volume-based LD particle size distribution of coarse fraction of granules with addition of different amount of 1-octanol. ....	113
<b>Figure 57:</b> SEM images of laser manufactured parts with a), b) powder 1, c), d) powder 2, e), f) powder 3. Images of the ceramic part obtained by the laser process g) before and h) after heat treatment at 1650 °C.....	120
<b>Figure 58:</b> Powders to evaluate the influence of coarse alumina variation on the part formation by PBF-LB. ....	121
<b>Figure 59:</b> Qualitative absorption spectrum evaluated by the Kubelka Munk method of the three different combinations.....	122
<b>Figure 60:</b> Shape imaged by optical microscopy and cross sections imaged by SEM of laser manufactured parts .....	123
<b>Figure 61:</b> Higher magnifications of internal structure imaged by SEM of laser manufactured parts. ....	124
<b>Figure 62:</b> Qualitative absorption spectrum evaluated by the Kubelka Munk method of pure granules, granules mixed with coarse aluminum oxide and pure coarse aluminum oxide AA18. ....	126
<b>Figure 63:</b> Compressive strength of parts produced with pure granules and granules mixed with different amount of coarse aluminum oxide AA18.....	126
<b>Figure 64:</b> Shape (left column) and cross-sections (center column) imaged by optical microscopy as well as internal structure imaged by SEM (right column) of laser manufactured parts produced with Fe <sub>2</sub> O <sub>3</sub> -doped (a, b) and MnO <sub>2</sub> /Mn <sub>2</sub> O <sub>3</sub> -doped (a, c, e: untreated; b, d, f: thermally pre-treated) powders. ....	129
<b>Figure 65:</b> High resolution powder diffraction pattern of a laser manufactured part revealing presence of the phases corundum and galaxite. Red dots are the measured data, blue and green lines are calculated patterns of corundum and galaxite phases, respectively.....	130
<b>Figure 66:</b> Tomographic microscopy imaging of two parts prepared with a), b) as-prepared (powder 2) and c), d) heat treated (powder 4) Mn-doped granules.....	131
<b>Figure 67:</b> Laser processed part density and Hausner ratio as function of tapped powder density. ....	133

<b>Figure 68:</b> a) Electron microscopy and b) tomography images of the parts processed from Mn-doped as-prepared (left) and thermal treated (right) granules presenting non-molten granules found in pores of the parts.....	134
<b>Figure 69:</b> EBSD mapped results of parts made from iron oxide doped granules with the laser scanning speeds of <b>a)</b> 2 mm/s, <b>b)</b> 5 mm/s and <b>c)</b> 10 mm/s (Colored areas represent grains with different crystal orientation; black areas represent the porosity within the laser processed parts). .....	135
<b>Figure 70:</b> Thermomechanical analysis illustrating the length change in respect to time and temperature of laser additive manufactured parts made from <b>a)</b> iron oxide or <b>b)</b> manganese oxide doped granules.....	137
<b>Figure 71:</b> Optical microscopy images of laser processed layers located on thermally pre-treated circular substrates <b>a)</b> 700°C and <b>b)</b> 1600 °C and corresponding manganese content in wt% measured at the marked line scans (blue lines in the optical microscopy images). The red and green line within the optical microscopy represent the measured aluminum and manganese amount, respectively.....	140
<b>Figure 72:</b> Schematics of the setup for the XRD-contrast microscopy experiments .....	149
<b>Figure 73:</b> SEM images of a) mullite WFM 0-10 and b) submicron mullite. Inlet in a) shows the optical appearance of WFM 0-10.....	150
<b>Figure 74:</b> X-ray diffraction pattern of mullite WFM 0-10. ....	151
<b>Figure 75:</b> Zeta potential of <b>a)</b> mullite WFM 0-10 and <b>d)</b> submicron mullite particles as a function of pH value and various citrate concentrations with corresponding <b>b), e)</b> volume change by HCl and NaOH addition as function of pH value. $pH_{IEP}$ of <b>c)</b> mullite WFM 0-10 and <b>f)</b> submicron mullite suspensions as function of ammonium citrate dibasic addition. ....	152
<b>Figure 76:</b> Volume based particle size distributions of mullite powders in water by optimized (ammonium citrate dibasic) dispersant amount (0.8 wt% (1.6 Vol%) for micron-sized mullite WFM 0-10 and 1.2 wt% (2.3 Vol%) for submicron mullite) and dispersing routine determined by Laser diffraction (LD). ....	153
<b>Figure 77:</b> SEM images of spray-dried <b>a), b)</b> granules A, <b>c), d)</b> granules D, <b>e)</b> granules D mixed with coarse aluminum oxide AA18 and <b>f)</b> granules E. ....	154
<b>Figure 78:</b> Element distributions within granules <b>a)</b> with micron sized and <b>b)</b> submicron sized mullite examined by energy-dispersive X-ray spectroscopy .....	157
<b>Figure 79:</b> <b>a)</b> Shape and <b>b)</b> cross-section of laser manufactured parts produced with granules A and 30 Vol% AA18 imaged by optical microscopy.....	158
<b>Figure 80:</b> Internal structure of laser manufactured parts produced with granules A and 30 Vol% AA18 imaged by <b>a), c)</b> SEM (secondary electrons), <b>b)</b> optical microscopy <b>d)</b> SEM (backscattered electrons). ....	158
<b>Figure 81:</b> <b>a)</b> Evaluated positions and corresponding element content as well as <b>b)</b> corresponding spectra of point 1 examined by energy-dispersive X-ray spectroscopy.....	159
<b>Figure 82:</b> High resolution powder diffraction pattern of laser manufactured parts.....	159
<b>Figure 83:</b> <b>a)</b> SEM images and optical appearance as well as <b>b)</b> x-ray diffraction pattern of CeO <sub>2</sub> nanoparticles.....	160
<b>Figure 84:</b> <b>a)</b> Zeta potential of CeO <sub>2</sub> nanoparticles as a function of pH value and various citrate concentrations. <b>b)</b> $pH_{IEP}$ of CeO <sub>2</sub> nanoparticles as function of ammonium citrate dibasic addition.....	161

<b>Figure 85:</b> Volume based particle size distributions of CeO <sub>2</sub> nanoparticles in water by optimized dispersant amount (2.5 wt% (10 Vol%) of ammonium citrate dibasic) and dispersing routine determined by <b>a), b)</b> laser diffraction (LD) and <b>c), d)</b> dynamic light scattering (DLS).	162
<b>Figure 86:</b> <b>a), b)</b> SEM images, <b>c)</b> volume based particle size distribution and <b>d)</b> properties of Al <sub>2</sub> O <sub>3</sub> /CeO <sub>2</sub> granules.	163
<b>Figure 87:</b> <b>a)</b> Zeta potential of Y <sub>2</sub> O <sub>3</sub> particles as a function of pH value and various citrate concentrations with corresponding <b>c)</b> conductivity and <b>d)</b> volume change by HCl and NaOH addition as function of pH value. <b>b)</b> pH <sub>IEP</sub> of Y <sub>2</sub> O <sub>3</sub> suspensions as function of ammonium citrate dibasic addition.	164
<b>Figure 88:</b> Volume based particle size distributions of Y <sub>2</sub> O <sub>3</sub> submicron particles in water by optimized dispersant amount (0.8 wt% (2.4 Vol%) of ammonium citrate dibasic) and dispersing routine determined by <b>a), c)</b> laser diffraction (LD) and <b>b), d)</b> dynamic light scattering (DLS).	165
<b>Figure 89:</b> <b>a)</b> Volume based particle size distributions of Fe <sub>2</sub> O <sub>3</sub> doped Al <sub>2</sub> O <sub>3</sub> /Y <sub>2</sub> O <sub>3</sub> granules in isopropanol determined by laser diffraction (LD). <b>d)</b> properties of Al <sub>2</sub> O <sub>3</sub> /Y <sub>2</sub> O <sub>3</sub> granules.	166
<b>Figure 90:</b> SEM images of Fe <sub>2</sub> O <sub>3</sub> doped Al <sub>2</sub> O <sub>3</sub> /Y <sub>2</sub> O <sub>3</sub> granules spray-dried with <b>a)</b> 40.2 Vol% and <b>b)</b> 44.8 Vol% solid load.	166
<b>Figure 91:</b> Laser consolidated layers on uniaxial pressed cylindrical substrates containing both rare earth oxide/aluminum oxide granules	167
<b>Figure 92:</b> X-ray diffraction measurements of <b>a)</b> the laser-processed alumina-yttria (power = 20 W, hatch distance = 100 µm, laser speed = 75 mm/s) and of <b>b)</b> laser processed alumina-ceria (power = 30 W, hatch distance = 100 µm, laser speed = 50 mm/s).	168
<b>Figure 93:</b> <b>a)</b> Zeta potential of TiO <sub>2</sub> particles as a function of pH value and various citrate concentrations. <b>b)</b> pH <sub>IEP</sub> of TiO <sub>2</sub> suspensions as function of ammonium citrate dibasic addition	170
<b>Figure 94:</b> Volume based particle size distributions of TiO <sub>2</sub> nanoparticles in water determined by <b>a), c)</b> laser diffraction (LD) and <b>b), d)</b> dynamic light scattering (DLS) and dispersed by optimized dispersant amount (2.6 wt%) and by vibration milling or a combination of roll milling and vibration milling	171
<b>Figure 95:</b> Thermal gravimetric analysis to evaluate the minimum temperature necessary to reduce the TiO <sub>2</sub> nanoparticles to TiO <sub>2-x</sub> in argon/hydrogen atmosphere by <b>a)</b> mass loss and <b>b)</b> derivation of the mass loss.	172
<b>Figure 96:</b> Optical appearance and SEM images of spray dried granules containing 1 Vol% of TiO <sub>2-x</sub> before and after thermal treatment in Ar/H <sub>2</sub> at maximum temperatures of 1400 °C and 1600 °C (idle times: 2 hours).	173
<b>Figure 97:</b> SEM images of spray dried granules containing 14.2 Vol% of TiO <sub>2-x</sub> before and after thermal treatment in Ar/H <sub>2</sub> at maximum temperatures of 1000 °C, 1200 °C, 1300 °C and 1400 °C (idle times: 2 hours).	175
<b>Figure 98:</b> SEM images of spray dried granules containing 68 Mol% of TiO <sub>2-x</sub> before and after thermal treatment in Ar/H <sub>2</sub> at maximum temperatures of 1000 °C, 1100 °C, 1200 °C, 1300 °C and 1400 °C (idle times: 2 hours).	176
<b>Figure 99:</b> Qualitative absorption spectrum at room temperature measured by the Kubelka Munk method of <b>a)</b> untreated and pure AA18 as well as of <b>b)</b> reduced granules.	178

<b>Figure 100:</b> Attenuation contrast tomographic microscopy of laser-manufactured parts made from powder combination A and with different processing speeds <b>a)</b> 2 mm/s and <b>b)</b> 10 mm/s.	180
<b>Figure 101:</b> XRD-contrast tomography of laser-manufactured parts made from powder combination A. The inlets show the laser manufactured part with the position of the analyzed cross section (left side) as well as the acquired intensities with the cross section at angles of 17.8° and 20.5° (right side).	181
<b>Figure 102:</b> Evaluation of <b>a), b), c)</b> parts density and cracks density as well as <b>d)</b> crack distribution in a cross section of laser printed doped alumina parts for three different dopants ( $\text{Fe}_2\text{O}_3$ , $\text{TiO}_{2-x}$ , $\text{Mn}_x\text{O}_y$ ) at different laser scanning speed (2 mm/s, 5 mm/s, 10 mm/s) from tomographic microscopy.	182
<b>Figure 103:</b> Internal structure imaged by optical microscopy and SEM of cross-sections ( <b>a-e</b> ) view in build direction and <b>f), g)</b> top view) of laser manufactured parts produced with powder combination B.	183
<b>Figure 104:</b> <b>a)</b> Shape imaged by optical microscopy. Internal structure imaged by SEM of cross-sections ( <b>b), c)</b> view in build direction and <b>d), e)</b> top view) of laser manufactured parts produced with powder combination C.	184
<b>Figure 105:</b> X-ray diffraction measurements of <b>a)</b> powder combination C (50 Mol% of $\text{TiO}_{2-x}$ ) before and after thermal treatment in $\text{Ar}/\text{H}_2$ at maximum temperatures (idle time: 2 hours) of 1000 °C and 1400 °C and of <b>b)</b> laser processed parts made from powder combination B (10 Vol% of $\text{TiO}_{2-x}$ ) and powder combination C.	186
<b>Figure 106:</b> SEM images of <b>a)</b> $\text{ZrO}_2$ and <b>b)</b> $\text{WO}_3$ nanoparticles.	187
<b>Figure 107:</b> <b>a)</b> Zeta potential of $\text{ZrO}_2$ particles as a function of pH value and various citrate concentrations. <b>b)</b> $\text{pH}_{\text{IEP}}$ of $\text{ZrO}_2$ suspensions as function of ammonium citrate dibasic addition. <b>c)</b> Zeta potential of $\text{WO}_3$ particles as a function of pH value and various citrate concentrations. <b>d)</b> Zeta potential of $\text{WO}_3$ suspensions as function of ammonium citrate dibasic addition at constant pH values of 1.5, 2.5 and 3.5.	188
<b>Figure 108:</b> Volume based particle size distributions of $\text{ZrO}_2$ particles in water dispersed by optimized dispersant amount (0.6 wt% (2.1 Vol%) of ammonium citrate dibasic) and roll milling for 24 hours or a combination of vibration milling (20 minutes) and roll milling (24 hours) and determined by <b>a), b), d)</b> laser diffraction (LD) and <b>c), e)</b> dynamic light scattering (DLS).	189
<b>Figure 109:</b> Volume based particle size distributions of $\text{WO}_3$ particles in water by optimized dispersant amount (0.2 wt% (0.9 Vol%) of ammonium citrate dibasic) dispersed by roll milling for 24 hours and determined by <b>a), c), d)</b> laser diffraction (LD) and <b>b)</b> dynamic light scattering (DLS).	190
<b>Figure 110:</b> Influence of <b>a)</b> solid load, <b>b)</b> pump rate, <b>c)</b> power output of ultrasonic nozzle and <b>d)</b> inlet temperature on volume based particle size distribution of spray-dried $\text{ZrO}_2/\text{WO}_3$ granules determined by laser diffraction (LD).	193
<b>Figure 111:</b> SEM images of $\text{ZrO}_2/\text{WO}_3$ granules spray-dried with different solid loads. ....	194
<b>Figure 112:</b> Correlation of pump rate to actual slurry feed flow during spray drying.	195
<b>Figure 113:</b> SEM images of $\text{ZrO}_2/\text{WO}_3$ granules spray-dried with a different ultrasonic power output.	196
<b>Figure 114:</b> <b>a)</b> SEM image and <b>b), c), d)</b> corresponding element distributions of W, O and Zr examined by energy-dispersive X-ray spectroscopy of $\text{ZrO}_2/\text{WO}_3$ granules.	197



<b>Figure 115:</b> SEM images of $\text{ZrO}_2/\text{WO}_3$ granules mixed with <b>a)</b> 3.1 Vol% and <b>b)</b> 50 Vol% coarse aluminum oxide AA18.....	198
<b>Figure 116:</b> Qualitative absorption spectrum evaluated by the Kubelka Munk method of pure granules, granules mixed with coarse aluminum oxide and pure coarse aluminum oxide AA18. ....	199
<b>Figure 117:</b> <b>a)</b> Laser consolidated layers on uniaxial pressed cylindrical substrates containing pure $\text{ZrO}_2/\text{WO}_3$ granules. <b>b)</b> Evaluation of $\text{Zr}(\text{WO}_4)_2$ phase after laser processing of $\text{ZrO}_2/\text{WO}_3$ substrates with different power, hatch distance, laser speed. ....	200
<b>Figure 118:</b> <b>a)</b> Optical microscope and <b>b-f)</b> SEM images of cross-sections (view of build direction) of laser-manufactured parts produced with powders containing 50 Vol% coarse alumina AA18 and 50 Vol% spray dried $\text{ZrO}_2/\text{WO}_3$ granules.....	202
<b>Figure 119:</b> <b>a)</b> Optical microscope and <b>b-e)</b> SEM images of cross-sections (top view) of laser-manufactured parts produced with powders containing 50 Vol% coarse alumina AA18 and 50 Vol% spray dried $\text{ZrO}_2/\text{WO}_3$ granules. <b>f)</b> Element content of evaluated position (marked in orange) in Figure 119e. ....	203
<b>Figure 120:</b> <b>a)</b> Shape imaged by optical microscopy and <b>a-d)</b> SEM images of cross-sections (top view) of laser-manufactured parts produced with powders containing 3.1 Vol% coarse alumina AA18 and 96.9 Vol% spray dried $\text{ZrO}_2/\text{WO}_3$ granules.....	204
<b>Figure 121:</b> Compressive strength of laser-manufactured parts produced with powders containing a different additive content to aluminum oxide.....	205
<b>Figure 122:</b> <b>a)</b> Avalanche angle and <b>b)</b> surface fractal of $\text{Fe}_2\text{O}_3$ doped granules mixed with different amounts of coarse aluminum oxide AA18 (standard deviations calculated from three measurements for each powder evaluating at least 127 avalanches per measurement). ....	212
<b>Figure 123:</b> Impact of thermal pre-treatment and mixing with 30 Vol% coarse aluminum oxide AA18 on avalanche angle and surface fractal of <b>a), b)</b> $\text{Fe}_2\text{O}_3$ doped granules and <b>c), d)</b> $\text{MnO}_2/\text{Mn}_2\text{O}_3$ doped granules (standard deviations calculated from three measurements for each powder evaluating at least 127 avalanches per measurement). ....	214
<b>Figure 124:</b> <b>a)</b> Avalanche angle and <b>b)</b> surface fractal of $\text{Fe}_2\text{O}_3$ - and $\text{MnO}_2/\text{Mn}_2\text{O}_3$ -doped aluminum oxide granules containing different dopant amounts of 1 and 5 Vol% (standard deviations calculated from three measurements for each powder evaluating at least 127 avalanches per measurement). ....	217
<b>Figure 125:</b> SEM images of <b>a)</b> 5 Vol% $\text{Fe}_2\text{O}_3$ - and <b>b)</b> 5 Vol% $\text{MnO}_2/\text{Mn}_2\text{O}_3$ -doped aluminum oxide granules as well as particle size distributions of the granules measured in Figure 124. ....	218
<b>Figure 126:</b> <b>a)</b> Avalanche angle and <b>b)</b> surface fractal of zirconia-tungsten oxide granules and alumina granules with mullite or rare earth oxide addition (standard deviations calculated from three measurements for each powder evaluating at least 127 avalanches per measurement). ....	220
<b>Figure 127:</b> Impact of thermal treatment in $\text{Ar}/\text{H}_2$ and mixing with 30 Vol% coarse aluminum oxide AA18 on avalanche angle and surface fractal of powders with a final $\text{TiO}_{2-x}$ content of <b>a), b)</b> 0.7 Vol%, <b>c), d)</b> 10Vol% and <b>e), f)</b> 50 Mol% (standard deviations calculated from three measurements for each powder evaluating at least 127 avalanches per measurement). ....	222
<b>Figure 128:</b> SEM images of as spray-dried $\text{Fe}_2\text{O}_3$ doped granules illustrating <b>a)</b> the morphology and <b>b), c), d)</b> the subsurface morphology of the granules.....	225
<b>Figure 129:</b> Impact of screening on <b>a)</b> apparent, tapped density and Hausner ratio and on <b>b)</b> the particle size distribution. ....	226

---

<b>Figure 130:</b> SEM images illustrating the morphology and the subsurface morphology of <b>a), b), c), d)</b> as spray-dried $\text{MnO}_2/\text{Mn}_2\text{O}_3$ -doped granules and <b>e), f) g), h)</b> thermal pre-treated granules in air (maximum temperature 1600 °C, heating and cooling rate: 2 K/min, idle time: 2 hours) .....	227
<b>Figure 131:</b> SEM images of as spray-dried $\text{Al}_2\text{O}_3/\text{CeO}_2$ granules illustrating <b>a)</b> the morphology and <b>b), c), d)</b> the subsurface morphology of the granules.....	228
<b>Figure 132:</b> SEM images of as spray-dried $\text{ZrO}_2/\text{WO}_3$ granules illustrating <b>a)</b> the morphology and <b>b), c), d)</b> the subsurface morphology of the granules.....	230
<b>Figure 133:</b> SEM images illustrating the morphology and the subsurface morphology of <b>a), b), c), d)</b> as spray-dried $\text{Al}_2\text{O}_3/\text{TiO}_2$ granules and <b>e), f) g), h)</b> thermally reduced $\text{Al}_2\text{O}_3/\text{TiO}_{2-x}$ granules in $\text{Ar}/\text{H}_2$ atmosphere (maximum temperature 1300 °C, heating and cooling rate: 2 K/min, holding time: 2 hours) .....	231

---

## List of Tables

<b>Table 1:</b> Advantages and disadvantages of laser additive manufacturing compared to other additive manufacturing processes specified in chapter 2.1.2 and 2.1.3. ....	13
<b>Table 2:</b> Process parameters of relevant publications regarding powder bed fusion of high performance aluminum oxide ceramics .....	25
<b>Table 3:</b> Properties of aluminum oxide parts processed by PBF-LB .....	34
<b>Table 4:</b> Absolute densities, specific surface area and BET average particle size of alumina powders .....	57
<b>Table 5:</b> Absolute densities, specific surface area and BET average particle size of dopants .....	57
<b>Table 6:</b> $d_{10}$ , $d_{50}$ and $d_{90}$ of volume based particle size distributions of alumina powders in water by optimized dispersant amount and dispersing routine determined by dynamic light scattering (DLS) and Laser diffraction (LD). ....	63
<b>Table 7:</b> $d_{10}$ , $d_{50}$ and $d_{90}$ of volume based particle size distributions of dopants in water by optimized dispersant amount and dispersing routine determined by dynamic light scattering (DLS) and Laser diffraction (LD). ....	67
<b>Table 8:</b> Impacts of different influencing factors on packing density and flowability of <b>a)</b> spray dried granules and <b>b)</b> granules mixed with additives. ....	76
<b>Table 9:</b> Powder combinations. ....	84
<b>Table 10:</b> Powder combinations calculated by the EMMA software (Mixtures 2, 4, 6, 7, 9) and powder combinations with coarse alumina AA18 (Mixtures 1, 3, 5, 8) made for comparison of the achieved results. ....	95
<b>Table 11:</b> Absorptance, reflectance and transmission values of the green laser light in the powder bed measured by an integrating sphere. ....	106
<b>Table 12:</b> Apparent and tapped density as well as Hausner ratio and yield of the granules with octanol amount. ....	112
<b>Table 13:</b> Characteristic values for $d_{10}$ , $d_{50}$ and $d_{90}$ of coarse fraction of granules with addition of different amount of 1-octanol. ....	114
<b>Table 14:</b> Summary of the impacts of different influencing factors on the properties of the laser manufactured parts. ....	115
<b>Table 15:</b> Properties of powders used for laser processing, which contain coarse alumina AA18 and spray dried granules (powder combination A, B and C). ....	118
<b>Table 16:</b> Properties of powders used for laser processing, which contain spray dried granules doped with iron oxide and a different amount of coarse alumina AA18. ....	122
<b>Table 17:</b> Archimedes density in % of the theoretical density (TD) of laser processed parts. ....	124
<b>Table 18:</b> Properties of powders used for laser processing, which contain spray-dried granules doped with manganese oxide and a different amount of coarse alumina AA18. ....	125
<b>Table 19:</b> Properties of powders used for laser processing, which contain coarse alumina AA18 and spray dried granules doped with either iron oxide or manganese oxide. ....	127
<b>Table 20:</b> Relative densities for parts processed by green-pulsed laser SLM with different powders .....	133

<b>Table 21:</b> Average manganese content measured by XRF line scans of <b>a)</b> spray-dried and thermal pre-treated granules and of <b>b)</b> laser processed parts made from spray-dried and thermal pre-treated granules .....	139
<b>Table 22:</b> Average manganese content measured by XRF line scans of laser-processed layers consolidated on thermal pre-treated substrates (700 and 1600 °C).....	141
<b>Table 23:</b> theoretical principle of crack reduction in the PBF-LB processed aluminum oxide parts by the use of these additives .....	143
<b>Table 24:</b> Way of incorporation of mullite WFM 0-10 on the basis of Fe <sub>2</sub> O <sub>3</sub> doped Al <sub>2</sub> O <sub>3</sub> granules. ....	154
<b>Table 25:</b> Way of incorporation of submicron mullite on the basis of Fe <sub>2</sub> O <sub>3</sub> doped Al <sub>2</sub> O <sub>3</sub> granules. ....	154
<b>Table 26:</b> Properties of spray-dried powders containing micron-sized mullite WFM 0-10. ....	155
<b>Table 27:</b> Properties of spray-dried powders containing submicron-sized mullite.....	156
<b>Table 28:</b> Evaluation of crystalline phases after laser processing of Al <sub>2</sub> O <sub>3</sub> /CeO <sub>2</sub> substrates with different power, hatch distance, laser speed.....	169
<b>Table 29:</b> Evaluation of crystalline phases after laser processing of Al <sub>2</sub> O <sub>3</sub> /Y <sub>2</sub> O <sub>3</sub> /Fe <sub>2</sub> O <sub>3</sub> substrates with different power, hatch distance, laser speed.....	169
<b>Table 30:</b> Properties of spray dried granules and thermal treated granules with 1 Vol%, 14.2 Vol% and 68 Mol% TiO <sub>2-x</sub> mixed with 30 Vol% coarse aluminum oxide AA18. ....	177
<b>Table 31:</b> Powder combinations used for laser processing .....	179
<b>Table 32:</b> Properties of powder combinations A, B and C.....	179
<b>Table 33:</b> Influence of <b>a)</b> solid load, <b>b)</b> pump rate, <b>c)</b> power output of ultrasonic nozzle and <b>d)</b> inlet temperature on properties of spray-dried ZrO <sub>2</sub> /WO <sub>3</sub> granules .....	192
<b>Table 34:</b> Properties of powders used for laser processing containing coarse alumina AA18 and spray dried ZrO <sub>2</sub> /WO <sub>3</sub> granules. ....	199
<b>Table 35:</b> Compressive strength and standard deviations of laser-manufactured parts produced with powders containing a different additive content to aluminum oxide.....	205
<b>Table 36:</b> Comparison of the avalanche angles and Hausner ratios of Fe <sub>2</sub> O <sub>3</sub> doped granules in terms of the impact on the flowability by addition of coarse aluminum oxide AA18.....	213
<b>Table 37:</b> Comparison of the avalanche angles and Hausner ratios of Fe <sub>2</sub> O <sub>3</sub> - and MnO <sub>2</sub> /Mn <sub>2</sub> O <sub>3</sub> -doped granules in terms of the impact on the flowability by thermal pre-treatment and mixing with 30 Vol% coarse aluminum oxide AA18. ....	215
<b>Table 38:</b> Comparison of the avalanche angles and Hausner ratios of Fe <sub>2</sub> O <sub>3</sub> - and MnO <sub>2</sub> /Mn <sub>2</sub> O <sub>3</sub> -doped granules in terms of the impact on the flowability by changing the dopant amount... ..	219
<b>Table 39:</b> Comparison of the avalanche angles and Hausner ratios of zirconia-tungsten oxide granules and alumina granules with mullite or rare earth oxide addition in terms of the impact on the flowability. ....	220
<b>Table 40:</b> Comparison of the avalanche angles and Hausner ratios of powders with a final TiO <sub>2-x</sub> content of <b>a)</b> 0.7 Vol%, <b>b)</b> 10Vol% and <b>c)</b> 50 Mol% in terms of the impact on the flowability by thermal treatment in Ar/H <sub>2</sub> and mixing with 30 Vol% coarse aluminum oxide AA18. ...	223

---

<b>Table 41:</b> Strategies to solve the densification and absorption issue in laser powder bed fusion aluminum oxide and visualization of the success by red signal (unsuccessful) and green signal (successful).....	234
<b>Table 42:</b> Theoretical principle of crack reduction in PBF-LB processed aluminum oxide parts by the use of different additives and visualization of the success by red signal (unsuccessful) and green signal (successful).....	236
<b>Table 43:</b> Impact of slurry and spray drying parameters on granule size and shape for different material compositions. ....	240